AFCRL-64-364
MAY 1964

2.13
435 pg - $6.00

Environmental Research Papers
No. 15

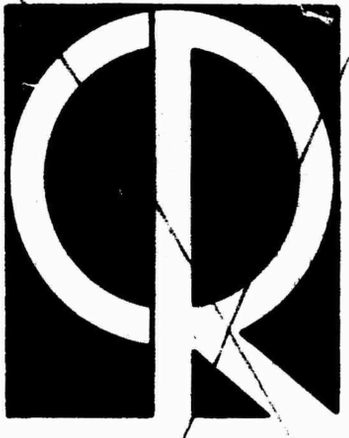

Project Firefly 1962-1963

N.W. ROSENBERG
EDITOR

UPPER ATMOSPHERE PHYSICS LABORATORY PROJECT 7635

DISCLAIMER NOTICE

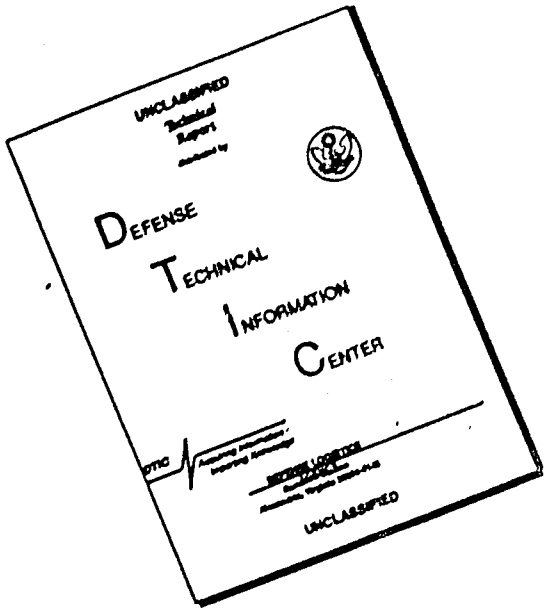

THIS DOCUMENT IS BEST QUALITY AVAILABLE. THE COPY FURNISHED TO DTIC CONTAINED A SIGNIFICANT NUMBER OF PAGES WHICH DO NOT REPRODUCE LEGIBLY.

BLANK PAGES
IN THIS
DOCUMENT
WERE NOT
FILMED

AFCRL-64-364
MAY 1964

Environmental Research Papers
No. 15

Project Firefly 1962-1963

N.W. ROSENBERG
EDITOR

RESEARCH JOINTLY SUPPORTED BY

U. S. Air Force Office of Aerospace Research
U. S. Air Force Research and Technology Division
Advanced Research Projects Agency
Defense Atomic Support Agency
U. S. Army Electronic Research and Development Agency
Department of Defense, Ft. Meade, Maryland
National Aeronautics and Space Administration

UPPER ATMOSPHERE PHYSICS LABORATORY PROJECT 7635

AIR FORCE CAMBRIDGE RESEARCH LABORATORIES, OFFICE OF AEROSPACE RESEARCH, UNITED STATES AIR FORCE, L.G. HANSCOM FIELD, MASS.

Abstract

This is a compilation of papers reporting the preparation, observations, data reduction and interpretation of upper atmosphere experiments. The general objective of these experiments is a study of the dynamics, transport processes, state, and composition of natural and artificial perturbations of the upper atmosphere. For these studies, techniques are employed wherein various chemicals are released in the upper atmosphere from rocket-borne containers, followed by observations from the ground of the effects resulting from the release.

Contents

PROJECT FIREFLY, 1962-1963

I. A Summary Report

N. W. Rosenberg and D. Golomb
Air Force Cambridge Research Laboratories
Bedford, Massachusetts

Abstract

This paper provides a summary of the test objectives, techniques and results of upper atmosphere chemical release experiments carried out during 1962 and 1963 from Eglin AFB, Florida, under management of AFCRL.

1. INTRODUCTION

The general objective of Project Firefly has been a study of the dynamics, transport processes, state, composition, and artificial perturbations of the upper atmosphere. For these studies, a technique is employed wherein various chemicals are released in the upper atmosphere from rocket-borne containers,

---

(Received for publication 24 February 1964)

followed by observations from the ground of the effects resulting from the release. The ground-based sensors are of the following types: (1) optical, (2) radio frequency, and (3) acoustical. The results obtained in the Firefly experiments have a military significance in addition to their basic geophysical significance, insofar as they help to understand processes associated with missile launch, weapons effects, and RF propagation in the ionosphere.

Since the last Firefly Report was issued in August 1962, three series of experiments have been carried out in the Fall of 1962, Spring 1963 and Fall 1963. About 40 sounding rockets were launched, with many of the rockets carrying multiple payload. The experiments can be classified in the following groups:

(1) Generation of localized high electron density regions (electron clouds) for propagation studies and measurements of transport processes.

(2) Generation of localized electron-deficient regions (electron holes) for transport processes studies and the simulation of missile effects.

(3) Generation of chemiluminescent and resonance light emitters in the upper atmosphere, for the study of transport processes, composition and state of the upper atmosphere, and for simulation of optical effects resulting from the deposition of missile exhausts and comet trails.

(4) Explosive releases in the upper atmosphere for simulation of missile and weapon effects, and for the study of acoustic wave propagation.

Table 1 gives a list of the 1962-1963 Firefly experiments arranged in chronological order. The table includes the nicknames, date, payload, release time, altitude and coordinates. Detailed accounts on experimental and observational techniques, data reduction and interpretation are found in the individual papers of the participants. In this summary report, some of the results are cross-correlated, and the major conclusions are pointed out. Plans for future experiments are also set forth.

2. PARTICIPANTS

The following organizations took active part in the program:

(1) AFCRL, Bedford, Mass.
(2) USAELRDL, Ft. Monmouth, N. J.
(3) DOD, Ft. Meade, Md.
(4) Rome Air Development Center, Rome, N. Y.
(5) NBS, Boulder, Colo.
(6) Eglin AFB, Florida
(7) Georgia Institute of Technology, Atlanta, Ga.
(8) Melpar, Inc., Falls Church, Va.

(9) Martin Corporation, Baltimore, Md.
(10) Atlantic Research Corporation, Alexandria, Va.
(11) Device Development Corporation, Weston, Mass.
(12) Stanford Research Institute, Menlo Park, Calif.
(13) University of Georgia, Athens, Ga.
(14) University of Michigan, Ann Arbor, Mich.
(15) Cornell Aeronautics Labs, Buffalo, N. Y.
(16) Avco Research Corporation, Wilmington, Mass.
(17) AeroChem, Inc., Princeton, N. J.
(18) Geophysics Corp. of America, Bedford, Mass.
(19) Mithras, Inc., Cambridge, Mass.
(20) Air Reduction Company, Murray Hill, N. J.
(21) Wentworth Institute, Boston, Mass.
(22) CNRS, Verrieres-le-Buisson, Seine et Oise, France
(23) Ionosphaeren Institut, Breisach, Germany

3. GROUND BASED INSTRUMENTATION

3.1 Optical Instrumentation

The following optical instrumentation was used:

(1) K-24 aerial cameras (f/2.5, 175 mm focal length) deployed at several sites were operated by Georgia Institute of Technology.

(2) Framing cameras of the 16 mm type (GSAP and Millikon), 35 mm type (Praktina and Flight Research MOD IV), and 35 mm streak cameras (DuMont) were operated by Device Development Corporation.

(3) A Fastie-Ebert slitted spectrometer, f/6 mirror, 50 cm focal length, RCA 6810A photomultiplier was operated by the University of Georgia.

(4) A slitless spectrograph, f/0.87 lens, 76 mm focal length, 1800 lines/mm reflecting grating was operated by the University of Georgia.

(5) A Hunten auroral spectrometer with photoelectric sensor was operated by Device Development Corporation.

3.2 Radio Frequency Instrumentation

For propagation studies, an extensive array of radio frequency transmitters and receivers was deployed at various sites by the U. S. Army Electronics R & D Laboratories, Rome Air Development Center, and DOD, Ft. Meade, Md. In addition, the following RF equipment was used:

(1) Sweep ionosondes of the C-3 and C-4 types, sweeping between 0.25 and 20 Mcps with a sweep time of 30 seconds were operated by the National Bureau of Standards.

(2) A spaced-receiver drift recorder was operated by NBS and Ionosphaeren Institut, Breisach, Germany.

(3) A multiple fixed-frequency radar, phase-coherent, 3-30 Mcps range, with up to 150 pps, 200 μsec pulse duration was operated by Stanford Research Institute.

(4) A bistatic CW radar for Doppler shift measurements, transmitting in the 8.2, 14.9 and 27.6 Mcps ranges was operated by Stanford Research Institute.

3.3 Acoustics

Ground based highly sensitive microphones (capacitor, hot wire and microbarograph) were operated by the University of Michigan.

4. SUMMARY OF RESULTS

4.1 Electron Clouds

In the 1959 and 1960 series of experiments it was shown that long-lasting electron clouds can be deposited successfully in the 90-120 km altitude region by detonating explosive mixtures containing cesium. Electron clouds so formed reflect or scatter radio frequency waves for several minutes at night and tens of minutes in daylight. In daylight, photoionization of cesium augments the initial thermal ionization. The reflected, scattered radio signal intensity and duration are dependent on a altitude, time of day and wind shears.[1,2,3]

In the Fall 1962 series, 16 experiments were devoted to the development of the propagation technique by electron clouds. The clouds were of three types:

(1) Single Point Electron Clouds (SPEC) formed by a detonation of a $CsNO_3$-Al-RDX mixture. The payload was similar in composition and weight to those used in 1959/60, except that the components were cast instead of pressed.

(2) Multiple Point Electron Clouds (MPEC) formed by four releases, each with 1/4 the weight of a SPEC. The four explosions occurred at intervals of 3-5 km, spanning an altitude region of 10 to 15 km. This was an attempt to increase the probability of placing at least one cloud into the variable optimum altitude region, where signal strength and duration are maximum.

(3) Trail Electron Clouds (TEC) formed by the release of the combustion products of a 4 lb mixture of cesium nitrate and aluminum powder without added high explosive. This mixture burned deflagratively over a period of 40 to 100 seconds, venting the exhaust products along the rocket trajectory as a trail. Usually, three units were flown in a single rocket, of which one or two burned properly. The

expected advantages of trail electron clouds were increased thermal ionization by virtue of the high flame temperature (estimated at 4000°K) and a relatively low chamber pressure (~ 20 atm),[4] and a higher probability of encountering the optimum altitude region with a trail deposit.

The single point electron clouds of the 1962 series (LOUISE, KITTY) gave about the same reflectivity (or transmission loss) and duration as the 1959/60 clouds when released at the same altitude and time of day, notwithstanding the different packing technique (casting).

The multiple point electron clouds eliminated the difficulty of the altitude sensitivity, allowing a wider tolerance in the rocket trajectory for cloud deposition. The signal duration of the best MPECs was similar to that of the best SPECs, and cloud cross sections were also comparable.[3]

The trail electron clouds were the poorest RF reflectors. Signals could be transmitted only during the burning period of the plasma generator, and cloud cross sections were less than 10% of the detonation-produced clouds. It remains to be determined whether this is due to the decreased release rate of the ionized combustion products (about 50 gr/km from each of the two burners), or to the shape of the reflector which was a thin cylindrical cloud as compared to the spherical MPECs.*

In summary, the feasibility of the electron cloud technique for sustaining transmissions in the HF and lower end of VHF band has been clearly demonstrated. The transmissions are not bandwidth limited, the fade rate is not excessive, and the scattering is not severely limited either in azimuth or elevation. Average cloud life-times have been determined, the optimum altitude region has been defined, and specifications have been compiled for vehicle, payload, and electronic equipment requirements. Further improvements can be expected in increasing life times and transmission capabilities of electron clouds, but this is considered more a task for a system development agency than for AFCRL. Thus, no plans exist at present in this laboratory to develop the electron cloud technique further. This does not preclude the utilization of artificially generated ionized regions for daytime wind studies, determination of expansion and diffusion rates, and studies of geomagnetic confinement of electron drift.

4.2 Electron Holes

The objectives of the release of electron attaching species were to study the nature of reflected radio frequency waves from the perturbed ionosphere and to determine the rate of return of the region to normal by diffusion and photoionization.

---

* It should be noted that the TECs, however poor RF reflectors, turned out to be excellent light emitters. TECs released at night produced luminous trails lasting for 3 - 5 minutes, enabling them to be utilized for upper atmosphere wind studies.[5]

Four rockets were flown for this purpose. ETHEL carried a payload of 28 kg sulfur hexafluoride to E-region altitudes at daytime, KAREN and LAURA carried a double payload of 5.5 kg CO_2 and 18 kg SF_6 each, to F-layer altitudes at night, and MARTHA carried 22.7 kg SF_6 to the F-layer at daytime.

The E-layer release was detected by NBS sounders. The ionograms resemble those obtained during the 1960 SF_6 release (RENA). J. W. Wright attributes the ionogram patterns to an electron deficient region due to electron removal by SF_6 within a bounded region.[6] The effect lasted for about 3 minutes. No detailed analysis of this release has yet been performed.

The effects of KAREN were masked by perturbations caused by a large meteor passing at a low elevation angle. Telemetry aboard LAURA indicated the release of CO_2 at 220 km altitude. Telemetry ceased at this point, and there is no evidence for the release of SF_6 which was scheduled to occur 120 seconds later. There is a possibility that both the telemetry and the release activator of the SF_6 tank were knocked out by the CO_2 release. The ionograms, obtained following the CO_2 release, display echoes which may be associated with an electron hole. However, J. W. Wright, who analyzed the ionograms, is uncertain whether the echoes are in fact due to the release, since the frequencies affected are lower than the plasma frequency at the altitude of release.[7] Further releases of carbon dioxide would be required to clarify this question.

The clearest case of an electron hole was obtained by the noontime release of SF_6 (MARTHA). Telemetry aboard the vehicle reported the successful release. The ionograms before the release were normal, and perturbations were noted at the appropriate time and frequencies. The returns obtained in subsequent radar sweeps were clearly of the kind described by Booker[8] as the typical echo pattern from a region of reduced electron density embedded in the ionosphere. A full description of the phenomenon is found in this issue.[9] The effect lasted for about 2000 seconds; that is, it required a rather long time to restore the region to normal by diffusion and photodissociation of negative ions. Since diffusion time constants of neutral species at the altitude of release are in the order of seconds, it is obvious that electron drift into the hole proceeds at a much slower rate. Golomb and Oldham[10] set up a model of the ionospheric hole in which electrons are allowed to diffuse only along the magnetic field lines. They have shown that with electron motion so constrained the center of the hole still has a less-than-ambient electron density after thousands of seconds, which explains the radar observations.

4.3 Artificial Luminescence

4.3.1 CHEMILUMINESCENCE OF ALUMINIZED COMPOUNDS

It had been reported previously by this group and other workers that persistent glows result at night, in the altitude region above 90 km, following the passage of

missiles with aluminized propellants. Similar glows have been observed following the explosion of grenades containing aluminum.[11,12] The trail electron cloud generator (TEC) (see Section 4.1 and Ref 5), consisted of a mixture of cesium nitrate and aluminum powder. When ignited at night above 90 km, it also formed a glowing trail with a continuum spectrum which persisted for several minutes in the 100-120 km region, becoming less persistent at higher altitudes.

To investigate the cause of these glows further, a mixture of aluminum granules imbedded in a purely organic explosive, without any other inorganic constituent, was exploded at 114 km. A spherical glow developed after burst, lasting for about 100 seconds. The same explosive, without aluminum, gave no glow under the same conditions.

Thus, it was definitely established that a luminescence is due to aluminum or its oxides. The 'aluminum' glow consists of a continuous spectrum, peaking around 5000-5500A. Most probably, the following reactions are involved:

(1) $AlO + O \rightarrow AlO_2^*$ formation of excited state

(2) $AlO_2^* \rightarrow AlO_2$ + Pseudo-continuum

(3) $AlO_2^* + M \rightarrow AlO_2$ collisional deactivation

(4) $AlO_2 + O \rightarrow AlO + O_2$ regeneration

In the denser regions of the atmosphere, reaction (3) predominates over reaction (2), explaining the fact that persistent glows result only above 90 km. Reaction (4) in which the active species are regenerated may account for the high photon yield observed in these releases.

The TEC glows proved to be excellent markers for ionospheric wind measurements. However, in view of their high cost and low reliability, a more economical and effective method was sought to disperse gaseous aluminum compounds in the upper atmosphere. This was achieved by the release of liquid trimethyl aluminum which flash-vaporizes in the rarefied atmosphere. A deposit of as little as 20 g TMA per km resulted in a bright night glow in the 85 to 150 km region, sufficiently persistent to measure wind vectors.[13,14] The spectrum of the TMA night glow was also a continuum. The postulated reaction mechanism for th TMA luminescence is:

(5) $(CH_3)Al + O_2$ or $O \rightarrow AlO$ + fragments

(1 to 4) as shown above.

Both the TEC and TMA releases have been used extensively for nightime wind studies. Important information has been obtained on nighttime wind patterns and magnitudes. These studies are described in full in this issue.[15,16,17] Simultaneous wind measurements and ionosonde observations enabled a correlative analysis of wind shears and Sporadic-E formations.[18] The TMA glow has also been used to observe the propagation of an acoustic wave through the luminescent trail (see Section 4.4.1)

4.3.2 FLUORESCENCE OF TRIMETHYL ALUMINUM

In one experiment (BECKY), TMA was released at twilight so that the trail was sunlit but the sky background was dark. This experiment was primarily performed to find out whether any reaction products or intermediates can be detected by observing the resonance radiation of the sunlit trail. The spectrum displayed AlO bands, establishing this compound as a product or intermediate in the TMA-oxygen reaction. The AlO electronic spectrum of sunlit grenade explosions has been used to obtain upper atmosphere temperatures.[19, 20, 21] Thus, sunlit releases of TMA trails can provide a convenient method to obtain this geophysical parameter. The advantage of the trail TMA release as compared with point explosions is that the altitude variation of temperature can be made with any desired degree of altitude resolution.

4.3.3 LUMINESCENCE OF NITRIC OXIDE

Nitric oxide was released at night as a trail in three experiments (MABEL, DINAH, EVA). The release altitudes and conditions were identical, only the times after sunset were different. The purpose of the releases was to measure the persistence of the NO trails for possible use as a wind marker, and to obtain atmospheric oxygen concentrations from the observed light intensities as a function of altitude and time of the night.

The spectrum of the trail consisted of a continuum from 3900 to 6300A, peaking at 5200A and with half-peak intensities at 4600 and 6000A. There does not appear to be a major shift in wavelength distribution with time or altitude.[22]

The persistence of the trails was quite adequate for wind measurements, in particular in the 90-100 km region.[5] However, TMA is far superior for this purpose and the latter compound will be used in future synoptic wind measurements.

It was of greater interest to analyze the light emission intensity as an indicator of ambient oxygen atom concentrations. The first, although qualitative, conclusion is that since in all three trails, released 30 minutes, 5 hours, and 11 hours after sunset, respectively, a similar luminosity was observed, at least to an order of magnitude, it appears that the ambient oxygen atom concentration does not vary greatly through the night. A quantitative study of the light emission should reveal the rate of oxygen depletion during the night as a function of altitude.

To obtain absolute oxygen concentrations, the reaction volume and time, and nitric oxide densities along the trail have to be defined exactly. The nitric oxide trail consisted of two distinct parts. (1) An intense glow, tens of meters wide, following the vehicle closely, and of very short duration (less than 0.1 sec). This is the so-called headglow and is associated with the mixing region around the NO jet expanding to ambient pressure. (2) The other trail feature was an afterglow,

of longer persistence (up to 150 sec at 100 km), but orders of magnitude less intense than the headglow.

It was felt that an aerodynamic analysis of the headglow would be simpler than for the afterglow, especially since the latter is changing rapidly due to wind drag and diffusion. Hill and Alden prepared a gasdynamic analysis of the flow generated by the release of nitric oxide from a supersonic vehicle into the upper atmosphere.[23] The initial mixing between the NO and the ambient is found to occur in a layer forming roughly a paraboloid surrounding the vehicle. In this layer the actual mixing zone is sandwiched between two shockwaves. The average NO densities and entrained ambient densities in the mixing layer have been calculated. An attempt is also made to calculate the residence time of the species in the mixing layer, but this time can be evaluated from streak and framing photographs of the headglow. The calculated mixing zone diameters correspond very well with the observed headglow diameters.

Having defined, thus, the NO density in the mixing zone and the reaction time, the oxygen atom density can be obtained from the relation

$$O = \frac{\int Idt}{kt\left[NO\right]} \qquad (1)$$

where $\int Idt/t$ is the integrated photon emission over the reaction time t, and k is the reaction rate constant, obtained in laboratory studies.[24] Preliminary calculations not included in this issue, using data from one trail only, indicate the surprising result that either the laboratory rate constant is too low or ambient oxygen atom concentrations are much higher than postulated in the literature. Since the discrepancy may be as high as three orders of magnitude, it is felt that the excessive photon flux from the nitric oxide glow must be due to a much higher reaction rate for the nitric oxide-oxygen atom radiative recombination than obtained in the laboratory[24] ($k = 2.7 \times 10^{-17} cm^3 sec^{-1}$). A possible explanation is that some of the ambient oxygen atoms may be in an excited state and react at a faster rate than ground state atoms. This is only a conjecture, not based on sufficient evidence. However, a higher than expected photon emission rate has been observed previously by Armstrong from grenade glows.[19]

4.3.4 THE ACETYLENE GLOW

Acetylene was released to simulate the luminous and RF effects observed following the passage through the upper atmosphere of hydrocarbon-LOX burning missiles. Acetylene probably comes closest to the hydrocarbon fragments and radicals found in missile exhausts. These fragments are believed to be responsible for the

CH and C_2 band emission in missile plumes. The highly energetic radicals may also enter into chemi-ionization reactions, causing the enhanced RF reflectivities of missile plumes at E-layer altitudes.

Acetylene was released in two flights using different deposition rates. In NETTY, 150 moles/km were released at 100 km tapering to 15 moles/km at 115 km, resulting in a short, large diameter trail. In OLGA, 15 moles/km were released at 100 km, tapering to 6 moles/km at 130 km.

No radar returns were observed from either trail, although chemi-ionization is known to occur in acetylene-oxygen reactions in the laboratory.[25] No detailed analysis can be carried out to estimate the electron densities in the mixing region surrounding the acetylene trail until laboratory sutdies provide the rate constants permitting such analysis. It would be premature to conclude that no chemi-ionization occurred at all, since the trail electron cloud releases showed that radar reflectivity from elongated cylinders is very small compared to spherical clouds. Thus, the absence of radar reutrns from the acetylene trails may simply be due to the geometrical configuration.

The optical effects showed a striking difference between the nitric oxide and acetylene releases. The nitric oxide glow was brightest in the vicinity of the rocket and developed almost instantaneously upon release. The acetylene glow required one to several seconds after release to develop. This is explained on the basis of different reaction mechanisms. Whereas in the NO + O reaction, photons are produced in a single step, the acetylene-oxygen reaction must produce first intermediates which later react with emission of photons. A possible reaction sequence, suggested by Hand and Kistiakowsky[26] is

(1) $O + C_2H_2 \rightarrow C_2H + OH$

(2a) $C_2H + O_2 \rightarrow CO_2 + CH^*$

(2b) $C_2H + O \rightarrow CO + CH^*$

(2c) $C_2H + O \rightarrow OH + C_2^*$

(3) $CO + O \rightarrow CO_2^*$

(4) $CH^* + O \rightarrow CHO^+ + e^-$

All these steps are exothermic, except (2c) which probably requires an excited oxygen atom. The light emission occurs in the following steps

(5) $CH^* \rightarrow$ CH (3890 and 4315A system)

(6) $C_2^* \rightarrow C_2$ (5165A system)

(7) $CO_2^* \rightarrow CO_2$ (pseudo-continuum)

Reaction (4) produces the RF effect, if any.

Another proposed mechanism involves as an intermediate a highly energetic unsaturated complex $[C_2H_2O]$:

(8) $C_2H_2 + O \rightarrow [C_2H_2O]$

(9) $[C_2H_2O] \rightarrow C_2^* + H_2O$

$\searrow CH^* + CHO$

Laboratory work is at present being performed to elucidate the mechanism of the low pressure chemiluminescent reaction of acetylene and oxygen.[27]

The spectra obtained from the acetylene releases by Cooper[22] show an underlying continuum upon which there are superposed the CH 4315A band (strong), the CH 3890A band (weak), and the C_2 5165A band (weak). In addition, there is a pronounced emission at about 5770A, which is unexplained [$O(^1S) \rightarrow O(^1D)$?].

Laboratory studies of the acetylene-oxygen luminescence indicate[27] that the CH bands become relatively more intense than the C_2 bands as the pressure is decreased. A similar effect has been observed in the upper atmosphere experiments.

The number of photons resulting from NETTY was $1X10^{24}$. In this experiment about $4X10^{26}$ molecules were released in the 100 to 110 km region. Thus, the photon yield of acetylene in this oxygen atom rich altitude region is $2.5X10^{-3}$.

4.3.5 MISCELLANEOUS LUMINOUS RELEASES

Nitrogen Dioxide (STELLA). A payload of 2 kg of liquid nitrogen dioxide was released at 93 km altitude. This was an attempt to provide a simple liquid alternative to the more complex and space consuming gaseous nitric oxide release. This compound is also of interest as the oxidant of the Titan II missile. Light emission was expected due to the following reaction mechanism:

(1) $NO_2 + O \longrightarrow NO + O_2$

(2) $NO + O \longrightarrow NO_2$ + pseudo-continuum

The payload functioned properly but no significant glow was observed or recorded. Calculations indicate[28] that chemicals requiring two reaction steps for the emission of one photon will be less effective upper atmosphere emitters than those requiring one step, even if the rate constant of the first step is very fast. This has been confirmed in the nitrogen dioxide experiment.

Carbon Disulfide (BECKY). A payload of 3 kg of liquid carbon disulfide was released between 90 and 100 km. This was another attempt to provide an oxygen atom titrant. The carbon disulfide-oxygen atom reaction has been studied in the laboratory by Harteck and Reeves.[29] In closed vessels, at pressures of 0.01-0.1 mmHg, carbon disulfide gave an intense glow. However, in the upper atmosphere, a very low intensity trail was recorded on film with a persistence of about 60 seconds. It was not detected by the unaided eye. The low intensity is again explained by the two step reaction mechanism required for light emission:

(1) $CS_2 + O \longrightarrow CS + SO$

(2) $SO + O \longrightarrow SO_2$ + pseudo-continuum

Ammonia (BECKY). Ammonia is postulated to be a significant constituent of comets, since the spectra of cometary trails contains prominent NH_2 bands. A sunlit release of NH_3 at an altitude of 180 km, well above the solar horizon of 130 km, was executed to determine if significant NH_2 band structure could be recorded.

The release of 2 kg of NH_3 was spread over 5 km. A large bluish cloud with 10 to 20 second persistence developed and was photographed and spectrographed. However, the spectrum showed no band structure but only a weak continuum, almost certainly due to solar scatter from frozen ammonia ice. The use of a faster spectrometer would be required to show NH_2 bands if they were a minor perturbations on this scattered light.

Sodium (SHARON, SARAH, BLANCHE). Sodium was released in three experiments at twilight in the framework of an international wind study program under the coordination of NASA. The twilight sodium releases were supplemented with the night releases of aluminum compounds to obtain the first direct morphology of ionospheric winds over the whole night.[16,17] These experiments showed a relationship between heights of sporadic-E layers and wind shears.[18] The wind pattern as measured by the subsequent trails followed the general characteristics predicted by Hines.[30]

4.4 Explosive Releases

4.4.1 OPTICAL AND ACOUSTIC STUDIES OF HIGH ALTITUDE EXPLOSIONS

In Firefly GILDA, four explosive releases were made in sunlight at 138, 155, 237 and 250 km, respectively. In all releases, an initial radial growth rate of 2.7 km/sec was obtained from streak photos, independent of altitude and ambient temperature. This confirms our previous conclusion that the observed growth rate is associated with expanding particulate matter (smoke) of submicron size from which the sunlight is scattered. The scattered light was highly polarized. Similar growth rates have been observed for expanding missile trails in the ionosphere, under twilight conditions, indicating the presence of particulate matter in missile exhausts.

The acoustic detectors emplaced by the University of Michigan[31] revealed compression waves lasting 0.3 to 3 seconds following detonations of 4 kg explosives at altitudes to 117 km. Travel times corresponded to average sound speeds of 300 m/sec. These detectors readily separated the four charges contained in a MPEC payload. In this technique, the detonations were monitored on the ground by capacitor microphones, hot-wire microphones and microbarographs.

Applying the equations derived by Groves,[32] the initial shock wave velocity can be calculated. This shock wave attenuates subsequently to become a sound wave. The shock wave velocity is related to the temperature in the vicinity of the detonation.

To measure the velocity of a shock wave resulting from a high-altitude detonation, the following technique was used (for more details see Ref 33). A chemiluminous trail (see Section 4.3.1) was released from a rocket (WANDA) followed

by a detonation of a grenade from the same rocket. The shock wave from the detonation moved out as an approximately spherical shell intersecting the luminous trail. The overpressure of the shock created a brighter band of light moving along the trail. This movement was photographed by a streak camera. From the streak photo, the propagation velocity of the shock wave was calculated to be 350 m/sec at 108 km altitude. Since the shock wave velocity is related to the ambient temperature, the latter was estimated to be $300 \pm 50^{\circ}K$, in good agreement with U. S. Standard Atmosphere tabulated values. Thus, a new method has been provided for measuring shock wave characteristics and ambient temperatures to corroborate the acoustic sensor technique.

4.4.2 RADIO FREQUENCY STUDIES OF HIGH ALTITUDE EXPLOSIONS

The RF effects of sunlit and night detonations of cesium seeded and unseeded high explosives in the 140 to 160, and 230 to 250 km altitude regions were explored in Firefly FANNY and GILDA.

In general, the RF effects of the detonations can be divided into two categories. The direct, 'hard' echo from the expanding contact surface or shock wave, and the perturbations of the normal ionosphere caused by the detonations. The direct echo was monitored by Barnes and Chesnut[34] on pulsed and CW radar at higher frequencies than the plasma frequency at the point of release.

The 250 km releases created no shock waves, and were essentially invisible at high frequencies. The 140 km releases of high explosive were detected, both sunlit and at night, at frequencies of 10 to 30 Mcps for a few seconds. The 160 km release of a cesium-seeded detonation was detected only when sunlit at 15 to 20 Mcps for a few seconds, and at 4 to 6 Mcps for several minutes, presumably due to photo-ionization. Only the sunlit cesium cloud gave a Doppler shifted reflection at 14 and 28 mc, probably from the contact surface, since if it were at the shock surfaces, the high explosive release of equal strength would have been detected.

The ionospheric perturbations were monitored by Wright[6] using C-4 ionosondes sweeping over the plasma frequencies of the ionosphere. There is no clear evidence that the 140 to 160 km bursts produced any perturbations of the normal F-region returns, so that the effects of a few kilograms of high explosive in regions of low electron density do not seem significant, whether sunlit or not, seeded or unseeded. No effects were synchronous with the unseeded release at 240 km or the seeded release at 240 km which followed 2 minutes later. However, a new type of F-region disturbance began about one minute after the unseeded release, and continued after the seeded release. These echoes were seen first at high frequencies, spreading at later times to lower frequencies; that is, to lower electron densities and lower heights. These disturbances are what could be expected from a region of reduced

electron density surrounded by an unaffected region, similar to the effects noticed in the sulfur hexafluoride release (see Section 4.2 and Ref 9). The degree of ionization of the expanded unseeded cloud is apparently lower than that of the ambient, the latter being about 10^{-4}. The degree of ionization of the seeded cloud is probably similar to that of the ambient, therefore the observed perturbations may have been related to the unseeded explosive only. The effect lasted for about 15 to 20 minutes, both in the sunlit and the dark release.

Further work is required to understand the RF effects of high altitude detonations, both as a distrubance of the ionosphere and as a localized RF target.

5. FUTURE PLANS

The future plans for chemical release studies by the AFCRL group will be in two areas: (1) Coordinated studies of several geophysical properties, and (2) missile effects. The missile effects studies are discussed in a classified report, and the planned geophysical studies are set forth briefly here.

5.1 Ionospheric Morphology

Simultaneous rocket-borne experiments for measurements of electron and ion densities and temperatures, neutral densities and temperatures, winds, shears, turbulence and acoustic velocities, are planned in the altitude region 60 to 160 km, each experiment being repeated several times during a single 24 hour period. The electron and ion data will be obtained between 60 and 160 km both by RF impedance probes and by spherical electrostatic analyzers. The neutral densities and temperatures will be obtained between 60 to 110 km by the falling sphere technique. These three experiments will be carried in a single 90 lb payload. A second rocket will be used to determine the neutral winds, shears, and turbulence (from dusk to dawn) by TMA releases. From the same second vehicle, acoustic velocities in the 60 to 110 km region will be determined by a series of grenade releases detected acoustically at the ground. They will also be optically recorded by streak photos of compressional waves traversing a TMA trail deposited in the 100 to 140 km region. Temperatures will be measured in the 130 to 160 km region by A10 resonance spectrum technique.

A test round of each of the two payload types is scheduled for launch on 1 July 1964 from Eglin AFB; the actual test program is scheduled for 1 November 1964 from Eglin AFB.

Ground based ionosondes and spaced drift sounders will also be emplaced for interrelation of their recordings with the simultaneous measurements described above.

5.2 Wind Studies

The wind morphology from several locations may be studied simultaneously to determine spatial and temporal divergences. A light payload aboard a small rocket (boosted Arcas type), or a gun probe will make this experiment feasible. Observation will be made at the corners of a 600 km triangle throughout the night with about five launches per site. The divergence among these sites in wind patterns would give significant further insight to ionospheric metorology. Possible sites are Eglin AFB, Cape Kennedy, and a mobile launcher in the Myrtle Beach, South Carolina, area.

5.3 Chemiluminous Titration of Upper Atmosphere Constituents

The development of reliable titration techniques through laboratory calibration of chemiluminous reactions is planned. Specifically, the pressure and O/O_2 ratio dependence of TMA luminescence and NO glow studies could lead to experiments permitting estimation of oxygen atom concentrations and variations in concentrations with height more reliably and less expensively than by mass spectrometry.

5.4 The Constraint on Ionic Diffusion by Magnetic Fields

Development of a reliable payload releasing ionized and neutral barium vapor is now under study. Interference filter photography is planned to establish the relative motion of the non-ionized and ionized fractions of the released vapor at altitudes of 150 to 250 km and to measure molecular and ambipolar diffusion rates. This experiment may allow the determination of the altitude at which postulated field confinement of ion motion takes place.

References

1. Project Firefly, Volume IV, AFCRL 62-826.
2. N. W. ROSENBERG and D. GOLOMB, in this issue.
3. Classified Appendix to this report.
4. R. FRIEDMAN, et al., in this issue.
5. N. W. ROSENBERG, D. GOLOMB and E. F. ALLEN, Chemiluminescent Techniques for Studying Nighttime Winds, in this issue.
6. J. W. WRIGHT, in this issue.
7. J. W. WRIGHT, private communication.
8. H. BOOKER, Geophys Res., 66: 1073, 1961.

9. D. GOLOMB, et al., in this issue.

10. D. GOLOMB and B. OLDHAM, in this issue.

11. E. B. ARMSTRONG, Planet, Space Sci., 11: 733, 1963.

12. D. D. WOODBRIDGE, High Altitude Glow Measurements in Australia, in Chemical Reactions in the Lower and Upper Atmosphere, Interscience Publishers, New York, 1961.

13. N. W. ROSENBERG, D. GOLOMB and E. F. ALLEN, Chemiluminescence of Trimethyl Aluminum, in this issue.

14. N. W. ROSENBERG, D. GOLOMB and E. F. ALLEN, Resonance Radiation of AlO, in this issue.

15. H. D. EDWARDS, in this issue.

16. H. D. EDWARDS, et al., in this issue.

17. N. W. ROSENBERG and H. D. EDWARDS, in this issue.

18. M. A. MACLEOD, in this issue.

19. E. B. ARMSTRONG, Planet. Space Sci., 11: 743, 1963.

20. B. AUTHIER, et al., Compt. Rend., 256: 3870 1963.

21. O. HARANG, Planet. Space Sci., in press.

22. D. C. COOPER, in this issue.

23. J. A. F. HILL and H. L. ALDEN, in this issue.

24. A. FONTIJN, C. B. MEYER and H. I. SCHIFF, J. Chem. Phys., in press.

25. A. FONTIJN, in this issue.

26. C. W. HAND and G. B. KISTIAKOWSKY, J. Chem. Phys., 37: 1239, 1962.

27. N. JONATHAN and G. DOHERTY, in this issue.

28. D. GOLOMB and J. MASON, Computer Solution of Simultaneous Diffusion - Chemical Kinetics Equations Relating to Upper Atmosphere Releases, AFCRL 62-1132.

29. P. HARTECK and R. REEVES, Rensselaer Polytechnic Institute, Troy, New York, Private Communication.

30. C. O. HINES, Can. J. Phys., 38: 1441, 1960.

31. H. F. ALLEN, in this issue.

32. G. V. GROVES, in this issue.

33. N. W. ROSENBERG, in this issue.

34. D. R. ALLISON and W. G. CHESNUT, in this issue.

TABLE 1. List of Firefly 1962/63 Experiments

Experiment No.	Date	Name	Launch Time CST	Solar Depression degree	Solar Horizon km	Payload type	Payload kg	Release Time after Launch sec	Release Time CST	Altitude km	Lat. degree	Long. degree	Slant Range from Launch Site (km)
1	15 Oct 62	Bonnie	0515:00	7.73	59.3	TEC	4.9	95.	0516:36	91.1	30.246	86.727	92.7
2	16 Oct	Alice	0515:00	7.76	59.8	PEC	3.66	114.7	0516:54	90.	30.32	86.67	91.
						PEC	3.66	140.1	0517:20	96.	30.29	86.69	97.
						PEC	3.66	144.8	0517:24	97.	30.29	86.69	98.
3	16 Oct	Dagmar	1840:00			TEC	4.9	90.	1841:30	88.8	30.283	86.689	89.7
4	17 Oct	Cindy	0516:00	7.73	59.3	TEC	4.9	90.	0517:30	86.1	30.214	86.690	88.6
5	17 Oct	Brenda	1900:00			MPEC		Failed					
6	19 Oct	Queenie	0517:00	7.67	58.5	PEC	3.66	100.5	0518:40	91.4	30.352	86.819	92.3
						PEC	3.66	110.3	0518:50	96.4	30.341	86.825	97.4
						PEC	3.66	124.9	0519:04	103.	30.34	86.86	105
						PEC	3.66	136.5	0519:20	106.	30.34	86.87	106.
7	22 Oct	Louise	0519:00	7.65	58.0	SPEC	16.90	99.92	0520:40	96.8	30.119	86.739	101.9
8	23 Oct	Kitty	0519:00	7.68	58.5	SPEC	16.73	121.93	0521:02	108.0	30.095	86.680	115.6
9	23 Oct	Ethel	1309:59			SF6	27.9	121.36	1312:00	137.			
10	25 Oct	Enid	0030:00			TEC	3.27	81.	0031:21	88.6	30.293	86.761	89.7
								121.	0032:01	112.	30.25	86.79	113.
11	25 Oct	Paula	0521:00	7.56	56.5	PEC	3.66	121.0	0523:01	95.3	30.251	86.915	98.9
						PEC	3.66	131.3	0523:11	98.1	30.230	86.906	102.0
						PEC	3.66	146.15	0523:26	100.3	30.027	86.943	105.3
						PEC	3.66	166.5	0523:46	100.6	30.191	87.003	107.5
12	31 Oct	Hazel	1730:00			MHEX		Failed					
13	1 Nov	Ruby	0525:00	7.56	56.5	PEC	3.66	101.5	0526:41	96.0	30.263	86.788	97.2
						PEC	3.66	118.32	0526:58	(109.)			
						PEC	3.66	131.59	0527:11	(113.)			
						PEC	3.66	152.98	0527:33	117.2	30.22	86.83	
14	1 Nov	Lisa	2225:00			MHEX		Failed					
15	2 Nov	Carol	0525:00			MPEC		Failed					
16	5 Nov	Sally	0529:00	7.36	53.5	PEC	3.66	104.6	0530:44	97.1	30.249	86.709	98.6
						PEC-H	3.60	115.20	0530:55				
						PEC L	3.57	126.79	0531:06	108.6	30.208	86.705	110.7
						PEC	3.66	140.81	0531:20	112.3	30.190	86.713	114.3
17	6 Nov	Beverly	0200:00			PEC	3.66	105.5	0201.45	89.2	30.257	86.852	91.9
						PEC-H	3.60	115.11	0201:55	94.	30.24	86.87	97.
						PEC-L	3.57	No release					
						PEC	3.66	140.12	0202:20	101.8	30.207	86.910	106.2

TABLE 1. List of Firefly 1962/63 Experiments (Cont)

Experiment No.	Date	Name	Launch Time CST	Solar Depression degree	Solar Horizon km	Payload type	Payload kg	Release Time after Launch sec	Release Time CST	Altitude km	Lat. degree	Long. degree	Slant Range from Launch Site (km)
18	10 Nov	Fanny	1903:00			HEX	3.03	107.7	1904:47	(140.)			
						PEC	3.94	119.74	1904:59	157.	30.091	86.634	161.
						HEX	3.03	184.2	1906:04	(230.)			
						PEC	3.94	318.93	1908:19	260.	29.405	86.507	284.
19	13 Nov	Gilda	1730:00	9.00	80	HEX	3.03	106.9	1731:47	137.7	30.114	86.735	142.
						PEC	3.94	119.19	1731:59	155.	30.059	86.745	159.
						HEX	3.03	212.67	1733:32	250.	29.71	86.80	259.
						PEC	3.94	338.75	1735.38	237.	29.23	86.86	270.
20	15 Nov	Karen	1926:00			7 Grenades	0.020	90. First	1927.31	107.	30.242	86.699	108.
								102. Last	1927:43	123.	30.214	86.699	124.
						CO_2	5.44	215.5	1929:34	234.			
						SF_6	17.91	335.5	1931:34	225.			
21	27 Nov	Mabel	1800:00			NO	10.89	84.8	1801:24	92.3	30.180	86.609	95.9
22	1 Dec	Terry	1720:00	7.71	59	N_a	7.3	40.	1720:40	42.	30.27	86.70	45.
23	3 Dec	Sharon	1720:00	7.70	58.8	N_a	7.3	40.	1720:40	70.	30.27	86.69	72.
24	3 Dec	Ivy	1801:00			TEC	4.9	73.	1802:13	82.4	30.153	86.703	87.0
25	3 Dec	Esther	2145:00			TEC	4.9	74.4	2146:14	87.4	30.165	86.746	91.4
26	3 Dec	Dinah	2245:00			NO	11.34	80.7	2246:20	90.	30.13	86.686	95.
27	4 Dec	Patsy	1951:00			MHEX		Failed					
28	6 Dec	Eva	0421:00			NO	10.91	79.2	0422:19	88.6	30.228	86.620	90.0
29	7 Dec	Laura	1908:00			7 Grenades	0.020	83.3 First	1909:23	91.9	30.134	86.706	96.6
								93.7 Last	1909:34	107.9	30.078	86.707	113.7
						CO_2	5.68	215.	1911:35	(220.)			
						SF_6	17.14	335.	1913:35	(220.)			
30	10 Dec	Dana	1929:59			HEX-A1	10.89	108.8	1931:47	108.1	30.250	86.791	109.4
31	12 Dec	Netty	1745:59	12.90	162.	C_2H_2	18.14	95.96	1747:35	101.	30.07	86.79	108.
32	14 Dec	Olga	1752:00	13.93	188.5	C_2H_2	18.37	76.6	1753:16	90.	30.17	86.63	94.
33	15 Dec	Martha	1130:00			SF_6	22.68	274.02	1134:34	222.	29.59	86.64	
34	15 May 63	Claire	2000:00			NO_2	2.01	100	2002:00	95.2	30.265	86.692	96.4
						TMA	3.04						
						CS_2	4.45						
35	17 May	Sarah	1906:00	6.00	35.1	Na	7.3	40	1906:40	41.0	30.301	86.691	42
36	17 May	Stella	2218:00			NO_2	2.07	80	2219:20	93.8	30.140	86.694	98.2
						TEC	3.2						

TABLE 1. List of Firefly 1962/63 Experiments (Cont)

Experiment No.	Date	Name	Launch Time CST	Solar Depression degree	Solar Horizon km	Payload type	Payload kg	Release Time after Launch sec	Release Time CST	Altitude km	Lat. degree	Long. degree	Slant Range from Launch Site (km)
37	18 May	Doris	0255:00			TMA	1.13	94	0256:34	91.7	30.169	86.655	95.3
						TEC	3.2						
38	18 May	Blanche	0406:00	8.45	69.9	Na	7.3	40	0406:40	42.3	30.325	86.695	43.
39	21 May	Irene	1910:00	6.22	37.3	Na	7.3	40	1910:40	41.6			
40	23 Sept	Irma	2215:00			TMA	1.81	64	2216:04	89.7	30.181	86.858	94.2
						TMA	1.54	271	2219:31	136.8	29.523	86.334	171.4
						HEX	6.26	291	2219:51	121.2	29.450	86.396	163.1
41	25 Sept	Wanda				TMA	1.77	70	2238:09	88.9	30.355	86.738	89.1
						HEX	6.26	85	2238:24	106.7	30.341	86.740	109.0
42	25 Sept	Violet	2330:00			CS_2	2.72	75	2331:15	91.	30.306	86.721	91.6
						TMA	1.63	380	2336:20				
43	1 Oct	Becky	0447:00	11.03	119.9	TMA	1.81	70	0448:10	88.3	30.383	86.710	88.4
				10.75	113.8	NH_3	1.36	153	0449:33	164.2	30.361	86.723	164.2
				10.39	106.2	TMA	1.72	262	0451:22	172.8	30.320	86.740	173.1

FOOTNOTES:

TEC - Trail Electron Cloud
PEC - Point Electron Cloud
MPEC - Multiple Point Electron Cloud
SPEC - Single Point Electron Cloud
MHEX - Multiple Point High Explosive
PEC-H - Point Electron Cloud With High Aluminum Content
PEC-L - Point Electron Cloud With Low Aluminum Content
Grenades - 30 g Flash Grenades ($KClO_4$, CaF_2, Al)
TMA - Trimethyl Aluminum

II. Payload Compositions and Release Systems

N. W. Rosenberg, E. F. Allen, Jr. and A. W. Berger*
Air Force Cambridge Research Laboratories
Bedford, Massachusetts

Abstract

Details on chemical compositions, conditions and thermodynamic calculations of Firefly payloads are reported. Release system engineering features are described. Statistics of successes and failures are given.

1. INTRODUCTION

This report presents the Firefly III payload chemical compositions and the calculated release products and/or rates, including a brief description of the payloads, instrumentation, and release methods. All releases were initiated by a timer activated at launch.

---

* Present affiliation: Monsanto Research Corp., Boston, Mass.

2. TRAIL ELECTRON CLOUD (TEC) $CsNO_3$ + Al BURNER

The TEC composition was formed as a solid pressed charge in a steel cylinder. Release was made by igniting the mix and venting it at high temperature ($3500^{o}K$) through a convergent tungsten nozzle (0.187 in. throat). The mix was ignited by timer ignition of a pyrotechnic train, consisting of squib, ignition pellets, and the solid propellant igniter (see Figure 1).

The initial composition of the charge and the calculated chamber composition at 175 psi are given in Table 1. Three or two nominal 1.63 kg (net) generators were flown per payload. The burners were simultaneously ignited and then simultaneously separated 50 ms later with shaped charges.

On the basis of a nominal 100 second uniform burning time, the reaction rate is 16.3 grams constituents/sec. The stoichiometric reaction may be written per kilo as

$$8.97\ M(111) + 3.91\ M(1)\ NO_3 \longrightarrow 3.91\ M(1) + 1.96\ N_2 + 8.97\ M(111)\ O_{1.31}$$

where the magnesium constituent has been included as equivalent moles aluminum to show the metal-rich nature of the composition. (The ratio 0/1.5 M (111) is 0.873 (see Section 5).

3. POINT ELECTRON CLOUDS (PEC) AND HIGH EXPLOSIVE (HEX)

Each chemical composition was cast into an aluminum cylinder. Explosive release was made by timer ignition of an RDX booster. Multiple releases were dispensed at a given time, with separate time delay devices providing successive detonations at different times (and altitudes).

3.1 PEC

The point electron clouds are treated in three categories: (1) Multiple Point Electron Cloud (MPEC) (Figure 2), (2) Single Point Electron Cloud (Figure 3), and (3) High and Low Balance MPEC, MPEC-H and MPEC-L, respectively. The compositions and calculated products for (1) and (2) are identical.

Charge weights, total moles gas released, and moles cesium released are given in Table 2. The initial compositions and calculated products for all three categories are given in Appendix (classified).

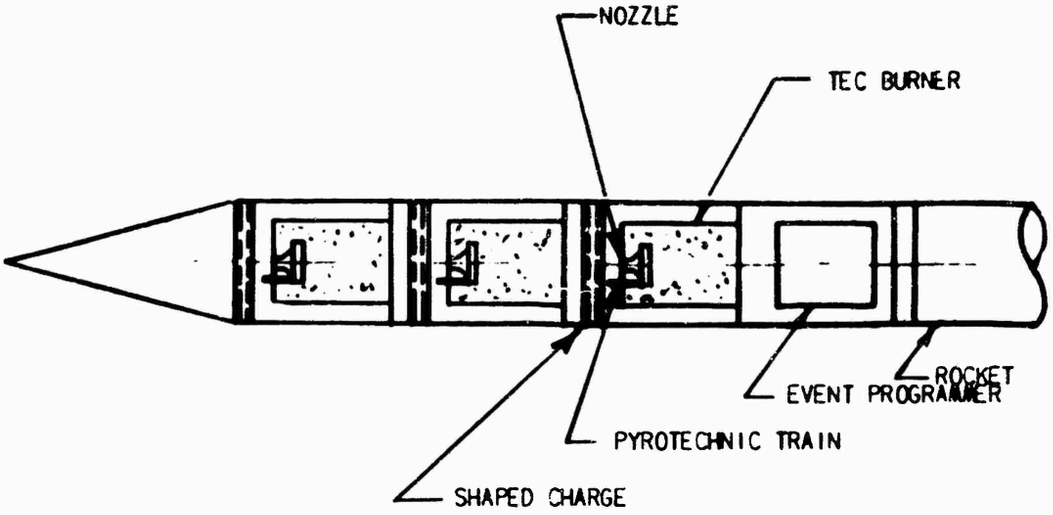

Figure 1. TRI-TEC Burner Payload

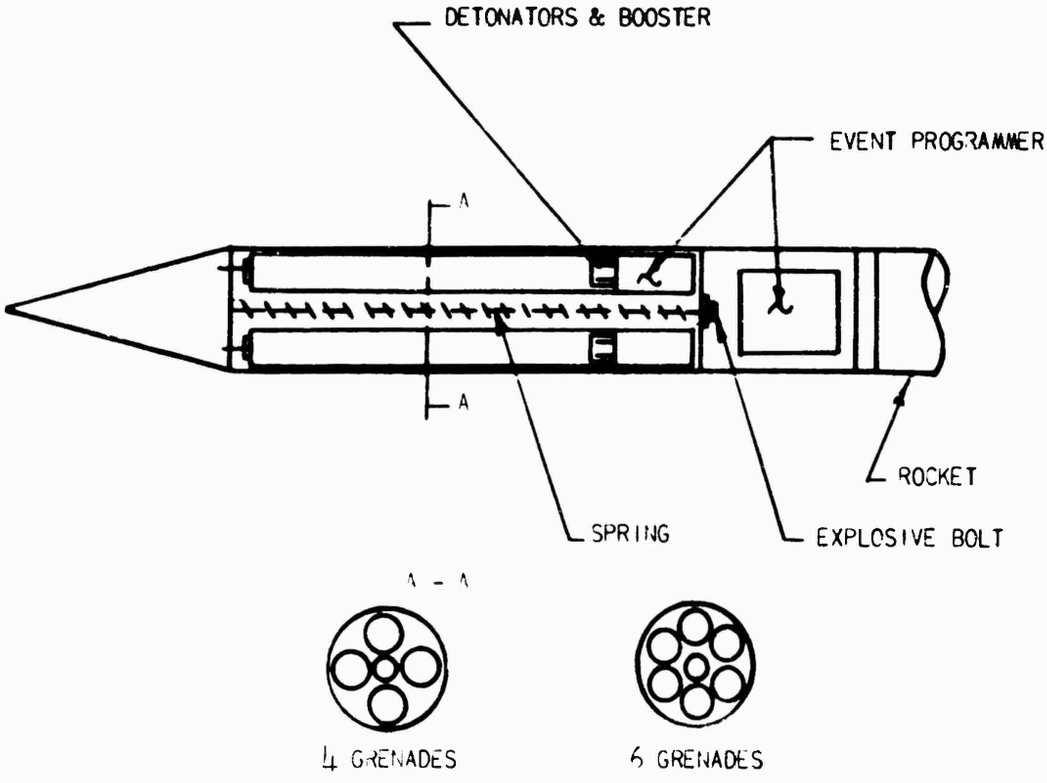

Figure 2. MPEC Payload

TABLE 1. Calculations for pressed charge at 175 PSI (Refs 1, 2)

Reactants		Products	
Initial Composition	Moles/Kilo	Constituent	Millimoles/Kg
71.143% $CsNO_3$	3.65	Mg	1.222×10^3
22.905% Al	8.11	O	3.195×10^2
3.095% Mg	1.28	N	3.480×10^0
2.857% KNO_3	0.258	Cs^+	1.268×10^2
100.000%		e	1.253×10^2
		Al	0.682×10^3
$T = 4141.9^oK$		K^+	2.997×10^0
$e/[Cs] = 3.5 \times 10^{-2}$		MgO	5.040×10^1
$e/moles\ gas = 1.4 \times 10^{-2}$		O^-	4.505×10^0
		O_2	3.694×10^1
		N_2	1.921×10^3
		NO	0.871×10^2
		Cs	3.502×10^3
		Cs_2	1.073×10^1
		AlO	2.556×10^2
		Al_2O	1.523×10^2
		Al_2O_2	2.101×10^1
		K	2.794×10^2
		K_2	0.586×10^{-2}
		total gas	0.880×10^4
		Al_2O_3 liq	3.604×10^3
		C solid	0
		MgOliq	0

TABLE 2. PEC parameters (Ref 2)

Type	Wt, kilo	Moles gas/kilo		Moles ($Cs + 2Cs_2$)	
		1 atm	1000 atm	1 atm	1000 atm
MPEC*	3.66	26.27	22.86	1.537	1.365
MPEC-H	3.60	25.93	21.72	1.271	1.116
MPEC-L	3.57	27.05	25.15	1.507	1.403

* SPEC is of identical composition. Net weight is 16.7 $\pm$ 0.1 kilos.

3.2 HEX

The conventional high explosive packages were loaded with Composition B (60% RDX/40% TNT). The composition of the detonation products, according to Cook, is given in Table 3.

TABLE 3. Detonation parameters of composition B (ρ_o = 1.56 g/cc) (Ref 3)

Species	Moles/kg		
CO	8.0		
CO_2	5.9		
H_2	0.01	n (moles gas/kg)	31.3
H_2O	0.1	T, ^oK	4,420
N_2	10.6	P, atm	1.90×10^5
NH_3	0.2		
CH_4	0.6		
CH_3OH	5.0		
CH_2O_2	0.9		

It should be noted that Cook's calculation is presumably more realistic than the ideal gas calculations of Atlantic Research Corp at an arbitrary 100 atm. Comparison of the two methods for a similar aluminized high explosive shows reasonable agreement for total moles of gas/kg, but major disagreement even to the predominant species. For comparison, the CO mechanism stoichiometric products are given in Table 4.

TABLE 4. 'Stoichiometric' reaction products of composition B (Ref 4)

Species	Moles/kg
CO	20.44
H_2O	6.35
H_2	6.17
N_2	11.10
total gas	44.06

It is clear that a rather sophisticated analysis is required before attempting a detailed study of the chemistry of the explosive releases.

4. SULFUR HEXAFLUORIDE (LIQUID) - AND COMPOSITION C-4 - FIREFLY ETHEL

The SF_6 was field loaded and carried in two cylindrical steel tanks (28 liters total volume). Release was made by detonating a composition C-4 explosive charge and simultaneously fracturing both tanks (see Figure 4).

The Firefly ETHEL payload contained 28 kilo of SF_6 at 15° C, released upon detonation of the 3.2 kilo breaking charge of composition C-4. The constituents of Composition C-4 and the nominal products based upon the 'CO mechanism' are given in Tables 5 and 6.

TABLE 5. Composition C-4 constituents

Constituent	Wt fraction	Formula	Moles/kilo
RDX	0.91_0	$C_3H_6O_6N_6$	5.10
di(2 ethyl hexyl) sebacate	0.053	$C_{26}H_{50}O_4$	0.124
polyisobutylene	0.021	$(C_4H_8)_n$	$\frac{0.661}{n}$
motor oil	0.016	say $(C_4H_8)_n$	

TABLE 6. 'Stoichiometric' reaction products of composition C-4

Species	Moles/kg
CO	18.2
H_2O	6.9
H_2	11.2
N_2	12.3
total gas	48.6

On this basis, 3.2 kilo of Composition C-4 will produce, crudely, 154 moles of gas.

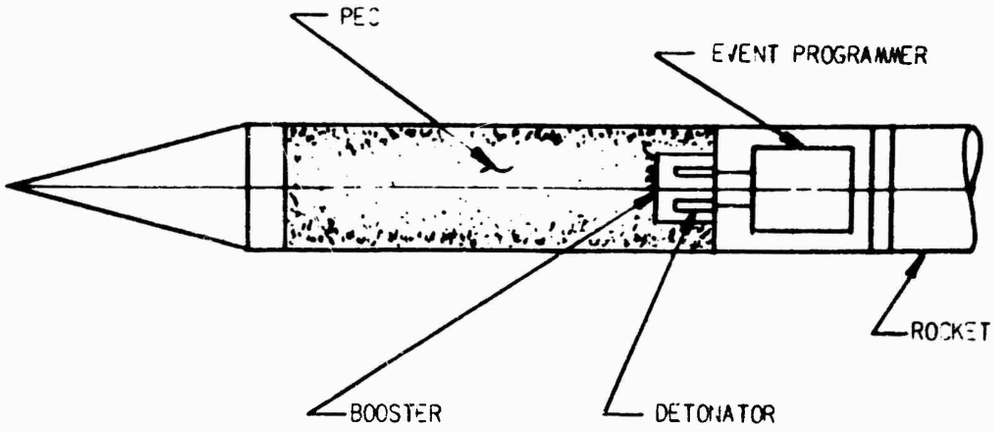

Figure 3. SPEC Payload

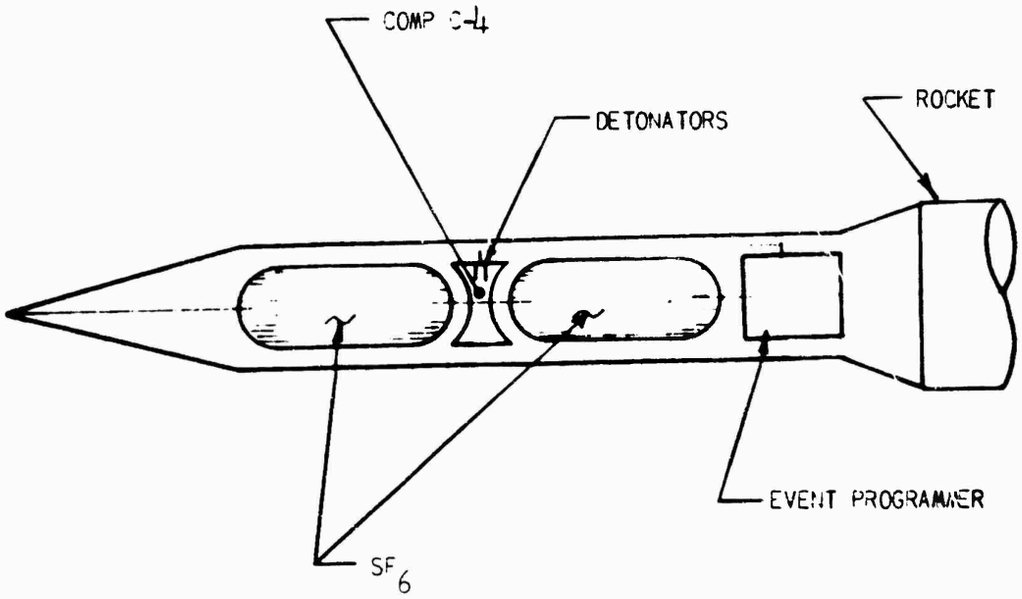

Figure 4. SF_6 (Liquid) Payload - ETHEL

As a good approximation, the SF_6 may be considered to be entirely in the liquid phase prior to release. (Tank volume ~ one ft^3.) Assuming that vaporization after release becomes insignificantly slow at 180^oK (which may not be valid for the 10 to 20 minute duration of the ionospheric effects observed), 68% of the SF_6 (ℓ) vaporizes immediately to provide 130 moles of gaseous SF_6(see Ref 2).

The significant point deduced from these calculations is that the mole fraction of SF_6(g) in the release is approximately 0.5.

5. ALUMINIZED HIGH EXPLOSIVE - FIREFLY DANA

The Firefly DANA payload was a field loaded package containing alternate layers of Composition C-4 and coarse aluminum granules (-20 mesh). The overall composition was 7.3 kilo Composition C-4 and 3.6 kilo aluminum. Explosive release was made by a timer actuated detonator (see Figure 5).

It is widely recognized that aluminized high explosives react relatively slowly,[2,3,4] and that the degree of reaction of the aluminum is sensitive to the particle size and containment. It appears likely, therefore, that relatively little aluminum reacted. It is clear from the observation of high altitude glow, however, that a significant but unknown amount of the aluminum reacted and/or volatilized.

Assuming no aluminum reaction, the 'stoichiometric' moles of gas may be obtained from the data given for Composition C-4 in Section 4 as 353 moles total gas or 48.6 mole/kilo. As the other limit we may consider the reaction products of a conventional aluminized explosive of similar balance. We may define the stoichiometric balance as the ratio $0/(1.5\ Al + C)$ of the constituents (where 0 represents oxygen available for Al reaction). For Firefly DANA, this ratio (assuming complete reaction) is 0.545. Some comparisons are given in Table 7 for the explosives TNT/RDX/Al = 28/46/26 (Atlantic Research Corporation) and the very similar 30/45/35 (Cook) of ratio ~ 0.67 and a high ratio explosive, $r \simeq 0.98$.

It is again clear that rather serious diagreement exists between the Cook and Atlantic Research Corporation results for (essentially) the same explosive. Within this framework, it appears that for high ratio (low aluminum or low reactivity) explosive both Al and Al_2O concentration become quite small as expected. Attention should therefore be paid to the possibility of decomposition of Al_2O_3(c) as a possible source of reactive radicals.

TABLE 7. Reaction products of aluminized explosives

r = O/(1.5 Al+C)	0.67		0.98*
	Cook	ARC	ARC
Total gas, moles/kilo	22.5	30.9	25.2
Al(g) moles/kilo	----	0.61	0.105
Al_2O	3.36	0.59	0.063
Al_2O_3(c)	1.27	9.66	3.24
AlN	----	4.03	----
T, ^oK	4400	3663	3651
Pressure, atm.	1.05×10^5	103	103
ρ_o, g/cc	1.51	----	----

6. SULFUR HEXAFLUORIDE (SUPERCRITICAL), CARBON DIOXIDE AND FLASH CARTRIDGES, FIREFLY KAREN, LAURA AND MARTHA

The SF_6 and CO_2 were each contained in titanium flanged spherical tanks (17.8 liters volume). Each chemical was released through a 4.52 in. diameter opening in the tank produced by severing the tank flange with a shaped explosive charge. Payload telemetry was used to indicate the time in flight that this flange was severed. Prior to launch, tank temperature was monitored and controlled by appropriate sensors and heaters. (Figure 6)

(1) SF_6. 18.2 kilo of sulfur hexafluoride was field loaded at a density of 102 g/cc and heated to a nominal 65° C (P = 990 psia). Calculation[2, 5] indicates 100% vaporization upon sudden release for these conditions. The nominal moles SF_6(g) released (Firefly KAREN and LAURA) is therefore 124 moles. Firefly MARTHA also included an auxiliary tank with another 4.5 kilo of SF_6 and therefore provided a nominal yield of 155 mole SF_6(g).

(2) CO_2. 5.4 kilo carbon dioxide was loaded at a density of 0.306 g/cm^3. A nominal release temperature of 18° C may be assumed for both releases (P≃800 psia) (Firefly KAREN and LAURA). 123 moles of CO_2 were loaded of which ~ 50% is vapor phase at the conditions given. By extrapolation from the higher temperature results,[5] vaporization (immediate) should be ~70% upon release.

(3) Flash Cartridge Compositions. Firefly KAREN and LAURA each carried seven (Poppy) flash cartridges. Each cartridge was sequentially ejected and

---

* For further details see classified appendix.

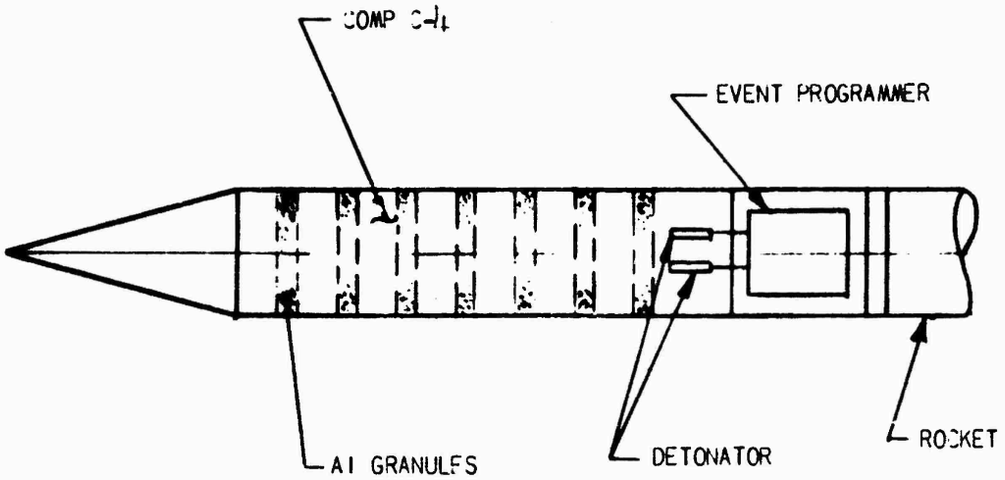

Figure 5. Aluminized HEX Payload - DANA

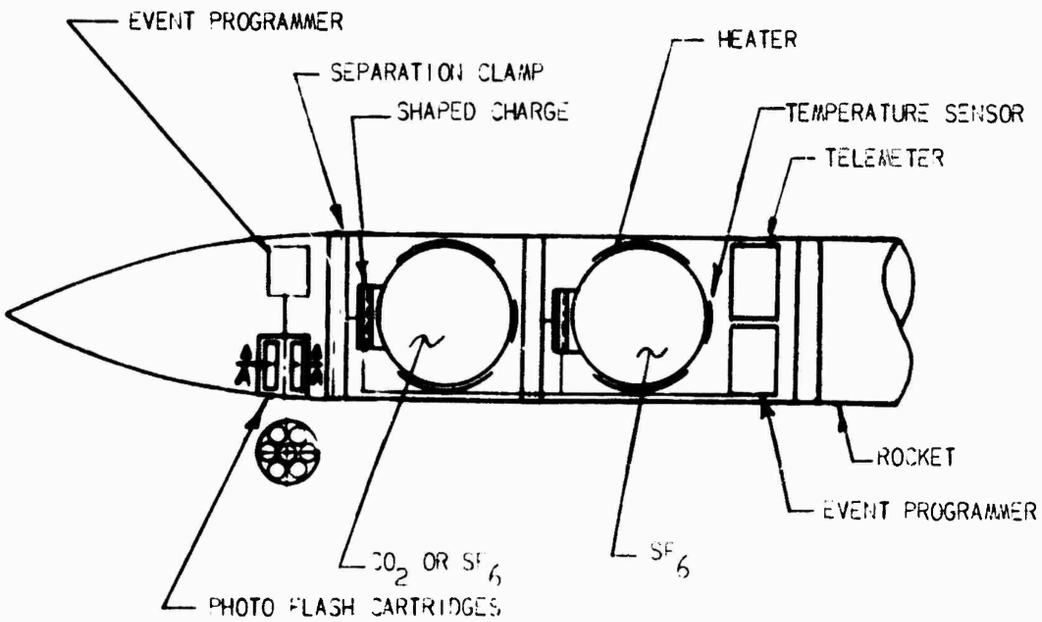

Figure 6. CO_2/SF_6 and Flash Cartridge Payload

detonated at a given time, by timer actuation of a squib and pyrotechnic delay column. The composition of the Firefly KAREN cartridges and of cartridges Nos. 2, 4 and 6 of Firefly LAURA is given in Table 8.[6]

TABLE 8. Calcuim Fluoride Cartridge Composition

Constituent	Wt %
Aluminum	31
$KClO_4$	49
CaF_2	20

Considering CaF_2 and KCl to be inert products, the stoichiometric balance, 0/1.5 Al = 0.82. Although the total stoichiometric moles of gas produced is not meaningful for this reaction, in view of its sensitivity to the assumed reaction products and consitions, it is remarkable to note that the nominal cartridge load is 19 grams of mixture. The observed reaction therefore occurs with ~ 6 grams or 0.25 mole total aluminum.

Flares Nos. 1, 3, 5 and 7 of Firefly LAURA contained the Picatinny Type III Class A composition given in Table 9.

TABLE 9. Type III Class A Flash Composition

Constituent	Wt%
Aluminum	40
$KClO_4$	30
$Ba(NO_3)_2$	30

For reaction to the gross products KCl, BaO and N_2, the stiochiometric balance 0/1.5 Al = 0.65 is considerably more reducing than the previous composition. Nominal cartridge load is 20 grams, of which ~ 8 gram is aluminum (0.3 mole).

7. SODIUM-LITHIUM THERMITE - FIREFLY TERRY AND SHARON

The nominal active contents of the Geophysics Corporation of America sodium-lithium thermite vaporizer are 1.0 kg sodium metal, 0.3 kg lithium metal and 16.7 kg thermite. Release was made by timer actuation of the pyrotechnic booster, and thermite starter. The sodium-lithium vapor is released through ports in the payload envelope (Figure 7). The design burning time is 150 $\pm$ 25 sec (Ref 7). This provides 43 moles of each vapor species at a nominal rate of $\sim$0.3 mole/sec for each metal.

Dr. Edward Manring of GCA estimates that the effective release rate for Firefly SHARON was an order of magnitude below the nominal rate.[8]

8. NITRIC OXIDE AND ACETYLENE

Each chemical was field loaded into a steel (86.6 liters volume) cylindrical tank. Release was initiated through a solenoid-operated valve and throttled through two adjustable orifices in parallel. A payload telemeter was used to transmit tank pressure versus time during release. A potentiometer transducer was used as the pressure sensor. On the C_2H_2 tanks, temperature sensors were used to determine tank, temperature prior to launch (Figure 8).

8.1 NO - Firefly MABEL, DINAH, and EVA

The nitric oxide releases were nominally 11.4 kilo (378 moles) at an initial pressure of $\sim$1500 pisa at 18^{o}C. The (smoothed) total moles released and the release rate as a function of time from launch from the Firefly EVA telemetry record (pressure) are given in Table 10. All three releases used similar orifices and similar release histories are expected.

TABLE 10. NO Release Parameters (Smoothed)

From initiation of release t, secs	Integrated moles released	Release rate, mole/sec
0	0	19
5	94	14
10	163	10
15	213	7
20	248	4
30	288	2.4

TABLE 10. NO Release Parameters (Smoothed) (Cont.)

From initiation of release t, secs	Integrated moles released	Release rate, mole/sec
40	312	1.4
50	326	1.0_5
60	336.5	0.7_4
70	344	0.4
95	354	0.2
120	359	

8.2 C_2H_2 (Supercritical) - Firefly NETTY and OLGA

The launch and prerelease payload parameters are given in Table 11.

TABLE 11. Acetylene Payload Parameters

	Firefly NETTY		Firefly OLGA*	
	Launch	Release	Launch	Release
Mass, kilo	18.2		18.4	
Density, g/cm^3	0.214		0.217	
Temp., ^oC	60	62.3**	63	(63)**
Pressure (psia)	1315	1425	1240	1432

Data Reduction Procedure: Isentropic internal expansion within the tank was assumed. The temperature-entropy diagram for acetylene extrapolated by Massey and Simmons[2,9] was used to obtain the temperature and molar volume from the smoothed pressure data. The molar volume-temperature data were smoothed and used to obtain a mass vented versus pressure function and, in turn, a mass versus time function. The mass versus time plot was differentiated by increments to obtain finally the release rate given in Figures 9 and 10.

---

* The initial conditions listed for OLGA are inconsistent with those for NETTY and with the thermodynamic data. This may be attributable to the use of external surface temperature probes. Since more weight was given to the pressure data the pre-release parameters used were based upon the pressure and a consistent temperature (for $\rho = 0.217$); that is, identical with Firefly NETTY.

** Calculated

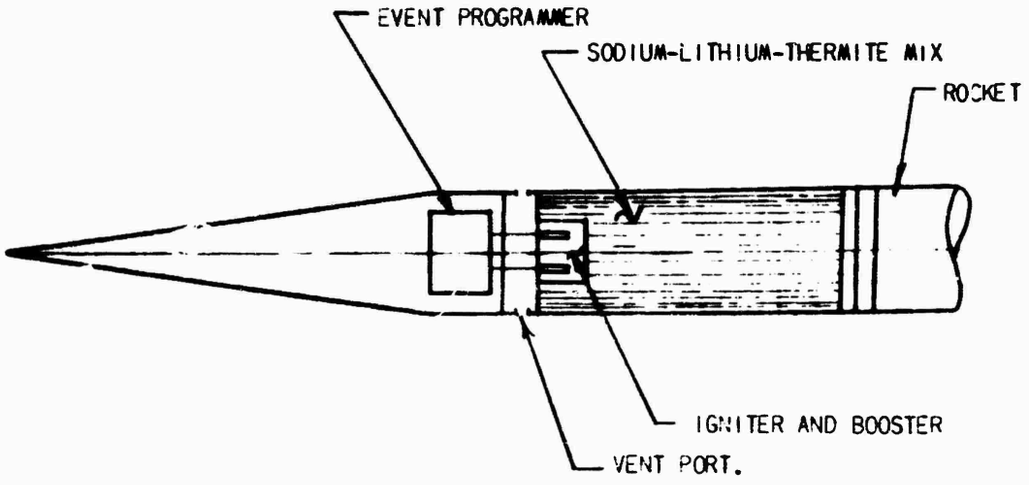

Figure 7. Sodium-Lithium-Thermite Payload

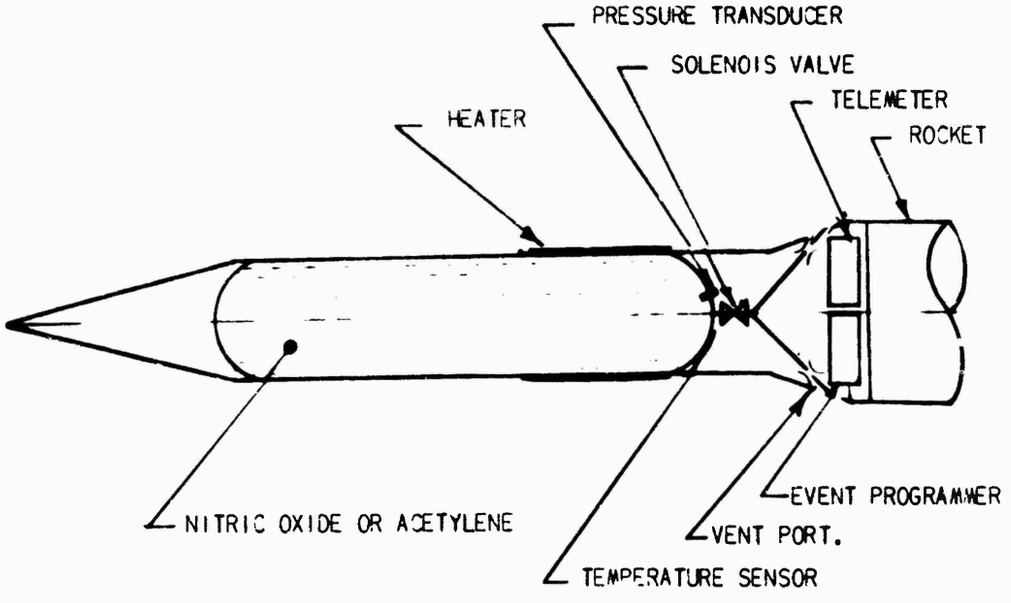

Figure 8. Nitric Oxide and Acetylene Payloads

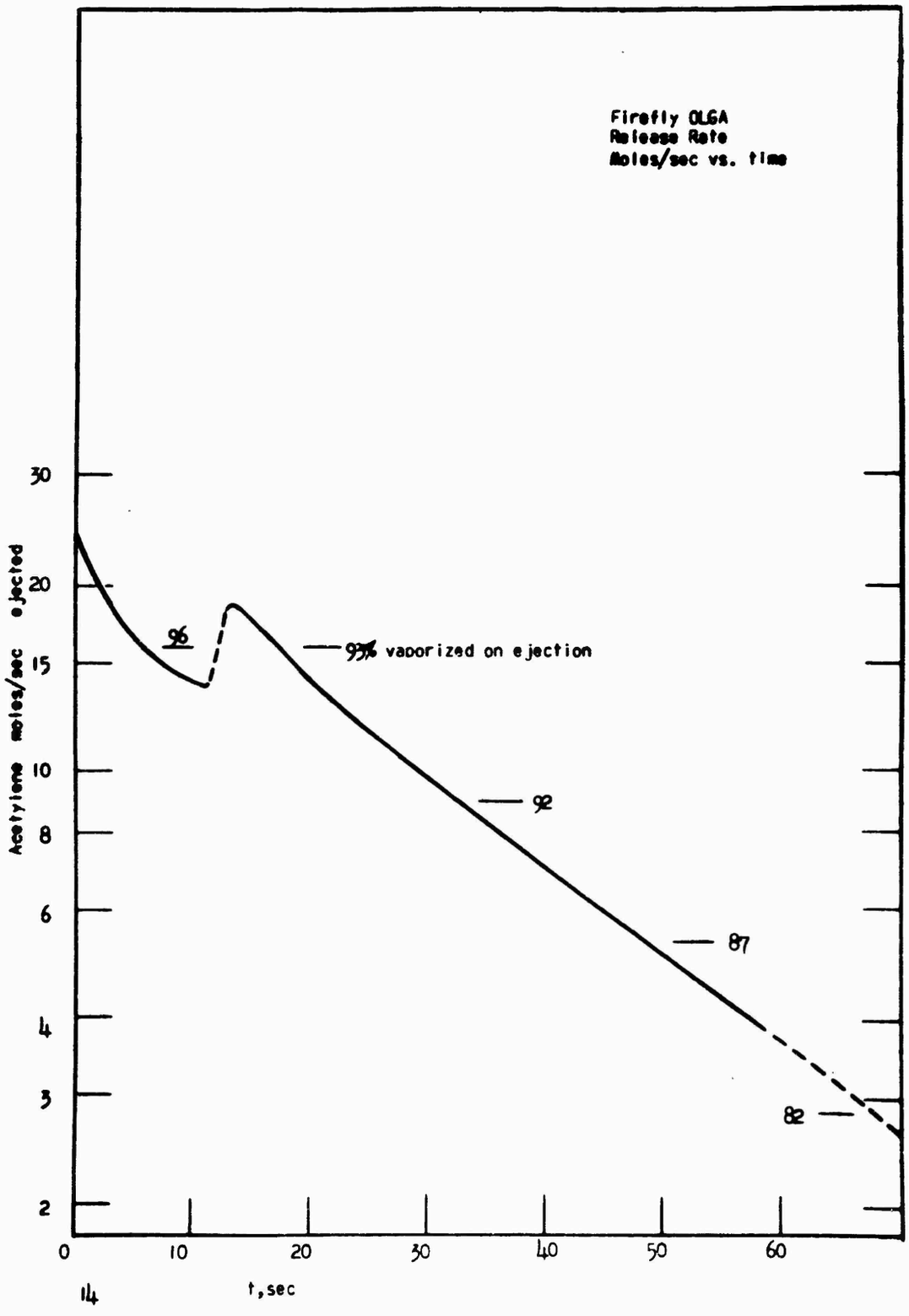

Figure 9. Firefly OLGA - Release Rate Moles/sec vs Time

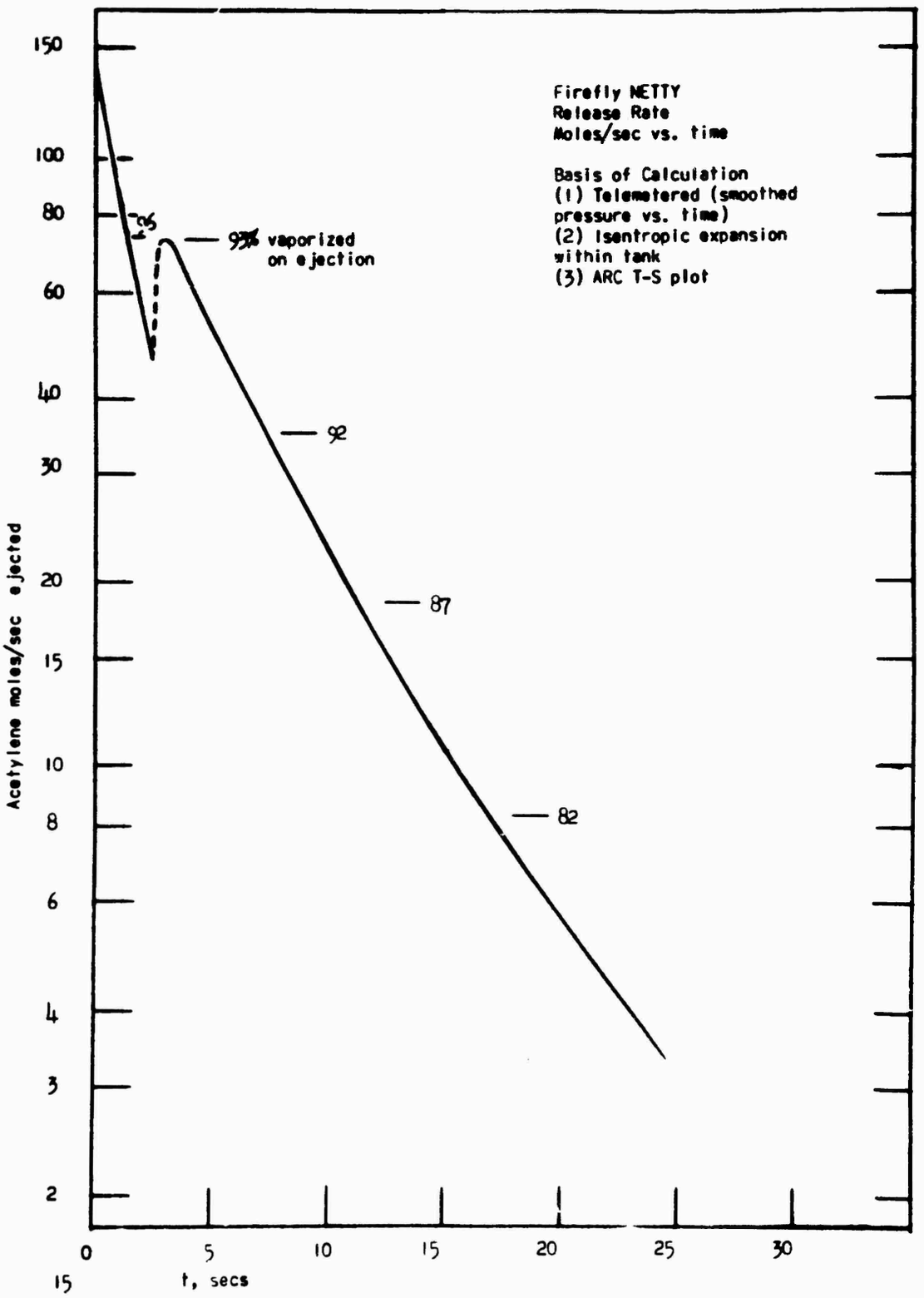

Figure 10. Firefly NETTY - Release Rate Moles/sec vs Time

Several cautions must be borne in mind in using these gross release rates. The results presented are many steps from the raw data and involve many approximations. For example, the upturn in the gross rate, is not observed in the pressure curve, but is derived from the thermodynamic data. This, in turn, is dependent upon not only its validity but also the assumption (certainly not a good one) that the gas and liquid is at equilibrium throughout (before venting). On the other hand, the adiabatic venting assumption is certainly better than the isothermal (infinite mass tank in equilibrium with gas) since the latter predicts 90% dumping for NETTY within seven seconds.

Note that the rate increase is associated with the formation of liquid phase within the tank. This occurs in both cases at ~ 0.3 mass removed. The effective moles gas vaporizing has been calculated by Atlantic Research Corporation[2, 10] for initial conditions $t = 67^{\circ}C$, $\rho = 0.214\ g/cm^3$ and is given in Table 12.

TABLE 12. Acetylene Fraction Vaporized ($t_i = 67^{\circ}C$, $\rho_i = 0.214\ g/cm^3$)

Fraction Withdrawn	Incremental Fraction Vaporized
0	1.00
0.2	0.96
0.4	0.93
0.6	0.92
0.8	0.87
0.9	0.82

9. NITROGEN DIOXIDE, TRIMETHYL ALUMINUM AND CARBON DISULFIDE - FIREFLY CLAIRE, STELLA AND DORIS

NO_2 and CS_2 were field loaded into steel tanks at loading densities of 1.44 gr/cc and 1.26 gr/cc, respectively. Due to its pyrophoric nature, trimethyl aluminum (TMA) was factory loaded into steel tanks at loading densities of 0.752 gr/cc. Each chemical was released as a liquid by circumferentially severing the tank by detonating a shaped explosive charge and venting the chemical through 1/2 and 1 inch diameter ports in the payload envelope. Prior to launch the tanks were each preheated to about $72^{\circ}C$. Firefly CLAIRE carried three tanks with NO_2, TMA and CS_2 (programmer was designed to release chemicals sequentially) (Figure 11). Firefly STELLA and DORIS carried a single tank and dual TEC burners programmed to release chemical simultaneously (Figure 12).

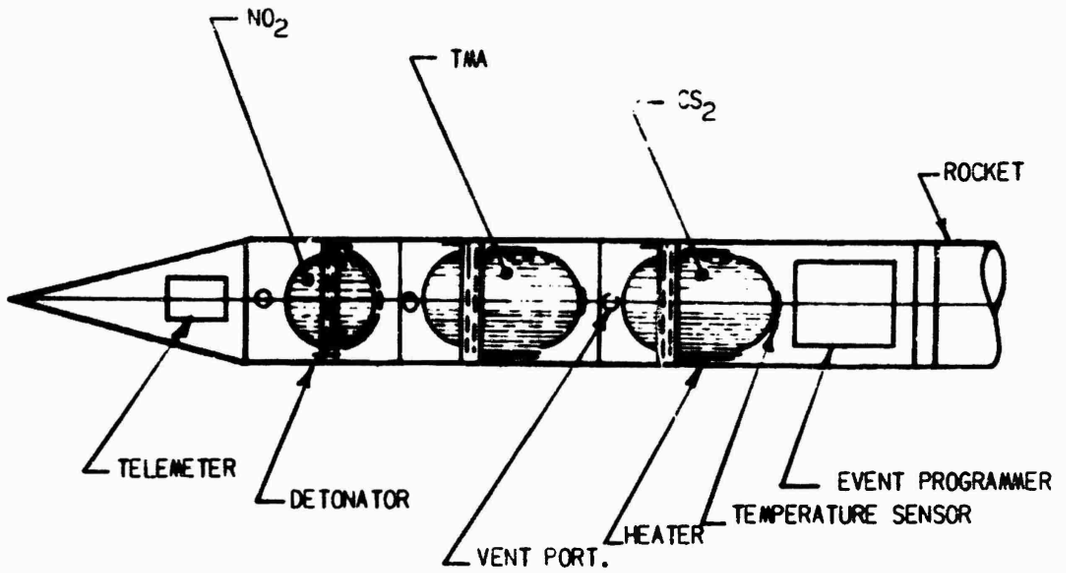

Figure 11. NO_2, TMA and CS_2 Payload - CLAIRE

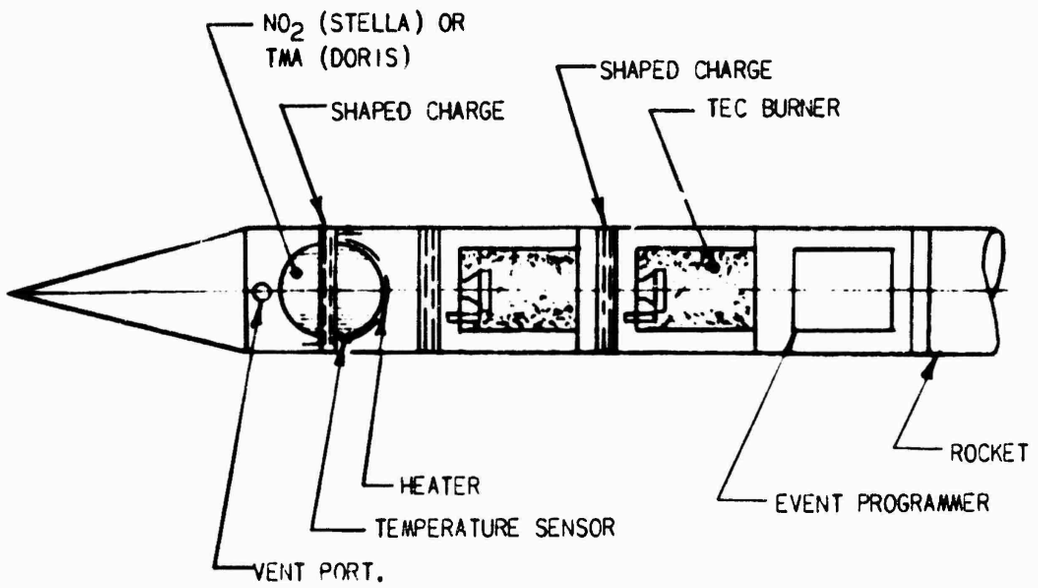

Figure 12. NO_2/TMA and Dual TEC Payloads - STELLA and DORIS

9.1 NO_2

Firefly CLAIRE and STELLA each carried 2.01 and 2.07 kg of NO_2 respectively, in 1820 cc tanks at a pressure of one atmosphere. At 72°C the calculated fraction of NO_2 vaporized was approximately 35% or 0.725 kg.

9.2 CS_2

Firefly CLAIRE carried 4.45 kg of CS_2 in a 4510 cc tank at approximately 250 psig N_2 pressure. At 72°C the calculated fraction vaporized was approximately 19% or 0.844 kg.

9.3 TMA

Firefly CLAIRE and DORIS each carried 3.04 kg of TMA in a 4590 cc tank and 1.13 kg in a 1820 cc tank, respectively. The tanks were pressurized to nominally 400 psig N_2, and it was calculated that the fraction of TMA vaporized at 72°C was approximately 40% while the remainder would freeze, or 1.22 kilo for CLAIRE and .45 kilo for DORIS. Release duration time for CLAIRE was not recorded; for DORIS a 15 second TMA release was observed (1/2 in. dia ports).

10. STATISTICS OF FIREFLY RESULTS

Of the thirty-nine rocket flights conducted in 1962 and May of 1963, thirty-three experiments were considered completely successful or partially successful; whereas, six experiments failed from an engineering standpoint.

10.1 Failures

The Firefly HAZEL, LISA AND PATSY MHEX payloads consistently failed to dispense grenades until approximately forty km altitude on re-entry where a point detonation of all grenades was observed. Payload development criterion had been based upon one rps vehicle spin rate, whereas the vehicles were spun at approximately six rps. Post-flight ground tests showed that at six rps, centrifugal acceleration forced the grenades hard against the ejectable payload skin and thus held the skin and grenades in place. As the spin rate decreased to approximately three rps, the skin slowly moved forward, but did not release the grenades. Aerodynamic heating during re-entry probably caused the grenades to cook off.

Firefly BRENDA and CAROL Nike Cajun MPEC experiment failures were attributed to vehicle malfunctions. A Cajun failure during burning was observed for Firefly BRENDA, and the Firefly CAROL Cajun rocket was not ignited as a result of improper hook-up of the firing circuit.

10.2 Partial Successes

Three MPEC releases out of four were observed from Firefly ALICE and BEVERLY. On the MABEL NO payload, the telemeter failed prior to launch; and on the Firefly LAURA, $CO_2 + SF_6$ payload, telemeter did not give positive indication of chemical release, since telemeter signal was lost at the time of the first release. The Firefly CLAIRE NO_2, TMA, CS_2 payload, two and probably three releases were initiated simultaneously. It is possible that aerodynamic heating, added to the heat of the chemicals, combined with the shock of explosively breaking the first tank, may have detonated the pyrotechnics on the other tanks. Also, telemeter signal, which was to indicate the release from the NO_2 tank, was lost immediately after launch.

References

1. L. W. FAGG and R. FRIEDMAN, Electron Yield of the 'TEC' -- Generators, Summary Report, Atlantic Research Corp., 16 July 1962.
2. C. H. MC DONNELL, 1962 Firefly Experiments, Final Report, Atlantic Research Corp., Contract AF19 (628) -295, 20 Jan 1963.
3. M. A. COOK, The Science of High Explosives, Reinhold, New York 1958, page 306.
4. The KISTIAKOWSKY-WILSON rules. For discussion and application to aluminized explosives, see H. W. Sexton, ARDE Rept (MX) 3/61 (Confidential)
5. R. FRIEDMAN, letter of 6 Nov 1962, Atlantic Research Corp.
6. F. SHELTON, Picatinny Arsenal, Dover, N. J. Private communication. For a general discussion see S. Lopatin, FRL-TR-29, October 1961.
7. J. BEDINGER, Geophys Corp., of America, private communication.
8. Private communication.
9. F. LIN, Thermodynamic Functions of Gases, Vol. II, Butterworths, 1956.
10. R. FRIEDMAN, letter report, Atlantic Research Corporation, 25 Sept 1962.

III. Photographic and Photometric Observations of Chemical Releases, Data Reduction, Interpretation and Analysis

Howard D. Edwards
Georgia Institute of Technology
Atlanta, Georgia

Abstract

Horizontal wind velocities have been computed for five of the twilight releases and for the 14 night releases which took place during Firefly III, and for the six releases of May 1963. Analyses of the six remaining twilight releases from Firefly III are in process at the time of this report.

Data are presented which give the wind heading in degrees east of north, magnitude of wind speed in meters per second, and north-south and east-west components in meters per second. Plots of north-south and east-west components are also given for each rocket release.

Data and plots of wind data as well as wind component contours are given for the four releases occuring on the night of 17-18 May 1963.

1. INTRODUCTION AND OBJECTIVES

The overall objectives of this effort are to perform photographic and photometric observations of chemical releases and to perform data reduction, interpretation and analysis. This report represents the results of project efforts which have been devoted to the analysis of data acquired during two field operations. These were

the Firefly III operations which took place at Eglin Air Force Base, Florida from 15 October 1962 until 15 December 1962, and a second field operation which took place at Eglin from 15 May to 21 May 1963.

2. SUMMARY AND CONCLUSIONS

Horizontal wind velocities have been computed for five of the twilight releases and for the 14 night releases which took place during Firefly III, and for the six releases of May 1963.

Analyses of the six remaining twilight releases from Firefly III are in process. No data was obtained from eight of the thirty-three Firefly III rocket firings since two were fired during daylight and hence could not be photographed, and six failed to release material due to either rocket or payload failure.

Table 1 gives a summary of the altitude ranges over which wind data was obtained for the 25 releases reported here. The six remaining releases include one SPEC (LOUISE) and five MPEC (ALICE, QUEENIE, PAULA, RUBY, SALLY). All of these were released in the altitude range of 90-117 km during the period of morning twilight.

A special study was made of the four releases which occurred on the evening of 3 December 1962 in which wind shears and turbulence were correlated with sporadic E activity. A paper entitled 'Ionospheric Winds: Motions into Night and Sporadic E Correlations' by N. W. Rosenberg, H. D. Edwards and J. W. Wright was presented

TABLE 1. Summary of altitude range covered with the 25 releases reported here

Twilight Shots		
Type	Name	Altitude Range (Km)
MPEC	Gilda	150-164, 218
SPEC	Kitty	105.5-114
TEC	Bonnie	90.5-117
	Cindy	87-114
Sodium	Sharon	93-135
	Sarah	71-170
	Blanche	99-165
	Irene	69-140

TABLE 1. Summary of altitude range covered with the 25 releases reported here (Cont)

Night Shots		
Type	Name	Altitude Range (Km)
TMA	Clair	96-113
	Doris	93-114
MPEC	Beverly	94, 104
	Fanny	--
SPEC	Dana	109
TEC	Dagmar	98-115
	Enid	101-112
	Ivy	96-143
	Esther	97-135
	Stella	96-130
NO	Mabel	93-108
	Dinah	90-115
	Eva	89-108
C_2H_2	Netty	103-114
	Olga	89-126
Grenade	Karen	107-122
	Laura	100-108

at the COSPAR meeting in Warsaw, Poland on 6 June 1963 and is being published in Space Research IV by North-Holland Publishing Company and as NASA Technical Note D-2114.

Table 2 summarizes the correlations of the height of strong east-west wind shear with the height of sporadic E. Dashes in Table 2 indicate that the wind data did not cover the altitude range at which the sporadic E was reported.

Plots which combine the N-S and E-W components are given for the four releases occuring on the night of 17-18 May 1963 in which wind data was obtained from evening twilight to the following morning twilight. The contours of the north-south and east-west components indicate a general tendency for the wind component pattern to decrease in altitude throughout the entire night. This phenomenon was observed in the data from the 3 December releases which covered only the period from evening twilight to about midnight. Unlike the 3 December results, the 17-18 May north-south wind components are generally decreasing in magnitude as the

TABLE 2. Correlation of sporadic E with East-West wind shear

Rocket Name	Height of Sporadic E (Km)	Height of Wind Shear (Km)	Direction of Shear, Lower to Upper Height
Kitty	105	107	W-E
Beverly	100	---	---
Enid	90 weak 100 strong	---	---
Eva	100	97	E-W
Sharon	96, 109	97, 108	W-E, E-W
Ivy	96, 108	96, 107	W-E, E-W
Esther	103	101	E-W
Dinah	100	99	E-W
Mabel	113	---	---
Dagmar	88	---	---
Dana	94, 99	---	---
Netty	101	---	---
Olga	103	102.5 103.5	E-W W-E

night progresses. The east-west component contour for the May data, like the December data, shows the same tendency for the magnitude to increase throughout the night at the upper altitudes. At the lower altitudes no general tendencies are immediately obvious, and it seems that wind data more closely spaced in time is needed to clarify the east-west component contour in this region.

No ionosonde data was taken during the May releases, so correlation between sporadic E and wind shears is not possible for this series of firings.

Upon completion of the determination of horizontal wind velocities for the six remaining twilight releases (ALICE, QUEENIE, LOUISE, PAULA, RUBY, SALLY), studies are planned on: (1) the diurnal and seasonal variation of the horizontal wind motion; (2) vertical wind motion; (3) turbulance and diffusion.

Appendix A

A.1 HORIZONTAL WIND VELOCITIES FOR 14 NIGHT RELEASES

The horizontal wind velocities as a function of altitude for the 14 night releases which took place during firefly III launchings (15 October 1962 to 15 December 1962) are presented in the following data and plots. Wind headings are given in degrees east of north. A minus sign indicates a wind component toward either the south or west.

BEVERLY

LAUNCH DATE	LAUNCH TIME (CST)	PAYLOAD MATERIAL	HEIGHT (KM)	NORTH LATITUDE	WEST LONGITUDE
11-6-62	0200	MPEC	88.70	30.2604	86.8506

HEIGHT (KM)	WIND HEADING (DEGREES)	HORIZONTAL WIND SPEED (M/S)	NORTH-SOUTH COMPONENT (M/S)	EAST-WEST COMPONENT (M/S)
94.1	128	67	-28	38
103.7	37	56	42	35

DAGMAR

LAUNCH DATE	LAUNCH TIME (CST)	PAYLOAD MATERIAL	HEIGHT (KM)	NORTH LATITUDE	WEST LONGITUDE
10-16-62	1840	TEC	87.86	30.2625	86.6895

HEIGHT (KM)	WIND HEADING (DEGREES)	HORIZONTAL WIND SPEED (M/S)	NORTH-SOUTH COMPONENT (M/S)	EAST-WEST COMPONENT (M/S)
98.0	98	90	-12	90
99.0	101	98	-18	96
100.0	108	106	-33	101
101.0	121	116	-59	100
102.0	134	131	-90	102
103.0	124	135	-75	112
104.0	137	130	-95	89
105.0	152	123	-108	58
106.0	163	120	-112	33
107.0	175	106	-106	10
108.0	181	55	-56	-1
109.0	187	33	-33	-4
109.3	189	20	-20	-3
109.6	188	18	-18	-2
110.0	194	16	-16	-4
111.0	228	11	-5	-10
111.7	301	12	6	-10
112.0	297	14	6	-11
112.2	310	11	7	-8
113.0	315	14	9	-10
114.0	352	25	24	-7
115.0	360	44	44	0

DANA

LAUNCH DATE	LAUNCH TIME (CST)	PAYLOAD MATERIAL	HEIGHT (KM)	NORTH LATITUDE	WEST LONGITUDE
12-10-62	1930	SPEC	107.43	30.2496	86.7917

HEIGHT (KM)	WIND HEADING (DEGREES)	HORIZONTAL WIND SPEED (M/S)	NORTH-SOUTH COMPONENT (M/S)	EAST-WEST COMPONENT (M/S)
109.1	354	111	110	-12

DINAH

LAUNCH DATE	LAUNCH TIME (CST)	PAYLOAD MATERIAL	HEIGHT (KM)	NORTH LATITUDE	WEST LONGITUDE
12-3-62	2245	NO	90.00	30.1274	86.6898

HEIGHT (KM)	WIND HEADING (DEGREES)	HORIZONTAL WIND SPEED (M/S)	NORTH-SOUTH COMPONENT (M/S)	EAST-WEST COMPONENT (M/S)
90.2	264	43	-5	-42
91.0	284	45	8	-43
91.3	300	45	22	-39
92.0	319	56	41	-36
92.6	334	52	46	-23
93.0	332	70	56	-31
94.0	346	88	89	-17
94.5	349	77	75	-15
95.0	8	82	82	2
96.0	29	46	44	19
97.0	60	36	19	30
98.0	100	55	-42	35
99.0	200	80	-82	-43
100.0	220	120	-108	-72
100.5	225	125	-86	-86
101.0	225	129	-108	-91
101.5	225	133	-93	-97
102.0	225	138	-106	-95
102.5	227	130	-87	-95
103.0	230	133	-89	-112
103.5	240	139	-70	-121
104.0	244	139	-64	-134
104.5	249	134	-48	-125
105.0	255	140	-33	-135
105.5	260	150	-15	-138
106.0	270	150	5	-144
106.5	280	142	22	-134
107.0	290	130	44	-118
107.5	297	120	55	-106
108.0	310	109	66	-76
108.5	326	101	72	-49
109.0	339	100	84	-36
109.5	350	95	84	-22
110.0	355	85	83	-10
111.0	20	72	66	34
112.0	40	72	56	54
113.0	53	97	62	82
114.0	70	125	64	105
115.0	75	139	62	136

ENID

LAUNCH DATE	LAUNCH TIME (CST)	PAYLOAD MATERIAL	HEIGHT (KM)	NORTH LATITUDE	WEST LONGITUDE
10-25-62	0030	DTEC	87.09	30.2952	86.7655

HEIGHT (KM)	WIND HEADING (DEGREES)	HORIZONTAL WIND SPEED (M/S)	NORTH-SOUTH COMPONENT (M/S)	EAST-WEST COMPONENT (M/S)
101.0	21	69	64	24
102.0	30	52	45	26
103.0	32	38	32	20
104.0	28	24	22	11
105.0	187	10	-8	-3
106.0	214	13	-10	-7
107.0	209	17	-14	-8
108.0	224	27	-18	-18
109.0	227	34	-23	-25
110.0	233	36	-20	-29
111.0	245	43	-18	-38
112.0	257	47	-11	-46

ESTHER

LAUNCH DATE	LAUNCH TIME (CST)	PAYLOAD MATERIAL	HEIGHT (KM)	NORTH LATITUDE	WEST LONGITUDE
12-3-62	2145	TEC	86.40	30.1682	86.7446

HEIGHT (KM)	WIND HEADING (DEGREES)	HORIZONTAL WIND SPEED (M/S)	NORTH-SOUTH COMPONENT (M/S)	EAST-WEST COMPONENT (M/S)
96.5	55	17	10	14
97.0	97	17	-2	17
97.5	134	35	-24	25
98.0	128	52	-32	41
98.5	125	59	-34	48
99.0	125	59	-34	48
99.5	133	49	-33	36
100.0	112	32	-12	30
101.0	219	61	-48	-38
102.0	226	121	-85	-86
103.0	237	151	-83	-126
104.0	236	152	-87	-125
105.0	243	160	-74	-142
106.0	252	144	-46	-136
107.0	262	150	-20	-143
108.0	290	118	40	-111

ESTHER (CONTINUED)

HEIGHT (KM)	WIND HEADING (DEGREES)	HORIZONTAL WIND SPEED (M/S)	NORTH-SOUTH COMPONENT (M/S)	EAST-WEST COMPONENT (M/S)
109.0	285	145	38	-140
110.0	301	146	75	-125
111.1	329	95	80	-49
111.7	345	88	85	-22
113.5	17	97	93	28
114.4	32	107	90	57
115.8	46	116	81	83
116.9	54	125	73	101
118.6	68	124	46	114
119.0	63	127	58	112
120.0	71	118	41	109
122.0	88	109	9	98
124.0	102	91	-19	89
126.0	122	91	-49	77
128.0	130	89	-57	68
130.0	137	88	-64	60
135.0	154	83	-74	36

EVA

LAUNCH DATE	LAUNCH TIME (CST)	PAYLOAD MATERIAL	HEIGHT (KM)	NORTH LATITUDE	WEST LONGITUDE
12-6-62	0421	NO	87.99	30.2306	86.6126

HEIGHT (KM)	WIND HEADING (DEGREES)	HORIZONTAL WIND SPEED (M/S)	NORTH-SOUTH COMPONENT (M/S)	EAST-WEST COMPONENT (M/S)
89.0	67	51	20	47
90.0	62	62	29	55
91.0	57	57	36	58
92.0	59	93	48	80
93.0	54	115	60	98
94.0	54	147	87	117
95.0	67	75	36	83
96.0	71	76	20	45
97.0	64	19	9	17
98.0	324	13	9	-7
99.0	295	34	14	-31
100.0	292	53	20	-26
102.0	277	60	7	-59
104.0	243	34	-15	-30
106.0	120	21	-11	18
108.0	43	58	42	40

FANNY

LAUNCH DATE	LAUNCH TIME (CST)	PAYLOAD MATERIAL		HEIGHT (KM)	NORTH LATITUDE	WEST LONGITUDE
11-10-62	1903	HEX-PEC	(2)	156.38	30.0998	86.6332
			(4)	257.7	29.423	86.507

IVY

LAUNCH DATE	LAUNCH TIME (CST)	PAYLOAD MATERIAL	HEIGHT (KM)	NORTH LATITUDE	WEST LONGITUDE
12-3-62	1801	MTEC	81.58	30.1575	86.7041

HEIGHT (KM)	WIND HEADING (DEGREES)	HORIZONTAL WIND SPEED (M/S)	NORTH-SOUTH COMPONENT (M/S)	EAST-WEST COMPONENT (M/S)
96.0	72	17	5	17
97.0	83	33	4	33
98.0	89	59	1	59
99.0	94	85	-6	84
100.0	98	100	-15	99
101.0	104	110	-28	107
102.0	111	119	-42	111
103.0	116	123	-54	111
104.0	117	127	-58	113
105.0	120	121	-60	106
105.2	114	87	-36	79
106.0	127	98	-58	79
107.0	161	50	-47	16
107.2	171	31	-27	7
108.0	247	36	-9	-33
109.0	263	52	-5	-52
110.0	272	61	2	-61
110.4	274	68	5	-68
112.0	292	73	26	-64
114.0	307	72	43	-57
114.2	305	68	39	-56
116.0	300	66	43	-56
118.0	314	65	41	-44
120.0	311	46	31	-34
122.0	300	24	13	-18
124.0	316	22	16	-15
124.7	303	17	9	-12
127.0	244	18	-9	-12
130.0	188	39	-39	-5
135.0	166	43	-42	10
140.0	153	52	-46	24
143.0	138	58	-43	39

KAREN

LAUNCH DATE	LAUNCH TIME (CST)	PAYLOAD MATERIAL		HEIGHT (KM)	NORTH LATITUDE	WEST LONGITUDE
11-15-62	1926	GRENADE	(1)	106.68	30.2472	86.6986
			(2)	109.53	30.2426	86.6987
			(3)	112.21	30.2379	86.6985
			(4)	114.80	30.2335	86.6984
			(5)	117.47	30.2289	86.6983
			(6)	122.23	30.2208	86.6975

HEIGHT (KM)	WIND HEADING (DEGREES)	HORIZONTAL WIND SPEED (M/S)	NORTH-SOUTH COMPONENT (M/S)	EAST-WEST COMPONENT (M/S)
106.8	224	109	-79	-75
109.6	267	110	-5	-110
112.2	286	82	20	-78
115.3	308	64	39	-51
117.6	331	48	41	-23
122.2	78	31	7	31

LAURA

LAUNCH DATE	LAUNCH TIME (CST)	PAYLOAD MATERIAL		HEIGHT (KM)	NORTH LATITUDE	WEST LONGITUDE
12-7-62	1908	GRENADE	(1)	91.68	30.1324	86.7059
			(2)	94.56	30.1222	86.7063
			(3)	97.24	30.1126	86.7065
			(4)	99.73	30.1041	86.7066
			(5)	102.18	30.0955	86.7063
			(6)	104.66	30.0864	86.7063
			(7)	107.49	30.0760	86.7064

HEIGHT (KM)	WIND HEADING (DEGREES)	HORIZONTAL WIND SPEED (M/S)	NORTH-SOUTH COMPONENT (M/S)	EAST-WEST COMPONENT (M/S)
100.2	235	49	-28	-40
105.3	257	156	-34	-153
108.0	294	124	51	-114

MABEL

LAUNCH DATE	LAUNCH TIME (CST)	PAYLOAD MATERIAL	HEIGHT (KM)	NORTH LATITUDE	WEST LONGITUDE
11-27-62	1800	NO	91.87	30.1807	86.6094

HEIGHT (KM)	WIND HEADING (DEGREES)	HORIZONTAL WIND SPEED (M/S)	NORTH-SOUTH COMPONENT (M/S)	EAST-WEST COMPONENT (M/S)
92.7	26	51	43	26
93.0	37	44	36	27
93.6	38	47	36	28
94.0	31	56	48	29
94.5	31	65	55	34
95.0	34	66	55	37
96.0	34	49	41	27
97.0	46	39	24	28
98.0	117	55	-25	49
99.0	130	85	-55	65
100.0	140	92	-78	65
101.0	148	112	-94	59
102.0	154	116	-105	49
103.0	161	115	-109	37
104.0	172	106	-105	16
105.0	176	101	-101	8
106.0	178	99	-99	4
107.6	197	83	-79	-25

NETTY

LAUNCH DATE	LAUNCH TIME (CST)	PAYLOAD MATERIAL	HEIGHT (KM)	NORTH LATITUDE	WEST LONGITUDE
12-12-62	1746	ACETYLENE	100.36	30.0702	86.7865

HEIGHT (KM)	WIND HEADING (DEGREES)	HORIZONTAL WIND SPEED (M/S)	NORTH-SOUTH COMPONENT (M/S)	EAST-WEST COMPONENT (M/S)
102.5	118	21	-14	14
103.0	97	15	-2	15
103.5	37	22	17	13
104.0	9	20	20	3
105.0	327	40	34	-22
106.0	308	64	40	-50
108.0	302	85	46	-72
110.0	315	90	65	-63
112.0	327	84	70	-46
113.5	315	53	37	-37
114.0	321	47	37	-30

OLGA

LAUNCH DATE	LAUNCH TIME (CST)	PAYLOAD MATERIAL	HEIGHT (KM)	NORTH LATITUDE	WEST LONGITUDE
12-14-62	1752	ACETYLENE	88.61	30.1771	86.6365

HEIGHT (KM)	WIND HEADING (DEGREES)	HORIZONTAL WIND SPEED (M/S)	NORTH-SOUTH COMPONENT (M/S)	EAST-WEST COMPONENT (M/S)
89.0	111	31	-11	29
90.0	103	35	-8	34
91.0	123	29	-16	24
92.0	142	25	-20	15
93.0	151	26	-23	13
94.0	154	28	-25	12
95.0	145	19	-16	11
96.0	135	12	-9	9
97.0	182	12	-12	0
98.0	217	11	-9	-7
99.0	253	14	-4	-13
100.0	276	16	2	-16
101.0	300	17	9	-15
102.0	301	16	8	-14
103.0	293	101	39	-93
104.0	307	78	47	-63
105.0	315	33	23	-24
106.0	295	32	13	-29
107.0	292	37	14	-35
108.0	294	43	18	-39
109.0	292	61	23	-56
110.0	285	48	13	-46
112.0	245	36	-15	-32
114.0	230	44	-28	-34
116.0	204	49	-44	-20
118.0	199	49	-47	-16
120.0	197	40	-38	-12
122.0	173	35	-35	5
124.0	153	29	-25	13
126.0	150	30	-26	15

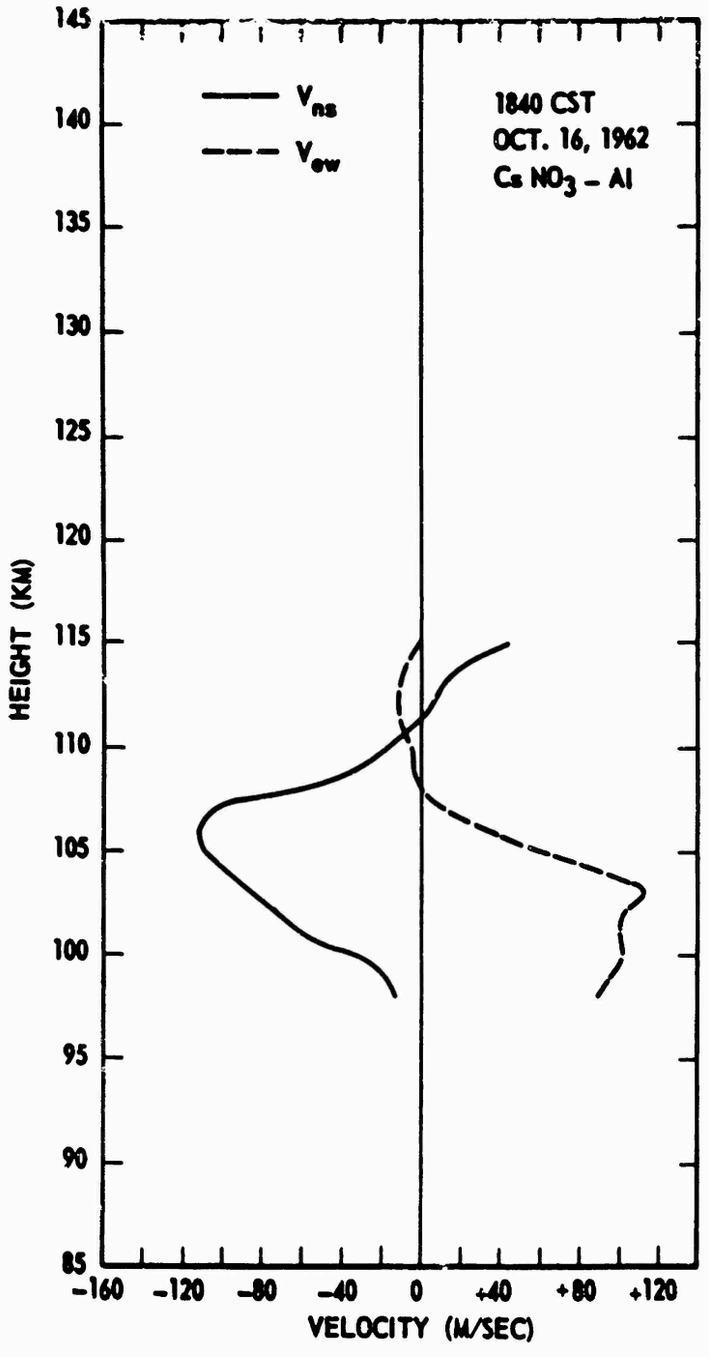

Figure A1. North-South and East-West Components of the Wind Velocity for DAGMAR

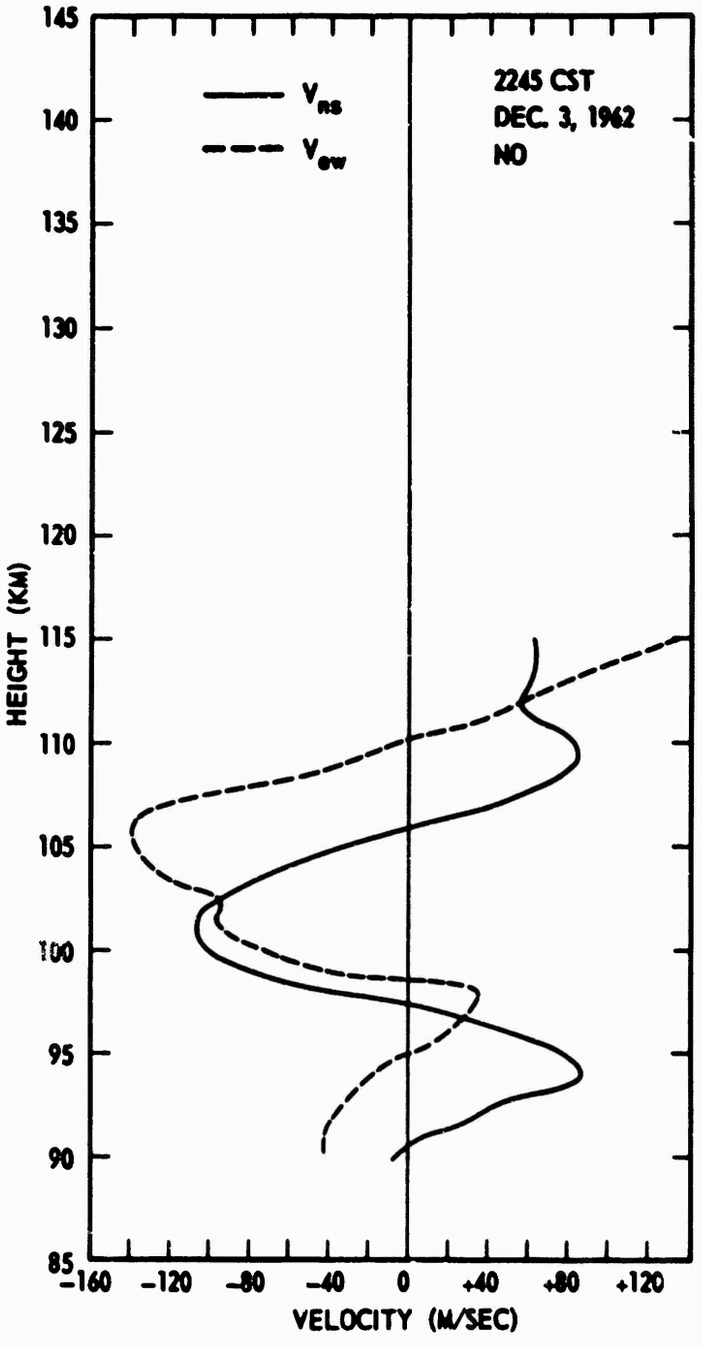

Figure A2. North-South and East-West Components of the Wind Velocity for DINAH

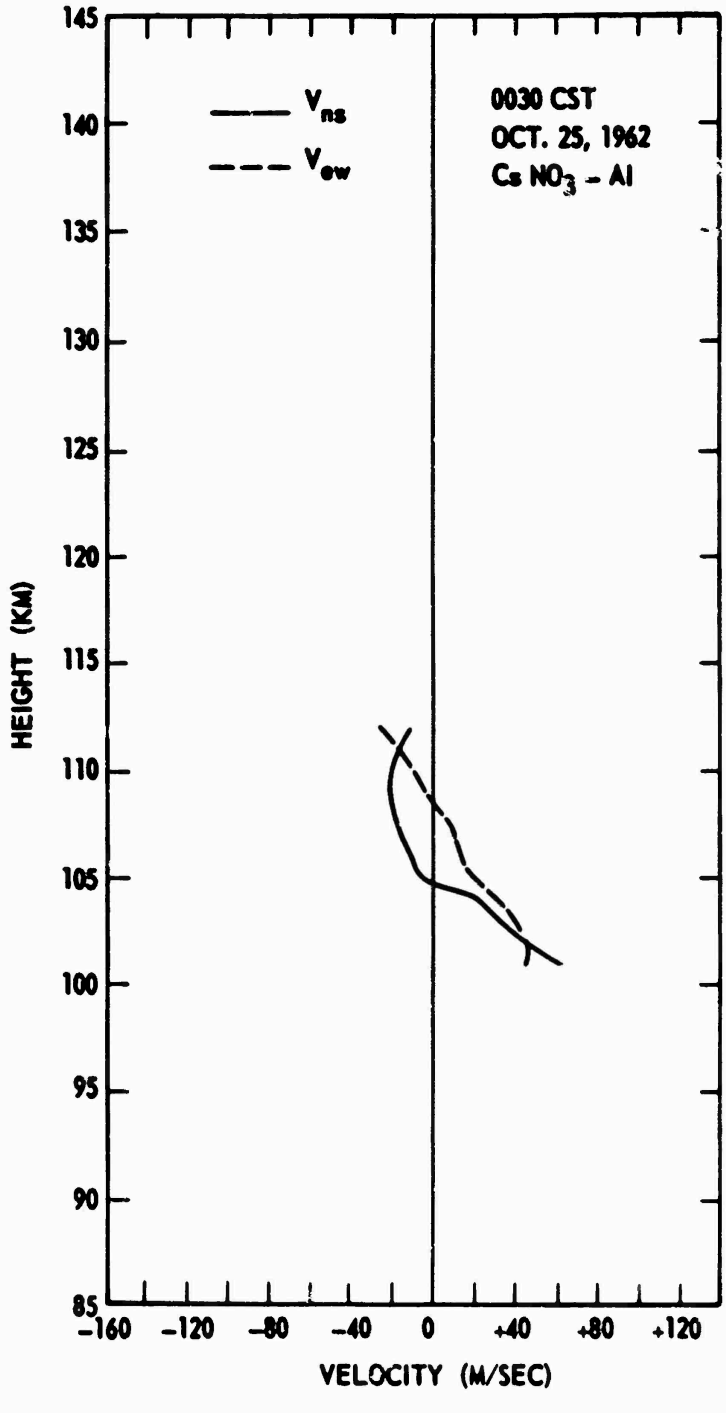

Figure A3. North-South and East-West Components of the Wind Velocity for ENID

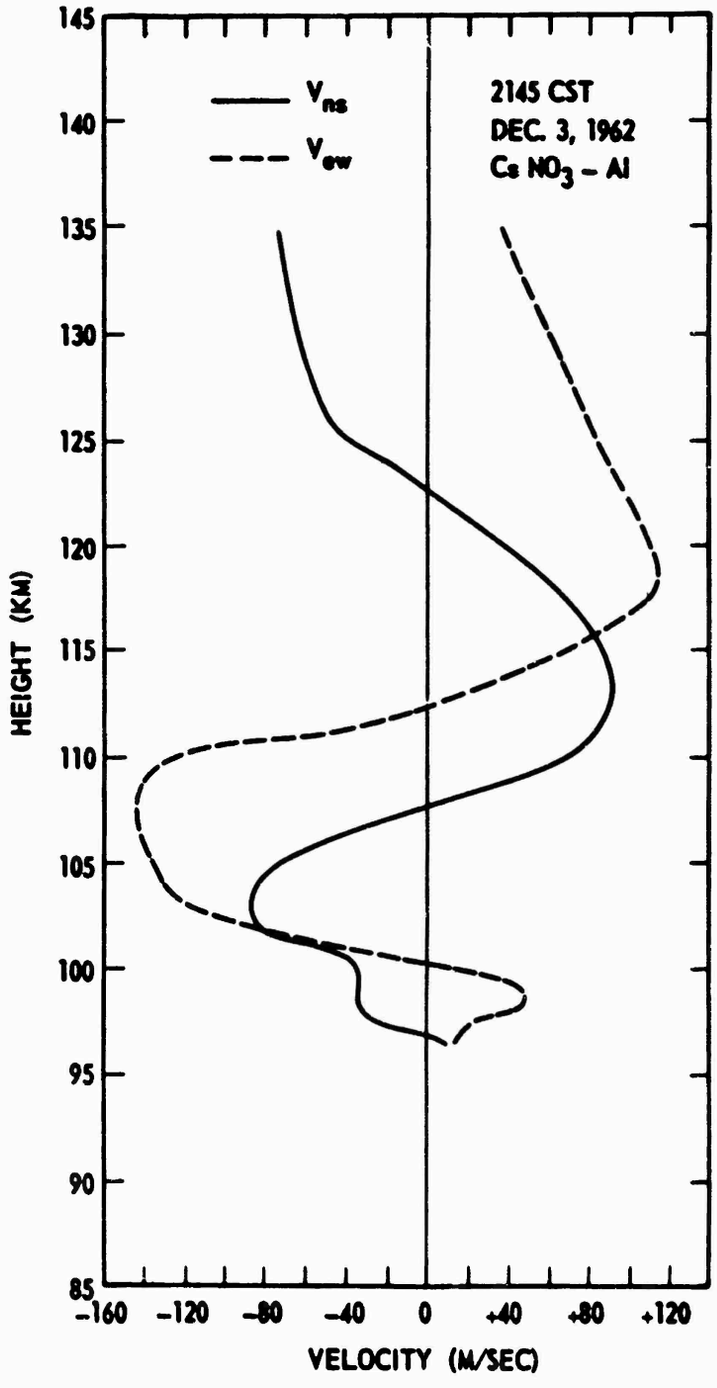

Figure A4. North-South and East-West Components of the Wind Velocity for ESTHER

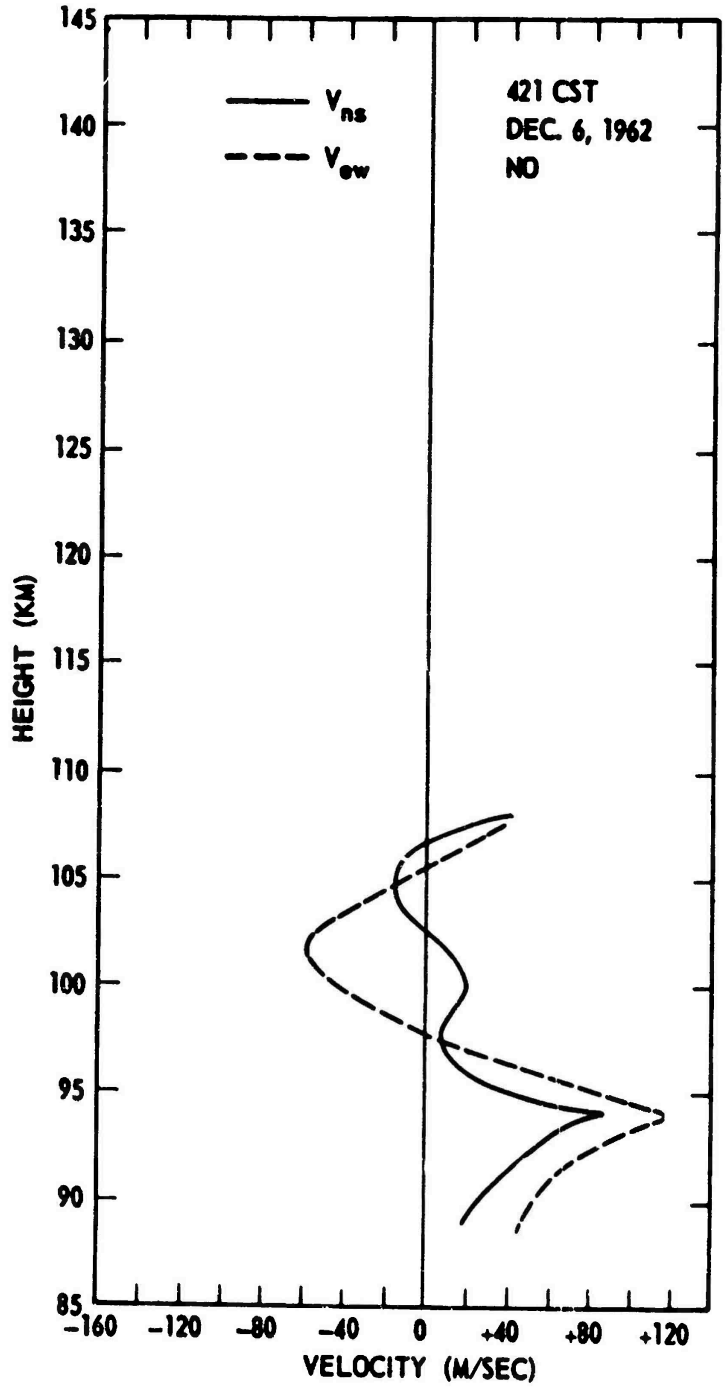

Figure A5. North-South and East-West Components of the Wind Velocity for EVA

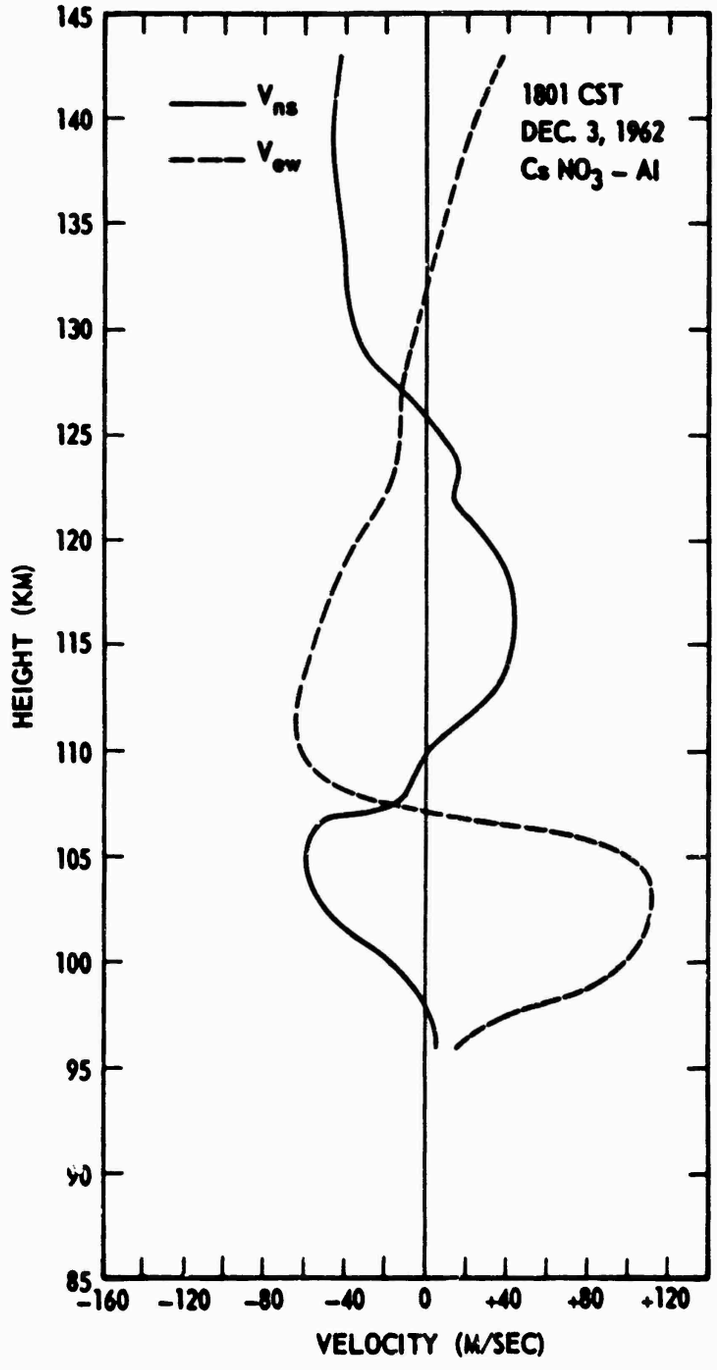

Figure A6. North-South and East-West Components of the Wind Velocity for IVY

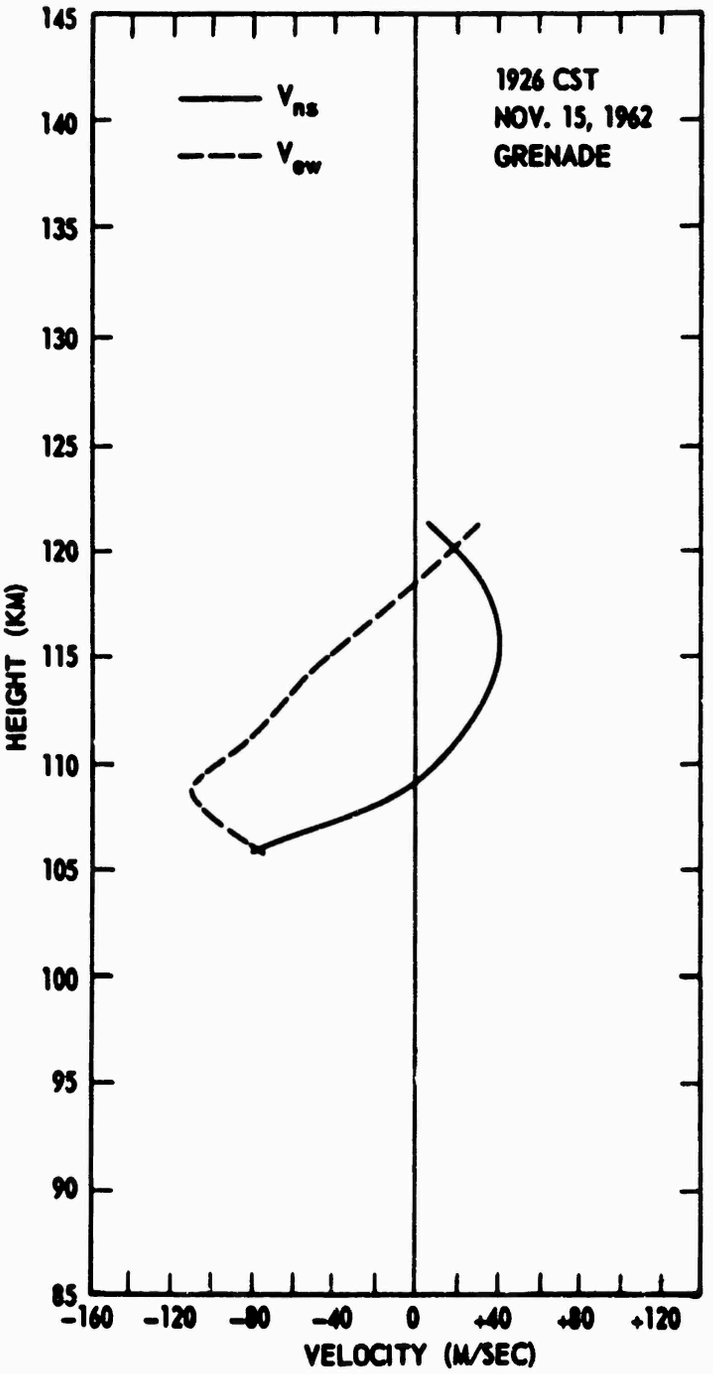

Figure A7. North-South and East-West Components of the Wind Velocity for KAREN

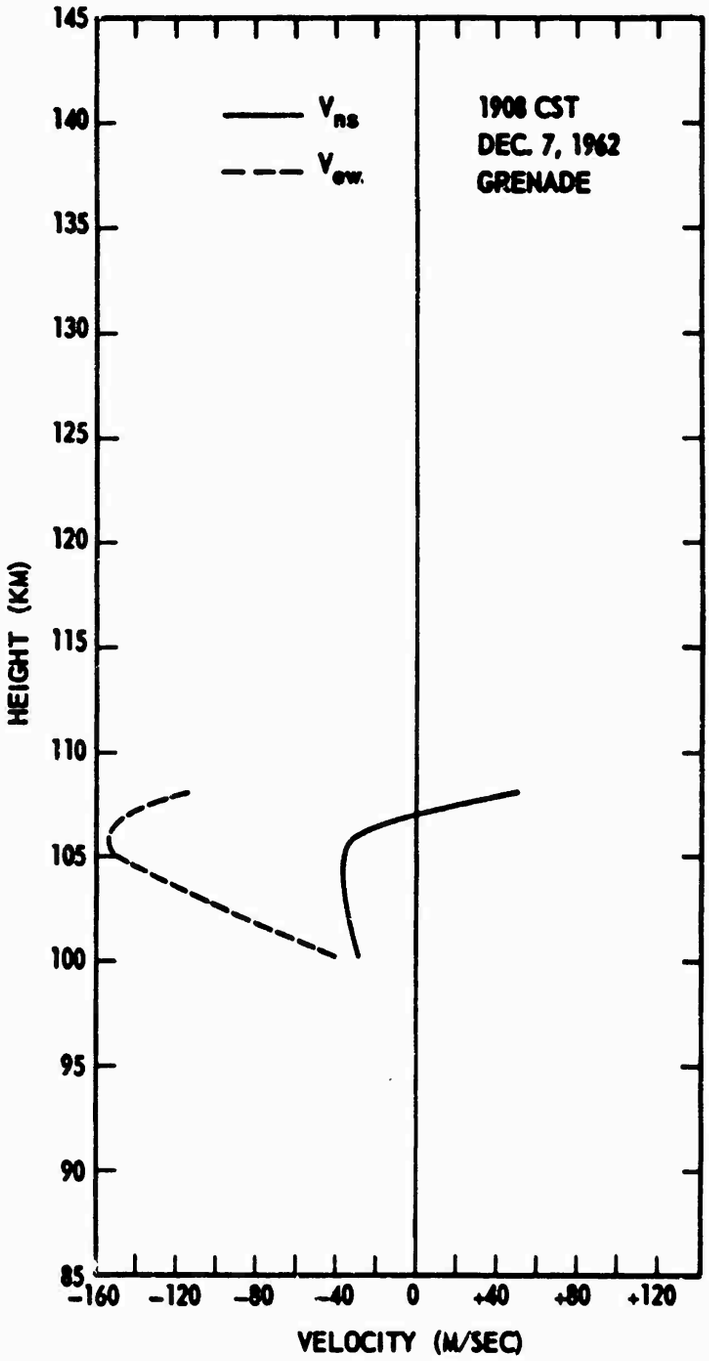

Figure A8. North-South and East-West Components of the Wind Velocity for LAURA

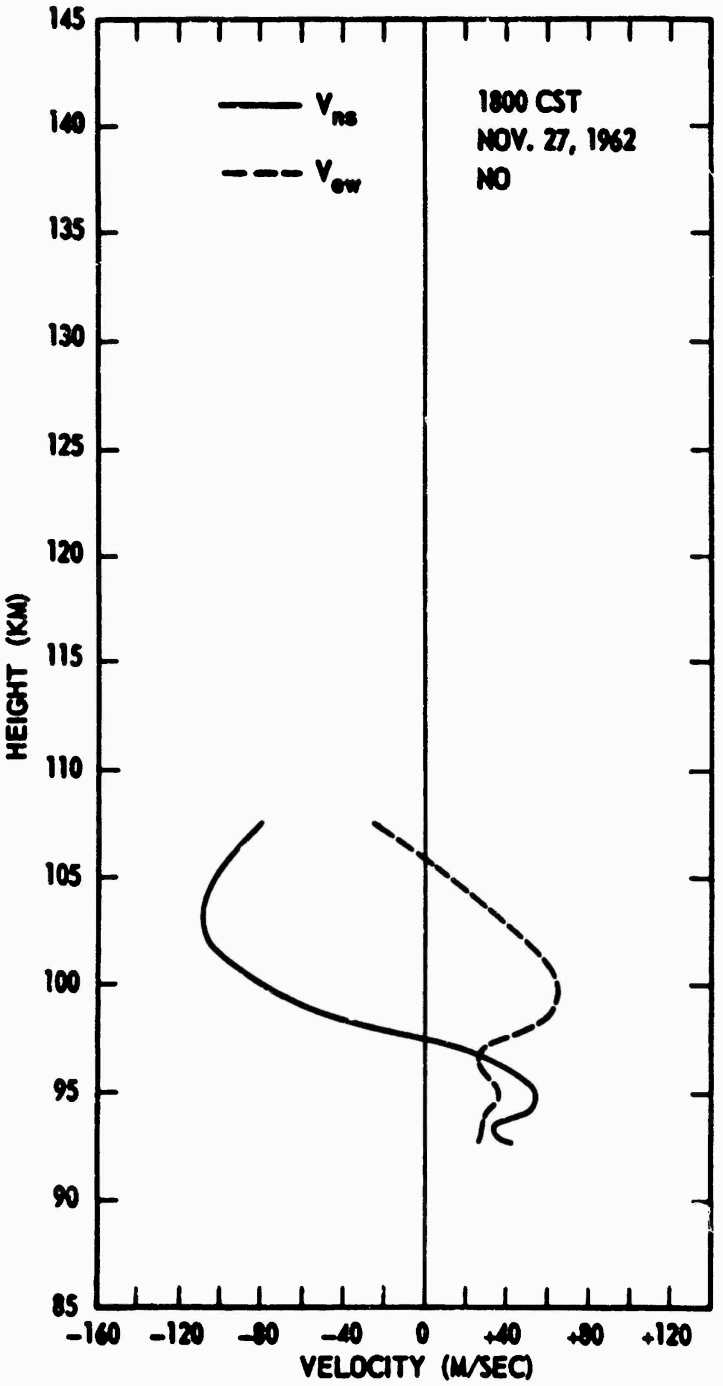

Figure A9. North-South and East-West Components of the Wind Velocity for MABEL

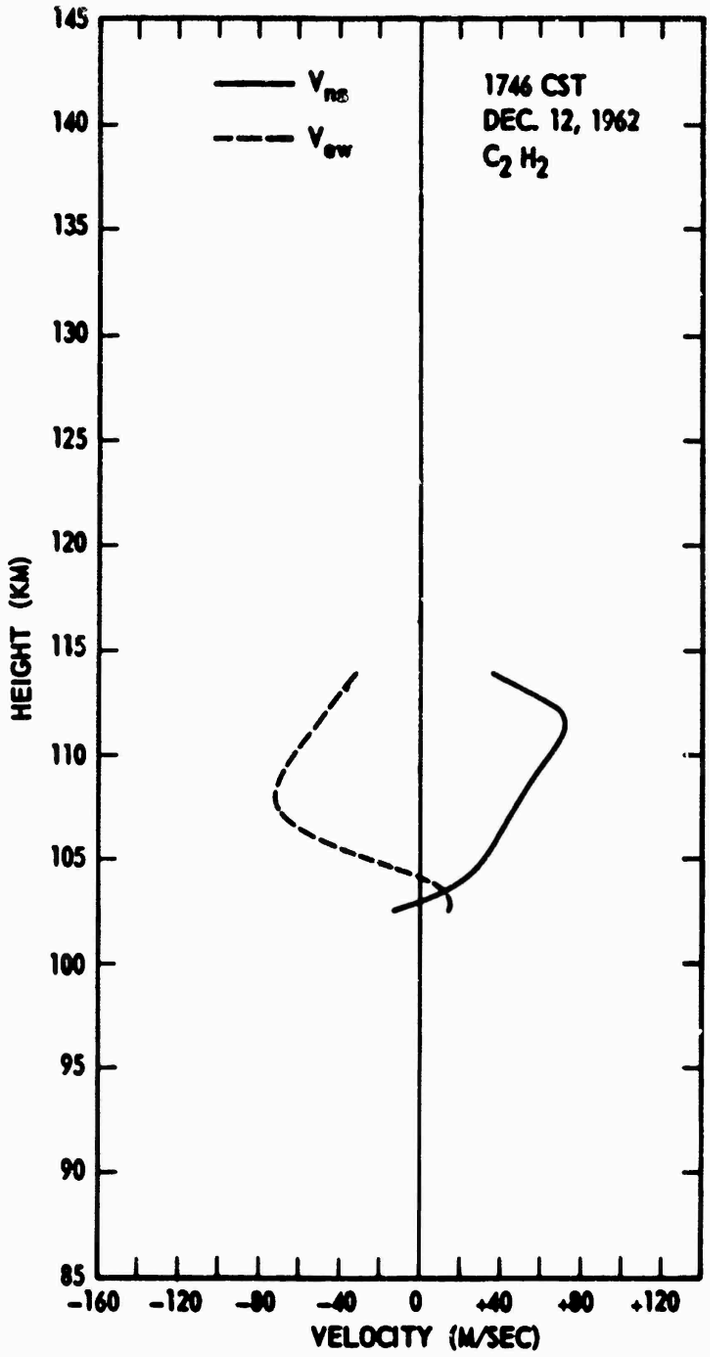

Figure A10. North-South and East-West Components of the Wind Velocity for NETTY

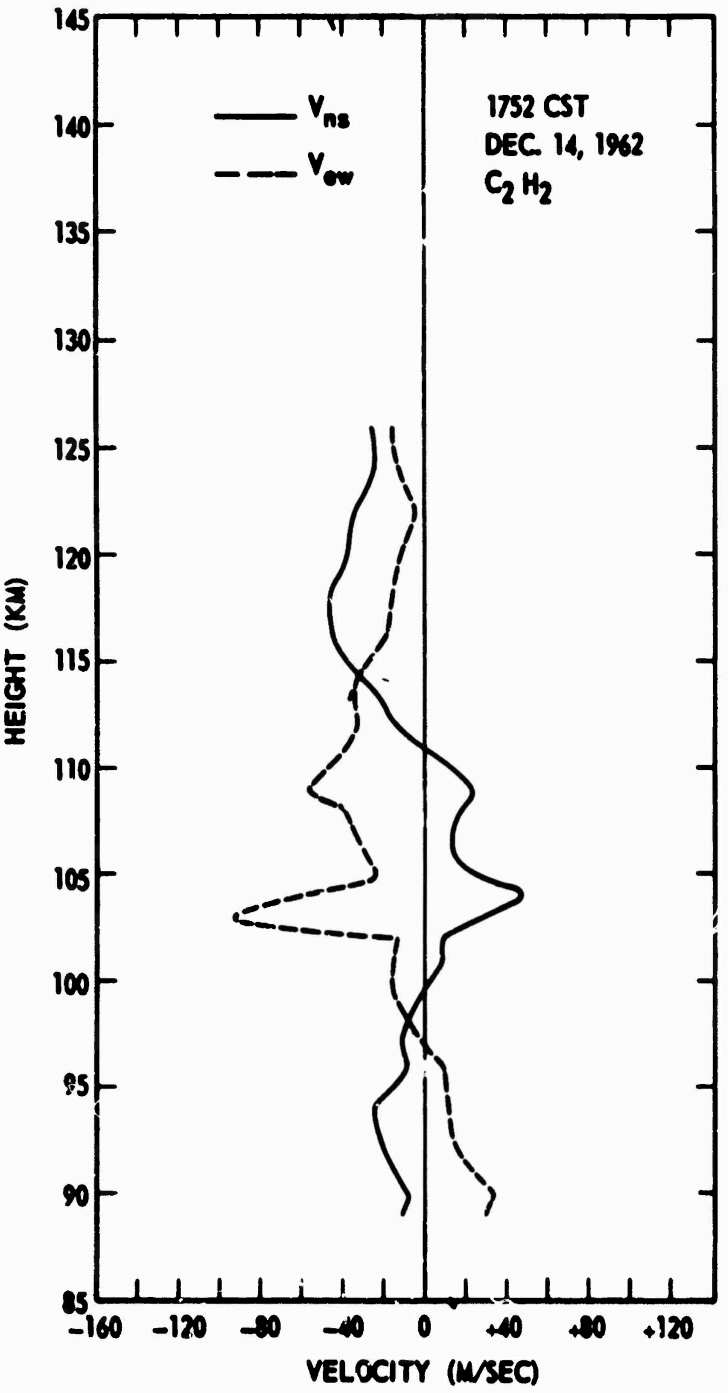

Figure A11. North-South and East-West Components of the Wind Velocity for OLGA

Appendix B

B.1 HORIZONTAL WIND VELOCITIES FOR FIVE TWILIGHT RELEASES

The horizontal wind velocities as a function of altitude for five twilight releases which took place during firefly III launchings (15 October 1962 to 15 December 1962) are presented in the following data and plots. Wind headings are given in degrees east of north. A minus sign indicates a wind component toward either the south or west.

BONNIE

LAUNCH DATE	LAUNCH TIME (CST)	PAYLOAD MATERIAL	HEIGHT (KM)	NORTH LATITUDE	WEST LONGITUDE
10-15-62	0515	TEC	90.47	30.2471	86.7267

HEIGHT (KM)	WIND HEADING (DEGREES)	HORIZONTAL WIND SPEED (M/S)	NORTH-SOUTH COMPONENT (M/S)	EAST-WEST COMPONENT (M/S)
90.5	16	55	53	15
91.0	20	61	58	21
91.9	28	68	61	32
92.0	25	67	60	29
92.7	32	70	59	37
93.0	40	73	55	47
94.0	55	78	45	64

BONNIE (CONTINUED)

HEIGHT (KM)	WIND HEADING (DEGREES)	HORIZONTAL WIND SPEED (M/S)	NORTH-SOUTH COMPONENT (M/S)	EAST-WEST COMPONENT (M/S)
95.0	53	73	45	58
95.5	72	80	24	76
96.0	78	83	18	81
96.8	84	88	9	87
97.0	87	85	4	84
97.8	91	86	-1	86
98.0	94	85	-6	85
100.0	104	84	-20	82
100.8	115	84	-36	76
101.4	117	92	-42	82
102.0	121	84	-43	72
102.0	109	83	-27	78
102.3	123	89	-48	75
103.0	129	74	-46	58
103.1	140	75	-57	49
104.5	216	22	-18	-13
104.7	248	30	-11	-28
104.8	229	32	-21	-24
104.9	244	36	-15	-32
105.0	235	40	-23	-33
105.0	248	41	-15	-38
105.1	234	36	-21	-29
105.3	238	39	-21	-33
105.9	228	50	-34	-37
106.0	224	51	-37	-35
106.9	199	59	-56	-19
107.0	193	67	-65	-15
107.1	195	63	-61	-17
107.5	188	63	-63	-8
107.7	182	70	-70	-2
108.0	177	95	-95	4
108.0	179	80	-80	1
108.5	174	96	-96	11
109.0	173	109	-109	13
109.1	171	110	-109	18
109.2	171	108	-106	17
109.3	173	119	-118	14
109.4	174	113	-113	12
109.9	170	115	-113	20
109.9	171	120	-119	19
110.0	175	103	-102	10
111.0	181	70	-70	-1
112.0	187	66	-66	-8
113.0	195	51	-49	-14
114.5	213	39	-33	-21
114.8	209	39	-34	-19
115.7	204	43	-40	-17
116.8	211	40	-34	-21

CINDY

LAUNCH DATE	LAUNCH TIME (CST)	PAYLOAD MATERIAL	HEIGHT (KM)	NORTH LATITUDE	WEST LONGITUDE
10-17-62	0516	TEC	86.60	30.2127	86.6903

HEIGHT (KM)	WIND HEADING (DEGREES)	HORIZONTAL WIND SPEED (M/S)	NORTH-SOUTH COMPONENT (M/S)	EAST-WEST COMPONENT (M/S)
87.0	67	62	24	56
87.8	72	57	18	54
88.0	71	49	16	47
89.0	38	48	38	30
89.7	32	68	58	36
90.0	41	62	47	41
91.0	38	91	72	55
91.4	46	93	65	66
92.0	60	94	42	76
93.0	70	104	35	99
94.0	70	113	38	107
94.0	73	109	32	104
95.0	79	110	20	108
96.0	93	107	-6	107
97.0	91	99	0	99
97.9	112	73	-27	68
98.0	101	77	-15	75
98.3	103	71	-16	69
99.0	103	71	-17	69
99.2	79	33	7	32
100.0	107	60	-17	57
100.4	341	31	30	-10
100.5	11	25	25	5
101.0	325	40	33	-23
101.8	324	50	40	-29
102.2	326	53	44	-29
102.5	325	50	41	-28
102.6	332	53	46	-26
102.6	325	58	47	-33
102.8	327	64	54	-35
103.0	334	57	50	-25
103.0	327	50	40	-27
103.5	331	60	52	-29
103.5	331	64	56	-31
104.0	338	54	50	-21
104.3	335	63	58	-27
104.3	335	66	60	-27
104.7	339	63	59	-22
104.7	349	63	62	-12
105.0	330	66	57	-32
105.3	343	64	61	-18
105.4	347	68	65	-16
105.5	346	61	59	-15
105.6	353	66	65	-9
105.7	4	61	61	4

CINDY (CONTINUED)

HEIGHT (KM)	WIND HEADING (DEGREES)	HORIZONTAL WIND SPEED (M/S)	NORTH-SOUTH COMPONENT (M/S)	EAST-WEST COMPONENT (M/S)
105.8	9	56	56	8
105.8	10	59	58	11
105.9	15	53	51	13
106.0	17	54	51	15
106.0	23	57	52	21
106.6	37	58	46	35
106.7	65	35	15	31
106.8	91	30	0	30
107.0	98	32	-4	31
107.0	100	39	-7	38
107.1	134	42	-29	30
107.2	121	44	-23	37
107.5	131	44	-28	33
107.8	141	50	-39	31
107.9	151	62	-54	30
108.0	156	76	-69	31
108.0	143	59	-47	30
108.3	157	87	-80	34
108.5	161	96	-91	31
108.6	161	93	-88	30
109.0	163	97	-93	28
109.0	159	84	-78	30
109.7	174	87	-86	10
110.0	167	74	-62	15
111.0	171	88	-87	12
111.3	185	80	-79	-7
112.0	177	88	-88	4
113.7	203	84	77	-32

GILDA

LAUNCH DATE	LAUNCH TIME (CST)	PAYLOAD MATERIAL		HEIGHT (KM)	NORTH LATITUDE	WEST LONGITUDE
11-13-62	1730	HEX-PEC	(1)	136.71	30.1144	86.7357
			(2)	154.16	30.0686	86.7407
			(3)	242.7	29.721	86.785
			(4)	236.07	29.2524	86.8597

HEIGHT (KM)	WIND HEADING (DEGREES)	HORIZONTAL WIND SPEED (M/S)	NORTH-SOUTH COMPONENT (M/S)	EAST-WEST COMPONENT (M/S)
150.0	150	60	-52	30
152.0	143	55	-44	33
154.0	135	55	-39	40

GILDA (CONTINUED)

HEIGHT (KM)	WIND HEADING (DEGREES)	HORIZONTAL WIND SPEED (M/S)	NORTH-SOUTH COMPONENT (M/S)	EAST-WEST COMPONENT (M/S)
156.0	129	57	-36	44
156.3	130	53	-34	41
158.0	125	56	-32	46
160.0	118	55	-26	49
162.0	115	56	-23	51
164.0	108	55	-17	53
217.8	30	76	66	39

KITTY

LAUNCH DATE	LAUNCH TIME (CST)	PAYLOAD MATERIAL	HEIGHT (KM)	NORTH LATITUDE	WEST LONGITUDE
10-23-62	0519	SPEC	107.74	30.0369	86.6721

HEIGHT (KM)	WIND HEADING (DEGREES)	HORIZONTAL WIND SPEED (M/S)	NORTH-SOUTH COMPONENT (M/S)	EAST-WEST COMPONENT (M/S)
105.5	288	83	26	-79
105.6	281	85	16	-84
105.8	286	86	24	-83
106.0	283	83	19	-81
106.4	272	79	3	-79
108.1	230	37	-23	-28
108.5	185	68	-68	-6
108.5	217	41	-33	-25
108.6	191	48	-48	-9
108.8	185	79	-79	-6
109.1	178	87	-87	3
109.4	178	79	-79	3
110.3	179	94	-94	1
111.0	188	100	-99	-14
112.3	197	93	-89	-28
113.1	215	83	-67	-48
113.8	289	67	21	-64
114.4	274	78	5	-78

SHARON

LAUNCH DATE	LAUNCH TIME (CST)	PAYLOAD MATERIAL	HEIGHT (KM)	NORTH LATITUDE	WEST LONGITUDE
12-3-62	1720	SODIUM	69.90	30.2717	86.6886

HEIGHT (KM)	WIND HEADING (DEGREES)	HORIZONTAL WIND SPEED (M/S)	NORTH-SOUTH COMPONENT (M/S)	EAST-WEST COMPONENT (M/S)
70.5	45	33	23	23
92.7	207	65	-58	-29
93.4	216	65	-53	-38
94.0	223	72	-52	-49
94.1	237	57	-31	-48
95.0	242	55	-26	-48
96.0	286	19	5	-18
96.5	286	10	3	-9
97.0	12	2	2	1
97.4	78	36	8	35
98.0	81	56	11	72
99.0	83	79	9	78
100.0	88	101	1	100
101.0	91	108	-2	108
102.0	100	119	-20	117
103.0	105	128	-34	122
103.8	106	131	-37	126
104.0	107	133	-39	126
105.0	107	127	-35	121
106.0	106	110	-30	105
107.0	109	96	-29	91
107.5	118	62	-25	55
108.0	139	29	-22	19
108.5	185	21	-21	2
109.0	247	59	-22	-55
110.0	254	59	-14	-57
110.7	257	67	-15	-65
112.0	267	63	-3	-63
115.0	285	66	17	-59
120.0	315	52	36	-36
125.0	348	29	28	-7
130.0	50	19	12	13
135.0	85	31	2	31

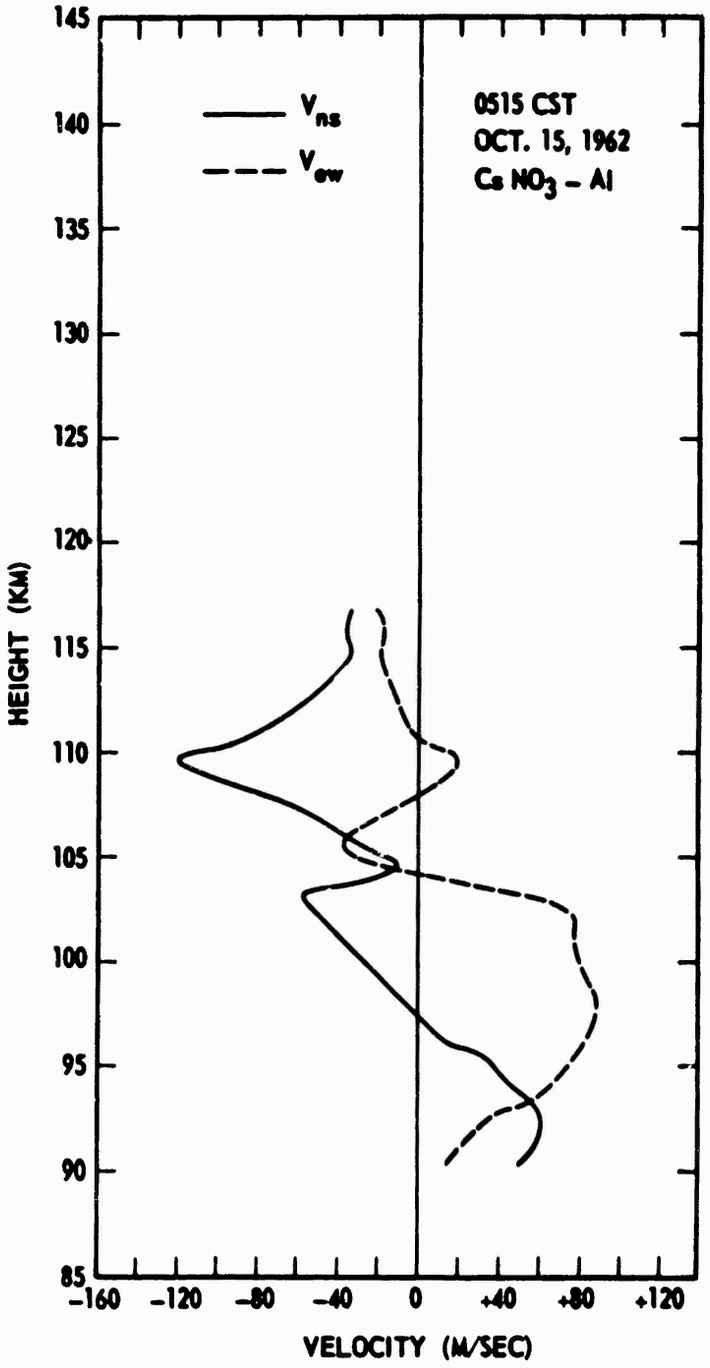

Figure B1. North-South and East-West Components of the Wind Velocity for BONNIE

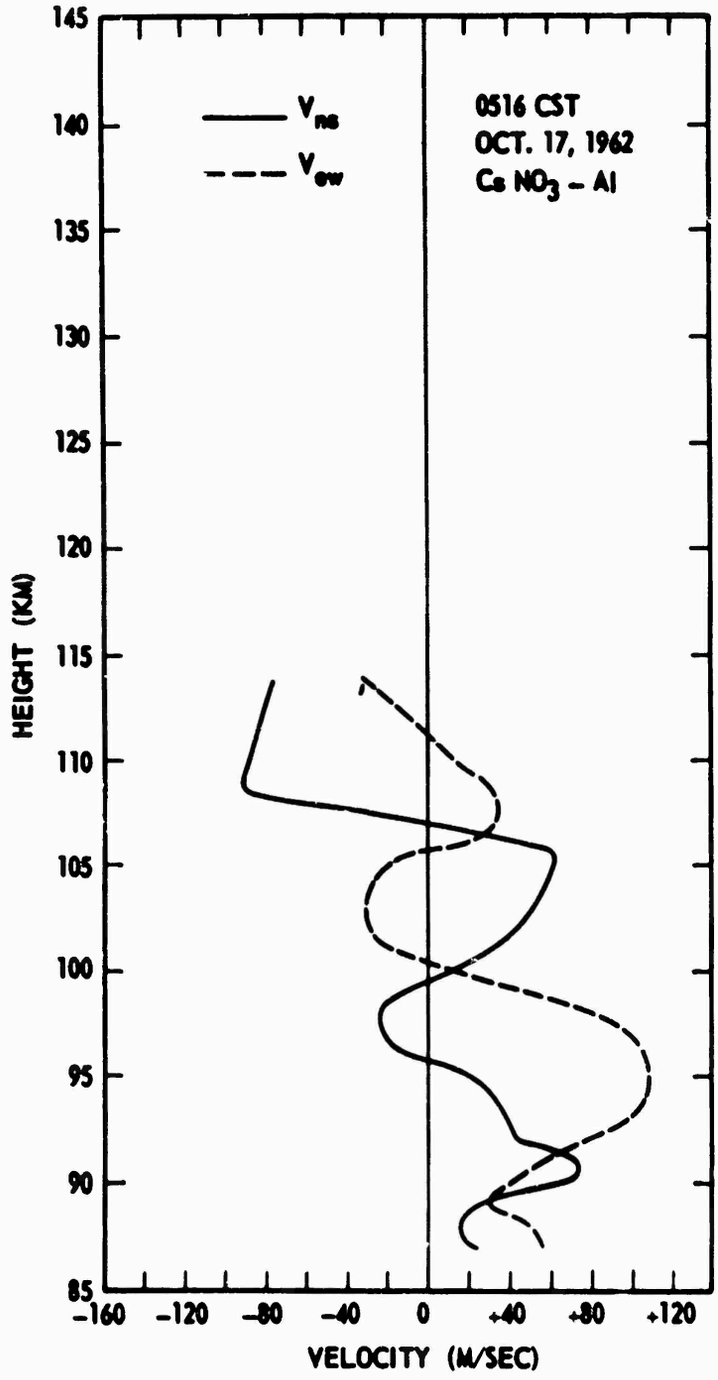

Figure B2. North-South and East-West Components of the Wind Velocity for CINDY

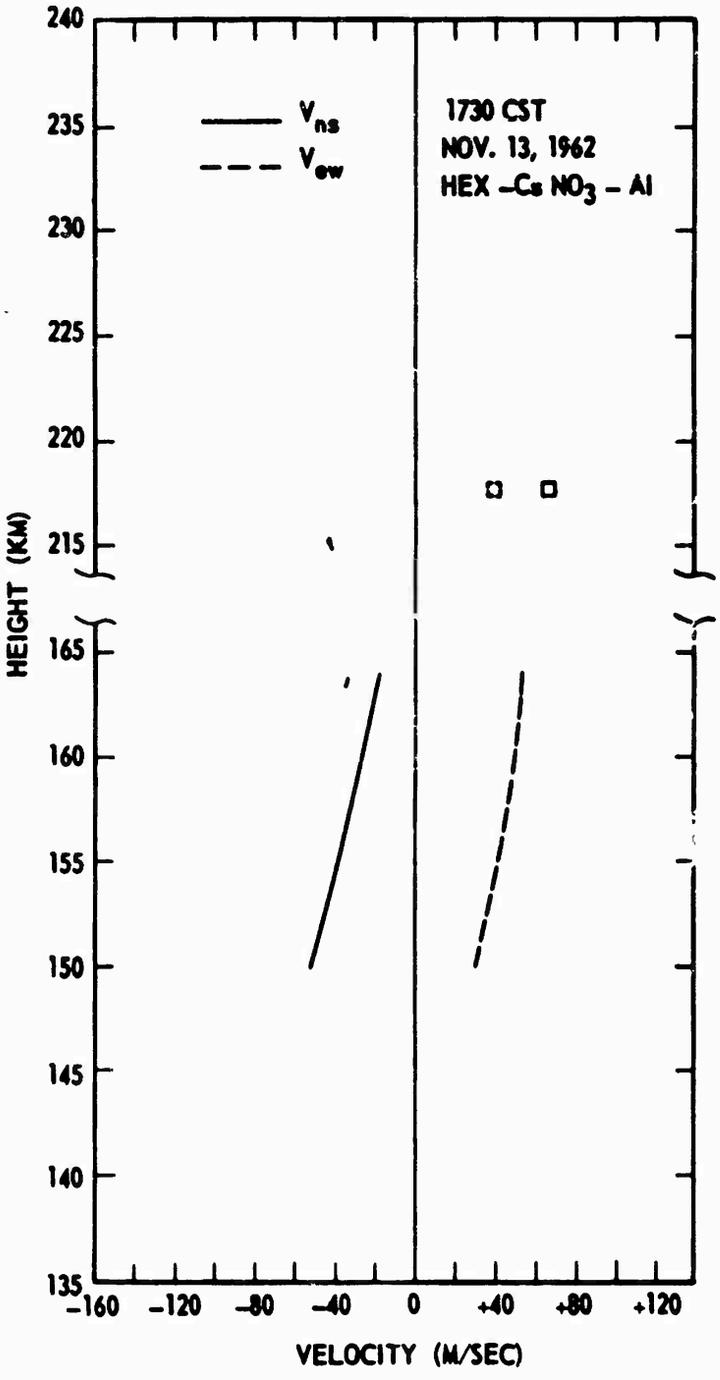

Figure B3. North-South and East-West Components of the Wind Velocity for GILDA

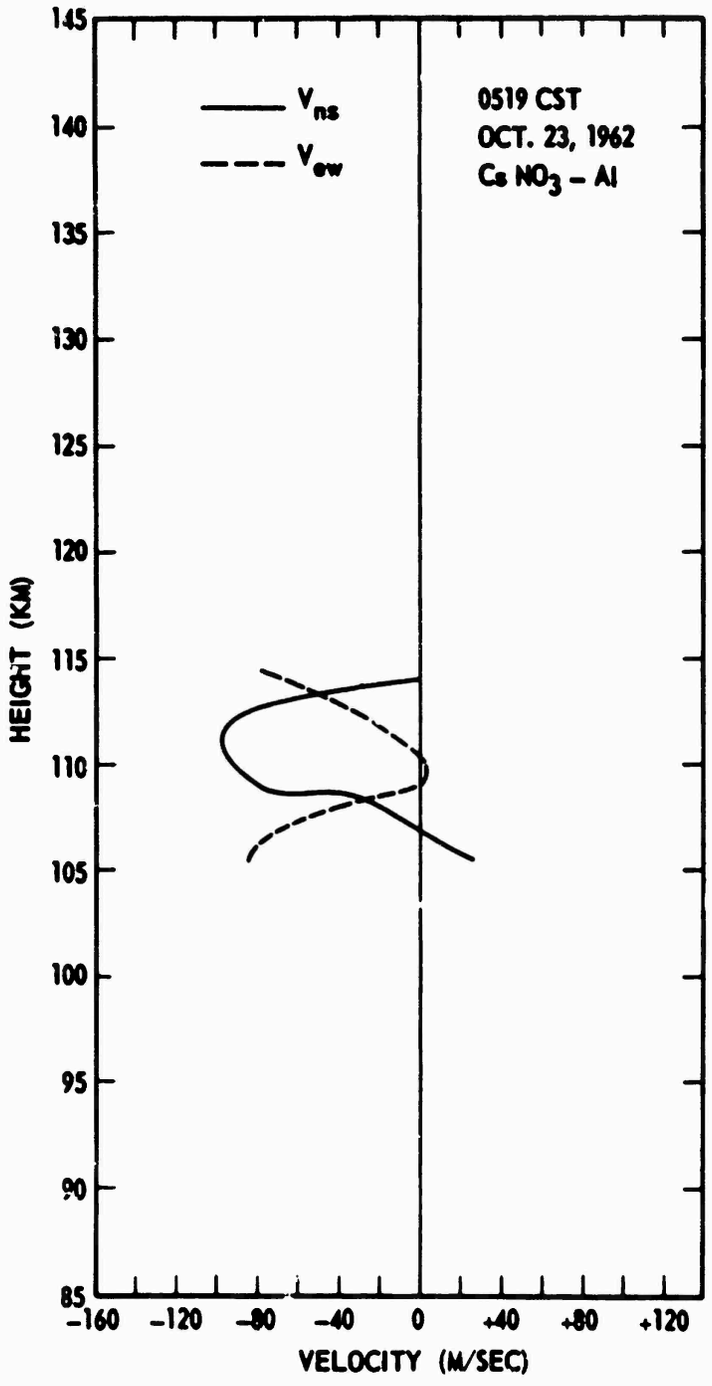

Figure B4. North-South and East-West Components of the Wind Velocity for KITTY

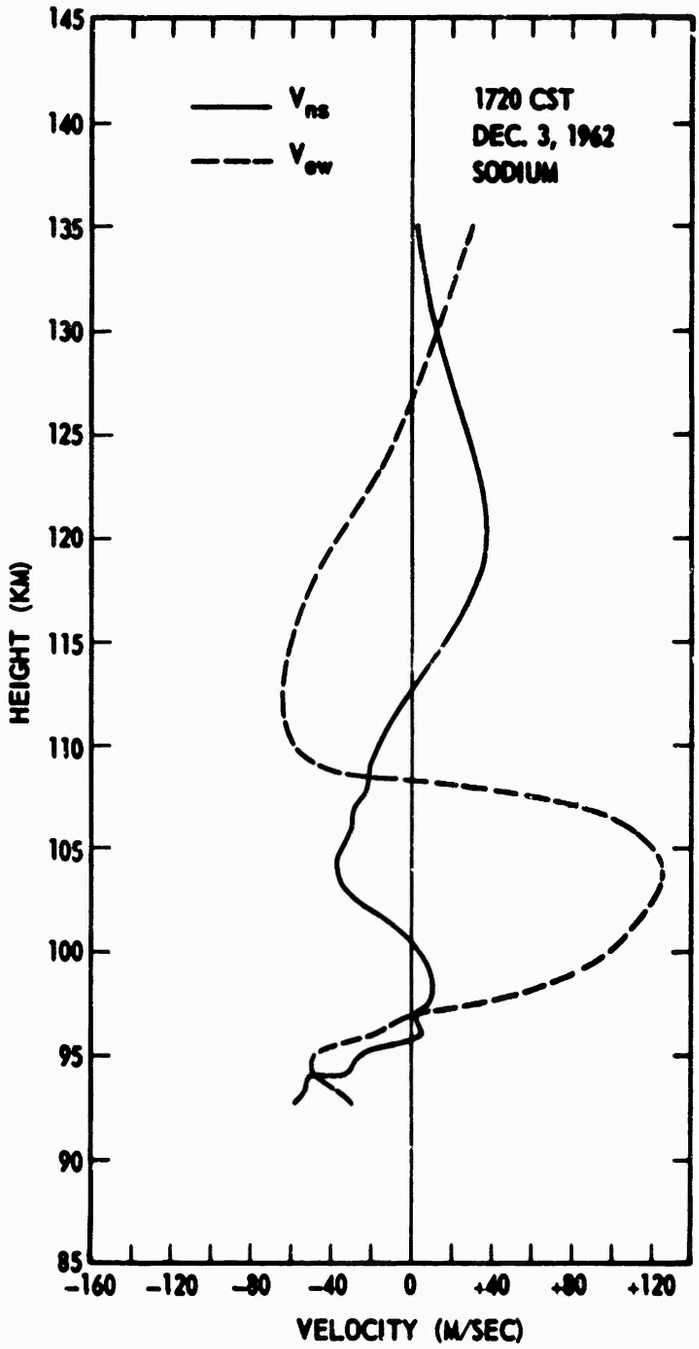

Figure B5. North-South and East-West Components of the Wind Velocity for SHARON

Appendix C

C.1 HORIZONTAL WIND VELOCITIES FOR THE SIX RELEASES IN MAY

The horizontal wind velocities as a function of altitude for the six releases which took place from 15 May to 21 May 1963 are presented in the following data and plots. Wind headings are given in degrees east of north. A minus sign indicates a wind component toward either the south or west.

CLAIR

LAUNCH DATE	LAUNCH TIME (CST)	PAYLOAD MATERIAL	HEIGHT (KM)	NORTH LATITUDE	WEST LONGITUDE
5-15-63	2000	TMA	95.19	30.2658	86.6916

HEIGHT (KM)	WIND HEADING (DEGREES)	HORIZONTAL WIND SPEED (M/S)	NORTH-SOUTH COMPONENT (M/S)	EAST-WEST COMPONENT (M/S)
96.0	57	64	35	54
97.0	52	78	48	61
98.0	46	81	56	58
98.3	45	79	56	56
99.0	55	66	38	56
99.0	50	74	48	57
100.0	63	53	24	47
100.0	58	62	33	52

CLAIR (CONTINUED)

HEIGHT (KM)	WIND HEADING (DEGREES)	HORIZONTAL WIND SPEED (M/S)	NORTH-SOUTH COMPONENT (M/S)	EAST-WEST COMPONENT (M/S)
100.6	70	45	15	42
100.7	56	42	24	35
101.0	69	35	13	33
101.3	65	47	20	42
101.8	84	25	3	25
101.9	147	31	-26	17
102.1	81	29	5	29
102.2	157	35	-32	14
102.2	154	33	-30	14
102.3	166	30	-29	7
102.3	160	36	-63	12
102.3	146	18	-15	10
102.4	100	19	-4	19
102.4	162	30	-29	9
103.5	166	28	-27	6
103.7	185	28	-27	-2
103.7	165	26	-25	7
103.8	116	38	-37	9
104.3	192	39	-38	-8
104.9	196	30	-28	-9
105.0	195	29	-28	-8
105.1	194	36	-35	-8
105.4	201	29	-27	-11
106.0	225	21	-15	-15
107.0	233	21	-13	-17
108.0	244	10	-4	-9
109.0	319	43	32	-28
110.0	295	44	19	-40
111.0	329	22	19	-11
112.0	283	28	6	-27
113.0	266	51	-4	-50

SARAH

LAUNCH DATE	LAUNCH TIME (CST)	PAYLOAD MATERIAL	HEIGHT (KM)	NORTH LATITUDE	WEST LONGITUDE
5-17-63	1906	SODIUM	76.6 *	30.275	86.732

HEIGHT (KM)	WIND HEADING (DEGREES)	HORIZONTAL WIND SPEED (M/S)	NORTH-SOUTH COMPONENT (M/S)	EAST-WEST COMPONENT (M/S)
71.4	234	53	-31	-43
74.6	264	27	-3	-27

* - LOWEST POINT DETERMINED ON THE TRAIL AT T+67 SEC.

SARAH (CONTINUED)

HEIGHT (KM)	WIND HEADING (DEGREES)	HORIZONTAL WIND SPEED (M/S)	NORTH-SOUTH COMPONENT (M/S)	EAST-WEST COMPONENT (M/S)
75.8	302	30	16	-26
76.0	240	53	-27	-46
80.6	300	72	38	-65
82.0	336	68	62	-27
83.0	90	53	0	53
83.4	88	64	2	64
85.4	101	64	-12	63
88.1	93	84	-5	83
91.0	143	74	-59	45
91.4	141	72	-47	46
91.8	153	66	-58	30
91.9	147	67	-56	36
92.1	149	74	-64	38
92.6	162	63	-61	19
95.3	312	14	9	-10
95.6	316	16	12	-11
96.0	278	12	2	-12
98.0	193	74	-72	-15
98.1	194	69	-67	-15
100.0	211	77	-67	-30
102.0	212	58	-49	-60
103.0	219	51	-39	-32
104.0	212	31	-26	-16
105.0	182	28	-27	-1
105.0	175	27	-26	2
105.0	175	27	-26	2
105.3	196	16	-15	-4
106.0	334	13	11	-6
107.0	345	41	40	-11
108.0	346	73	70	-17
108.3	344	80	77	-21
109.0	345	79	76	-21
109.0	343	75	71	-23
110.0	354	99	96	-5
110.0	354	99	96	-5
111.0	6	125	124	12
112.0	7	136	134	17
114.0	14	166	160	40
115.4	15	170	164	44
116.0	15	173	168	44
118.0	14	164	159	39
120.0	12	93	91	16
122.0	22	39	36	15
125.0	175	84	-83	8
130.0	178	155	-154	5
135.0	184	192	-191	-15
135.5	185	203	-202	-18
145.0	187	179	-176	-23
150.0	194	151	-147	-36
155.0	195	123	-119	-33
160.0	204	110	-90	-45
165.0	203	79	-72	-31
170.0	203	62	-60	-24

STELLA

LAUNCH DATE	LAUNCH TIME (CST)	PAYLOAD MATERIAL	HEIGHT (KM)	NORTH LATITUDE	WEST LONGITUDE
5-17-63	2218	NO2,TOC	93.83	30.1400	86.6944

HEIGHT (KM)	WIND HEADING (DEGREES)	HORIZONTAL WIND SPEED (M/S)	NORTH-SOUTH COMPONENT (M/S)	EAST-WEST COMPONENT (M/S)
95.0	139	25	-19	17
96.0	168	26	-26	6
97.0	175	24	-24	2
98.0	186	22	-22	-2
99.0	198	20	-19	-6
100.0	213	17	-14	-9
101.0	210	10	-9	-5
102.0	115	7	-3	7
103.0	90	23	0	23
104.0	116	26	-7	25
105.0	121	33	-17	29
105.7	154	18	-16	8
106.0	146	18	-15	10
107.0	5	40	40	3
107.7	23	77	71	30
108.0	26	85	77	37
109.0	46	98	68	70
110.0	59	110	57	94
111.0	65	111	47	100
112.0	72	98	31	93
113.0	79	82	16	80
114.0	90	67	0	67
117.4	165	88	-85	23
120.0	191	122	-120	-24
122.1	201	147	-137	-52
125.0	210	141	-122	-70
130.0	214	117	-97	-66

DORIS

LAUNCH DATE	LAUNCH TIME (CST)	PAYLOAD MATERIAL	HEIGHT (KM)	NORTH LATITUDE	WEST LONGITUDE
5-18-63	0255	TMA,TOC	91.73	30.1694	86.6551

HEIGHT (KM)	WIND HEADING (DEGREES)	HORIZONTAL WIND SPEED (M/S)	NORTH-SOUTH COMPONENT (M/S)	EAST-WEST COMPONENT (M/S)
93.4	89	67	1	68
94.0	85	67	7	66
95.0	87	70	3	70
96.0	97	65	-8	64
96.4	102	65	-14	64
97.0	104	64	-15	61
98.0	108	69	-31	64
99.0	109	70	-28	66
99.5	114	76	-30	69
100.0	109	76	-25	71
101.0	125	89	-51	74
101.4	132	93	-62	67
102.0	129	98	-62	77
103.0	122	105	-53	82
104.0	132	113	-75	84
105.0	156	122	-112	50
106.0	168	131	-128	30
107.0	199	111	-106	-36
108.0	207	103	-91	-47
109.0	220	93	-71	-60
110.0	226	94	-65	-68
111.0	243	101	-45	-90
112.0	254	100	-29	-96
112.7	263	100	-12	-99
113.0	261	93	-15	-92
114.0	262	101	-14	-100

BLANCHE

LAUNCH DATE	LAUNCH TIME (CST)	PAYLOAD MATERIAL	HEIGHT (KM)	NORTH LATITUDE	WEST LONGITUDE
5-18-[illegible]3	0406	SODIUM	93.5 *	30.205	86.715

HEIGHT (KM)	WIND HEADING (DEGREES)	HORIZONTAL WIND SPEED (M/S)	NORTH-SOUTH COMPONENT (M/S)	EAST-WEST COMPONENT (M/S)
99.0	165	28	-27	7
101.0	191	50	-49	-10
102.0	225	95	-67	-67
103.0	235	97	-56	-79
104.0	251	87	-29	-82
105.0	245	86	-36	-78
106.0	245	85	-36	-77
107.0	244	83	-36	-75
108.0	248	81	-31	-75
109.0	254	80	-22	-76
110.0	270	83	0	-83
111.0	288	87	27	-83
112.0	305	90	52	-73
113.0	319	100	75	-65
114.0	329	112	95	-58
115.0	332	115	102	-53
116.0	338	107	99	-40
117.0	340	97	92	-33
118.0	342	99	94	-30
119.0	346	96	93	-24
120.0	349	91	90	-17
122.0	8	91	90	13
124.0	14	92	89	22
126.0	20	90	84	31
128.0	23	78	72	30
130.0	25	61	55	25
132.0	20	57	53	20
134.0	21	38	36	14
136.0	24	26	24	11
249*1	55	28	24	23
138.0	44	17	13	12
140.0	92	15	0	15
145.0	146	16	-12	9
150.0	146	23	-19	13
155.0	165	41	-40	11
160.0	174	58	-58	6
165.0	181	72	-72	-2

---

* - LOWEST POINT DETERMINED ON THE TRAIL AT T+97 SEC.

IRENE

LAUNCH DATE	LAUNCH TIME (CST)	PAYLOAD MATERIAL	HEIGHT (KM)	NORTH LATITUDE	WEST LONGITUDE
5-21-63	1910	SODIUM	69.2 *	30.301	86.703

HEIGHT (KM)	WIND HEADING (DEGREES)	HORIZONTAL WIND SPEED (M/S)	NORTH-SOUTH COMPONENT (M/S)	EAST-WEST COMPONENT (M/S)
69.2	255	33	-9	-32
70.8	257	30	-7	-29
71.4	273	26	1	-26
72.4	275	43	4	-43
72.7	288	20	6	-19
77.1	255	43	-11	-41
80.5	358	27	27	-1
81.7	312	8	5	-5
82.2	204	28	-26	-12
83.4	199	27	-25	-9
83.9	192	53	-52	-11
85.3	195	53	-51	-14
85.7	107	32	-9	30
88.1	78	59	12	58
91.6	97	70	-8	69
95.2	178	54	-54	2
96.0	124	42	-23	34
97.0	147	55	-46	30
98.0	116	43	-19	38
99.0	86	45	3	44
99.5	76	64	16	62
100.0	69	58	21	54
101.0	68	66	26	61
102.0	78	79	18	75
103.0	94	94	-7	92
104.0	106	111	-30	105
104.3	111	125	-45	117
105.0	125	126	-71	103
106.0	127	141	-85	113
106.1	131	130	-85	98
107.0	135	122	-86	87
108.0	143	92	-73	56
109.0	159	54	-50	20
110.0	238	43	-23	-36
111.0	249	59	-21	-55
113.0	265	66	-7	-65
113.8	276	90	10	-89
115.0	272	72	3	-72
120.0	283	73	15	-72
125.0	288	47	14	-45
130.0	295	31	13	-27
135.0	307	14	9	-11
140.0	315	15	10	-11

* - LOWEST POINT DETERMINED ON THE TRAIL AT T+63 SEC.

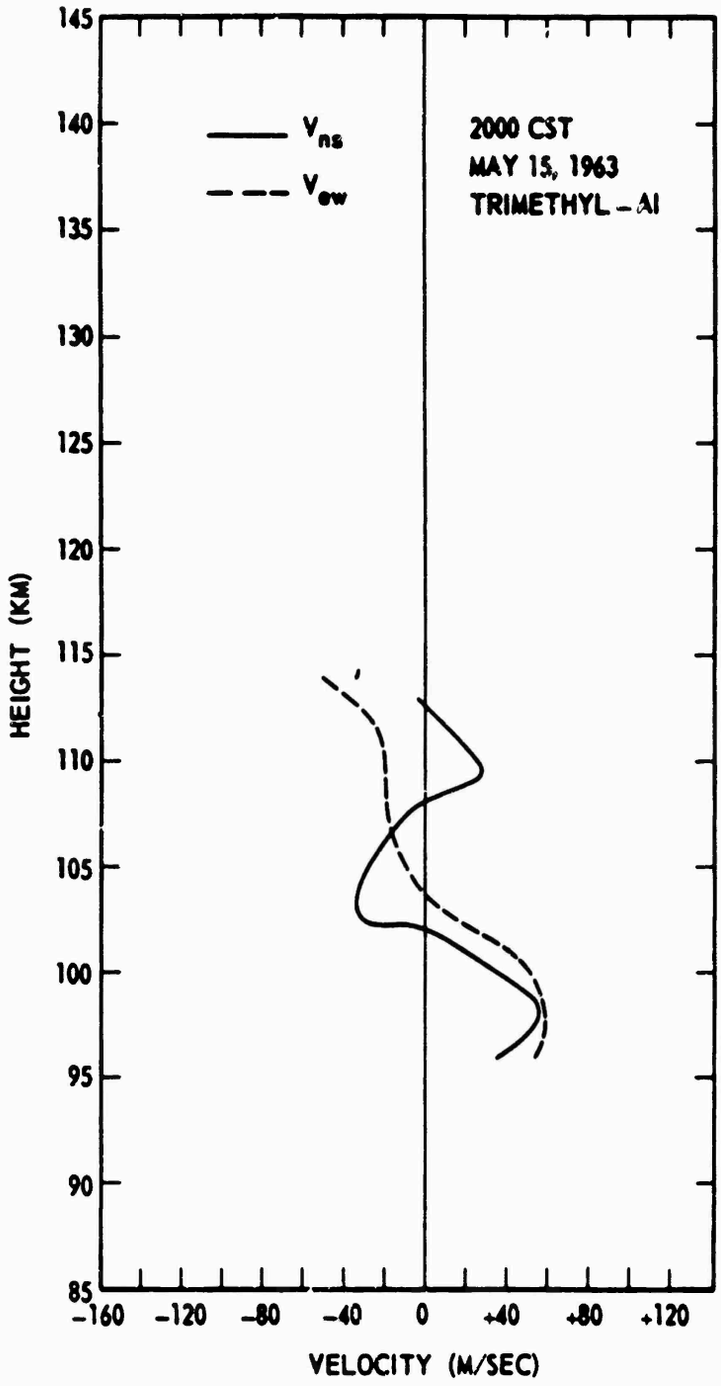

Figure C1. North-South and East-West Components of the Wind Velocity for CLAIR

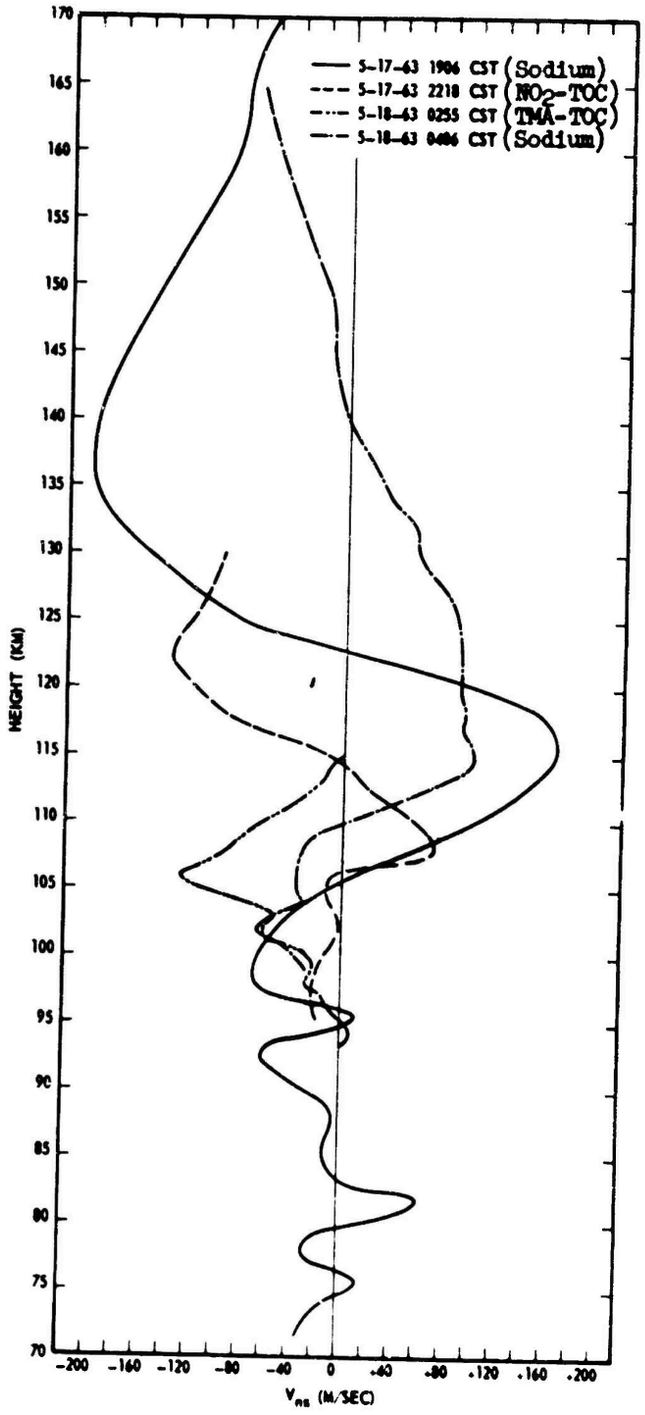

Figure C2. North-South Component of the Wind Velocity for Four Chemical Releases During the Night of May 17, 1963 - SARAH, STELLA, DORIS, and BLANCHE

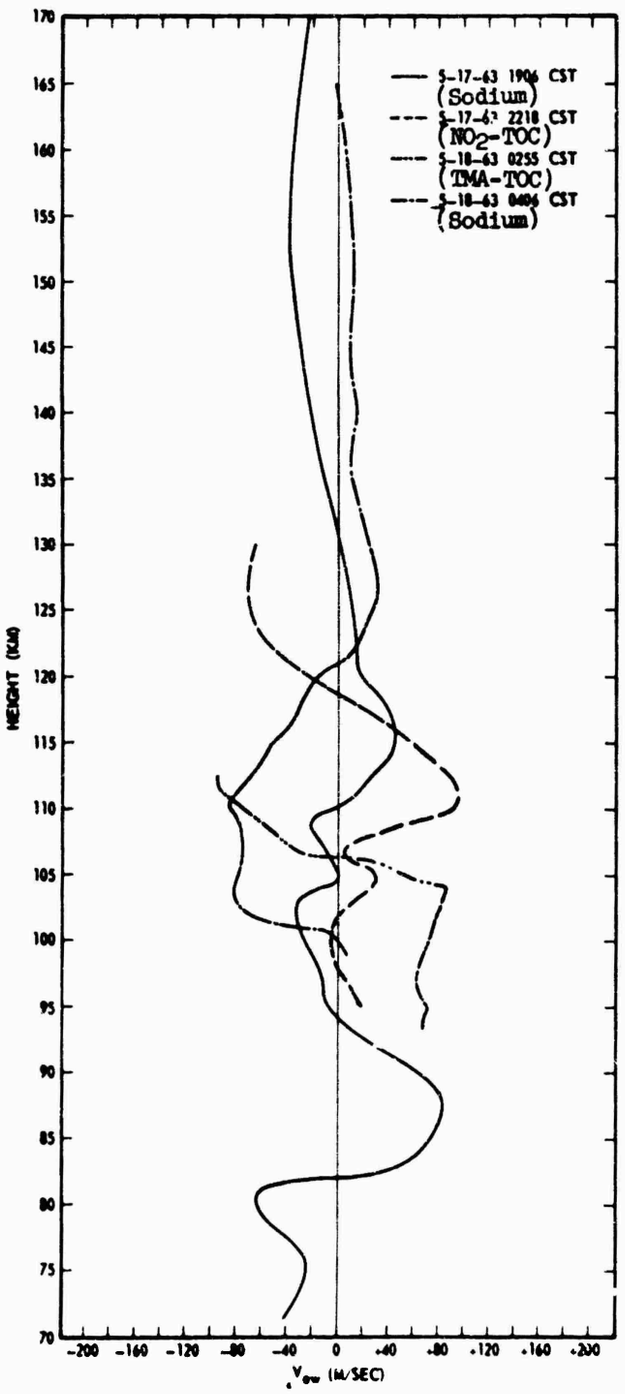

Figure C3. East-West Component of the Wind Velocity for Four Chemical Releases During the Night of May 17, 1963 - SARAH, STELLA, DORIS, and BLANCHE

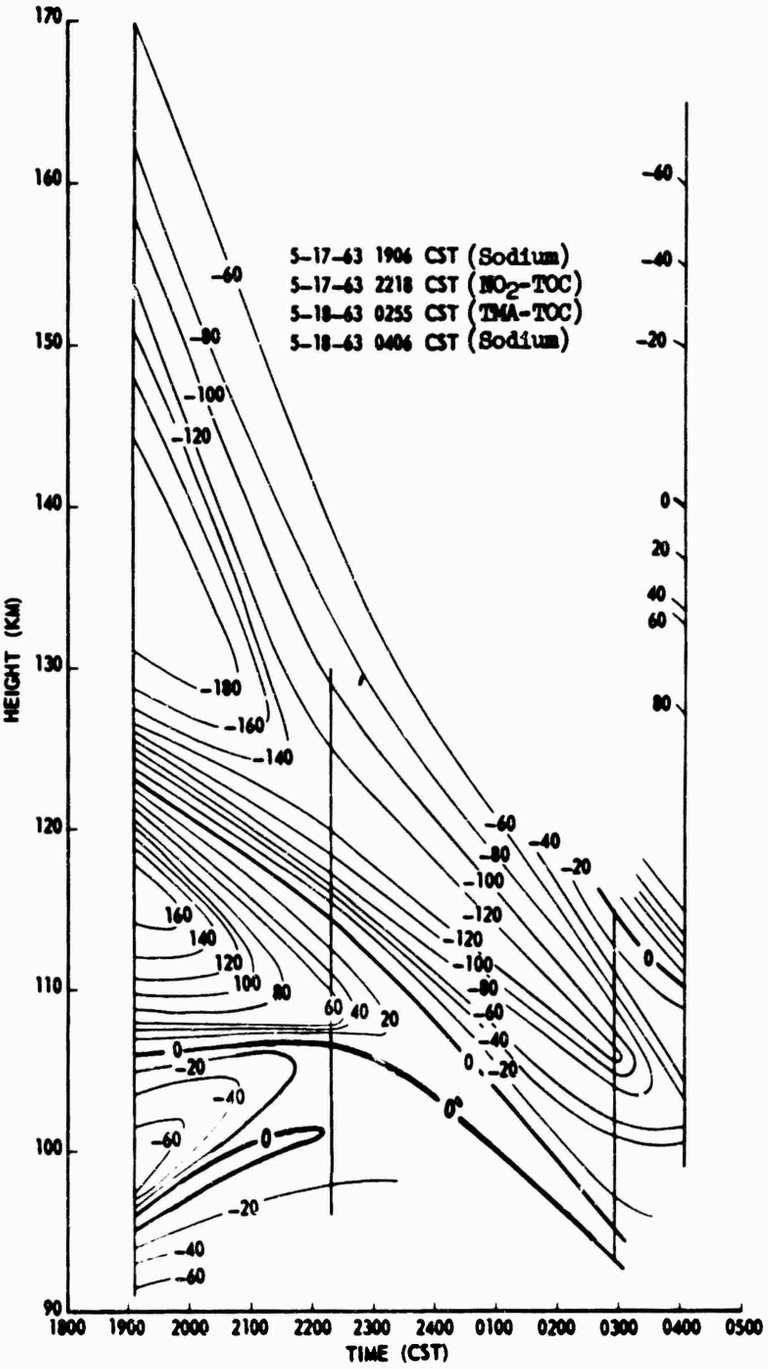

Figure C4. Contour of the North-South Component of the Wind Velocity for the Night of May 17, 1963 - SARAH, STELLA, DORIS, and BLANCHE

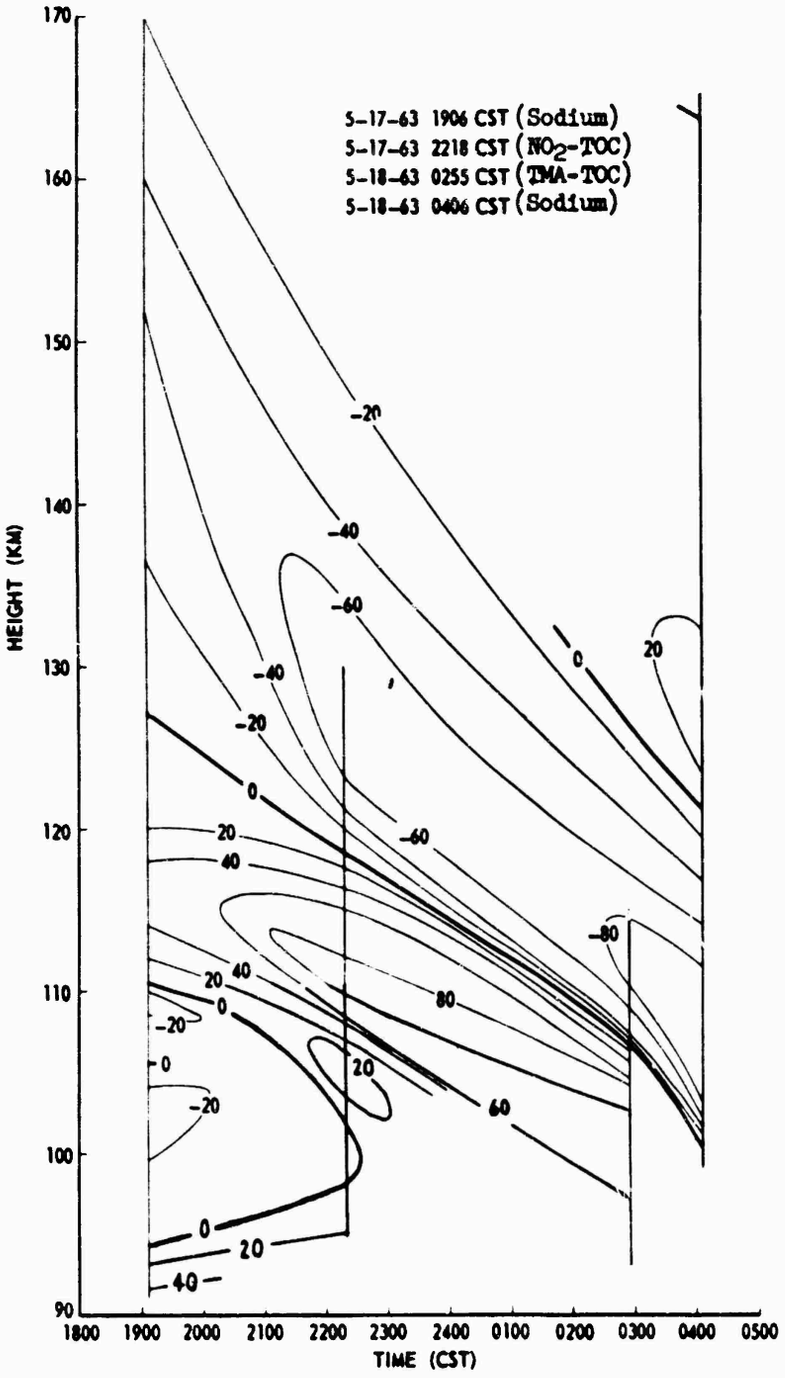

Figure C5. Contour of the East-West Component of the Wind Velocity for the Night of May 17, 1963 - SARAH, STELLA, DORIS, and BLANCHE

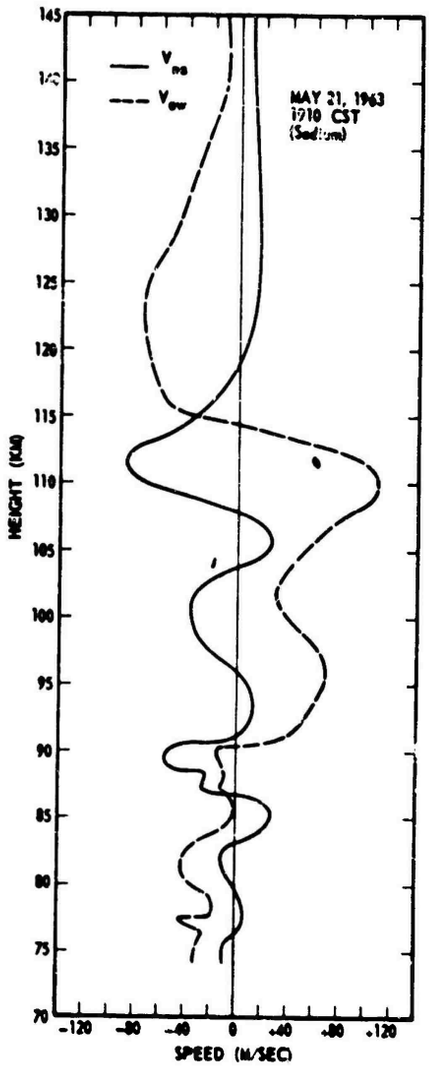

Figure C6. North-South & East-West Component of the Wind Velocity for the Chemical Release of May 21, 1963 for IRENE

IV. Photography and Photometry from Luminous Chemical Releases*

R. B. Holt
Device Development Corporation
Weston, Massachusetts

Abstract

A major new approach to the problem of the interpretation and analysis of photo-optical and other types of data gathered during the Project Firefly series of vertical probe launches has been initiated. These new techniques involve the use of electronic data processing methods and equipment and are expected to make possible data analysis of a nature and extent not heretofore feasible and to greatly reduce the time and cost involved in future data analysis work. Essentially all of the organization and planning of the electronic data processing approach to this problem has been completed. Data has been extracted from films obtained during a number of Firefly experiments and has been converted into computer input forms. Several analytical programs have been written which manipulate the raw data and present it in printed form in response to several different lines of experimental investigation.

1. INTRODUCTION AND OBJECTIVES

Extensive amounts of photo-optical and photo-electric data were acquired during the Firefly III series of upper atmosphere chemical releases conducted at

*Prepared under Contract AF19(628)1642. Supported under ARPA Project Defender Order 42.

Eglin Air Force Base, Florida in the fall of 1962. Since early in 1963, our primary task has been the reduction and interpretation of this data and its presentation in a manner useful for further scientific analysis. Earlier this year we initiated a major new approach to the very sizeable problem of reducing, handling, and analyzing the very large backlog of raw data available from experiments in the field. This new attack is centered around the use of electronic data processing methods and equipment and the devising of computer techniques applicable to the scientific questions and the type of data which are here involved.

During January and February of 1964, a considerable amount of hand reduction was carried out in conjunction with the photographs obtained on a few of the films. It rapidly became apparent that it would require, in order to do an adequate job, a number of man years of effort to accomplish even a moderately satisfactory data reduction program. A few specific results were obtained on individual shots using this hand data reduction technique, such as the total rate of emission versus time curve shown in Figure 1 of this report for Firefly DANA. This curve was obtained by hand plotting of values calculated for the equivalent total energy emitted as a function of time (as obtained from individual frames of movie film), and integrating the resulting values with a polar planimeter. The tedious and lengthy individual steps of this process involved conversion of the logarithmic units of photographic density to linear energy values, integration of these in the X and Y directions in space, and finally integration of the results with respect to time; this process occupies the full time of one technician for more than a month. This discouraging example of the difficulties inherent in hand processing of some of the data forced us into the present machine type operation. Based on our best available estimates, the equivalent job can now be done in less than 10 minutes by the machine (as soon as final revisions are made in one of the manipulative programs).

An important factor to consider in this work, which at least for the present makes it necessary to interpose an operator in the chain of data processing, is the fact that photographs contain many more bits of information in the form of developed or undeveloped individual grains (mostly redundant) that can be processed in any reasonable time by even the largest computer. Attempts to limit this amount of information by optical means such as using scanning slits much larger than grain size, or electrical smoothing or integrating techniques on microdensitometer output, involve arbitrary choices of parameters which may vary greatly from film to film. In order to keep the cost within practical bounds, and to gain experience in the handling of the type of data involved to aid in the possible design of more automatic systems later, an experienced operator can select the pertinent data points to be used from graphical microdensitometer output information. This operation keeps to a maximum of a few hundred data points the input required to give an essentially complete description of all the significant information contained in a photograph.

The objectives of this undertaking are several. During the initial phase, one objective has been to devise methods and techniques, appropriate to the overall goals of the project, of extracting all basic data from the raw data records. Procedures were devised for the conversion of raw photographic data into computer input forms using a Joyce-Loebl double beam recording microdensitometer. Methods and formats have also been devised for encoding the microdensitometer output traces, which are in graph form, and for punching these coded traces into cards for subsequent handling by electronic computers. A second phase, more or less concurrent with the first, required programming of the computers themselves in such a way as to provide a capability for data manipulation in response to several different areas of investigation suggested by the scientific objectives of the overall program. The major programming objective up to the time of this report, in addition to the working out of specific techniques for the conversion of raw data into computer input form, has been the design of generalized methods of handling and processing the data once it has been presented to the computer. While programs yielding specific presentations of manipulated data have been written, initial emphasis has been placed on the overall planning and organization of electronic data processing methods so as to make possible the multiple reuse of the same basic computer input data in many different ways to yield answers to a broad range of analytical questions.

2. SUMMARY AND CONCLUSIONS

As of the writing of this report, the general planning and organization of the electronic data has been completed. The systems analysis work required to construct the framework, within which may be designed methods and techniques for extracting raw data from photographic film, has been carried out. Most of these methods and techniques have themselves also been perfected. Through use of the Joyce-Loebl microdensitometer, data is being obtained from photographic records in a form and completeness required for integrated data processing by a wide range of computer programs, each specifically oriented toward a particular data analysis problem. In general, the planning of data extraction techniques has been directed toward the goal of obtaining from the raw film records virtually all of the useful information lodged in those records; also, of organizing the extracted data in such a manner that it may be manipulated by the computers in a number of different ways, permitting answers to be obtained to various data analysis questions which may be of interest now or in the future. Thus, when data has been converted from the raw photographic records into computer input form, it will be available for use in a variety of ways such as: analysis to yield information on a specific problem; comparison with data from other experiments; or comparison with data from the non-photographic aspects of the same experiment.

In addition to being general in the sense of providing data which can be manipulated by different computer programs in different ways, data extraction techniques have also had to be generalized to allow for variability in nearly every data acquisition parameter. During field experimentation, cloud size, distance, and configuration, camera type, lens, exposure, and operational mode, film type and processing were among the many parameters which had to vary with circumstances. Data extraction techniques, as well as the computer programs themselves, have had to be organized with sufficient built-in generality to permit smooth handling of this extremely wide range of variability. The task of setting up extraction methods of this type is now essentially complete.

In addition to these basic computer loading programs, a group of utility programs has also been written. These are programs which, for example, display with wide optional variability of format, the various types of tape stored data files generated by the load programs, programs which obtain logarithms or anti-logarithms, interpolate between point-array data records, or plot out in graph form (again, with a wide optional variability of output format) the results of computer generated calculations. Examples of most of these programs are shown in this report.

The next stage, that of writing the specific analytical programs which will interpret the tape-stored files of data in any desired fashion, is proceeding as planned. Analytical programs have been written which convert the data files into brightness contours for each frame extracted from the raw film. A program has also been written to integrate the energy output of any desired selection of frames from a given series to determine rates of photon emission and total photon emission. A program to determine rates of cloud expansion is nearly complete but still presents enough difficulties to necessitate its omission from this report. Work has begun on a program to yield spectral intensities versus wavelength. Several other analytical programs are also planned.

3. BACKGROUND

Optical observations and data analysis have been underway by this company over the past several years under AFCRL contracts. This work has included participation in several Firefly series, and in the observation of missile trails from a site at Jupiter, Florida. It has involved photographic recording of chemical releases and missile phenomena with high and medium speed cameras, use of scanning spectrometers, operation of closed circuit television cameras, and interpretation of data obtained from this type of equipment.

The primary emphasis in this program has been on the military evaluation of missile trails and related phenomena occurring principally in the altitude region of 100 to 200 kilometers. A by-product of these investigations has been the addition

to already existing knowledge of the properties of the upper atmosphere of whatever data and interpretations which arise naturally from the conduct of the work.

One of the most promising aspects of the extremely useful data analysis tool represented by electronic data processing is the feasibility of a far more detailed analysis of data acquired in earlier Firefly series than has heretofore been possible. through hand methods of reduction. Such use of raw data from earlier experiments will take place as it is desired to examine the earlier films for further information regarding past experiments or for purposes of comparison with more recent data. Proper planning of data extraction techniques has made it possible to approach earlier films in precisely the same manner used for current films and to manipulate extracted data similarly. This will make is possible to obtain results with precisely comparable meanings from both sets of data. No additional programming or planning work is required to accomplish this new and more extensive utilization of past data. It is necessary only to perform an original data extraction on the earlier films as desired. The data extraction and computer loading aspects of this operation have been specifically planned so that once data from a particular film has been extracted it can be used without basic change in form to yield information on questions which have not yet arisen but which present themselves in the future as a result of further analysis and experimentation. When such future questions arise, analytical programs applying directly to them can be written to utilize data files already prepared on tape.

4. SOURCES OF DATA

Up to the writing of this report, data has been extracted only from photographic records obtained during the source of recent field experiments. At such time as the extraction and analysis of data from this source has proceeded to the point where the priority attached to that aspect of the task has diminished somewhat, the scope of the work will be broadened to include as sources of data other types of instrumentation which have yielded data records on upper atmosphere chemical release experiments. These would include instrumentation such as the Hunten type auroral spectrograph, the 16 channel photomultiplier array used as a photoelectric spectrum analyzer, multilens photographs of chemical release clouds obtained at various wave lengths and polarizations, and others. The planning of data extraction techniques has been accomplished in a manner which will permit the inclusion of data from these sources as part of the complete program of data analysis.

5. EXPERIMENTAL TECHNIQUES

The data extraction methods and techniques which form the basis of the electronic data processing operations are comprised of three separate operational areas. First, data is converted from its raw form into trace or graphic form. In the case of raw photographic data, this is accomplished through the use of the Joyce-Loebl microdensitometer which reduces a photographic image to a series of two dimensional traces showing instrument deflection as a function of position on the film. Second, the raw data in graph form is encoded and punched into cards. Third, the cards are loaded into the computer where the data is partially pre-edited, arranged, and converted into data files stored on magnetic tape.

The operation of the Joyce-Loebl densitometer is based on the use of a double beam light system, in which two beams of light from a single source of light are switched alternately to a single photomultiplier. If the two beams of light are of different intensity, a signal is produced by the photomultiplier which causes a servomoter to move an optical attenuator so as to reduce the intensity difference to zero. In this way a continuously balanced system is obtained in which the position of an optical attenuator is made to record the density at any particular part of a specimen.

The specimen table and the recording table are mechanically linked together with a known ratio. This enables the accurate measurement of distances on the image. When the recording table moves in the X direction, the specimen table will also move in the X direction so that a complete scan of one line is made across the film by the measuring beam. Controls are provided for moving the specimen table in the Y direction. A control on the pen enables the pen to be moved in the D direction so that any one scan line can be recorded in any part of the paper in the D direction.

The operator, before taking traces, has to determine the proper ratio arm of linkage between recording and specimen table to be used. The ratio has to be chosen in such a way that the whole image width is recorded.

The film is fixed to the specimen table between two pieces of optically flat glass and so positioned that the portion of the film of interest is scanned during the travel of the specimen table.

To start with, the film is moved away from the measuring beam and only the two glass plates will be under scan. A small trace is taken of these two glass plates. This gives the zero reference density reading. Next the film is moved back under the measuring beam so that the first one or two lines of scan will be of the image background near the edge of the image. After each line scan, the film is moved in the Y direction by a small known amount so that after a number of scans the image would be completely scanned and the image background will again come under the

measuring beam. The pen is moved to a new equivalent background density value each time before the film is moved for the next scan. This is done to avoid superposition of recordings of different scans of the image. Normally, a sheet of recording paper can accommodate about four to five traces. When a sheet of paper is filled, the operator inserts a new sheet and records the deflection of the pen on this new sheet before moving the pen and the film. The value of this deflection is known as the P value (or the zero value from the previous page). The value of the densitometer deflection after the pen is moved is known as the Z value (or zero value) for the next trace. The value of deflection after the film has been moved is known as the S value (starting value). Knowing the P, Z and S values, the relative densities above that of glass of any portion of the image or film can be determined from densitometer recording.

The Y value of the first line of scan is always made 0. The knob used for moving the film is graduated to 1/10 a turn and, since the movement of film for 1/10 a turn is known, each consecutive trace can be numbered consecutively. The film is moved in the Y direction a known amount each time. After the whole image has been scanned, the film is moved in the same direction as before until the edge of the film comes within the measuring beam and distance moved is recorded in terms of the number of turns. Thus the total distance from the first line of scan to the edge of the film and also the distance of each line of scan from the edge of the film are known. Traces of the film across the bottom and top sprocket holes are also made.

After all the traces for an image are recorded, significant data points are marked on the traces. For traces of image background (that is, the first one or two traces and the last one or two traces in which no portion of the image is present) only two data points per trace are selected. One of these points is selected anywhere at the beginning of the trace and another at the end of the trace. For all other traces where a portion of the image is present, the usual two data points at the beginning and end of the traces are selected. In addition, a number of significant data points are chosen to represent the portion of the image on the trace. Data points from the microdensitometer traces on a particular frame of film, taken at sufficiently close intervals to allow a complete description of the images on the film based on a collection of points designated from the microdensitometer traces, are recorded on TRACE cards. Each TRACE card contains 10 data points (position and density for each point). As many TRACE cards as are required for one trace are used. Coding and column assignment in cards is described in Appendix A. The TRACE cards also contain, in coded form, the position at which the traces start, the length of the trace, the background density recorded for glass, a coding indicating the film from which the frame was taken, and sequence coding, by frame, for a particular film. Various other details such as zero shift on the microdensitometer between traces, identification of the reference points used for determining

a position of the image on the film (grid lines, star position, film defects or sprocket holes), and data for calculating cumulative density-reading errors over the entire frame are also included.

A collection of TRACE cards on a particular frame is described by a FRAME card. This card contains: the frame identification; all of the pertinent information concerning the densitometer settings which were used during the taking of the traces for the frame (ratio arm, slit height, slit width, magnification, speed, gain, iris setting); the time at which the exposure was taken with respect to a reference point (in the case of an explosion, the time of the explosion; otherwise, absolute time); the duration of the exposure; the length of the trace scan; the position on the film of the trace scan; and provisions for the optional insertion of information for further identifying the location of the images of interest. High and low X and Y limit values are inserted for subsequent plotting or data calculation purposes.

A single FRAME card suffices for all traces taken under identical conditions on a particular frame of film. If conditions are changed (microdensitometer settings, area of the frame scanned, etc.), a new FRAME card is made with the same coding, but with a next-in-sequence indication. TRACE cards to which this FRAME card pertains follow it in the deck. This deck will ultimately be used by the manipulative programs.

Any group of frames which use identical camera conditions are described on a FILM card. This card contains in coded form, the camera code (specifying type and serial number), the camera orientation, focal length of the lens used, film type employed in coded form, and any other special features of the data acquisition instrumentation which are required to be known by the manipulative programs. In case any camera parameters except exposure time (which is registered on the FRAME card) are changed, a new FILM card must be prepared carrying information on the change. Finally, the data deck, which includes the FILM, FRAME and TRACE cards, is provided with a PROGRAM card which specifies the operations which are to be performed on the DATA cards, and thus allows the computer to select the correct manipulative programs for the processing of the data. This PROGRAM card determines not only the steps to be taken, but the sequence in which they are to be taken, and includes provision for summaries to be made of results from data on more than one frame, or on more than one experiment. The development temperature, time and chemicals for the film processing are also coded on this card.

In addition, a WEDGE card is provided for calibration of the energy received per unit area by the film in various parts of the image. This wedge is described on one, two or three cards (depending upon the number of steps in the wedge) and is coded in terms of absolute exposure (ergs per square centimeter) versus density on the wedge. The wedge is further coded as to the film from which it is taken, the length of the wedge exposure, and the film development procedure.

The manipulative programs are arranged so that an individual deck of DATA cards can be run with one or more individual decks of PROGRAM cards in order to give rapid specific answers for specific frames. A more efficient utilization of machine time results (particularly when multiple references will be made to specific data over an extended period of time) if this data is pre-edited and placed in tape storage.

The film loading program arranges in computer storage the FILM card, FRAME card, WEDGE cards and TRACE cards in that order, and edits several of these in preparation for the actual tape storage operation. For example, all densities recorded for the film are corrected for glass background, and for zero position of the trace on the microdensitometer. Furthermore, wedge values are similarly corrected and a determination is made of the noise level to be expected on the film. This noise level is based on data from the TRACE cards which specify the average noise level encountered with the particular setting of the densitometer slit size and other parameters employed. Differentials less than the noise level can (optionally) be set to zero. Superfluous information on various cards (supplying such information as sequence number of individual TRACE cards, changes in zero settings, etc.) is discarded at this point, and the entire record made more compact by eliminating vacancies due to empty columns on cards, etc. The entire assemblage for a particular frame is then loaded as a single record onto tape in such a fashion that is can be retrieved, at will, for further processing.

The basic philosophy in this entire loading program is to retain the data in as near to its original form as can be done, and still prevent a large amount of duplication of computation in succeeding steps. The preliminary edit described will serve to record, in one conveniently accessible record, all of the instrument settings and pertinent factors concerning the data (both in terms of the original instrument settings for taking the data and the subsequent densitometer settings for reading the data) in a form convenient to subsequent processing steps.

In selecting the particular computer to be used in connection with this work, the principal consideration that governed the choice was the availability of a computer of medium size and moderate cost which would be suitable for the task. The IBM 1401 equipment was chosen not so much because of its superiority technically, but mainly because several installations in the immediate neighborhood posses such computers that were available for lease on an hourly basis. This choice has proved to be a very satisfactory one, in that it has been possible to program in such a way that the basic manipulative program framework can be used on larger and faster computers if and when the volume of data processed and the complexity of processing steps indicates the desirability of making a change. At the present time, we are entirely satisfied with the choice that has been made, and find that we are not really limited by the speed of the computer itself. However, it would be desirable if the computer had additional storage for the manipulation of the large arrays of

data points which are sometimes encountered in particular situations, such as efforts to rotate coordinate axes or to perform other manipulations on large arrays of points.

6. DISCUSSION

The actual job of manipulation and interpretation of raw data is accomplished by a series of analytical programs which convert the data files stored on magnetic tape into printed output in any one of a number of different forms depending on the problem being attacked.

Early in the programming effort, we prepared a program for the examination of the FILM, TRACE, and FRAME cards to simply plot out iso-density contours for particular photographs involved. Although our techniques for handling the data have been refined considerably since then, this program is still very useful, particularly in the detection of errors in TRACE cards. Examples of the output of this program are shown in Figures 2 through 5. This program, which operates quite rapidly because it does not require the correction for all of the parameters treated by the more sophisticated iso-brightness and integration programs, usually detects errors made on TRACE cards by giving an output which is quickly recognized by an experienced operator as containing such errors.

It is useful, in interpreting photographs of extended sources, to present the data in the form of contours of equal apparent brightness. Obviously, such brightness figures are only truly valid in the case of a surface which is radiating according to Lambert's law. Even in the case of a collection of point radiators, however, such figures are of use in interpretation of experimental results, so that a manipulative program for preparing this type of information from the FRAME, FILM and TRACE cards has been prepared. In this way, the results from a number of cameras can be represented in a format which is compatible and allows the interpretation of data taken under various conditions and with various pieces of equipment to be made coherent. For this purpose, a program has been written which will accept either card input data or pre-loaded tape data and will perform the necessary editing functions to reduce the individual FRAME data to a compatible and absolute basis.

The first series of steps in this program will re-edit the WEDGE data to take into account the reciprocity effect which results because the wedge and the actual frame exposures were different. In this step, and in all other steps in this procedure, the original data stored on cards or on the original tape is not disturbed in any way. The basic data for this reciprocity law correction is contained on the FILM card in coded form. The corrected WEDGE values are then converted to apparent brightness factors by taking into consideration: the f number of the lens;

the attenuation factor of any neutral density or polarizing screens present; and the variation of photon energy with wavelength which filters selecting various wavelengths are employed, for other factors which include the dependence of film sensitivity on wavelength; and the variation in spectral sensitivity with exposure level. Also, an optional feature in the program is included for subtracting out sky background intensities, should this be desired. A further feature corrects for specular-diffuse density differences due to scanning aperture size. Finally, logarithmic interpolation on each data point in the collection of traces pertaining to the particular frame involved is performed, in order to assign brightness values to each of the points taken.

A further optional feature is provided for the edit procedure for correction of the vignetting effect of lenses. In order to make use of this feature, it is necessary to code on the PROGRAM card the vignetting effect as a function of distance on the film from the center to use the already coded position data included with the TRACE cards.

The program provides for the optional punching of revised cards or for loading the revised data from this step onto tape. The various computation programs will accept either this revised data, or in some cases the raw data from the previous loading process, depending on the accuracy desired and the PROGRAM card instructions specified by the user.

After each of the edit steps described herein (and in general, after any process performed on the data in any of these programs), the machine records in an index location the facts that the operation has been completed on the data and also specifies the nature of the operation. This means in subsequent programs that a test can be made for the completion or non-completion of a particular edit step, in order to determine the procedure to be used by the program for the treatment of the data.

In general, iso-brightness edited data should be used (to conserve machine time) in total energy integration programs, in radial growth programs, in programs involving either interpretation of data from wavelength filters or of data from spectrographs, and generally whenever the absolute values of energy received by the film are important. It need not be used in wind shear programs, programs involving absolute position data using triangulation or star maps, wind direction and speed programs, or in other similar programs where absolute energy per unit area is not of critical importance.

As an example of the approach outlined above, a detailed printout of the processing of an individual frame, including a number of the immediate results obtained during the processing, is given in Figures 6 through 30. The first step in the procedure (not shown in detail) involves the preparation of an edited WEDGE card, taking into account exposure duration, reciprocity failure, spectral sensitivity, and, in general, all of the factors mentioned in the above discussion. This synthetic

WEDGE card can then be used for direct interpolation between the observed densitometer readings for translation of these readings directly to brightness values for the conditions involved. Program NRG1P prepares these cards automatically, from the pertinent FRAME cards, FILM cards, and UNEDITED WEDGE cards. These EDITED WEDGE cards, together with the FILM, FRAME, and TRACE cards are loaded onto tape in program NWR1P. An example of the format of the data in storage is given in Figure 6. Following this step, the data is interpolated in the X direction, taking into account the appropriate X multiplier and X start values from the FRAME card. The output of this step is a tape record containing header information (positions 577 through 999 of the above mentioned tape record) together with individual records for each Y value, containing 132 log E values derived from the wedge and trace data given for each individual Y value. An example of such output is shown in Figure 7. Following this step, which has been performed by program ISC1P, the data is ready for plotting or for other steps (such as energy integration), which are done by succeeding programs. Examples are shown in Figures 8 through 30 of the type of iso-brightness plot which can be done by the use of program BRP1P. In order to demonstrate the versatility of the plotting method, there is also included an inverted plot which can be specified by the appropriate symbol in the FILM card. An intermediate program called ROT1P, would have rotated coordinates by 90 degrees (or by a smaller amount, if required) in case the camera orientation had so dictated. The program is under rather powerful operator control through the selection of PROGRAM cards, in that any arbitrary zero level can be selected, corrections to the log E values can be inserted at this point, scale changes can be made, and various values of starting and stopping Y coordinates can be selected. Additional examples, from another release, are given in Figures 31 through 33. An alternate type of printout, using solid blocks of letters rather than merely indicating equal value contours, is shown in Figures 34 and 35. We generally prefer the type plot shown in Figures 31 through 33.

Most of the work has been completed, although a few details remain to be corrected, on a program for taking the output of the NRG1P, NWR1P, ISC1P programs outlined above and performing an integration with respect to the X and Y coordinates in order to determine the total rate of energy emission as measured by the densities recorded by a particular frame of the film. Following this, an integration with respect to time is performed, resulting in the determination of the total energy radiated in a particular wavelength range.

As an example of the type of data which can be produced (and in large volume at high rates of speed), a series of iso-brightness plots has been included in this report for Firefly DANA. While this by no means represents all of the available data frames, several very interesting features of the development of the cloud are evident from the examination of these isophotes, many of which would have been missed in a cursory or even fairly careful evaluation of the film itself.

Commenting on these iso-brightness plots themselves (see Figures 8 through 30), it will be noted that after extremely bright initial burst, at about 0. 1 sec the intensity has decreased markedly and there is a beginning (observable in the upper right hand corner of the plot) of a double maximum brightness condition, which persists through the next few tenths of seconds. After approximately one-half a second, however, the double maximum begins to disappear, and the cloud assumes a slowly decaying configuration with fairly steep brightness gradients towards its edges. The maximum intensity actually increases until almost one second after burst, at which time it begins to decay slowly, and the iso-brightness contour denoted by 3 on the graph (corresponding to approximately a factor of two above background) starts shrinking in toward the center as would be expected. While the cloud, of course, continues to expand, its edges rapidly approach background intensities for the short exposure used in making these early time photographs, which could (and will, in future computer runs) be shown by the existing programs. A series of pictures such as these, it will be seen, can be used for studying rate of cloud expansion, although a later manipulative program will present the data in somewhat easier to use form. While we have not yet begun the work of trying to understand the cloud dynamics which produce such a display, it should be very interesting to compare the various bursts with one another, and with previous releases. This will be done during the next period.

To show the considerable modification which can be made in the appearance of identical data, an additional printout of the frame for 2. 45 seconds after burst is shown in Figure 36 with lower background cut-off figures and with a different scale. We find that it is sometimes useful to plot the same data in different ways, because the interpreter of the data may wish somewhat different formats for investigating different physical phenomena.

An additional rather powerful technique which has been developed for the presentation of data has been the construction of a macro instruction (to be included with the program library used in the rapid preparation of manipulative programs) which allows the plotting of data in the form of graphs. This technique will be particularly useful when forms of data other than the present photographic ones are to be treated. Although such programs have previously existed for IBM 1401 machines, they have been based on a card input (rather than tape) and are much slower in operation and not so flexible as this plotting technique. Up to 8 single valued functions can be plotted on the same graph, with great variety and latitude with respect to labels, suppression or inclusion of borders, suppression or inclusion of coordinate markings, scale markings. Simple modifications can place printed comments alongside any trace being plotted, and graphs can be constructed in either the X or the Y direction. As examples of this program output, Figure 37 shows a plot of mount position versus time for shot DANA for the two large modified gun mounts used in the recent Firefly program. Figure 38 shows a plot of the

product of film sensitivity and filter factor for Kodak RXP film and Wratten filter #8. Any other functions desired can be plotted, and we expect to make large scale use of this technique for future data presentation.

7. INTERPRETATION

It seems clear that the use of electronic data processing techniques (as a tool for the handling and analysis of experimental data of the nature with which the present program is involved) has and will in the future prove to be of very great value in the continuing work of data interpretation under the contract. An examination of the appendices reveal a very great quantity of data which has been interpreted and presented in ways which would have been, in a practical sense, impossible under hand methods of data reduction. In terms of time, cost, and feasibility of analysis, these techniques are far superior to earlier methods. As the operation is expanded through the creation of additional analytical programs suggested by examination of the results yielded by current programs, it is expected that increasing amounts of useful information can be obtained from existing and future data records.

8. RECOMMENDED FURTHER STUDY

Perhaps the most important aspect of the recommendations for continued work in this field involves the completion, testing, and use of manipulative programs referred to earlier. Several of these are well along towards completion and have been referred to above. In addition, we plan to write programs for taking into account the positions on the film of images of stars in cases where it is desirable to use these positions for wind drift and other types of positional determinations; and for recognizing and excluding from consideration other types of artifacts, such as scratches and spots caused during development. Furthermore, a program is contemplated for treating photometer data, an additional program for reducing the wavelengths and intensity information obtainable from slitless spectrograph photographs, and a program to enable the computer to follow and study the development of eddies and other turbulent effects are contemplated.

The basic long term goal of the operation is to provide what will amount, in terms of past efforts, to almost real-time data interpretation of data records obtained during field experiments. It is expected that once the necessary computer programs are fully perfected and the proper instrument installations arranged, a basic analysis of field data can be carried forward and completed within a few days of the occurrence of a chemical release experiment.

This will enable the program to provide experimenters in the field with analytical results in the light of which revisions and modifications to later experiments can be made. It is not expected that this ultimate goal is one which can be reached in the immediate future. It is expected, however, that, within possibly a year, this goal will have become a rapidly attainable reality.

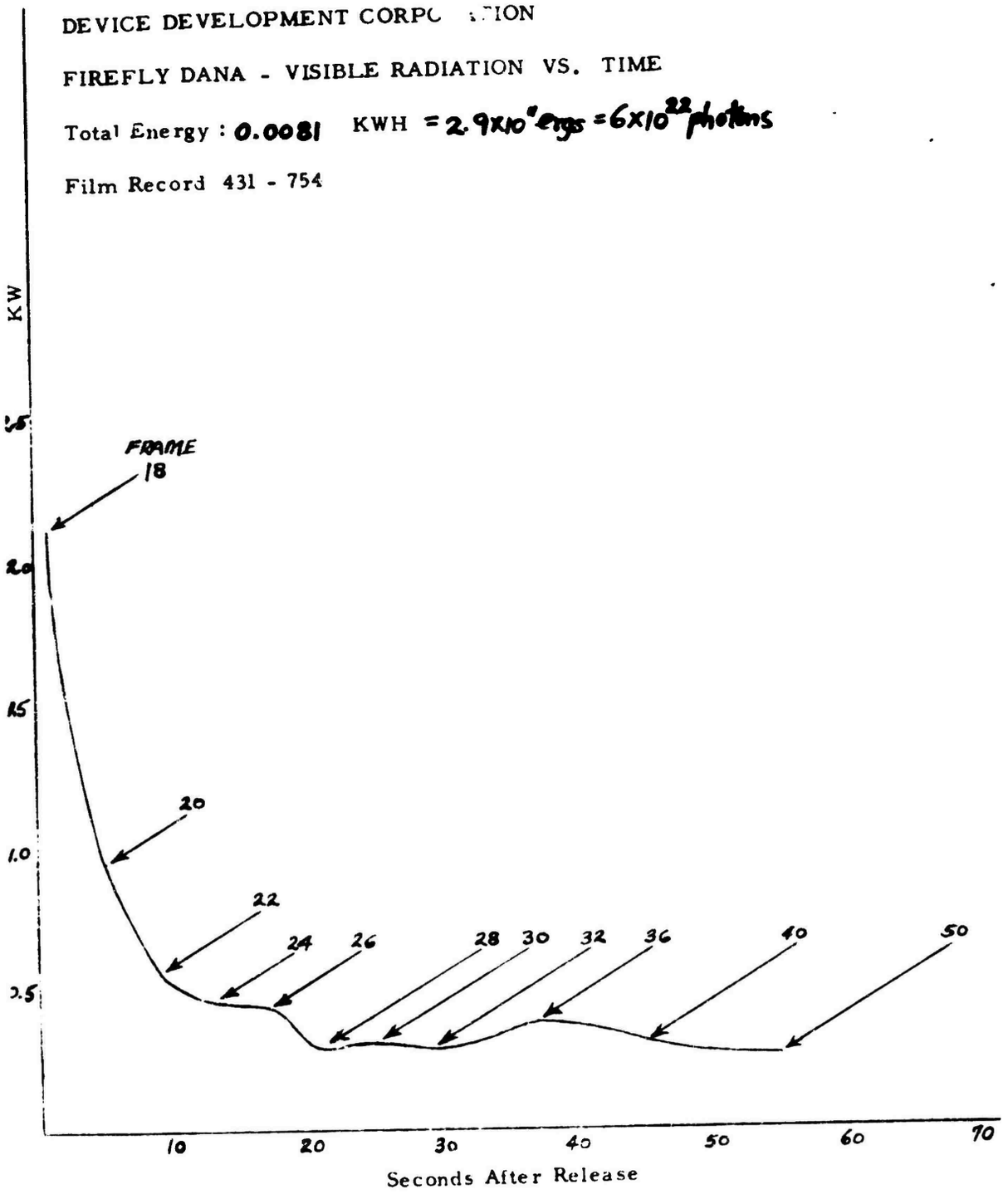

Figure 1. Hand Integration of Total Emission, Firefly DANA

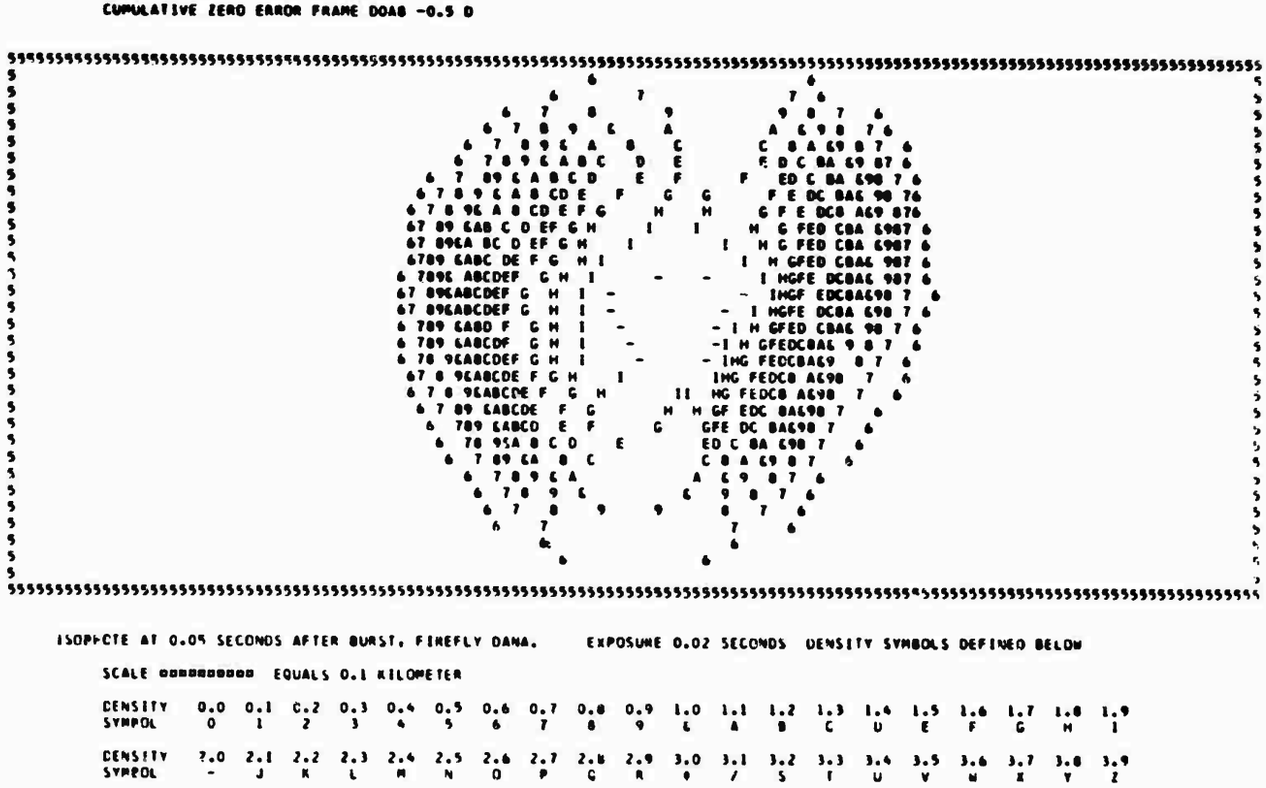

Figure 2. Example of Isodensity Plot

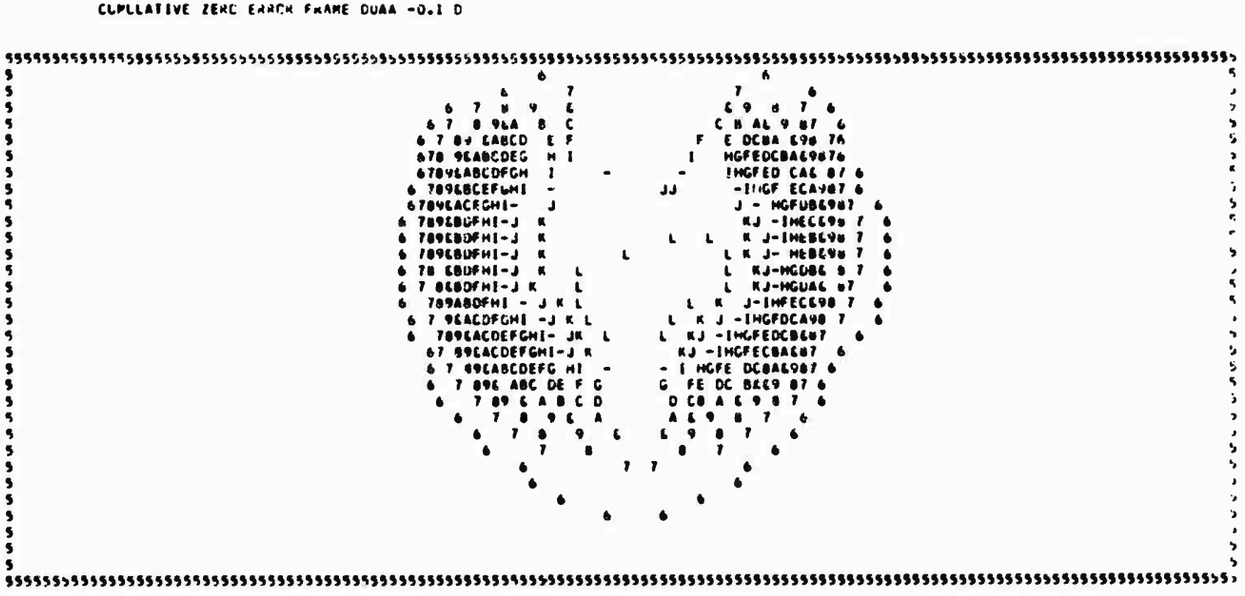

Figure 3. Example of Isodensity Plot

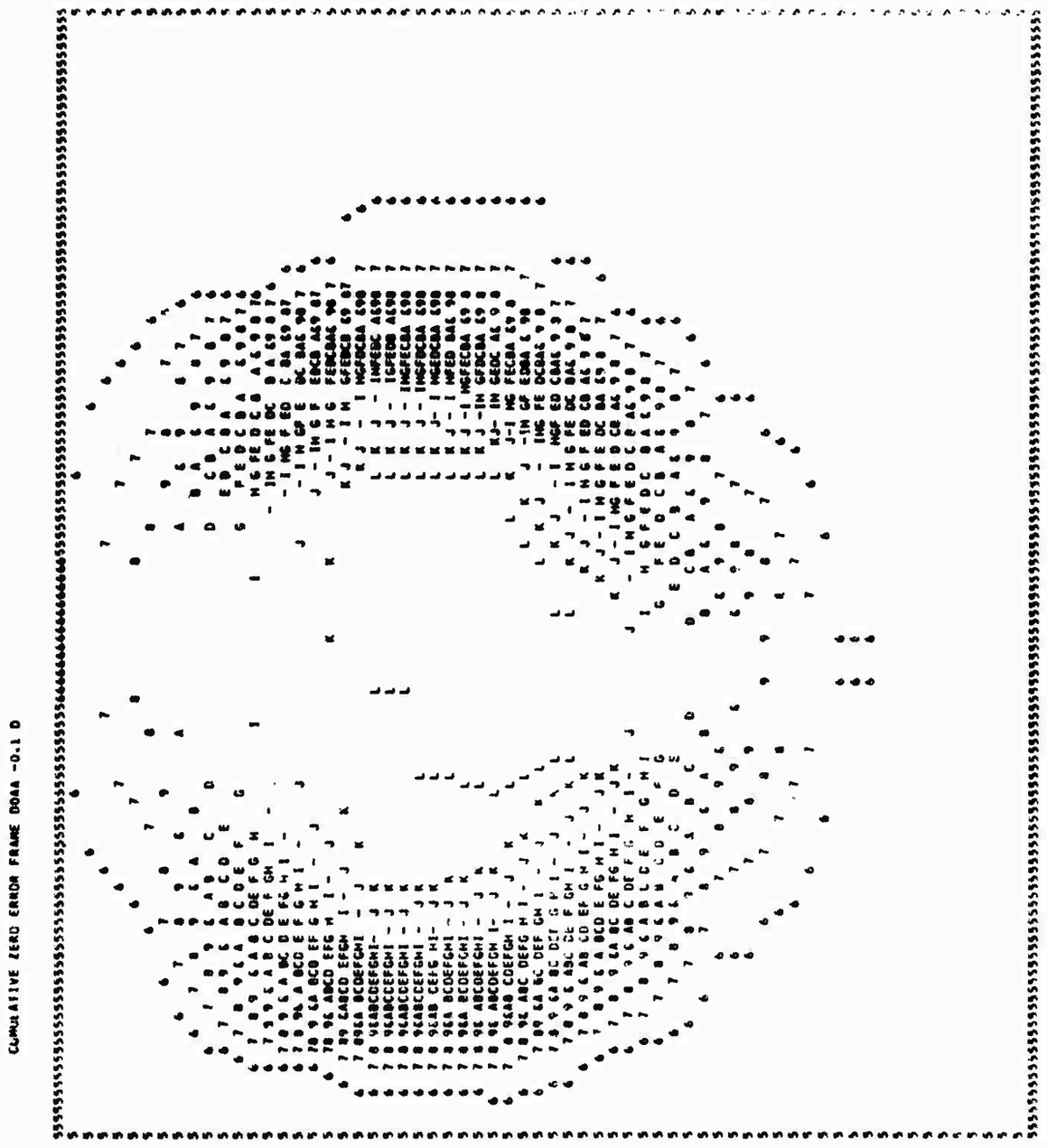

Figure 4. Example of Isodensity Plot

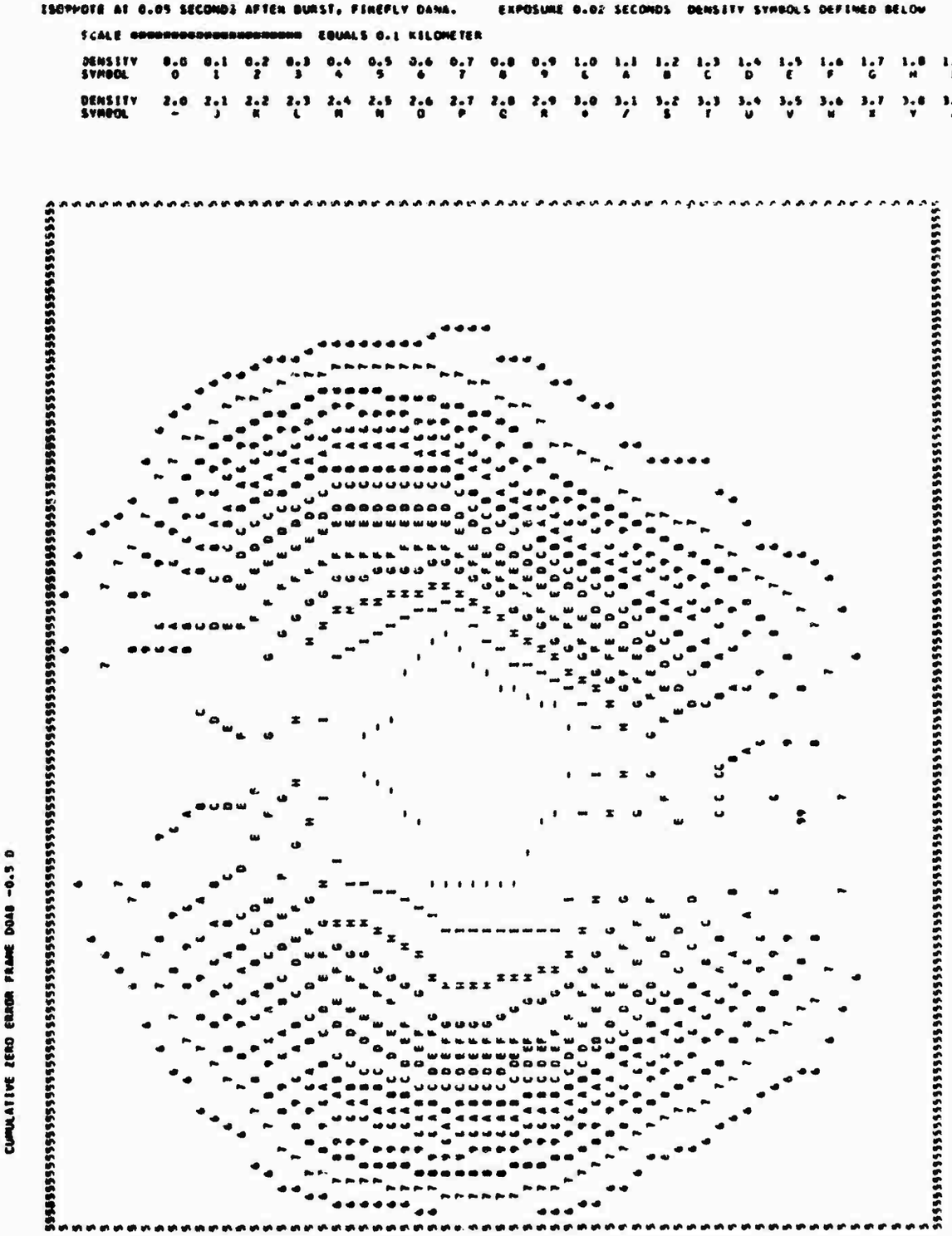

Figure 5. Example of Isodensity Plot

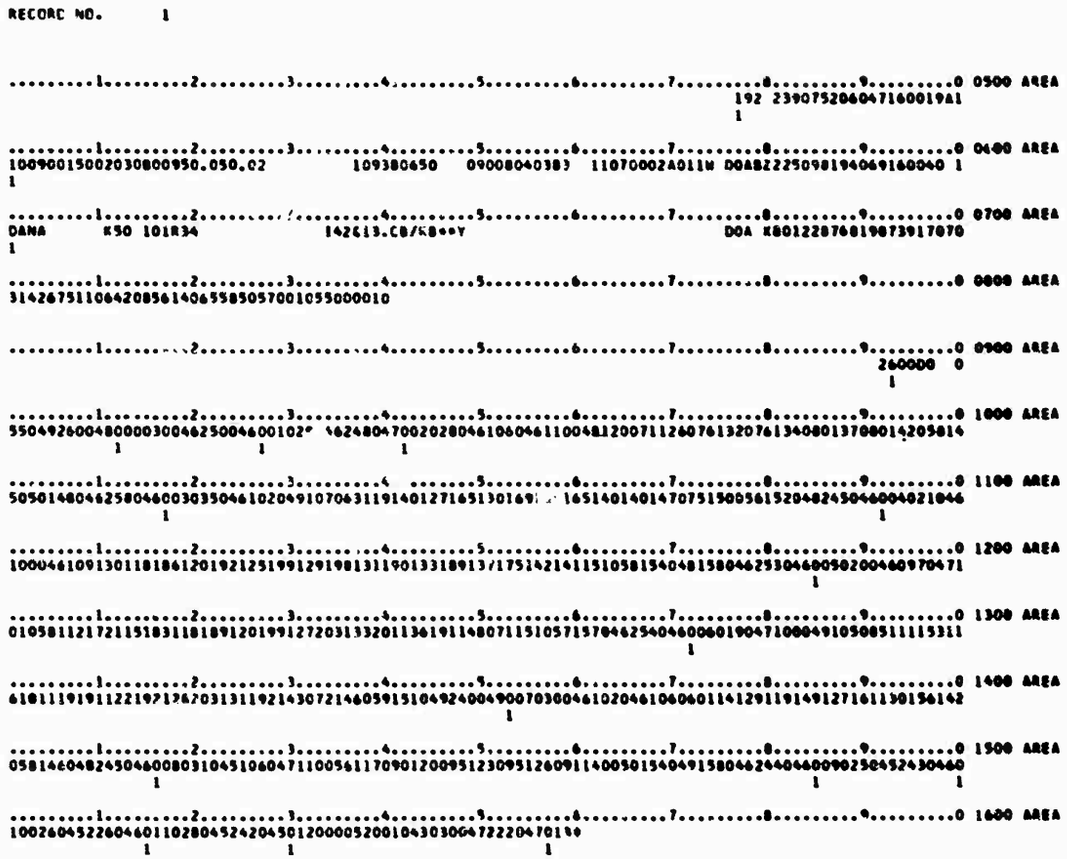

Figure 6. Program NWR, Output Example

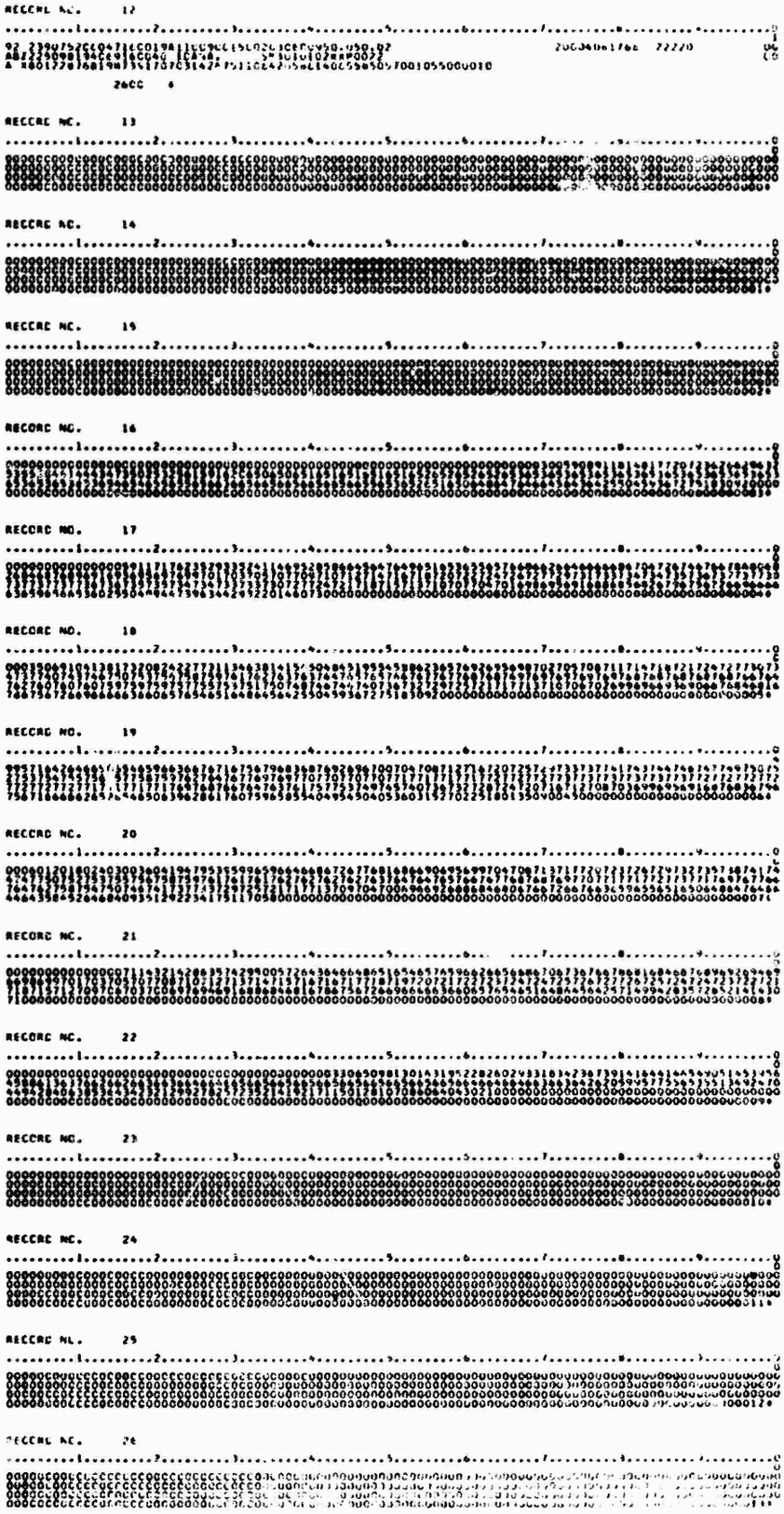

Figure 7. Program ISC, Output Example

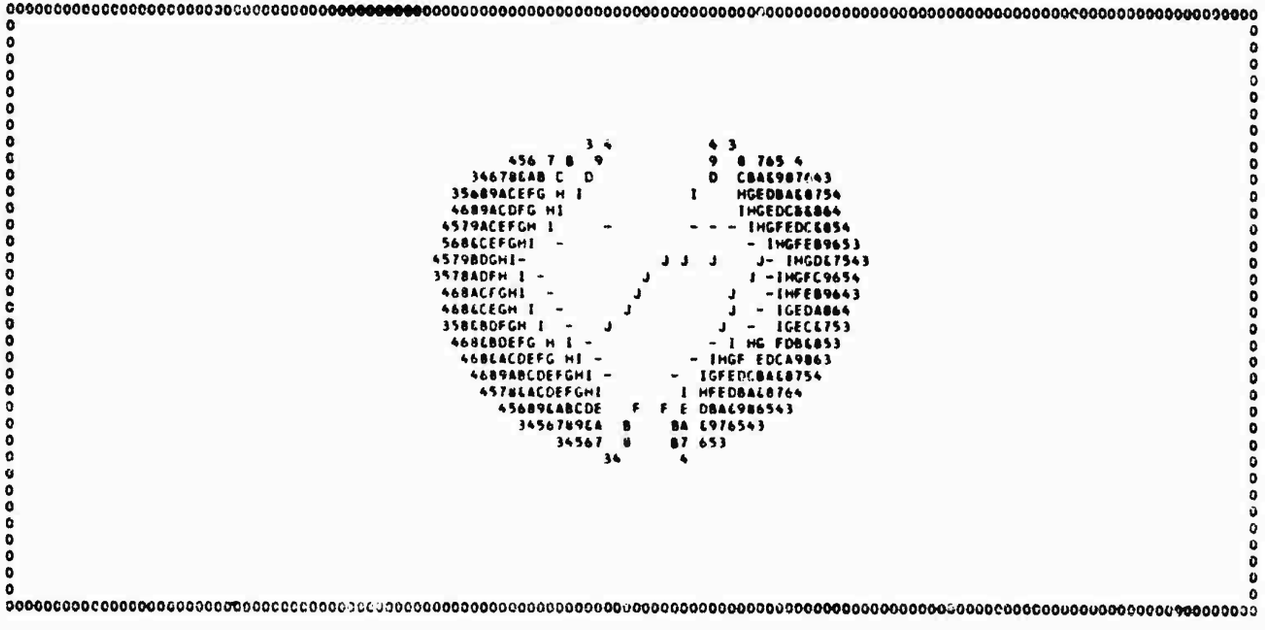

ISOBRIGHTNESS CONTOURS, FIR-FLY DANA TIME 0000 SECONDS AFTER RELEASE. EXPOSURE DURATION 0.02 SECONDS.

SCALE ▪▪▪▪▪▪▪▪▪▪ EQUALS 0.1 KILOMETER. WAVELENGTH RANGE 380-650 MILLIMICRONS.
VALUES IN TERMS OF ERGS PER SQ. CM. PER STERADIAN PER SECOND. SYMBOLS DEFINED BELOW.

SYMBOL	0	1	2	3	4	5	6	7	8	9	A	B	C	D	E	F	G	H	I
LOG E	0.0	0.1	0.2	0.3	0.4	0.5	0.6	0.7	0.8	0.9	1.0	1.1	1.2	1.3	1.4	1.5	1.6	1.7	1.8	1.9

SYMBOL	-	J	K	L	M	N	O	P	Q	R	S	/	S	T	U	V	W	X	Y	Z
LOG E	2.0	2.1	2.2	2.3	2.4	2.5	2.6	2.7	2.8	2.9	3.0	3.1	3.2	3.3	3.4	3.5	3.6	3.7	3.8	3.9

Figure 8. Selected Frames, Firefly DANA - Burst Frame

BRIGHTNESS CONTOURS, FIREFLY DANA TIME 300 SECONDS AFTER RELEASE. EXPOSURE DURATION 0.02 SECONDS.

SCALE ========== EQUALS 0.1 KILOMETER. WAVELENGTH RANGE 380-650 MILLIMICRONS.
VALUES IN TERMS OF ERGS PER SQ. CM. PER STERADIAN PER SECOND. SYMBOLS DEFINED BELOW.

SYMBOL	0	1	2	3	4	5	6	7	8	9	A	B	C	D	E	F	G	H	I
LOG E	0.0	0.1	0.2	0.3	0.4	0.5	0.6	0.7	0.8	0.9	1.0	1.1	1.2	1.3	1.4	1.5	1.6	1.7	1.8	1.9

SYMBOL	-	J	K	L	M	N	O	P	Q	R	S	/	S	T	U	V	W	X	Y	Z
LOG E	2.0	2.1	2.2	2.3	2.4	2.5	2.6	2.7	2.8	2.9	3.0	3.1	3.2	3.3	3.4	3.5	3.6	3.7	3.8	3.9

Figure 8. Selected Frames, Firefly DANA - Burst Frame, Mirror Image (Coordinate inversion example)

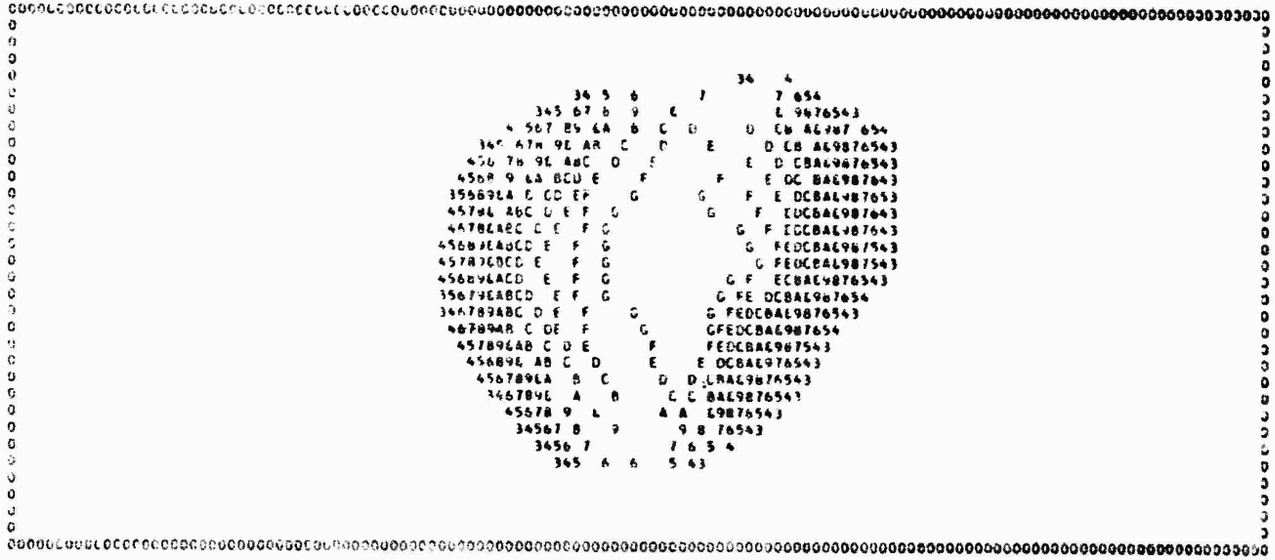

ISOBRIGHTNESS CONTOURS, FIREFLY DANA TIME 0.05 SECONDS AFTER RELEASE. EXPOSURE DURATION 0.02 SECONDS.

SCALE ⋯⋯⋯⋯ EQUALS 0.1 KILOMETER. WAVELENGTH RANGE 380-650 MILLIMICRONS.
VALUES IN TERMS OF ERGS PER SQ. CM. PER STERADIAN PER SECOND. SYMBOLS DEFINED BELOW.

SYMBOL	0	1	2	3	4	5	6	7	8	9	A	B	C	D	E	F	G	H
LOG E	0.0	0.1	0.2	0.3	0.4	0.5	0.6	0.7	0.8	0.9	1.0	1.1	1.2	1.3	1.4	1.5	1.6	1.7	1.8	1.9

SYMBOL	-	J	K	L	M	N	O	P	Q	R	S	T	U	V	W	X	Y	Z
LOG E	2.0	2.1	2.2	2.3	2.4	2.5	2.	2.7	2.8	2.9	3.0	3.1	3.2	3.3	3.4	3.5	3.6	3.7	3.8	3.9

Figure 10. Selected Frames, Firefly DANA - Time 0.05 Seconds After Release

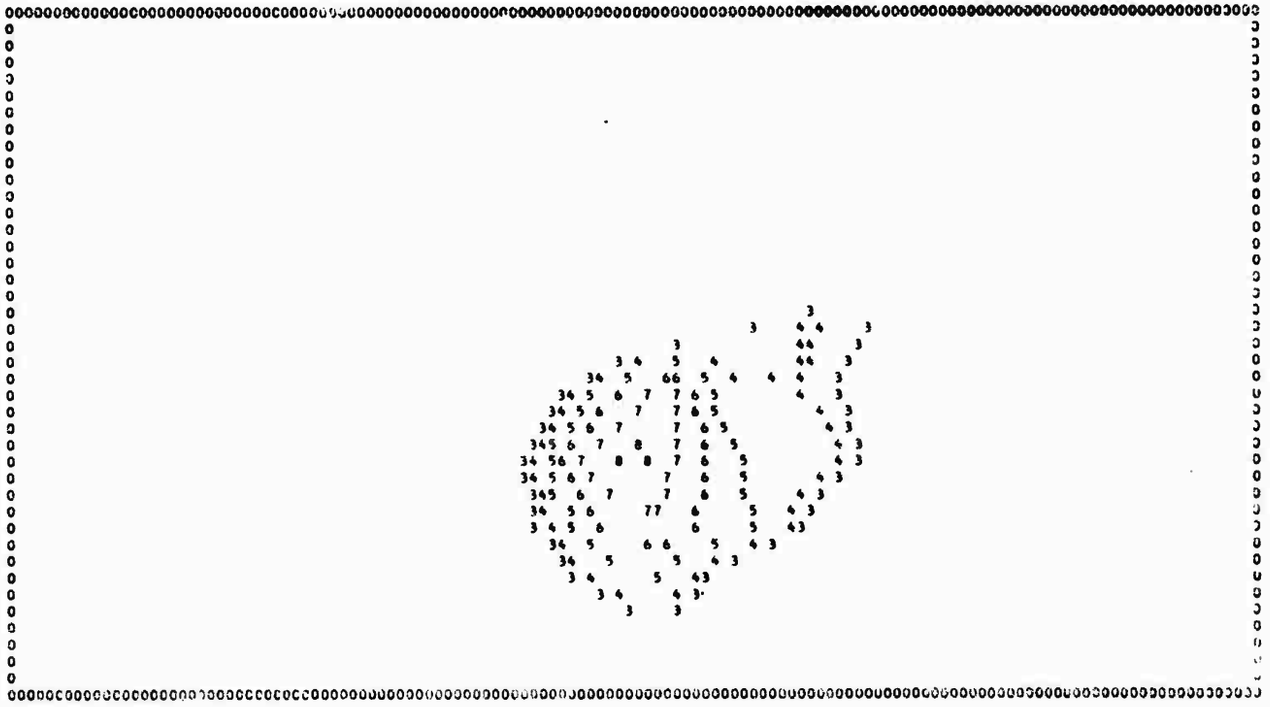

ISOBRIGHTNESS CONTOURS, FIREFLY DANA TIME 0.10 SECONDS AFTER RELEASE. EXPOSURE DURATION 0.02 SECONDS.

SCALE 0000000000 EQUALS 0.1 KILOMETER. WAVELENGTH RANGE 380-650 MILLIMICRONS.
VALUES IN TERMS OF ERGS PER SQ. CM. PER STERADIAN PER SECOND. SYMBOLS DEFINED BELOW.

SYMBOL	0	1	2	3	4	5	6	7	8	9	A	B	C	D	E	F	G	H	I
LOG E	0.0	0.1	0.2	0.3	0.4	0.5	0.6	0.7	0.8	0.9	1.0	1.1	1.2	1.3	1.4	1.5	1.6	1.7	1.8	1.9

SYMBOL	-	J	K	L	M	N	O	P	Q	R	S	T	U	V	W	X	Y	Z
LOG E	2.0	2.1	2.2	2.3	2.4	2.5	2.6	2.7	2.8	2.9	3.	3.1	3.2	3.3	3.4	3.5	3.6	3.7	3.8	3.9

Figure 11. Selected Frames, Firefly DANA - Time 0.10 Seconds After Release

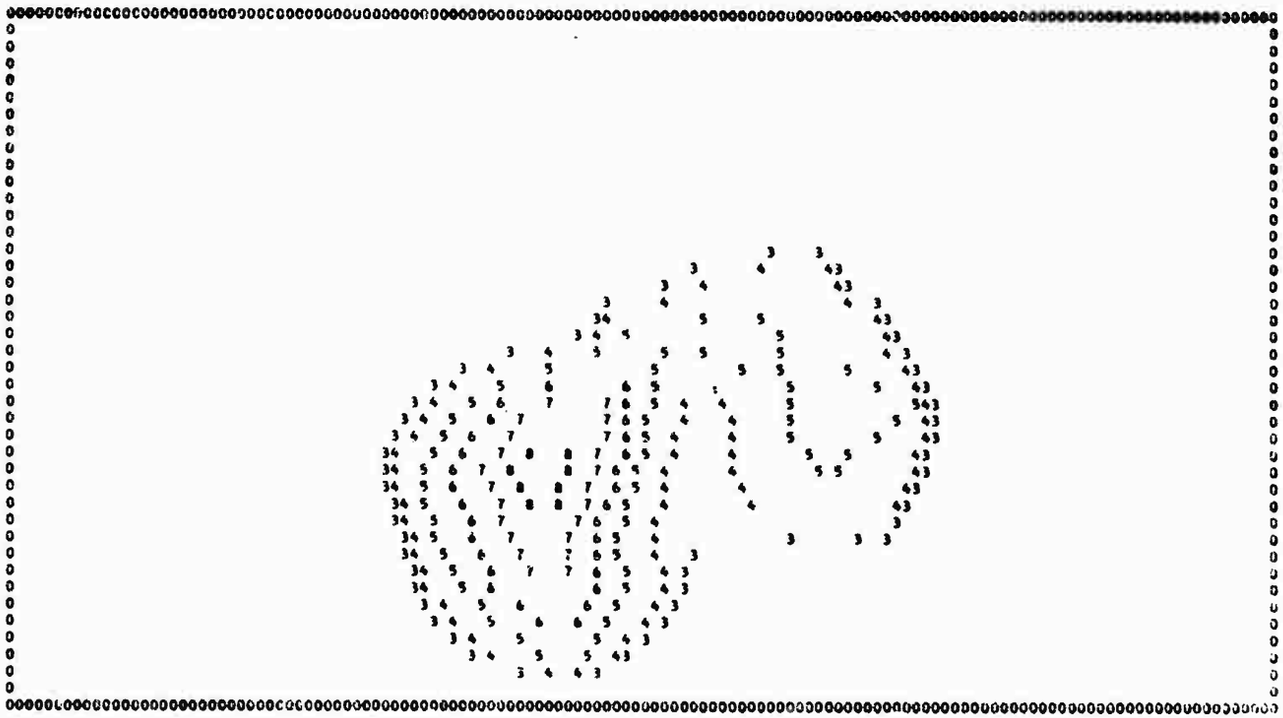

ISOBRIGHTNESS CONTOURS, FIREFLY DANA TIME 0.15 SECONDS AFTER RELEASE. EXPOSURE DURATION 0.02 SECONDS.

SCALE ⊕⊕⊕⊕⊕⊕⊕⊕⊕ EQUALS 0.1 KILOMETER. WAVELENGTH RANGE 380-650 MILLIMICRONS.
VALUES IN TERMS OF ERGS PER SQ. CM. PER STERADIAN PER SECOND. SYMBOLS DEFINED BELOW.

SYMBOL	0	1	2	3	4	5	6	7	8	9	A	B	C	D	E	F	G	H	I
LOG E	0.0	0.1	0.2	0.3	0.4	0.5	0.6	0.7	0.8	0.9	1.0	1.1	1.2	1.3	1.4	1.5	1.6	1.7	1.8	1.9

SYMBOL	-	J	K	L	M	N	O	P	Q	R	S	T	U	V	W	X	Y	Z
LOG E	2.0	2.1	2.2	2.3	2.4	2.5	2.6	2.7	2.8	2.9	3.0	3.1	3.2	3.3	3.4	3.5	3.6	3.7	3.8	3.9

Figure 12. Selected Frames, Firefly DANA - Time 0.15 Seconds After Release

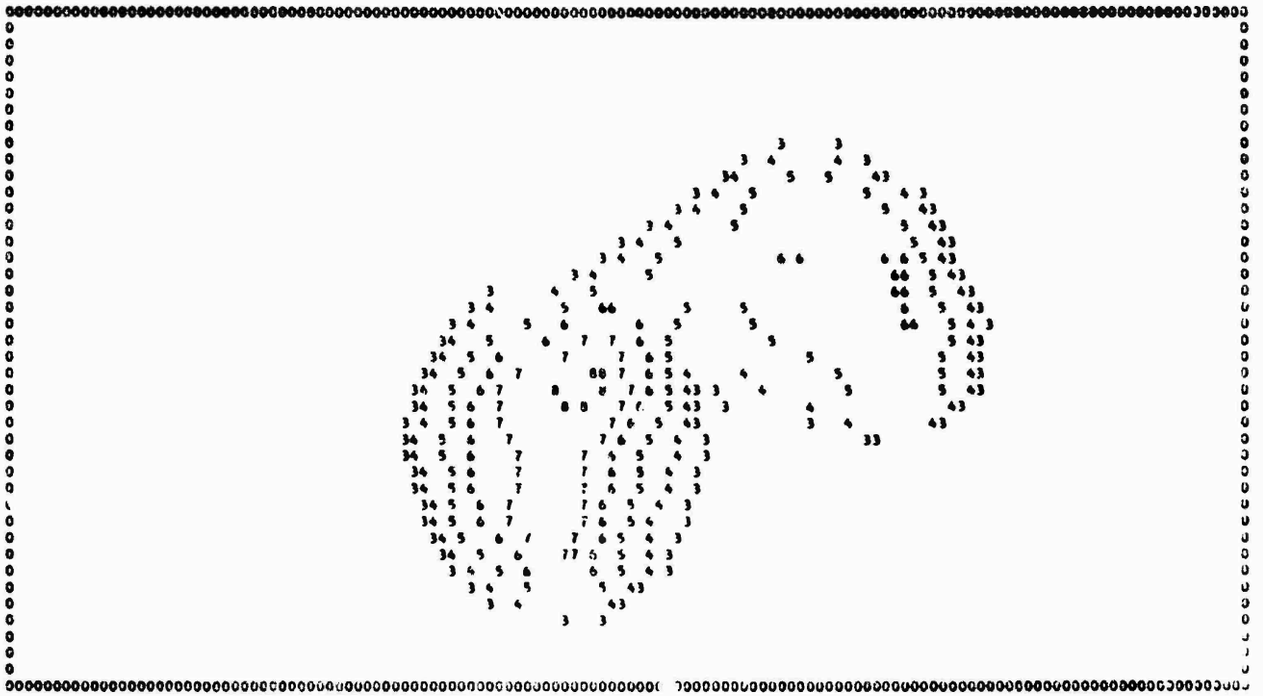

ISOBRIGHTNESS CONTOURS, FIREFLY DANA TIME 0.20 SECONDS AFTER RELEASE. EXPOSURE DURATION 0.02 SECONDS.

SCALE ▪▪▪▪▪▪▪▪▪▪ EQUALS 0.1 KILOMETER. WAVELENGTH RANGE 380-650 MILLIMICRONS.
VALUES IN TERMS OF ERGS PER SQ. CM. PER STERADIAN PER SECOND. SYMBOLS DEFINED BELOW.

SYMBOL	0	1	2	3	4	5	6	7	8	9	A	B	C	D	E	F	G	H	I
LOG E	0.0	0.1	0.2	0.3	0.4	0.5	0.6	0.7	0.8	0.9	1.0	1.1	1.2	1.3	1.4	1.5	1.6	1.7	1.8	1.9

SYMBOL	-	J	K	L	M	N	O	P	Q	R	S	/	S	T	U	V	W	X	Y	Z
LOG E	2.0	2.1	2.2	2.3	2.4	2.5	2.6	2.7	2.8	2.9	3.0	3.1	3.2	3.3	3.4	3.5	3.6	3.7	3.8	3.9

Figure 13. Selected Frames, Firefly DANA - Time 0.20 Seconds After Release

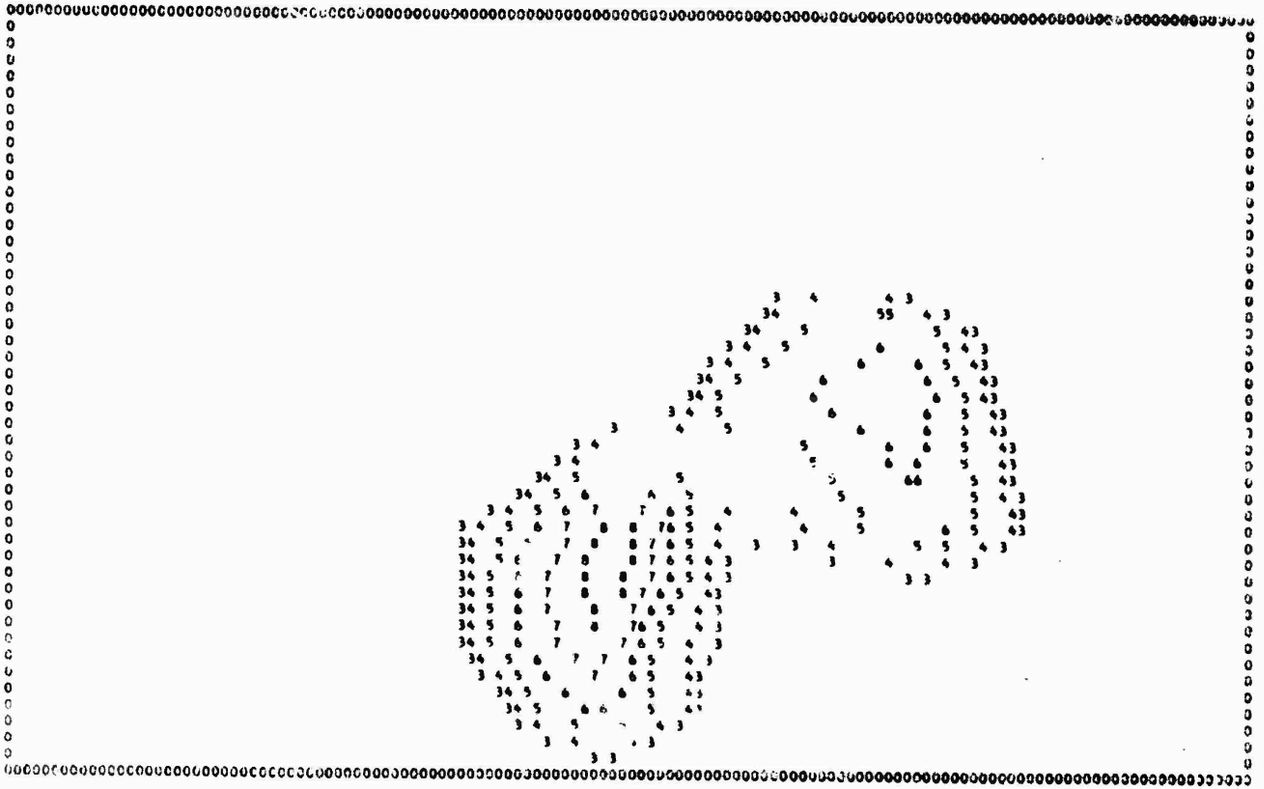

ISORNIGHENESS CONTOURS, FIREFLY DANA TIME 0.25 SECONDS AFTER RELEASE. EXPOSURE DURATION 0.02 SECONDS.

SCALE 0000000000 EQUALS 0.1 KILOMETER. WAVELENGTH RANGE 380-650 MILLIMICRONS.
VALUES IN TERMS OF ERGS PER SQ. CM. PER STERADIAN PER SECOND. SYMBOLS DEFINED BELOW.

SYMBOL	0	1	2	3	4	5	6	7	8	9	A	B	C	D	E	F	G	H	I
LOG E	0.0	0.1	0.2	0.3	0.4	0.5	0.6	0.7	0.8	0.9	1.0	1.1	1.2	1.3	1.4	1.5	1.6	1.7	1.8	1.9

SYMBOL	.	J	K	L	M	N	O	P	Q	R	S	T	U	V	W	X	Y	Z
LOG E	2.0	2.1	2.2	2.3	2.4	2.5	2.6	2.7	2.8	2.9	3.0	3.1	3.2	3.3	3.4	3.5	3.6	3.7	3.8	3.9

Figure 14. Selected Frames, Firefly DANA - Time 0.25 Seconds After Release

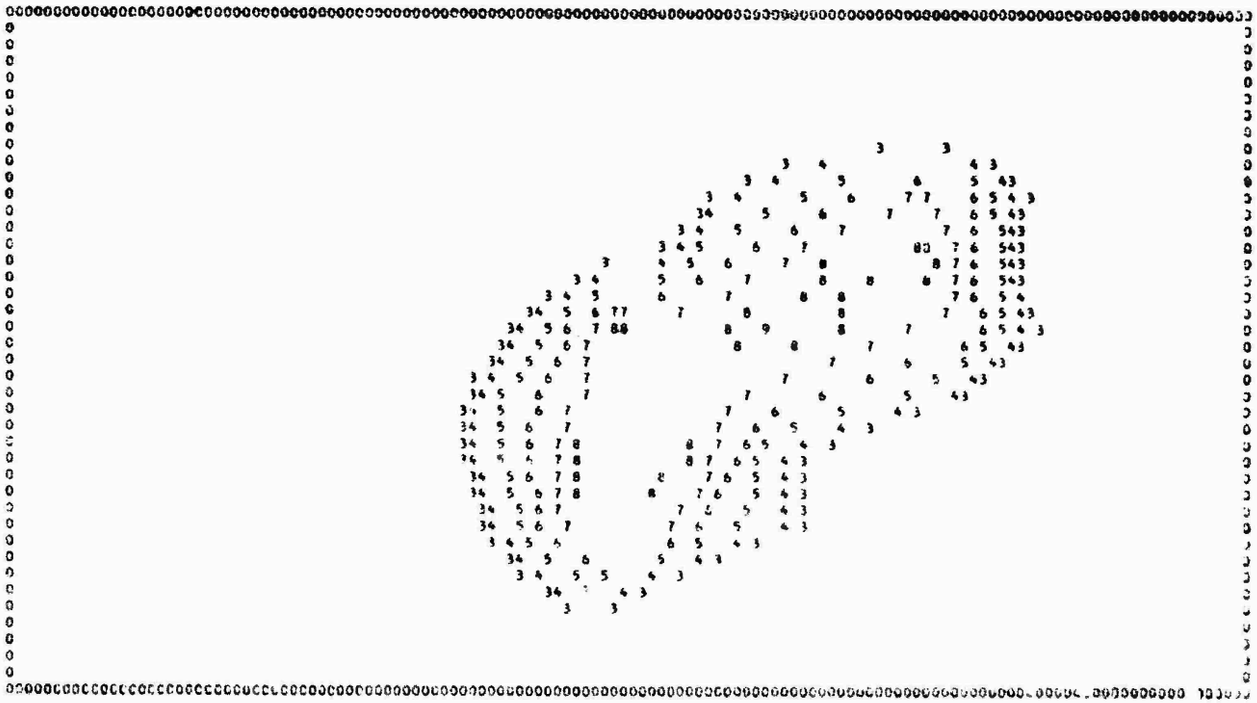

ISOBRIGHTNESS CONTOURS, FIREFLY DANA TIME 0.40 SECONDS AFTER RELEASE. EXPOSURE DURATION 0.02 SECONDS.

SCALE ∞∞∞∞∞∞∞∞ EQUALS 0.1 KILOMETER. WAVELENGTH RANGE 380-650 MILLIMICRONS.
VALUES IN TERMS OF ERGS PER SQ. CM. PER STERADIAN PER SECOND. SYMBOLS DEFINED BELOW.

SYMBOL	0	1	2	3	4	5	6	7	8	9	A	B	C	D	E	F	G	H	I
LOG E	0.0	0.1	0.2	0.3	0.4	0.5	0.6	0.7	0.8	0.9	1.0	1.1	1.2	1.3	1.4	1.5	1.6	1.7	1.8	1.9

SYMBOL	-	J	K	L	M	N	O	P	Q	R	S	T	U	V	W	X	Y	Z
LOG E	2.0	2.1	2.2	2.3	2.4	2.5	2.6	2.7	2.8	2.9	3.0	3.1	3.2	3.3	3.4	3.5	3.6	3.7	3.8	3.9

Figure 16. Selected Frames, Firefly DANA - Time 0.40 Seconds After Release

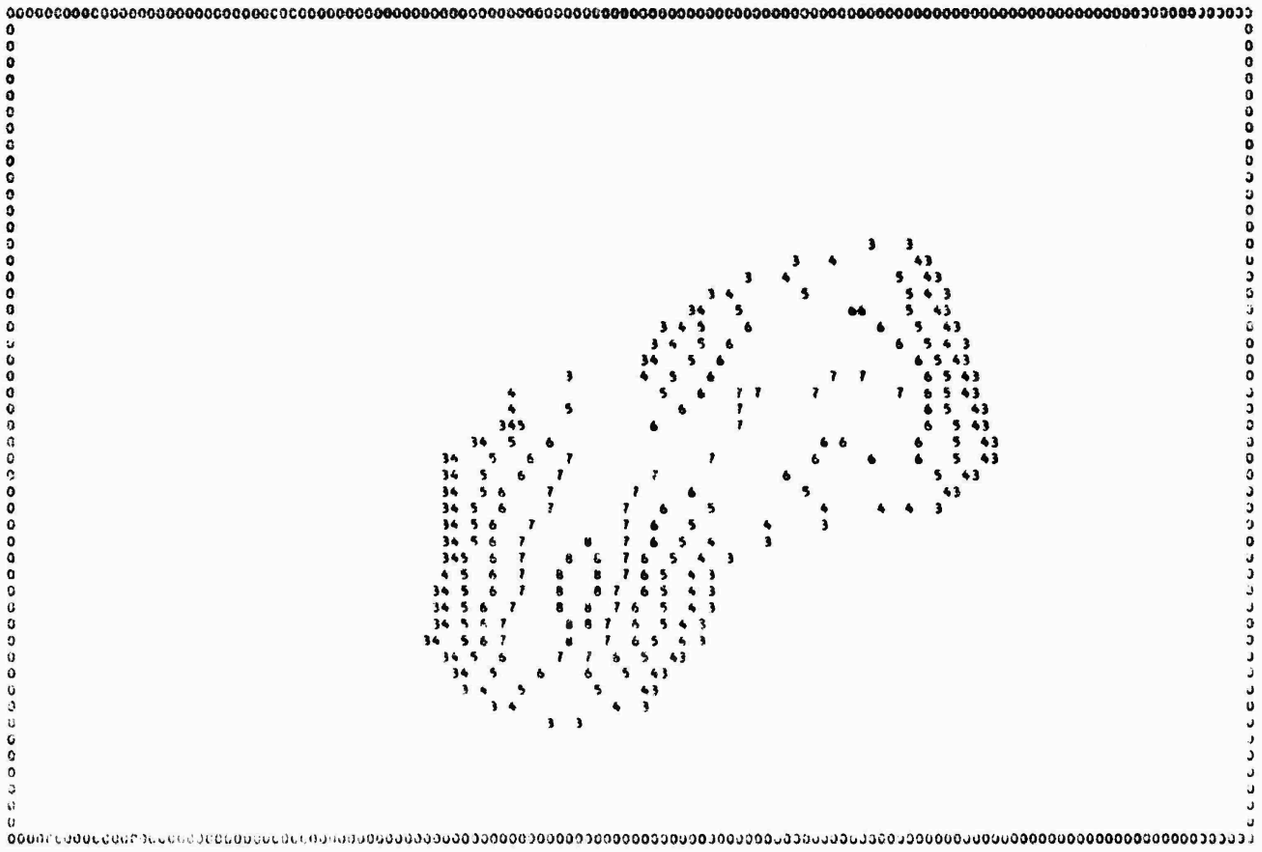

Figure 15. Selected Frames, Firefly DANA - Time 0.35 Seconds After Release

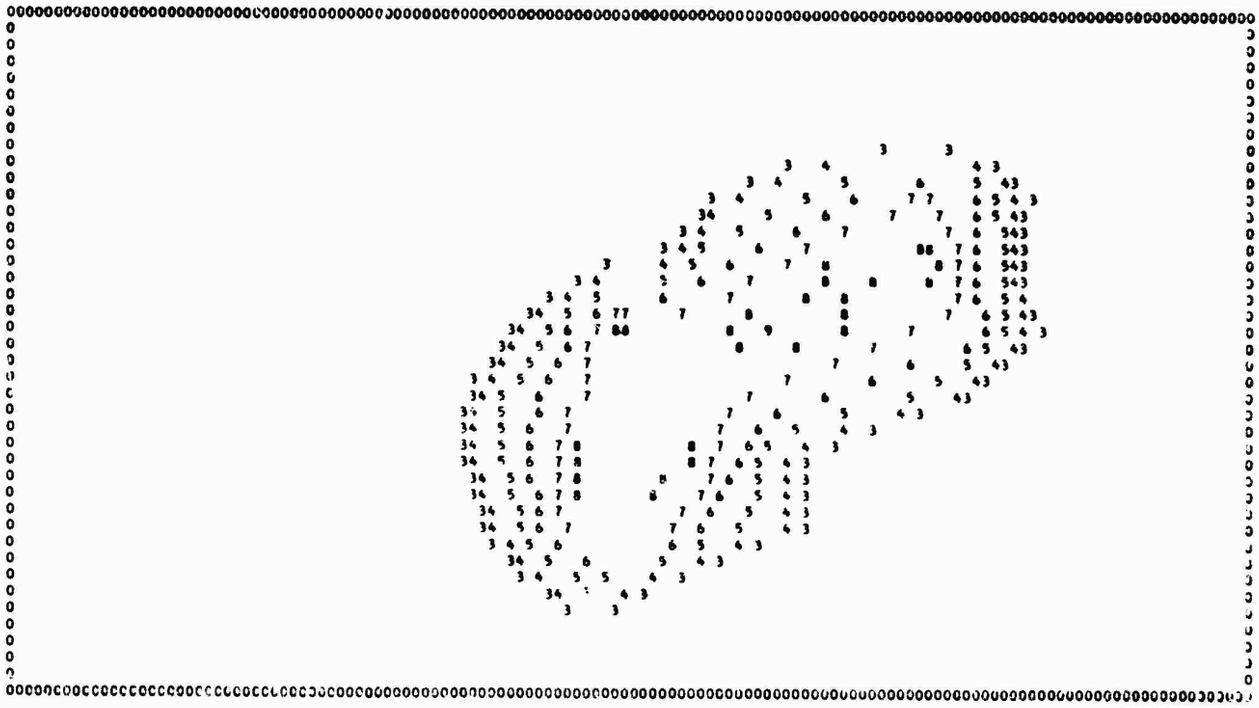

ISOBRIGHTNESS CONTOURS, FIREFLY DANA TIME 0.40 SECONDS AFTER RELEASE. EXPOSURE DURATION 0.02 SECONDS.

SCALE ⊏⊏⊏⊏⊏⊏⊏⊏⊏ EQUALS 0.1 KILOMETER. WAVELENGTH RANGE 380-650 MILLIMICRONS.
VALUES IN TERMS OF ERGS PER SQ. CM. PER STERADIAN PER SECOND. SYMBOLS DEFINED BELOW.

SYMBOL	0	1	2	3	4	5	6	7	8	9	L	A	B	C	D	E	F	G	H	I
LOG E	0.0	0.1	0.2	0.3	0.4	0.5	0.6	0.7	0.8	0.9	1.0	1.1	1.2	1.3	1.4	1.5	1.6	1.7	1.8	1.9

SYMBOL	-	J	K	L	M	N	O	P	Q	R	S	T	U	V	W	X	Y	Z
LOG E	2.0	2.1	2.2	2.3	2.4	2.5	2.6	2.7	2.8	2.9	3.0	3.1	3.2	3.3	3.4	3.5	3.6	3.7	3.8	3.9

Figure 16. Selected Frames, Firefly DANA - Time 0.40 Seconds After Release

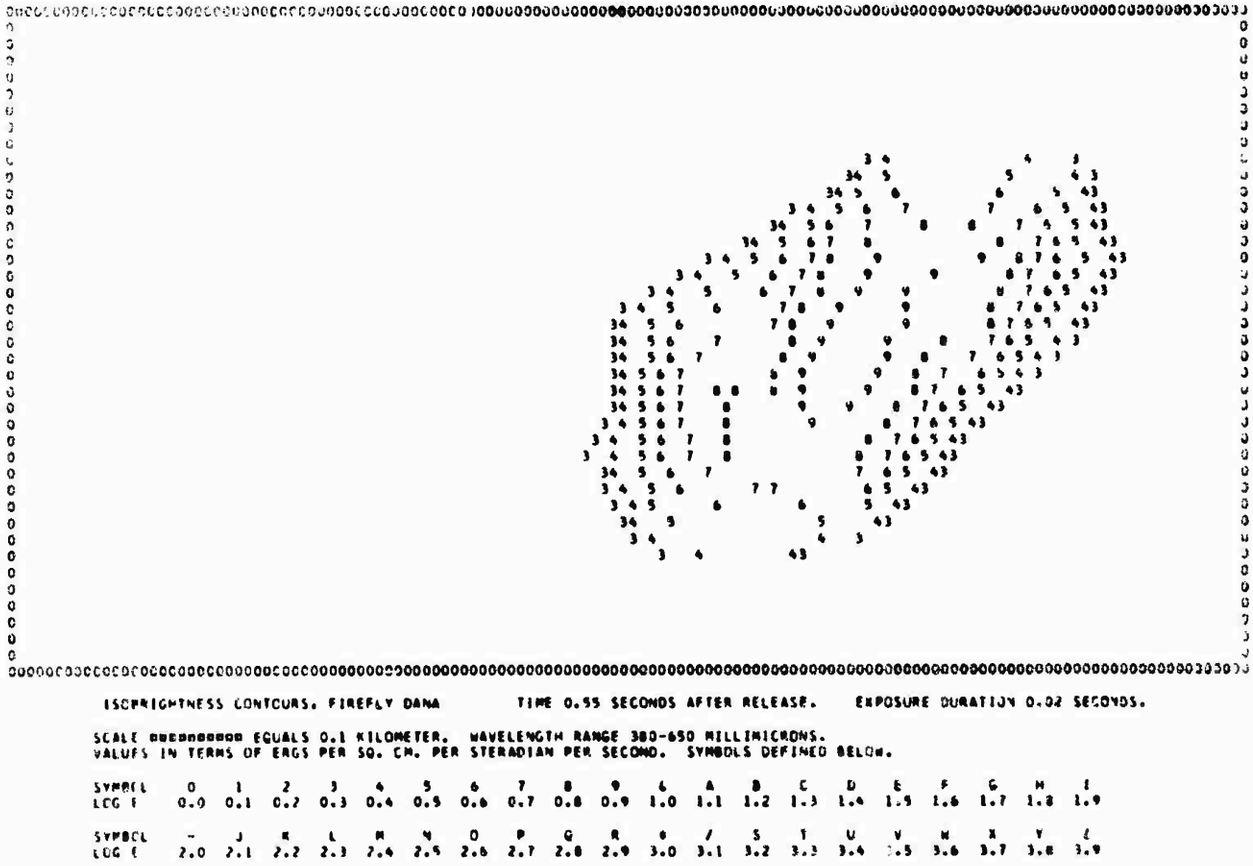

Figure 17. Selected Frames, Firefly DANA - Time 0.55 Seconds After Release

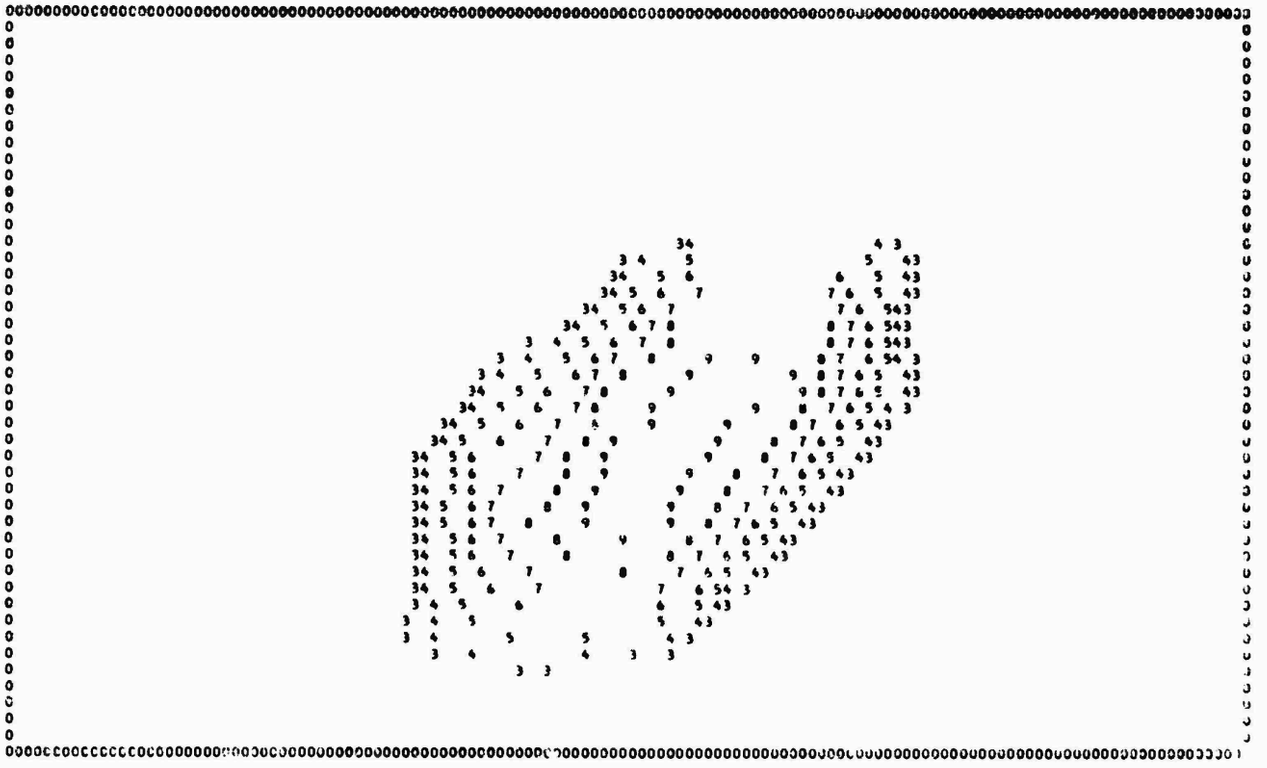

ISOBRIGHTNESS CONTOURS, FIREFLY DANA TIME 0.60 SECONDS AFTER RELEASE. EXPOSURE DURATION 0.02 SECONDS.

SCALE ▫▫▫▫▫▫▫▫▫ EQUALS 0.1 KILOMETER. WAVELENGTH RANGE 380-650 MILLIMICRONS.
VALUES IN TERMS OF ERGS PER SQ. CM. PER STERADIAN PER SECOND. SYMBOLS DEFINED BELOW.

SYMBOL		1	2	3	4	5	6	7	8	9	L	A	B	C	D	E	F	G	H	I
LOG E	0.0	0.1	0.2	0.3	0.4	0.5	0.6	0.7	0.8	0.9	1.0	1.1	1.2	1.3	1.4	1.5	1.6	1.7	1.8	1.9

SYMBOL	-	J	K	L	M	N	O	P	Q	R	S	/	S	T	U	V	W	X	Y	Z
LOG E	2.0	2.1	2.2	2.3	2.4	2.5	2.6	2.7	2.8	2.9	3.0	3.1	3.2	3.3	3.4	3.5	3.6	3.7	3.8	3.9

Figure 18. Selected Frames, Firefly DANA - Time 0.60 Seconds After Release

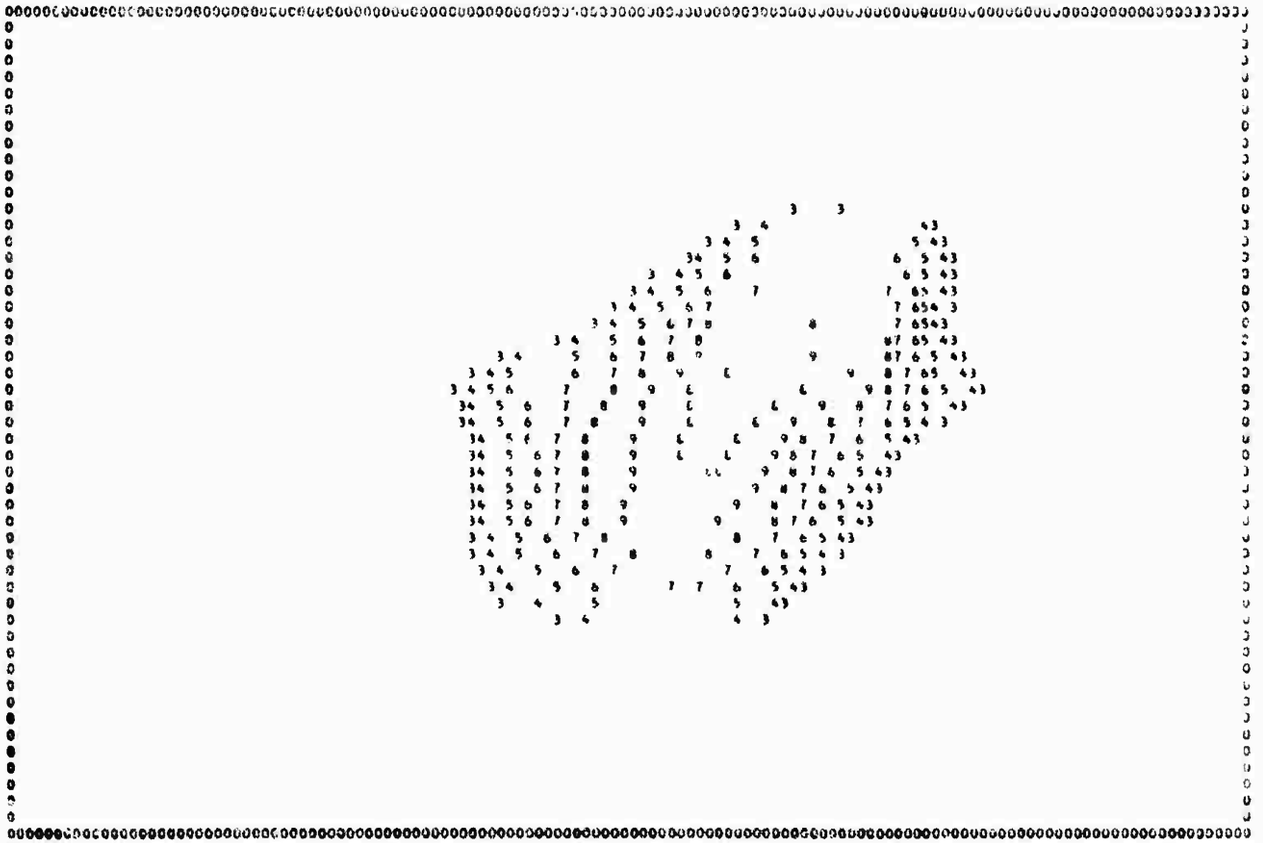

ISOBRIGHTNESS CONTOURS, FIREFLY DANA TIME 0.75 SECONDS AFTER RELEASE. EXPOSURE DURATION 0.02 SECONDS.

SCALE ⊙⊙⊙⊙⊙⊙⊙⊙⊙⊙ EQUALS 0.1 KILOMETER. WAVELENGTH RANGE 380-650 MILLIMICRONS.
VALUES IN TERMS OF ERGS PER SQ. CM. PER STERADIAN PER SECOND. SYMBOLS DEFINED BELOW.

SYMBOL	0	1	2	3	4	5	6	7	8	9	A	B	C	D	E	F	G	H	I
LOG E	0.0	0.1	0.2	0.3	.4	0.5	0.6	0.7	0.8	0.9	1.0	1.1	1.2	1.3	1.4	1.5	1.6	1.7	1.8	1.9

SYMBOL	-	J	K	L	M	N	O	P	Q	R	S	/	U	V	W	X	Y	Z
LOG E	2.0	2.1	2.2	2.3	2.4	2.5	2.6	2.7	2.8	2.9	3.0	3.1	3.2	3.3	3.4	3.5	3.6	3.7	3.8	3.9

Figure 19. Selected Frames, Firefly DANA - Time 0.75 Seconds After Release

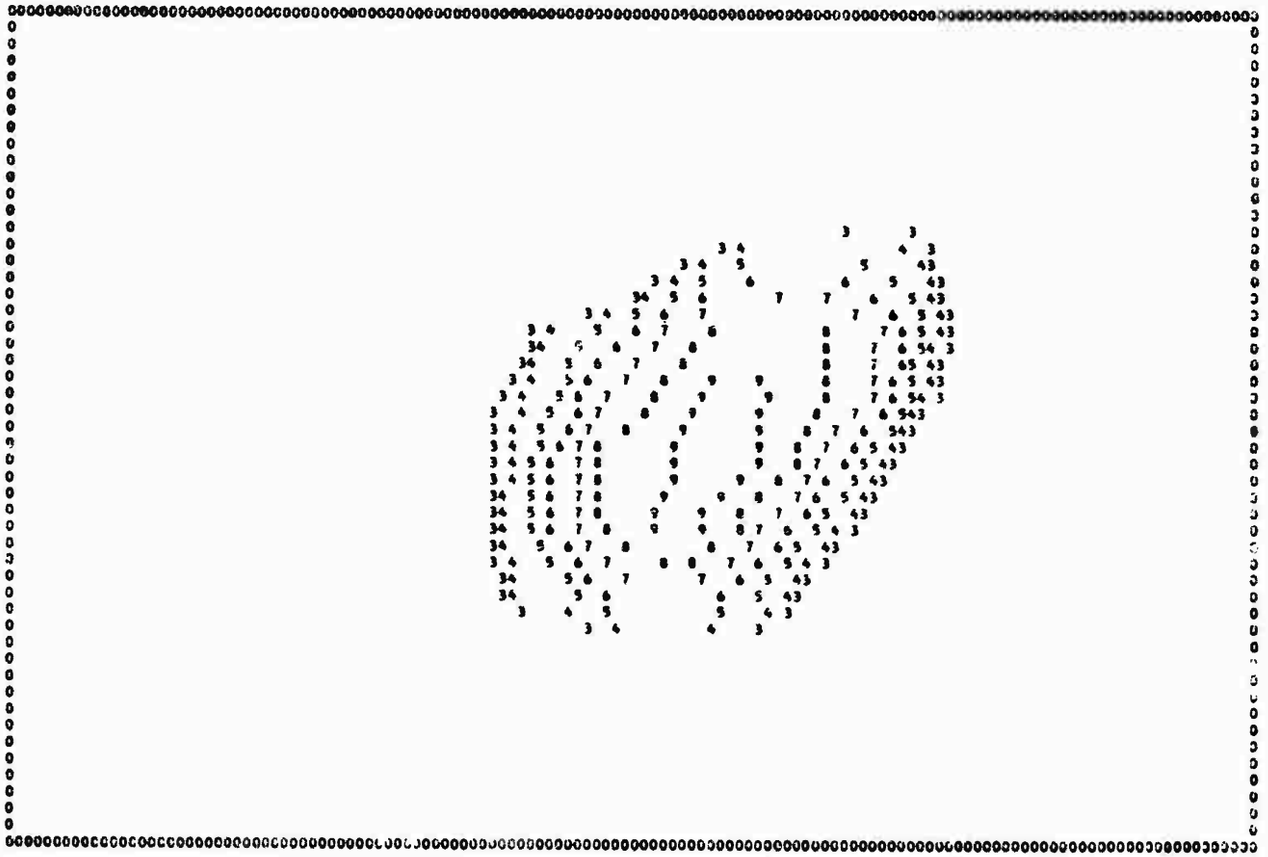

ISOBRIGHTNESS CONTOURS, FIREFLY DANA TIME 0.80 SECONDS AFTER RELEASE. EXPOSURE DURATION 0.02 SECONDS.

SCALE ▪▪▪▪▪▪▪▪▪▪ EQUALS 0.1 KILOMETER. WAVELENGTH RANGE 380-650 MILLIMICRONS.
VALUES IN TERMS OF ERGS PER SQ. CM. PER STERADIAN PER SECOND. SYMBOLS DEFINED BELOW.

SYMBOL	0	1	2	3	4	5	6	7	8	9	A	B	C	D	E	F	G	H	I
LOG E	0.0	0.1	0.2	0.3	0.4	0.5	0.6	0.7	0.8	0.9	1.0	1.1	1.2	1.3	1.4	1.5	1.6	1.7	1.8	1.9

SYMBOL	-	J	K	L	M	N	O	P	Q	R	S	T	U	V	W	X	Y	Z
LOG E	2.0	2.1	2.2	2.3	2.4	2.5	2.6	2.7	2.8	2.9	3.0	3.1	3.2	3.3	3.4		3.6	3.7	3.8	3.9

Figure 20. Selected Frames, Firefly DANA - Time 0.80 Seconds After Release

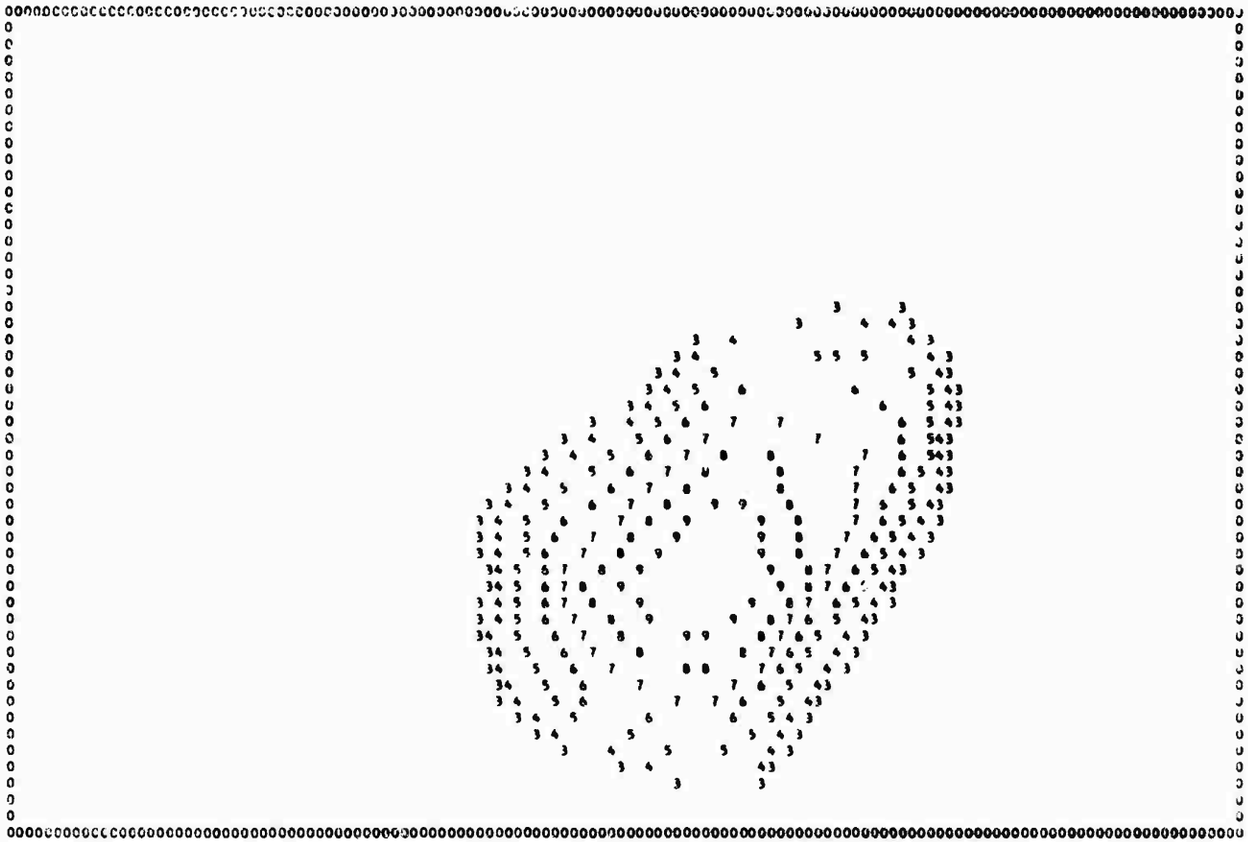

ISOBRIGHTNESS CONTOURS, FIREFLY DANA TIME 0.90 SECONDS AFTER RELEASE. EXPOSURE DURATION 0.02 SECONDS.

SCALE ▪▪▪▪▪▪▪▪▪▪ EQUALS 0.1 KILOMETER. WAVELENGTH RANGE 380-650 MILLIMICRONS.
VALUES IN TERMS OF ERGS PER SQ. CM. PER STERADIAN PER SECOND. SYMBOLS DEFINED BELOW.

SYMBOL	0	1	2	3	4	5	6	7	8	9	A	B	C	D	E	F	G	H	I
LOG E	0.0	0.1	0.2	0.3	0.4	0.5	0.6	0.7	0.8	0.9	1.0	1.1	1.2	1.3	1.4	1.5	1.6	1.7	1.8	1.9

SYMBOL	-	J	K	L	M	N	O	P	Q	R	S	/	T	U	V	W	X	Y	Z
LOG E	2.0	2.1	2.2	2.3	2.4	2.5	2.6	2.7	2.8	2.9	3.0	3.1	3.2	3.3	3.4	3.5	3.6	3.7	3.8	3.9

Figure 21. Selected Frames, Firefly DANA - Time 0.90 Seconds After Release

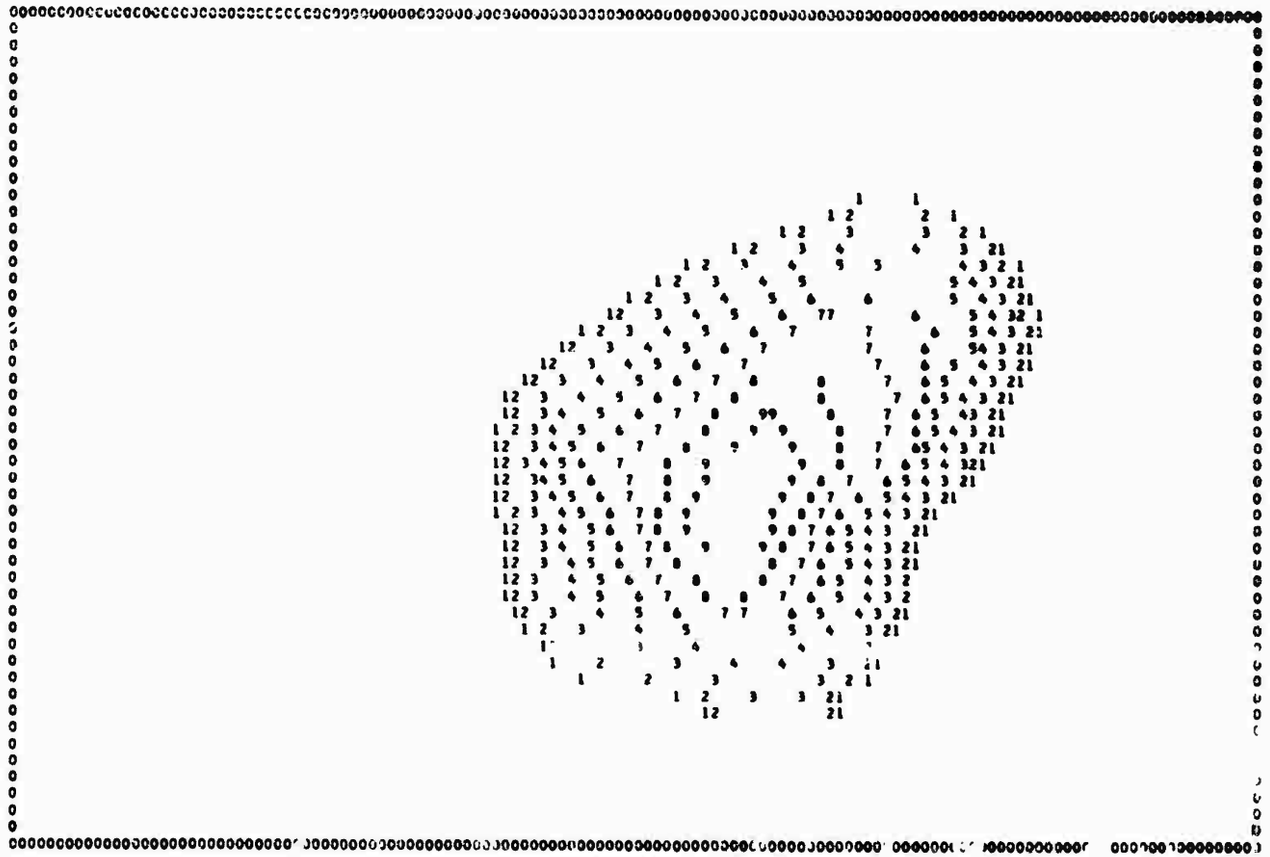

Figure 22. Selected Frames, Firefly DANA - Time 0.95 Seconds After Release

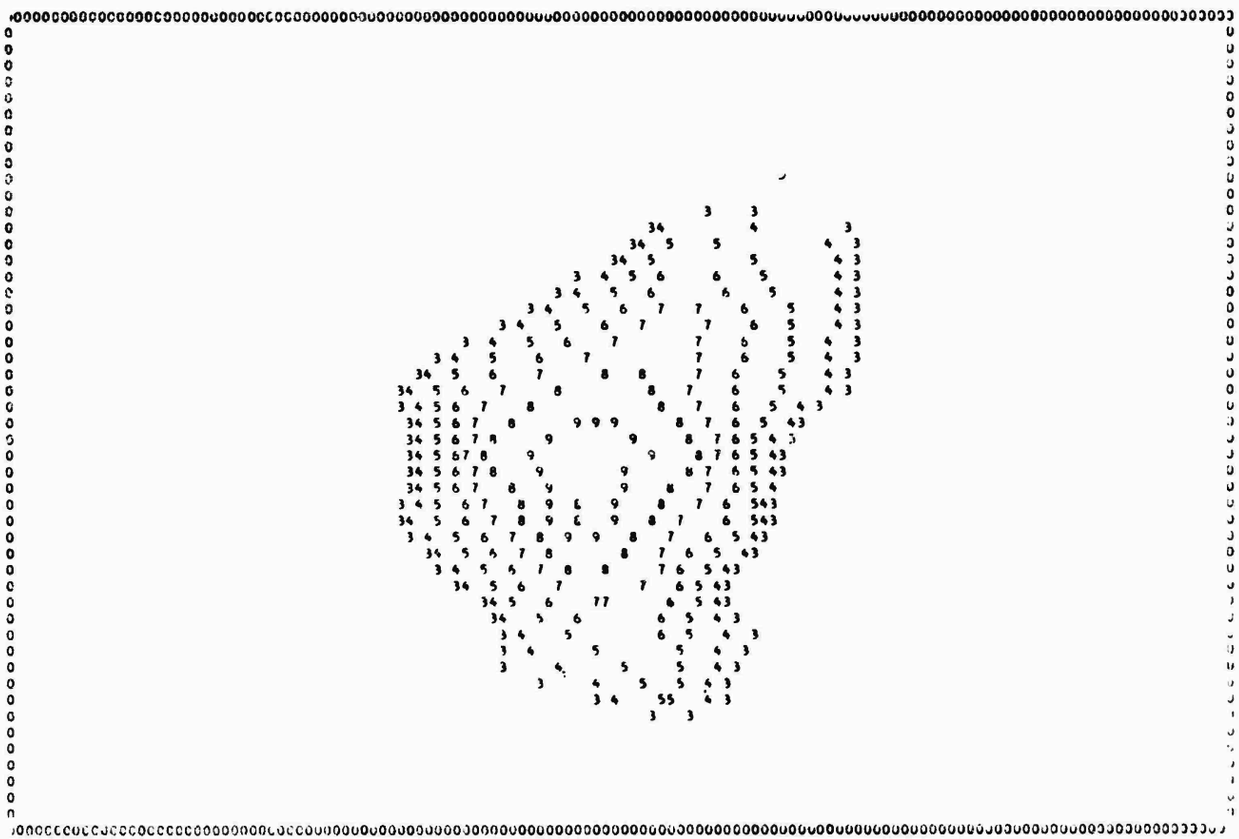

ISOBRIGHTNESS CONTOURS, FIREFLY DANA TIME 1.20 SECONDS AFTER RELEASE. EXPOSURE DURATION 0.32 SECONDS.

SCALE 00000000 EQUALS 0.1 KILOMETER. WAVELENGTH RANGE 380-450 MILLIMICRONS.
VALUES IN TERMS OF ERGS PER SQ. CM. PER STERADIAN PER SECOND. SYMBOLS DEFINED BELOW.

SYMBOL	0	1	2	3	4	5	6	7	8	9	A	B	C	D	E	F	G	H	I
LOG E	0.0	0.1	0.2	0.3	0.4	0.5	0.6	0.7	0.8	0.9	1.0	1.1	1.2	1.3	1.4	1.5	1.6	1.7	1.8	1.9

SYMBOL	-	J	K	L	M	N	O	P	Q	R	S	/	S	T	U	V	W	X	Y	Z
LOG E	2.0	2.1	2.2	2.3	2.4	2.5	2.6	2.7	2.8	2.9	3.0	3.1	3.2	3.3	3.4	3.5	3.6	3.7	3.8	3.9

Figure 23. Selected Frames, Firefly DANA - Time 1.20 Seconds After Release

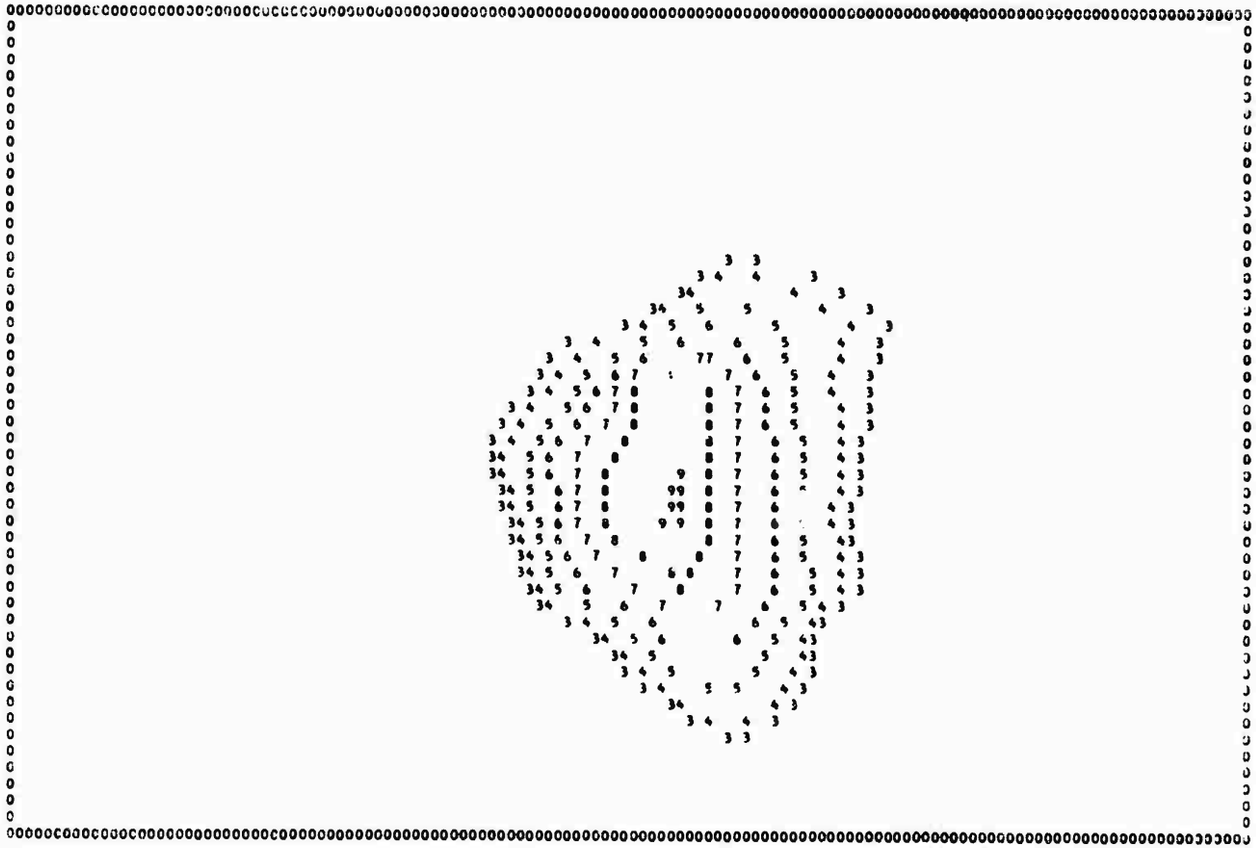

ISOBRIGHTNESS CONTOURS, FIREFLY DANA TIME 1.45 SECONDS AFTER RELEASE. EXPOSURE DURATION 0.02 SECONDS.

SCALE ▫▫▫▫▫▫▫▫▫▫ EQUALS 0.1 KILOMETER. WAVELENGTH RANGE 380-650 MILLIMICRONS.
VALUES IN TERMS OF ERGS PER SQ. CM. PER STERADIAN PER SECOND. SYMBOLS DEFINED BELOW.

SYMBOL	0	1	2	3	4	5	6	7	8	9	&	A	B	C	D	E	F	G	H	I
LOG E	0.0	0.1	0.2	0.3	0.4	0.5	0.6	0.7	0.8	0.9	1.0	1.1	1.2	1.3	1.4	1.5	1.6	1.7	1.8	1.9

SYMBOL	-	J	K	L	M	N	O	P	Q	R	$	/	S	T	U	V	W	X	Y	Z
LOG E	2.0	2.1	2.2	2.3	2.4	2.5	2.6	2.7	2.8	2.9	3.0	3.1	3.2	3.3	3.4	3.5	3.6	3.7	3.8	3.9

Figure 24. Selected Frames, Firefly DANA - Time 1.45 Seconds After Release

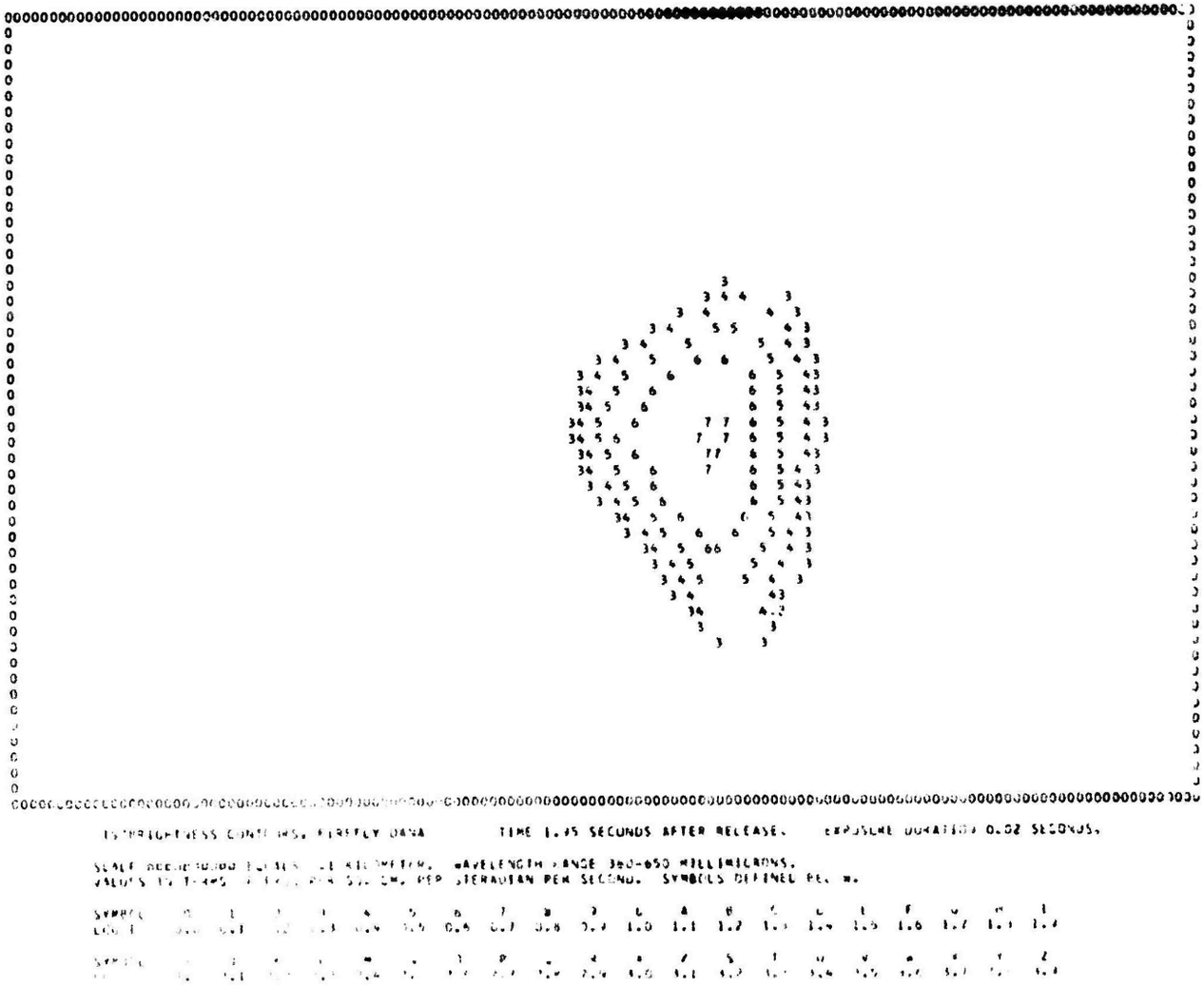

Figure 25. Selected Frames, Firefly DANA - Time 1.95 Seconds After Release

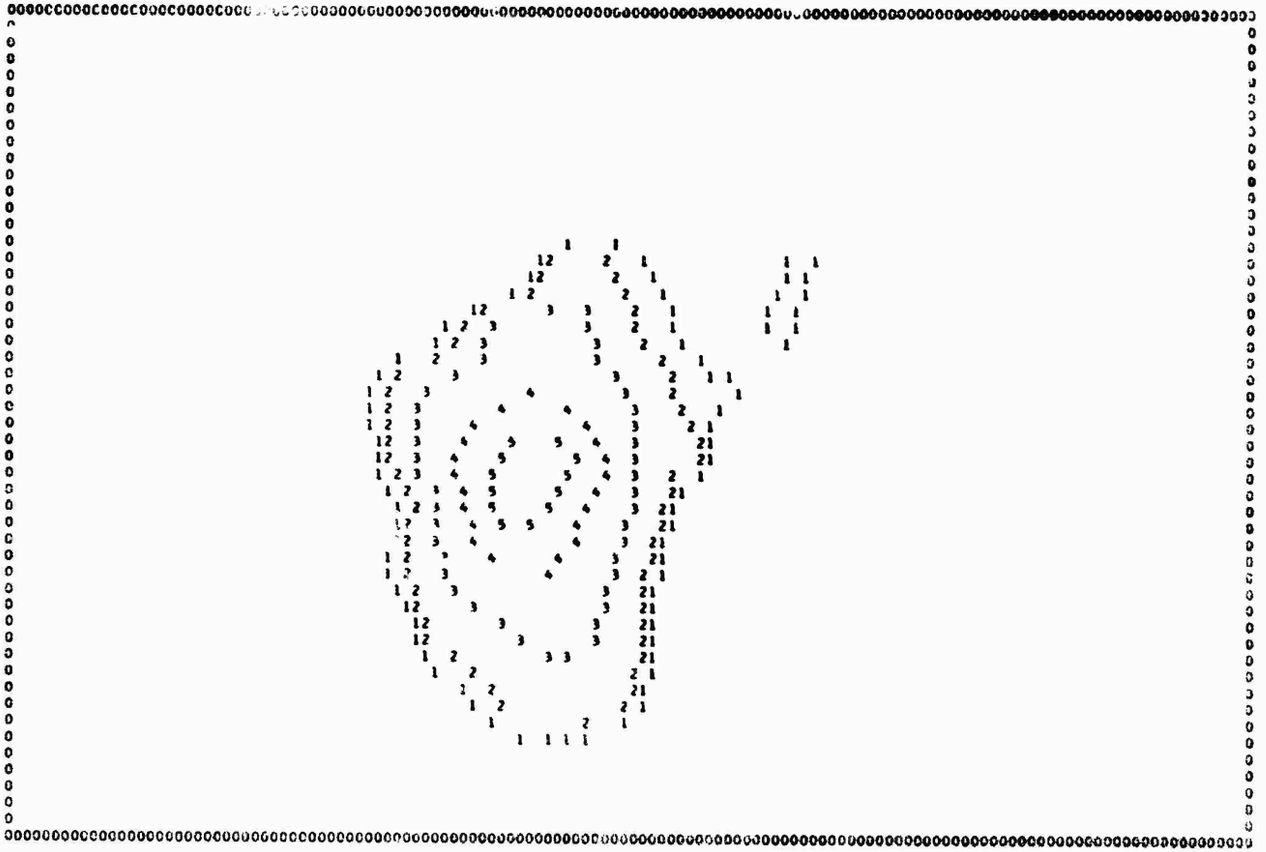

ISOBRIGHTNESS CONTOURS, FIREFLY DANA TIME 2.45 SECONDS AFTER RELEASE. EXPOSURE DURATION 0.02 SECONDS.

SCALE ooooooooo EQUALS 0.1 KILOMETER. WAVELENGTH RANGE 380-650 MILLIMICRONS.
VALUES IN TERMS OF ERGS PER SQ. CM. PER STERADIAN PER SECOND. SYMBOLS DEFINED BELOW.

SYMBOL	0	1	2	3	4	5	6	7	8	9	L	A	B	C	D	E	F	G	H	I
LOG E	0.0	0.1	0.2	0.3	0.4	0.5	0.6	0.7	0.8	0.9	1.0	1.1	1.2	1.3	1.4	1.5	1.6	1.7	1.8	1.9

SYMBOL	-	J	K	L	M	N	O	P	Q	R	S	/	S	T	U	V	W	X	Y	Z
LOG E	2.0	2.1	2.2	2.3	2.4	2.5	2.6	2.7	2.8	2.9	3.0	3.1	3.2	3.3	3.4	3.5	3.6	3.7	3.8	3.9

Figure 26. Selected Frames, Firefly DANA - Time 2.45 Seconds After Release

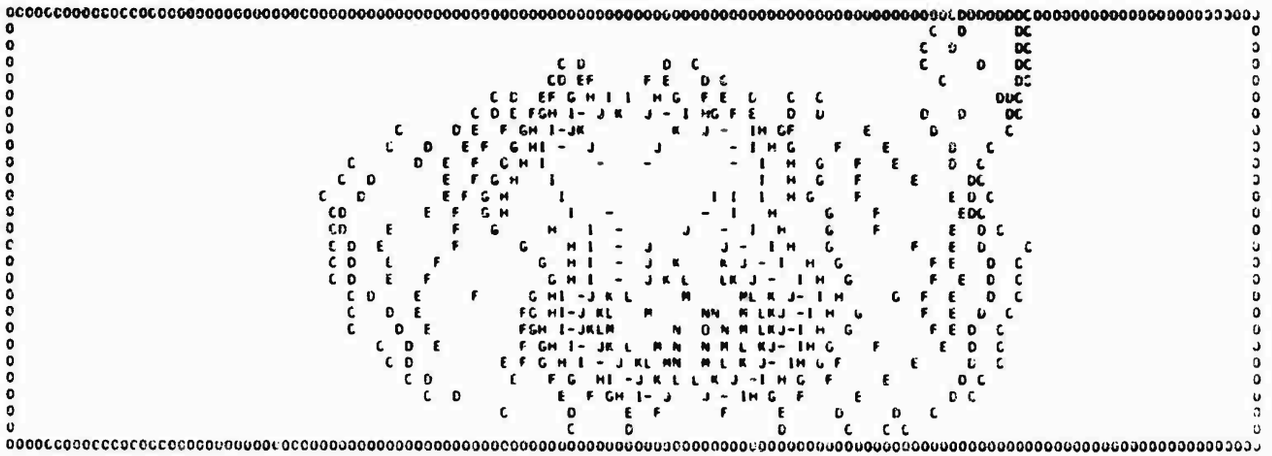

ISOPHOTENESS CONTOURS, FIREFLY DANA TIME 12.0 SECONDS AFTER RELEASE. EXPOSURE DURATION 1.00 SECONDS.

SCALE 0000000000000000000000000000000000 EQUALS ONE KILOMETER. WAVELENGTH RANGE 380-650 MILLIMICRONS.
VALUES ARE IN MILLIERGS PER SQ. CM. PER STERADIAN PER SECOND. SYMBOLS DEFINED BELOW.

SYMBOL	0	1	2	3	4	5	6	7	8	9	A	B	C	D	E	F	G	H	I
LOG E	0.0	0.1	0.2	0.3	0.4	0.5	0.6	0.7	0.8	0.9	1.0	1.1	1.2	1.3	1.4	1.5	1.6	1.7	1.8	1.9

SYMBOL	-	J	K	L	M	N	O	P	Q	R	S	T	U	V	W	X	Y	Z
LOG E	2.0	2.1	2.2	2.3	2.4	2.5	2.6	2.7	2.8	2.9	3.0	3.1	3.2	3.3	3.4	3.5	3.6	3.7	3.8	3.9

Figure 27. Selected Frames, Firefly DANA - Time 12.0 Seconds After Release

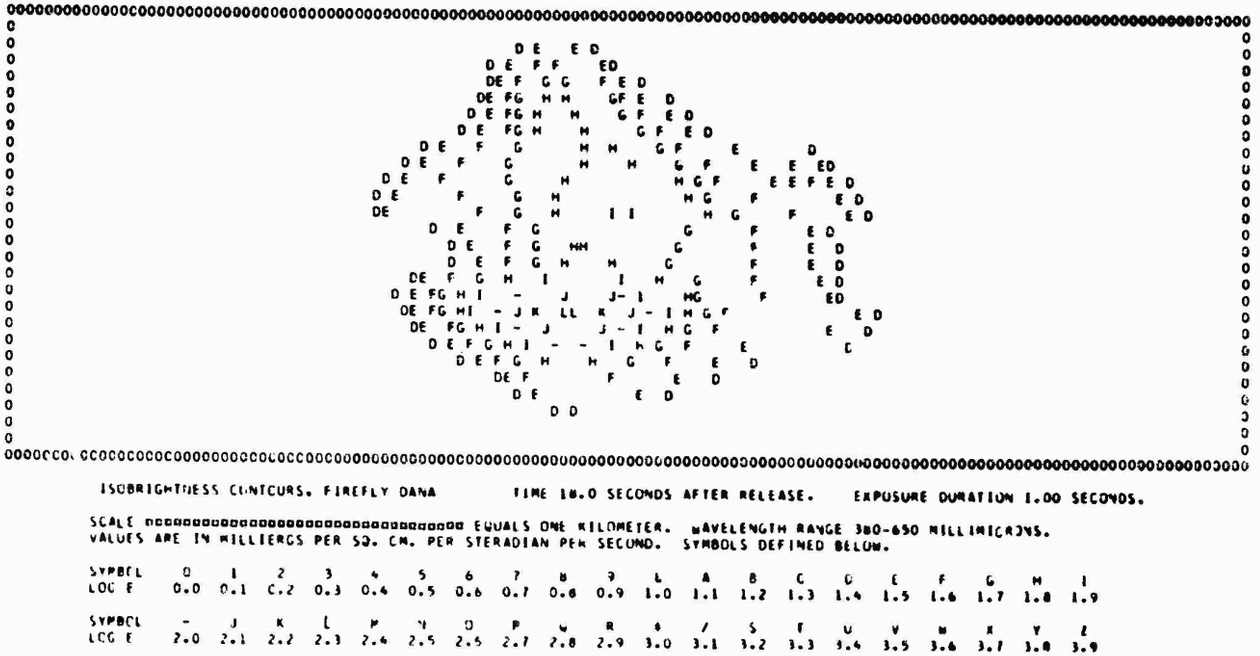

ISOBRIGHTNESS CONTOURS. FIREFLY DANA TIME 18.0 SECONDS AFTER RELEASE. EXPOSURE DURATION 1.00 SECONDS.

SCALE ▫▫▫▫▫▫▫▫▫▫▫▫▫▫▫▫▫▫▫▫▫▫▫▫▫▫▫▫▫▫▫▫▫▫ EQUALS ONE KILOMETER. WAVELENGTH RANGE 380-650 MILLIMICRONS.
VALUES ARE IN MILLIERGS PER SQ. CM. PER STERADIAN PER SECOND. SYMBOLS DEFINED BELOW.

SYMBOL	0	1	2	3	4	5	6	7	8	9	L	A	B	C	D	E	F	G	H	I
LOG E	0.0	0.1	0.2	0.3	0.4	0.5	0.6	0.7	0.8	0.9	1.0	1.1	1.2	1.3	1.4	1.5	1.6	1.7	1.8	1.9

SYMBOL	-	J	K	L	M	N	O	P	Q	R	S	/	S	T	U	V	W	X	Y	Z
LOG E	2.0	2.1	2.2	2.3	2.4	2.5	2.6	2.7	2.8	2.9	3.0	3.1	3.2	3.3	3.4	3.5	3.6	3.7	3.8	3.9

Figure 28. Selected Frames, Firefly DANA - Time 18.0 Seconds After Release

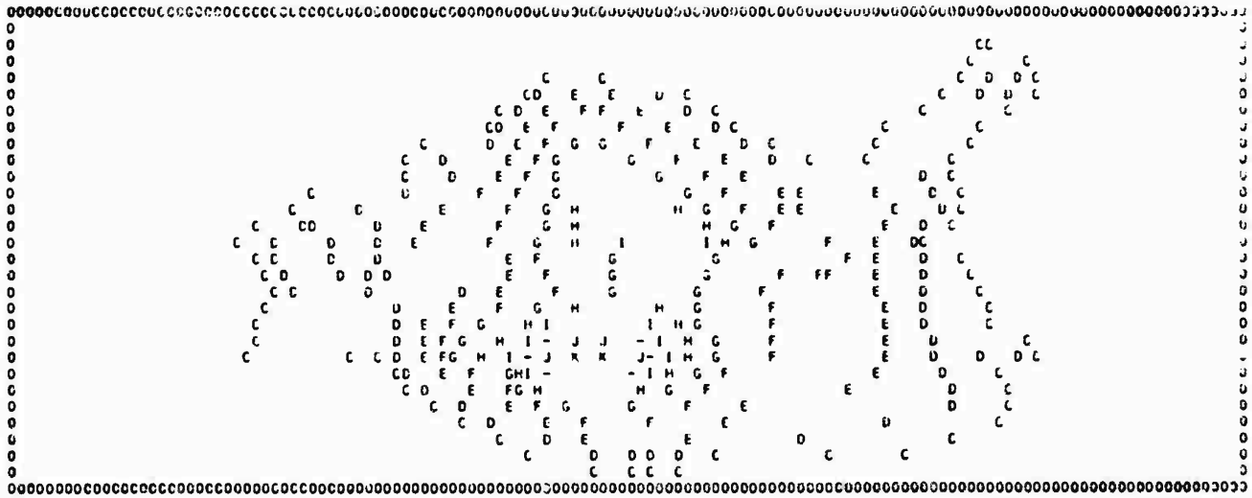

ISOBRIGHTNESS CONTOURS, FIREFLY DANA TIME 20.0 SECONDS AFTER RELEASE. EXPOSURE DURATION 1.00 SECONDS.

SCALE 0000000C0000C000000000000000000 EQUALS ONE KILOMETER. WAVELENGTH RANGE 380-650 MILLIMICRONS.
VALUES ARE IN MILLIERGS PER SQ. CM. PER STERADIAN PER SECOND. SYMBOLS DEFINED BELOW.

SYMBOL	0	1	2	3	4	5	6	7	8	9	0	A	B	C	D	E	F	G	H	I
LOG E	0.0	0.1	0.2	0.3	0.4	0.5	0.6	0.7	0.8	0.9	1.0	1.1	1.2	1.3	1.4	1.5	1.6	1.7	1.8	1.9

SYMBOL	-	J	K	L	M	N	O	P	Q	R	S	/	S	T	U	V	W	X	Y	Z
LOG E	2.0	2.1	2.2	2.3	2.4	2.5	2.6	2.7	2.8	2.9	3.0	3.1	3.2	3.3	3.4	3.5	3.6	3.7	3.8	3.9

Figure 29. Selected Frames, Firefly DANA - Time 20.0 Seconds After Release

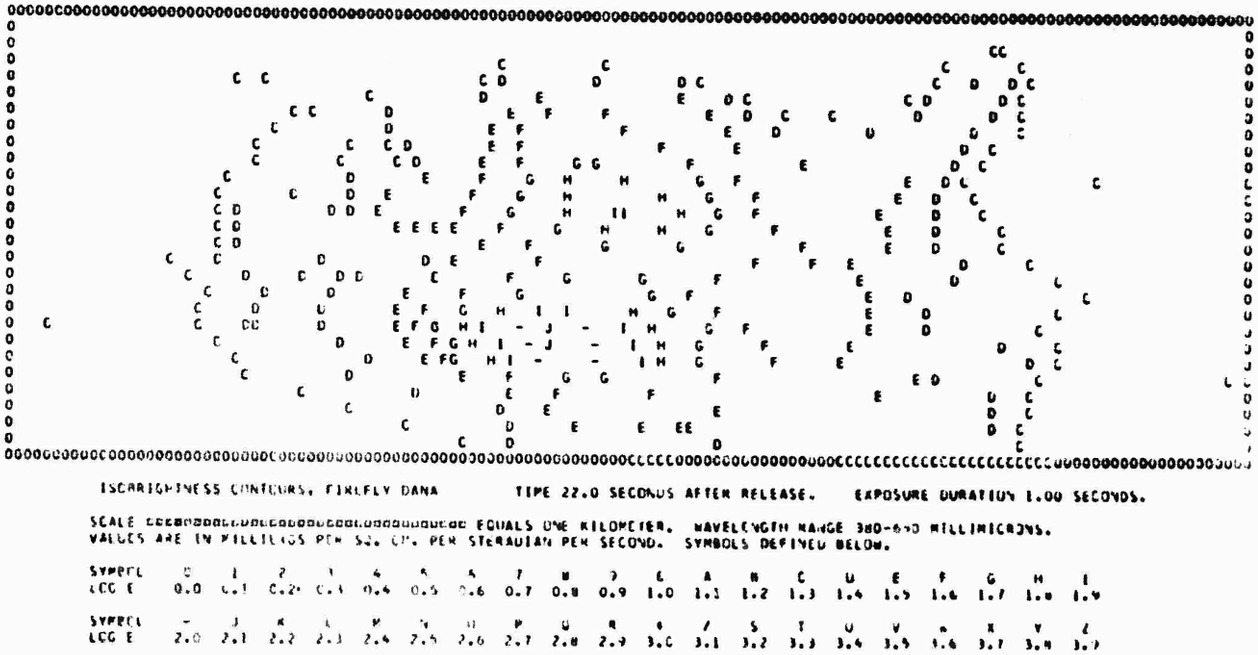

Figure 30. Selected Frames, Firefly DANA - Time 22.0 Seconds After Release

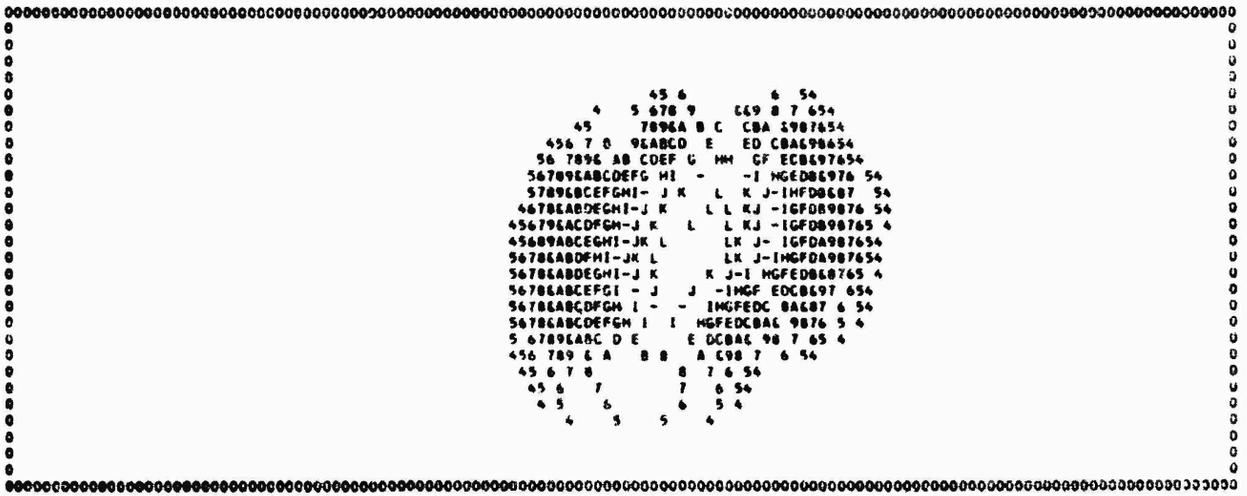

ISOBRIGHTNESS CONTOURS, FIREFLY SALLY TIME 0.00 SECONDS AFTER RELEASE. EXPOSURE DURATION 0.02 SECONDS.

SCALE ▪▪▪▪▪▪▪▪▪▪ EQUALS 0.1 KILOMETER. WAVELENGTH RANGE 380-650 MILLIMICRONS.
VALUES IN TERMS OF ERGS PER SQ. CM. PER STERADIAN PER SECOND. SYMBOLS DEFINED BELOW.

SYMBOL	0	1	2	3	4	5	6	7	8	9	A	B	C	D	E	F	G	H	I
LOG E	0.0	0.1	0.2	0.3	0.4	0.5	0.6	0.7	0.8	0.9	1.0	1.1	1.2	1.3	1.4	1.5	1.6	1.7	1.8	1.9

SYMBOL	-	J	K	L	M	N	O	P	Q	R	S	/	T	U	V	W	X	Y	Z
LOG E	2.0	2.1	2.2	2.3	2.4	2.5	2.6	2.7	2.8	2.9	3.0	3.1	3.2	3.3	3.4	3.5	3.6	3.7	3.8	3.9

Figure 31. Selected Frames, Firefly SALLY - Burst Frame

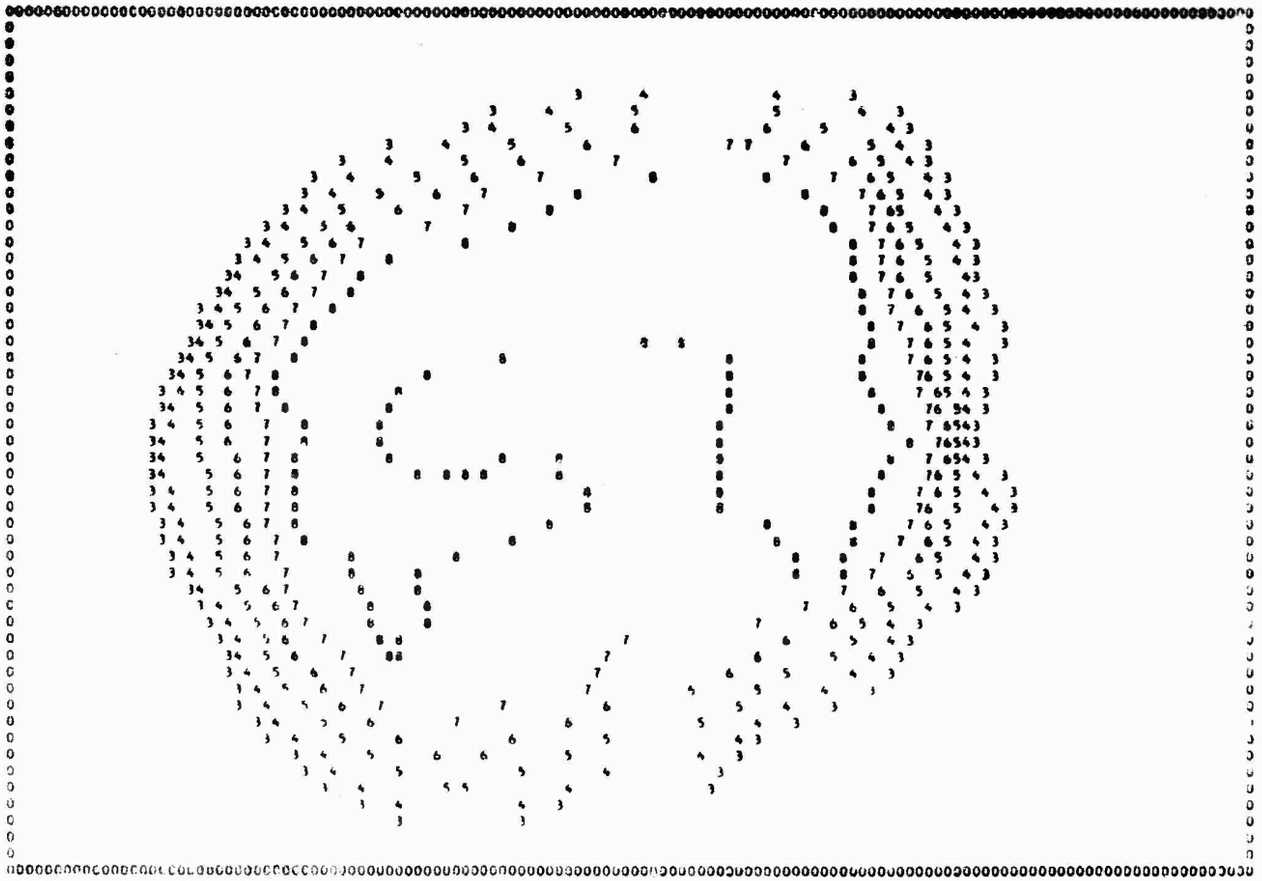

ISOBRIGHTNESS CONTOURS, FIREFLY SALLY TIME 0.20 SECONDS AFTER RELEASE. EXPOSURE DURATION 0.02 SECONDS.

SCALE 0000000000 EQUALS 0.1 KILOMETER. WAVELENGTH RANGE 380-650 MILLIMICRONS.
VALUES IN TERMS OF ERGS PER SQ. CM. PER STERADIAN PER SECOND. SYMBOLS DEFINED BELOW.

SYMBOL	0	1	2	3	4	5	6	7	8	9	A	B	C	D	E	F	G	H	I
LOG E	0.0	0.1	0.2	0.3	0.4	0.5	0.6	0.7	0.8	0.9	1.0	1.1	1.2	1.3	1.4	1.5	1.6	1.7	1.8	1.9

Figure 32. Selected Frames, Firefly SALLY - Time 0.2 Seconds After Release

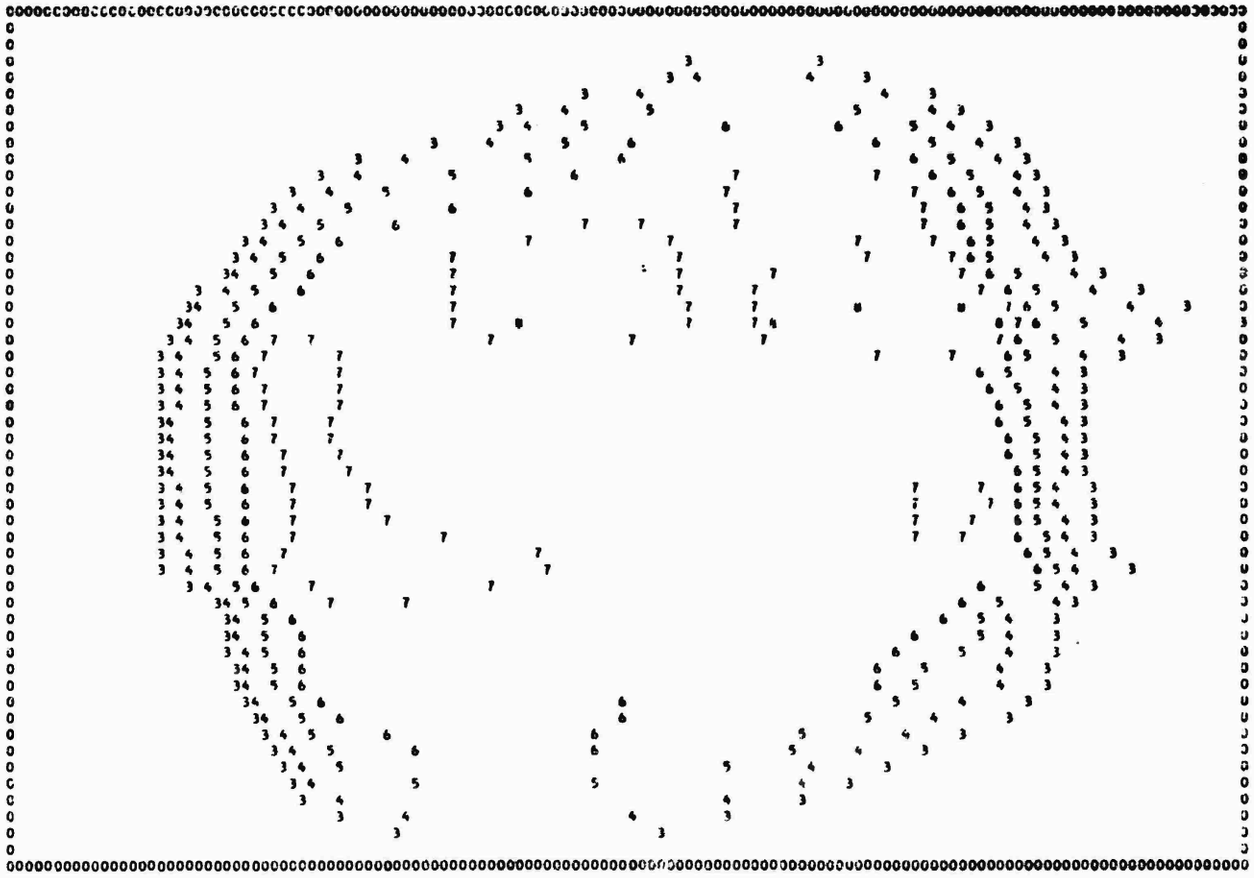

ISOBRIGHTNESS CONTOURS, FIREFLY SALLY TIME 0.30 SECONDS AFTER RELEASE. EXPOSURE DURATION 0.02 SECONDS.

SCALE ▫▫▫▫▫▫▫▫▫▫ EQUALS 0.1 KILOMETER. WAVELENGTH RANGE 380-650 MILLIMICRONS.
VALUES IN TERMS OF ERGS PER SQ. CM. PER STERADIAN PER SECOND. SYMBOLS DEFINED BELOW.

SYMBOL	0	1	2	3	4	5	6	7	8	9	A	B	C	D	E	F	G	H	I
LOG E	0.0	0.1	0.2	0.3	0.4	0.5	0.6	0.7	0.8	0.9	1.0	1.1	1.2	1.3	1.4	1.5	1.6	1.7	1.8	1.9

Figure 33. Selected Frames, Firefly SALLY - Time 0.3 Seconds After Release

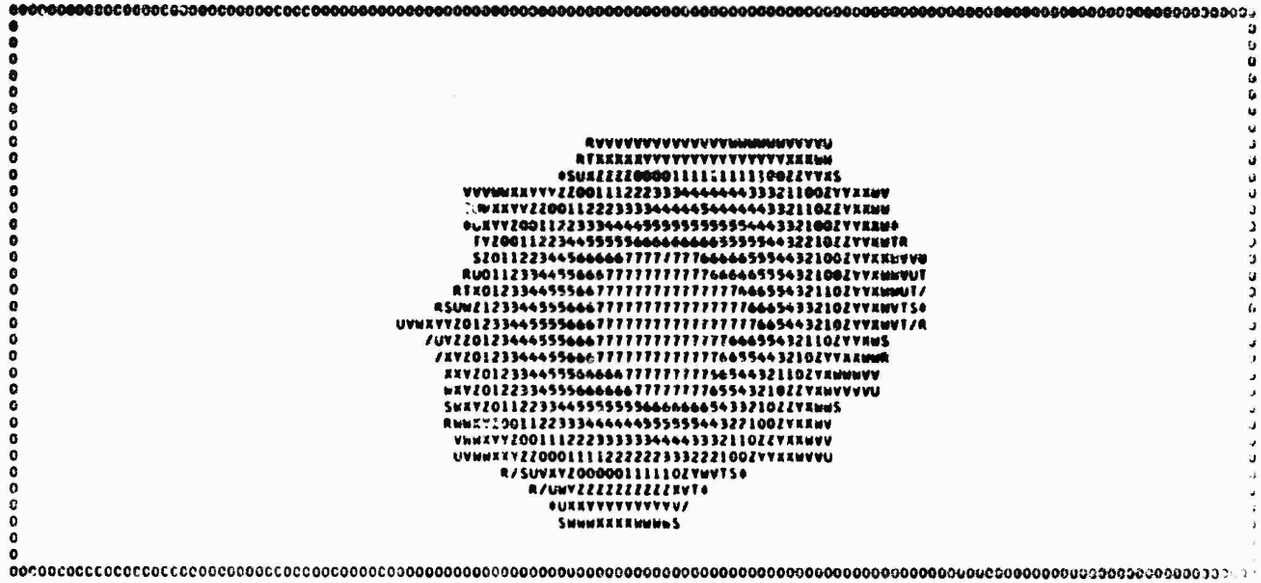

ISOBRIGHTNESS CONTOURS, FIREFLY DANA. TIME 0.05 SECONDS AFTER RELEASE. EXPOSURE DURATION 0.02 SECONDS.

SCALE ▯▯▯▯▯▯▯▯▯ EQUALS 0.1 KILOMETER.
VALUES ARE IN MILLIERGS PER SQ. CM. PER STERADIAN PER SECOND. SYMBOLS DEFINED BELOW.

SYMBOL	0	1	2	3	4	5	6	7	8	9	A	B	C	D	E	F	G	H	I
LOG E	0.0	0.1	0.2	0.3	0.4	0.5	0.6	0.7	0.8	0.9	1.0	1.1	1.2	1.3	1.4	1.5	1.6	1.7	1.8	1.9

SYMBOL	-	J	K	L	M	N	O	P	Q	R	S	/	T	U	V	W	X	Y	Z
LOG E	2.0	2.1	2.2	2.3	2.4	2.5	2.6	2.7	2.8	2.9	3.0	3.1	3.2	3.3	3.4	3.5	3.6	3.7	3.8	3.9

FOR LOG E VALUES GREATER THAN 3.9, ADD 4.0 TO VALUES IN TABLE TO OBTAIN SYMBOLS.

Figure 34. Solid Print Alternate, Isobrightness Data - Time 0.05 Seconds After Release

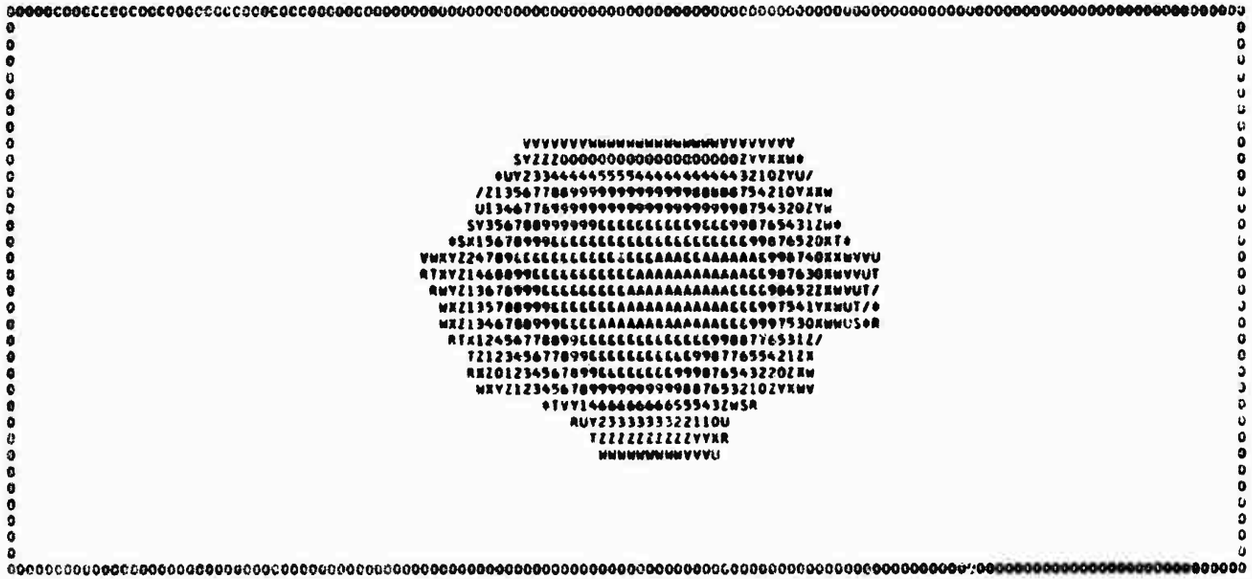

ISOBRIGHTNESS CONTOURS, FIREFLY DANA. TIME 0000 SECONDS AFTER RELEASE. EXPOSURE DURATION 0.02 SECONDS.

SCALE ⊙⊙⊙⊙⊙⊙⊙⊙⊙ EQUALS 0.1 KILOMETER.
VALUES ARE IN MILLIERGS PER SQ. CM. PER STERADIAN PER SECOND. SYMBOLS DEFINED BELOW.

SYMBOL	0	1	2	3	4	5	6	7	8	9	&	A	B	C	D	E	F	G	H	I
LOG E	0.0	0.1	0.2	0.3	0.4	0.5	0.6	0.7	0.8	0.9	1.0	1.1	1.2	1.3	1.4	1.5	1.6	1.7	1.8	1.9

SYMBOL	-	J	K	L	M	N	O	P	Q	R	$	/	S	T	U	V	W	X	Y	Z
LOG E	2.0	2.1	2.2	2.3	2.4	2.5	2.6	2.7	2.8	2.9	3.0	3.1	3.2	3.3	3.4	3.5	3.6	3.7	3.8	3.9

FOR LOG E VALUES GREATER THAN 3.9, ADD 4.0 TO VALUES IN TABLE TO OBTAIN SYMBOLS.

Figure 35. Solid Print Alternate, Isobrightness Data - Time 0.00 Seconds After Release

Change of cut-off level for background in plotting frame already included in Figures 8 through 30.

Note particularly the considerable apparent increase in size of the cloud (which, of course, is not real) and the greater difficulty in recognizing a particular contour level when a great deal of extra information is included in the graph.

As explained in the text, our present technique is to make both this kind of plot and the one shown in Figure 8 through 30 for the same time after burst for different interpretation purposes.

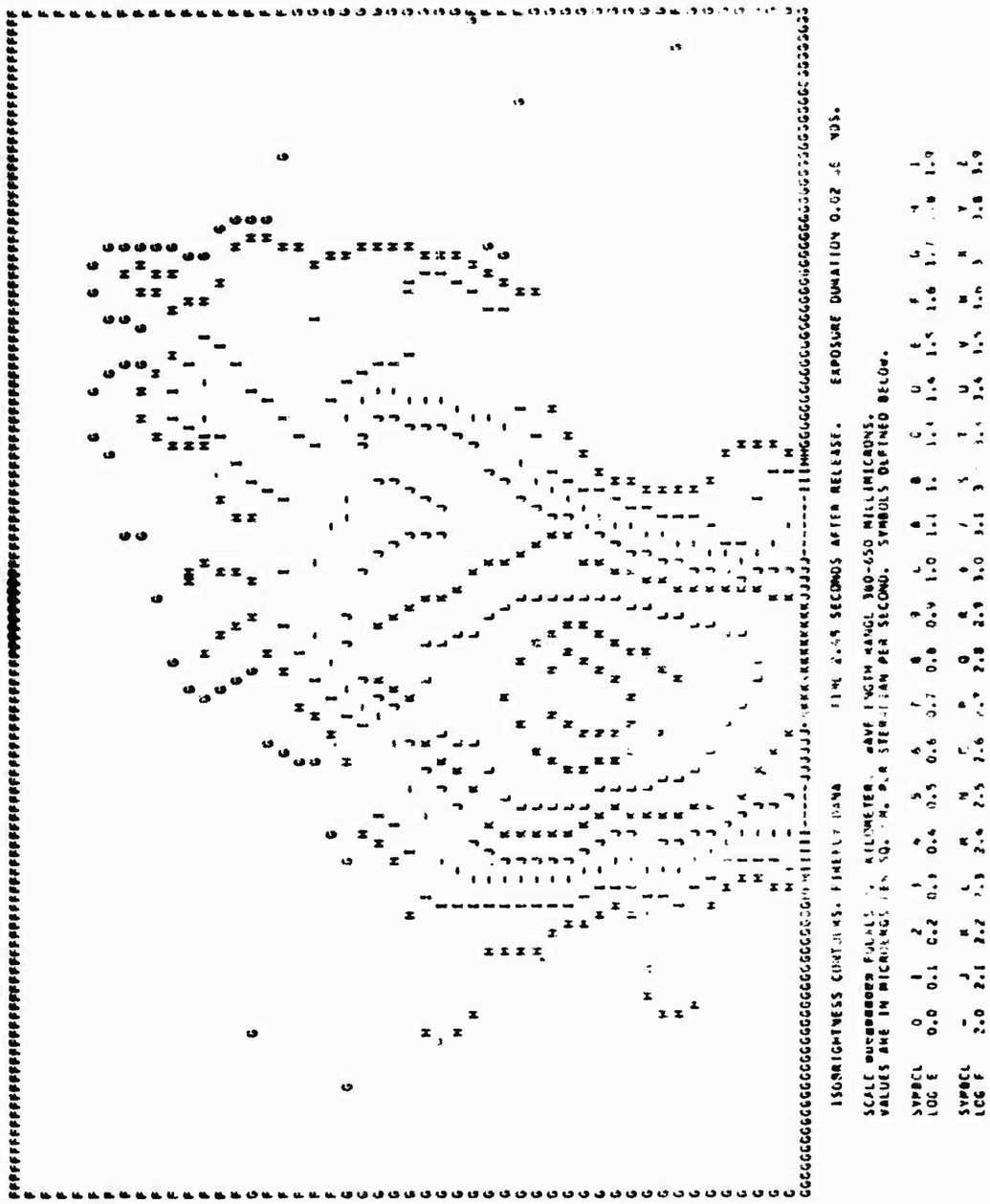

Figure 36. Alternate Background Level Selection at Lower Than Figures 8 Through 31 Value Example

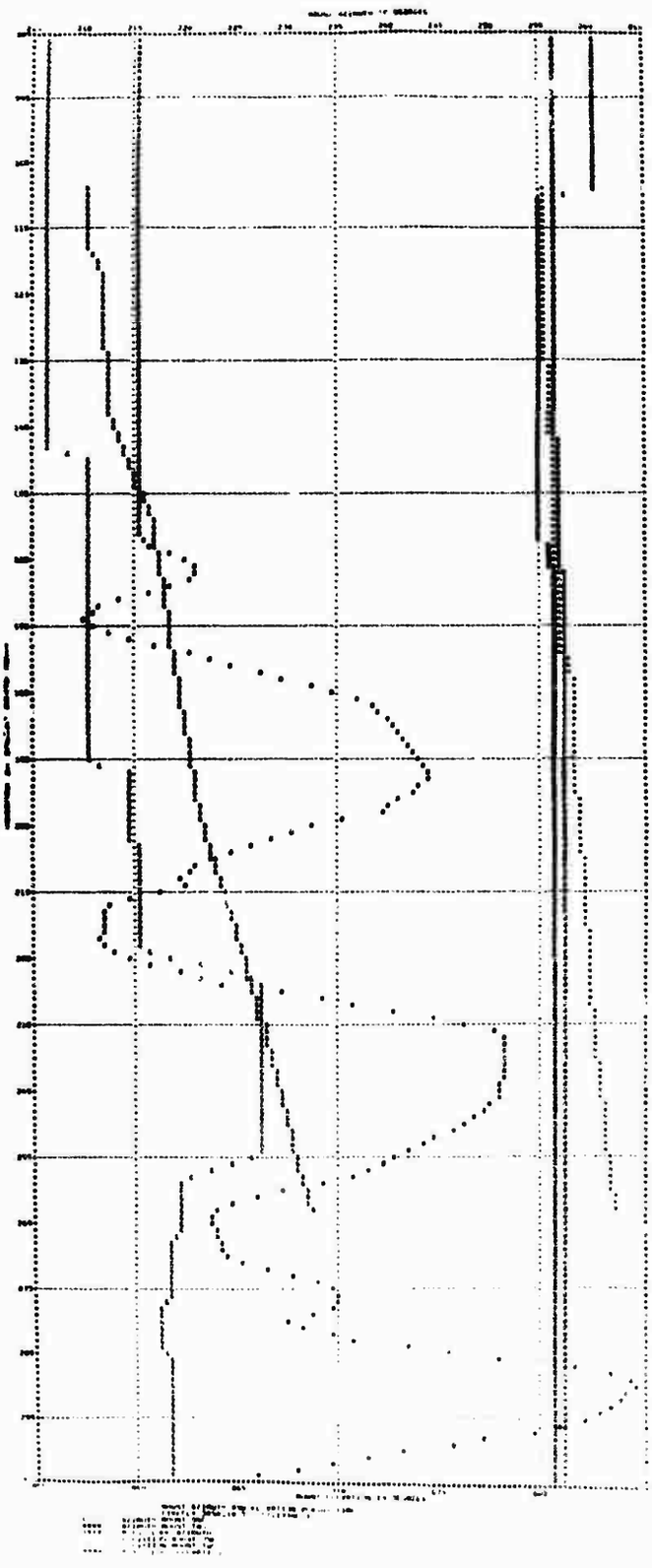

Figure 37. Computer Plotted Mount Azimuth and Elevation vs Time, Firefly DANA

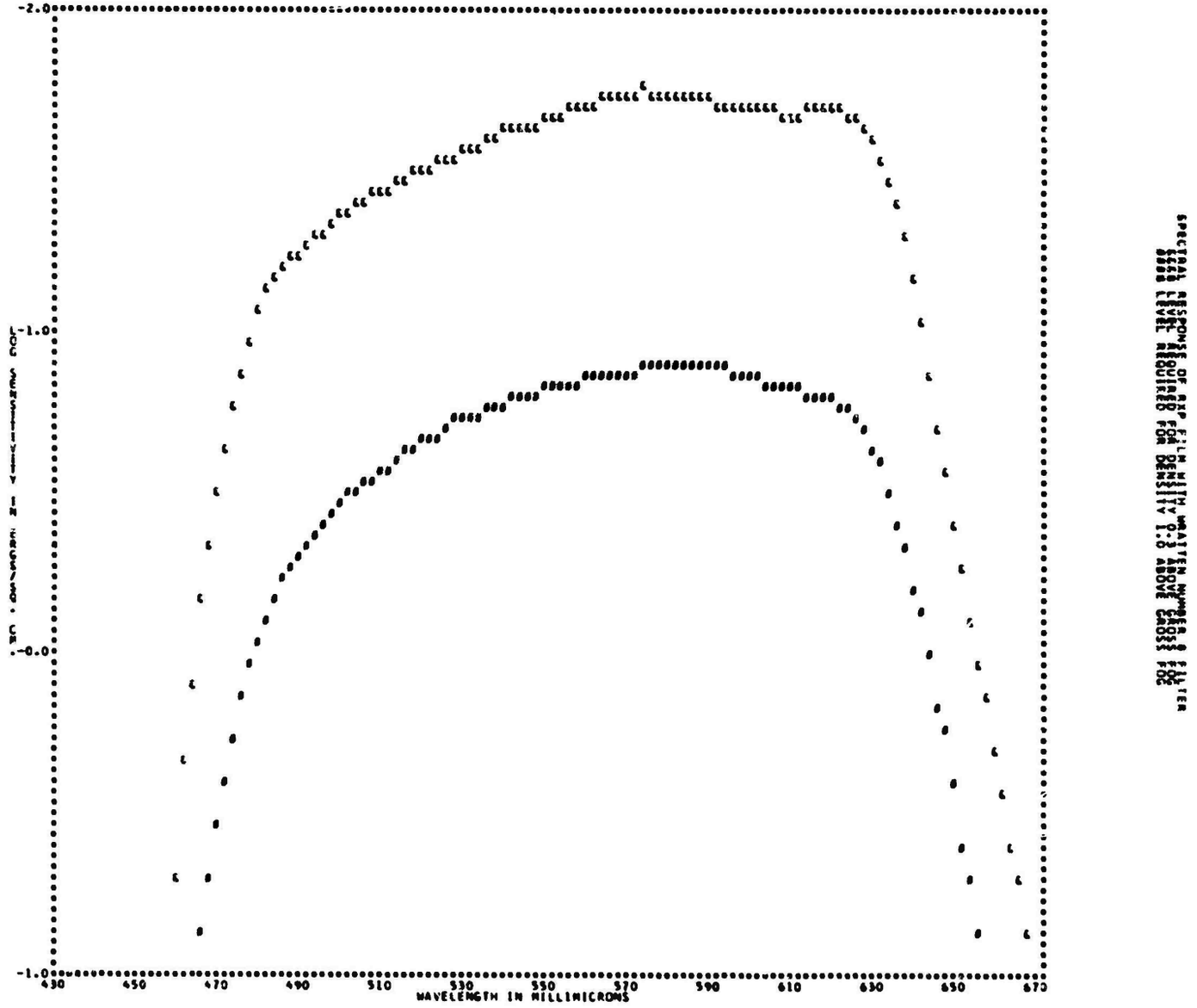

Figure 38. Computer Plotted Sensitivity Curve for Kodak RXP Film Plus Wratten No. 8 Filter

ISOBRIGHTNESS CONTOURS, FIREFLY DANA. TIME 0.[illegible] SECONDS AFTER RELEASE. EXPOSURE DURATION 0.02 SECONDS.

SCALE ▪▪▪▪▪▪▪▪▪▪▪▪▪▪▪▪▪▪▪▪ EQUALS 0.1 KILOMETER.
VALUES ARE IN MILLIERGS PER SQ. CM. PER STERADIAN PER SECOND. SYMBOLS DEFINED BELOW.

SYMBOL	0	1	2	3	4	5	6	7	8	9	A	B	C	D	E	F	G	H	I
LOG E	0.0	0.1	0.2	0.3	0.4	0.5	0.6	0.7	0.8	0.9	1.0	1.1	1.2	1.3	1.4	1.5	.6	1.7	1.8	1.9

SYMBOL	-	J	K	L	M	N	O	P	Q	R	S	T	U	V	W	X	Y	Z
LOG E	2.0	2.1	2.2	2.3	2.4	2.5	2.6	2.7	2.8	2.9	3.0	3.1	3.2	3.3	3.4	3.5	3.6	3.7	3.8	3.9

FOR LOG E VALUES GREATER THAN 3.9, ADD 4.0 TO VALUES IN TABLE TO OBTAIN SYMBOLS.

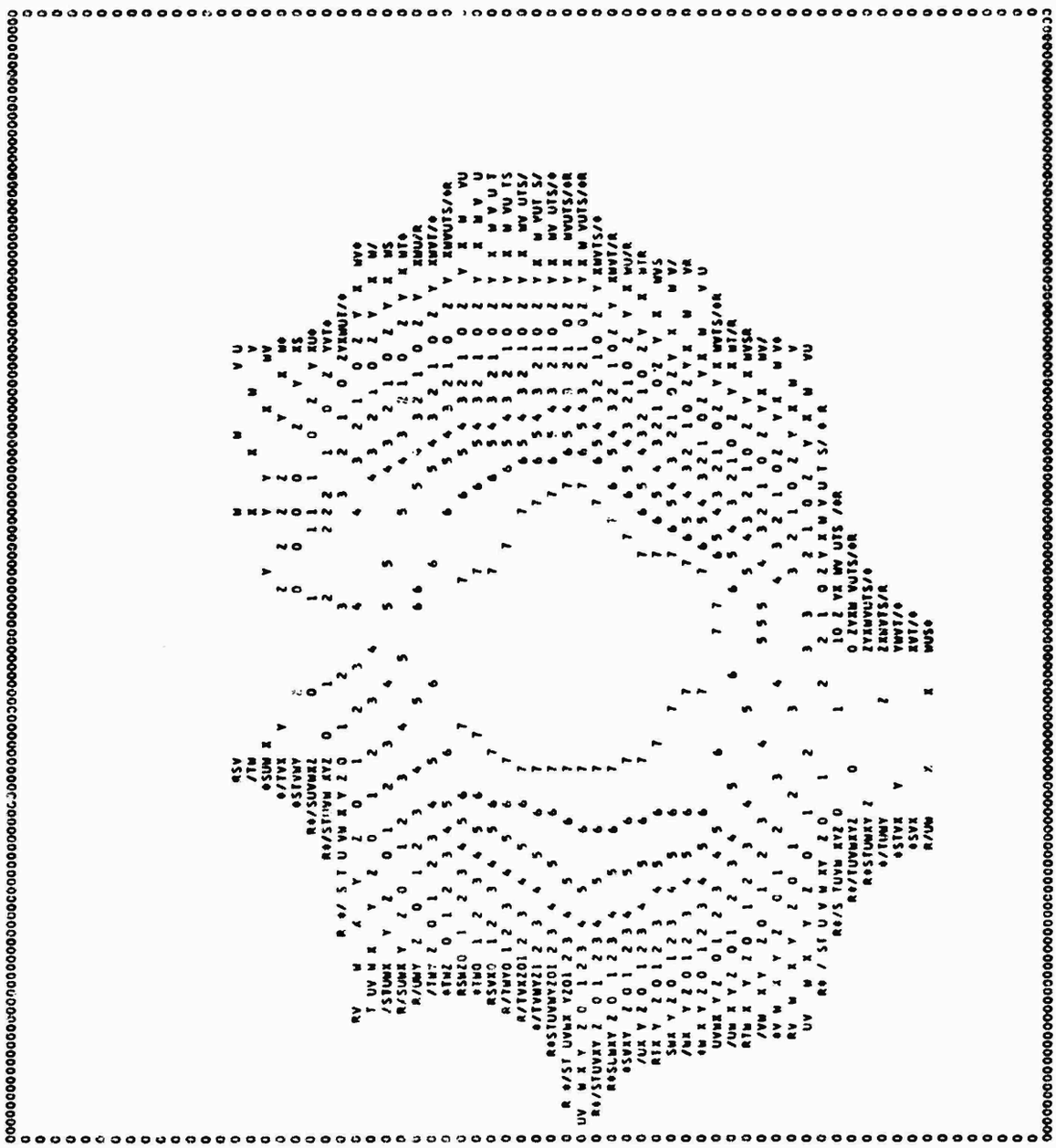

Figure 39. Alternate Background Treatment-Interpolation to Zero Level Rather Than Selection of Cut-off Level

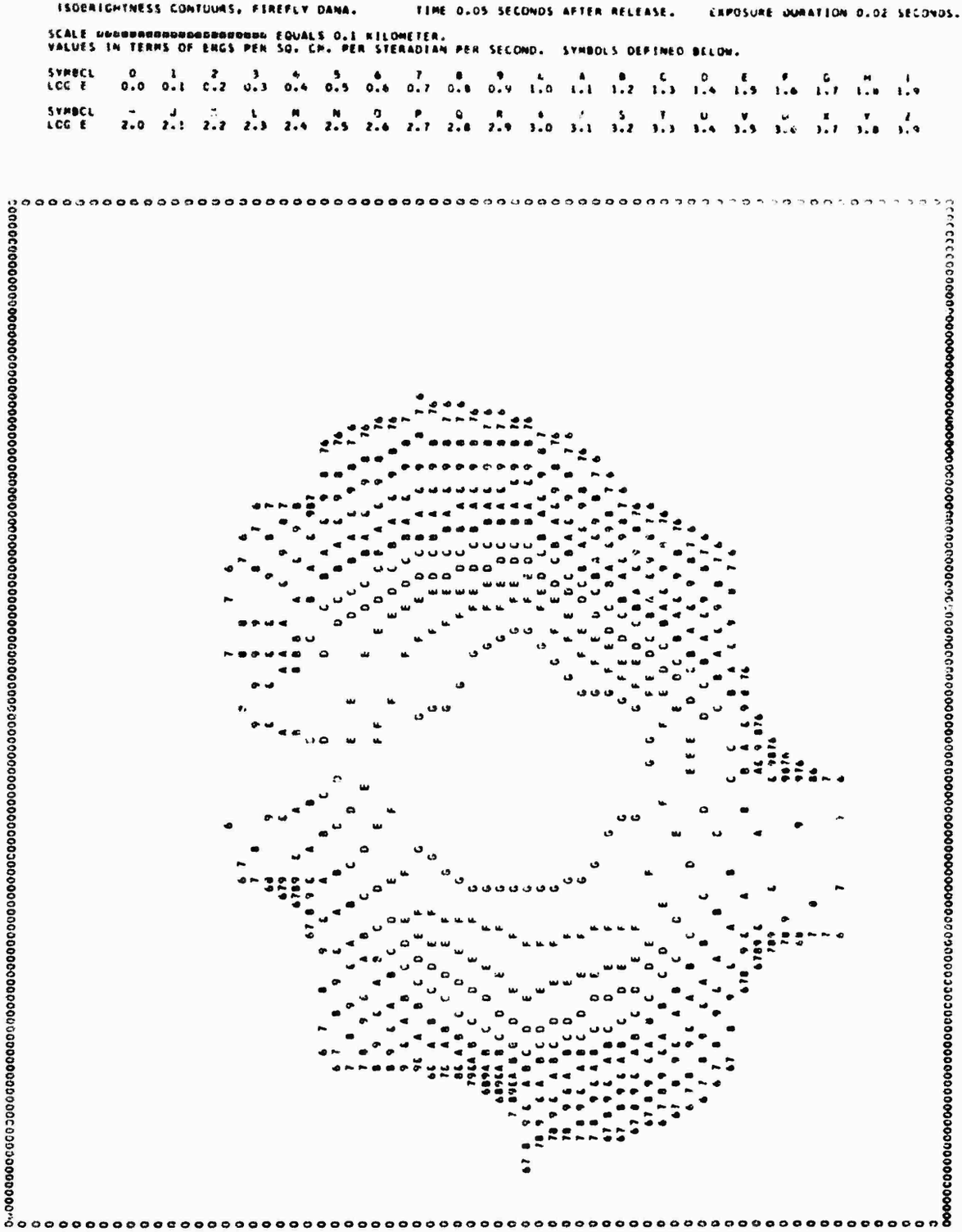

Figure 40. Alternate Background Level Selection at Higher Level Than in Figures 8 Through 30

Appendix A

A1. TRACE CARD

This card records the raw data from a densitometer trace through an image. The information regarding the image on a frame is conveyed by giving the X and D coordinates of significant points chosen on the trace. D value here indicates the instrument deflection at a particular value along the trace. Information regarding the particular frame, and Y value (location on the frame) of the trace are also given. A trace may use more than one card.

The information is entered in the cards in the following way:

(1) Columns 1-3. These readings indicate the zero value of deflection from prior trace sheet and are known as P values of the sheet. These columns are also used to record the density value of the glass trace in the last trace sheet, in which case the values are distinguished by a 12 Zone in column 1.

(2) Columns 4-6. These readings indicate the zero value of deflection from the previous trace, after the base line is shifted. These are known as Z value of the trace.

(3) Columns 7-9. These readings indicate the deflection value after the film position has been shifted and are known as the S value of the trace.

(4) Columns 10-69. These columns indicate the X values of significant points chosen and the deflections at those points. Each data field of six columns is defined by its coordinate measured in millimeters along the X axis of the trace and the readings entered in the first 3 columns. The deflection at the point, measured in millimeters along the other axis on the trace sheet, is entered in the next 3 columns.

Thus each data point will occupy a total of 6 columns, and there is provision for accommodating 10 points on a card.

(5) Columns 70-72. These columns indicate the Y value of each trace. Whenever a trace has more than 10 points, each card except the last card of the trace must have a 12 zone in column 70.

(6) Columns 76-79. These columns indicate the identification code for the frame to which the trace belongs.

(7) Column 80. This column indicates whether the card is a continuation of the previous card or not. If it is a continuation, it has a letter A for the 1st continuation card, a letter B for the 2nd continuation card, and so on. On continuation cards punching starts from column 10, giving only the data point coordinates, Y value of the trace, frame code and continuation card letter.

The exception to the punchings in the Z location (columns 4-6) is the first trace, where the density value corresponding to glass is entered. The exception to P punchings is in the last trace where the value of glass deflection is entered in columns 1-3 with an 11 zone over the digit in column 1. In the last trace, approximate noise values are indicated through the use of the following convention. The first data point to be recorded is the one with maximum deflection. This point is arbitrarily assigned an X value of 000. Second data point is the one with the minimum deflection. This point is arbitrarily assigned an X value of 001. The test of the data points are punched in the usual order. For the first sprocket hole trace, Column 1 contains 0 and three data points are punched in column 10 onward. Column 75 contains the digit 1. For the second sprocket hold trace, column 1 is blank and three data points from left to right are punched from column 10 onwards. Column 75 contains digit 2. As before both sprocket hole cards have frame code in columns 76-79.

Appendix B

B1. FRAME CARD

The FRAME card presents, in coded form, all the relevant information regarding the densitometer settings used, film used, etc., for any particular frame. It is important to note that whenever there is any change in any quantity or setting specified on the original FRAME card, a new FRAME card shall be made out. This new FRAME card shall be treated as if it describes a new frame.

The information contained in the various columns of a FRAME card is given below.

Columns

1-3	Ratio arm setting of the densitometer
4-6	Densitometer slit height (dial readings)
7-9	Densitometer slit width (dial readings)
10-12	Magnification of objective in the densitometer
13-14	Recording speed of densitometer
15-16	Gain or sensitivity of the densitometer
17-19	Slope of optical wedge used in the densitometer. (See notes)
20-23	Time in seconds from t = 0 to the beginning of the frame.
24-27	Duration of exposure of the frame in seconds
28-29	Iris setting of the densitometer
30-33	Summary code for the wedge that fits the film (See notes)
34-36	Logarithm of wedge exposure duration in microseconds
49-50	1 less than the printer spaces = 0.1 km. (or if column 49 contains a 12 zone, 1 less than the printer spaces = 1 km.) (See notes)

51-53	Y starts in terms of corrected values (see notes)
54-56	Y finish in terms of corrected values (See notes)
57-59	Y multiplier (See notes)
62-63	X multiplier
64-66	X start in terms of corrected values
76-79	Frame code
80	Z

B2. NOTES AND EXPLANATION

(1) Columns 17-19. Slope of optical wedge. The slope of the wedge is entered in the FRAME card in a coded form. The method of coding is as follows. Use only 3 significant digits with zone punches over the first digit; for example:

For a slope of 0. 95 code will be +095; that is, with 12 zone mark.

For a slope of 0. 095, code will be 095; that is, no zone mark.

For a slope of 0. 0095, code will be -095; that is, will 11 zone mark.

For a slope of 0. 00095 code will be ⊖095, that is; with 0 zone mark.

(2) Columns 62-63.— Z Multiplier. It is assumed that the printer has 132 printing positions for X values. The X multiplier is used in order to enlarge or diminish the size of the printed output in the X direction (that is, horizontal) relative to the trace. It can also be used to correct for any change in the ratio arm setting of the densitometer. The X multiplier can have any value between 0. 8 and 3. 5. For any given frame, choose the trace for the widest part of the image. On this trace, measure the number of units in the X direction between the two significant points on the curve which indicate the maximum width of the image. If the number of units is greater than 132, use an X multiplier of less than 1 or, if less than 132, vice versa in such a way that the maximum width of the trace is brought out to 132 spaces on the printer.

In the event it is desired to show the drift of the image in the successive frames, it is necessary to choose the X multiplier in such a way that with a fixed X start, the output image does not go beyond the limits either way of 132 print spaces for all the frames under study. In entering the value the decimal point is ignored.

It may be noted that the printer has 10 printing spaces per inch in the X (or horizontal) direction.

(3) Columns 64-66 - X Start. Choose the X start with reference to the trace of the widest part of the image and in such a way that the whole image will come within the 132 printing spaces. The entries in the columns 64-64 are the corrected X values; that is, after multiplication by the X multiplier chosen.

In the event it is desired to show the drift of image a fixed X start must be used for all frames. The X start must be so chosen that in the printouts of all frames the image does not go beyond the 132 spaces of the printer either way.

(4) Columns 57-57 - Y Multiplier. The Y multiplier must be compatible with the X multiplier. It is calculated in the following way:

For a ratio arm of 100 in the densitometer, Y multiplier = 3.41 x X multiplier when the printer is set for 6 lines/inch in the Y direction. Y multiplier = 4.55 x X multiplier when the printer is set for 8 lines/inch in the Y direction.

For any other value (r) of ratio arm, Y multiplier = 3.41 x X factor x $\frac{r}{100}$ for 6 lines/inch; and Y multiplier = 4.55 x X factor x $\frac{r}{100}$ for 8 lines/inch.

In entering the value, the decimal point is ignored.

(5) Columns 51-53 - Y Start. This indicates the start of the image in the printed output. Choose the Y value of the trace for the top edge of the image. (that is, the trace in which the image is just beginning to show up). The values entered are always cor. ected ones; that is, multiplied by the Y multiplier.

(6) Columns 54-56 - Y finish. This indicates the finish of the image in the printed output. As before, choose the Y value of the trace for the bottom edge of the image (that is, the trace where the image has just faded out). The values entered are corrected ones after being multiplied by the Y multiplier.

(7) Columns 49-50 - Scale:

(a) For number of print spaces per 0.1 km. the value is given by the formula

$$S = \frac{0.1}{D} FRX-1$$

where S = the value entered in columns 49-50

D = slant range in kilometers of the burst

F = focal length of the lens in mm in the camera used for recording the burst

X = X multiplier

R = ratio arm of densitometer used

(b) To convert the value from (a) above to the number of print spaces for 1 km, multiply by a factor of 10 and place a 12 zone in column 49.

Appendix C

C1. FILM CARD

This card contains all the necessary information regarding the camera, film, filter, etc., used in the recording of the burst.

The card has all the information in a coded form in the following manner:

(1) Columns 1-10 have the Firefly Shot name; for example, DANA will occupy 4 columns, the rest being blank.

(2) Columns 11-12 have the Camera code. Column 11 has a letter; A for 35 mm amateur camera, D for Dumont oscilloscope recording camera, K, L for Data cameras, M for Millikan cameras, N for FASTEX cameras. Column 12 has a serial number or symbol (assigned to each of the cameras of a particular type).

(3) Columns 13-14 have the camera orientation in degrees, with respect to film transport, or with respect to the top of the camera when there is no film movement.

(4) Columns 15-17 have the focal length in millimeters. Column 16 has also a multiplier as shown below:

12 zone - x 100
11 zone - x 10
0 zone - 0.1
no zone - no multiplier

(5) Column 18 has the code for the film emulsion. A partial listing of the code follows: I for High Speed Infra Red, R for Royal X Pan., S for Superior No. 4, T for TR-X.

(6) Columns 19-20 have the mantissa of the logarithm of the f number used on the camera, with zone punches in column 19 for the characteristic. The zone punches assignments are 12 zone for a characteristic of 2, 11 zone for 1 and no zone punch for 0. Also, Column 20 will have a 12 zone punch if the Log is positive and 11 zone if negative.

(7) Columns 21-25 are reserved for future use on data giving the relationship between wavelength and film gamma.

(8) Columns 26-33 have the reciprocity law data. In treating the reciprocity data, an array of values for density above fog of 1.0 and 0.3 is created. This array is in increments of log 1/10 units. A table of values, for density above fog of 1.0, is made. A table of corrections for density 0.3 above fog, each with respect to the minimum of the curve, is also made. The code starts at 1 μsec exposure time. Increments in time are automatic for all alphmeric characters. If there is no zone mark it means 1 log unit increment, an 11 zone mark means 2 log units increment, a 0 zone mark means a 3 log unit increment. If there is a 12 zone mark it means that the next point in the curve is a minimum and that the present point is the decrement needed to reach the minimum. All changes are assumed to be 0.1 unless there is a code for a scale change. The code is as follows:

.	add 1)	of whatever precision
¤	add 2)	is current to latest
[	add 3)	value of present point
<	add 5)	to get correction for 0.3
+	add 7)	density point.
$	subtract 1)	of whatever precision
*	subtract 2)	is current to latest value
]	subtract 3)	of present point to get
;	subtract 5)	correction for 0.3
-	subtract 7)	density point.
#	.01 log unit)	
:	.04 log unit)	
@	0.11 log unit)	precision indicators
,	no data at 1st point	
%	no data at 1st 2 points	
\	no data at 1st 3 points	
>	end of curve.	

(9) Columns 34-50 have the Film Spectral Code. The coding is done by choosing significant points on the curve and coding the points by means of their X and Y values with respect to a predefined wavelength and a reference line. The coding occupies a maximum of 17 spaces in columns 34-50 on the FILM card.

In the coding of film curves, the following will be assumed unless otherwi specified:

(1) The zero or the starting point along the X axis of the curve shall be 3000 Å in all cases.

(2) The standard increment along the X axis shall be 400 Å.

(3) The standard increment along the Y axis shall be 1/10 of a log unit.

(4) The first character in the spectral sensitivity curve coding shall always be an absolute value indicator establishing the reference line and will be in 1/10 log units.

(5) The reference line and X values of points will be coded as follows:

12 zone for 1 log unit or 1 increment above standard increment along X axis.

11 zone for 2 log units or 2 increments above standard increment along X axis.

0 zone for 3 log units or 3 increments above standard increment along X axis.

(6) In coding, the X value is taken as 1 less than the number of increments from the previous point, since there is always a standard increment which is not coded.

(7) In establishing the reference line, the sensitivity is the reciprocal of the exposure (ergs/cm^2) required to produce a density D = 0. 3 above gross fog. In the event the spectral sensitivity curves for a film are given for any density other than D = 0. 3 the absolute value of the reference line should be given for D = 0. 3 after appropriate conversion. The conversion is done as follows:

$\text{Log}\, S_2 = \text{Log}\, S_1 + \frac{AD}{\gamma}$ where γ is the slope of the straight portion of Log E = Density curve of the film, where log S_2 = sensitivity value for D = 0. 3.

Log S_1 = sensitivity value for D = any value other than 0. 3, $\Delta D = D_1 - D_2 = D_1 - 0.3$

(8) Sensitivity value is always measured from the reference line <u>downwards</u>, which is considered to be the positive direction.

The following symbols are used in coding:

+	400 Å increment	
.	100 Å increment	
¤	20 Å increment	
[	5 Å increment	
<	1 Å increment	
-	add 5)	of
*	add 10)	whatever precision
,	add 20)	units are
]	subtract 5)	currently used with
;	subtract 10)	respect to the
%	Subrtact 20)	reference line.
#	precision 0. 01 log unit	
:	precision 0. 03 log unit	
@	precision 0. 1 log unit	
$	back space origin 1000 Å	

If the total of 17 spaces is not filled up in coding, use to denote the finish of coding.

To code a curve proceed as follows:

(1) Draw the reference line parallel to the X axis in such a way that its Y value is in multiples of 1/10 of log units and that the curve lies below it and preferably with the highest point on the curve lying on, or within 1/10 log unit of, the reference line.

(2) Next mark the significant points on the curve such that their X values measured from the previous point are codable multiples of the increments chosen.

C2. EXAMPLE OF FILM SPECTRAL CODING OF KODAK HIGHSPEED INFRARED FILM

The curve supplied by Kodak is for a sensitivity equal to the reciprocal of exposure required to produce D = 1.0 above gross fog.

Draw the reference line at a log sensitivity value of 1.4.

The log sensitivity value of the reference line for a D = 0.3 will be

$$\text{Log } S_2 = \text{Log } S + \frac{\Delta D}{\gamma}$$

$$= 1.4 + \frac{1-0.3}{\gamma} \qquad = 1.4 + \frac{0.7}{0.9} \quad = 1.4 + 0.8 = 2.2 \text{ assumming } \gamma = 0.9$$

2.2 log units can be coded as 11 zone 2, which is K; K will denote the position of the reference line in the coding.

1st point. Now the first point on the curve can be chosen at a wavelength of 4200 Å; that is, the point is 120 Å (or 3 x 400 Å) away from the starting point of 3000 Å. The point is on the reference line so that its Y value is 0. The first point can be coded as follows: Since there are 3 increments of 400 Å, the coded X value will be 2, which is an 11 zone. The first point will be coded 11 zone 0 which is !

2nd point. Second point is 400 Å away, a standard increment. Its Y value is 2. The point will be coded simply 2.

3rd point. Standard increment of 400 Å and a Y value of 9 the point will be coded 9.

4th point. This point is 200 Å away from the last point. The standard increment will be changed from 400 Å to 100 Å. This will be denoted by . The Y value of this point is 13. This calls for a shift in reference line by 10 units and can be denoted by * (that is, add 10). The new Y value of the point with respect to the new reference line will be 3. The coding for the point will be 12 zone 3 (since there is 1 increment above the standard increment of 100 Å) which is C. The full coding for the point will be *C denoting the changes in standard increment and reference line as well.

5th point. This is 1200 Å away, so change back to 400 Å standard increment, denoted by +. The number of increments is 3. The Y value is 8 with respect to the original reference line. Denote changing back to the original reference line by ; (that is, subtract 10). The point can be coded 11 zone 8 which is Q. The full coding for the point will be + ; Q.

6th point. This is 1600 Å away of 4 increments away and its Y value is 4. The point can be coded 0 zone 4 which is U.

7th point. This is 800 Å or 2 increments away and its Y value is 7. The point can be denoted 12 zone 7 which is G.

8th point. This point is 800 Å or 2 increments away. The Y value is 32 with respect to the reference line. Shift the reference line by 30. This is denoted by, * (add 20, add 10). The Y value with respect to the new reference line is 2 so the point can be denoted by ,*B. The coding for the curve will be: K! 29. *C+;QUG, *B. This occupies only 15 spaces. The full coding is: K! 29. *C+;QUG,*B>

Columns 51-70 will have the Filter Spectral Code. The method of coding, in general, is the same as for film spectral coding except for the following assumptions:

(1) The 100% transmission line is assumed to be the reference line.

(2) Upward direction from the reference line is considered to be a positive direction.

(3) Standard increment in the Y direction shall be 1/10 of a density unit. Since the 100% transmission line is assumed to be the reference line, the first character in the code will pertain to the first significant point.

As before, unless otherwise specified, zero or starting point shall be 3000 Å in all cases.

Standard increment in the Y direction shall be 400 Å

Scale along the Y axis will be 1/10 of a density unit.

Coding for the X values of points shall be:

12 zone for 1 increment above standard increment

11 zone for 2 increments above standard increment

0 zone for 3 increments above standard increment.

Symbols:

+	400 Å increment	
.	100 Å increment	
¤	20 Å increment	
[	5 Å increment	
<	1 Å increment	
-	add 5)	of whatever
*	add 10)	precision units are
.	add 20)	currently being
]	subtract 5)	used to form
;	subtract 10)	new reference
%	subtract 20)	line.

#	precision 0.01 density unit
:	precision 0.03 density unit
@	precision 0.1 density unit
$	back space origin 1000 Å.

If the total of 20 spaces is not filled, indicate finish by >. To code a filter absorption curve, proceed as follows: Mark significant points on the curve in such a way that the distance of it from the previous point is a codable multiple of the standard increments used.

C3. EXAMPLE OF FILM SPECTRAL CODING OF WRATTEN FILTER NO. 8

1st point. The first point chosen is at 4600 Å or 4 standard increments away from the zero or starting point of 3000 Å. Its coded X value will be 3 (that is, 0 zone). The Y value of the point is 2.5, so shift the reference line up to 20 (that is, add 20). This is denoted by , and coding for the point will be 0 zone 5 which is V. The complete coding for the point will be , V.

2nd point. The second point is at 4700 Å with a Y value of 1.2, so change standard increment from 400 Å to 100 Å and shift reference line down by 10 (subtract 10). The point is coded simply 2. Full coding for the point will be . ; 2

3rd point. Third point is at 4800 Å standard increment of 100 Å and Y value of 7. Shift reference line down by 10 (subtract 10). Coding for the point will be ; 7

4th point. Fourth point is at 4900 Å. Standard increment of 100 Å and Y value = 4. Coding for the point will be 4.

5th point. Fifth point is at 5000 Å. Standard increment of 100 Å Y value is 0.2. Coding for the point will be 2.

6th point. Sixth point is at 5100 Å. Standard increment of 100 Å Y value is 0.1. Coding is 1.

7th point. Seventh point is at 5200 Å. Standard increment Y value is 0.1. Coding is 1.

8th point. Eighth point is at 6800 Å. Change of 1600 Å, change standard increment to 400 Å so the number of increments is 4. Y value is 1. Coding for the point will be +/. Complete coding will be: , V . ; 2 ; 74211+/>

Columns 71 - 73 have the code for developer used. The code is as follows: Column 71 has the development time in minutes. If there is a 0 zone mark, add 10 minutes. Column 72 has the development temperature in degrees C starting at 10°C = 0. If there is a 0 zone mark, add 10°C. Column 72 has the chemical code (A for DK 60, B for D19, etc.)

Columns 74 - 75 are blank.

Columns 76 - 78. Code name of the film.

Column 79 is blank.

Column 80 has an X.

Appendix D

D1. WEDGE CARD

The wedge card is made as follows:

(1) Columns 1-3 have the logarithm of microergs/cm^2/sec for the exposure from the standard light box corresponding to the highest density step on the wedge image.

(2) Columns 4-6. Densitometer deflection reading for this step.

(3) Columns 7-72 have the same information as above for the succeeding steps in the wedge, with 6 columns per step being used.

(4) Columns 73-75 have the log of wedge exposure in microseconds. Column 75 has no zone mark for the first card, has a 11 zone mark for the first continuation card, and a 12 zone mark for the second continuation card. The last but one point has 001 as log energy value for density deflection corresponding to film background. The last point has 000 log energy value corresponding to deflection for glass.

(5) Columns 76-79 have the code name of the film; for example, DOA. Column 79 has a letter pertaining to a frame of the film referred to which used the same densitometer settings as were employed in tracing the wedge.

(6) Column 80 has W for an unedited wedge, and V for an edited wedge.

V. Spectrography and Spectrometry of Luminous Chemical Releases

C. Dewey Cooper
University of Georgia
Athens, Georgia

Abstract

The spectrographic and spectrometric data which were obtained from Project Firefly have been studied, and those which appeared to be the most promising for furnishing intensity measurements were processed to provide such information. The equipment used, calibration, and data reduction techniques are discussed.

1. EXPERIMENTAL APPARATUS

The spectra recorded in this report were obtained with a spectrometer and a slitless spectrograph. The spectrometer was a Fastie-Ebert mount using an f/6 mirror of 50 cm focal length, an 1800 groove/mm grating, and adjustable curved slits 5 cm in length. An RCA 6810A photomultiplier was used as a detector and the signal recorded with a Sanborn recorder. The cloud was imaged on the entrance slit with an f/6, 24 in. focal length lens.

The slitless spectrograph used an f/0.87 lens of 76 mm focal length and an 1800 groove/mm grating which was blazed for 500 nm.

2. CALIBRATION AND DATA REDUCTION

The signal recorded by the spectrometer depends upon several variables which must be known before quantitative intensities can be obtained from the traces. The f/value, and the transmissivity of the collecting lens determines the light flux intercepted and passed by the lens. The size of the image on the slit is determined by the focal length of the collecting lens, and the size of the slit limits the light flux into the spectrometer. Both the efficiency of the spectrometer and the sensitivity of the photomultiplier varies with the wavelength.

Dr. H. D. Edwards at the Georgia Institute of Technology calibrated the various elements of the spectrometer. The transmissivity of the collecting lens, the efficiency of spectrometer, and the photomultiplier sensitivity were obtained as a function of wavelength. The photomultiplier response was found to be S11, identical to that given by RCA. With the photomultiplier voltage set at 1400 volts, which is the same voltage setting used in many of the field tests, the peak sensitivity was found to be 13,300 microamperes per microwatt. Utilizing the measured efficiencies of the various components and the S11 response curve, each of the spectrometer traces were converted to graphs of wavelength versus the light flux which arrived at the collector lens and was focussed to pass through the entrance slit. The spectrometer slit width used on most of the releases was 4 mm and this gave a 40A or 4 nanometer band pass over the visible region. Our data on Figures 1 through 7 are plotted in microwatts x 10^7 per 4 nm for wavelengths between 370 and 620 nm.

Additional corrections to these data are needed if the total energy radiated from the cloud is desired. Considering the cloud as a point source placed x kilometers away, the total energy radiated per second by the cloud is given by

$$P_n = \frac{4\pi x^2 P}{\pi r^2 S} \qquad (1)$$

where r is the radius of the collecting lens, and P is the power per 4 nm recorded on the charts. S is the fraction of the energy collected by the collimator which is passed by the entrance slit. Taking r = 50 mm and x = 110 km we obtain $P_n = 1.93 \times 10^{13} \frac{P}{S}$. As an example, let us take P for λ = 525 nm from Trace 4 in Figure 1. Here P is found to be 100 x 10^{-13} watts/4nm, and P_n = 193 watts/4nm. To obtain the energy radiated within the 4nm or 40A band pass, we simply multiply by the time necessary to sweep 4nm which was 0.22 sec., or in this case E_n = 42.5 joules/4nm.

If the total energy radiated between 620 and 370 nm is desired, then the total area under the traces is required and this has been recorded for each trace. The correct equation in this case is

$$E = 1.93 \times 10^{13} \frac{At}{4S} \qquad (2)$$

where A is the area under the curve recorded in watts-nanometers; the number 4 enters the denominator because of the 4 nm band width. The parameter t, which is 14 seconds in this case, is the time for recording the entire spectrum. Again using Trace 4 of Ivy (Figure 1) as an example, E is found to be 1.7×10^5 joules. The computed values of E are included in Table 1.

The data obtained with the slitless spectrograph has been reduced to provide relative intensities as a function of wavelength for several releases. A microphotometer was used to measure the density of the film. Figure 8 shows typical curves for the Ivy release. Before intensity readings can be obtained from the film densities, a calibration of the film as it was used in the spectrograph must be performed. This was accomplished using a standard lamp and different angles of incidence. This film calibration used with a sensitometric strip, which was developed with the film in the field operation, provided a means of obtaining light intensity from the film density. The results of these efforts are depicted in Figures 9 through 11. It is to be noted that the curves have approximately the same shape as those obtained with the spectrometer.

3. DISCUSSION

The spectrometric data presented herein provides intensity measurements for several of the chemiluminescent clouds which were observed. Obvious errors which could not be controlled resulted from the difficulty in tracking the cloud and the estimates made from photographs concerning the portion of the cloud which fell on the slit. It is worthwhile to compare the total visible energy obtained for Dana from T + 113 to T + 127 with that reported by Device Development Corporation. We report 8×10^{11} ergs while they obtained 2.9×10^{11} ergs for the entire light output. If all of the light which was collected by our spectrometer collecting lens was passed through the entrace slit, then S in Table 1 for Dana would be 1 instead of 0.6 as estimated. If S is taken as 1, then we would report a value of 4.8×10^{11} ergs which is still higher than that reported by Device Development Corp. The source of this discrepancy is not apparent at this time.

The results in Figures 7 and 11 show that the TEC releases provided a continuum which was much stronger in the 5700A region than was provided by the aluminum release.

TABLE 1. Visible energy radiated by several chemical clouds. Data obtained from figures 1 through 7

Rocket and Trace No.	Time of Recording	Area under Trace in watt nanometers	S	E(joules)
IVY 2	T* +95 -109	38×10^{-10}	0.7	3.6×10^{5}
IVY 4	T +125 -139	18×10^{-10}	0.7	1.7×10^{5}
IVY 8	T +185 - 199	8.8×10^{-10}	?	?
ESTHER 2	T +104 -118	24×10^{-10}	0.7	2.4×10^{5}
ESTHER 4	T +134 -148	12×10^{-10}	0.3	2.9×10^{5}
ESTHER 8	T +194 -208	6×10^{-10}	0.15	2.7×10^{5}
DANA B	Background moonlight	14×10^{-10}		0.92×10^{5}
DANA 1	T +113 -127	21×10^{-10}		
DANA 1- DANA B		7×10^{-10}	0.6	0.80×10^{5}
EVA 1	T +85 -99	31×10^{-10}	0.7	3.0×10^{5}
EVA 2	T +100 -114	12×10^{-10}	0.8	1.0×10^{5}
EVA 3	T +115 -129	3.0×10^{-10}	0.6	0.3×10^{5}
EVA 4	T +130 -144	1.8×10^{-10}	<0.5	0.2×10^{5}
DINAH 1	T +90 -104	23×10^{-10}	0.8	1.9×10^{5}
DINAH 2	T +105 -119	6.7×10^{-10}	0.5	0.9×10^{5}
DINAH 3	T +120 -134	2.7×10^{-10}	0.5	0.4×10^{5}
OLGA 2	T +107 -121	7.8×10^{-10}	0.8	0.66×10^{5}
OLGA 3	T +122 -136	3.0×10^{-10}	0.9	0.25×10^{5}
NETTY 2	T +111 -125	39×10^{-10}	0.7	$>3.8 \times 10^{5}$
NETTY 3	T +126 -140	18×10^{-10}	0.6	$>2.0 \times 10^{5}$
NETTY 4	T +141 -155	3.8×10^{-10}	0.3	0.7×10^{5}

*T = o is the time of launch.

E in this table was computed using:

$$E = \frac{x^2 At}{r^2 S}, \text{ where}$$

x = 110 km,
r = 50 mm,
t = 14 seconds.

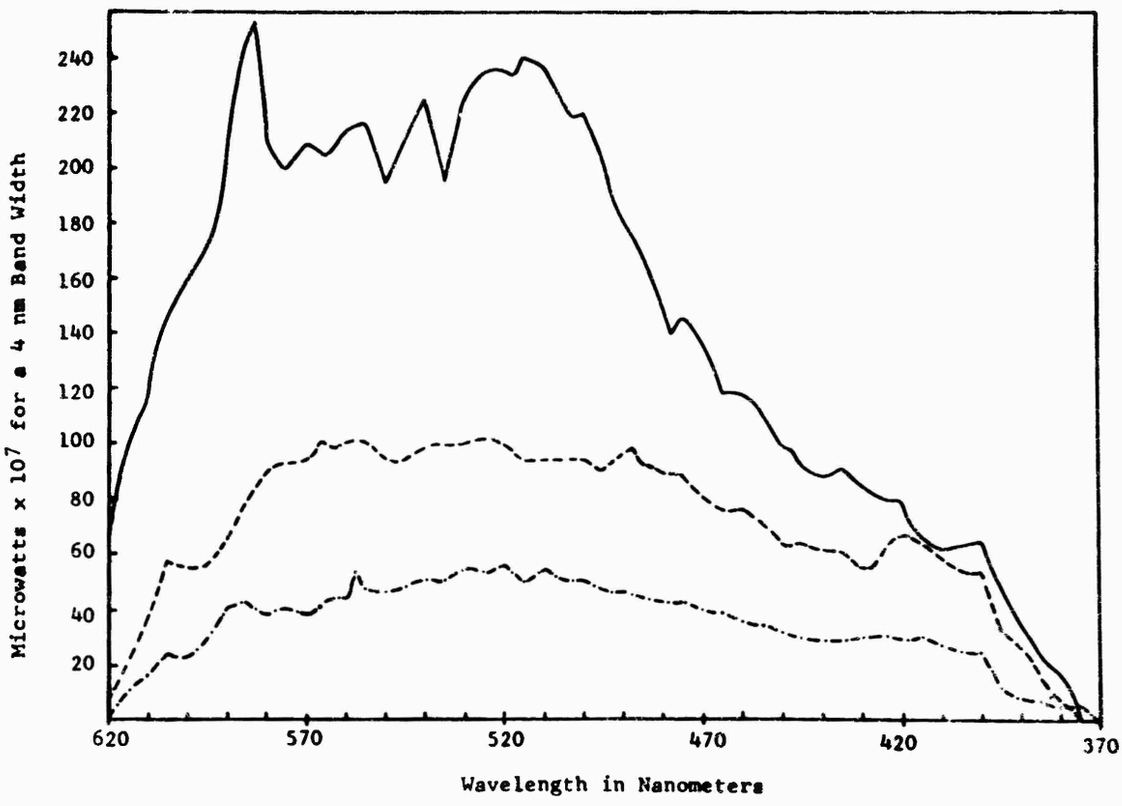

Figure 1. Power Versus Wavelength as Recorded with a Spectrometer for IVY. Trace 2 ——, Trace 4 - - -, Trace 8 -·-·-.

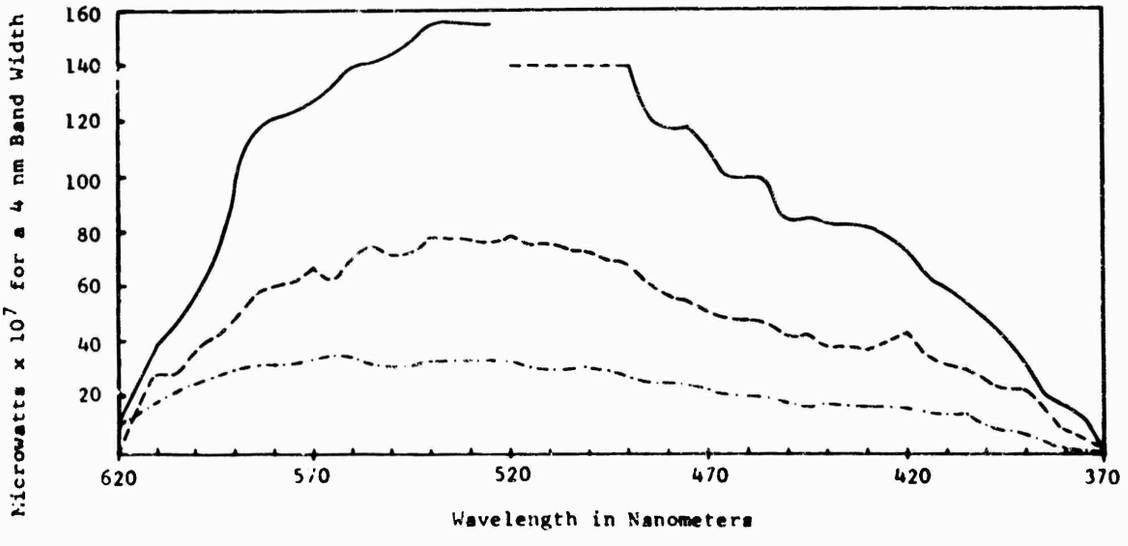

Figure 2. Power Versus Wavelength as Recorded with a Spectrometer for ESTHER. Trace 2 ——, Trace 4 - - -, Trace 8 -·-·-.

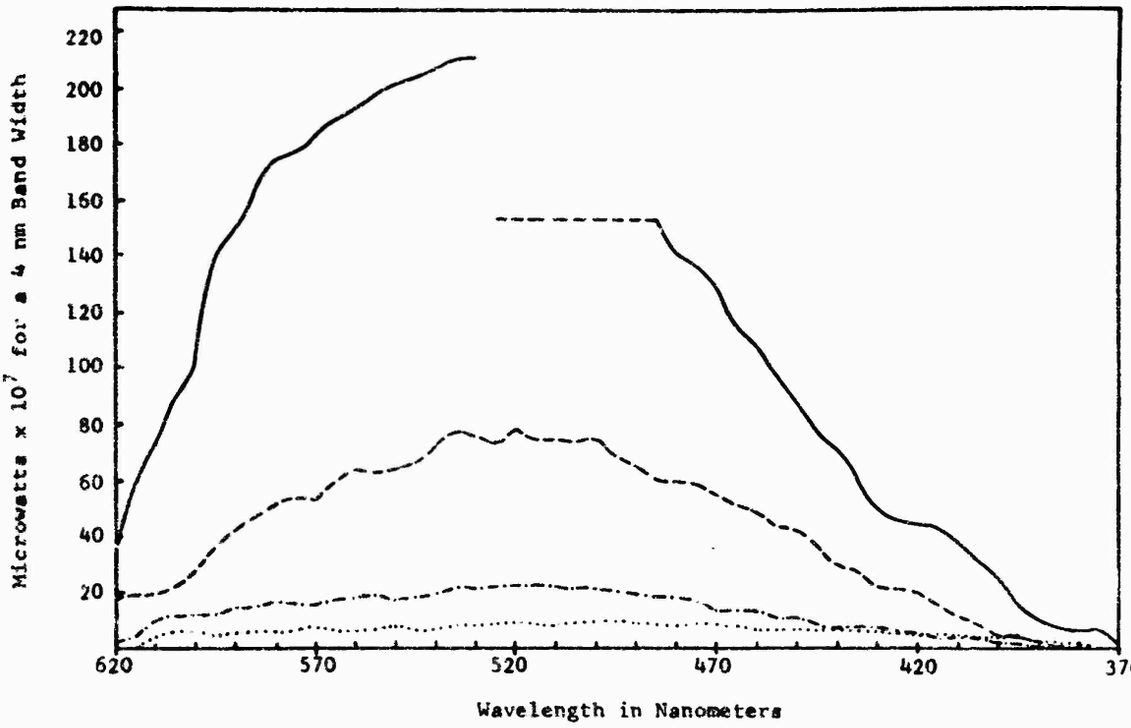

Figure 3. Power Versus Wavelength as Recorded with a Spectrometer for EVA. Trace 1——, Trace 2 - - -, Trace 3 ·····, Trace 4 . . . .

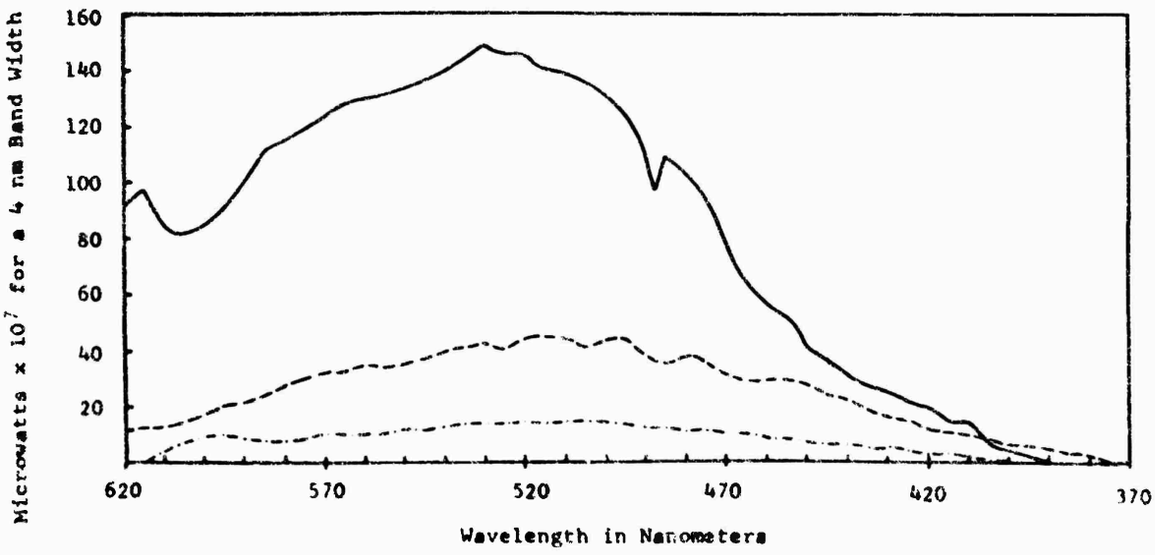

Figure 4. Power Versus Wavelength as Recorded with a Spectrometer for DINAH. Trace 1——, Trace 2 - - -, Trace 3 ·····.

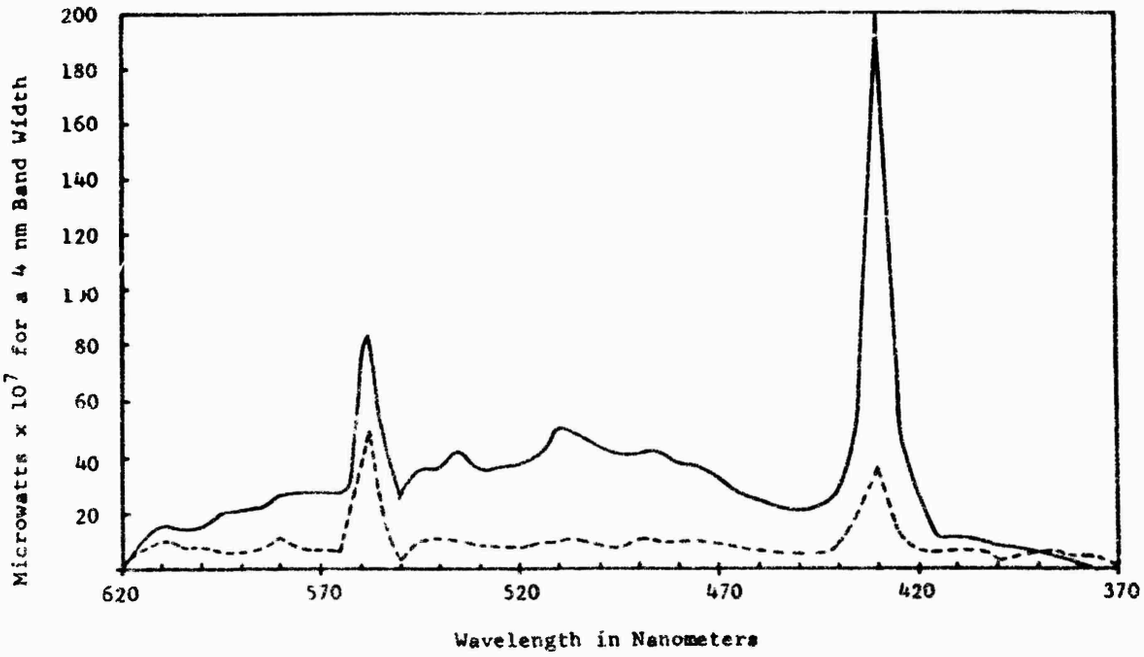

Figure 5. Power Versus Wavelength as Recorded with a Spectrometer for OLGA. Trace 2——, Trace 3 - - -.

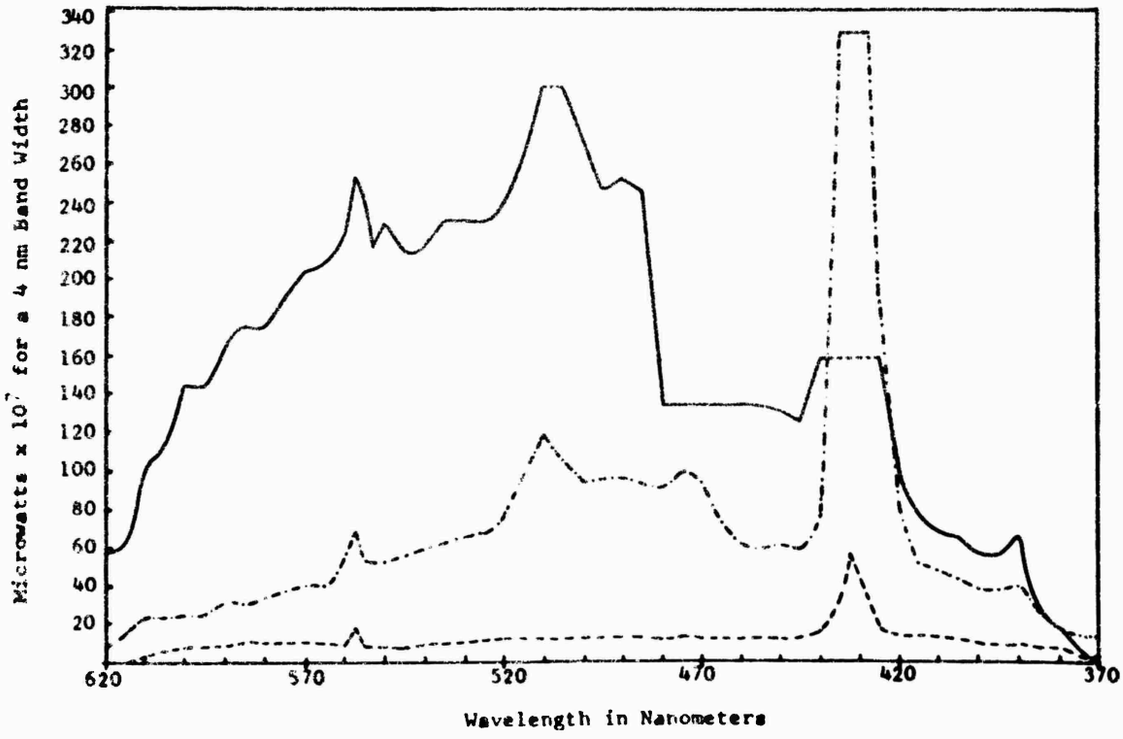

Figure 6. Power Versus Wavelength as Recorded with a Spectrometer for NETTY. Trace 2——, Trace 3 -·-·-, Trace 4 - - -.

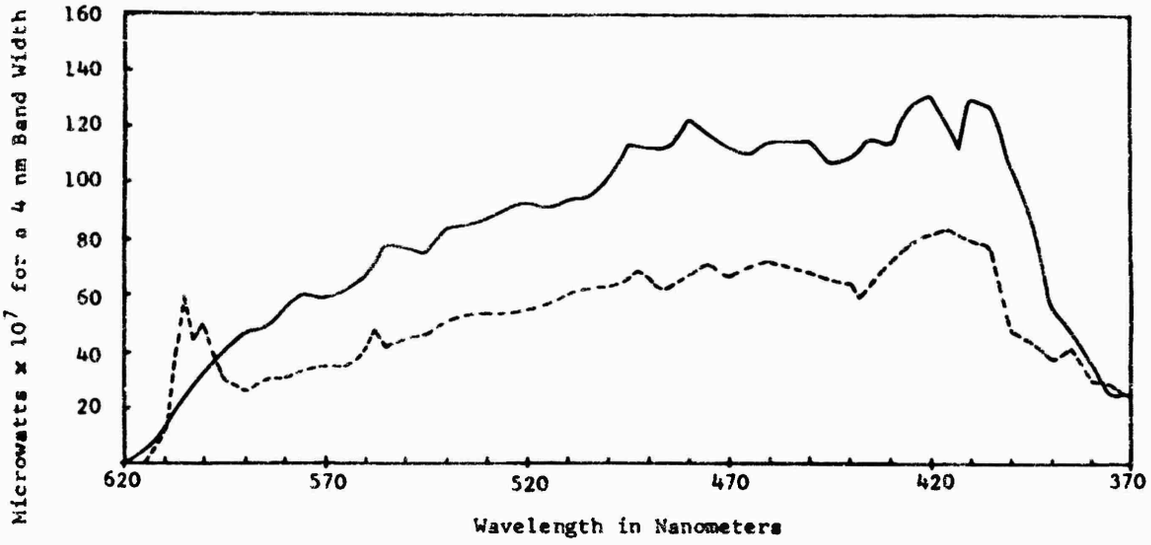

Figure 7. Power Versus Wavelength as Recorded with a Spectrometer for DANA. Background Trace - - -, Trace 1 ——.

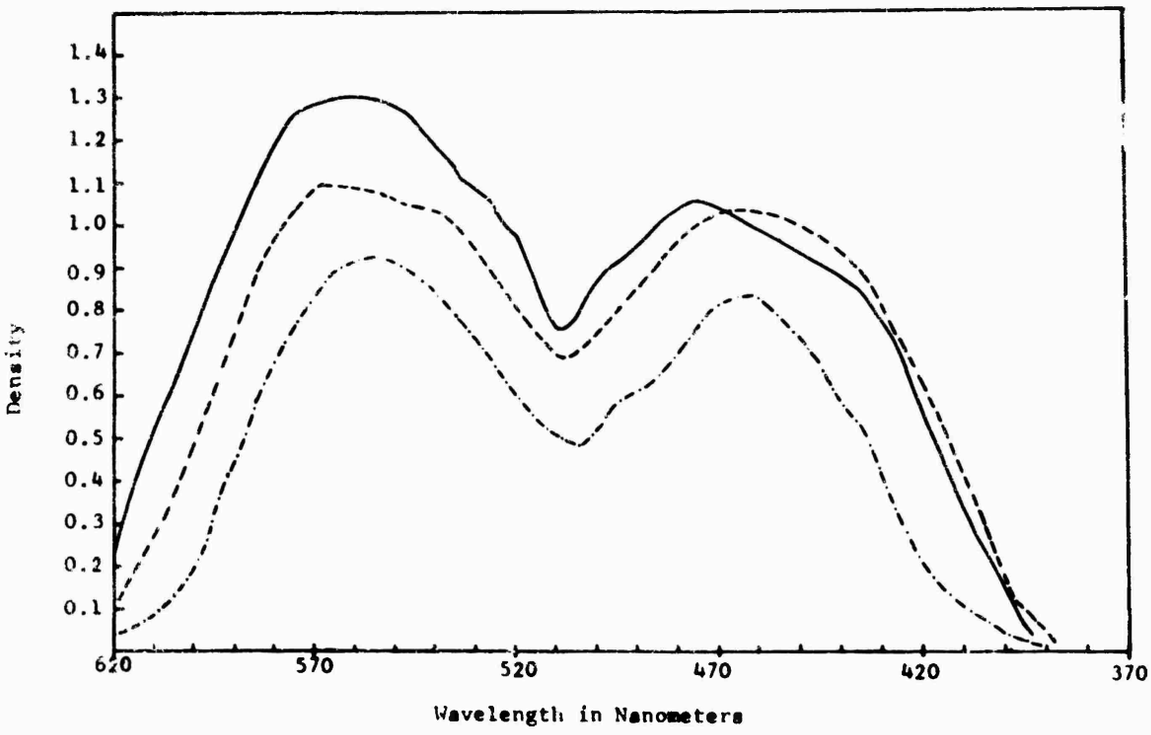

Figure 8. Film Density Versus Wavelength as Recorded with Slitless Spectrograph for IVY. Exposure Time 10 sec. No. 3 - - -, No. 4 ——, No. 5 -·-·-.

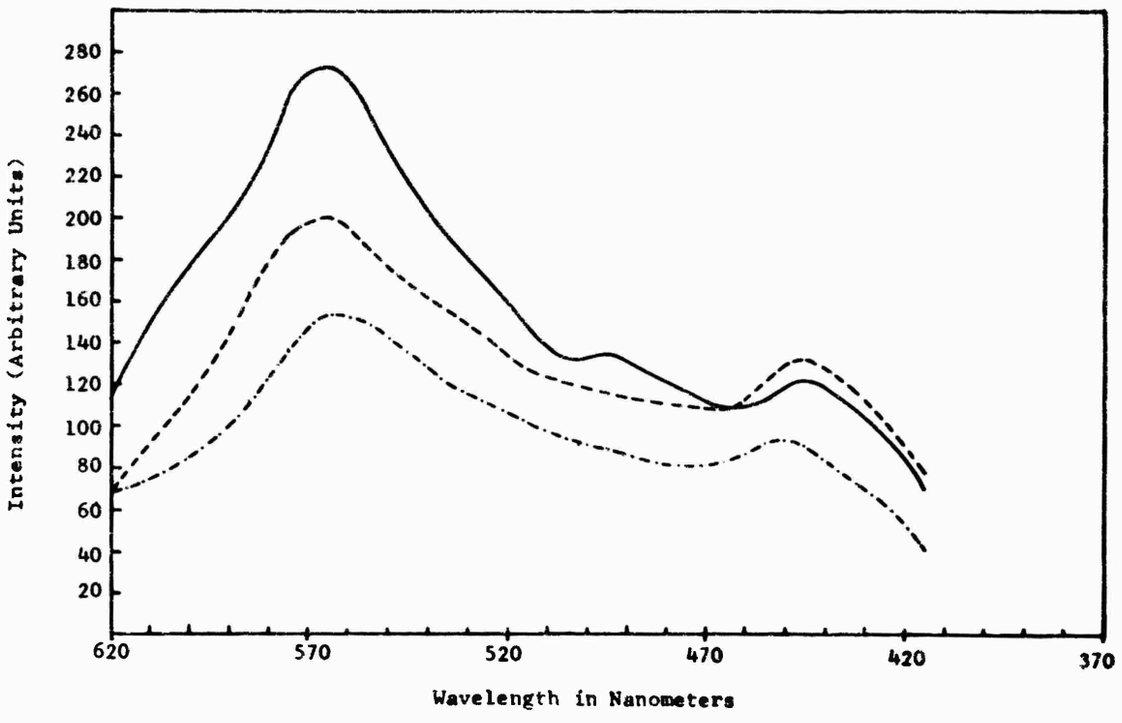

Figure 9. Relative Intensity Versus Wavelength as Recorded with Slitless Spectrograph. IVY 3 - - -, 4 ——, 5 -·-·-.

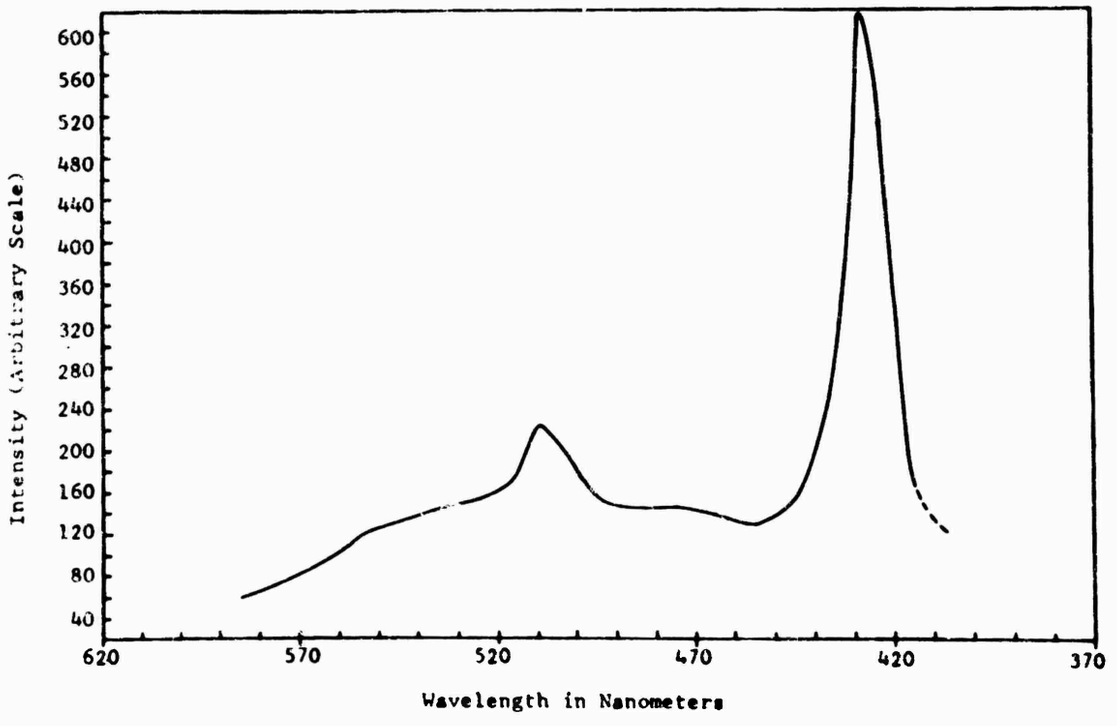

Figure 10. Relative Intensity Versus Wavelength as Recorded with Slitless Spectrograph for NETTY 2.

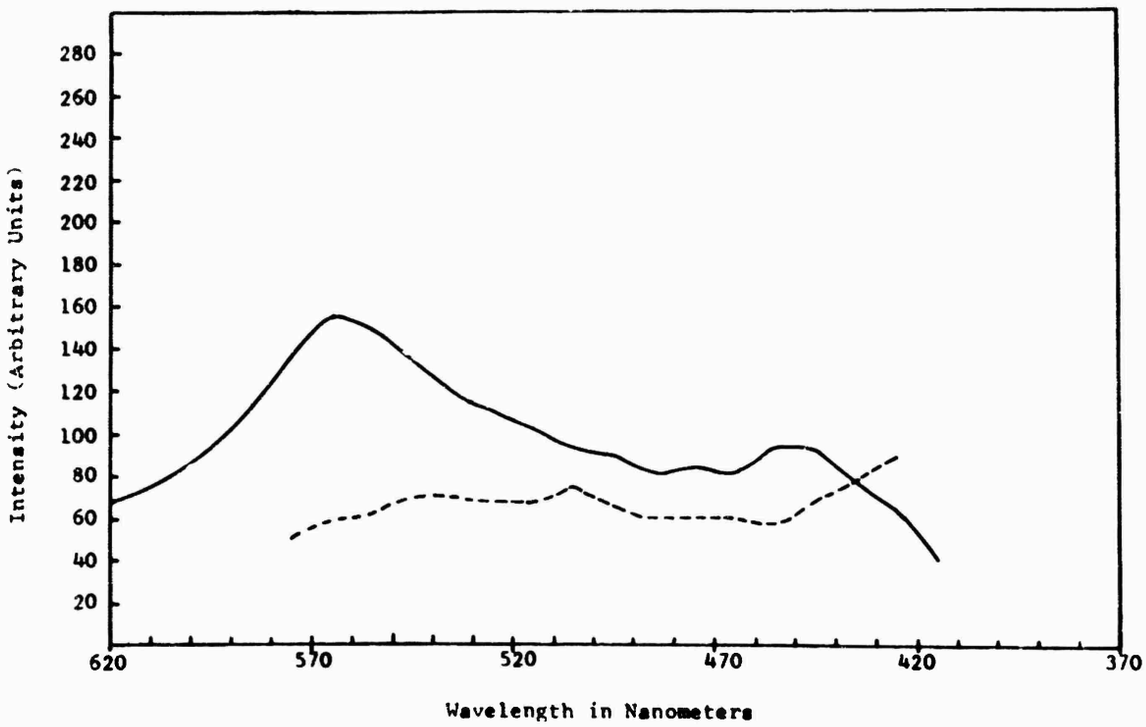

Figure 11. Relative Intensity Versus Wavelength as Recorded with Slitless Spectrograph. IVY 5 ——, DANA - - -.

VI. Studies of RF Scattering Processes from Ionized Chemical Releases in the Upper Atmosphere

D. R. Allison and W. G. Chesnut
Stanford Research Institute
Menlo Park, California

Abstract

This semi-annual Technical Summary Report describes the results of converting field data stored on magnetic tape into a visual format. The field data (on magnetic tape) contain recordings of radar backscatter and forward scatter signals reflected from chemical releases in the E and F regions during Project Firefly 1962. The conversion of this data into 'Z-scope' format, as is currently being done, is the first and most important step in the data analysis.

This report presents the data from Events FANNY and GILDA, night-time and sun-lit F-region probes, respectively. Also included are the data from releases KITTY (Cesium release at 108 kilometers in sunlight) and DANA (Aluminum doped high explosive at 101 kilometers altitude). The FANNY and GILDA release data were converted with high priority at the request of Dr. N. W. Rosenberg of AFCRL. Releases KITTY and DANA were converted for purposes of instrumentation normalization.

1. INTRODUCTION

The release of various chemicals into the ionosphere can have a pronounced effect upon the electromagnetic properties of the region of release. As a result, electromagnetic radiation (radar signals for example) can be used as a diagnostic tool to better understand the physical processes which occur during these releases.

The Radio Physics Laboratory of the Stanford Research Institute provided such electromagnetic probes during Project Firefly 1962. Specifically, S. R. I. provided and operated three backscatter radars, a three site CW bistatic radar system, and a short path forward and oblique scattering system.

The current research program is directed toward a reduction and analysis of the data recorded in the field during Project Firefly 1962. During this reporting period, the major effort has been directed toward reducing the recorded data by converting it into a form which is amenable to analysis by simple visual inspection. Involved in this effort was a re-evaluation and improvement of data processing techniques in order to provide greatest signal detectability possible. Some data may require more sophisticated reduction techniques to find positive effects. These special problems may be attacked at a later date should time and resources permit.

2. PROCEDURES

The Radio Physics Laboratory of SRI operated a variety of backscatter radars or sounders and CW bistatic radars during Project Firefly 1962. Table 1 lists the primary instrumentation used by SRI along with their nominal operating characteristics. Figure 1 presents a pictorial map of the field sites and release area used during Project Firefly 1962. A more detailed description of the generic types of equipment and how their data is reduced will be given in this section.

Much of the data taken by S. R. I. during Project Firefly 1962 was obtained with phase coherent backscatter radars, or 'Phase Sounders'. To properly orient the reader, a description of the principles of operation and of data reduction techniques will be described here.

2.1 Phase Sounder

A phase coherent sounder is essentially a radar in which the IF output, in our case offset by 9.6 kcps, is maintained phase coherent with respect to the transmitted pulse, the prf source, and the offset frequency source. As a result, a shift in phase of the reflected signal from pulse to pulse corresponds to a real motion of the target or to a change in the total phase path from transmitter to target and return. The measurement of pulse to pulse change of phase (which is conceptually equivalent to measuring the doppler shift) is an additional bit of information that is provided by a phase coherent sounder which is not obtainable by ordinary sounders. Since pulse to pulse phase coherence is maintained, long term, very slow changes in phase can be measured, and, hence, very small velocities resolved. Large velocities can be resolved with fair accuracy by measuring the time rate of change of target range; intermediate velocities lead to an ambiguity in velocity interpretation.

This ambiguity in velocity determination arises in the following way. A phase change of 2π radians/pulse interval* is seen as no phase change at all; a velocity of $N\lambda/2$ km/pulse interval (where N is an arbitrary integer, λ is the wavelength of the transmitted pulse in km) will give just such a phase change. In general, any velocity measured using a phase sounder has the form $v = v_o + n\lambda\,(prf)/2$ where v is the actual velocity, v_o is the zeroth order velocity measured from phase changes, n is an integer, λ is the wavelength, and prf is the pulse repetition frequency (cycles per second). The value of n may possibly be determined from the physical situation. Since a phase sounder is a sampling device, for the record to have any phase coherence, the correlation time of the process being observed must be greater than the pulse repetition interval.

Generally, information is desired at more than one frequency. This can be done by building several exciters at various frequencies and having these exciters sequentially drive a power amplifier feeding a common antenna. All of the sounders used by SRI in Firefly 1962 were of this type. We call them multiple frequency, time multiplexed, phase coherent sounders. The sole exception to this rule was the two vhf channels of the twelve frequency sounder at Saufly Field which were not phase coherent. Due to equipment difficulties, little data was obtained from these channels and this report will not discuss them.

The data from the phase sounders, an amplitude modulated 9.6 kcps IF signal and the time multiplexed outputs from the various receivers, are recorded on one channel of magnetic tape in amplitude mode. Other channels of the same tape record time marks, operator comments, the offset reference frequency, and the key pulse train with the initial pulse of each string inverted.

2.2 Data Presentation Technique for Phase Sounders

A standard Z-scope record presentation of phase sounder data for Firefly 1962 was prepared by running the IF signal (9.6 kcps carrier) from the playback recorder through a 10 kcps bandpass filter (± 5 kcps bandwidth) to remove hum and tape noise, then through an amplifier into an intensity modulated oscilloscope.

The sync channel from the tape recorder was run into a device which detected the proper time multiplexed frequency and then triggered the oscilloscope. Timing was introduced from the tape by adding either at reduction time or at operation time, a timing tone on the timing channel of the tape. This tone activated a relay to remove the sync signal for a short period producing a white line on the record once every minute. For all Project Firefly sounder records, the timing was initiated by hand and is accurate only to the normal human reaction time (approximately 0.1 second).

---

* Note that a phase change of 2π radians for the received signal corresponds to a π radian phase shift in target range for a backscatter configuration.

The signal records were produced by photographing the Z-scope trace with a moving film camera. Setting the light intensity of the trace has proven to be critical in order to obtain optimum detection of low level signals. An attempt was usually made to have the background noise slightly darken the film. In this way weak signals could be readily detected, yet strong signals would not saturate the record.

The oscilloscope was adjusted in the following way. With no signal present, the intensity control of the oscilloscope was increased until a trace was just barely visible. The signal was then applied and the gain of the amplifier driving the cathode ray tube of the scope monitored by hand so that the light output of the trace measured by a photocell remained approximately constant. Ideally, the light detector should see only a small portion of the trace on which only noise was present; the instrumentation borrowed for this analysis measured the total oscilloscope light intensity, including the transmitter feed-through. Therefore, hand monitoring of the light intensity met with varying degrees of success as interference levels varied.

With the oscilloscope adjusted in this manner for each sweep, a series of dark and light spots separated by the offset frequency period of 10^{-4} second (or 15 km range in backscatter) would be displayed. The intensity of the bright spots were a function of the amplitude of the signal. As film moved past the oscilloscope trace, a series of lines were produced. The intensity of a line was a function of the amplitude of the return; an angle with respect to the time axis was a function of the rate of change of total phase path or of the velocity of the target. A negative slope corresponded to a motion toward the radar, a positive slope to motion away.

We introduce the idea of fringes as a quick and simple way of getting information from these sounder records. A fringe is a continuous line on the record formed by many radar returns. As often happens, these lines are at an angle and eventually pass completely through the echo and start again. The number of fringes per unit time gives the velocity in terms of half-wavelengths per unit, including, of course, the possibility of the $N\lambda/2$ ambiguity discussed earlier.

This discussion holds completely for all channels of the four frequency sounder and all but the vhf channels of the Saufly Field twelve frequency phase coherent sounder. Any echoes seen on the vhf channels give only range information. The three frequency short pulse sounder used a pulse length of 10 μ seconds rather than the 200 μ seconds used by the other sounders; this sounder used an offset frequency of 100 kcps. Other than for this minor difference, the sounder data from this unit was reduced in the same manner as that for the other sites.

2.3 CW Bistatic Radar

SRI operated two CW bistatic radar receiving sites. These sites shared common transmitters which operated on three frequencies (27.6, 14.9, and 8.2 Mcps). The transmitting site was located at Saufly Field, Naval Air Station, Pensacola; the

receiving sites were located at Eglin Site A-4 (direct path 75 km) and at Cape San Blas (direct path 205km).

The transmitters were crystal controlled and had a rated power of 1 kw. At the receiving sites the transmission was received with the upper sideband suppressed and the receiver tuned with a 1.5 kcps offset. As a result, the received signal would be detected as a 1.5 kcps tone. The bandwidth of the receivers was 2.6 kcps. The detected output was recorded on 1/4-inch tape. Timing was introduced by recording countdown directly on the data channel from approximately 5 minutes before launch to 20 seconds before the first release, and at approximately 300 second intervals following the first release.

The primary purpose of this experiment was to obtain information on the early growth of the scattering cloud; that is, velocity and radial size. For a moving reflecting interface (see Figure 2), the velocity that the interface is moving is given by

$$v = (\lambda_o \Delta f/2) \sec(\phi/2) \qquad (1)$$

where v is the velocity of the moving interface, Δf is the measured frequency shift in r-f space, λ_o is the wavelength of the transmitted signal, and ϕ is the total scattering angle.

Generally, the reaction one expects to see is a positive doppler due to the material moving toward the observer initially of about 500 cps and decreasing to zero in approximately 0.5 second.* Additionally, if the cloud is underdense (that is, the angle of reflection is less than the angle of total reflection), a simultaneous negative shift could be observed. Experience has shown that this occurs more readily for the higher altitude events.

Once given the frequency-shift versus time signature of the event, application of Eq. (1) gives the velocity versus time profile. Integration of the velocity versus time data gives a measure of the radial growth.

For a given velocity of the interface, the shift observed varies in magnitude as cos ($\phi/2$). It is at a maximum in backscatter and at a near minimum in forward scatter. The scattering angles for both the San Blas and Eglin A-4 sites have been calculated; the observed shift will be greater than 70% of the shift that would have been observed in backscatter, for all cases except Sharon and Terry events.

The early growth data is obtained by running spectrograms of the data and constructing a time versus frequency plot. Several methods of doing this were explored and they met with varying degrees of success.**

---

* These characteristic times and frequency shifts refer to an E-layer electron cloud.

** See Quarterly Letter Reports 1 and 2.

The spectrum analysis was generally performed using a Rayspan Spectrum analyzer. This consists of a bank of 420 mangetostrictive filters with nominal bandwidth of 10 cps spaced every 8 cps covering the range from 84.7 to 88.052 kcps along with a mixing apparatus which allows analysis of any 3.352 kcps and between 20 cps and 13.428 kcps. The filters are fed in parallel and their output scanned by a commutator switch either 30 or 60 times per second.

In order to find out what events produced responses on the CW bistatic radar systems, all tapes have been processed by a technique which provides records on which the signatures are visible, but may not be measurable to sufficient accuracy to give a reasonably accurate velocity profile.

The signal from the magnetic tape was run through a bandpass filter centered at 1.5 kcps with cutoff points at 500 cps and 4 kcps to minimize hum, loran interference, teletype, and the like, then amplified and analyzed by the Rayspan between 20 and 3000 cps. The output of the Rayspan was used to intensity modulate an oscilloscope beam. The oscilloscope trace was photographed by a moving film camera on 70 mm paper.

On some events (mostly the F-region HEX and PEC series), minor modification of this was used. The data tape was played back at four times real time, thereby multiplying frequencies by a factor of four. The Rayspan filter was adjusted to allow for this frequency change; the r-f carrier was approximately centered on the Z-scope record. This procedure results in an effective reduction of the Rayspan filter bandwidth from 10 cps to 2.5 cps, increases the integration time by a factor of four, and decreases the noise seen by each filter by a factor of four. It is not completely clear that this technique really increases the detectability of effects as one's intuition would, at first sight, suggest.

The CW experiment suffered somewhat from interference. The CW transmitters were fixed frequency and were unable to move to a nearby quiet region when interference was present. This problem was particularly pronounced on the 8.2 Mcps channel which generally was obscured by teletype.

At the receiving sites, the data was recorded on 1/4-inch tape using two channels of a Webcor recorder and one channel of an Ampex 601. The running speed of these machines in the field were subject to variation due to local power frequency variations, and other uncertain causes. Since timing was recorded on the same channel as the data, and the only timing is the voice countdown referred by hand to WWV, reinserting time even to voice countdown accuracy is a difficult procedure. For most of the quick look records, timing was reinserted by measuring in the laboratory the percentage discrepancy between two time marks on each tape and compensating the time mark generator to allow for the measured error.

3. RESULTS

As of this writing, all 'no-problem' magnetic tapes* of the twelve frequency backscatter sounder, four frequency backscatter sounder, three frequency backscatter sounder and three frequency bistatic CW radars have been processed in the data reduction laboratory. Approximately half of these records, now in visual form, have been positioned and pasted on supporting material. Approximately 1/6 have been labeled, though not titled. Only the data from FANNY, GILDA, KITTY and DANA are in a form suitable for inclusion in this report. However, a cursory scanning of the records has allowed a 'quick-look' evaluation as to whether effects are clearly present or not. We present in this section, first, tables of condition of data, and second, the presentable data from Events FANNY, GILDA, KITTY and DANA.

3.1 Condition of Data-Summary

3.1.1 TWELVE FREQUENCY PHASE COHERENT SOUNDER.

Preliminary data reduction has been completed on all but five of these tapes. Table 2 presents a summary of the results seen. Of the five remaining tapes, one was neglected due to bookkeeping errors; one (BONNIE) starts sixteen minutes after launch; the other three are considered to be salvageable with effort.

3.1.2 FROM FREQUENCY VERTICAL INCIDENCE SOUNDER

Preliminary data reduction has been completed on all but four of these tapes. Table 3 presents a summary of the results seen. Of the four remaining tapes, all are considered salvageable.

3.1.3 THREE FREQUENCY SHORT PULSE SOUNDER

Due to damage in shipping, this instrument was not operative until 1 November 1962. The preliminary data reduction on all shots were the unit was operative has been completed and the results presented in Table 4.

3.1.4 CW BISTATIC RADAR

Preliminary data reduction of the Bistatic Radar tapes has been partially completed. Table 5 summarizes the results presently available.

---

* A 'no-problem' tape is one in which data may be easily converted to visual form. To clarify this concept somewhat, problem tapes may contain, through oversight, no sync signal, or countdown information, or may be physically damaged (needing replacing), etc., etc. Some of these data will be salvageable with effort.

3.2 Data Records for Events FANNY, GILDA, KITTY, and DANA

The four events from Project Firefly 1962 FANNY, GILDA, KITTY, and DANA have been converted to visual form. The events FANNY and GILDA were converted with high priority at the request of Dr. N. W. Rosenberg of AFCRL. Simultaneously, releases KITTY and DANA, both thought to give positive responses, were converted in order to provide standard for comparison for FANNY and GILDA. Table 6 reviews for the reader the important parameters of these four particular events.

Figures 3 through 11 are reproductions of the visual records for Event FANNY. Figures 12 through 19 are the records for Event GILDA. Figures 20 through 22 are the KITTY records, and Figures 23 through 25 are the DANA records.

The timing on the phase coherent sounder records is probably accurate to an order of a second. The CW records may have a large time disparity due to the fact that those tape recordings carried no timing signals, only voice countdown. Referring to Figure 22, one notes a very strong signature at about 120 seconds. The timing of the signature varies from 116.5 seconds for 27.6 Mcgs Eglin to 120.5 seconds for 14.9 Mcps - Eglin. This time disparity is not real, but may be used as a guide to the timing accuracy of these tapes. With effort, the timing errors can be reduced substantially.

4. DISCUSSION

In this section as attempt will be made to summarize the nature of the responses observed in Events FANNY, GILDA, KITTY, and DANA. One notes from Table 1 that the various phase sounders have differing 'nominal' detection sensitivities. For instance, the twelve frequency sounder has greater nominal peak power than either the four frequency or three frequency sounders. In fact, the evidence seems to indicate that the radiated power varied considerably from channel to channel of the twelve frequency sounder.

As a very approximate guide for first order analysis, Table 7 constructs nominal relative sensitivities of the various sounders for point targets and, presumably, for operation at the same frequency. This table cannot include differing levels of interference. Neither can it adequately convey the problems attendant with imperfect equipment operation.

The data-reduction-receiver-bandwidths have been used in the tables instead of direct receiver-bandwidth inasmuch as the data-reduction procedure further reduced the effective receiver bandwidth. The 20 cps figure indicated for the CW Bistatic radar is used rather than the individual filter bandwidths (2.5 cps for the data presented here). The photo reduction technique seems to provide a minimum display width of about 20 cps.

The rather large normalized sensitivity for the CW Bistatic radar may be somewhat misleading for the diagnostic work being attempted with the Project Firefly releases. For a frequency modulated (doppler modulated) signal, narrow bandwidth does not necessarily improve signal detection compared with wide bandwidth. For a linearly frequency-modulated signal, the energy supplied in a filter will be linearly proportional to the filter bandwidth. If the signal transit time across the filter passband is rapid compared with the filter response time (integration time), then narrowing the filter bandwidth does decrease the background noise, but it also decreases the signal energy. The signal-to-noise ratio may not improve.

4.1 Event FANNY

Event FANNY consisted of two high explosive releases and two cesium clouds below the F-layer. Table 8 simmarizes the effects observed.

4.1.1 TWELVE FREQUENCY SOUNDER

The first HEX release is observable at 107 seconds on some channels of the 12 frequency sounder records. The effects last for only about one second. The first PEC may provide a delayed effect on 6.4 Mcps. This effect, quite weak, begins at about 132 seconds and may last for 8 seconds. There is no assurance that the effect is release related.

The rather large disturbance on the 10.66 and 13.75 Mcps channels which begins at 313 seconds, precedes the published release time for the second PEC (318.93) by 5 seconds. Though the slant range is nearly correct, on the basis of timing it is difficult to believe that the effect is indeed caused by the release.

4.1.2 FOUR FREQUENCY SOUNDER

This instrument appears to give a short response to the first PEC at about 120 seconds on all except the 9.415 Mcps channel. On the two lower frequencies, 6.57 and 6.62 Mcps, respectively, a strong delayed effect is observed starting at approximately 139 seconds. This disturbance displays a very constant velocity, based upon fringe behavior, and appears like no natural disturbance observed with these instruments. We are inclined to assume that it is release induced. From the fringe shifts, a zero order velocity of 57 meters per second is indicated. The two frequencies on which this effect is observed are not sufficiently separated in order to determine if the actual velocity is greater than this, say the velocity of sound.

The fourth release, PEC #2, provides a similarly delayed response. This response also shows constant fringe shifts implying a constant velocity. Its zeroth order velocity is 45 meters per second.

4.1.3 THREE FREQUENCY SOUNDER

This instrument did not appear to respond to the FANNY releases.

4.1.4 CW BISTATIC RADARS

Only the 8.2 Mcps receiver at Eglin seems to have responded unambigously tothe FANNY releases. This response occurred at about the time of the second release, PEC #1.

4.2 Event GILDA

The parameters of the GILDA releases were very similar to those of Event FANNY. However, the GILDA releases occurred in sunshine. Table 9 summarizes the effects observed.

4.2.1 TWELVE FREQUENCY SOUNDER

Many channels of the twelve frequency sounder responded to this first release HEX #1. The response was strongest at intermediate frequencies. The response appeared to be 'transparent', showing an 'upper' and a 'lower' (greater and lesser range) altitude response. The upper and lower reflections appear to be range separated by nearly 70 kilometers. Both are initiated within one tenth of a second of each other. The simultaneity of effects at such great range separation is difficult to understand.

The second release, PEC #1, produces short lived effects on many channels of the sounder. This effect does remain on the low frequency channels for longer periods. The third and fourth releases do not appear to affect this instrument. The fourth release probably took place outside of the 3 db limits of the sounder antenna pattern.

4.2.2 FOUR FREQUENCY SOUNDER

The four frequency sounder does not appear to respond to the first release, HEX #1. However, all channels respond strongly to the second release, PEC #2. This strong response is probably the result of solar ionization of the PEC - cesium cloud. The third and fourth releases do not provide obvious effects. These appear at 384, on the 4.419 Mcps channel, a response similar to the delayed responses seen during FANNY. It shows a constant velocity as did the FANNY reactions. But the range is too small to correspond to even the first release.

4.2.3 THREE FREQUENCY SOUNDER

The three frequency sounder did not respond to the GILDA releases.

4.2.4 CW BISTATIC RADAR

The CW Bistatic radar may have responded to the first GILDA release, HEX #1.

The second release, PEC #1, gave a strong signature on several channels. Releases 3 and 4 gave no response.

4.3 Event KITTY

The parameters of Event KITTY are summarized in Table 6. KITTY was a 16.73 Kg PEC release at 108 kilometers at launch plus 121.93 seconds. The E region was sunlit so that solar ionization of Cesium could occur. Table 10 summarizes the effects observed.

4.3.1 TWELVE FREQUENCY SOUNDER

The twelve frequency sounder responded strongly to this release. The effects of delayed solar ionization are quite evident in that the return signal strength increases as time progresses.

4.3.2 FOUR FREQUENCY SOUNDER

All channels of the four frequency sounder responded to the KITTY release. Again, the effects of solar ionization are quite pronounced.

4.3.3 THREE FREQUENCY SOUNDER

The three frequency sounder did not respond to release KITTY.

4.3.4 CW BISTATIC RADAR

All channels of the bistatic radar, except 8.2 Mcps - Eglin responded to release KITTY. Failure of this channel to respond is quite surprising.

4.4 Event DANA

The parameters of Event DANA are given in Table 6. DANA was a 10.89 Kg HEX-Al (aluminum doped high explosive release at night time at an altitude of 108.1 kilometers. The release occurred at launch plus 108.8 seconds. Table 11 summarizes the responses to DANA.

4.4.1 TWELVE FREQUENCY SOUNDER

The twelve frequency sounder responded on its higher frequencies to the DANA release. Though the low frequency channels (three channels between 3.6 and 3.8 Mcps) appear to have been operating well, the release does not appear on those records.

4.4.2 FOUR FREQUENCY SOUNDER

No unambiguous response to DANA was obtained on this sounder.

4.4.3 THREE FREQUENCY SOUNDER

No response to release DANA was observed with this instrument.

4.4.4 CW BISTATIC RADAR

Some of the channels responded to release DANA. The release produces a nearly vertical line on the CW records.

5. CONCLUSIONS

At this writing it is not possible to give a detailed analysis of the observed effects (or lack of observed effects) on the four events included in this report. However, an attempt will be made to suggest plausible reasons for the existence or non-existence of responses.

Table 12 is a brief review of the PEC releases and equipment responses to them. Table 13 is a similar one compiled for HEX releases. Table 7 compared nominal sensitivities of the various instruments. For 'stationary signals', meaning not frequency modulated (by doppler), the twelve frequency and four frequency sounders had approximately the same sensitivities, while the CW Bistatic radar was approximately 25 times more sensitive. However, the doppler nature of the CW signals would have a profound effect on the CW Bistatic radar sensitivity. If a signal is doppler shifted 500 cps during 1/2 second, then the transit time of the signal through the 2.5 cps filters is 2.5 milliseconds. This is about 1/100 the filter integration time. We shall guess at this point that such a signal will be detected by the CW Bistatic radar with a sensitivity approximately one hundred times less than indicated in Table 7. Therefore, the CW Bistatic radar sensitivity might be more nearly like that of the sounders; or they might even be less sensitive by a factor of 3 or 4.

Table 12 indicates that the low altitude PEC (KITTY) provides positive doppler. The higher altitude releases give negative doppler. Table 13 shows that HEX releases do not give as large a CW response as do PEC's. The 108 km HEX-AC (DANA) also is 'transparent' in that positive and negative doppler are seen. One would guess that intermediate altitude PEC's (greater than 108 and less than 150 km) might also show 'double doppler.' The negative doppler suggests a transparent scatterer with reflections coming from the 'back' surface. One notes that for the intermediate altitude releases, ionosonde data suggests that the ambient electron densities were comparable. Therefore, the positive responses for PEC's on the CW Bistatic radar and negative response for HEX's suggest that the Cesium ionization (free electrons) are responsible for these observations. Shock wave compression by HEX releases at 135 to 140 kilometers is not sufficient to give a strong return.

With the exception of the strange, delayed responses on the four frequency sounder following the FANNY PEC's, one notes that the four frequency and twelve

frequency sounders do respond together. One important difference is the fact that the four frequency sounder is nearly under the releases where as the twelve frequency sounder observes the releases at about a 45° elevation angle. Thus, any layering mechanisms (flat bottomed clouds, etc.) may produce reflection cross sections which will be larger as seen from underneath. Perhaps this is why the four frequency sounder observes delayed FANNY responses which were not seen by the twelve frequency sounder. This geometry effect is the only plausible explanation for the lack of response at 5.0 and 6.4 Mcps on the twelve frequency sounder as compared with the very strong return on the four frequency sounder (at 5.6 Mcps in particular) following the first GILDA PEC. This cloud is undoubtedly solar ionized.

We conclude at this time that there are plausible explanation for the presence or absence of returns on the four events discussed. The rather strange delayed response to the FANNY PEC releases, if they are release associated, are unusual. We have no explanation for these at this time.

We conclude that 3.94 Kg release weights are of marginal size for F-region chemical probes for equipment with the sensitivities employed in this experiment.

Acknowledgments

Mr. Robert Barnes of the Stanford Research Institute has assisted the authors with many problems during the course of this work. Dr. N. W. Rosenberg of AFCRL has provided able guidance, assistance, and stimulating conversations concerning the data acquired.

TABLE 1. SRI operated instrumentation for Project Firefly 1962

Instrument Description and Location	Frequency MC (Approx)	Antenna	Polarization
12 Frequency Phase Coherent Oblique Sounder Pulse Length - 200 μsec Peak Power - 15 kw PRF - 12.5 pps/freq (approx) Located at Saufly Field	5.1 6.5 8.1 10.7 13.7 18.1 23.0 30.0 40.0 50.0 100.0 200.0	Log Periodic (approx 6 db gain) Main Beam Oriented at 45° elevation AZ directed toward Release ground zero 3 Element Yagi (~6 db gain)	Horizontal " " " " " " " " " "
4 Frequency Phase Coherent Vertical Incidence Sounder Pulse Length - 200 μsec Peak Power - 5 kw PRF - 3.75 pps/freq. Located at Eglin AFB Site A-13	#1<f_oF2* #2<f_oF2 #3≃f_oF2 #4>f_oF2	Log Periodic Oriented Vertically	Horizontal " " "
3 Frequency Short Pulse Phase Coherent Sounder Pulse Length - 10 μsec Peak Power - 4 kw PRF - 37.5 pps/freq. Located at Eglin Site A-13	11.7 17.7 30.6	3 Element Yagi " " " " " " All oriented in anticipated direction of release (about 45° elevation angle)	Horizontal " "
CW Bistatic Radar Transmitter Pulse Length - CW Peak Power - 1 kw (approx) Frequency Crystal Controlled Located at Saufly Field	8.2 14.9 27.6	Dipole Yagi Yagi	Horizontal " "
CW Bistatic Radar Receiver Receiving Sites located at Eglin Site A-4 and at Cape San Blas	Each of 3 tuned to 1500 cps offset from transmitter frequency	Dipole 3 Element Yagi 3 Element Yagi	Horizontal " "

*Frequencies generally chosen to be fairly near, but spanning the f_oF2 maximum, as indicated.

TABLE 2. Twelve frequency sounder records - summary of response

Nature of Release	Event Title	Frequency - Mc (nominal)											
		200	100	50	40	29	23	18	13	10	8	6	5
F Region Hex & Pec	Fanny	N	N	-	-	(+)	-	(+)	+	+	-	+	-
	Gilda	N	N	-	-	+	+	+	+	+	(+)	+	+
Hex-Al	Dana	N	N	-	-	(+)	(+)	+	+	+	-	-	-
Spec	Kitty	N	N	-	-	+	-	+	+	N	+	+	+
Mpec	Alice	N	N	-	(N)	-	-	+	+	+	+	+	+
	Queenie	N	N	-	-	-	-	+	+	+	+	+	+
Spec	Louise	N	-	-	-	-	-	-	+	+	+	+	-
Mpec	Paula	N	N	+	+	+	+	+	+	+	+	+	+
	Ruby	NOT RUN -- Timing Error -- Salvageable											
	Sally	N	N	+	+	+	+	+	+	+	+	+	+
	Beverly	+	+	+	+	+	+	+	+	+	+	-	-
Tec	Bonnie	NOT RUN -- Data Begins at T + 16 Min.											
	Dagmar	N	N	-	-	-	(N)	(+)	(+)	-	-	(+)	-
	Cindy	N	N	-	-	-	-	-	(+)	-	(+)	(+)	(+)
	Ivy	-	-	(N)	-	+	(+)	+	+	+	(+)	(+)	(+)
	Esther	-	-	-	-	+	-	+	+	+	-	-	-
NO	Mabel	NOT RUN -- Sync Error - Salvageable											
	Dinah	-	-	-	-	-	-	(+)	-	-	-	-	-
Na	Terry	N	N	-	-	-	-	-	-	-	-	-	-
	Sharon	N	-	(N)	-	-	-	-	-	-	-	-	-
C_2H_2	Netty	(N)	(N)	-	-	-	-	-	-	-	-	-	-
	Olga	N	N	-	-	-	-	-	-	-	-	-	-
SF_6	Ethel	NOT RUN -- Accounting Error											
	Martha	N	N	-	-	-	-	-	-	-	+	+	+
SF_6 CO_2	Karen	-	-	-	-	+	(+)	(+)	-	-	-	-	+
	Laura	-	-	-	-	+	+	-	-	-	-	-	-
NO	Eva	-	-	-	(+)	(+)	(+)	(+)	(+)	(+)	-	(+)	+
Tec	Enid	N	N	-	-	-	-	-	+	-	-	+	-

LEGEND: N = No data

+ = Probable release induced response

- = No obvious response

Parentheses indicate some question concerning our decision

TABLE 3. Four frequency vertical incidence sounder -- summary of response

Nature of Release	Event Title	Channel Number			
		1	2	3	4
		lowest	$< f_o F2$	$\approx f_o F2$	$> f_o F2$
Mpec	Queenie	+	+	+	+
	Sally	+	+	+	+
	Beverly	+	+	+	+
	Paula	+	+	+	+
	Ruby	+	+	+	+
	Alice	+	+	+	+
Spec	Louise	+	+	+	+
	Kitty	+	+	+	+
Hex-Al	Dana	+	+	+	+
Tec	Dagmar	+	+	-	-
	Ivy	-	-	-	-
	Cindy	+	+	-	+
	Esther	-	-	+	+
	Bonnie	N	N	N	N
	Enid	N	N	N	N
Hex & Pec	Fanny	+	+	+	-
	Gilda	+	+	+	+
SF_6	Martha	(+)	(+)	+	+
	Ethel	+	-	-	-
CO_2 & SF_6	Karen	+	+	+	+
	Laura	(-)	(-)	(-)	(-)
C_2H_2	Olga	-	-	-	-
	Netty	-	-	-	-
NO	Mabel	-	-	-	-
	Dinah	-	-	-	-
	Eva	-	-	-	-
Na	Terry	-	-	-	-
	Sharon	-	-	-	-

LEGEND: N = No data

+ = Probable release induced response

- = No obvious response

Parentheses indicate some question concerning our decision

TABLE 4. Three frequency short pulse sounder -- summary of data
(Instrument not in operation until 1 November 1962)

Generic Type	Shot	11.7	17.7	30.6
Mpec	Ruby	+	-	-
	Beverly	+	-	-
	Sally	+	-	-
Hex - Pec	Fanny	-	-	-
	Gilda	-	-	-
CO_2 & SF_6	Martha	-	-	-
	Karen	-	-	-
	Laura	-	-	-
Hex - Al	Dana		-	-
C_2H_2	Olga	N	N	N
	Netty	-	-	-
Tec	Esther	-	-	-
	Ivy	-	-	-
NO	Dinah	-	-	-
	Mabel	N	N	N
	Eva	-	-	-
Na	Sharon	-	-	-
	Terry	-	-	-

LEGEND: N = No data
+ = Probable release induced response
- = No obvious response
Parentheses indicate some question concerning our decision

TABLE 5. CW bistatic radar -- summary of response

Nature of Release	Event Title	San Blas Radar			Eglin A-4 Radar		
		27.6 Mc	14.9 Mc	8.2 Mc	27.6 Mc	14.9 Mc	8.2 Mc
Mpec	Alice	- - - -		- - - -			
	Queenie	- - - -	+ + + +	- - + +			
	Sally	+ + + +	+ + + +	+ + + +		- - - -	
	Beverly	-	+ + - +	-	(+) + - +	-	
	Paula					+ + + +	
	Ruby	+ + + +					
Spec	Louise		(-)	-	-		
	Kitty	+	+	+	+	+	-
Hex-Al	Dana	+	+	+	+	-	-
Tec	Dagmar	-					-
	Ivy	-					
	Cindy				-		-
	Esther	(+)	+	-		-	
	Bonnie	-					
	Enid	-		(+)			(+)
Hex & Pec	Fanny	- - - -	- (+) - -	- - - -	(+)(+) - -	N - - -	- (N) - -
	Gilda	- + - -	(+) + - -		(+) + - -	N N N -	- - - -

TABLE 5. CW bistatic radar -- summary of response (Cont.)

Nature of Release	Event Title	San Blas Radar			Eglin A-4 Radar		
		27.6 Mc	14.9 Mc	8.2 Mc	27.6 Mc	14.9 Mc	8.2 Mc
SF_6	Martha	N	N	N	N	N	N
	Ethel	-	-	-	-		
SF_6 & CO_2 Grenades	Karen						
	Laura						
C_2H_2	Olga	N	N	N	N	N	N
	Netty	N	N	N	N	N	N
NO	Mabel		-	-		-	-
	Dinah		-	-			
	Eva		-	-	+	-	
Na	Terry	?	?	?			
	Sharon	?	?	?	-		

LEGEND: N = No data

+ = Probable release induced response

- = No obvious response

Parentheses indicate some question concerning our decision

TABLE 6. Parameters for events Fanny, Gilda, Kitty and Dana

Event Title	Condition of Ionosphere	Release Number	Time of Release (referred to launch) (seconds)	Altitude (kilometers)	Nature and Weight of Release Package
Fanny	Night Time	#1	107.7	140	HEX-3.03 Kg
		#2	119.74	157	PEC-3.94 Kg
	f_0 F2-4.3 Mc	#3	184.2	230	HEX-3.03 Kg
	at ~ 270 km*	#4	318.93	260	PEC-3.94 Kg
Gilda	Sunlit	#1	106.9	137.7	HEX-3.03 Kg
	Ionosphere (Sunset)	#2	119.19	155	PEC-3.94 Kg
	f_0 F2~4.4 Mc	#3	212.67	250	HEX-3.03 Kg
	at ~ 240 km*	#4	338.75	237	PEC-3.94 Kg
Kitty	Sunlit E-Region (Sunset) E_s at 105 km to 1.6 Mc Ambient E to 0.9 Mc	#1	121.93	108.0	SPEC-16.73 Kg
Dana	Night time E_s at 94 km to 1.0 Mc E_s at 99 km to 1.7 Mc Ambient E ~ $10^4/cm^3$ at altitude	#1	108.8	108.1	HEX-A1-10.89 Kg

*NOTE: All ionospheric data quoted here comes from "Ionosonde Results" - Firely III, Quick-Look Report; J. W. Wright, Central Radio Propagation Laboratories - National Bureau of Standards, Boulder, Colorado, PM-62-6103 (N. B. S. internal document).

TABLE 7. Comparison of detection capability of various sounders

Sounder	Nominal Peak Power (kw)	Two Way Antenna Gain	Data Reduction Receiver Bandwidth	Normalized Range to Releases	Normalized Sensitivity
12 Freq.	15	16	10	1.5	6
4 Freq.	5	16	10	1.0	8
3 Freq.	4	16	100	1.0	0.6
CW Bistatic	11	16	.020	1.5	200

TABLE 8. Summary of results -- Project Firefly Fanny

Site	Frequency	Release and Payload			
		#1 - HEX	#2 - PEC	#3 - HEX	#4 - PEC
Twelve Frequency Phase Coherent Sounder					
	50.11 Mc	-	-	-	-
	40.16 Mc	-	-	-	-
	29.41 Mc	-	-	-	-
	22.88 Mc	-	-	-	-
	18.01 Mc	106s/<1s very weak	-	-	-
	13.735 Mc	107/<1s	-	-	-
	10.66 Mc	-	-	-	-
	8.02 Mc	-	-	-	-
	6.41 Mc	107s/2s weak	132s/8s weak	-	-
	5.04 Mc	-	-	-	-
Four Frequency Vertical Incidence Sounder					
	9.415 Mc	-	123s/1s	-	-
	9.245 Mc	-	-	-	-
	6.617 Mc	-	120s/1s & 139s/14s	-	323s/8s
	6.574 Mc	-	120s/1s & 139s/14s	-	329s/~6s
CW Bistatic Radars					
San Blas	27.6 Mc	No	No	No	No
San Blas	14.9 Mc	No	Yes	No	No
San Blas	8.2 Mc	No	No	No	No
Eglin A-4	27.6 Mc	(Yes)	(Yes)	No	No
Eglin A-4	14.9 Mc	No data	No	No	No
Eglin A-4	8.2 Mc	No	(Yes)	No	No

Parentheses indicate uncertainty.

Hyphen indicates no response.

TABLE 9. Summary of results -- Project Firefly Gilda

Site	Frequency	Release and Payload			
		#1 - HEX	#2 - PEC	#3 - HEX	#4 - PEC
Twelve Frequency Phase Coherent Sounder					
	50.11 Mc	-	-	-	-
	40.16 Mc	-	-	-	-
	29.41 Mc	106s/1s transparent	-	-	-
	22.88 Mc	106s/1s transparent	119s/1s	-	-
	18.01 Mc	106s/2s transparent	119s/2s	-	-
	13.67 Mc	106s/2s transparent	119s/4s	-	-
	10.665 Mc	106s/2s transparent	125s/10s	-	-
	8.02 Mc	100s/2s transparent	-	-	-
	6.41 Mc	-	~119s/20s	-	-
	5.04 Mc	-	~120s/6s very weak	-	-
Four Frequency Vertical Incidence Sounder					
	5.598 Mc	-	119s/>5m	-	-
	4.742 Mc	-	123s/>5m weak off 15s	-	-
	4.419 Mc	-	123s/8s	-	-
	4.208 Mc	-	123s/12s	-	-
CW Bistatic Radars					
San Blas	27.6 Mc	No	Yes	No	No
San Blas	14.9 Mc	(Yes)	Yes	No	No
San Blas	8.2 Mc	?	?	?	?
Eglin A-4	27.6 Mc	(Yes)	Yes	No	No
Eglin A-4	14.9 Mc	No data	No data	No data	No data
Eglin A-4	8.2 Mc	HIGH INTERFERENCE LEVEL			

Hyphen indicates no response.

Parentheses indicate uncertainty.

TABLE 10. Summary of results -- Project Firefly Kitty

Twelve Frequency Phase Coherent Sounder		
Site	Frequency	Release & Payload SPEC
	50.10 Mc	-
	40.15 Mc	-
	29.42 Mc	~122s/>4m
	22.82 Mc	-
	18.06 Mc	~220s/>2.5m
	13.67 Mc	~200s/~2.5m
	10.67 Mc	Inoperative - receiver failure
	8.08 Mc	~121s/>4m -- stronger after 240s
	6.58 Mc	~121s/>4m -- stronger after 215s
	5.09 Mc	170s/>4m -- very weak
Four Frequency Vertical Incidence Sounder		
	11.269 Mc	123s/>5m -- weak; stronger after 233s
	9.590 Mc	125s/>5m -- stronger after 224s
	7.235 Mc	122s/>5m
	4.593 Mc	121s/>5m
CW Bistatic Radars		
San Blas	27.6 Mc	Yes
San Blas	14.9 Mc	Yes
San Blas	8.2 Mc	Yes
Eglin A-4	27.6 Mc	Yes
Eglin A-4	14.9 Mc	Yes
Eglin A-4	8.2 Mc	No

Hyphen indicates no response.

TABLE 11. Summary of results -- Project Firefly Dana

Site	Frequency	Release & Payload HEX - A1
Twelve Frequency Phase Coherent Sounder		
	50. Mc	-
	40. Mc	-
	29.41 Mc	109s/>1s
	22.9 Mc	109s/ -- very short
	18.06 Mc	109s/>1s
	13.66 Mc	109s/1s
	10.72 Mc	-
	3.800 Mc	-
	3.690 Mc	-
	3.649 Mc	-
Four Frequency Vertical Incidence Sounder		
	3.610 Mc	0
	3.478 Mc	0
	3.394 Mc	0
	3.000 Mc	0
CW Bistatic Radars		
San Blas	27.6 Mc	Yes
San Blas	14.9 Mc	Yes
San Blas	8.2 Mc	No
Eglin A-4	27.6 Mc	Yes
Eglin A-4	14.9 Mc	No data
Eglin A-4	8.2 Mc	Yes

Hyphen indicates no response.

TABLE 12. Summary of PEC releases Fanny, Gilda and Kitty

PEC			Response Summary		
Alt	Wt	n_e	12 Freq.	4 Freq.	CW Bistatic
103	17Kg	$\sim 10^4$ day (Kitty)	Yes	Yes^{**}_{4-11}	Yes (positive doppler)
155	3.9Kg	$6 \cdot 10^4 (2 \cdot 10^4)^*$ day(Gilda)	Yes	$Yes_{5,4}$	Yes (negative doppler)
157	3.9Kg	$3 \cdot 10^4$ night (Fanny)	Yes(weak)	$Yes_{9,6}$	Yes (negative doppler)
230	3.9Kg	$19 \cdot 10^4$ day (Gilda)	No	$No_{5,4}$	No
260	3.9Kg	$17 \cdot 10^4$ night (Fanny)	No	Yes	No

*Alternative profiles, J.W. Wright, Loc. Cit.
**Subscripts indicate approximate frequencies used.

TABLE 13. Summary of HEX releases Fanny, Gilda, and Dana

HEX			Response Summary		
Alt	Wt	n_e	12 Freq.	4 Freq.	CW Bistatic
108	10.9Kg	10^4 night (Dana)	Yes	$No^{**}_{3-3,6}$	Yes (positive and negative doppler)
137.7	3.0Kg	$4 \cdot 10^4$ day (Gilda) $(2 \cdot 10^4)$	Yes	No_{4-6}	(Yes)
140	3.0Kg	$2 \cdot 10^4$ night (Fanny)	Yes(weak)	No_{6-9}	Uncertain
230	3.0Kg	$14 \cdot 10^4$ night (Fanny)	No	No_{6-9}	No
250	3.0Kg	$19 \cdot 10^4$ day (Gilda)	No	No_{4-6}	No

*Alternative Profiles, J. W. Wright, Loc. cit.
**Subscripts indicate approximate frequencies used.

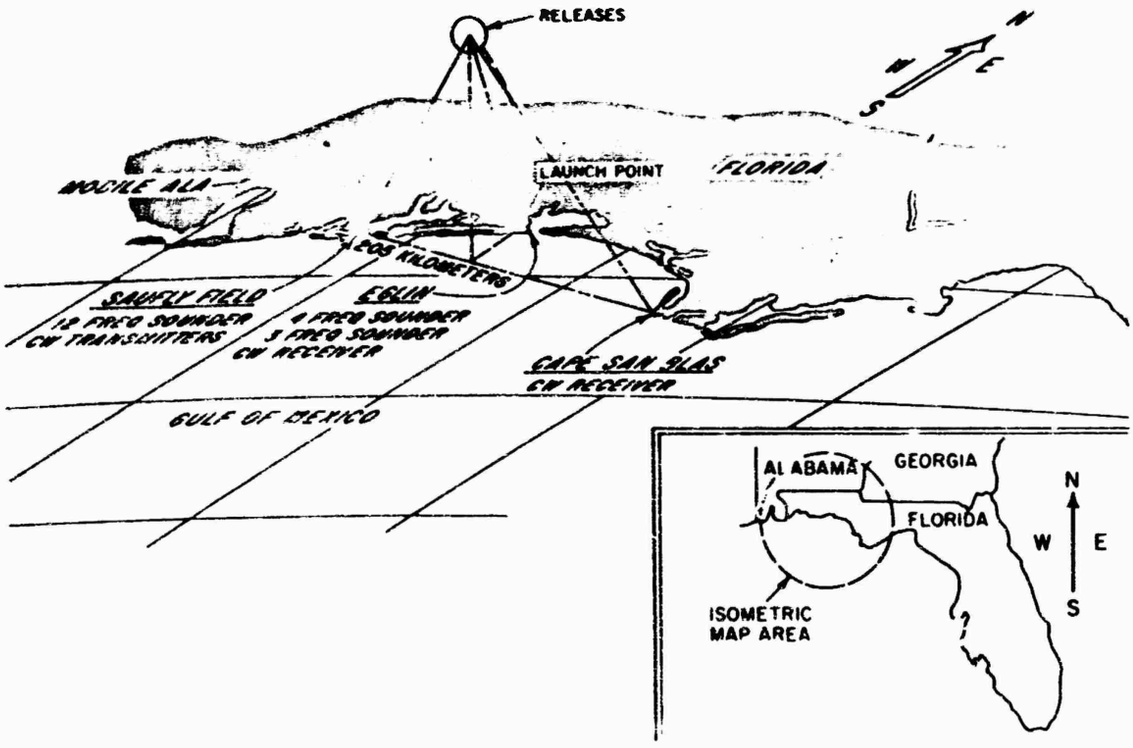

Figure 1. Map of Release Area

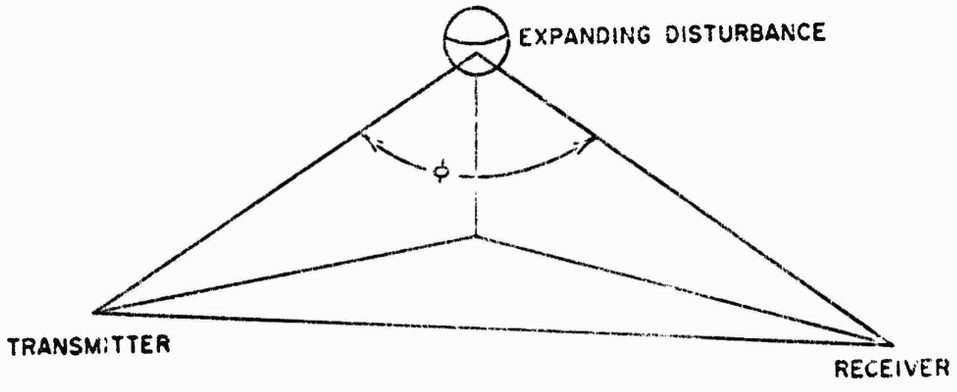

Figure 2. CW Bistatic Radar Geometry

(½ f)

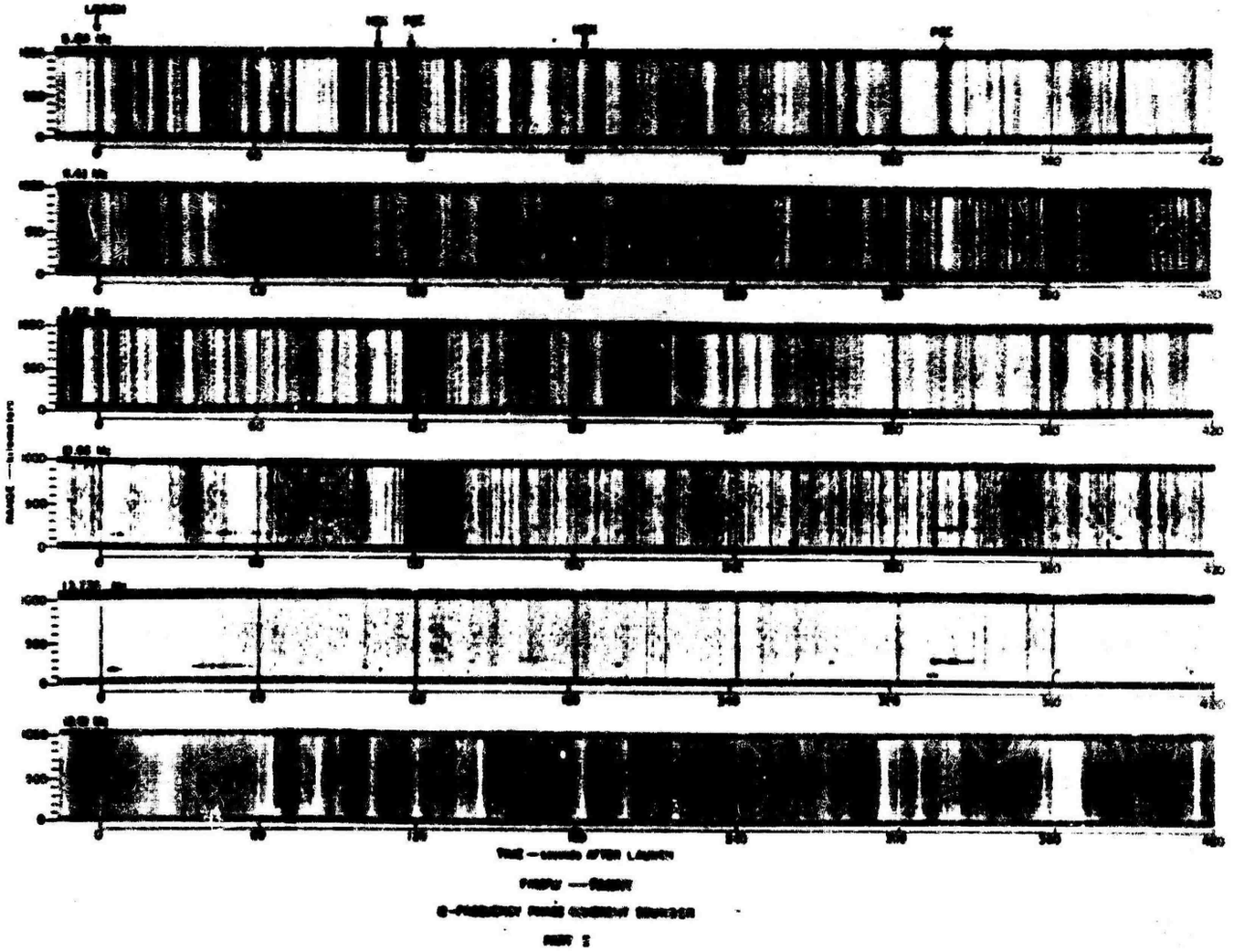

Figure 3. FANNY - Twelve Frequency Sounder

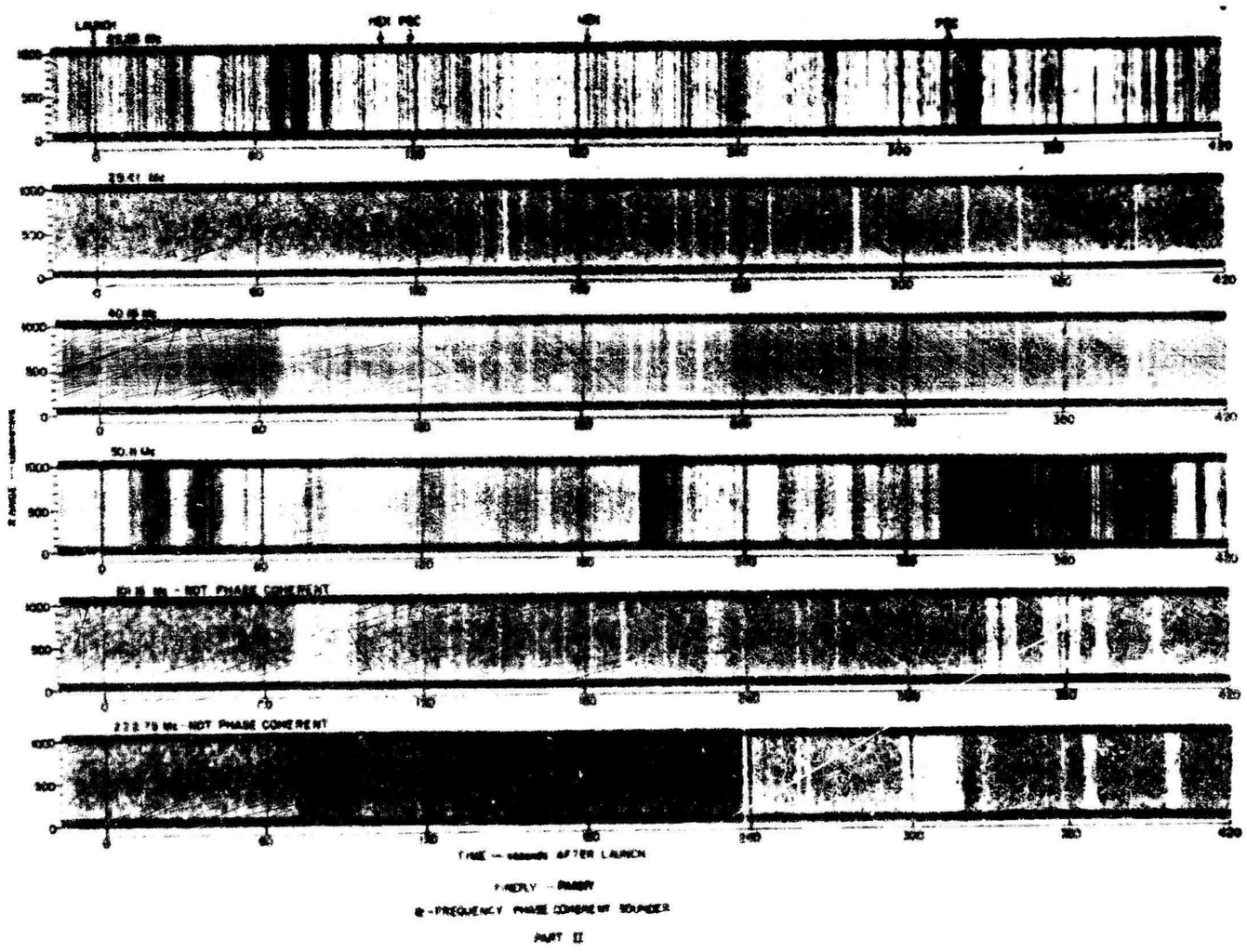

Figure 3. (Cont) FANNY - Twelve Frequency Sounder

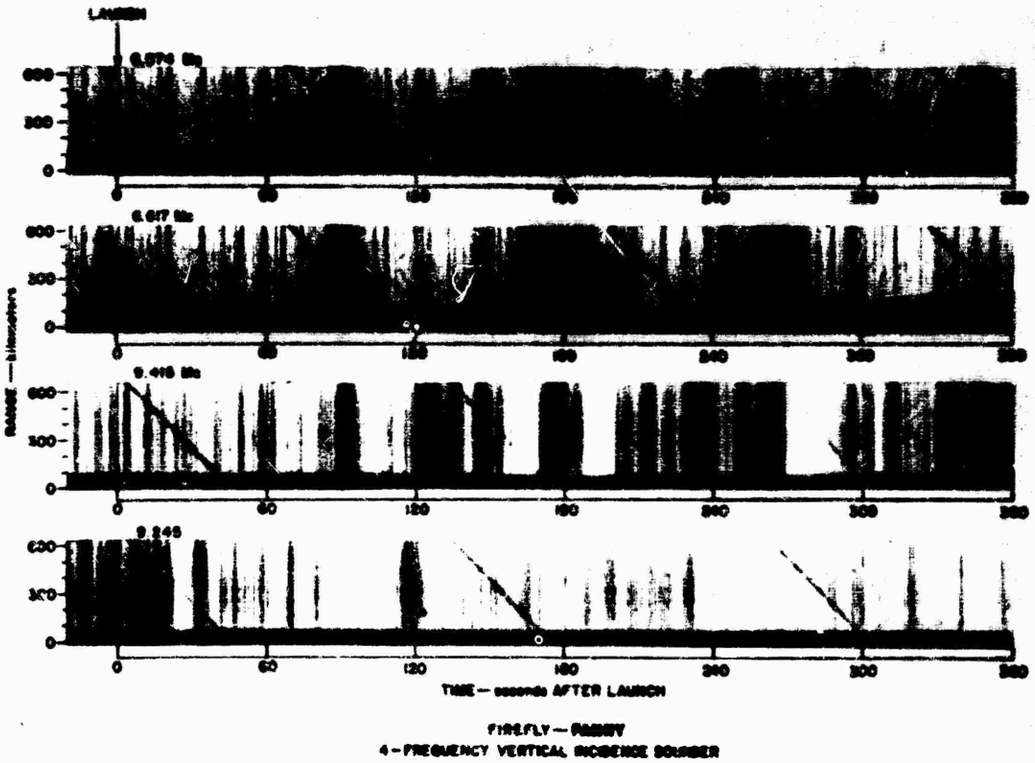

Figure 4. FANNY - Four Frequency Sounder

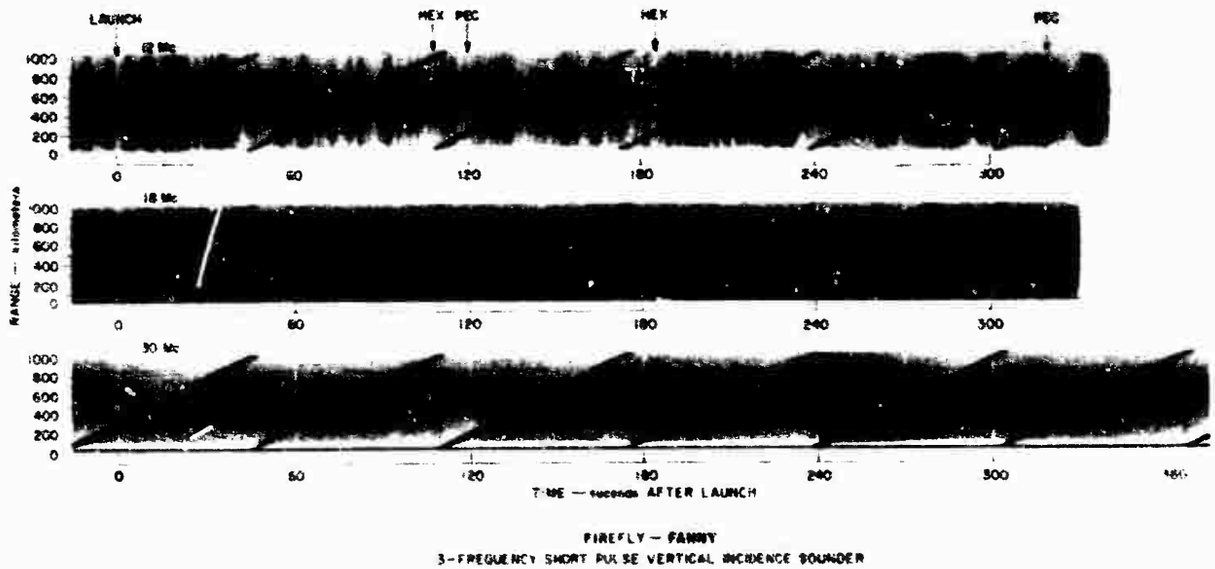

Figure 5. FANNY - Three Frequency Sounder

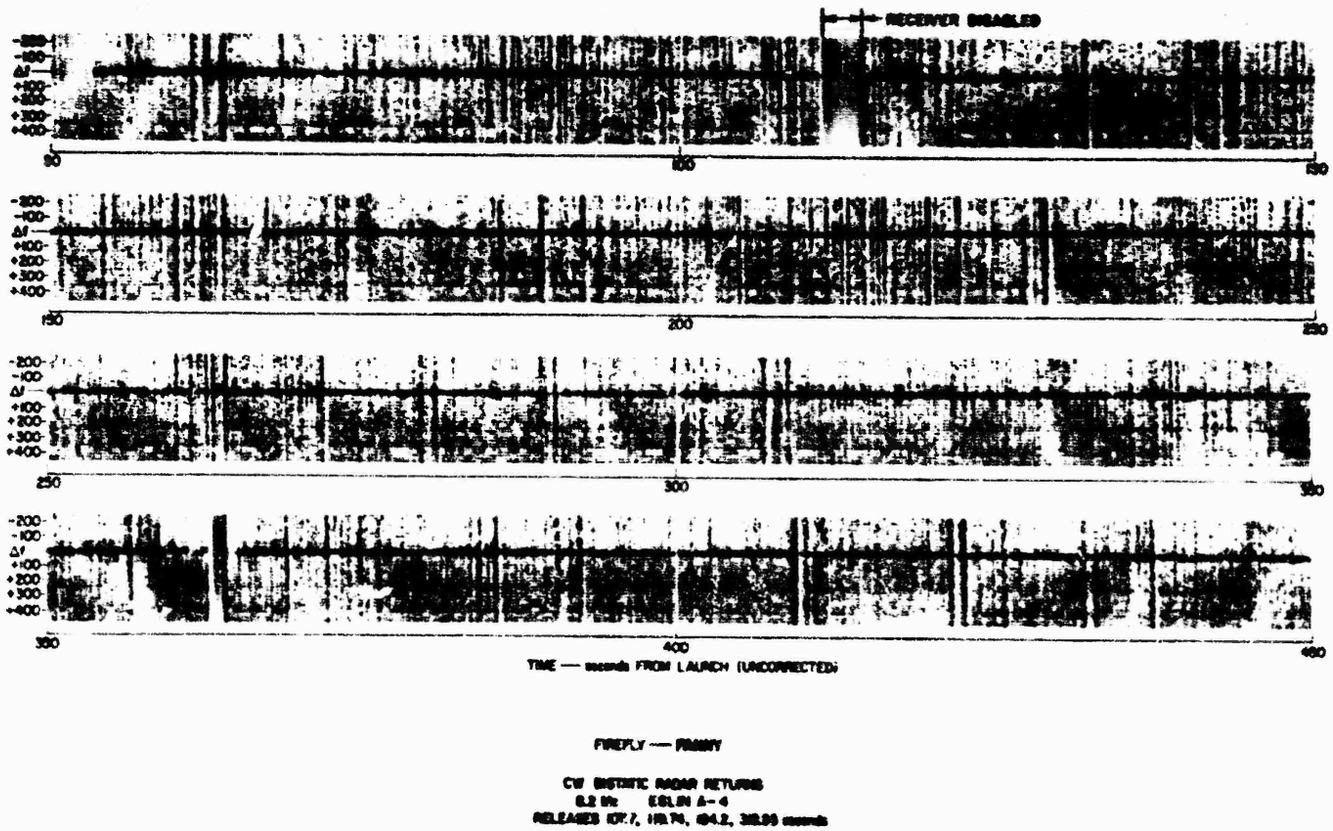

Figure 6. FANNY - CW Radar - 8.2 Mcps Eglin

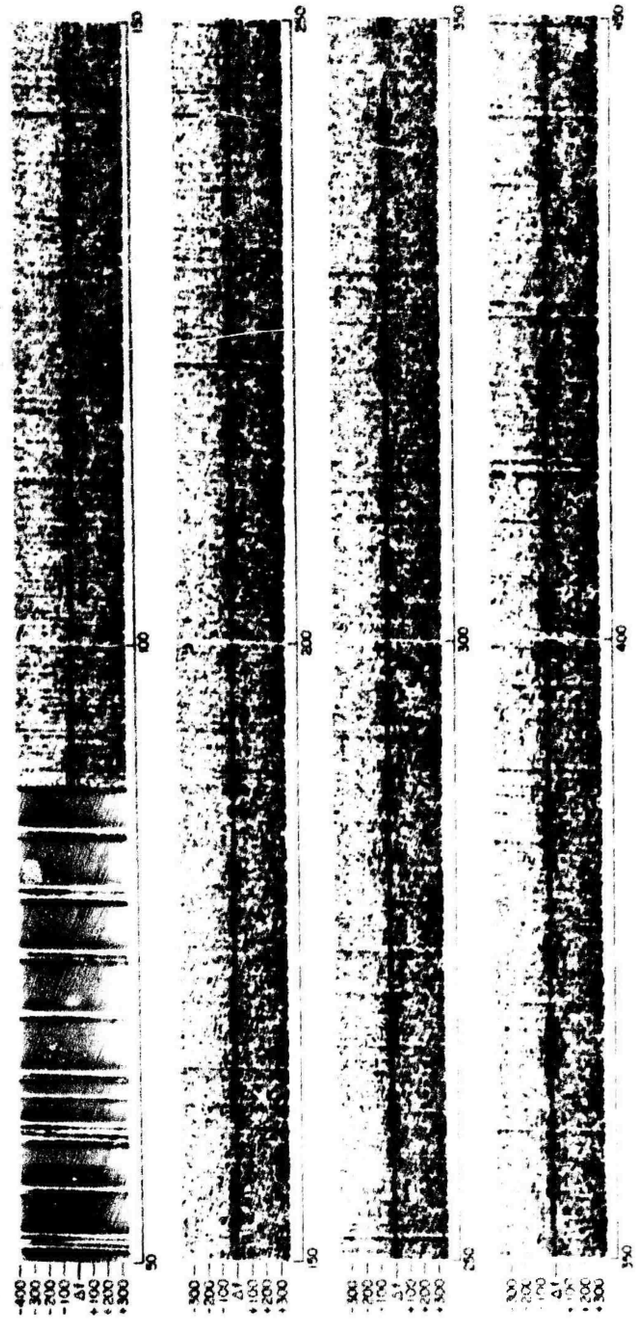

Figure 7. FANNY - CW Radar - 8.2 Mcps San Blas

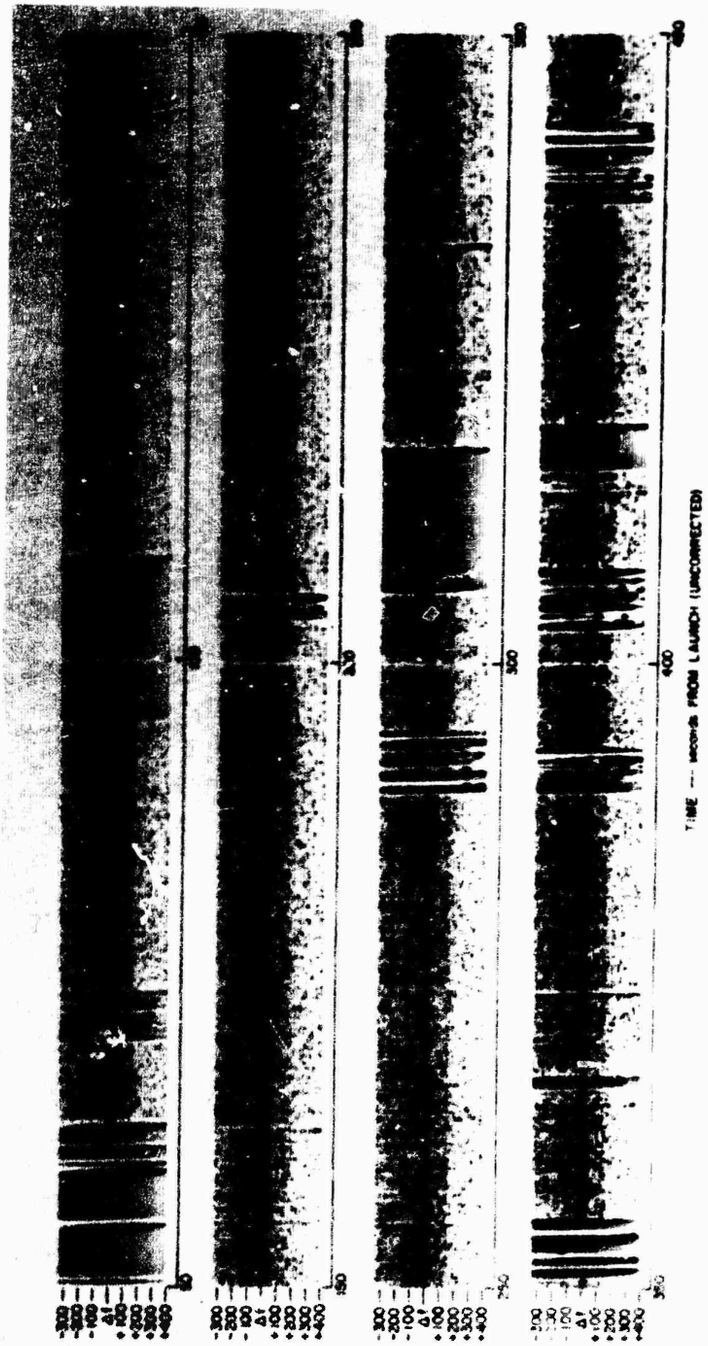

Figure 8. FANNY - CW Radar - 14.9 Mcps Eglin

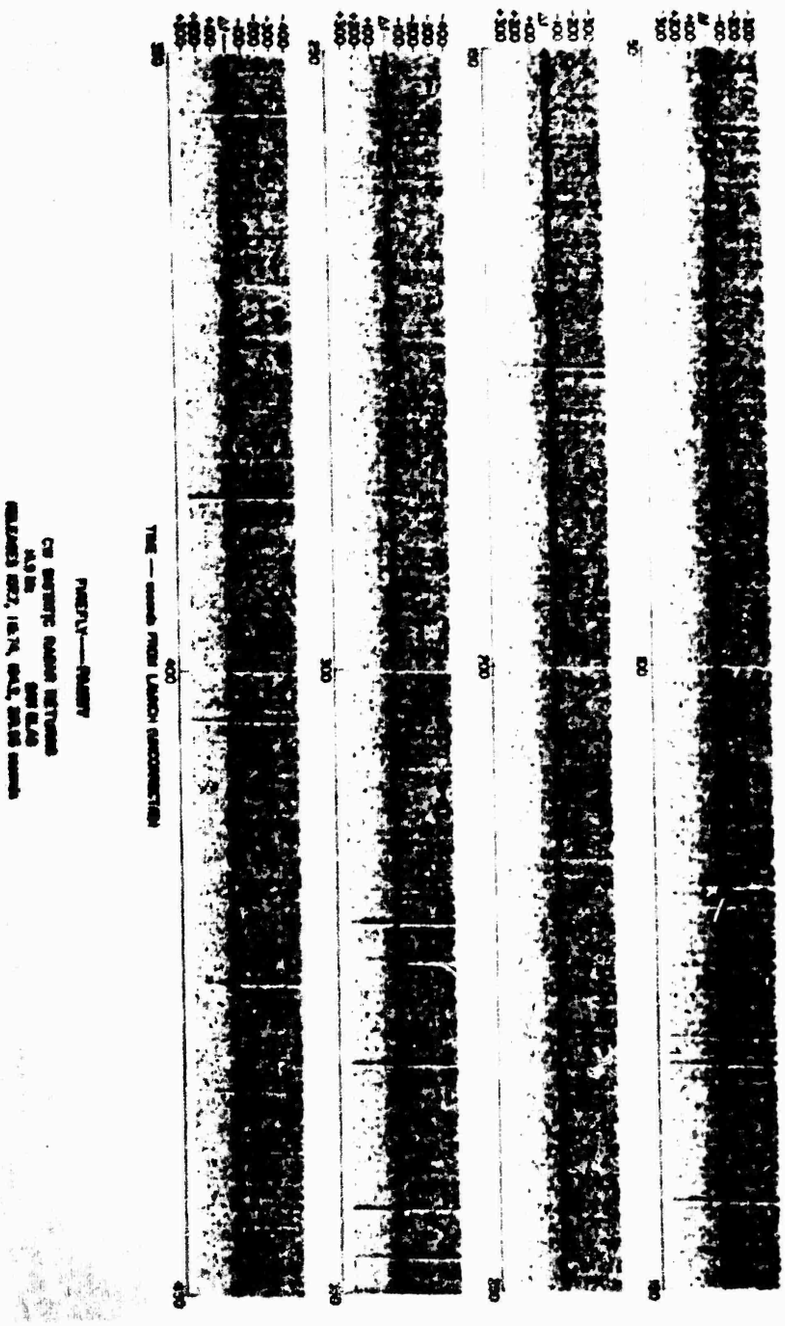

Figure 9. FANNY - CW Radar - 14.9 Mcps San Blas

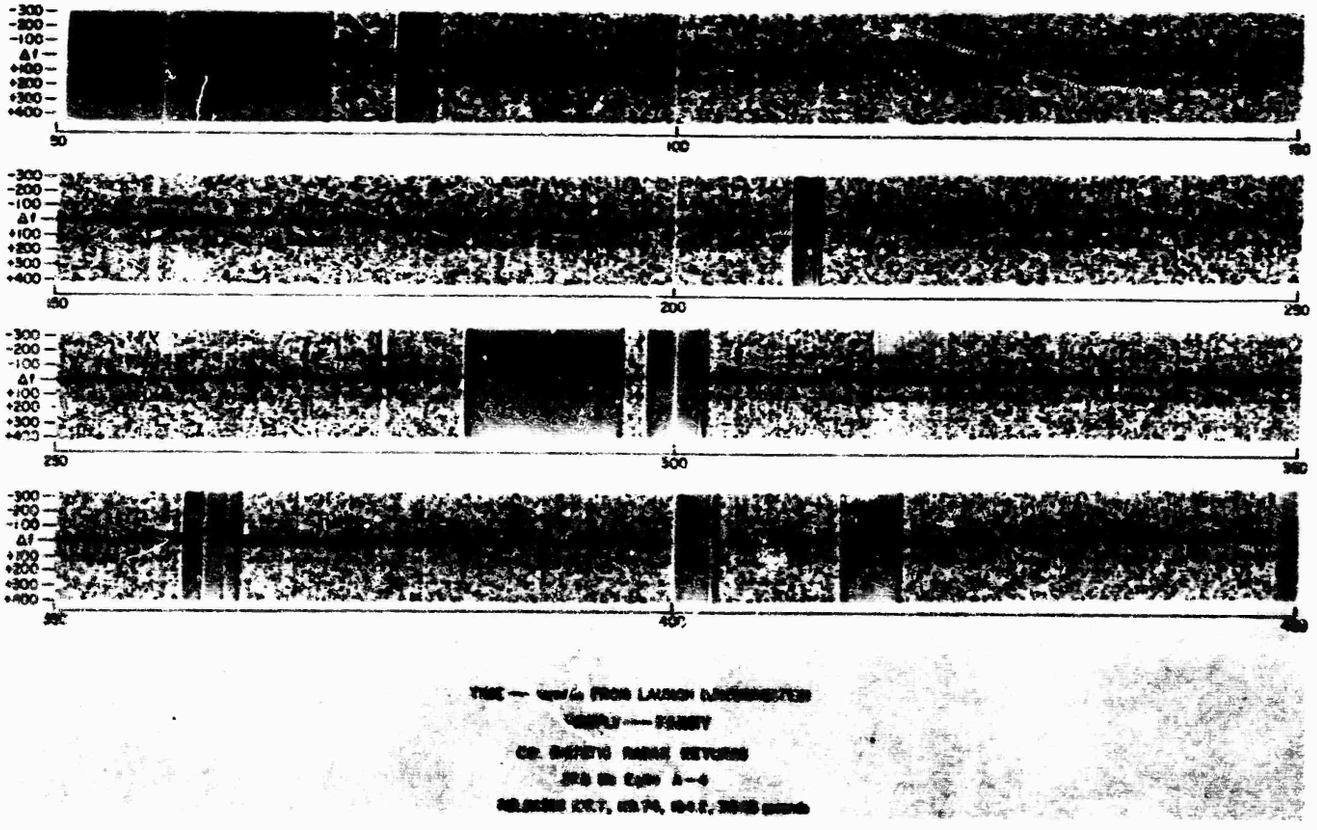

Figure 10. FANNY - CW Radar - 27.6 Mcps Eglin

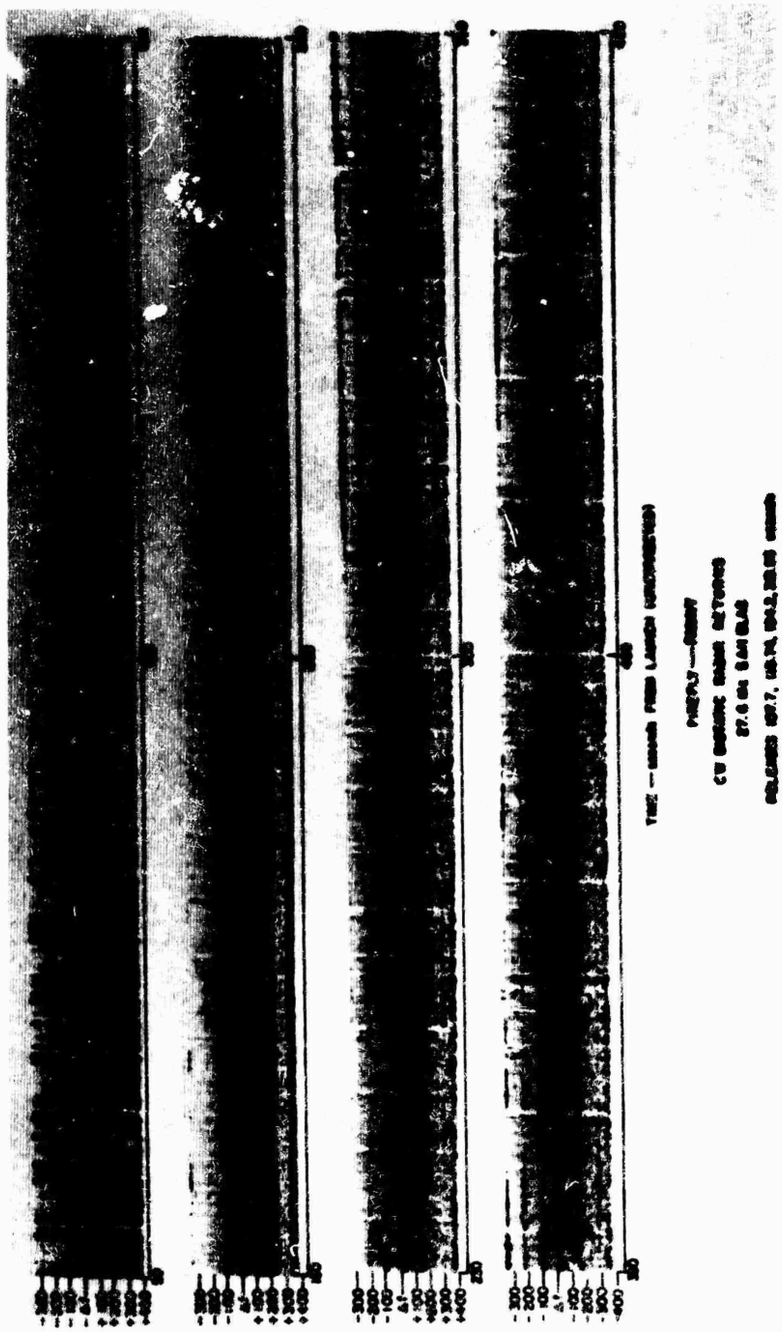

Figure 11. FANNY - CW Radar - 27.6 Mcps San Blas

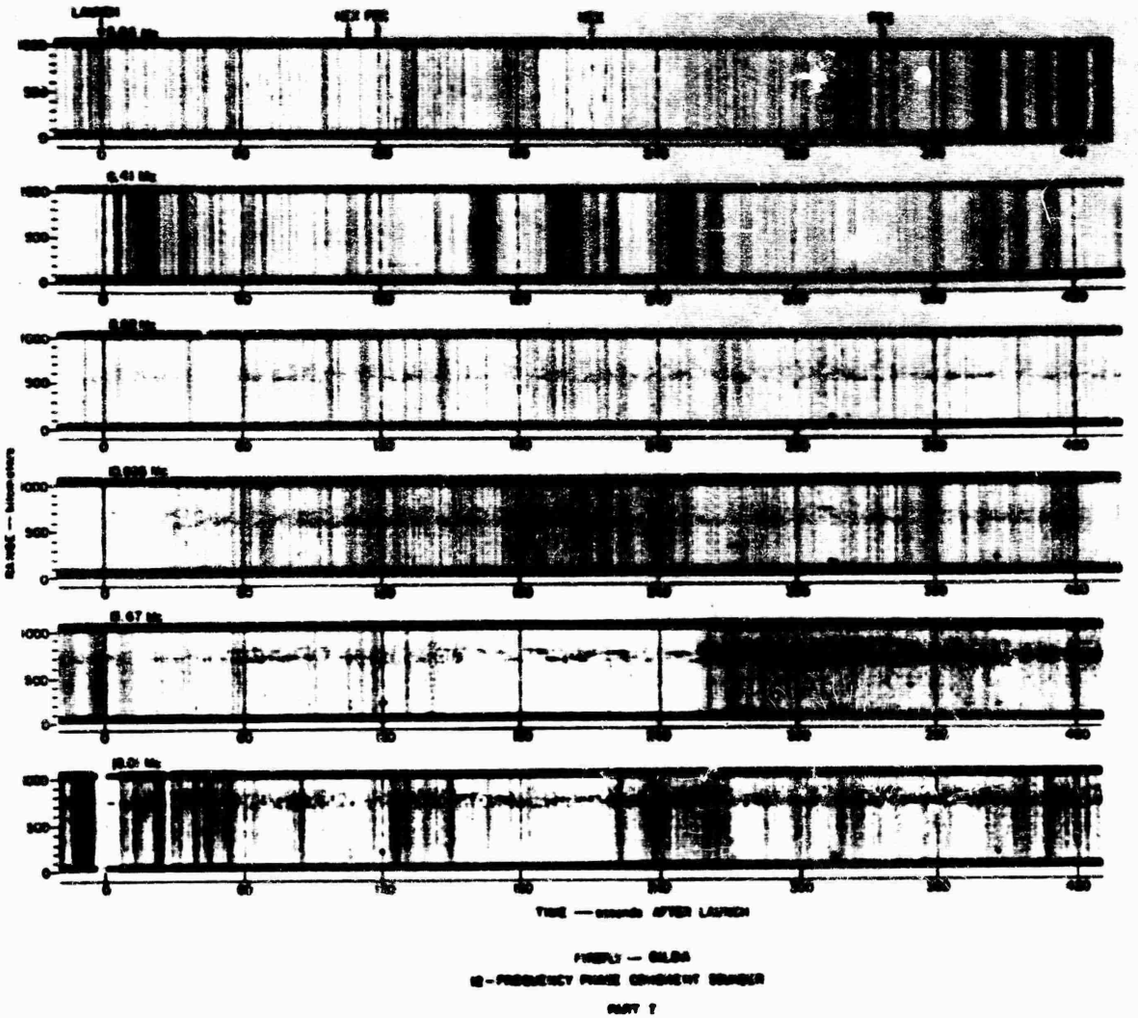

Figure 12. GILDA - Twelve Frequency Sounder

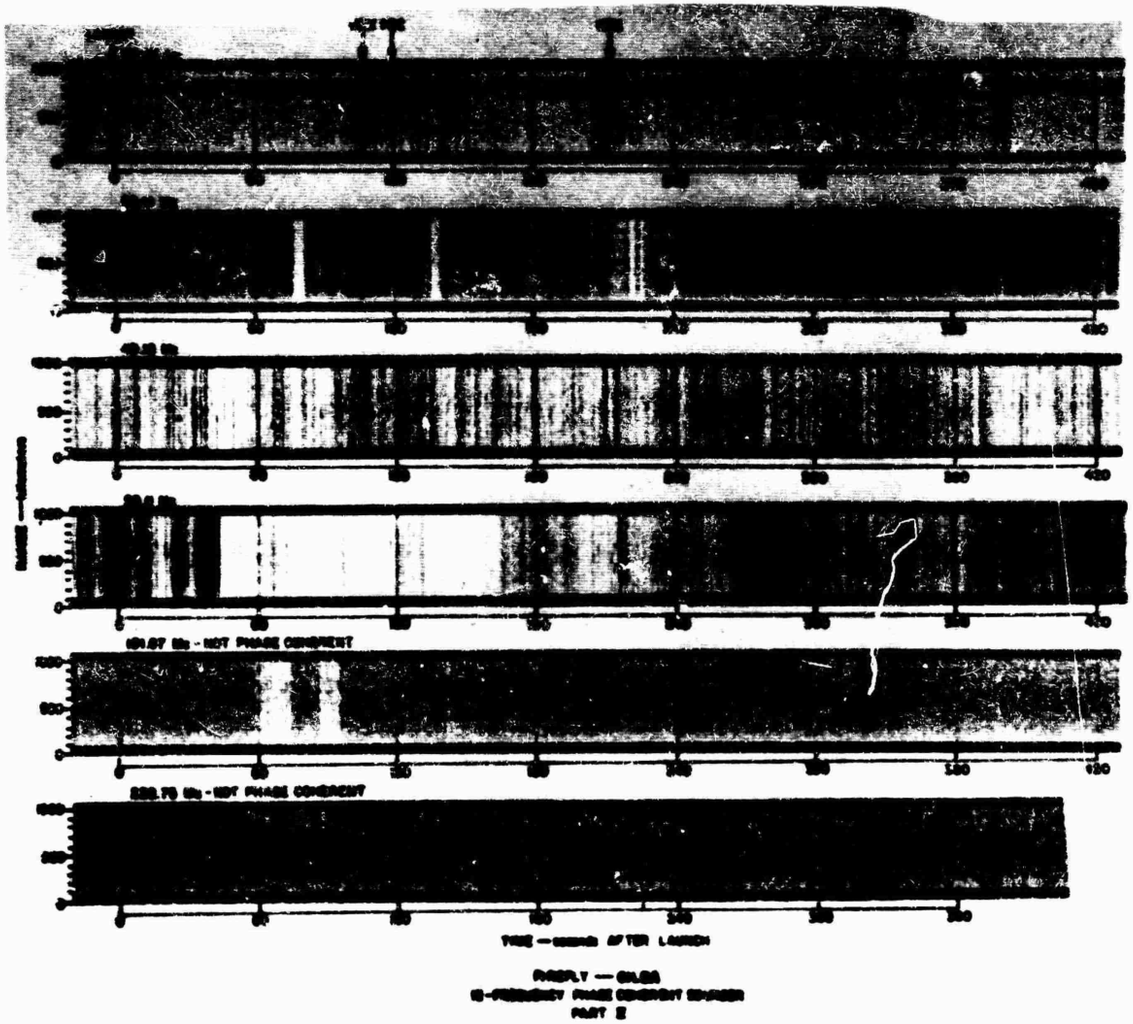

Figure 12. (Cont) GILDA - Twelve Frequency Sounder

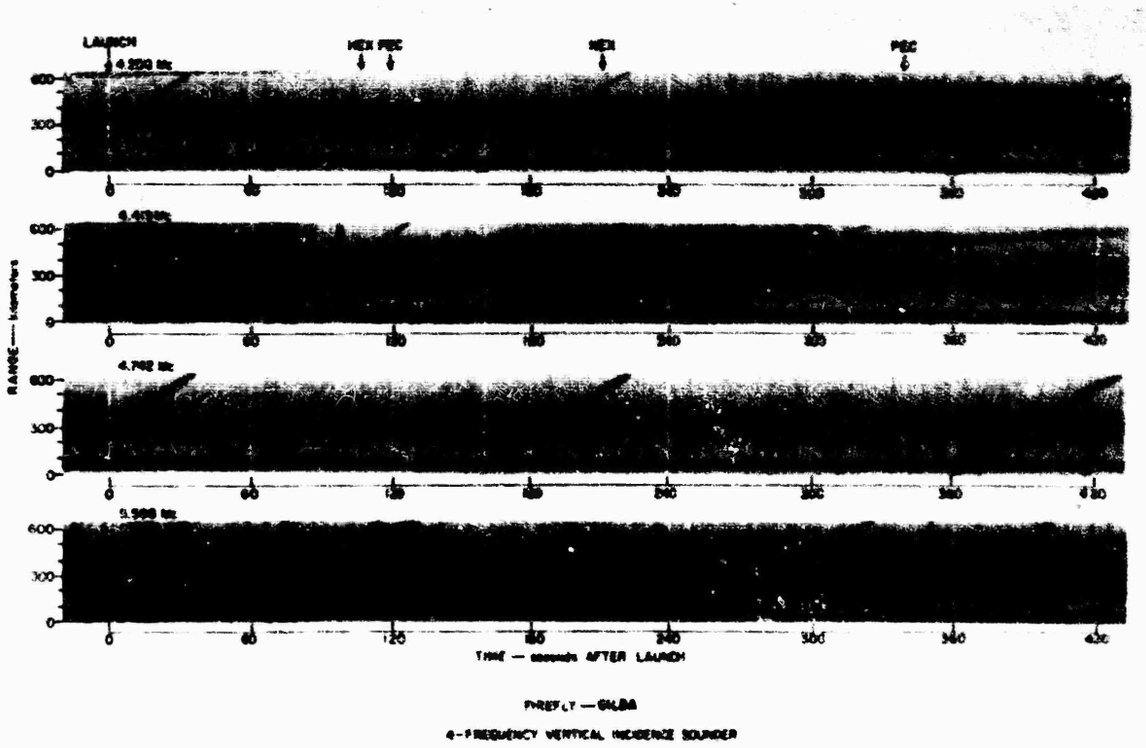

Figure 13. GILDA - Four Frequency Sounder

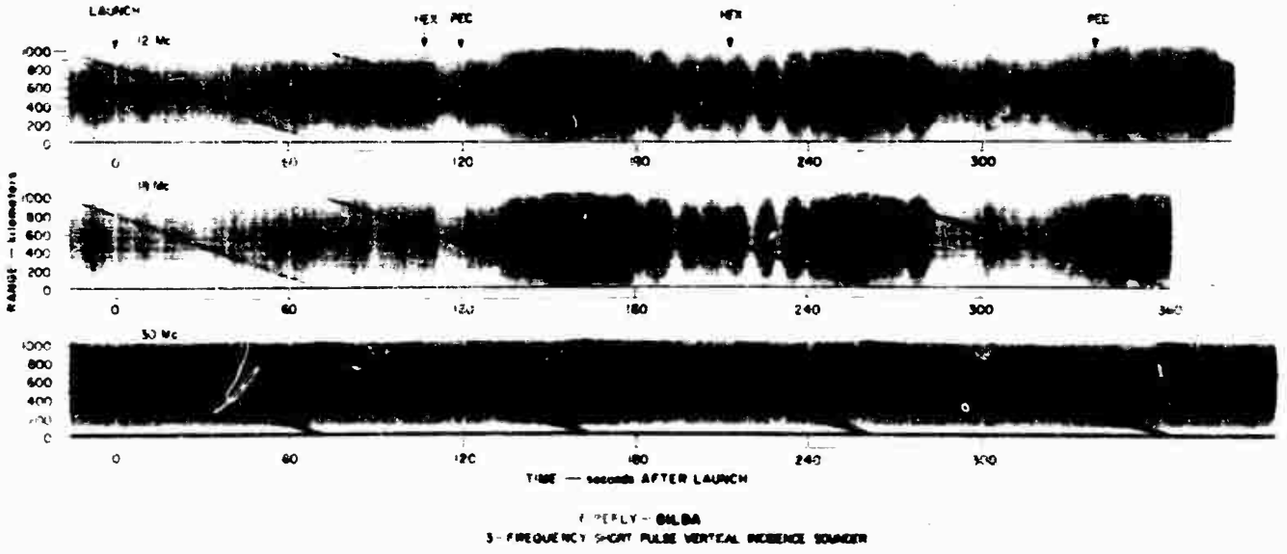

Figure 14. GILDA - Three Frequency Sounder

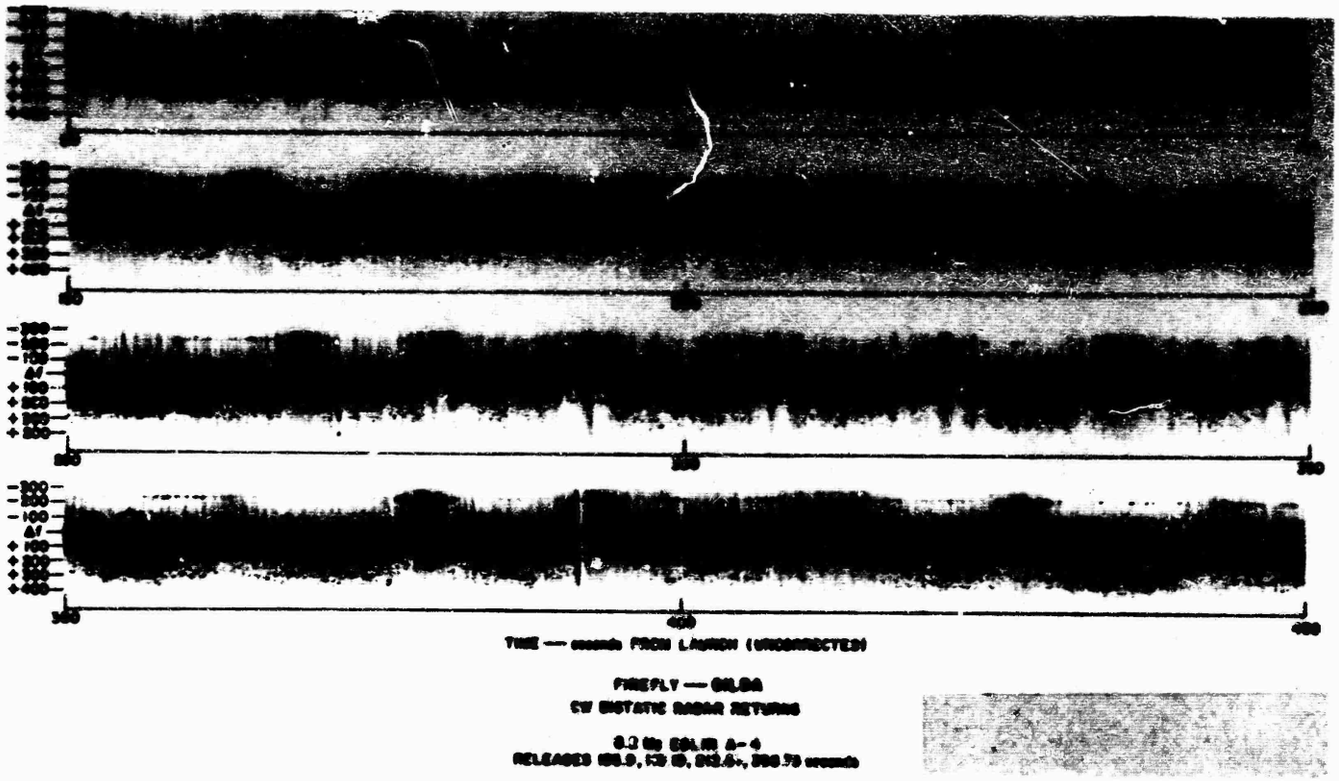

Figure 15. GILDA - CW Radar - 8.2 Mcps Eglin

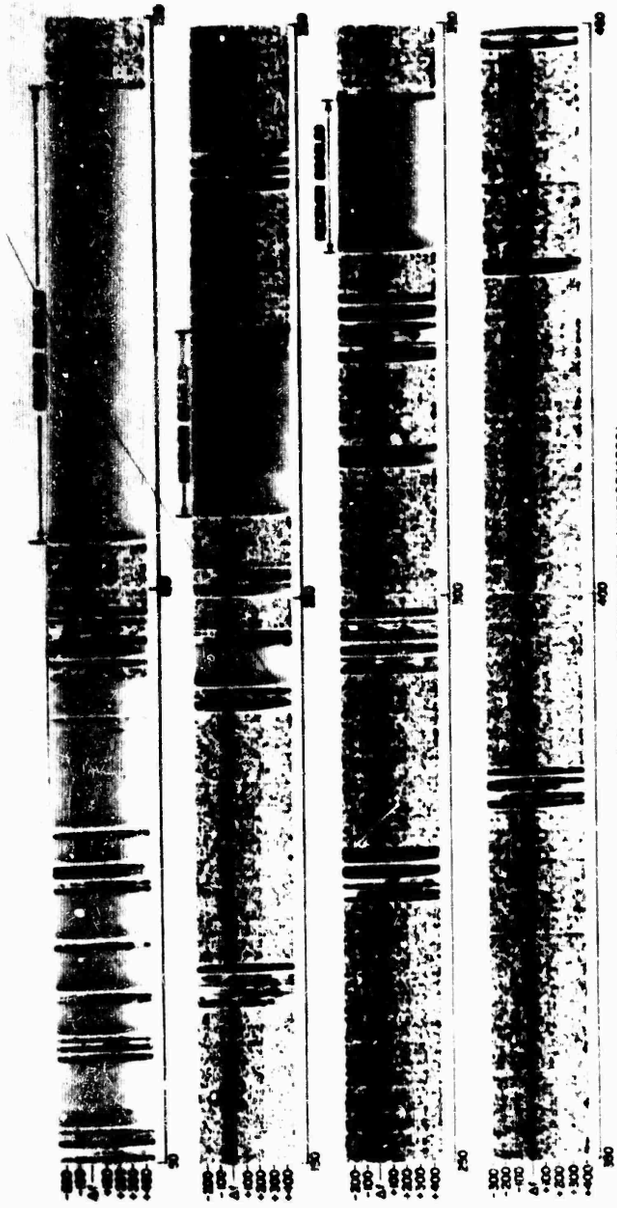

Figure 16. GILDA - CW Radar - 14.9 Mcps Eglin

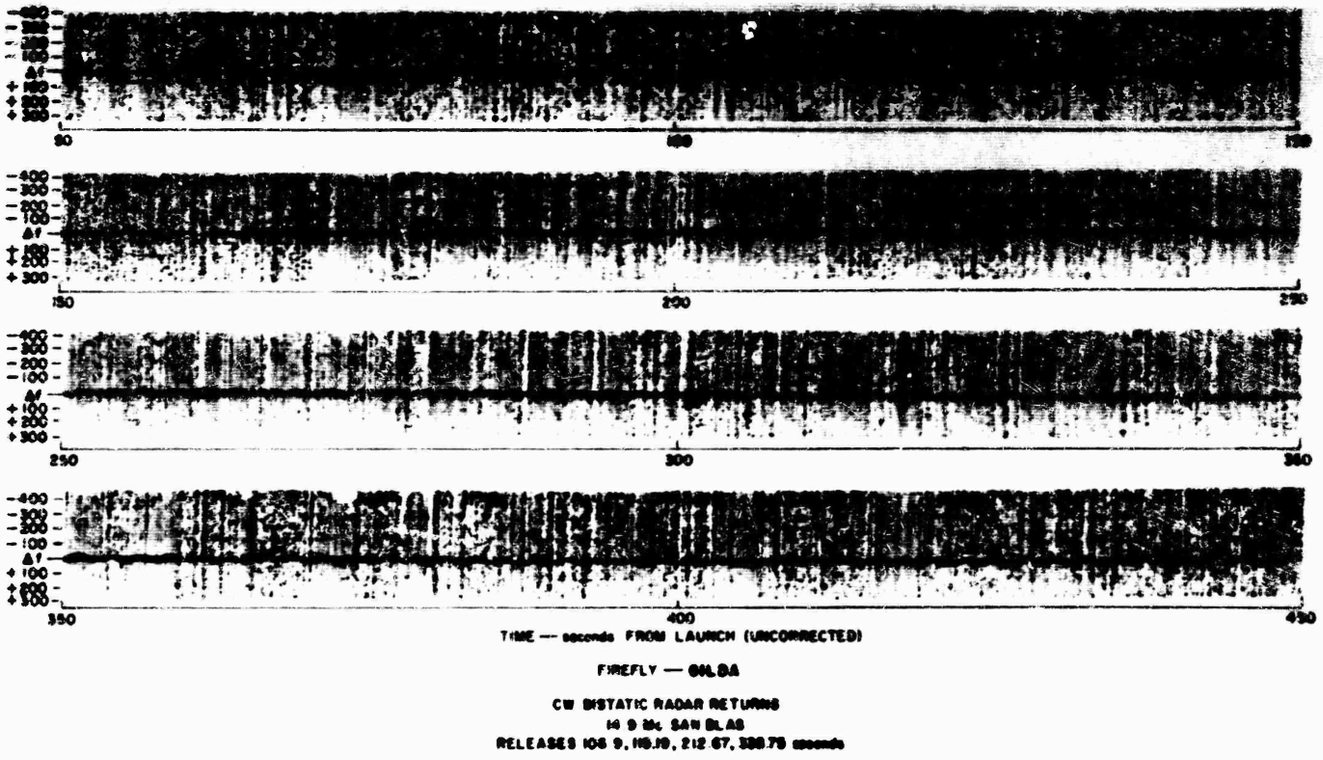

Figure 17. GILDA - CW Radar - 14.9 Mcps San Blas

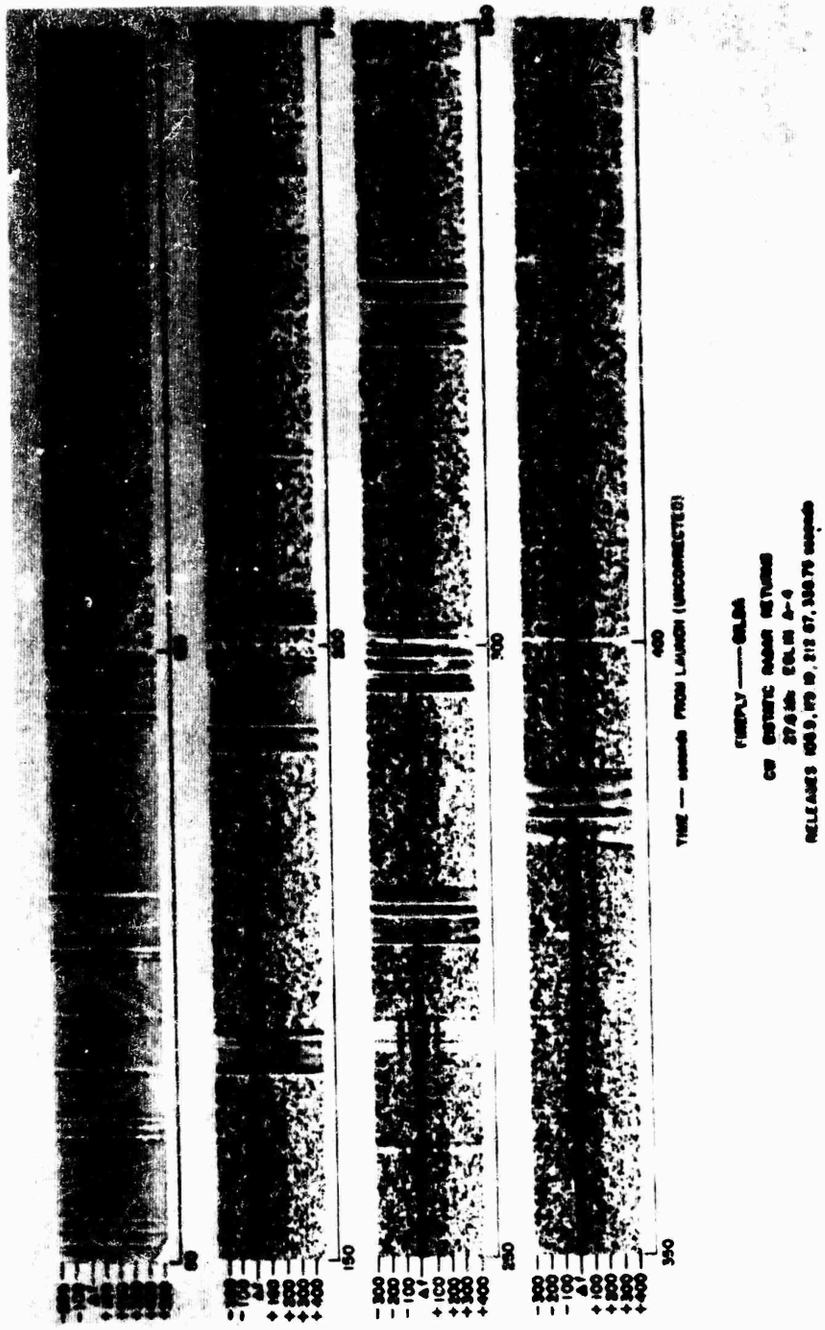

Figure 18. GILDA - CW Radar - 27.6 Mcps Eglin

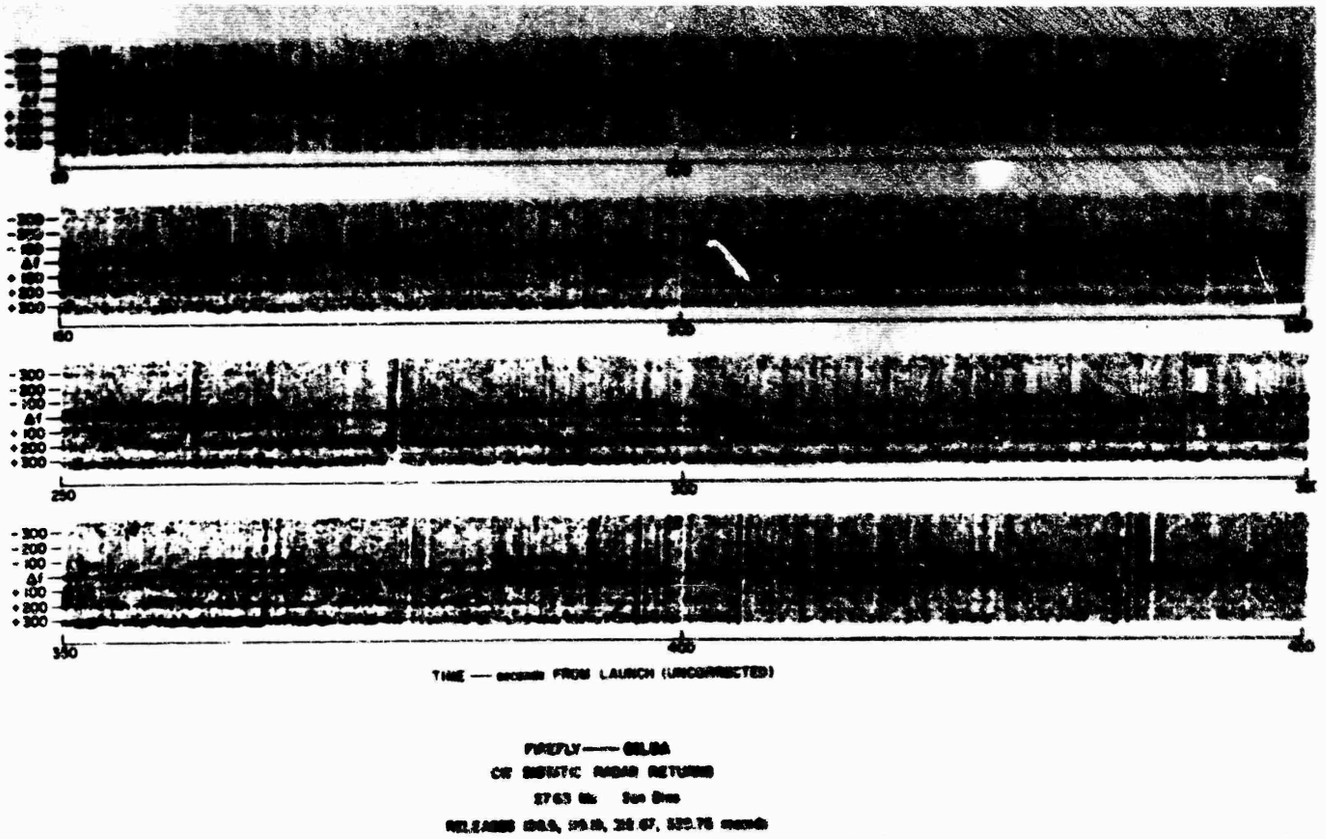

Figure 19. GILDA - CW Radar - 27.6 Mcps San Blas

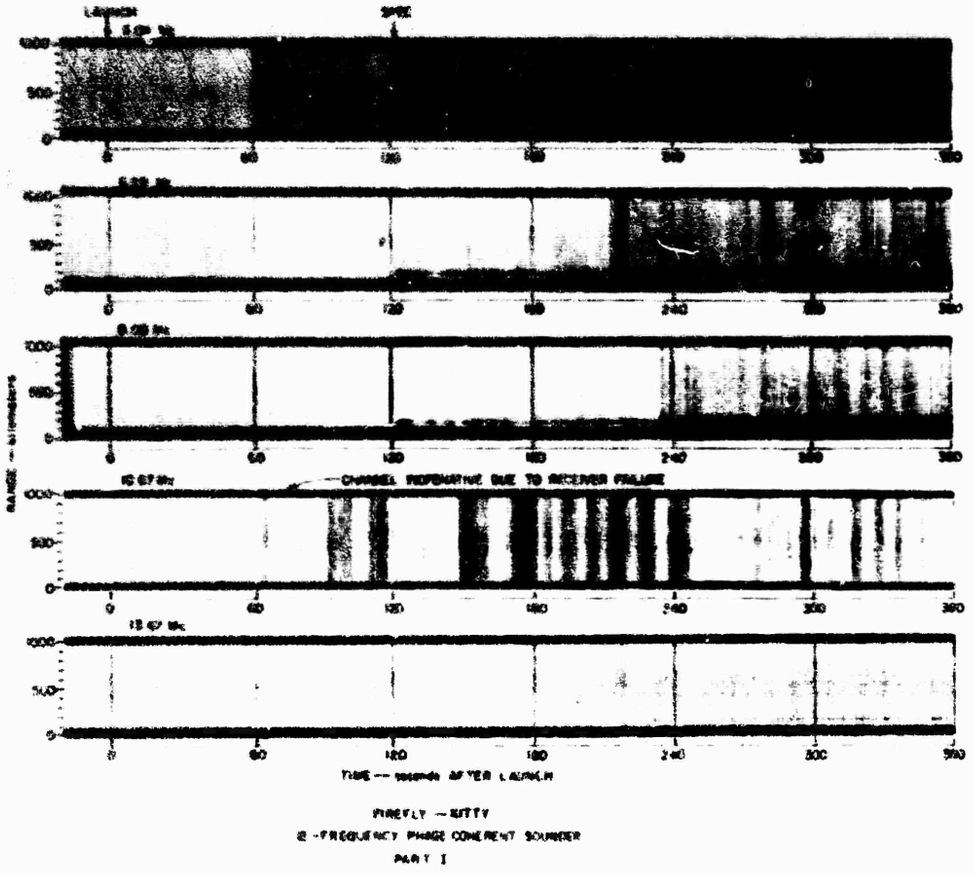

Figure 20. KITTY - Twelve Frequency Sounder

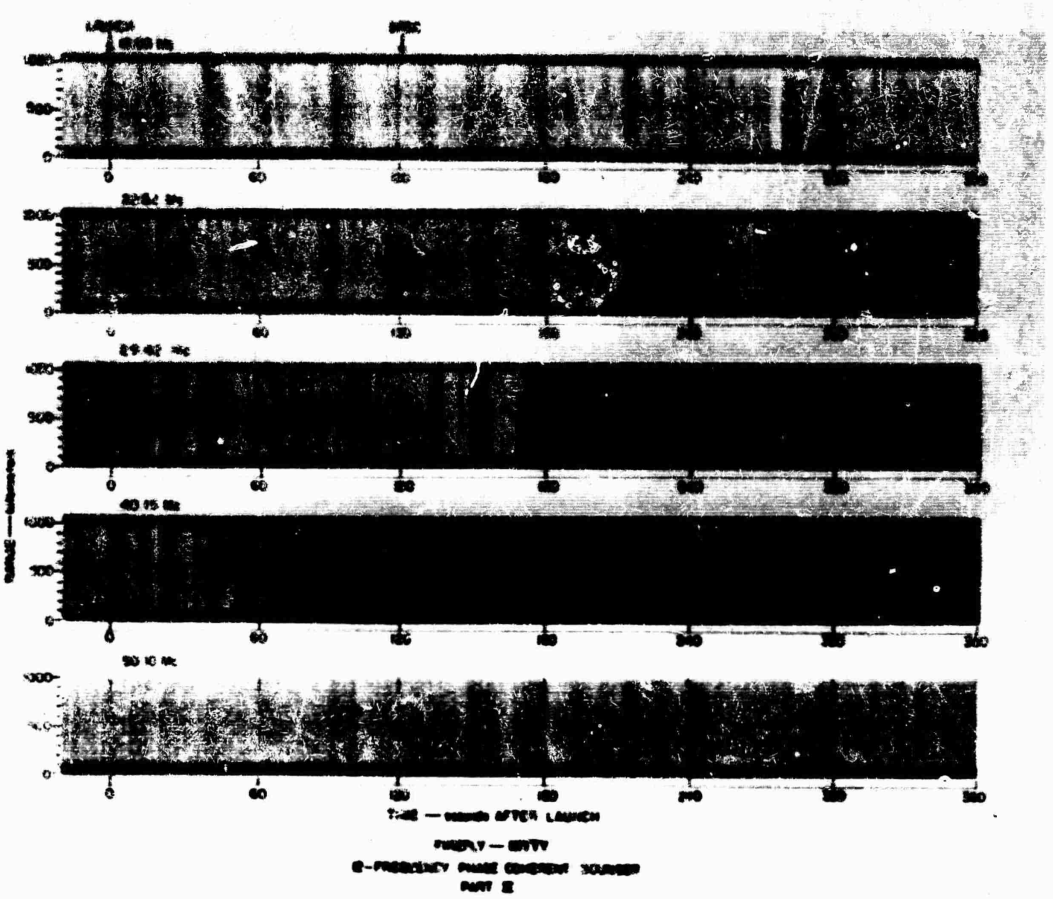

Figure 20. (Cont) KITTY - Twelve Frequency Sounder

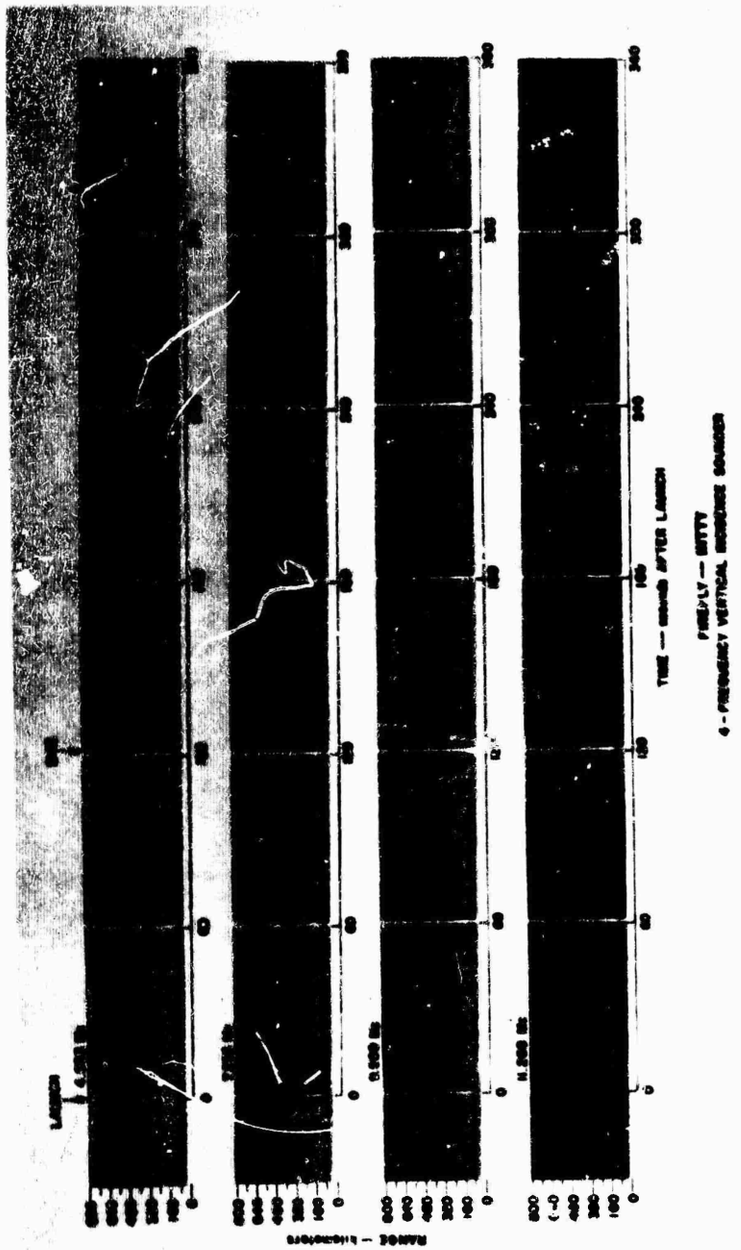

Figure 21. KITTY - Four Frequency Sounder

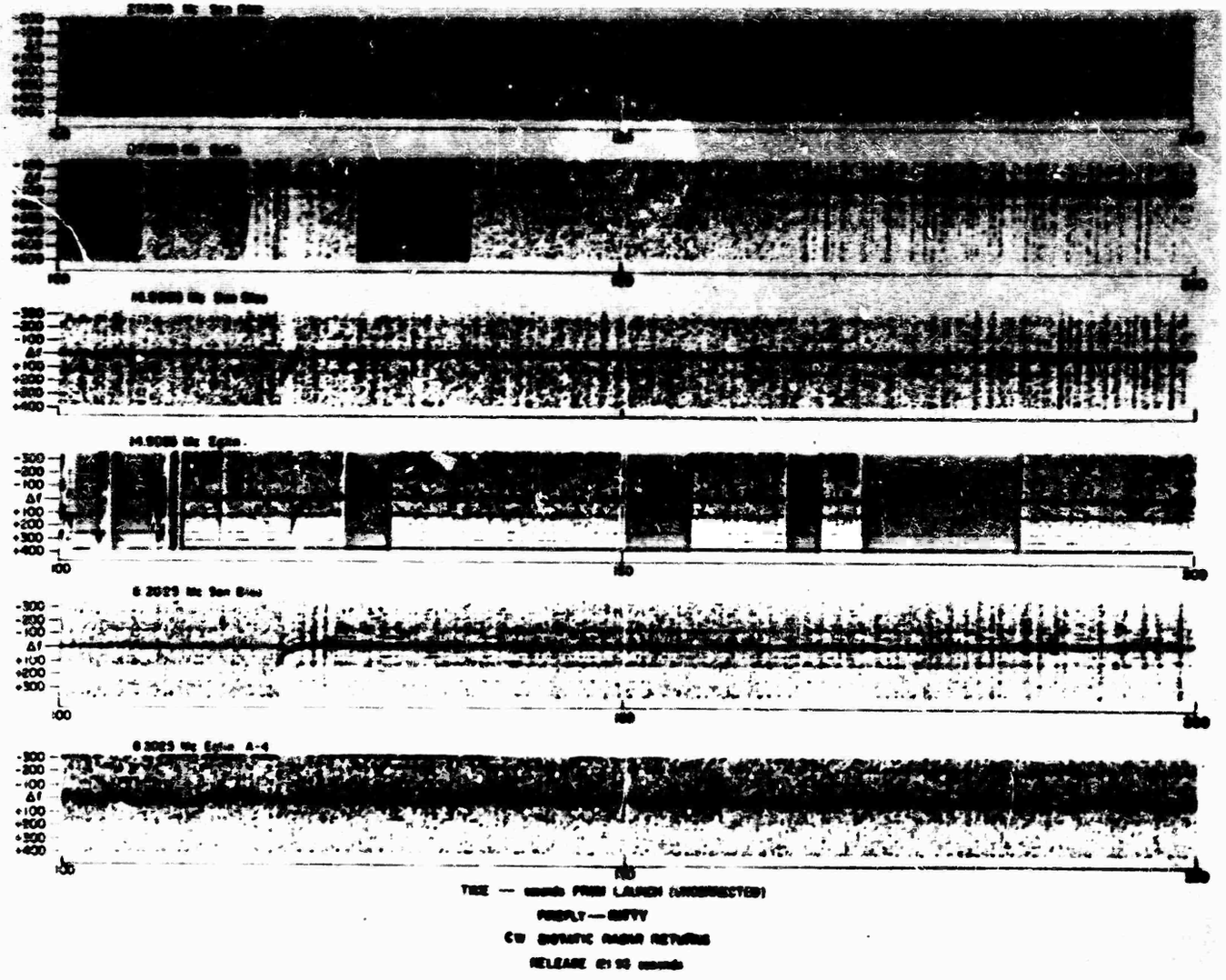

Figure 22. KITTY - CW Radar

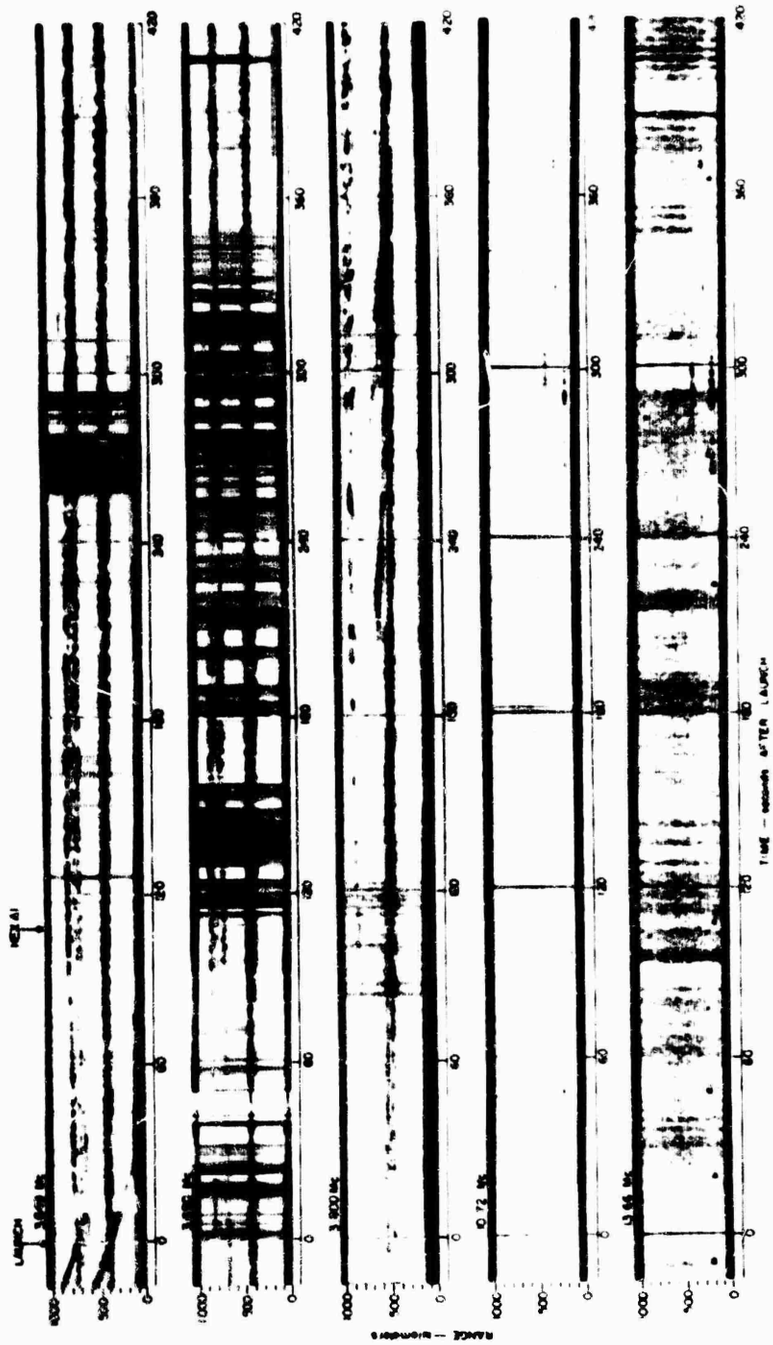

Figure 23. DANA - Twelve Frequency Sounder

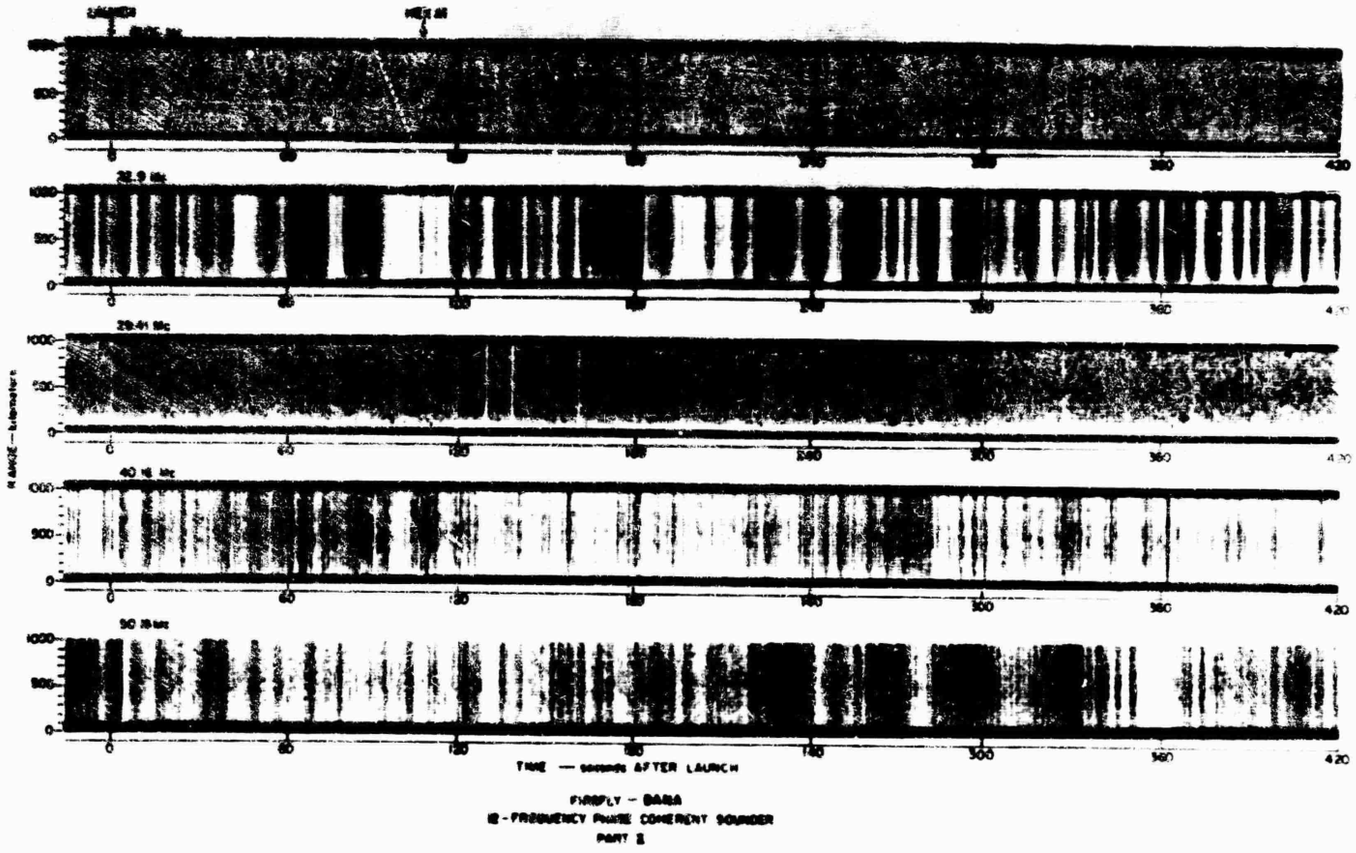

Figure 23. (Cont) DANA - Twelve Frequency Sounder

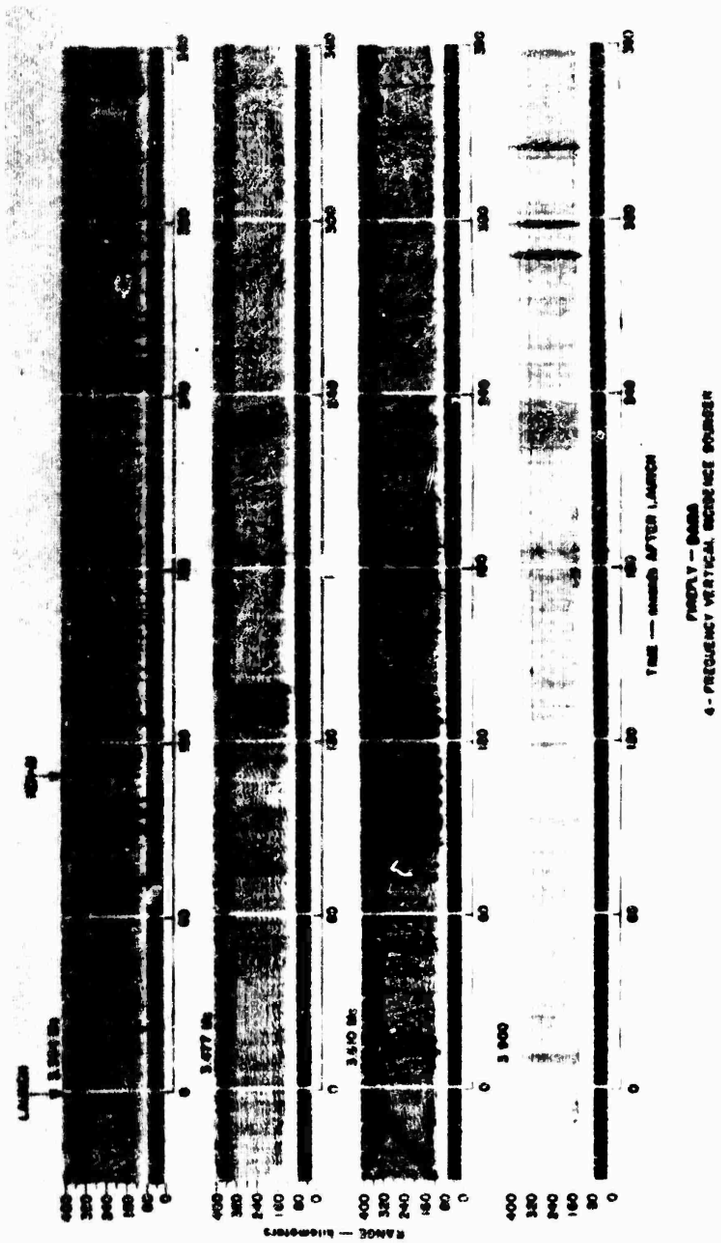

Figure 24. DANA - Four Frequency Sounder

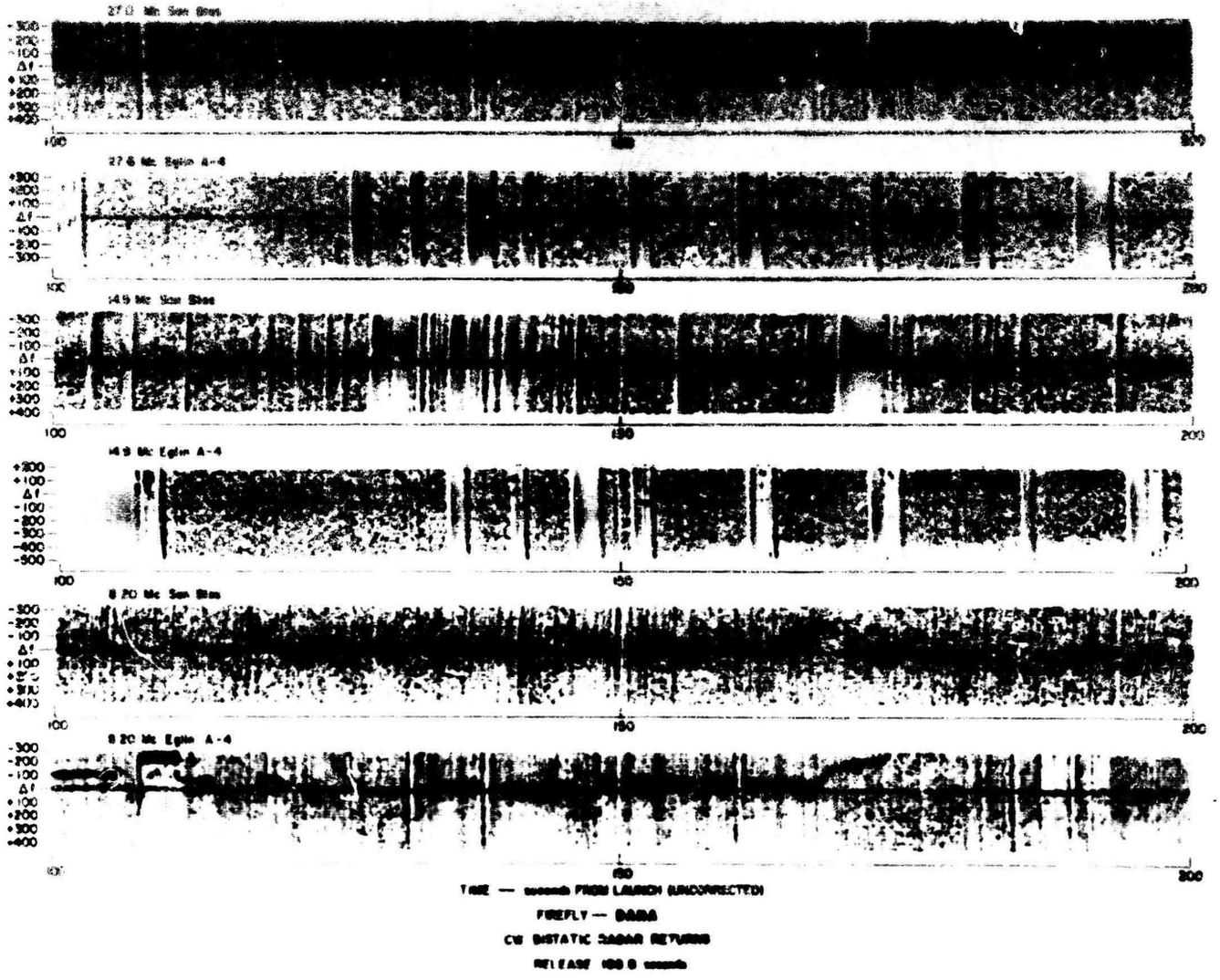

Figure 25. DANA - CW Radar

VII. Ionosonde Studies of Chemical Releases

J. W. Wright
Central Radio Propagation Laboratory
Boulder Laboratories
National Bureau of Standards
Boulder, Colorado

Abstract

A description is presented of ionosonde observations obtained during the release of chemicals and high explosive detonations in the E and F regions of the ionosphere during Project Firefly 1962. Several experiments were designed to reduce locally the ambient electron density. The effects are discussed in comparison with the calculated ambient electron distributions.

1. INTRODUCTION

Virtually all of the radio techniques exercised over many years for ionospheric explorations are sensitive to only a trace-element in the upper atmosphere, the electrons. Despite the significance attached to electrons because of their importance for radio communication, their concentration is to a great extent the incidental by-product of a complex of photochemical and chemical reactions; the complicated variability of the electron concentration, as observed by radio means, is largely a

It is reasonable that no effects are apparent much below the level of the F1 layer (145 km). In this region the rate of electron production becomes small. These processes limit the effectiveness of SF_6 at this level or below.

Acknowledgments

The efficiency and careful planning of the program of twenty-seven rocket launchings by AFCRL, under the leadership of Dr. N. W. Rosenberg, was essential to the success of the observations by the participating agencies. Many of the NBS staff contributed directly to the observations reported here, especially by G. H. Stonehocker, Mr. E. J. Violette, and Mr. J. J. Pitts.

The author expresses his appreciation to Mr. T. N. Gautier for many helpful discussions.

References

1. A. K. PAUL, and J. W. WRIGHT, Some results of a new method for obtaining ionospheric N(h) profiles with a bearing on the structure of the lower F region, J. Geophysics Res. In press, 1963.
2. A. K. PAUL. Bestimmung der wahren aus der scheinbaren Reflexionshöhe, Arch Elek. Ubertrag. 14: 468, 1960.
3. A. K. PAUL, Kritische Bemerkungen zur Berechnung der "wahren Höhen", Geophys. Pura e Appl. 47: 69, 1960.
4. E. J. VIOLETTE, An Improved Antenna System for Ionospheric Vertical Soundings, Private Communication.
5. D. GOLOMB, Private Communication.
6. J. W. WRIGHT. Ionosonde observations of artificially produced electron clouds, Firefly 1960, NBS Tech. Note 135, April 1962.
7. H. G. BOOKER. A local reduction of F-region ionization due to missile transit, J. Geophys. Res. 66: 1073, 1961.
8. BANNISTER and DAVIS, 1962.
9. GRANZOW, 1962.
10. C. SHERMAN. Qualitative considerations of diffusion in the earths gravitational field, Physics of Fluids, 5: 863, 1962.
11. I. HARRIS, and W. PRIESTER. Theoretical models for the solar-cycle variations of the upper atmosphere, NASA Institute for Space Studies, 24 April 1962.

12. J. W. WRIGHT. Diurnal and seasonal changes in structure of the mid-latitude quiet ionosphere, NBS J. Res. 66D: 297, 1962.

13. J. W. WRIGHT. A model of the ionosphere above hmaxF2, J. Geophys. Res. 65: 185, 1960.

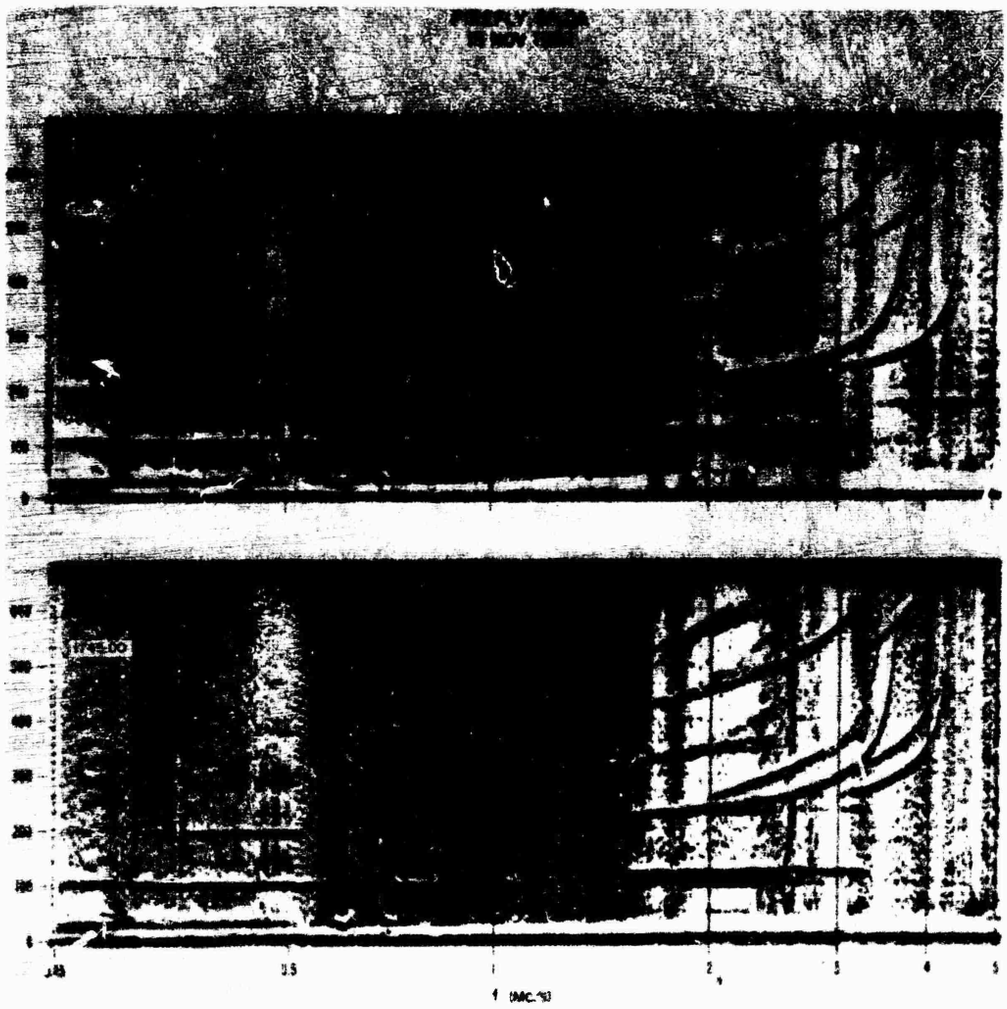

Figure 9. Ionograms During Firefly GILDA Just After Burst 2 (1732:00) and Almost 10 Minutes Following Burst 4 (1745).

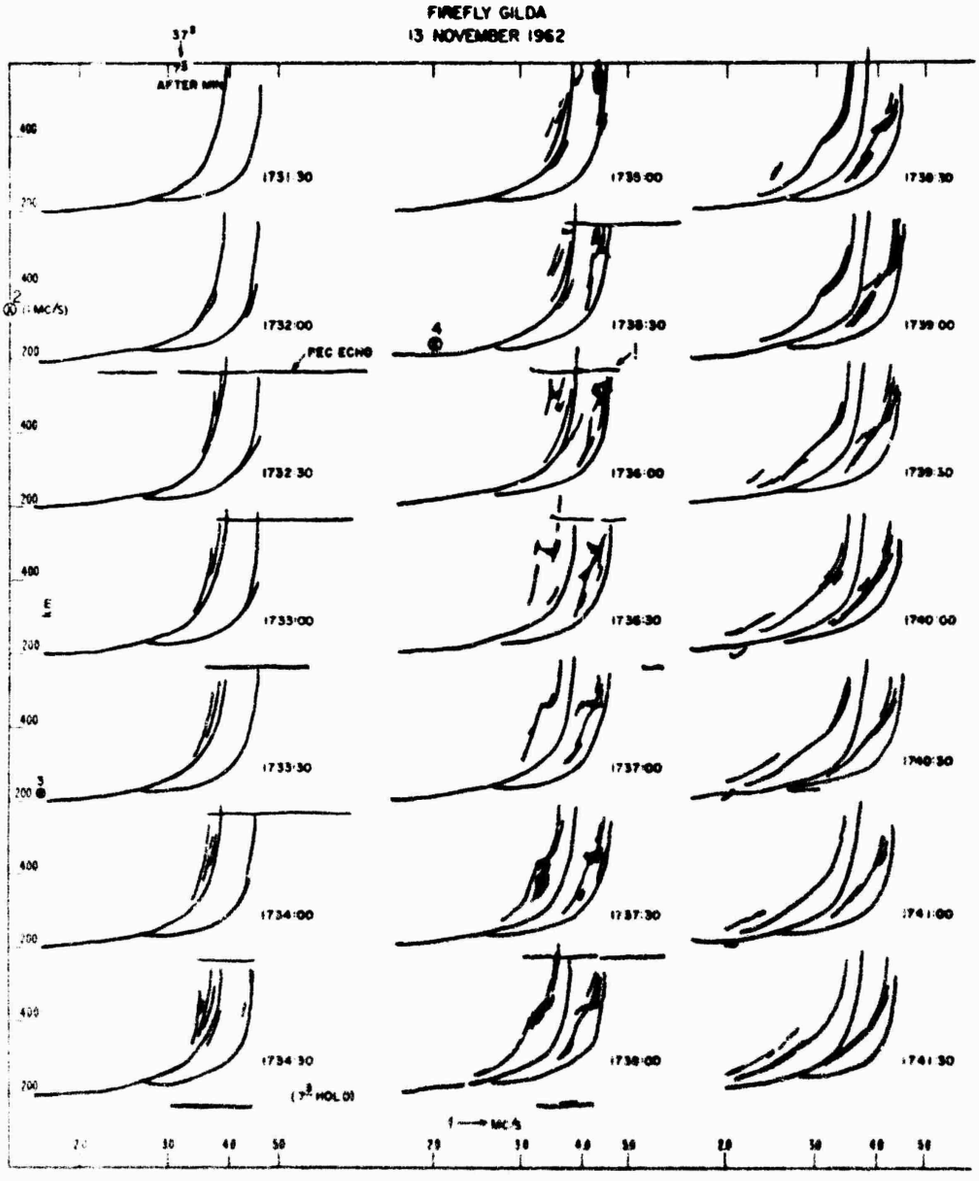

Figure 10. Tracings of Ionogram Sequence, Firefly GILDA, Each 30 Seconds, From 1731:30 Through 1752:00.

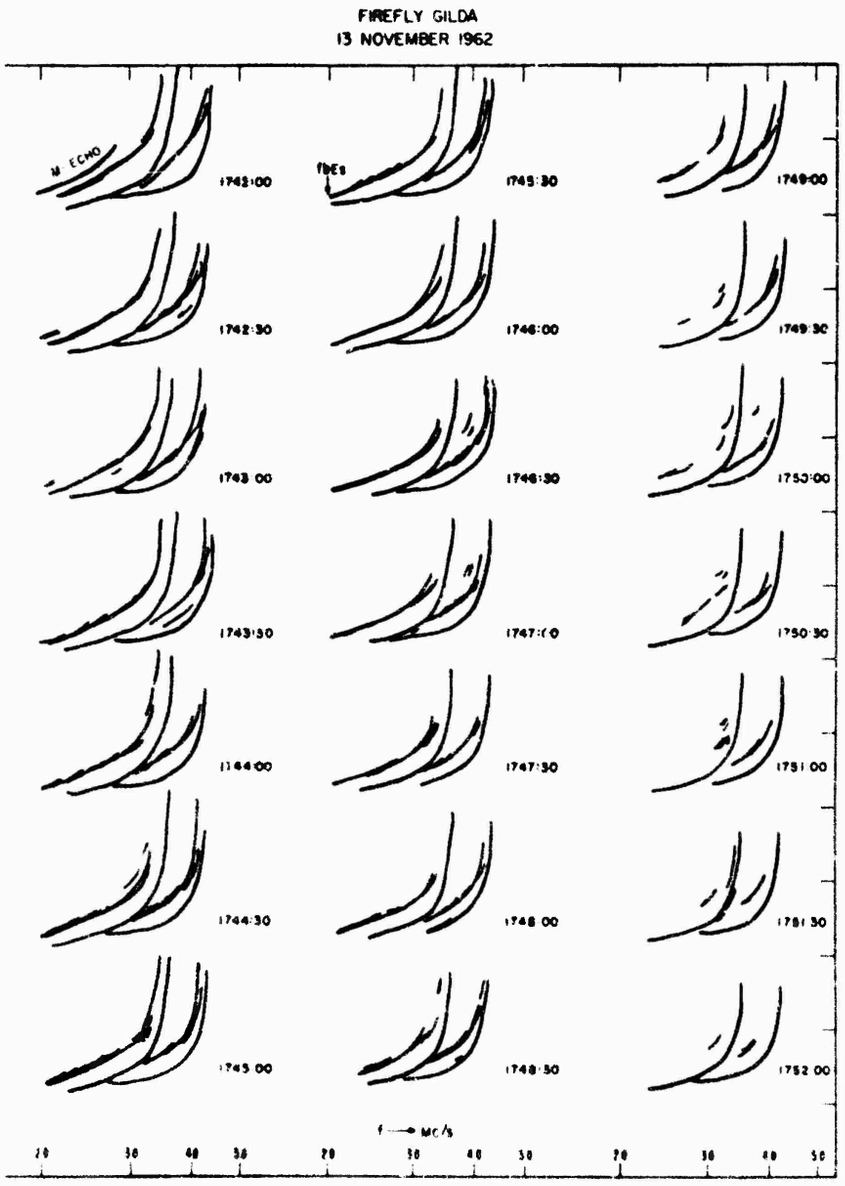

Figure 10.(Cont.) Tracings of Ionogram Sequence, Firefly GILDA, Each 30 Seconds, From 1731:30 Through 1752:00.

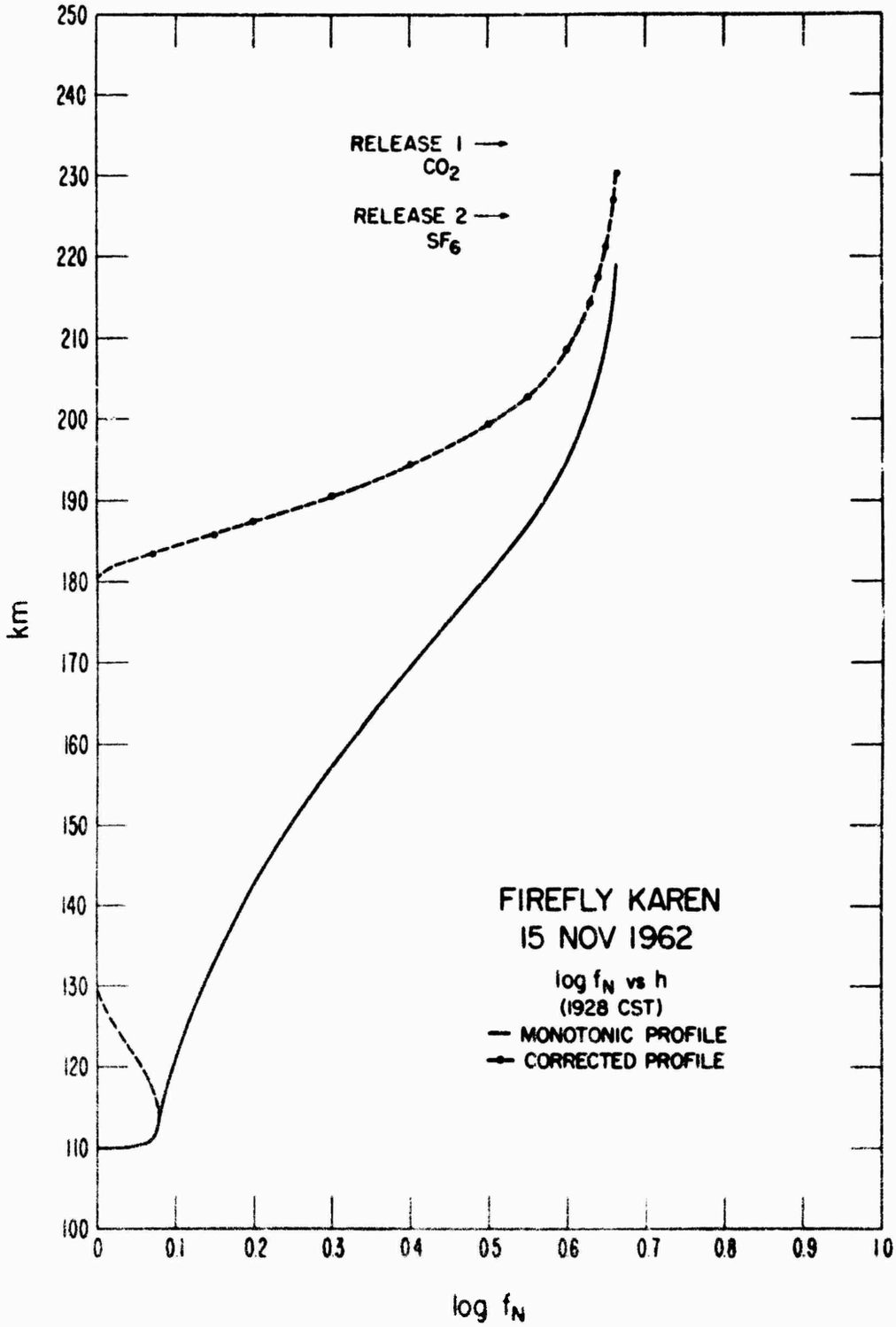

Figure 11. Electron Distribution During Firefly KAREN, 1928 CST 15 November 1962. Dashed Curve Represents a More Probable Profile, Taking Account of a Valley Above the E Layer.

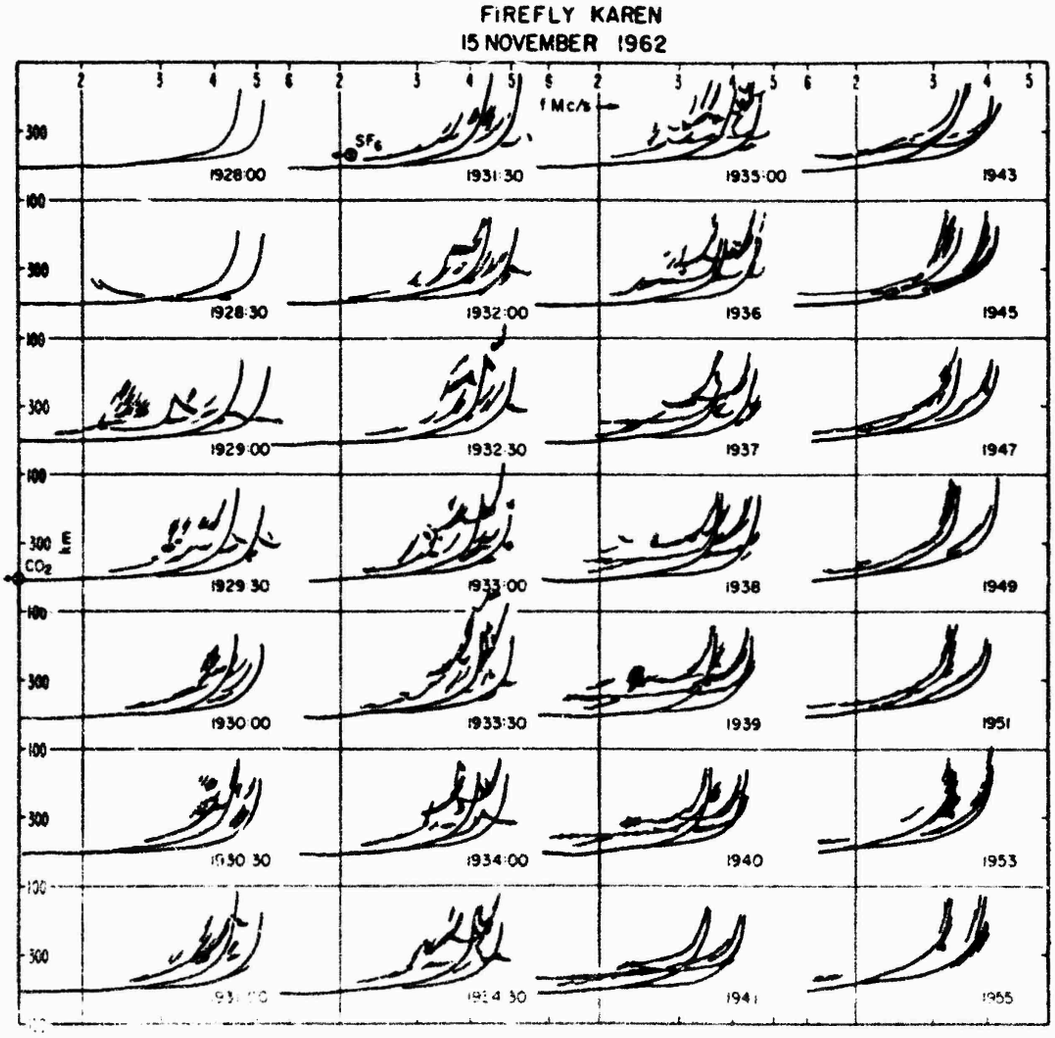

Figure 12. Tracings of Ionogram Sequence, Firefly KAREN, at Various Intervals as Shown Between 1928 - 1955 CST.

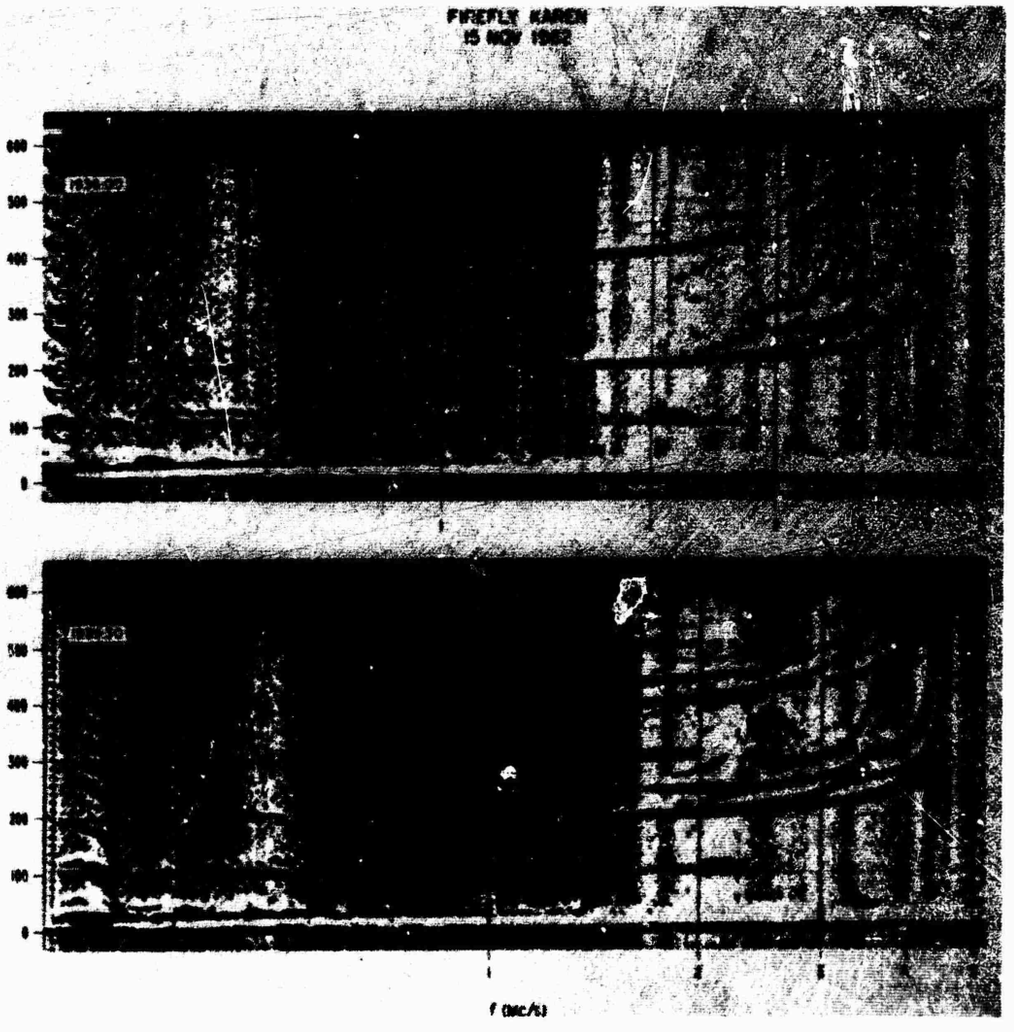

Figure 13. Ionograms During Firefly KAREN at Two Times Following Release of SF_6 Near the F2 Peak.

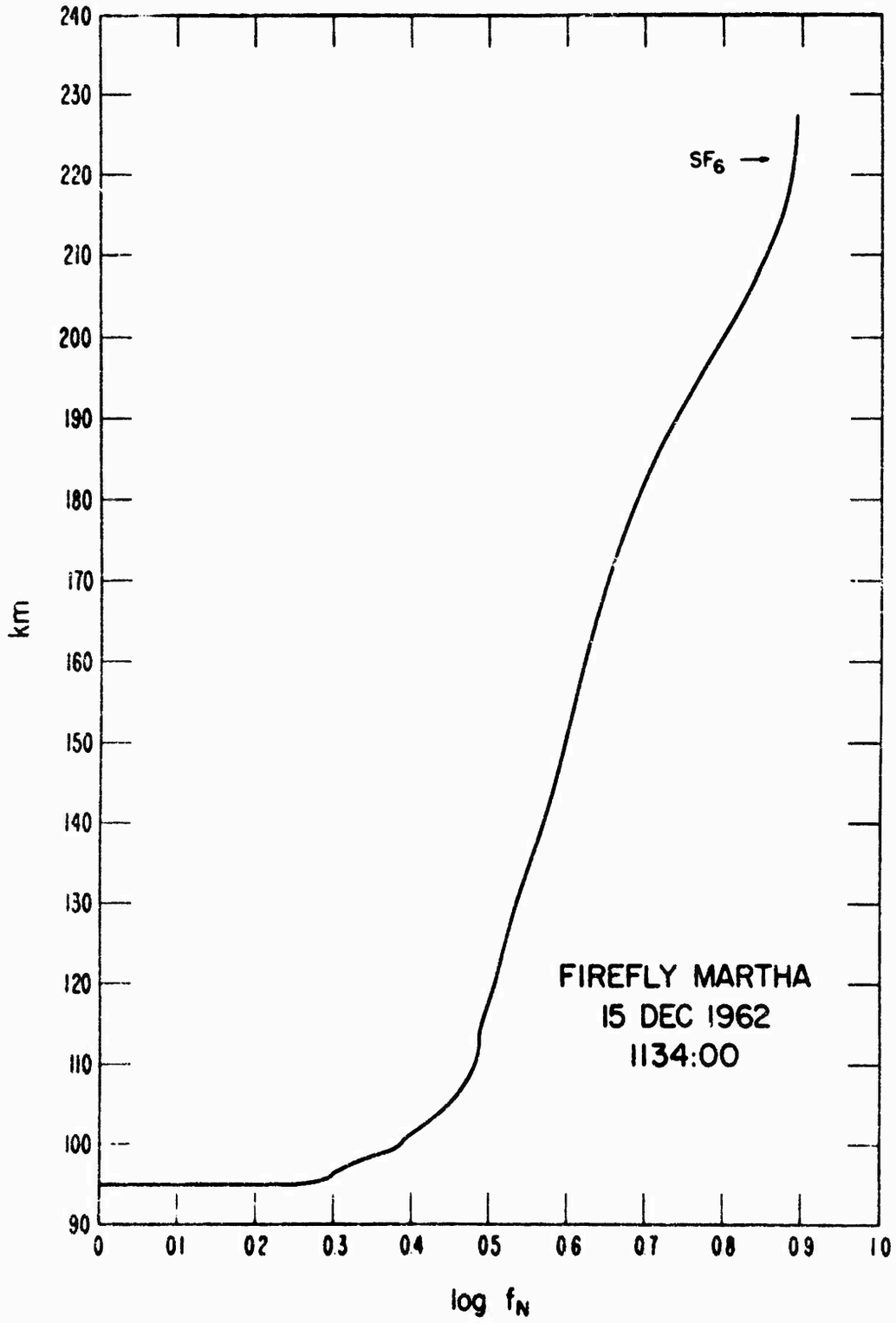

Figure 14. Electron Distribution During Firefly MARTHA, 1134 CST 15 December 1962. SF_6 Was Released at 222 km., Somewhat Below the F2 Peak.

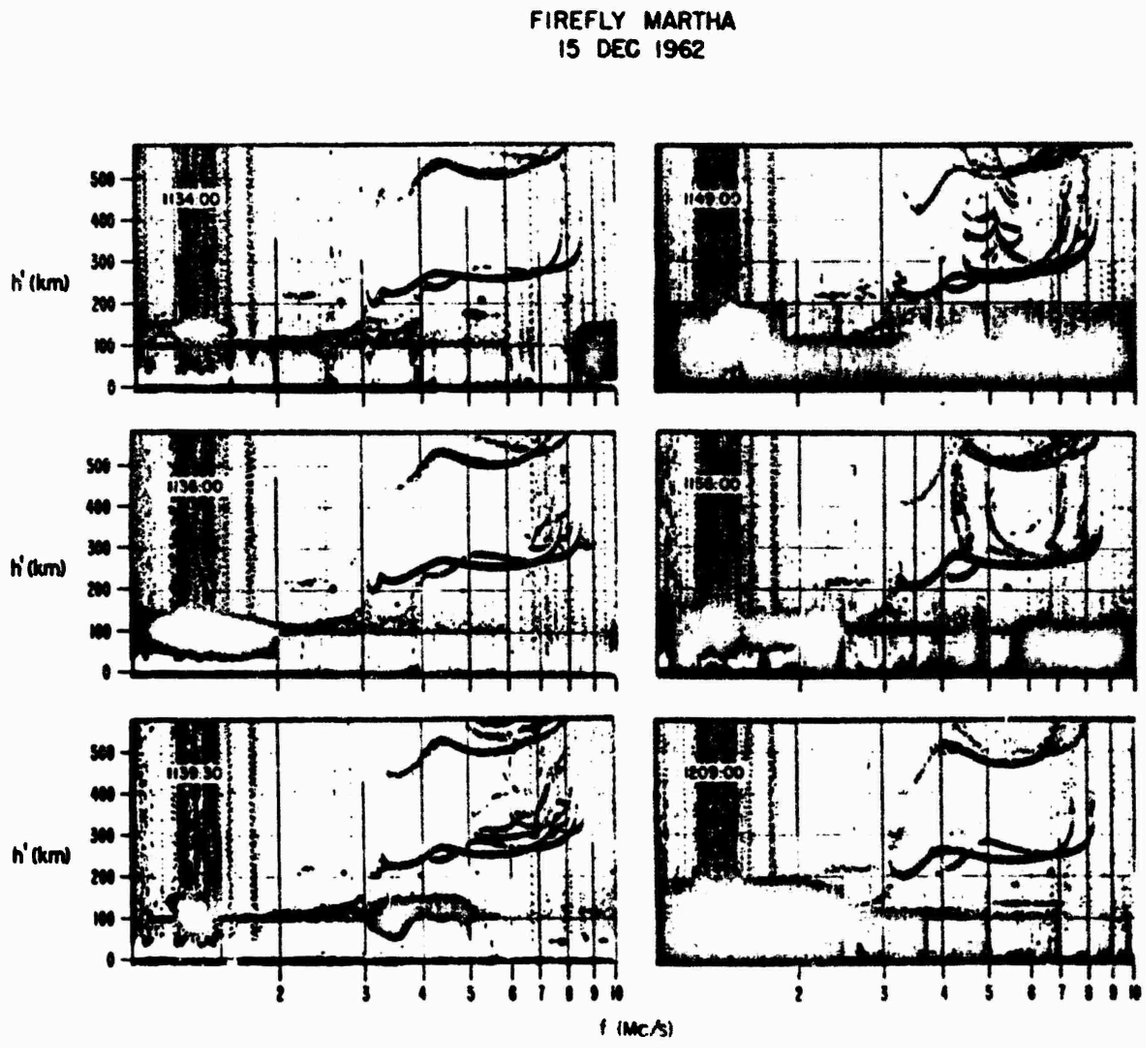

Figure 15. Ionograms During Firefly MARTHA at Six Typical Stages in the Development of the Disturbance. 1134: Slightly Before Release Near the F2 Peak. 1136: One and One-Half Minutes After Release; the Echo Exceeding fxF2 is Similar to an Oblique Sounding. 1139:30 Through 1156: Stages During the Downward Progress of the Disturbance.

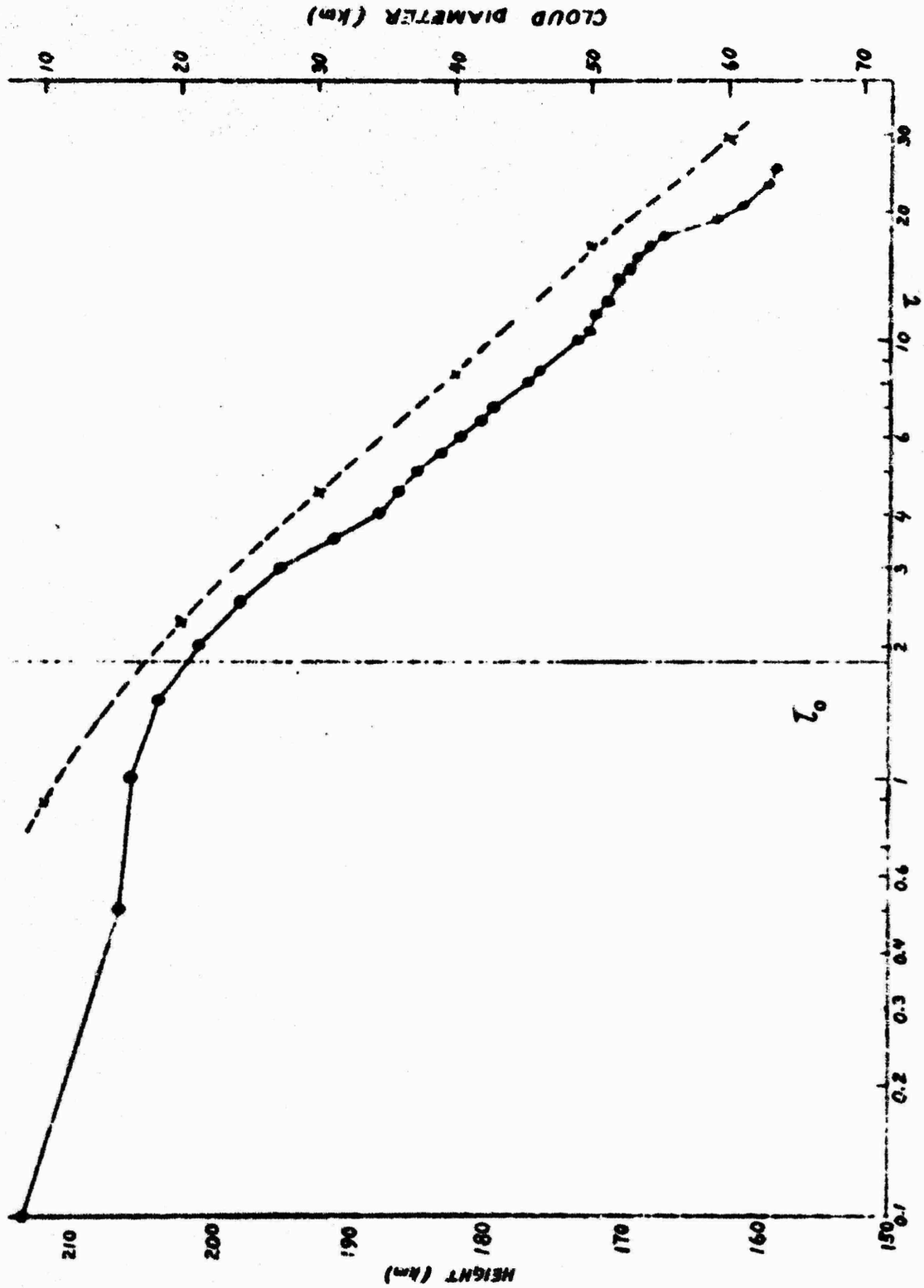

Figure 16. Height of the Lowest Electron Density Affected by SF_6 Vs-Time Firefly MARTHA, Together With Calculated Values. Right Hand Scale: Inferred Cloud Diameter.

VIII. Spaced Receiver Drift Results

Garth H. Stonehocker
Central Radio Propagation Laboratory
National Bureau of Standards
Boulder, Colorado

E. Harnishmacher
Ionospharen Institut
Breisach, Germany

Previous Firefly programs demonstrated that in addition to the RF-measurement objectives of electron cloud experiments, the long life and discreet size of such clouds provided convenient 'tracers' of the mass motion at E region altitudes. Studies of the motion of such clouds using spaced-ionosondes disclosed agreement with the optically-observed motions during the early visible phase of the cloud lifetime, and disclosed meaningful and consistent movements for periods of up to several hours later. Later work done with these observations during Firefly 1959, 1960, showed a significant height variation of drift speed, and agreement of the drift vector with the expected by ionospheric dynamo theory.

A number of questions were stimulated by this work, mainly based upon prior experience with the 'spaced-receiver' method which has long been a standard ground-based radio technique for making ionospheric drift measurements. In particular, it was of interest to know if the drift measured by this technique pertained

to 'wave motion' in the medium or to mass transport. Also, it was desirable to know if echoes from a single cloud would disclose a meaningful drift by the radio technique. Finally, it was recognized to be of interest to examine the relationship of ambient E region or Es drift, to the cloud motion measured optically, by spaced ionosondes, or by the spaced receiver technique.

Accordingly, arrangements were made via NBS and AFCRL, to enlist the participation of the Ionosphere Institute, where there has been broad experience in the spaced-receiver technique. Instrumentation was set up and operated at Eglin during Firefly 1962 by Mr. Harnischmacher of Breisach, and NBS personnel.

The observations are of a nature permitting approximate values for drift speed and direction to be obtained essentially by inspection of the recordings in cases where the drift itself is reasonably steady. These results are arranged in alphabetical order in Table 1. Each figure shows estimated values of the cloud drift vector direction and drift speed.

TABLE 1. Drift characteristics

Firefly 1962	Date	Time	Region	Direction Deg. E of N	Velocity m/s	Character
Alice	10-16	0515		No	Data	
Bonnie	10-15	0515		No	Data	
Cindy	10-17	0515	E	285	54	
Dagmar	10-16	1840	E	165	32	
Dana	12-10	1900	E	165	40	
Dinah	12-3	2245		No	Data	
Enid	10-25	0030		Not Available Yet		
Esther	12-3	2145		No	Data	
Ethel	10-23	1310	E	275	95	
Eva	12-6	0421		No	Data	
Fanny	11-10	1830	F	315	11	
Gilda	11-12	1730	E	45	27	Complex
			F	165-225	38	
Ivy	12-3	1801	E	195	42	
Laura	12-7	1900	E	200	30	
Louise	10-22	0520	E	105	95	
Mabel	11-27	1800	E	165	95	
Paula	10-25	0520	E	135	65	
Queenie	10-19	0517	E	345	54	
Ruby	11-1	0525	E	295	72	
Sharon	12-3	1720	E	195	65	

IX. Ground Based Acoustic Detection of High Altitude Explosions*

H. F. Allen
University of Michigan
Ann Arbor, Michigan

Abstract

Eight successful firings of Nike-Cajun rockets carrying high explosive charges were monitored from two sites, using three types of low frequency sound transducers. These included two capacitor microphones, two hot-wire microphones and a microbarograph.

1. INTRODUCTION

Eight successful firings of Nike-Cajun rockets carrying high explosive charges were monitored from two sites, using three types of low frequency sound transducers. These included two capacitor microphones, two hot-wire microphones and a microbaragraph. One microphone site was in dense vegetation, the other was in a open area about 100 feet across.

Twenty-two 8 lb and two 37 lb grenades were detonated at altitudes between 89.1 km and 117.2 km. An 8 lb grenade at 117.2 km did not produce a recognizable

*Excerpts from Technical Report, Contract No. NASr-54(02), December 1962.

sound return. All others were detected on the paper records, although some of the higher explosions were very faint, and were not distinguishable on the records of the hot-wire microphones. The highest recorded explosion was an eight lb grenade at 112.0 km.

During the last two firings, a longer pipe was used on one of the hot-wire microphones, and a new capacitor microphone with an acoustical filter replaced one of the original capacitor microphones. Both of these reduced the frequency of background noise, and made it slightly easier to detect the higher sound arrivals.

The eight pound grenades in the last two firings contained three variations of the explosive mix. Two grenades in each firing contained the standard mix, one had higher aluminum content and one had lower aluminum content. The low aluminum grenade failed to explode during the last firing, but during the preceding firing it detonated at 107.6 km and gave a stronger sound return than the high aluminum grenade which exploded 5km lower, and nearly as strong a return as the standard grenade which exploded at 96.7 km. The last standard grenade, at 112.0 km, was barely visible on the records of the capacitor microphones only. This was the highest explosion for which a sound return was detected.

2. EXPERIMENTAL

All microphone pickups were placed in shallow pits about 8 feet in diameter and 2 feet deep, with slanting sides. The microphones were placed in open-top containers buried in the bottoms of the pits. These were plastic waste baskets at the upper microphone site which was dry and sandy; but at the lower microphone site, where the bottom of the pit was only slightly above the water table, 5 gallon paint containers were used and staked down so they would not float up out of position.

At first, it was planned to place the hot-wire and capacitor microphones in the pits, and to use an acoustical filter with the microbarograph. This was to consist of a 100 foot length of pipe, decreasing in diameter from 2-1/2 inches at the center to 3/8 inch at the ends, with holes drilled at 12 inch intervals, as recommended by the Signal Corps manual. However, it was the recommendation of Schellenger Laboratory on the basis of experience at White Sands Missile Range, that the microbarograph also be placed in a pit, and it was decided to place it in the same pit with the capacitor microphone at the upper site. Accordingly, the east pit at the upper site was modified, and half of a 55 gallon oil drum was buried beside the plastic waste basket, to contain the microbarograph and associate equipment.

A six-channel Sanborn recorder, two four-channel Precision Instrument tape recorders, the hot-wire microphone terminator panel, and the power supply for the microbarograph were located in the van on top of the dune. The countdown was

received over the loudspeaker on top of the Sanborn recorder. The sequence of recording channels was as follows:

Item	Sanborn Recorder	Tape Rec. No. 1	Tape Rec. No. 2
Capacitor Mike, Upper site	1	2	-
Capacitor Mike, Lower site	2	3	-
Hot Wire Mike, Upper site	3	4	-
Hot Wire Mike, Lower site	4	-	2
Microbarograph	5	-	3
Timing	6	1	1
Voice	-	1	1
Events	6	-	-

Operating personnel usually reported to the van at T-3 hours for each firing. The microphones were placed in the pits and connected up, and all equipment was turned on at approximately T-2-1/2 hours. After half an hour of warming up, the system was checked by slamming an automibile door. This proved entirely adequate for checking the most distant microphone, and the shotgun which had been borrowed for the operation, was never used.

Background level was checked occasionally by operating the Sanborn recorder for short periods of time. Background noise was generally better than at Wallops Island, though not so good as at Fort Churchill, especially when wind velocities are low at Churchill. Location of the microphones about a third of a mile back of the launcher gives a higher sound arrival angle than at Wallops, but lower than at Churchill, where the array is located several miles down range. Aircraft and trucks gave little trouble during firings. Shipping on the intercoastal waterway occasionally caused concern during countdowns, but luckily no sound arrivals were obscured on this account. An offbeat note was provided by a skunk who resided in the area, and occasionally wandered across one of the wind screens. Background level was generally very low with southerly winds, and much higher with northerly winds, which produced waves on the adjacent shore of Santa Rosa Sound, and eddied over the north side of the dune. Audible surf noise was low during all firings, although surf may have contributed to the general low frequency background level.

The microbarograph was balanced at intervals, but seldom remained in balance very long. The balancing operation had to be carried out at the pit, but frequently a complete null could not be obtained, and the unbalance was compensated by unbalancing the Sanborn recorder. This involved shouting back and forth between the van and the microphone site, and when attempted near the firing time, resulted in much confusion. Light bulbs were installed in the pit to act as heat sources and reduce the humidity during night firings, but did not seem to impove the situation

noticeably. Consequently, the microbarograph was usually operated at fairly high attenuation, and seldom gave results of much value.

There was some difficulty with the tape recorders during certain firings, especially with the drive mechanism and the record and playback circuit cards. On one firing the voice channel (and therefore the timing) was inactive on one of the tape recorders, and during another firing, the first tape recorder was completely inactive on all channels, while the two capacitor microphones and the hot-wire microphone at the upper site were transferred to the second recorder, this being noted on the voice channel. During one of the firings, when much attention was being paid to the microbarograph at the last monent, the secondary countdown at T-1 minute was suddenly mistaken for the final countdown, and during the resulting confusion, the tape recorders were turned 'off' instead of 'on' just before actual T time. This mistake was not discovered until after the rocket had been fired, so that for this particular firing the tape recordings start about half a minute after the take-off.

Events, such as lift-off, Cajun ignition, and grenade explosions, were recorded by an outside observer, who pressed a push button, momentarily interrupting the timing trace on the Sanborn recorder, as soon as possible after observing the event. It is believed that the error inherent in this method is of the order of 0.1 second. On one occasion, the outside observer nearly broke his neck getting out of the van when he mistook a secondary countdown, one or two minutes before the actual firing, for the final countdown. The five-second secondary countdowns employed at this range before each 'mark' are frequently confusing, and appear to this observer to be entirely superfluous, if not downright dangerous.

The Sanborn recorder was usually operated at 2.5 mm/sec until T-20 seconds, at which time the speed was jumped to 25 mm/sec, and the tape recorders were turned on. Attenuation on the Sanborn recorder was kept at 1000 until the take-off noise has decreased to safe level. The attenuation on each channel was then reduced to the value indicated by the pre-firing background level. Some time after T + 100 seconds, the Sanborn recorder was cut back to 2.5 mm/sec to conserve paper, and was again operated at 25 mm/sec after T + 350 seconds. Immediately after each firing, the record was studied, preliminary explosion and sound arrival times were noted, and estimates of the heights of explosions were made on the basis of an average sound speed. These estimates were usually within one or two kilometers of actual heights, when these figures became available some time later.

Normally, when the station was left unattended, the microphone pickups were removed from the pits and returned to the van. Occasionally this procedure was not followed if the equipment were operated late at night and the schedule called for an early morning firing. On such occasions all microphones were left with power on, while personnel snatched a bit of badly needed sleep. After operating

continuously for several hours, the capacitor and hot-wire microphones seemed to be a bit more stable than after the customary 2-hour warm-up. The microbarograph retained its usual cantankerous disposition.

3. CONCLUSIONS

Under good listening conditions, the following conclusions appear valid:

(1) Eight pound grenades with the configuration and explosive listed in Table 1 can consistently be heard at altitudes in excess of 110 km, and possibly to 115 km with very low background noise, such as at Fort Churchill on calm nights.

(2) Sound returns from the higher altitudes are sometimes easier to detect with capacitor microphones than with hot-wire microphones.

(3) The improved capacitor microphones will probably pick up sound frequencies as low as can be used for reasonably accurate detection of sound arrival times.

(4) The microbarograph appears to be too temperamental for consistent field operation in its present form.

(5) The best sound ranging array probably should comprise a capacitor microphone and a hot-wire microphone in the same pit at each microphone site.

(6) The best microphone site is probably in a wooded area, but in a small opening in the trees.

(7) Low frequency sound background levels on Santa Rosa Island are generally as good or better than at Wallops Island, and a sound ranging array 2000 ft square, or 2000 ft by 4000 ft could be located at test site A-11.

(8) Low aluminum content in grenades, and consequent higher explosive content, will probably produce better sound arrivals.

(9) Higher RDX content may be a factor in the improved sound arrival of low aluminum grenade, and a grenade using compacted RDX as the explosive may be superior to cast explosives.

(10) The Cesium electron cloud trail from some of the non-explosive firings appears to be visible at night, in the absence of sunlight in the upper atmosphere, and may suggest a means of determining winds at night at altitudes above the upper limit of the grenade experiment.

TABLE 1. Types of payload - Firefly III

Designation	Principal Chemicals	Load	Nominal Release Altitudes	Vehicle Type	Vehicle Name
TEC	$CsNO_3$ Al	3 Trail Generators	90-115 km	Nike-Cajun	Bonnie Cindy Dagmar Enid Flora Gladys Helen
MPEC	$CsNO_3$ TNT RDX Al	Four 8-lb Explosive Charges	95, 102-109, 115 km	Nike-Cajun	Alice Brenda Carol Paula Queenie Ruby Sally Beverly
SPEC	$CsNO_3$ TNT RDX Al	One 38-lb. Explosive Charge	100 km	Nike-Cajun	Louise Kitty
BGEC	Acetylene	45 lb. tank	80-100 km	Honest John-Nike-Nike	Ethel
MHEX	TNT RDX Al $CsNO_3$ TNT RDX Al	Six 38-lb Explosive Charges Four 8-lb. Explosive	100, 105 125, 130 155, 160 km 190, 210 245, 250 km	Honest John-Nike-Nike Aerobee	Hazel Lisa Fanny Gilda

TABLE 2. Firefly acoustic measurements

Rocket	Payload	Date (1962)	Time (CST)	T_E (Seconds)	T_A (Seconds)	$T_A - T_E$ (Seconds)	Altitude (km)	Slant Range (km)	Av. Sound Speed (km/sec)
Alice	MPEC	10/16	0511	-	-	-	-	-	-
				115.04	430.79	315.75	93.0	93.65	.297
				140.44	484.07	343.63	101.2	102.35	.298
				145.14	492.17	347.03	101.5	102.60	.296
Queenie	MPEC	10/19	0517	100.76	400.92	300.16	90.7	91.45	.305
				110.62	429.29	318.67	95.7	96.60	.303
				125.20	465.18	339.98	101.9	103.0	.303
				136.79	497.68	360.89	106.0	107.5	.290
Louise	SPEC	10/22	0519	100.40	431.75	331.35	96.7	101.6	.306
Kitty	SPEC	10/23	0519	122.30	505.50	383.20	108.1	115.6	.302
Paula	MPEC	10/24	0521	121.27	437.85	316.58	95.0	98.4	.310
				131.53	486.33	354.80	93.0	101.6	.286
				146.50	510.29	363.79	100.4	105.1	.289
				166.80	532.32	365.52	100.4	106.9	.292
Ruby	MPEC	11/1	0525	101.81	418.98	317.17	96.0	97.15	.306
				118.69	441.5	322.8	-	-	-
				132.08	473.4	341.3	-	-	-
				153.35	551.5	398.1	117.2	119.4	.299
Sally	MPEC	11/5	0529	105.00	429.82	324.82	96.7	98.6	.304
				115.61	462.50	346.89	-	-	-
				127.14	489.83	362.69	107.6	109.7	.302
				141.16	518.4	377.2	112.0	114.3	.302
Beverly	MPEC	11/6	0200	105.99	401.03	295.04	89.1	91.5	.310
				115.56	426.76	311.20	93.7	96.5	.310
				-	-	-	-	-	-
				140	481.55	342	101.7	105.8	.309

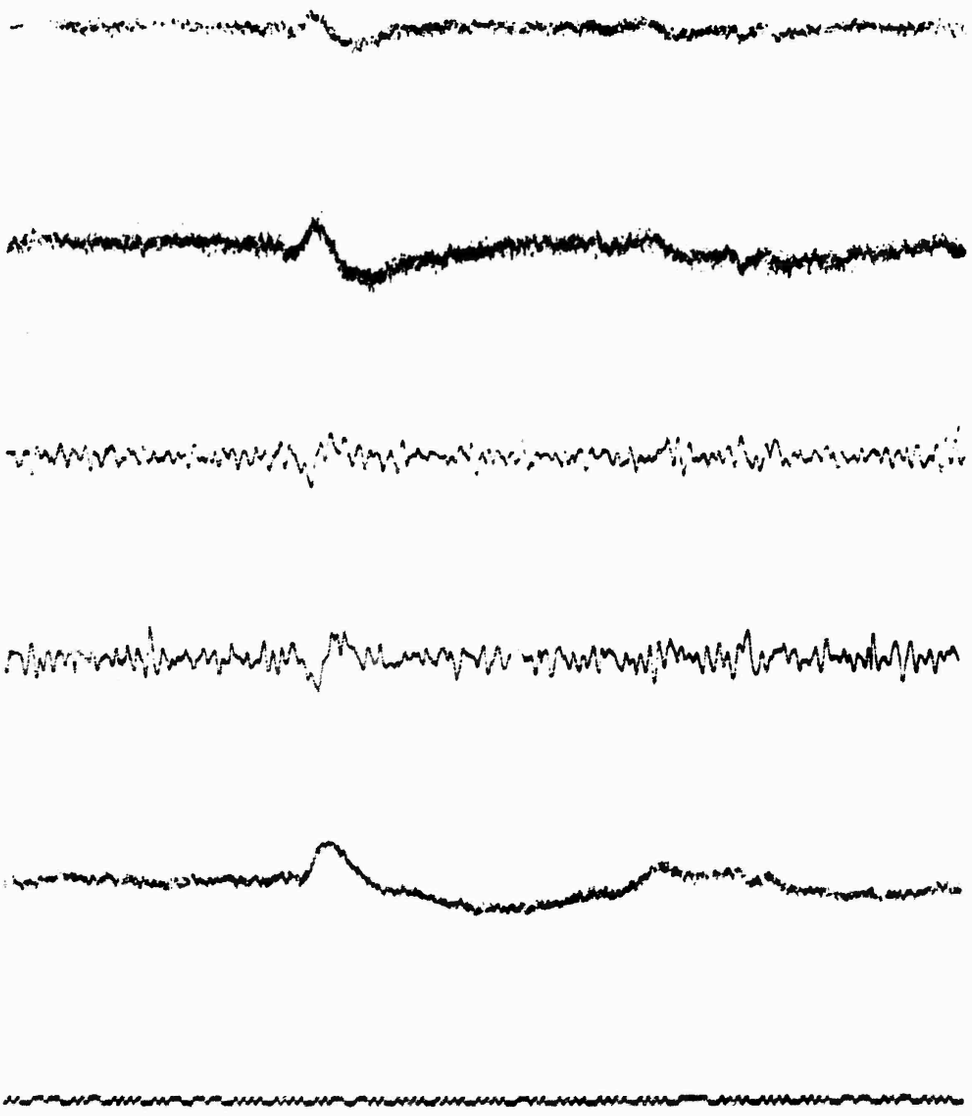

Channel 1 - Capacitor Microphone-Upper Site
Channel 2 - Capacitor Microphone-Lower Site
Channel 3 - Hot-Wire Microphone-Upper Site
Channel 4 - Hot-Wire Microphone-Lower Site
Channel 5 - Microbarograph-Upper Site
Channel 6 - Timing Trace

Figure 1. Sound Arrival from Eight Pound Grenade, Altitude 105 Kilometers

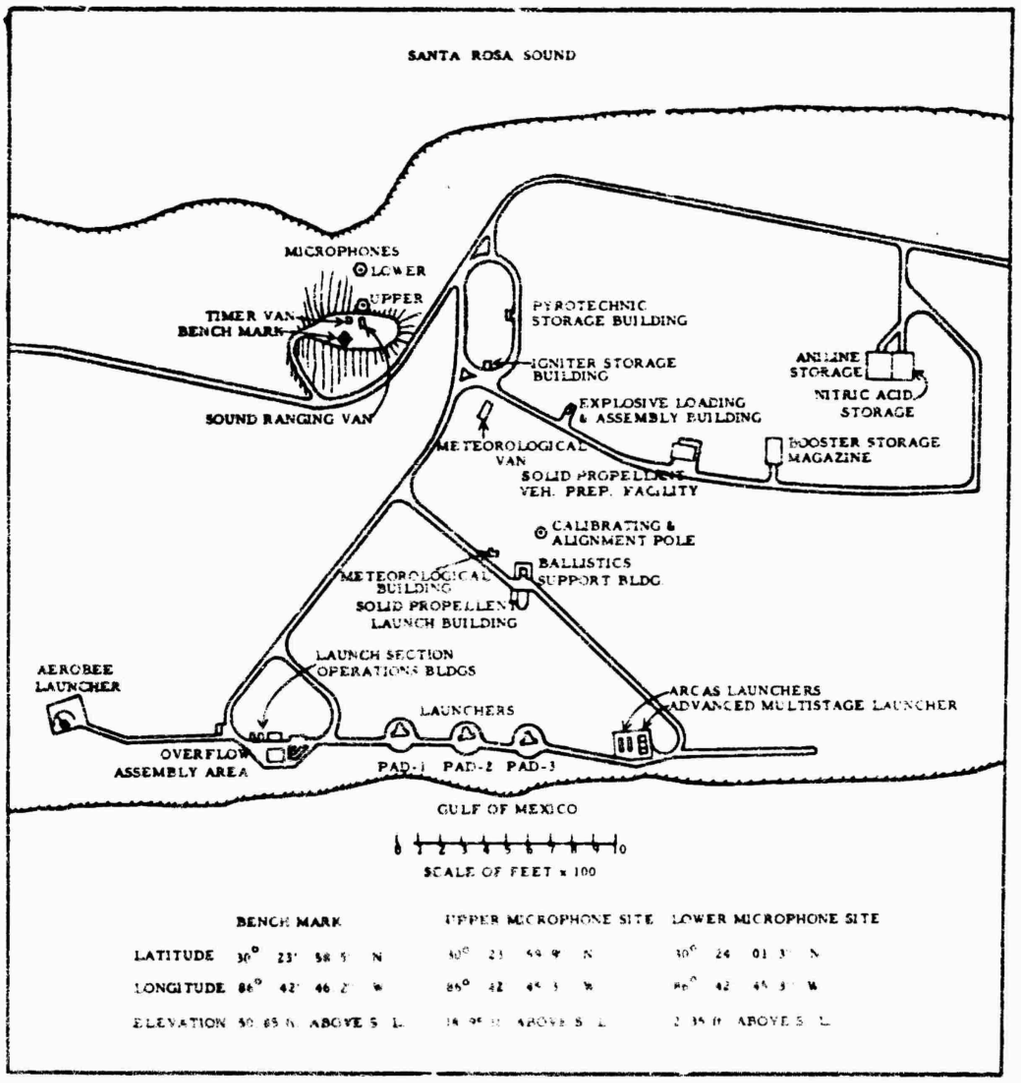

Figure 2 Map, Test Site A11

X. Infrared Radiometer Measurements

D. J. Edwards
Eglin AFB, Florida

Abstract

Two infrared radiometers, one in the near infrared, the other covering a wide region, were used to measure infrared radiation from a TMA and CS_2 release. An unexpected and unexplained result was that the TMA cloud emitted less IR energy than the equivalent area of clear sky, implying that the cloud was cooler than the background.

On 15 May 1963 the Applied Physics Branch personnel covered the multiple cloud launch (CLAIRE) conducted under the Firefly series. Two chemiluminous clouds were produced. One, white in appearance, was due to TMA; the second, blue in appearance, was due to CS_2. It was hoped that two IR radiometric instruments would be used during the launch, but only the Barnes R-8B2 could be readied on such short notice. One channel of the R-8B2 with a PbS detector-filter combination (50% points at 2.0 and 2.65 microns) had an NEI of 5×10^{-12} watts/cm^2, while the other channel with a thermister bolometer and a thin KRS-5 window had an NEI of 1.6×10^{-9} watts/cm^2. The R-8B2 field of view is nominally 8 milliradians diameter.

The R-8B2 radiometer was calibrated for irradiance, H, versus voltage output for both channels. This type calibration makes it easy to reduce data for either a point or extended source target. It was expected that the cloud would appear initially as a point target and then expand into an extended source target completely filling the instrument field of view.

The launch took place on schedule at 2000 hours on 15 May 1963. The first cloud was dispensed approximately 100 seconds after launch. It appeared first as a white dot and gradually enlarged. Unfortunately, the R-8B2 readiometer tripod was not 'jacked up' enough to allow an elevation look angle of almost 90 degrees. By the time the tripod was 'jacked up' enough to view the white cloud, it had enlarged to a size greater than the field of view of the radiometer. The lower elevation portion of the cloud was measured as an extended source. Several readings were taken later of the upper portion of the white cloud.

At approximately 180 seconds after launch, the second cloud (CS_2) appeared. This cloud was pale blue in color and was not visible until it had reached a size larger than the field of the radiometer. Several readings were taken on the blue cloud; however, it dissipated rapidly.

At no time throughout the mission was a signal from either background or target observed on the PbS channel. This indicates that the irradiance at the radiometer from both background and target was equal to or less than 5×10^{-12} watts/cm^2 in the 2.0 to 2.65 micron region. However, readings on the TMA cloud indicated an irradiance lower than the clear zenith sky background in the thermister bolometer region. The CS_2 cloud indicated an irradiance greater than the clear zenith night sky.

For the thermister bolometer channel, sufficient Electronic Temperature Offset (ETO) voltage was inserted to place the resultant signal at the system NEI. The resulting signal can then be expressed as:

$$NEI = H_{bb} - (H_b + H_{ETO}) \text{ and } H_b = H_{bb} - H_{ETO} - NEI \qquad (1)$$

where H_b is the sky background irradiance, H_{bb} is the internal blackbody irradiance, and H_{ETO} is the equivalent ETO voltage irradiance. Since all the values to the right of Eq. (1) are either calculated or calibrated, $H_b = 7.28 \times 10^{-7}$ watts/cm^2. The background irradiance was checked several times before, during and after the mission in the vicinity of the target position and found to be almost invariant. Since the background fills the radiometer field of view, the apparent radiance of the background may be expressed by:

$$N_b = \frac{H_b}{W_R} \tag{2}$$

where W_R is the field of view of the radiometer and is equal to 69×10^{-6} steradians. Therefore, $N_b = 1.053 \times 10^{-2}$ watts/cm^2 steradian. This is the apparent radiance since no attempt has been made to correct for atmospheric attenuation.

When the radiometer is placed on target, and the target fills the instrument field of view, the same technique is used so that

$$H_T = H_{bb} - H_{ETO} - NEI \tag{3}$$

where H_T is the target irradiance. At T_o + 160 seconds, the lower portion of the white cloud was measured. H_T was calculated as 7.19×10^{-7} watts/cm^2. The apparent radiance, $N_T = 1.02 \times 10^{-2}$ watts cm^2 steradian. Repeated measurements from T_o + 160 to T_o + 300 seconds, on various portions of the white cloud, produced approximately the same value of apparent radiance as indicated in Figure 1. Surprisingly, this apparent radiance is lower than the background radiance, indicating that the TMA cloud is 'cooler' than the background.

At approximately T_o + 200 seconds, measurements were made on the blue CS_2 cloud which filled the radiometer field of view. The irradiance values were greater than the sky background, indicating that the blue cloud is 'hotter' than the adjacent zenith clear sky background. The irradiance was calculated as $H_T = 7.35 \times 10^{-7}$ watts/cm^2, and the apparent radiance was calculated to be: $N_T = H_T/W_R = 1.065 \times 10^{-}$ watts/cm^2- steradian. The apparent radiance of the blue cloud diminished with time until approximately T_o + 260 seconds, when the irradiance fell to a level of the radiometer NEI. The reduced data is shown in Figure 1.

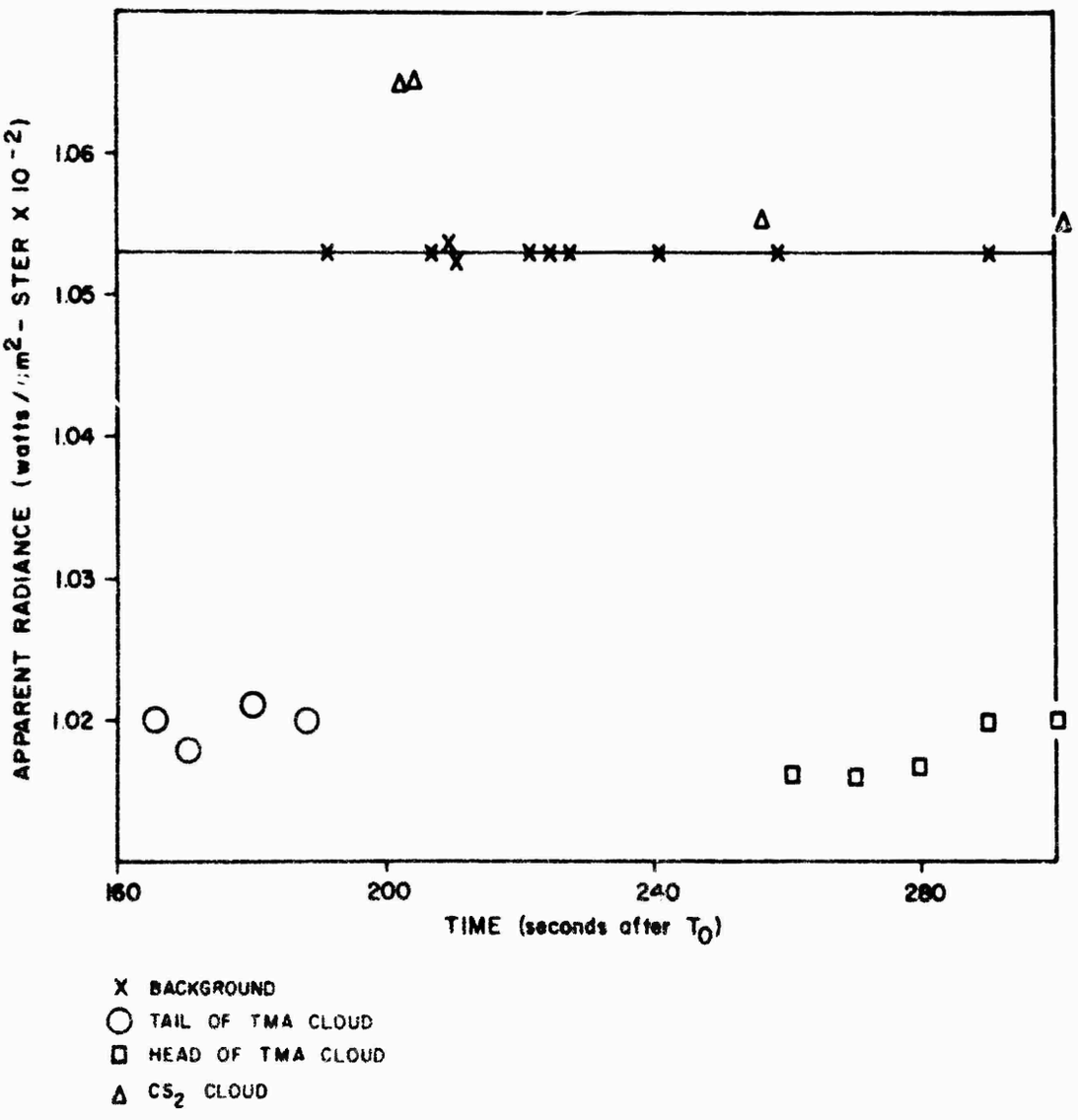

Figure 1. Apparent Radiance.

XI. Formation of an Electron Depleted Region in the Ionosphere by Chemical Releases*

D. Golomb and N. W. Rosenberg
Air Force Cambridge Research Laboratories
Bedford, Massachusetts

J. W. Wright
National Bureau of Standards
Boulder, Colorado

R. A. Barnes
Stanford Research Institute
Menlo Park, California

Abstract

The formation of an electron-depleted region in the ionosphere on release of a chemical with a high attachment coefficient for free electrons is reported. About 10^{26} molecules of sulfur hexafluoride were released from a rocket-borne pressurized tank at 220 km altitude. Marked perturbations were observed on sweeping and pulsed radio frequency sounders which can be interpreted as resulting from an electron depleted region as predicted by Booker. The frequencies returned from the region were initially in the 7 to 9 Mcps band, later spreading to cover the 4 to 8 Mcps band, indicating a growth of the electron depleted region. The effect lasted for about 30 minutes.

---

* Reprinted from Space Research IV, North-Holland Publ. Co., Amsterdam, 1964.

1. INTRODUCTION

In the Fall of 1962, a series of experiments was carried out by the U. S. Air Force Cambridge Research Laboratories in cooperation with other organizations to study the composition and dynamics of the upper atmosphere in the 80 to 250 km altitude region, as a continuation of the 'Firefly' program reported on at the Second COSPAR Symposium.[1] These experiments consist of releasing various chemicals from vertical sounding rockets and observing the effects with ground based instruments. Some of the releases were designed to produce night glows through chemiluminescent reactions of the released species (NO, AlO) with atmospheric oxygen atoms;[2] another group (cesium) produced clouds of increased electron densities in the 90 to 120 km region;[3] and some releases were performed to create electron-depleted regions in the F-layer. It is the latter type of experiment which will be described here in some detail.

The objectives of the electron removal experiment were to study the nature of reflected radio frequency waves from the perturbed ionosphere and to determine the rate of return of the region to normal by diffusion and photo-ionization.

The idea of forming a 'hole' in the ionosphere was put forward in 1960 by Sayers[4] and VanZandt.[5] VanZandt suggested the release of molecular oxygen to accelerate the particular ion-electon recombination reaction believed to be operative during the nighttime decrease of electron densities in the F-layer:[6]

$$O_2 + O^+ \xrightarrow{k_{CE}} O_2^+ + O \qquad \text{(charge exchange)} \qquad (1)$$

$$O_2^+ + e \xrightarrow{k_{DR}} O + O^* \qquad \text{(dissociative recombination)} \qquad (2)$$

Sayers proposed the release of ammonia instead of oxygen since the rate constant for charge exchange between O^+ and NH_3 was estimated as an order of magnitude higher than for $O^+ - O_2$. Preliminary calculations considering the diffusion and chemical kinetics characteristics of electron scavengers indicated that a single step electron attaching process would be more effective than a two step process.[7] Therefore, sulfur hexafluoride was selected for the release, which is known to attach thermal electrons in one step, with a high rate constant:[8]

$$SF_6 + e \xrightarrow{k_A} SF_6^- \qquad k_A = 10^{-9}\ \text{cm}^3\ \text{sec}^{-1} \qquad (3)$$

2. EXPERIMENTAL

An Aerobee vehicle was launched at 1130 CST, 15 December 1962, from Eglin AFB, Florida (29.6°N, 86.6°W), containing a payload of SF_6. A total weight of SF_6 of 22 kg (10^{26} molecules) was contained in two spherical tanks, heated to 65°C which is above the SF_6 critical temperature. At 1134:35 CST (275 seconds after launch), 10 cm dia holes were opened in the two tanks, releasing the gas within a fraction of a second, at an altitude of 222 km, 80 km S of the launch point and of the RF sounding equipment. Telemetry aboard the vehicle reported the successful release, and several observers reported visual sighting of a small white puff expanding and disappearing over about three seconds, against the noon sky background.

Two types of radio-frequency transmitter-receiver sounding were used to probe the release region and to characterize the electron-depleted region formed by the release. Thes included:

(1) A multiple fixed frequency pulse radar with 200 microsecond pulses, at a 37 pulse per second rate, 4 kw peak output. The four frequencies were between 6.3 and 7.8 Mcps.

(2) A sweep-frequency C-4 ionosonde, operating between 0.25 and 20 Mcps with a sweep time of 30 seconds. This frequency band permitted reflections from electron density contours between 10^3 and 5×10^6 electrons per cm. A high gain log-periodic and switched dipole antenna system was installed to provide useful observations throughout this range.

3. ELECTRON HOLE MODEL

It is considered that upon opening of the pressurized tanks, the sulfur hexafluoride expands into a spherical cloud with a Gaussian density distribution. The tails of the expanding Gaussian are overlapped by the tails of an inverted Gaussian density distribution of the ambient. Upon completion of the initial expansion, it can be assumed that the core of the cloud consists wholly of SF_6 and its density equals ambient density. After this stage, the released gas and the ambient interdiffuse while at the same time the cloud is falling under the force of gravitation, since sulfur hexafluoride is much heavier than air (See Figure 1).

Figure 1. Model of Density Profile of Released Gases and Ambient

During the lateral spread of the sulfur hexafluoride gas and its late-time descent through the ionosphere, free electrons will attach to the SF_6 molecules, as long as the concentration of SF_6 exceeds considerably the ambient electron concentration. Thus, an electron depleted region is created, the size and concentration gradients of which depend on the reaction rates (including photo-detachment in sunlight of the negative ions formed) and the diffusion rate of electrons into the hole. The diffusion of electrons at the altitude of release is probably affected by the geomagnetic field, the diffusion perpendicuar to the magnetic field lines being largely retarded. Rate equations including the appropriate kinetic and diffusion terms will be processed based on the method of Golomb and Mason[7] and reported at a later date.

Qualitatively, the electron depleted region can be represented as shown in Figure 2. Consider first Figure 2a where the electron density n_e and the critical frequency f_N in Mcps/sec ($f_N = 9 \times 10^{-3} n_e^{1/2}$) are plotted versus height for the normal ionosphere, and for vertical lines running (1) through the cloud center, (2) 5 km from the cloud center, and (3) 10 km from the cloud center. The time is taken as about 30 sec after release when the Gaussian half-width is about 5 km. Figure 2a permits construction of electron density contours shown in Figure 2b. Here a vertical plane through the hole center and the ground-based sounder is represented. Note that the electron density profile at 208 km ($f_N = 6.8$ Mcps) is undisturbed and will return no signal to the sounder (which views the cloud at a 70^o elevation angle). Deviation of rays is ignored, and it is assumed that only contour surfaces perpendicular to the sounder can reflect. At 210 km ($f_N = 7.1$ Mcps), the lowest distrubed region is encountered. A reflection from point A is possible, as well as a reflection from point B, which is at the same electron density. Two slant ranges will be observed corresponding to the two rays. At $f_n = 7.6$ Mcps, the points A and B will essentially merge because of the decreasing convexity. At about $f_n = 7.9$ Mcps, a surface will be encountered with no portion perpendicular to the sounder, and no direct echoes will be possible at higher frequencies. However, multiple reflections within the hole may permit higher frequencies to be returned by a less-than-perpendicular reflections.

It is also possible to qualitatively predict late-time behavior by similar arguments. Figure 2c might be representative of electron densities at late times when the Gaussian halfwidth is 10 km and the electron density is nowhere more than 20% below ambient. In this case, there are no negative gradients of electron density with ascending height. At such late times, the electron density contours of Figure 2d may be constructed, and show that only one reflection point from each contour is perpendicular to the sounder, so that only a single slant range should be expected for each frequency.

A more detailed discussion of the ionosonde results is now in order in the light of the above model for early and late time electron density contours.

An important adjunct to these experiments is the determination of the ambient electron distribution, N(h), into which the chemical is released. In a recent contribution, Paul and Wright[9] have described some results of N(h) calculations by the method of Paul.[10,11]

The electron density distribution at the time of the release is shown in Figure 3 No 'valley correction' was possible here, because of the configuration of the distribution near foE. Thus, the lower part of the correct F-region profile may be somewhat higher than shown, although little error is to be expected near the F2 peak.

4. RESULTS AND DISCUSSION

The SF_6 was released just below the F2 peak at 222 km. Figure 4 gives a series of ionograms obtained with the C-4 sweep frequency ionosonde. The first frame is the signature of the ionosphere shortly before release. The echo at a greater frequency than f_oF2 is attributed to a propagation by a triangular path with the F-peak. This echo, in its early stages, is similar to the virtual stant range versus frequency curve typical for oblique incidence pulse sounding.

At later times the ionograms indicate that many complicated raypaths have occurred between the cloud, surrounding F-region, and the ionosonde. Of course, each path appears twice, because of magnetoionic splitting. The lowest frequency echo, on each ionogram of the sequence, is part of a echo trace which may be followed with complete continuity of height, frequency and time.

Figure 5 presents a tracing of the ionograms of Figure 4, retaining only the ordinary direct F-region trace and the ordinary direct electron hole return. Note the dual return from the lower frequency portion of the electron hole return at early times and the single return at late times, in accordance with the contours of Figure 2. The returns are clearly of the kind described by Booker[12] as the typical echo pattern from a region of reduced electron density embedded in a surrounding medium. As the echoes develop to lower frequencies, this implies the downward progress of the perturbation. The very lowest frequency echo marks the lowest electron density contour sufficiently affected to render a reflection to the ionosonde. In the last ionogram of Figure 4, taken at about 2000 seconds after release, the region is restored to normal.

The multiple fixed frequency radar returns are shown in Figure 6. Severe perturbations are noticeable from the time of release (1134:35) at the three higher frequencies, and from 100 seconds after release at the lowest frequency used

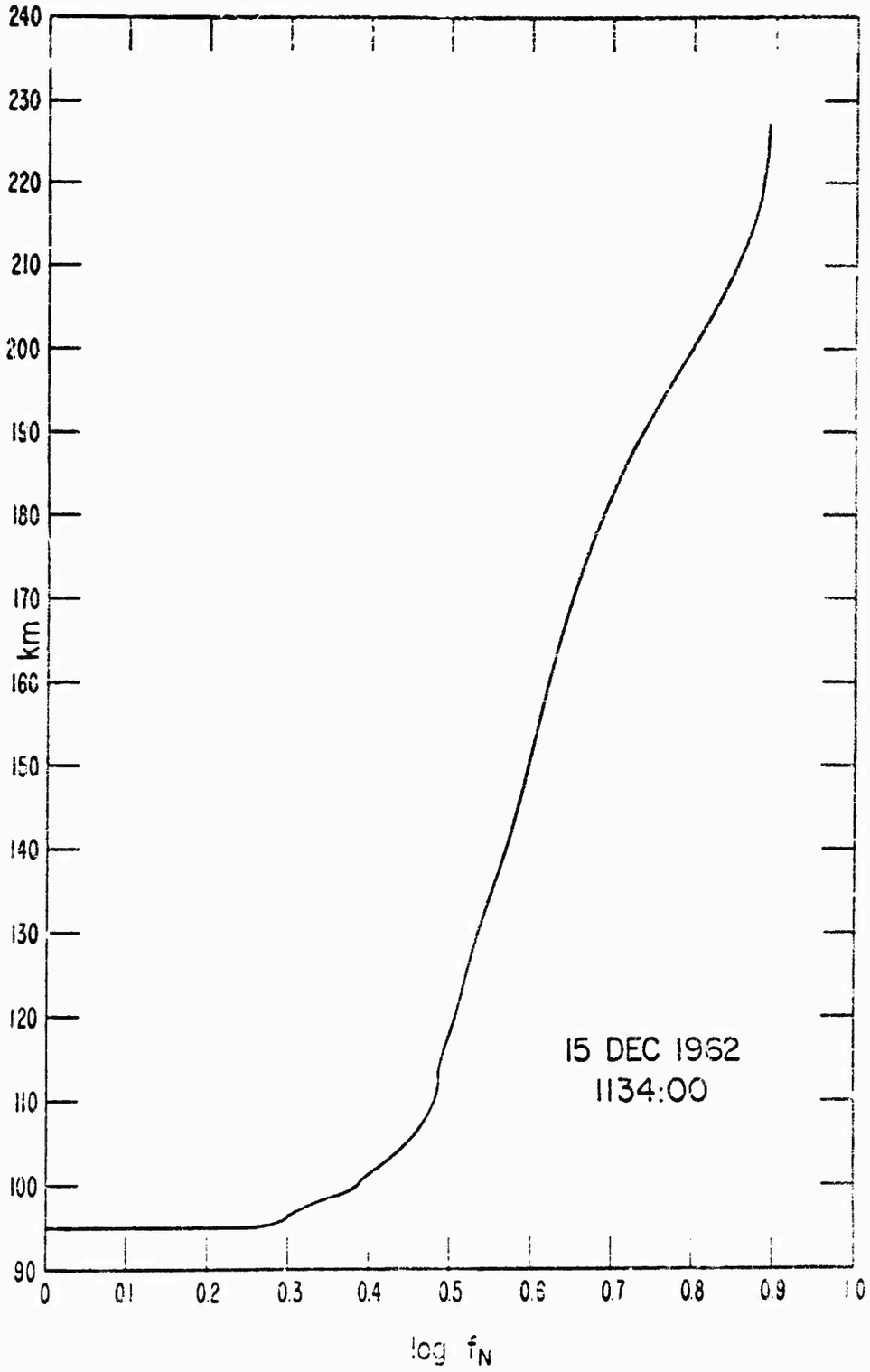

Figure 3. Electron Density Profile (in log of plasma frequency) vs Altitude Before SF_6 Release.

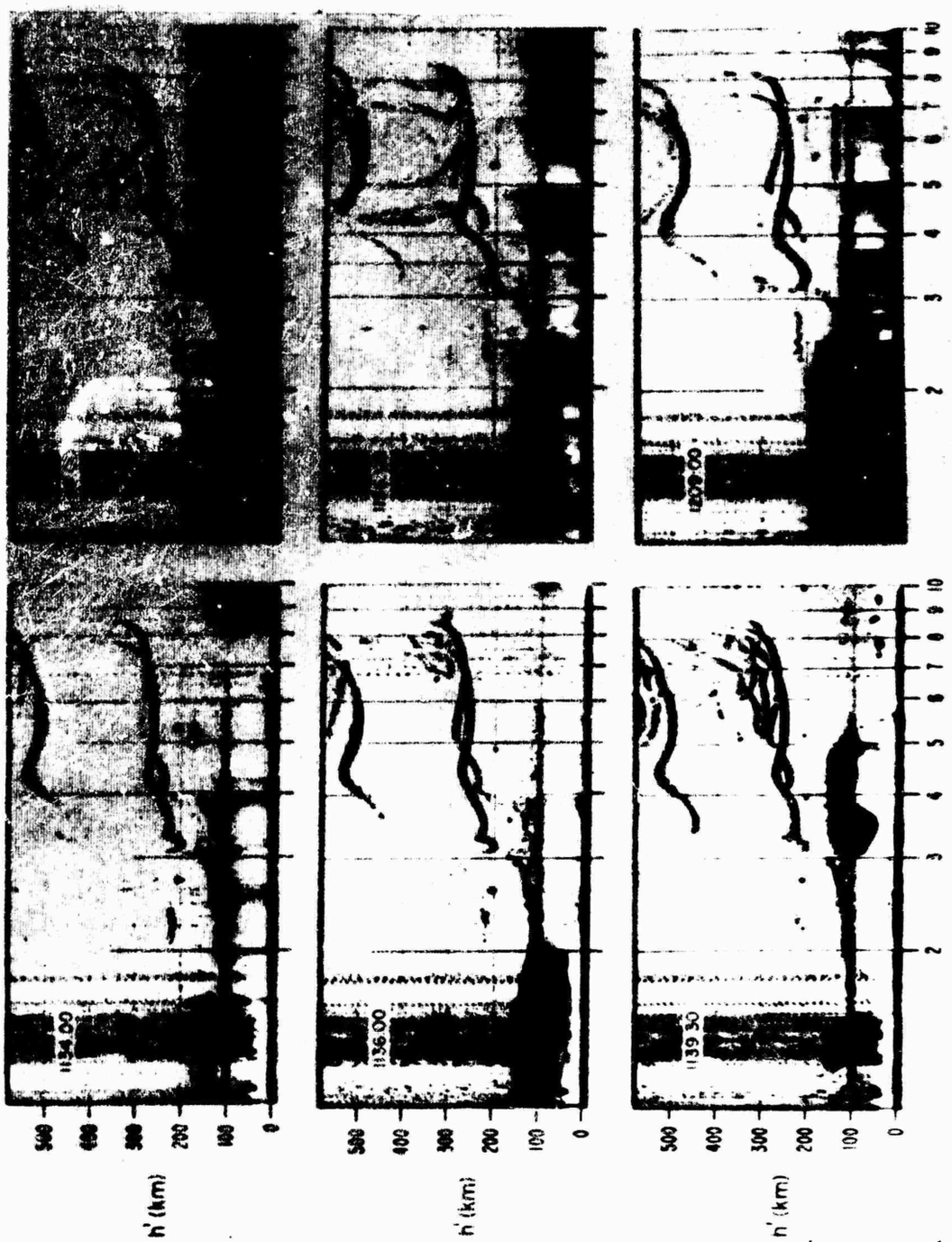

Figure 4. Ionograms of the SF_6 Release. Burst: 1134:35

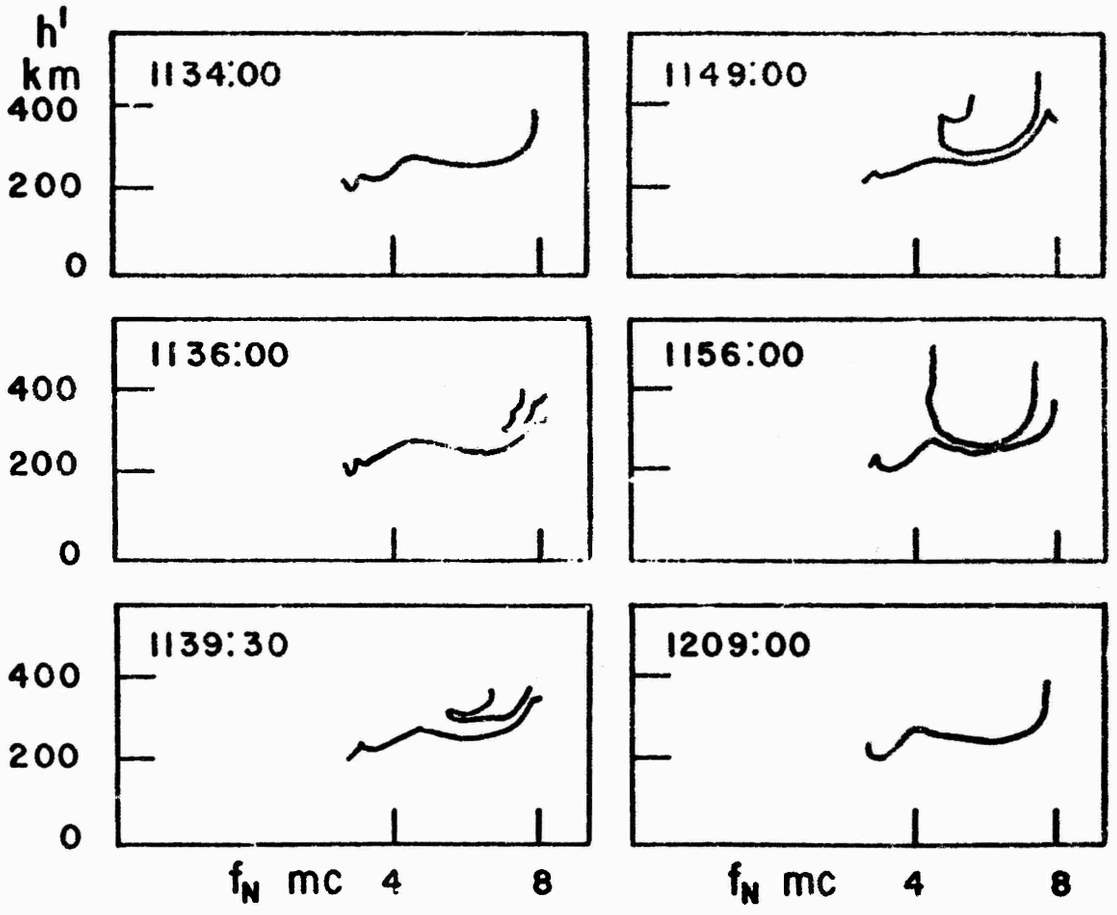

Figure 5. Tracings of the Ionograms.

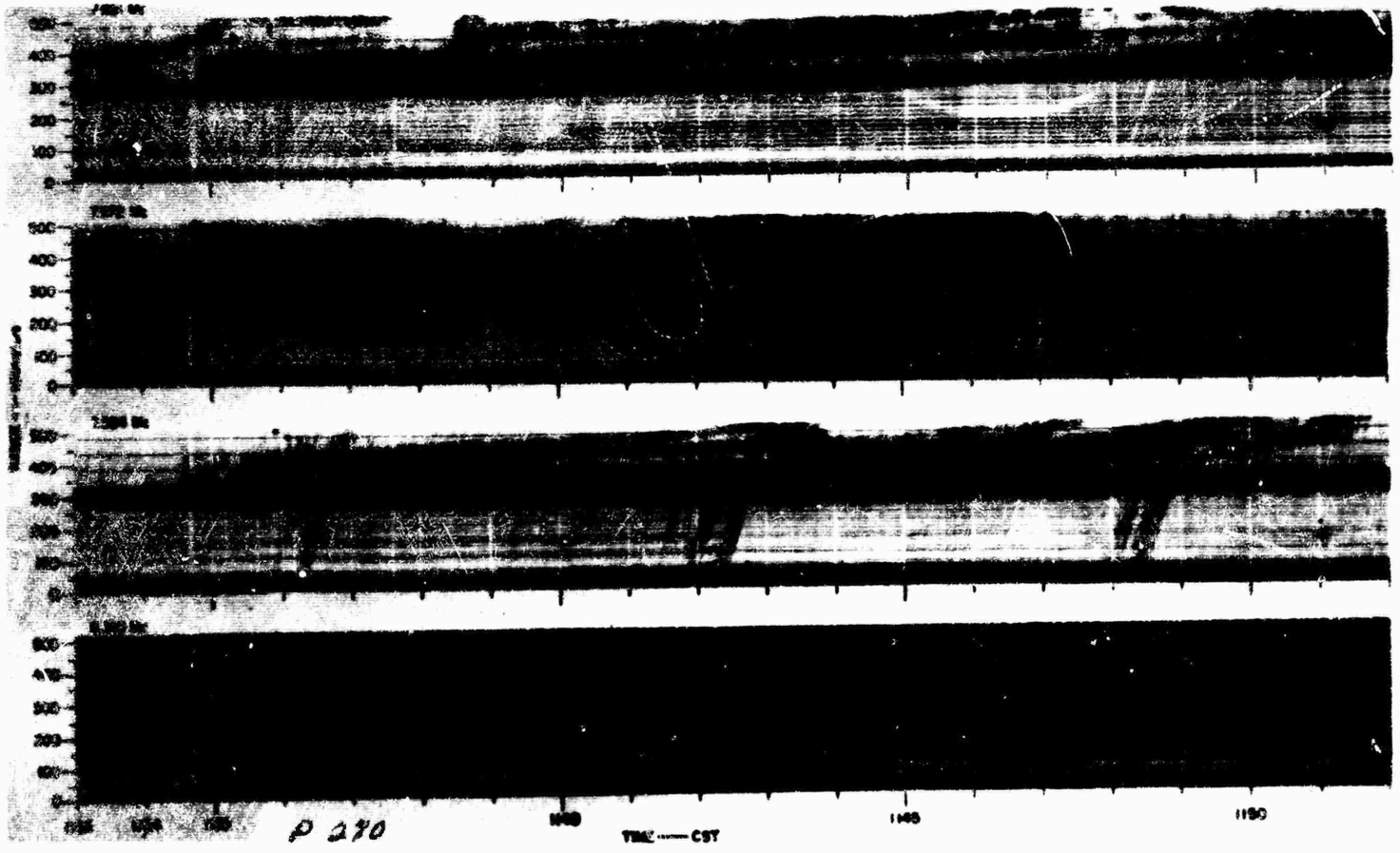

Figure 6. Phase Coherent Radar Returns for Firely MARTHA, SF_6. 15 December 1962. Release at 1134:35 CST.

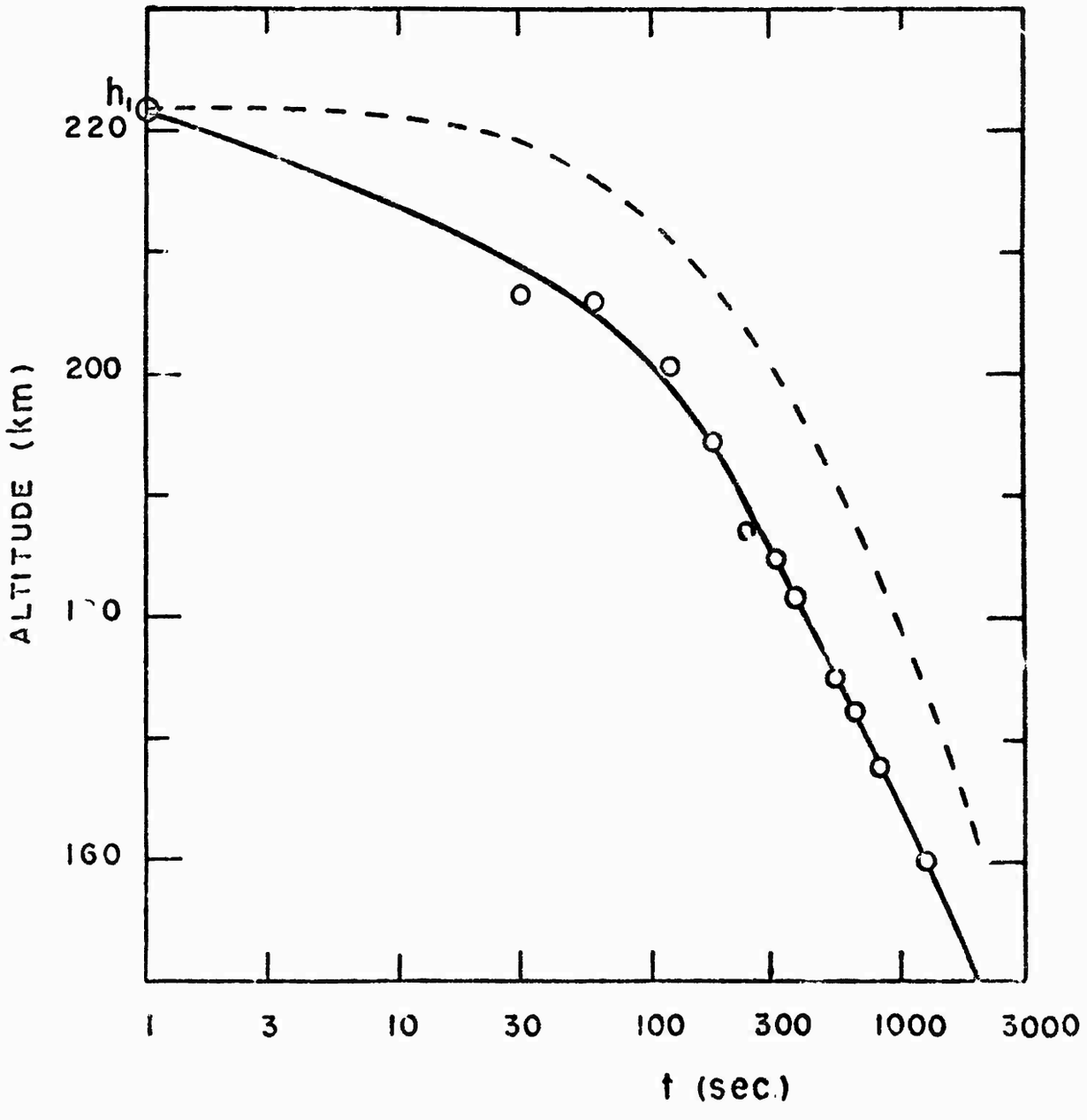

Figure 7. Descent of the RF Disturbance to Lower Altitudes.

(6.3 Mcps). The perturbations cease at all frequencies about 1500 seconds after release. Thus, according to the two types of radar measurements, the effect lasted between 25 and 35 minutes.

Since the minimum frequency at which a disturbance is returned is associated with the lowest altitude which the distrubance has reached, the descent of the perturbation to lower altitudes can be calculated from the sequence of ionograms and is presented in Figure 7 (solid curve).

The gravitational fall of a contaminant released into the upper atmosphere has been discussed by Banister and Davis[13] and by Sherman.[14] These authors derive the following equation for the fall rate of the maximum concentration point of the cloud

$$V = \frac{dx}{dt} = -(K/\rho_o) \exp(x/\lambda), \tag{4}$$

where ρ_o is the ambient density at the release point, λ is the e-fold distance of the isothermal atmosphere (scale height), x is the distance of descent (x = 0 at the release point), and K is a constant characteristic to the released molecules and the ambient.

$$K = \frac{3g\,[mM(m+M)]^{1/2}}{8(a+A)^2(2\pi kT)^{1/2}} \tag{5}$$

(a, A and m, M are the radii and masses of the respective molecules). Integration of Eq. (4) gives

$$x = \lambda \ln\left(1 + \frac{Kt}{\rho_o \lambda}\right) . \tag{6}$$

To compare the observed rate of descent with Eq. (6), we used the atmospheric parameters according to Harris and Priester[15] pertaining to a solar flux index 76. The scale height is obtained from the N(h) profile by the method of Wright[16] and equals 27 km for the release altitude (220 km). This value is consistent with the Harris and Priester model. Other parameters used are

$m = 4.8 \times 10^{-23}$ g	$T = 600^{o}$K
$M = 2.44 \times 10^{-22}$ g	$\rho_o = 6 \times 10^{-14}$ g/cm^3
$a = 1.7 \times 10^{-8}$ cm	$g = 9.2 \times 10^{2}$ cm/sec^2
$A = 2 \times 10^{-8}$ cm (estimate)	$k = 1.4 \times 10^{-16}$ erg/deg.

Accordingly, $K = 6.5 \times 10^{-10}$ g cm^{-2}sec^{-1}. The plot of Eq. (6) is represented by the dashed curve in Figure 7. It is seen that the fall rate as observed from the lowest RF reflecting contour (solid curve) is in good agreement with the theoretical fall rate of the maximum concentration point of the cloud (dashed curve) The altitude separation of about 10 to 15 km between the two curves is expected, since the observation stems from a lower contour of the descending cloud.

In summary it is concluded that the observed shift of the RF perturbation to lower frequencies is in reasonable agreement with the theoretical expansion and fall rate of the released SF_6 molecules. Further studies are planned to correlate the duration and intensity of the effect with estimates based on kinetic and dynamic considerations.

Acknowledgments

The authors are indebted to Dr. A. W. Berger of Monsanto, Inc., Boston, Mass., Mr. E. F. Allen, Jr., of AFCRL, and the engineers of Atlantic Research Corp., Alexandria, Virginia, for the design and preparation of the payloads, and to Mr. E. J. Violette of the National Bureau of Standards, Boulder, Colorado, for the design of the high gain antenna system.

References

1. N. W. ROSENBERG, Artificial Perturbation of the Ionosphere. Proceedings of the Second COSPAR Symposium, North Holland Publishing Co., Amsterdam 1961
2. N. W. ROSENBERG, D. GOLOMB and E. F. ALLEN, JR., Chemiluminescent techniques for studying nighttime winds in the upper atmosphere, J. of Geophys Res. 68: 3328, 1963.
3. N. W. ROSENBERG and D. GOLOMB, Generation and properties of high altitude chemical plasma clouds, in ions and electrons in combustion systems, American Inst. of Aeronautics and Astronautics Series, 12, in press, 1963.
4. J. SAYERS, University of Birmingham, England, private communication.
5. T. E. VANZANDT, National Bureau of Standards, Boulder, Colorado, private communication.
6. P. H. G. DICKINSON and J. SAYERS, Proc. Phys. Soc. 76: 137, 1960.
7. D. GOLOMB and J. MASON, Computer Solution of Simultaneous Diffusion - Chemical Kinetics Equations Relating to Upper Atmosphere Releases, AFCRL Technical Report 62-1132, 1962.

8. W. M. HICKAM and R. E. FOX, J. Chem. Phys. 25: 643, 1956.

9. A. K. PAUL and J. W. WRIGHT, Some results of a new method for obtaining ionospheric N(h) profiles with a bearing on the structure of the lower F-region, J. of Geophys Res., in press 1963.

10. A. K. PAUL, Arch. Elek. Ubertrag. 14: 468, 1960.

11. A. K. PAUL, Geophys. Pura e Appl. 47: 69, 1960.

12. H. BOOKER, J. of Geophys Res. 66: 1073, 1961.

13. J. R. BANISTER and H. L. DAVIS, Phys. of Fluids 5: 136, 1962.

14. C. SHERMAN, Phys. of Fluids 5: 863, 1962.

15. I. HARRIS and W. PRIESTER, Theoretical Models for the Solar-cycle Variations of the Upper Atmosphere, NASA Institute for Space Studies, 24 April 1962.

16. J. W. WRIGHT, Diurnal and seasonal changes in structure of the mid-latitude quiet ionosphere, J. Res. NBS, 66D: 297, 1962.

XII. Space and Time Variations of Electron Densities in an Ionospheric Hole

D. Golomb and W. J. B. Oldham, Jr.
Air Force Cambridge Research Laboratories
Bedford, Massachusetts

Abstract

A physical model and the equations for the space and time variation of electron densities within a electron depleted region are described. The equations include the effect of the geomagnetic field on the diffusion of charged particles. The full equations have to be solved by a computer. For a simplified set of equations an analytical solution is obtained which gives useful information on the kinetic and dynamic behavior of the ionospheric hole.

1. INTRODUCTION

In a preceeding paper,[1] an experiment is described whereby an electron-depleted region was formed in the ionosphere on release of about 10^{26} molecules (22 kg) of sulfur hexafluoride at 222 km altitude. Radio frequency soundings of the perturbed region indicated that the effect lasted for 1500 to 2000 seconds upon which time the ionographs regained a normal appearance as before the release.

In this report some attempts will be described to correlate the observed duration of the effect with estimates based on the dynamic and chemical-kinetic behavior of the dispersed sulfur hexafluoride and the ambient.

The basic physical model for the initial conditions of the phenomenon was given in the preceeding paper.[1] Briefly, it visualizes the released SF_6 vapor as a spherical cloud with a Gaussian density distribution immersed into the ambient with an inverted Gaussian density distribution in the region of the cloud. As the sulfur hexafluoride and the ambient particles interdiffuse, free electrons attach to the SF_6 molecules, forming the electron depleted region or so-called 'ionospheric hole'.

At an altitude of 200 km, the conductivity along the geomagnetic field lines is 1.3×10^{-11} emu, whereas transversely to the field lines it is 7.5×10^{-15} emu (Ref. 2). This means that the diffusion of the electron-positive ion gas into the depleted region proceeds predominantly along the field lines. The neutral SF_6 vapor is unrestricted by the magnetic field and diffuses in a radially symmetric fashion. The combined effect of the field-aligned motion of the electrons and the radial spread of SF_6 is to obtain a progressively shrinking ellipsoidal hole, with the major diameter in the plane along the field and the minor diameter transverse to the field.

As shown in the preceeding paper,[1] the cloud descended over a considerable altitude span during its life time. However, the inclusion of altitude (that is, time) dependent diffusion constants into the rate equations would render them hopelessly insoluble. Thus, the calculations are based on time invariant ambient parameters. It should be noted, however, that during the descent into denser regions, the cloud's diameter is decreasing due to the pressure increase and, consequently, it will take less time for the electrons to penetrate it, notwithstanding the larger diffusion constants. Thus, the two effects counterbalance each other to some degree and the constant altitude assumption may not be so bad.

2. THE RATE EQUATIONS

Since the release occurred in sunlight, the rate equations have to include also the photo-detachment of the negative ions formed by attaching electrons to sulfur hexafluoride. The reactions which occur after release are thus

$$SF_6 + e \xrightarrow{k_1} SF_6^- \quad \text{(attachment)} \tag{1}$$

$$SF_6^- + h\nu \xrightarrow{k_2} SF_6 + e \quad \text{(photo-detachment)} \tag{2}$$

The time and space variation of the reactants' density is determined by the set of coupled partial differential equations

$$\frac{\partial e}{\partial t} = D_A \nabla^2 e - k_1 e S + k_2 S^- \tag{3}$$

$$\frac{\partial S}{\partial t} = D_M \nabla^2 S - k_1 e S + k_2 S^- \tag{4}$$

$$\frac{\partial S^-}{\partial t} = D_A' \nabla^2 S^- + k_1 e S - k_2 S^- \tag{5}$$

Here e, S and S^- denote the number of electrons, SF_6 and SF_6^- molecules per cm^3, respectively. D_A and D_A' are the ambipolar diffusion coefficients for electrons and SF_6^-, respectively, and D_M is the molecular diffusion coefficient for sulfur hexafluoride.

It is convenient to use a cylindrical coordinate system for the definition of the space variables with the z - axis parallel to the magnetic field lines.

Assuming symmetry around the z - axis, the density distribution of the considered species at time t = 0 is given by

$$e(\ell, z) = e(\ell = z = \infty)\,[1 - \exp - (\ell^2 + z^2)/h^2] \tag{6}$$

$$S(\ell, z) = S(\ell = z = 0)\,[\exp - (\ell^2 + z^2)/h^2] \tag{7}$$

$$S^-(\ell, z) = S^-(\ell = z = 0) = 0 \tag{8}$$

Here h = Gaussian half-width, and $r^2 = \ell^2 + z^2$.

The Laplacian in cylindrical coordinates is

$$\nabla^2 n = \frac{1}{\ell} \frac{\partial}{\partial \ell} \left(\ell \frac{\partial n}{\partial \ell}\right) + \frac{1}{\ell^2} \frac{\partial^2 n}{\partial \theta^2} + \frac{\partial^2 n}{\partial z^2} \tag{9}$$

Since symmetry around the z - axis prevails at all times, the term containing $\partial^2 n/\partial\theta^2$ drops out for all species.

Since ambipolar diffusion is assumed to proceed only along the magnetic lines which run parallel to the z - axis, the term containing $\partial n/\partial \ell$ drops out for ionized species.

Thus, Eqs. (3) through (5) become

$$\frac{\partial e}{\partial t} = D_A \frac{\partial^2 e}{\partial z^2} - k_1 eS + k_2 S^- \tag{10}$$

$$\frac{\partial S}{\partial t} = D_M \left[\frac{1}{\ell} \frac{\partial}{\partial \ell} \left(\ell \frac{\partial S}{\partial \ell}\right) + \frac{\partial^2 S}{\partial z^2}\right] - k_1 eS + k_2 S^- \tag{11}$$

$$\frac{\partial S^-}{\partial t} = D_A' \frac{\partial^2 S^-}{\partial z^2} + k_1 eS - k_2 S^- \tag{12}$$

This is a set of coupled, partial, second-order, non-linear differential equations with two space variables and one time variable. At present, this set is being programmed for an analogue computer based on the method of finite differences.[3] However, for preliminary calculations, further simplifications can be introduced which will enable an analytical solution of Eqs. (10) through (12).

Let us assume that the density of sulfur hexafluoride, S, is constant over a limited time and space interval. Therefore, $k_1\bar{S} = k_1'$, where $\bar{S}$ is obtained by solving Eq. (11) separately, omitting the chemical terms:

$$\bar{S} = \frac{S(0)\, h^3}{(h^2 + 4D_M t)^{3/2}} \exp - \frac{\ell^2 + z^2}{h^2 + 4D_M t} \tag{13}$$

Putting $\psi = \frac{e(\ell, z, t)}{e(\infty, \infty, 0)}$ and $\phi = \frac{\bar{S}(\ell, z, t)}{e(\infty, \infty, 0)}$ (a normalizing procedure) and assuming for these preliminary calculations that $D_M = D_A = D$, we obtain

$$\frac{\partial \psi}{\partial t} = D \frac{\partial^2 \psi}{\partial z^2} - k_1' \psi + k_2 \phi \tag{14}$$

$$\frac{\partial \phi}{\partial t} = D \frac{\partial^2 \phi}{\partial z^2} + k_1' \psi - k_2 \phi \tag{15}$$

The solution to Eqs. (14) and (15), with the initial conditions of Eqs. (6) through (8) is

$$\psi = \frac{k_2 + k_1' \exp - Kt}{K} \left[1 - \frac{h \exp - (\ell^2/h^2) \exp - (z^2/G)}{G^{1/2}} \right] \tag{16}$$

$$\phi = \frac{k_1' (1 - \exp - Kt)}{K} \left[1 - \frac{h \exp - (\ell^2/h^2) \exp - (z^2/G)}{G^{1/2}} \right] \tag{17}$$

where $K = k_1' + k_2$ and $G = h^2 + 4Dt$.

3. RESULTS AND DISCUSSION

The following parameters have been used to solve Eqs. (16) and (17).

(1) $D = 2 \times 10^9$ cm^2 sec^{-1}, the diffusion coefficient for air molecules at 220 km altitude, according to U. S. Standard Atmosphere density and temperature values.[4]

(2) $h = 1.5 \times 10^5$ cm, obtained from $h = 1/\pi^{1/2}\ (N/n_a)^{1/3}$, where N is the total number of released SF_6 molecules ($150 \times 6 \times 10^{23} = 9 \times 10^{25}$) and n_a is the ambient density at 220 km (4.7×10^9 cm^{-3}).

(3) $k_1 = 1 \times 10^{-9}$ cm^3 sec^{-1}, from Hickam and Fox's data[5] assuming an electron energy of 0.1 - 0.2 ev.

(4) $k_2 = 0,\ 0.01,\ 1$ sec^{-1}. No data was found in the literature for the photodetachment rate of SF_6^-, therefore the calculations were performed for several values. The photodetachment rate for O_2^- is 0.1 - 1 sec^{-1} for photons in the UV,[6] for F^- it is 3×10^{-2} (Ref. 7).

(5) $S(0) = 4.7 \times 10^9$ cm^{-3}. This is the density of SF_6 in the center of the cloud at t = 0, a parameter used to obtain $\bar{S}$ values from Eq. (13). This density is assumed to be equal to the ambient density at 220 km, as tabulated in Ref. 4.

In Figure 1, ψ is plotted as a function of t for $\ell = z = 0$; that is, at the center of the perturbed region. As ψ approaches unity, the region restores to normal. The three curves pertain to the three photodetachment coefficient used in the calculations. It is seen that this coefficient has a marked effect on the restoration time. For $k_2 = 0$, which would be the case in a night release, the center electron density at 1000 seconds is only one-half the ambient value; for $k_2 = 0.01$ sec^{-1}, it is 90% of the ambient value; for $k_2 = 1$ sec^{-1}, it is 95%.

It is difficult to predict what minimum electron deficiency in the center of the perturbed region will cause a layer of a given plasma frequency to be tilted normal to the sounding frequency. The matter is complicated by the fact that the 'hole' in its later stages is oriented with regard to the magnetic field lines. This means that the crests of the wave-like electron density contours as depicted in Figure 2d of the preceeding paper[1] are perpendicular to the field lines. The field lines and the

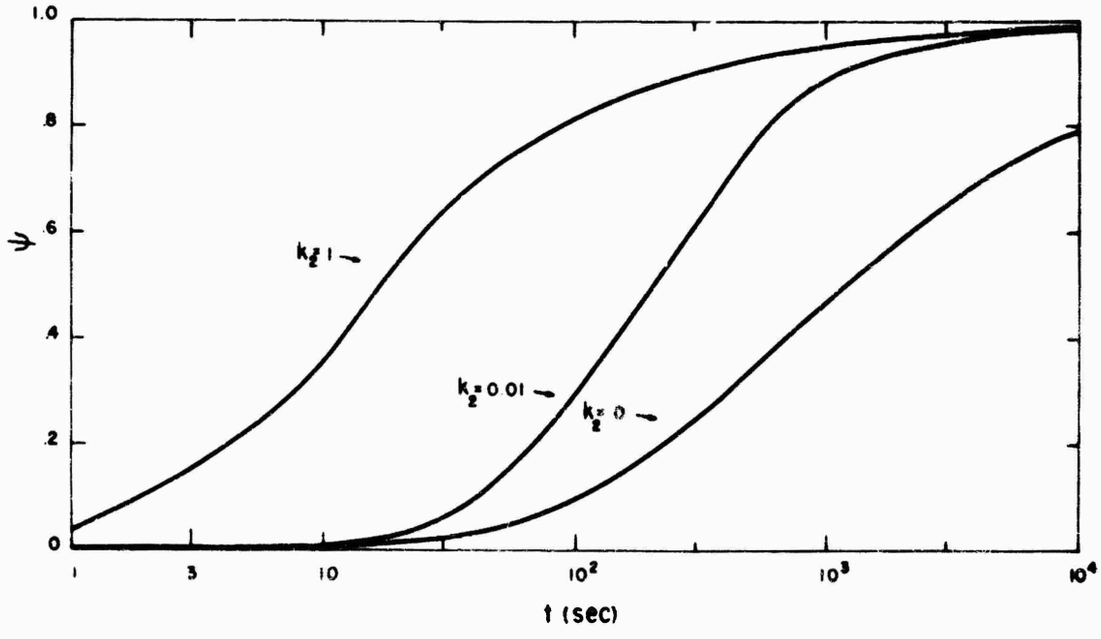

Figure 1.

incident rays cross at a certain angle. The magnetic dip angle at the latitude of release is about 60^{o}, and the ionosonde 'look-angle' was about 70^{o} with an azimuth due south. Thus, the field lines and the incident rays were (unintentionally) quite well aligned, and this might have been the reason that the effect was observed so long. Taking 2000 seconds as the duration of the effect, and a photodetachment rate between 0.01 - 1 sec^{-1}, it seems that for this geometry, when the electron density in the center of the hole approaches 95% of the ambient, the sounder ceases to record the phenomenon. It would be interesting to see in future experiments whether the same perturbation will be observed for different time periods by sounders placed at different locations.

In summary, it may be concluded that the model incorporating the chemical kinetics behavior of the released species and the field-restricted diffusion of electrons can provide at least a semi-quantitative estimate of the restoration time of the ionospheric hole. A computer solution of the unsimplified equations will give a better insight into the time and space variation of the electron densities.

References

1. D. GOLOMB, N.W. ROSENBERG, J.W. WRIGHT, and R.A. BARNES, Formation of an Electron Depleted Region in the Ionosphere by Chemical Releases, this issue.
2. S.K. MITRA, The upper atmosphere, Asiatic Society, Calcutta, p. 348, 1949.
3. D. GOLOMB and J. MASON, Computer Solution of Simultaneous Diffusion - Chemical Kinetics Equations Relating to Upper Atmosphere Releases, AFCRL Technical Report 62:1132, 1962.
4. U.S. Standard Atmosphere, 1962, Joint NASA-AF-Weather Bureau Publ., Washington, 1962.
5. W.M. HICKAM and R.E. FOX, J. Chem. Phys. 25:643, 1956.
6. D.S. BURCH, S.J. SMITH and L.M. BRANSCOMB, Phys. Rev. 112:171, 1958.
7. R.S. BERRY and C.W. REIMANN, J. Chem. Phys. 38:1540, 1963.

XIII. Ionospheric Winds and Sporadic E Correlations*

N. W. Rosenberg
Air Force Cambridge Research Laboratories
Bedford, Massachusetts

H. D. Edwards
Georgia Institute of Technology
Atlanta, Georgia

J. W. Wright
National Bureau of Standards
Boulder, Colorado

Abstract

The persistence of night winds and shears for more than 5 hours after sunset at altitudes between 100 and 150 km was evaluated during the COSPAR synoptic ionospheric winds program in December 1962. The method used was to release chemiluminous trails from rockets between 100 and 150 km with the times of release being 1720, 1801, 2145 and 2245 CST on 3 December 1962. The release times were respectively 13 minutes before sunset at the 100 km level and 28 minutes, 4 hours 12 minutes, and 5 hours 12 minutes post sunset. All rockets were launched from the Air Force Gulf Test Range, Eglin Air Force Base, Florida at a longitude of 86.6°W and a latitude of 29.6°N.

* Reprinted from Space Research IV, North-Holland Publ. Co., Amsterdam 1964.

It is believed that this is the first time such a morphology of winds and shears through the E region has been made available. Comparisons are made between the winds and shears observed under night conditions with those for the preceeding twilight period.

Theoretical discussions by Whitehead and others have suggested a wind shear origin for sporadic E. High east-west horizontal wind shears in the ionosphere and the natural magnetic field will act on ionized species to stratify these into relatively high vertical gradients.

Simultaneous measurements of ionospheric wind shears (measured by chemiluminescent trails) and of sporadic E (by sweep-frequency ionosondes) are discussed in this report. Occurrence at the same altitudes of maximum wind shears and strong sporadic E levels was found. In one case, for example, (86.6°W, 29.6°N, 1720 CST, 3 December 1962), sporadic E was found at 96±1 km to 1.0 mc and at 109±1 km at 6.2 mc. At this time, wind shear maxima of 45 m/s km bearing 85°E at 97±1 km and of 60 m/s km bearing 275°E at 109±1 km were found.

These data tend to verify the correlation between wind shear and sporadic E.

1. INTRODUCTION

The pattern of winds and shears in the E region of the ionosphere, including their time and altitude variation, and their relationship with sporadic E, has been the subject of considerable speculation and theoretical analysis.[1,2,3] The availability of sodium trails[4] has provided well-resolved altitude variations of winds in the 90 to 200 km region at sunrise and sunset. COSPAR-organized programs for simultaneous measurements at different locations have provided data on variation with geographic location of such sodium-trail winds and are being reported by Blamont at this metting.[5]

This report discusses a series of wind measurements made using recently developed chemiluminous gas trails[6] which permit measurements during the night. The pattern of winds from shortly before sunset into night is presented, and their relationships with simultaneous ionospheric soundings in the 0.2 to 20 Mcps region are noted, although no detailed theoretical analysis is given at this time.

2. EXPERIMENTAL

Four releases will be discussed, from rockets launched at 1720, 1801, 2145 and 2245 CST on 3 December 1962 from the Air Force Gulf Test Range, Eglin Air Force Base, Florida, Longitude 86.6°W, Latitude 29.6°N. The first release was a sodium payload[4] 13 minutes before sunset at 100 km, the second and third were $CsNO_3$-Al burners with chemiluminous trails (probably due to an Al-O reaction),[6] and the fourth was a nitric oxide trail.[6] The altitudes over which each gave useful data are presented in Figure 1.

Four photographic tracking stations equipped with modified K-24 aerial cameras[7] were used to take simultaneous photographs of the trails against a star background. Three of these stations were located approximately 100 km N, E, and W of the release, and the fourth was located near the launcher (about 20 km N of the release). Subsequent photogrammetry for winds was performed on a computer.[8]

Two ground-based ionosondes, one located about 20 km N and the other 100 km NE of the release, provided 30 second sweeps of frequencies between 0.2 and 20 Mcps for some time around each release. These are capable of providing estimates of Normal E-region and sporadic E frequencies and altitudes.

A spaced-receiver deift instrument, utilizing a standard ground-based radio technique for making ionospheric drift measurements and operating at 3 Mcps, was installed 20 km N of the release area and operated by Mr. E. Harnischmacher (Ionospharen Inst. Breisach) and Mr. G. H. Stonehocker (NBS Boulder). Their detailed results will be separately reported, but pertinent data have kindly been made available by them for this report.

3. OBSERVATIONS

3.1 Optical Wind Motions

Figure 2 is a photograph of a typical night wind trail as viewed from 100 km N of the release area. The altitudes and times after launch of various points along the trajectory are shown.

Figure 1 presents hodographs (wind patterns viewed from above) of the four releases. An appropriate presentation of wind patterns presents two problems. First, vertical motions have not yet been measured on these particular clouds, and may not be measurable except in the turbulent region around 100 km. This problem is not considered further here. The second problem is that a given wind vector must be represented by amplitude and direction, or by north-south and east-west components.

Figures 3 and 4 present NS and EW components for the four releases. A pattern varying through the night is better seen in contour displays such as given in Figures 5 and 6. In these figures, time is represented along the x-axis, and altitude along the y-axis. Equal wind components at the four times of observation are connected to form a contour map.

3.2 Radio Frequency Recordings of Ionospheric Condition

Figure 7 presents ionospheric sweep-frequency records taken at the time of the 1720 CST release. The scaled records, and the spaced receiver data (at 3 Mcps) are recorded in Table 1.

TABLE 1. RF ionosphere background

Time CST	f_oE(mc)	f_oE_s(mc)	hE_s(km)	Drift Receiver Direction	Drift Receiver Velocity
1720 Sharon	1.4	1.02 6.2	96 109	195°	65 m/s
1801 Ivy	0.8	0.8 6.2	96 108	195°	42 m/s
2145 Esther	0.8	2.7	103		
2245 Dinah	0.7	2.5	100		

For all releases, sporadic E was overhead and the assigned heights are probably good to ± 1 km.

No retardation corrections were necessary since a simple calculation showed that the underlying ionization could contribute less than 1 per cent of its thickness to retardation at the peak frequencies of the sporadic E.

4. DISCUSSION OF RESULTS

4.1 Wind Profiles

The data reported here were for a single night, and of course may not be typical of other nights.

Examination of Figures 3 and 5 shows that the altitude at which a given NS wind exists decreases by 5 to 10 km over the 5 to 6 hour period of observation. The altitudes at which the maximum NS or SN winds exist also decrease, but the maximum strengths (and shears) increase over the timer period. The NS winds appear to be quite regular in their variation, and a given pattern is sinusoidal with increasing wavelength at increasing altitude. Zimmerman[9] suggests that the period is close to a scale height and varies with the scale height of the ambient.

Examination of Figures 4 and 6 shows a similar effect for the EW wind component except for two anomalies; the velocity of the wind maximum in the 100 km region decreases as the night progresses (all other maximum winds increase in velocity); and in the region above 120 km, there is a rise in the altitude of a given contour with time in the early night followed by a decrease in altitude at later times.

It is tempting to associate the decreasing altitude of these winds with a thermal subsidence at night; that is, a given wind may exist at a given ambient density and that as a nighttime cooling occurs, these winds move downward together with the air mass in which they are embedded. It is also interesting that Hines[1] suggests a downward velocity of all wind profiles.

Spaced-receiver drift results for SHARON are shown in Figure 10. The direction sensed by the radio method is in good agreement with the cloud drift at the sporadic E altitude and, being mostly south-bound, agrees with the absence of an EW component implied by the wind shear theory of sporadic E. It would be useful to re-examine the great quantity of available spaced-receiver observations of sporadic E to determine how frequently the observed velocities are predominantly NS.

The velocities determined by the spaced-receiver technique are larger, however, than those deduced from the trails and this imples that:

(1) There may be a wave motion[10] superimposed upon the neutral drift. If so, a comparison of the two methods would permit the deduction of the wave motion separate from the neutral drift. The direction was observed to be toward the south and,

(2) The sporadic E reflection level may fluctuate about the level where $V_{EW}=0$, adding a variable EW component to the average NS component.

Acknowledgments

Our thanks to Mr. C. G. Justus for his untiring efforts in analysis of the photographic data.

Financial support for the studies conducted at the Georgia Institute of Technology has been supplied by the Air Force Cambridge Research Laboratories under contracts AF 19 (604) -5467 and AF 19 (628) -393, and by the National Aeronautics and Space Administration under Grant NsG 304-63.

References

1. C. O. HINES, Can. J. Phys. 38: 1441, 1960.
2. J. D. WHITEHEAD, J. Atmosph. Terr. Phys. 20: 49 1961.
3. W. I. AXFORD, J. Geophys. Res. 68: 769, 1963.
4. E. MANRING, J. F. BEDINGER, H. B. PETTIT, C. B. MOORE, J. Geophys. Res. 64: 587, 1959.
5. J. E. BLAMONT, COSPAR Meeting, 6 June 1963, Warsaw, Poland.
6. N. W. ROSENBERG, D. GOLOMB, E. F. ALLEN, J. Geophys. Res., In Press, 1963.
7. H. D. EDWARDS, M. M. COOKSEY, C. G. JUSTUS, R. N. FULLER, D. L. ALBRITTON, N. W. ROSENBERG, J. Geophys. Res. 68: May 15, 1963

8. D. L. ALBRITTON, L. C. YOUNG, H. D. EDWARDS, J. L. BROWN, Photogrammetric Engineering, September 1962.

9. S. P. ZIMMERMAN, Private Communication

10. C. O. HINES, Private Communication

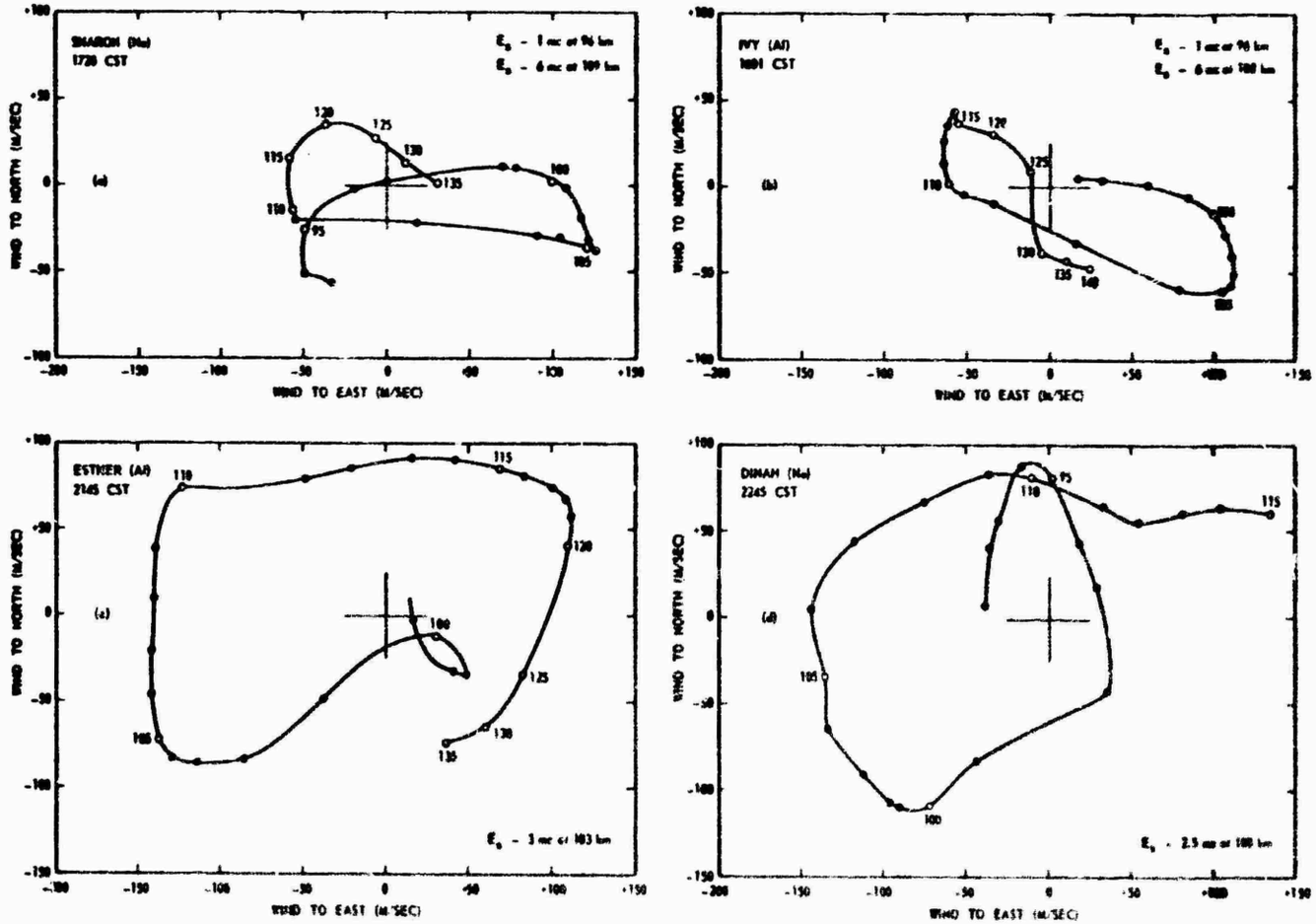

Figure 1. Hodographs of the Four Releases Showing East-West Components of the Wind Vector

Figure 2. Photograph of a Typical Night Wind Trail Showing East-West Wind Motion

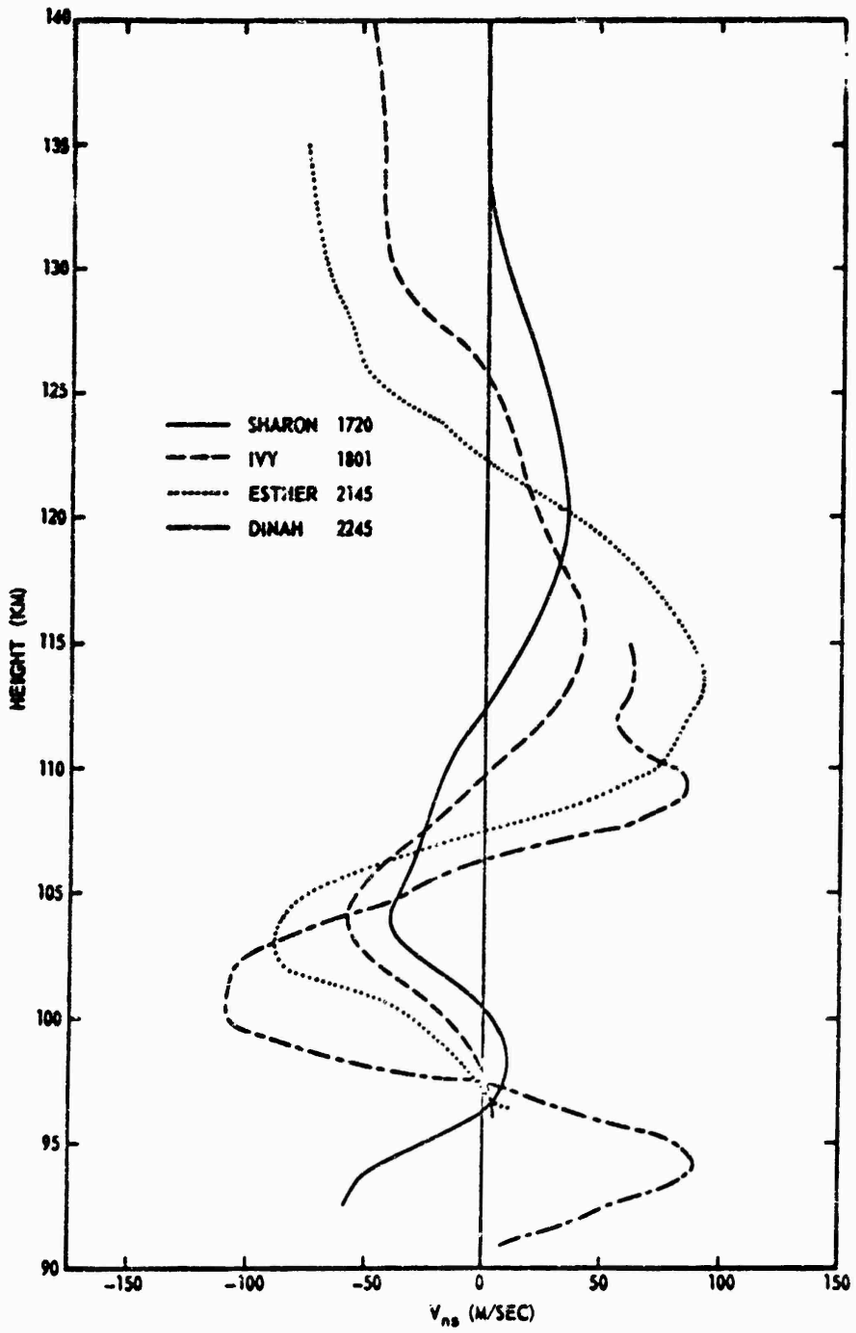

Figure 3. North-South Components of the Wind Velocity as a Function of Altitude for the Four Releases

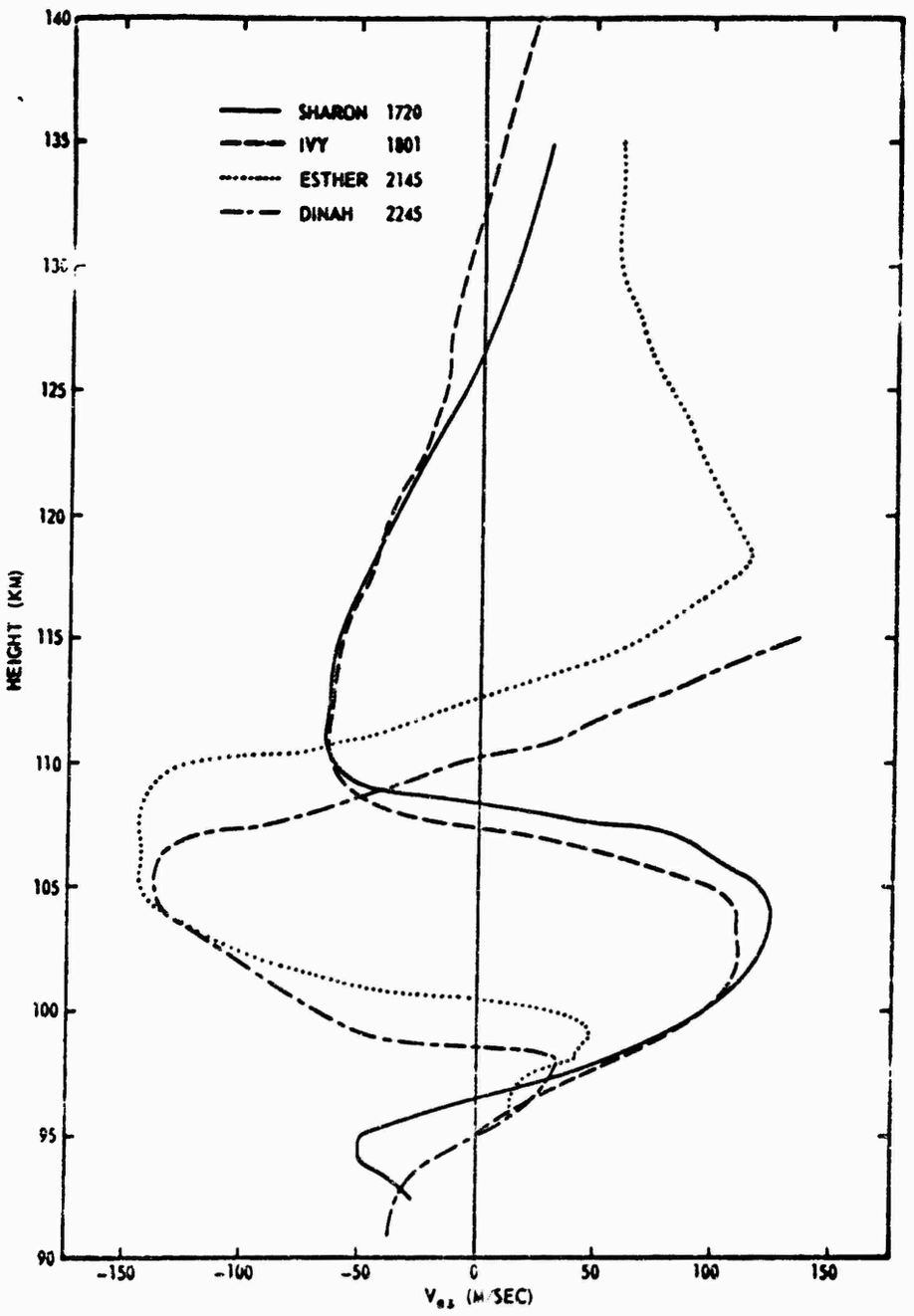

Figure 4. East-West Components of the Wind Velocity as a Function of Altitude for the Four Releases

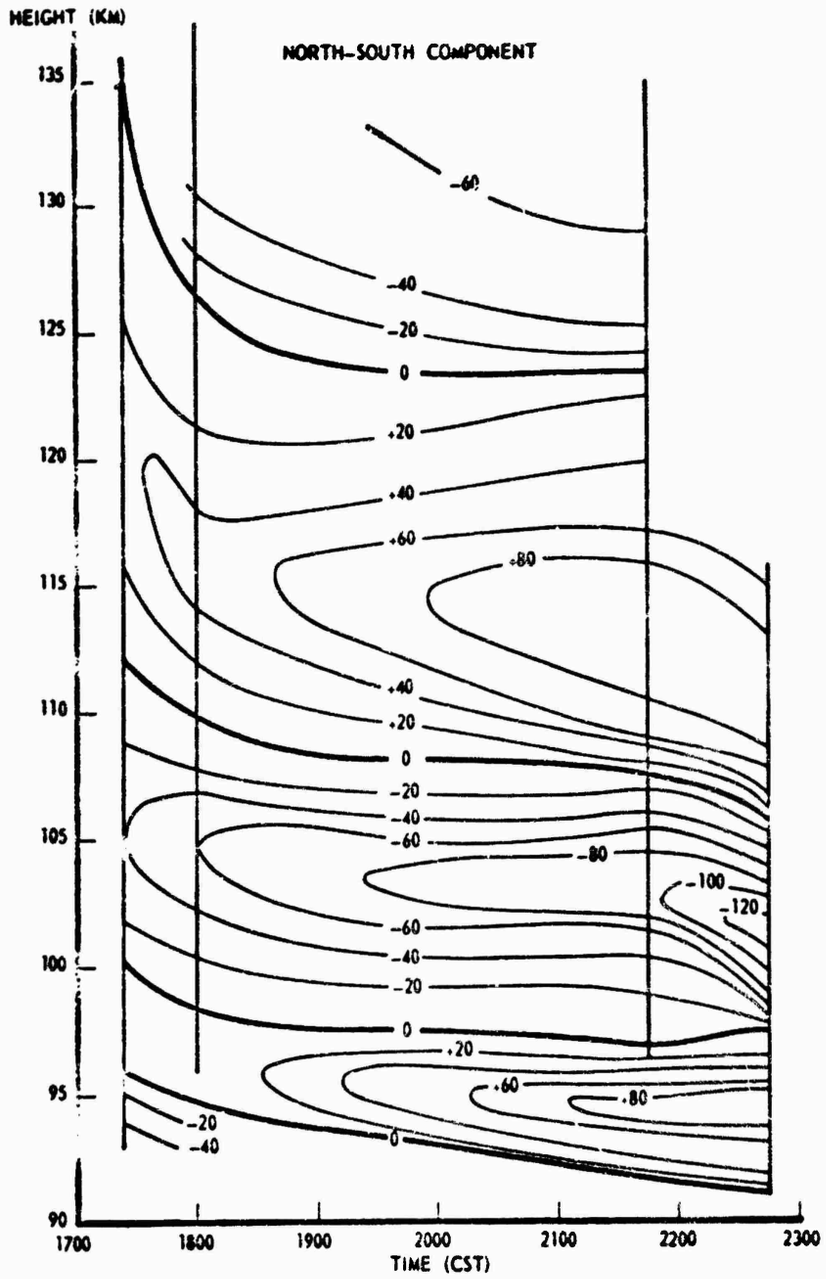

Figure 5. North-South Wind Contours from 1720 to 2245 CST on 3 December 1962 over Eglin Air Force Base, Florida as a Function of Altitude

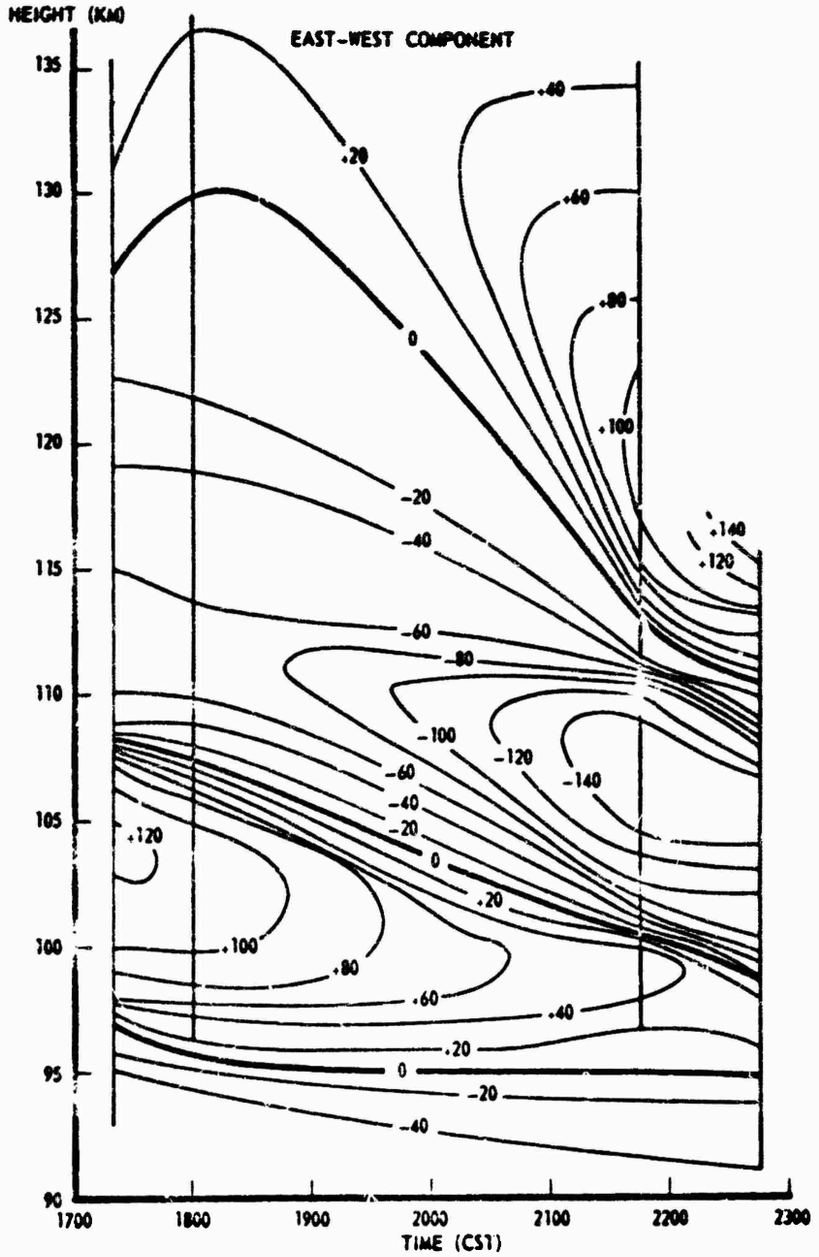

Figure 6. East-West Wind Contours from 1720 to 2245 CST on 3 December 1962 over Eglin Air Force Base, Florida as a Function of Altitude

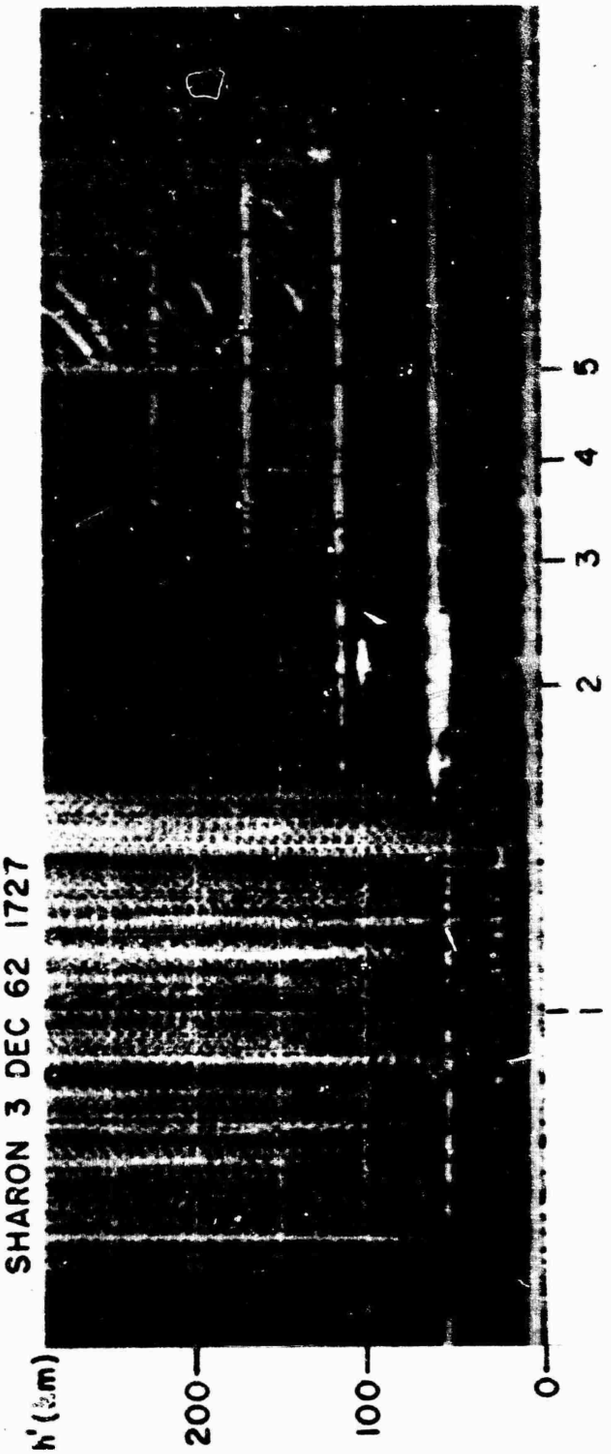

Figure 7. Ionospheric Sweep-Frequency Records Taken at the Time of Release 1726 CST

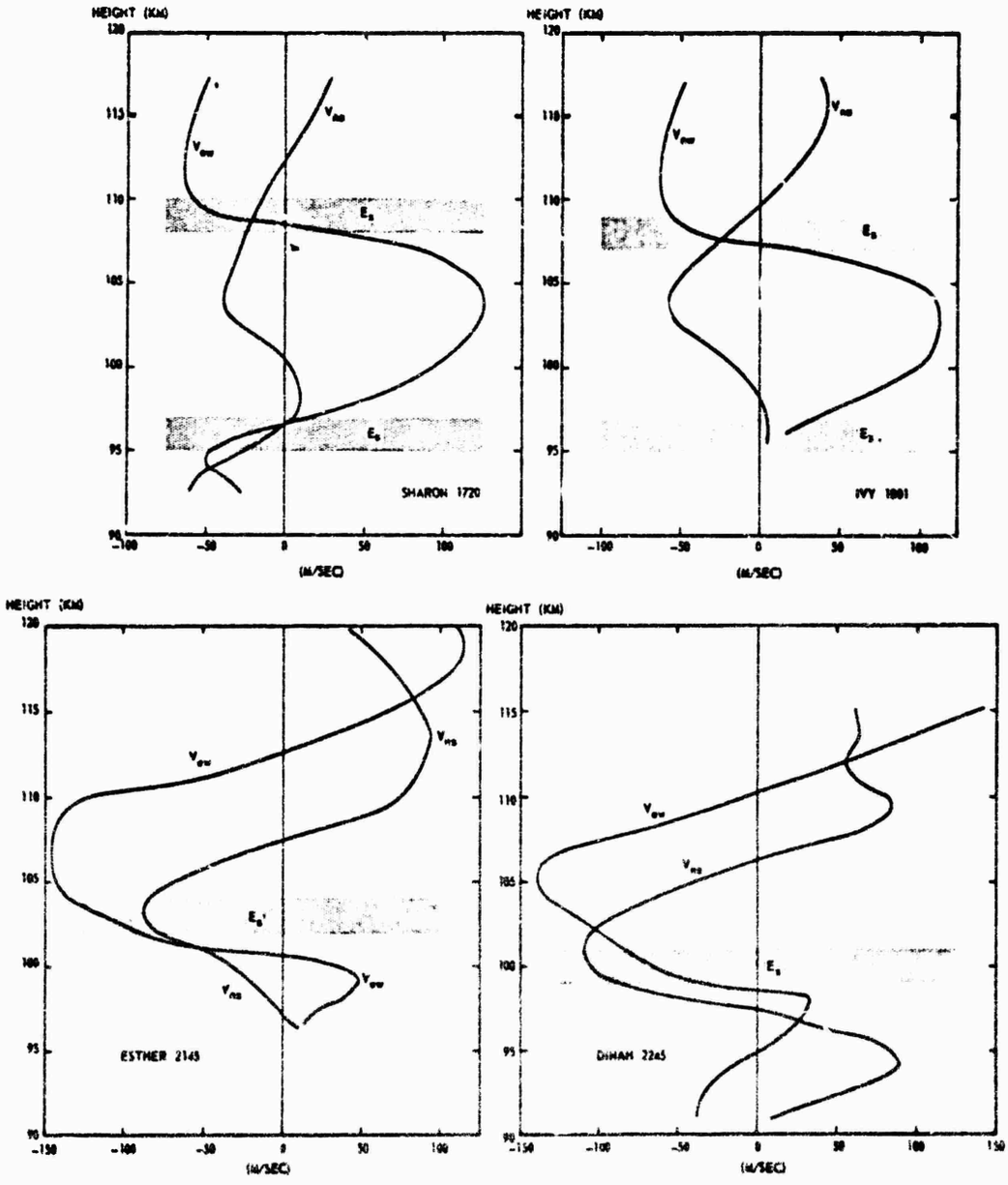

Figure 8. NS and ES Plots of Wind Speed as a Function of Altitude Showing Correlation with Observed Altitudes of Sporadic E

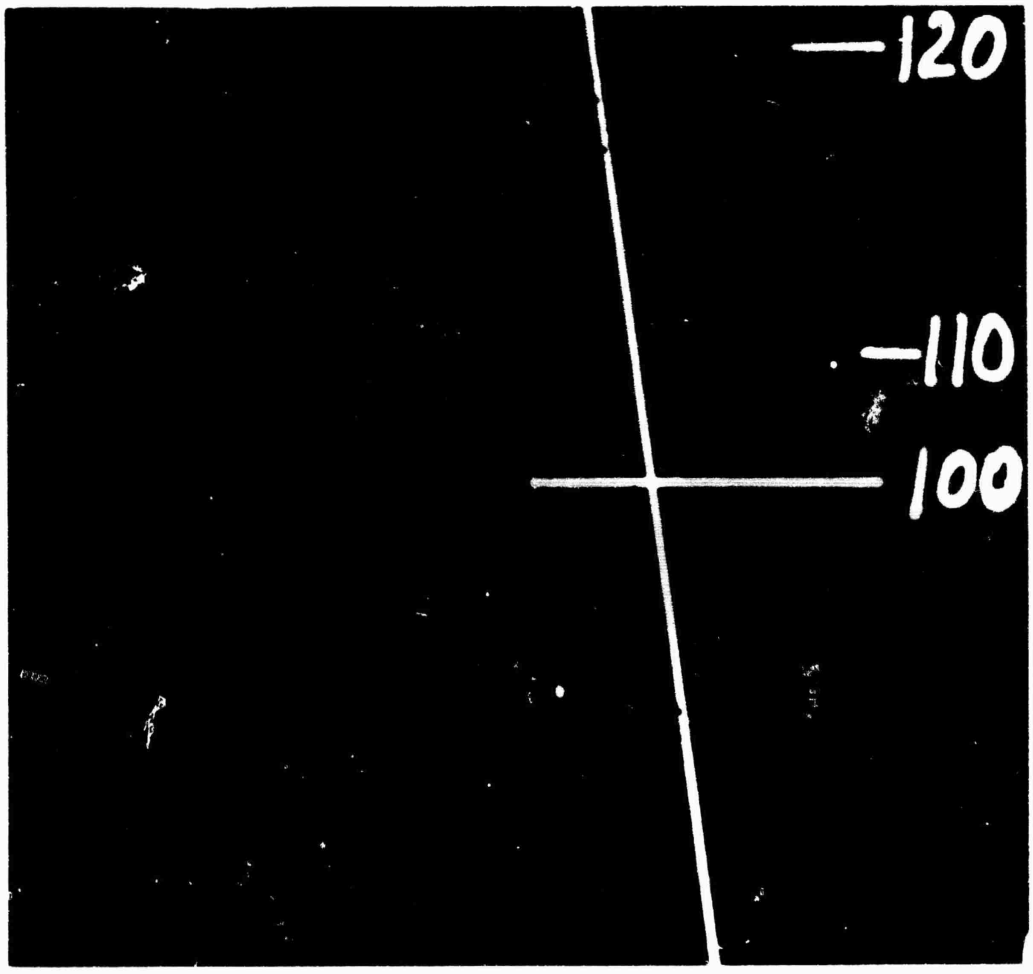

Figure 9. Photograph of the 1720 CST Twilight Release Showing High Wind Shears at 97 and 109 km

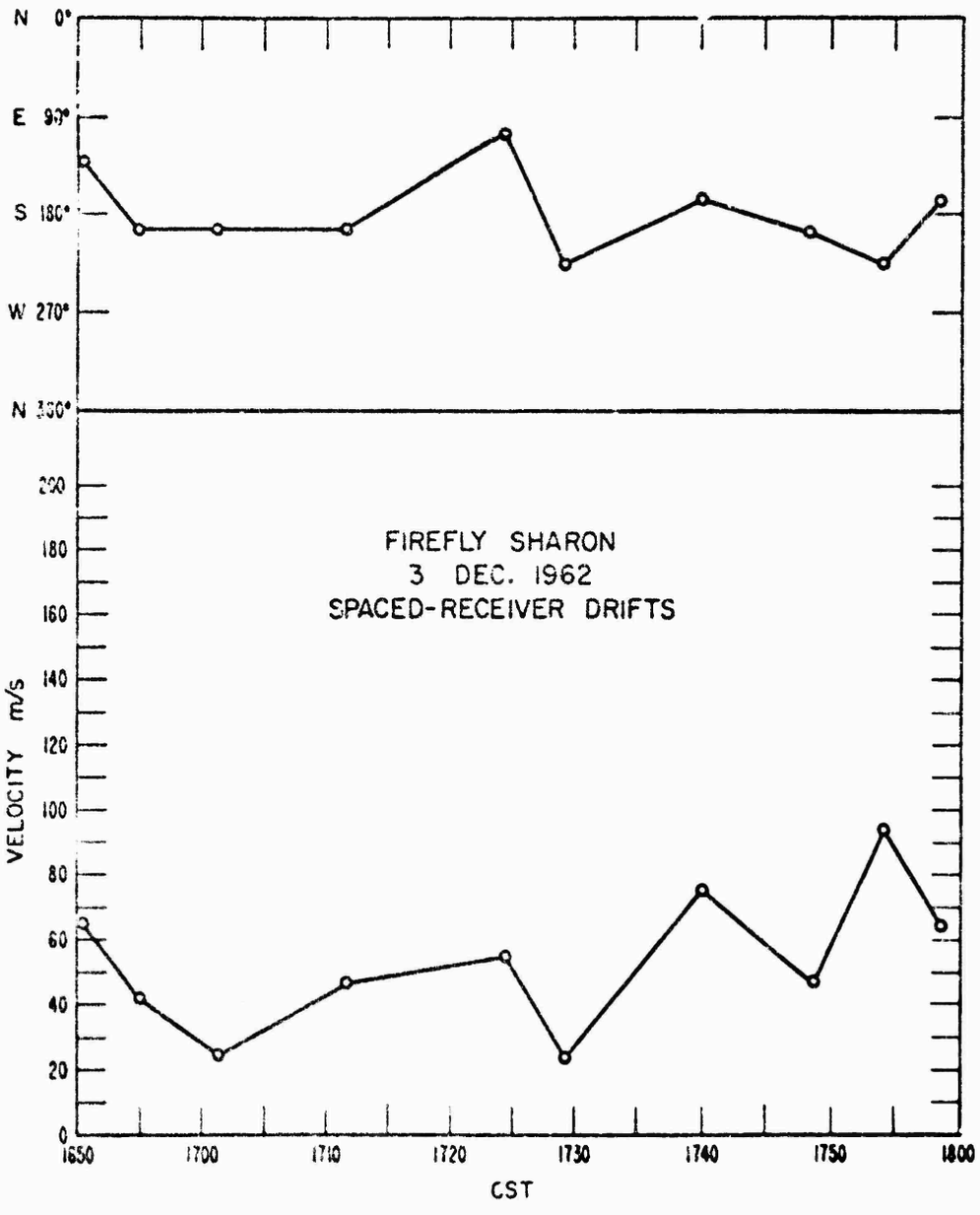

Figure 10. Magnitude and Direction of Wind Velocity as Observed by the Spaced-Receiver Techniques for the 1720 CST Release

XIV. Wind Shear Theory of Sporadic E

Malcolm A. MacLeod
Air Force Cambridge Research Laboratories
Bedford, Massachusetts

Abstract

Equilibrium electron density profiles have been obtained for wind shear induced layers of ionozation in the lower E region by assuming a constant shear neutral wind profile and neglecting the effect of diffusion. A comparison of the maximum electron densities predicted with those observed when simultaneous observations of sporadic E and wind shears were made gives order of magnitude agreement. The theoretical model appears to have the capability of explaining the formation of certain types of sporadic E layers.

1. INTRODUCTION

Recent observations[1] have confirmed that a close correlation exists between the occurrence of some sporadic E layers and the occurrence of large vertical shears in the neutral wind of the ionosphere. The purpose of this report is to present in condensed form the results of a study of a simplified theoretical model of a wind shear produced equilibrium sporadic E layer. A more detailed development of these results will be submitted for publication elsewhere.

Although the basis of the theory presented here is that of Axford,[2] the idea that neutral wind shears acting in conjunction with the geomagnetic field could produce changes in the ionization densities of the ionosphere seems to be traceable to Dungey.[3,4] Following the recognition of the correlation between the magnitude of the horizontal component of the geomagnetic field and the occurrence of sporadic E (Heisler and Whitehead[5]), Whitehead[6,7] suggested that vertical shear of the horizontal neutral wind should lead to the formation of thin layers of ionization. Whitehead discussed the formation of such layers under the influence of a sinusoidal neutral wind profile, including a quantitative estimate of the effects of photoionization and recombination, and a qualitative estimate of the effects of diffusion. Axford[2] subsequently developed a more general formulation of the theory, treating diffusion quantitatively, including the effect of vertical motion of the neutral component, and making somewhat different assumptions about the inclusion of the electric field effects. The portion of the discussion given by Axford which is applicable to the sporadic E problem was also expressed in terms of a sinusoidal wind profile. With the exception of a very idealized case (where the effects of recombination, photoionization, horizontal electric fields and the vertical neutral velocity were neglected), Axford relied on the numerical integration of a differential equation to obtain the equilibrium electron density profile, as did Whitehead. The current work is not restricted in this manner. The practical difference between the two treatments is that Whitehead allowed for a shear in magnitude and direction of the neutral wind, but did not treat diffusion quantitatively, whereas Axford allowed only a shear in magnitude, but did treat diffusion quantitatively.

The assumption of a sinusoidal neutral wind profile seems quite reasonable in view of the observational data available.[1] However, as may be seen by inspection of the electron density profiles which Whitehead and Axford obtained, the maximum ionization density occurs in the altitude region where the sine function may be approximated closely by the first term in its power series expansion. This corresponds to the case where the neutral wind profile exhibits a constant vertical shear. In this report, the results of an analytical investigation of the equilibrium electron density profiles produced in this constant shear region will be presented and compared with the pertinent Firefly data.[1]

2. TEMPERATE ZONE SPORADIC E CHARACTERISTICS

Certain assumptions and simplifications which are useful in the development of the theory are suggested by the characteristics of temperate zone sporadic E. The characteristics presented below have been excerpted from the review by Rawer.[8]

(1) There is no direct correlation with solar activity.

(2) The long term fluctuations in the occurrence of sporadic E are similar to fluctuations of climatological variables.

(3) A correlation exists between the strength of the sporadic E ionization density and the horizontal component of the geomagnetic field.

(4) The majority of sporadic E layers occur in the altitude range 90 to 130 km.

(5) Sporadic E layers are relatively thin with a thickness of about 1 km being typical.

(1) and (2) above suggest that the neutral winds of the ionosphere may be involved in the production of sporadic E layers, while (3) indicates that the geomagnetic field exercises some control over the formation process. If one accepts the altitude dependence of ρ_+ (the ratio of the ion-neutral collision frequency to the ion gyrofrequency) given by Axford,[2] then it can be shown that (4), together with (1) - (3), indicates that a coupled wind shear-geomagnetic force is responsible for the layer formation. (5) allows the mathematics to be simplified greatly by assuming that several atmospheric properties remain constant over the region where a sporadic E layer is being formed.

3. QUALITATIVE PHYSICAL BASIS FOR THE THEORY

The fact that appears basic to the theory is that the positive ion-neutral particle collision frequency is comparable with the ion gyrofrequency (give or take an order of magnitude) within the region where sporadic E is observed, while the electron gyrofrequency is much greater than the electron-neutral collision frequency in the same altitude region. The strong interactions affecting the ionization movement are then the ion-neutral collisions, the ion-geomagnetic field interaction, and the ion-electron Coulomb interaction.

Consider an ion alone in the ionosphere. Neglecting all other forces, it will gyrate about the local geomagnetic field direction. When the neutral particles are allowed to act on the ion through occasional collisions with no excess of momentum transfer in any direction at any altitude, the motion still consists of helical segments with no preferred direction of drift along the helical axes. However, when a vertical shear exists in the horizontal components of the neutral wind, a net vertical change in horizontal momentum transfer between the ions and neutrals is established which becomes converted by the geomagnetic field into a net momentum transfer along the geomagnetic lines of force; the ions move. The electrons, being much lighter than the ions, are dragged along with the ions in their movement by the Coulomb forces in an ambipolar diffusion process. In temperate zones, the geomagnetic field has a substantial vertical component; hence, vertical motion is produced by this mechanism. The vertical momentum transferred to the ions is clearly smallest where the neutral wind is smallest. Hence the ionization tends

either to converge to this altitude or diverge away from it, depending on the sign of the shear with respect to the direction of the horizontal component of the local geomagnetic field. If the ionization converges to some altitude, a sporadic E layer is formed. This view of the sporadic E production mechanism offers an explanation of the altitude dependence of the phenomenon. Below approximately 90 km, $\rho_+ \gg 1$; hence, collisions predominate and no E_s is expected. Above approximately 140 km, $\rho_+ \ll 1$; hence, the geomagnetic influence dominate and the collision-produced convergence and divergence becomes too slight to be observed. This behavior appears to coincide with the observational data.

4. QUANTITATIVE OUTLINE OF GENERAL THEORY

The object of this section is to sketch the derivation of the differential equation which governs the altitude dependence of the equilibrium electron density profile. Limitations of space do not permit a complete development of the theory. Hence only the basic equations of the theoretical model, the simplifying assumptions and the resulting equation will be given with very little discussion.

The basis of the theory presented here is essentially the same as that of Axford,[2] except that the neutral wind is allowed to have two horizontal components and attachment losses have been taken into account. Since the neutral wind generally exhibits a shear in direction as well as magnitude, and the consideration of attachment processes are essential for nighttime E_s layers, this amounts to an improvement on Axford's theory. It turns out that one of the simpler forms of this theory yields an expression for the coupling parameter, f, which is equal in magnitude to that derived by Whitehead,[6,7] but opposite in sign.

The basic mathematical model employed here is a macroscopic fluid dynamic one in which the ionosphere is considered to be a three component, partially ionized gas. The three components are: heavy neutral molecules, whose variables are indexed by a zero subscript; heavy positive ions of mass approximately equal to the neutral particle mass, indexed by a plus subscript; electrons, indexed by a minus subscript. The fundamental equations for each component are three:

The Equation of Motion:

$$\frac{d\vec{v}_i}{dt} = \sum_j K_{ij}(\vec{v}_i - \vec{v}_j) + \frac{e_i}{m_i}(\vec{\mathcal{E}} + \vec{v}_i \times \vec{B}) + \vec{g} - \frac{\nabla p_i}{n_i m_i} \tag{1}$$

The Equation of Continuity:

$$\frac{\partial n_i}{\partial t} + \nabla \cdot (n_i \vec{v}_i) = c_i - b_i n_i - a_i n_i^2 \tag{2}$$

The Equation of State:

$$p_i = n_i k T_i \tag{3}$$

where v_i, e_i, m_i, n_i, p_i, T_i denote the velocity, charge, mass, number density, pressure and temperature of the i th component, respectively, and K_{io} denotes the collision frequency of the i th species with the neutrals. It is assumed that there is no heat transfer in the process; hence the fourth hydrodynamic equation does not appear. Note that the continuity equation Eq. (2) contains terms representing ion creation (c), attachment (b) and recombination (a) processes.

It is convenient to adopt a right-handed local Cartesian coordinate system with y-axis directed along the horizontal component of the local geomagnetic field, z-axis directed upwards along the local vertical, and x-axis directed perpendicular to the other two in the proper sense. (In the north temperate zones, y is directed approximately northward, while x is directed eastward.)

The ratio of the number density of the ions to the number density of the neutrals is small. Hence the effect of the ion motion on the neutral motion may be neglected, and the motion of the neutral gas described fully by the wind profile:

$$\vec{U} = U_x \vec{i} + U_y \vec{j} + U_z \vec{k} \tag{4}$$

Plane symmetry is assumed; those quantities which are variable depend only on altitude.

Only the equilibrium situation is considered, hence

$$\frac{\partial n_i}{\partial t} = 0 \tag{5}$$

In view of the discussion of the preceding sections, it is assumed that the fractional rate of change with altitude of the temperature and the rates of creation, attachment and recombination are small and may be neglected.

The ion-electron gas is taken to be macroscopically neutral:

$$n_+ \approx n_- \tag{6}$$

The ratio of the ion-electron collision frequency to the electron gyrofrequency is negligible:

$$\rho_- \ll 1 \tag{7}$$

The net result of these assumptions is that the equations of motion may be solved to give an expression for the vertical ionization velocity which may then be substituted into the continuity equation Eq. (2) to yield the following general equation for the equilibrium electron density profile:

$$C_1 \frac{d^2n}{dz^2} - C_2 \frac{dn}{dz} - \frac{d}{dz}\left[n\left(\Gamma_1 U_x + \Gamma_2 U_y\right)\right] = c - bn - an^2 \tag{8}$$

where the expressions for the coefficients appropriate for the lower E region are as follows:

$$C_1 = \frac{k\left(T_+ + T_-\right)}{m + K_{+o}} \tag{9}$$

$$C_2 = \frac{\left(\frac{m_+ g}{eB_o} + \left(\rho_+ - \rho_-\right) U_z + \Gamma_3 \frac{\mathcal{E}_x}{B_o} + \Gamma_4 \frac{\mathcal{E}_y}{B_o}\right)\left(\psi_z^2 + \rho_+^2\right)}{\rho_+\left(1 + \rho_+^2\right)} \tag{10}$$

$$\Gamma_1 = - \frac{\rho_+ \psi_y}{1 + \rho_+^2} \tag{11}$$

$$\Gamma_2 = - \frac{\psi_y \psi_z}{1 + \rho_+^2} \tag{12}$$

$$\Gamma_3 = \psi_y \left(\frac{\rho_+}{\psi_z^2 + \rho_+^2} - \frac{\rho_-}{\psi_z^2 + \rho_-} \right) \tag{13}$$

$$\Gamma_4 = \psi_y \psi_z \left(\frac{1}{\psi_z^2 + \rho_+^2} - \frac{1}{\psi_z^2 + \rho_-^2} \right) \tag{14}$$

where ψ_x, ψ_y, ψ_z represent the direction cosines of the geomagnetic field with respect to the given coordinate system, with ψ_x being zero. (Note that Greek letters are used consistently to denote dimensionless quantities.) If C_1, C_2 and b are neglected, Eq. (8) takes essentially the form given by Whitehead,[6,7] but with minus signs before Γ_1, Γ_2. Eq. (8) represents the culmination of the general theory.

5. CONSTANT SHEAR, NO DIFFUSION THEORY

Neglecting diffusion (setting C_1 equal to zero), and assuming a linear neutral wind profile of the form

$$U_x = U_{xo} + U'_{xo}\, z$$

$$U_y = U_{yo} + U'_{yo}\, z\,, \tag{15}$$

allows Eq. (8) to be reduced to the form:

$$f \frac{d}{dz_s} (n\, z_s) = - C + bn + an^2 \tag{16}$$

where

$$f = \Gamma_1 U'_{xo} + \Gamma_2 U'_{yo} \tag{17}$$

and

$$z_s = z + (C_2 + \Gamma_1 U_{xo} + \Gamma_2 U_{yo}) / f \tag{18}$$

Eq. (16) may be simplified by putting it into dimensionless form. To that end, define the following variables:

$$\nu = \frac{n}{n_o}$$

$$\zeta = \frac{z_s}{z_o}$$

and the following parameters:

$$\tau_c = \frac{c}{n_o f}$$

$$\tau_a = \frac{b}{f}$$

$$\tau_r = \frac{a n_o}{f}$$

Here n_o, z_s denote the ambient electron density and the altitude where the electron density returns to the ambient density, respectively. The parameters τ_c, τ_a, τ_r, have simple interpretations. Each one represents the ratio of the time constant which is characteristic of the sporadic E production mechanism (1/f) to the time constant which is characteristic of the corresponding process taking place in the ambient (n_o/c, $1/b$ or $1/an_o$). On substituting the above definitions into Eq. (16), the dimensionless differential equation for the electron density profile becomes.

$$\zeta \frac{d\,\nu}{d\,\zeta} = - \tau_c + (\tau_a - 1)\, \nu + \tau_r\, \nu^2 \tag{19}$$

The solution of Eq. (19), which reduces to $\nu = 1$ where $\zeta = 1$, is easily found to be:

$$\zeta^{\sigma} = \left(\frac{\nu - \nu_+}{\nu - \nu_-}\right)\left(\frac{1 - \nu_-}{1 - \nu_+}\right) \tag{20}$$

or

$$\nu = \frac{(\nu_+ - \nu_-)\ (1 - \nu_-)}{(1 - \nu_-)\ \Gamma\ (1 - \nu_+)\ \zeta^{\sigma}} + \nu_- \tag{21}$$

where

$$\nu_{\pm} = \frac{1 - \tau_a \pm \sigma}{2\tau_r} \tag{22}$$

and

$$\sigma = [(1 - \tau_a)^2 + 4\tau_r \tau_c]^{1/2} \tag{23}$$

As $\zeta \to 0$, $\nu \to \nu_+$. To be physically reasonable, ν must be defined as being positive. Since ν_+ carries the sign of τ_r (that is, the sign of f), positive f implies a positive value of ν at $\zeta = 0$, and negative f implies the reverse. Thus, only positive values of the coupling parameter give physically acceptable solutions. If can be shown that if the (τ_c, τ_a, τ_r) values are such as to ensure equilibrium, then

$$\nu_+ \geq 1 \tag{24}$$

Now as $\zeta \to \infty$, $\nu \to \nu_-$, which by similar reasoning is negative for positive f. However, the solution is not used beyond $\zeta = 1$ ($z_s = z_o$) because it is the altitude at which it is assumed the perturbed electron density returns to ambient. The negative lower limit on ν is due to the non-physical assumption of a linear velocity profile which is valid over all space.

For positive f (the only case considered here), ν_+ is a maximum and ν_- a minimum of the normalized electron density profile. Typical profiles are shown in Figures 1 and 2, where it has been assumed that $\tau_a = 0$, $\tau_c = \tau_r$. When the sporadic E time constant becomes shorter than the other time constants, that is, when the wind shear-geomagnetic force predominates over the creation, attachment and recombination, the maximum E_s densities can become very high indeed (Figure 2). On the other hand, when the sporadic E time constant becomes much longer than the others, the maximum E_s density differs but little from ambient.

If is clear from Figure 2 that diffusion processes must modify the maximum electron density profile for large f (small τ_i) values, but the qualitative appearance of the profile should remain much the same. By examining the derivative of the

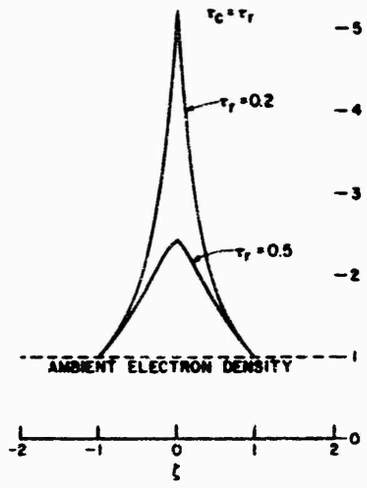

Figure 1. Sporadic E Electron Density Profile

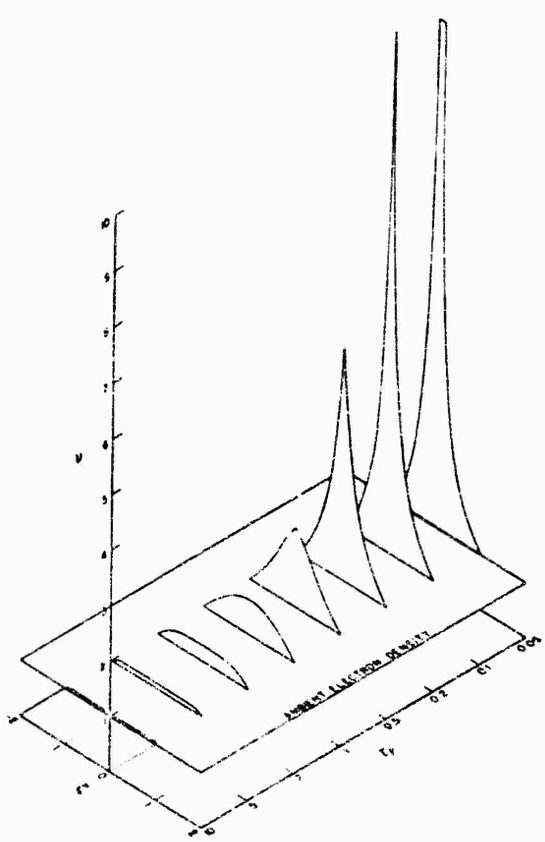

Figure 2. Sporadic E Electron Density Profile

electron density profile, $\nu'(\zeta)$, one can see a tendency for outward-moving particle currents to form at either side of the maximum at $\zeta = 0$. In a more rigorous treatment these tendencies must be offset by the wind shear-geomagnetic force, which decreases the layer formation tendency by an amount which is not taken into account here. Thus ν_+ will be decreased by an amount which is a function of the ratio of the wind shear-geomagnetic time constant to the diffusion time constant. The effect of diffusion will be discussed in more detail at a later date.

The simultaneous measurements of wind shear and $f_o E_s$ reported on in the preceding report allow the theory to be compared (incompletely) with observational data. The only point of comparison available is the sporadic E frequency which is a measure of $\nu(0)$ for which no electron density profiles are as yet available. According to the classic formula, the sporadic E frequency is given by Ratcliffe:[9]

$$f_o E_s = [n_{Es}]^{1/2} \times 1.12 \times 10^{-2} \qquad \text{(MCPS)} \tag{25}$$

where the maximum sporadic E electron density is given in general by:

$$n_{Es} = \nu_+ n_o \tag{26}$$

Thus, in order to predict $f_o E_s$, nine quantities must be known: $(a, b, c, n_o, \rho_+, \psi_y, \psi_z, u'_{xo}, u'_{yo})$. Of these quantities, only four are known with reasonable accuracy: $(\psi_y, \psi_z, u'_{xo}, u'_{yo})$; the values of the remaining ones must be estimated. A representative value of $a = 10^{-8}$ cm^3/sec was taken for the effective recombination coefficient, the possible variation with time after sunset being disregarded (see Ratcliffe[9]). Representative values of the effective attachment and creation coefficients were taken from the book of Nawrocki and Papa.[10] The direction cosines of the geomagnetic field were calculated using the values of the geomagnetic elements given in the USAF Handbook of Geophysics.[11] The altitude variation of ρ_+ was assumed to be given by the curve of Axford.[2] The data on wind shears and sporadic E frequencies and altitudes which are utilized here were taken from the results of four rocket flights launched from Eglin Air Force Base, Florida, on 3 December 1962 (see preceding report). The four flights with their launch times are as follows: SHARON, 1720 CST; IVY, 1801 CST; ESTHER, 2145 CST; DINAH, 2245 CST. A sporadic E return was observed six times during the four flights. In four of these cases, the shear was such that f was positive and the present equilibrium theory could be applied. A comparison of the predicted and observed sporadic E altitudes and frequencies is given in Table 1. The values of the parameters used in the calculations are given in Table 2. The values of u'_{xo} and u'_{yo} were estimated from the north-south and east-west velocity profiles given by Rosenberg, Edwards and Wright[1] after applying the appropriate coordinate transformation.

TABLE 1. Comparison of predicted and observed sporadic E altitudes and frequencies

Flight	Time (CST)	E_s Altitude (km)		$f_o E_s$ (MCPS)	
		Predicted	Observed	Predicted	Observed
Sharon	1720	-	96	-	1.02
		108	109	9.3	6.2
Ivy	1801	-	96	-	0.3
		107	108	7.9	6.2
Esther	2145	101	103	4.9	2.7
Dinah	2245	99	100	3.8	2.5

TABLE 2. Sporadic E parameters

$a = 10^{-8}$ cm^3/sec, $\psi_y = 0.47$, $\psi_z = -0.85$						
Flight	Predicted E_s Altitude (km)	b (sec^{-1})	ρ_+	u'_{xo} (sec^{-1})	u'_{yo} (sec^{-1})	f (sec^{-1})
Sharon	108	10^{-3}	3.45	-0.062	-0.002	$+7.9\times10^{-3}$
Ivy	107	9×10^{-4}	3.95	-0.051	+0.009	$+5.9\times10^{-3}$
Esther	101	8×10^{-4}	9.5	-0.054	-0.025	$+2.7\times10^{-3}$
Dinah	99	9×10^{-4}	12.9	-0.057	-0.012	$+2.1\times10^{-3}$

As it turns out, the ion creation rate is too small even to influence ν_+ for SHARON, so that the following approximation is valid:

$$\nu_+ = \frac{1 - \tau_a}{\tau_r} = \frac{f - b}{a n_o} \quad , \tag{27}$$

which permits the sporadic E frequency to be written as:

$$f_o E_s = \left[\frac{f - b}{a}\right]^{1/2} \times 1.12 \times 10^{-2} \qquad \text{(MCPS)} \tag{28}$$

Thus the ambient electron density does not exert any perceptible influence on the sporadic E frequency. The predictions of Table 1 were made with this formula.

It is seen from Table 1 that the simple constant shear theory predicts the E_s altitude and frequency rather closely. The difference between the predicted and observed altitudes is generally within the limits of error ($\pm$ 1 km) of the ionosonde method which was employed to determine the altitudes. All predicted sporadic E frequencies are higher than those observed, which is consistent with the view that diffusion should be taken into account, since the effect of diffusion will be to lower the maximum of the sporadic E electron density profile and hence to lower $f_o E_s$. The closeness of agreement between the calculated and observed values of $f_o E_s$ must be regarded as somewhat fortuitous in view of the uncertainties in the assumed parameters. When more exact values of some of these parameters are known, these numbers may have to change by as much as an order of magnitude either way. A change upwards in the numbers would seem more hopeful for the theory than the opposite change, since the inclusion of the effect of diffusion will certainly lower the sporadic E frequencies predicted by the present theory. The question as to whether or not the effect of diffusion is so large as to swamp the wind shear-geomagnetic effect completely will have to be left for clarification by future work. But the impression given by the present results is that the wind shear model possesses sufficient latitude to account for the formation of some sporadic E layers.

The problem of how to account for the two E_s layers which seem to occur where f is negative is unsolved at this writing. One possible explanation involves the generation of a non-equilibrium layer through a positive divergence mechanism (f negative) which pushes the ionization away from the reference altitude. Another possible explanation invokes an altitude shift, see Eq. (18), of an ionized layer from a region of negative divergence (f positive) to the edge of a region of positive divergence. For both cases here, this would be an upward shift. The solution of these difficulties lies in future work.

Acknowledgments

The writer wishes to record his indebtedness to Dr. Norman W. Rosenberg for suggesting this problem and for his continuing interest and assistance, and to Dr. Dan Golomb for several helpful discussions.

References

1. N.W. ROSENBERG, H.D. EDWARDS and J.W. WRIGHT, preceding paper.
2. W.I. AXFORD, J. Geophys. Res. 68: 769, 1963.
3. J.W. DUNGEY, J. Atmos. Terr. Phys. 8: 39, 1956.
4. J.W. DUNGEY, J. Geophys. Res. 64: 2188, 1959.
5. L.H. HEISLER, and J.D. WHITEHEAD, Nature, 187: 676, 1960.
6. J.D. WHITEHEAD, J. Atmos. Terr. Phys. 20: 49, 1961.
7. J.D. WHITEHEAD, The Formation of a Sporadic E Layer From a Vertical Gradient in Horizontal Wind, in Ionospheric Sporadic E, ed. by E. K. Smith and S. Matsushita, Pergamon Press, 1962.
8. K. RAWER, Structure of E_s at temperate latitudes, in Ionospheric Sporadic E, loc. cit.
9. J.A. RATCLIFFE, The Ionosphere, in Physics of the Upper Atmosphere, ed. by J.A. Ratcliffe, Academic Press, 1960.
10. P.J. NAWROCKI, and R.J. PAPA, Atmospheric Processes, Geophysics Corporation of America, August, 1961.
11. Handbook of Geophysics, United States Air Force Air Research and Development Command, Air Force Research Division, Geophysics Research Directorate, MacMillan Company, 1959.

XV. Chemiluminescent Techniques for Studying Nighttime Winds in the Upper Atmosphere*

N. W. Rosenberg and D. Golomb
Air Force Cambridge Research Laboratories
Bedford, Massachusetts

E. F. Allen, Jr.†
Device Development Corporation
Weston, Massachusetts

For the study of large-scale mass-transport processes (wind speed, direction, and shear, diffusion and turbulence), rocket-released smoke trails have been used for altitudes below 80 km, and the twilight, sodium trail has been used for higher altitudes.[1] However, the latter is restricted to a 20 to 40 minute period at sunset and sunrise, when the cloud is sunlit and the sky background is dark.

Two different types of payload for generating persistent, glowing trails under full night conditions have recently been designed and flown by this laboratory, and their effectiveness has been evaluated. Photographs of the trails can be treated by triangulation techniques to obtain mass motion parameters throughout the night.

The first type (1) of payload is based on the chemiluminescent reactions of vaporized aluminum and/or its oxides with the atomic oxygen of the upper atmosphere; the second type (2) on the reaction of atomic oxygen with nitric oxide.

---

* Reprinted from J. Geophs. Res., 68, 3328 (1963)
† Present affiliation: AFCRL

(1) The aluminum trail. A mixture consisting of 74 per cent cesium nitrate, 23 percent aluminum powder, and 3 percent nagnesium powder was pressed at a forming pressure of 20,000 lb/in^2 into a cylindrical grain (diameter, 7.11 cm; length, 15.5 cm; weight, 1.75 kg). The grain was placed in a phenolic-linen sleeve in a steel cylinder. The mix was ignited by a pyrotechnic train, consisting of squibs, ignition pellets, and a booster, and the reaction products were vented through a convergent tungsten nozzle with a 0.5 cm throat. In ground tests at an ambient pressure of 25 mm Hg, the unit burned for about 40 to 50 seconds. The initial chamber pressure was 35 atm and the average chamber pressure was 12 atm. The burning properties of the mix were somewhat erratic because of inhomogeneities and nozzle clogging. (The fabrication and ground testing of this payload were performed under contract by Atlantic Research Corporation, Alexandria, Virginia.)

Thermochemical claculations[2] indicate that at a chamber pressure of 12 atm, the flame temperature is about 4100°K and the major reaction products per kilogram of mix are as follows: 1.9 moles N_2 (gas), 3.5 moles Cs (gas), 3.6 moles Al_2O_3 (condensed), 0.7 mole Al (gas), 0.25 mole AlO (gas), 0.09 mole NO (gas), and 0.04 mole O_2 (gas). This composition may change, of course, during expansion of the exhaust products.

Three such units were mounted in the rocket. When the rocket attained an altitude of 80 km, the three units were ignited and separated by shaped charges. Each properly burning unit was visible as a bright point of light, following the rocket trajectory, some separation occurring between units because of the additional 3 kg thrust imparted by the exhaust gases. In the six rockets fired, about twelve (of eighteen) units ignited properly and burned for 40 to 100 seconds. At least one unit on each of five payloads burned for 100 seconds. Below 100 km there was no persistent afterglow, but above 100 km, at full night conditions, the exhaust gases formed a glowing trail readily photographed with an f/2.5 lens, 20 second exposure, and Royal-X Pan film. It persisted about 180 seconds after release in the region between 100 and 120 km and decreased gradually in persistence to about 30 seconds at 160 km. The visible trail was several hundred meters in diameter, depending on altitude and time after release. Figure 1 is a 20 second exposure of a trail during which the unit was still burning at an altitude of 140 to 150 km. The trajectory is marked with a dotted line. The still-glowing exhaust trail had already been subjected to severe wind shears, readily measured from two or more such photographs taken at separated sites. Spectrograms taken of the persistent (chemiluminescent) part of the trail showed a continuous emission peaking at 5300 A.

The photon yield of the trail gases was remarkably high. About 20 g/km of exhaust products were deposited; this is equal to about 1.2×10^{23} molecules/km

Figure 1. The Aluminum Trail at 100 to 150 km Altitude, 30°N, 87°W, 3 Dec 1962, at 2145 CST (6 hours after sunset). Royal-X Pan Film, 20 Second Exposure, f/2.5. Photograph Courtesy of H. Edwards, Georgia Institute of Technology.

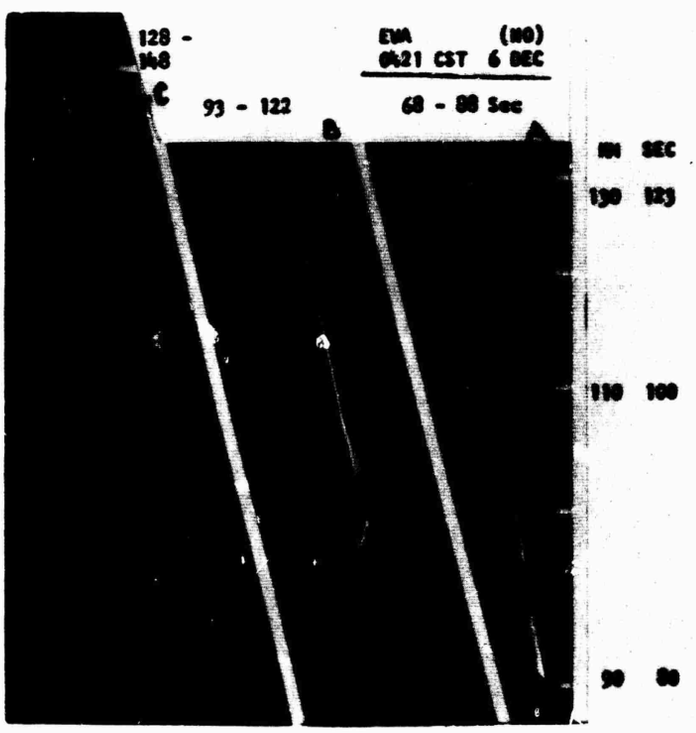

Figure 2. The Nitric Oxide Trail at 90 to 135 km Altitude, 30°N, 87°W, 6 Dec 1962, at 0421 CST (1 hour before sunrise). Royal-X Pan Film, f/2.5. Frame A: - 10 to +10 seconds from Initiation of Release, Frame B: +20 to +40 Seconds, Frame C: +50 to +70 Seconds. Courtesy of H. Edwards.

with the product composition listed above. Image densitometry of the exposed film showed that an average of 2×10^{20} photons/sec were emitted from each kilometer of the trail (containing 1.2×10^{23} molecules). Thus the photon yield per second per exhaust molecule was about 2×10^{-3}. Integrating over 30 seconds of trail glow at this intensity, we found a total photon yield of 0.06 per molecule. Since only a fraction of the exhaust molecules participated in the light-emission process, the photon yeild per active molecule must have been much higher. It was greater than unity if AlO, constituting 3 percent of the total number of molecules deposited, was the active molecule. This would require a cyclic light-emitting process in which the active molecule was regenerated. Although full analysis of the phenomenon is not yet complete and laboratory simulation of the glow is only beginning, we suggest the following possible reaction mechanism:

(a) $AlO + O \rightarrow AlO_2^*$ formation of excited state

(b) $AlO_2^* + M \rightarrow AlO_2 + M$ collisional deactivation

(c) $AlO_2^* \rightarrow AlO_2 + h\nu$ radiative decay

(d) $AlO_2 + O \rightarrow AlO + O_2$ regeneration of AlO

Below 100 km, were the atmosphere is dense and collisional deactivation is probable, process (b) would predominate over (c), and there would be no light emission from AlO_2^*. The role of aluminum in night glows was previously suggested by Woodbridge[3] in connection with explosions of aluminized grenades at high altitudes.

The glow has been proved to be due, at least in part, to aluminum and its oxides. In a separate experiment in this test series, a mixture of aluminum granules inbedded in a purely organic high explosive, without any other inorganic constituent, was exploded at 114 km. A spherical glow that developed after burst was photographable for about 100 seconds. It has a continuous spectrum similar to the trail glow. The same explosive, without aluminum, gave no glow under the same conditions.

(2) The nitric oxide trail. Nitric oxide was released as a trail from a rocket-borne, pressurized tank in the 90 to 160 km region. This release resulted in a continuous spectrum of shorter persistence (150 seconds at about 100 km, falling off below and above this altitude), but still sufficient for wind measurements. The advantage of the NO trail is that a lasting glow resulted in the 90 to 100 km region also, where the aluminum glow was not persistent. Furthermore, the more readily understood mechanism of the NO glow[4] may enable us to estimate the ambient atomic oxygen concentrations.

Figure 2 presents three 20 second exposures of a NO trail, with 10 seconds between successive frames. In frame A, the rocket traversed the 90 to 100 km region; in frame B, the 103 to 130 km region; in frame C, the 135 to 145 km region. The intense white line was a bright glow observed close to the nozzle of

the tank; it was associated with the mixing region around the NO jet expanding to ambient pressure. Its diameter (about 50 m at 100 km altitude) depended on altitude and the discharge rate of NO. This 'headglow' then developed into the persistent trail. In frame C, the 60 second trail was still clearly photographable and the work of wind shears is obvious.

It should be noted that concurrently with the experiments reported here a NO release was made by a Canadian group, and it will be described in a forthcoming paper.[5]

Detailed reports of these experiments, including wind vectors, molecular and turbulent diffusion coefficients, and ambient atomic oxygen concentrations, as functions of altitude and time of night are in preparation.

References

1. E. J. MANRING and H. KNAFLICH, Measurement of winds in the upper atmosphere during April 1961, J. Geophys. Res. 67: 3923, 1962.
2. R. FRIEDMAN, et al., Atlantic Research Corporation, Alexandria, Va., Final Report, to Air Force Cambridge Research Laboratories, Contract AF 19 (628)-295, 1962.
3. D. D. WOODBRIDGE, High altitude glow measurements in Australia, in Chemical Reactions in the Lower and Upper Atmosphere, 373-390, Interscience Publishers, New York, 1961.
4. A. FONTIJN and H. I. SCHIFF, Absolute rate constant for light emission of the air afterglow reaction for the wavelength region 3875-6200 A, in Chemical Reactions in the Lower and Upper Atmosphere, 239-254, Interscience Publishers, New York, 1961.
5. G. B. SPINDLER, The chemiluminescent reaction of nitric oxide with E-region atomic oxygen, Can. Auronautics Space Inst. J., in press 1964.

XVI. Chemiluminescence of Trimethyl Aluminum Released into the Upper Atmosphere*

N. W. Rosenberg, D. Golomb, and E. F. Allen, Jr.
Air Force Cambridge Research Laboratories
Bedford, Massachusetts

In a recent note,[1] two methods were described for the formation of persistent self-luminous trails in the upper atmosphere above 90 km. Such trails are useful for the measurement of winds, wind shears, and turbulence throughout the night. One method was based on the release from a rocket of the reaction products of a cesium nitrate-aluminum burner, the other on the release of gaseous nitric oxide. Since the resulting high-quantum-yield glow from the aluminized mixture was believed to be due to the interaction of vaporized aluminum or its oxides with atmospheric oxygen atoms, a more convenient method was sought for dispersing gaseous aluminum compounds into the upper atmosphere. This was recently achieved with the release of trimethyl aluminum (TMA).

About 1100 g of liquid TMA (8×10^{24} molecules) were contained in an inner cylindrical vessel of 1800 cm^3 volume mounted within an outer sleeve forming the payload skin. The void space in the inner vessel was pressurized with nitrogen to 25 atm. A heating tape wrapped around the inner vessel permitted heating of its contents to 70°C before launch. It was calculated that during flash vaporization

* Reprinted from J. Geophs. Res., 68, 5895 (1963)

at this temperature about 40 per cent of the liquid would vaporize and the remainder would freeze. A shaped charge was mounted around the inner vessel which cut it open upon initiation with a squib when the rocket attained the proper altitude. Two 1.2 cm diameter portholes were drilled through the outer skin of the payload to allow the escape of the liquid and vapor into the atmosphere.

The experiment was conducted over Eglin AFB, Florida, on 18 May 1963, at 0255 CST. The release was initiated at 94 km altitude, but about 15 seconds were required for the liquid to escape through the portholes as the rocket climbed to 102 km altitude. An intensely luminous cylindrical trail about 20 km long developed along the rocket trajectory with maximum diameters of 2 km at 7 seconds, 3 km at 22 seconds, and 7 km at 100 seconds. At about 100 km altitude, the trail was visible to the naked eye and photographable for about 1000 seconds. Photography[2] permitted triangulation of the cloud from which diffusion, turbulence, and wind data may be obtained.

Figure 1 is a montage of selected photographs taken from Mexico Beach, Florida, 120 km east of the release area with a K-24 camera(175 mm, f/2.5, 5 second exposure) and Royal-X Pan film. Times (after release) are noted on each frame, and approximate altitudes are noted along the left side of the figure. A $CsNO_3$-Al burner[1] was carried in the same payload and may be seen leaving a trail at higher altitudes.

Spectral analysis was provided, and Figure 2 presents densitometer traces of the spectrums of the TMA glow, of the $CsNO_3$-Al burner glow, and of an unidentified star in the field of view which may be considered a continuum blackbody source. (The star image is noisy because of the small image size compared with the film grain size.) It is noted that the aluminum burner and the TMA glows are nearly identical continua over the film sensitivity range (4000 to 6800 A) and have a considerably higher red content than the star image. The dip in all spectrums at 5000 A is due to a dip in the film sensitivity. The spectrum extended well into the infrared, since the image was also photographed on IR film with a Wratten 87 filter (7000 to 8500 A).

The film image diameter of the K-24 images and the growth rate were measured with a densitometer at various film densities and are plotted in Figure 3. From the known slant range, the actual cloud diameter was computed and is noted in Figure 3. A similar diagram was prepared for image area versus time, and a calibrated sensitometric strip permitted photometric estimates to be made of image brightness, total energy flux, and photon yields from the cloud. The actual surface brightness of the cloud equivalent to each density contour is included in Figure 3. The energy of all wavelengths emitted by the cloud was assumed to be as effective in film darkening as the 4500 to 5600 A radiation used to prepare the sensitometric strip. Figure 4 shows the radiated energy of the cloud, peaking

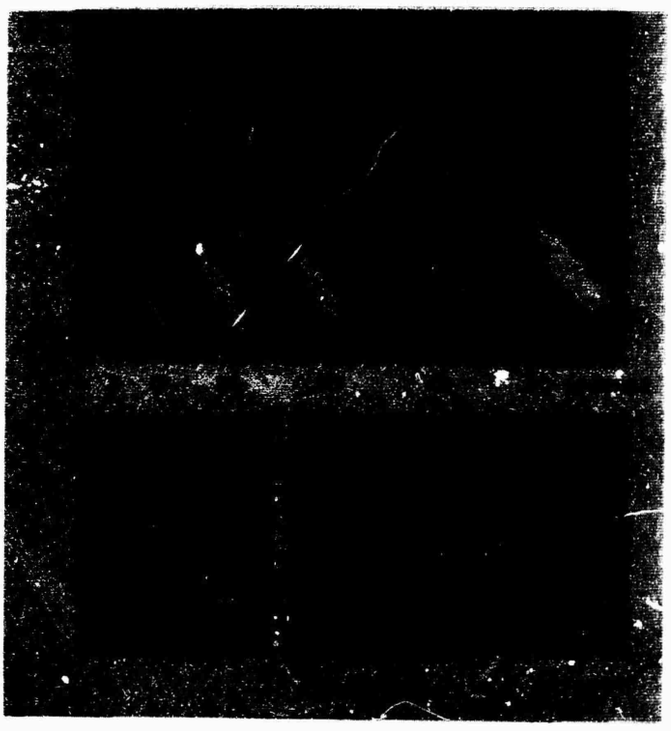

Figure 1. Montage of Photographs Showing Trimethyl Aluminum Release.

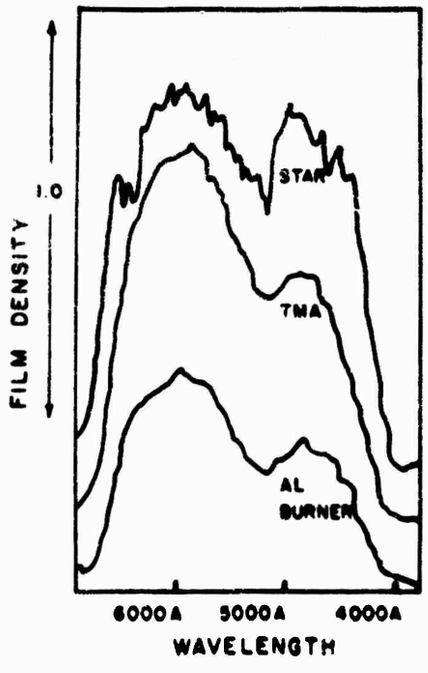

Figure 2. Spectrums of Glows From TMA Release and From Aluminum Burner Release Compared With Continuum Spectrum of a Star.

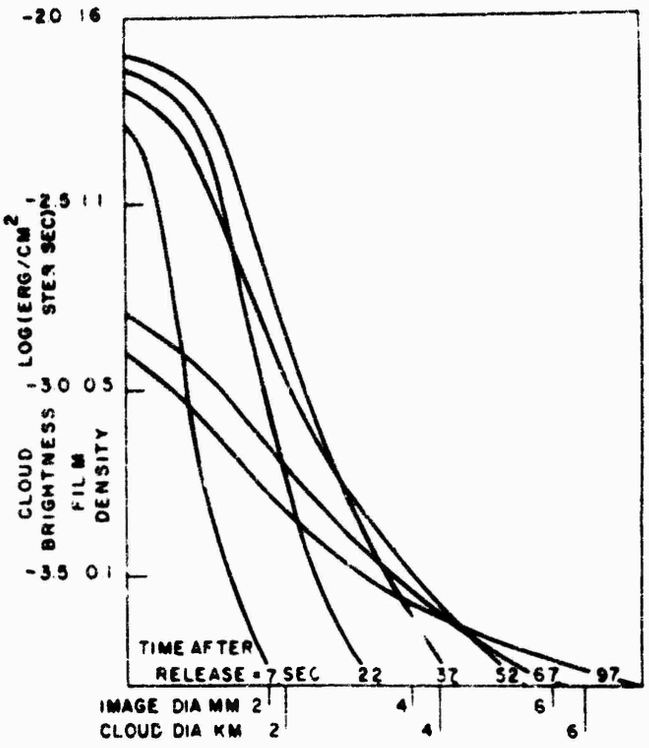

Figure 3. Brightness of TMA Release Versus Trail Diameter at Various Times After Launch.

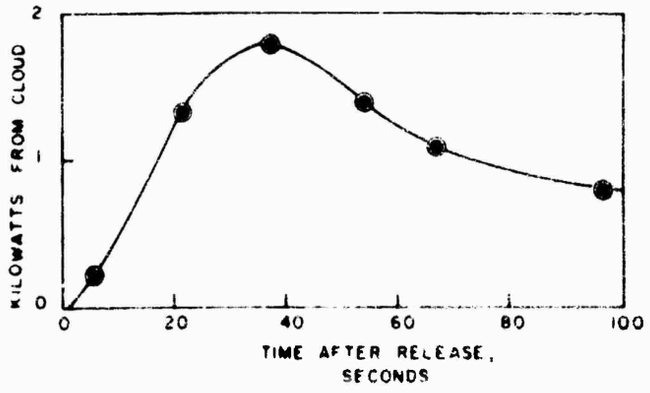

Figure 4. History of Light Emission Rate From TMA Release.

at 2 kw and averaging 1 kw over the first 100 seconds. Over the total cloud life about 200 kw sec = 2×10^{12} ergs = 4×10^{23} effective photons were emitted. However, because the radiation was more intense in the red and infrared where film sensitivity is less or nil), it is estimated that 1 to 2 $\times 10^{24}$ photons were actually produced.

Approximately 8×10^{24} molecules of TMA were released, of which about 3×10^{24} were available as vapor (5×10^{24} molecules froze). The quantum yield is thus 0.3 to 0.6 photon per vaporized TMA molecule. Few, if any, noncyclic reactions have such high quantum yields. The high yield of this reaction is probably related to the regeneration of the active species.

Another interesting estimate is the approximate over-all reaction rate, which may be derived from the following considerations. The maximum brightness of $10^{-2.1}$ erg/cm^2 ster sec occurs at 37 seconds (Figure 3). At this time, the cloud brightness falls to 1/e of its maximum at a diameter of 1.5 km = $10^{5.2}$ cm. The cloud is considered to be a cylinder 20 km long and 1.5 km in diameter, with a constant composition throughout this volume. This yields only an approximation to the actual concentration distribution, and the accuracy of the rate constant calculated below is therefore restricted to an order of magnitude. The volumetric emission must then average $10^{-7.3}$ erg/cm^3 ster sec, or in a 4π geometry $10^{-6.2}$ erg/cm^3 sec, throughout the cylinder volume of $10^{16.5}$ cm^3. The cylinder thus emits a total of $10^{10.3}$ ergs/sec equal to 2 kw, in agreement with Figure 4. The gaseous TMA (3×10^{24} molecules) may be considered to be spread over this volume, averaging $10^{8.0}$ molecules/cm^3 and reacting with a concentration of about $10^{12.5}$ oxygen atoms/cm^3 (at 100-km altitude). The total photon yield is $10^{-6.2}$ erg/cm^3 sec $\times 10^{11.3}$ photons/erg $\times$ 4 total emitted photons per film-recorded photon, or $10^{5.5}$ photons/cm^3 sec. If the reaction is between TMA and atomic oxygen, a nominal rate equation may be written as $\phi = k[O][TMA]$, where ϕ is the photon flux/cm^3 sec. Inserting the above values yields a value for k of the order of 10^{-15} cm^3/sec, a relatively slow reaction rate constant.

Regardless of the emission mechanism, the high photon yield of TMA and the simplicity of providing a trail release offer an excellent opportunity for synoptic measurements of ionospheric winds, shears, turbulence, and diffusion constants throughout the night. At present, laboratory studies of the reaction mechanism and experiments to investigate the complete altitude range in which TMA gives a persistent glow are planned.

References

1. N. W. ROSENBERG, D. GOLOMB and E. F. ALLEN, JR., Chemiluminescent techniques for studying nighttime winds in the upper atomsphere, J. Geophys. Res. 68: 3328-3338, 1963.

2. H. D. EDWARDS, M. M. COOKSEY, C. G. JUSTUS, R. N. FULLER, D. L. ALBRITTON and N. W. ROSENBERG, Upper-atmosphere wind measurements determined from twelve rocket experiments, J. Geophys. Res. 68: 3021-3032 1963.

XVII. Resonance Radiation of AlO from Trimethyl Aluminum Released into the Upper Atmosphere*

N. W. Rosenberg, D. Golomb, and E. F. Allen, Jr.
Air Force Cambridge Research Laboratories
Bedford, Massachusetts

1. INTRODUCTION

In a recent report,[1] an experiment was described in which trimethyl aluminum (TMA) was released from a rocket at night into the upper atmosphere. A persistent luminous trail formed, presumably due to the interaction of atmospheric oxygen atoms with TMA or its degradation products. The chemiluminescent trail provides an excellent marker for nighttime wind measurements in the upper atmosphere between 85 and 160 km.[2]

In this report, a similar experiment is reported in which TMA was released at twilight, so that the trail was sunlit but the sky background was dark. The purpose of the experiment was to ascertain the reaction mechanism for the TMA-oxygen interaction by spectroscopy of the resonance radiation from reaction products or intermediate species. AlO bands were observed in the sunlit part of the trail, making possible the future utilization of TMA to obtain a diatomic molecular resonance spectrum from which ambient temperatures can be determined.

---

* Submitted for publication in the J. of Geophys. Res.

2. EXPERIMENTAL

A rocket-borne chemical dispenser was designed to release TMA at a controlled rate over a desired altitude range along the rocket trajectory. About 2 kg of liquid TMA was contained in a cylindrical tank. The total payload weighed 10 kg (Figure 1). The cylinder was separated into two components by a freely-sliding piston. One compartment (2.5 liter volume) contained the liquid TMA, and the other compartment (0.8 liter volume) contained gaseous nitrogen at 15 atm pressure. When the rocket reached the desired altitude, a timer-activated explosive valve was opened, permitting the discharge of TMA. Flow control was achieved by selecting appropriate orifice sizes for the vents. A release of 20 g TMA/sec (obtained by using two 0.8 mm orifices) and a vehicle velocity of 1 km/sec gave a bright night glow in the 85-150 km region, sufficiently persistent to measure wind vectors. Heating of the TMA was unnecessary; about 40% of the TMA released at 15°C flash-vaporized in the upper atmosphere. The TMA used in this experiment contained 20% triethyl aluminum to lower the freezing point and thereby increase the fractional vaporization.

The sunlit trail was dispersed from a Nike-Apache rocket over Eglin AFB, Florida, on 1 October 1963, initiated at 04:49:22 CST on the downleg of the trajectory. The release started at 170 km and continued for 93 seconds, by which time the rocket has descended to 80 km.

The solar horizon was at about 110 km during the time of the release. A brilliant bluish-green emission was seen above the solar horizon while the lower part of the trail showed a whitish luminescence. The blue-green glow was visually observed for about 2000 seconds when it was lost against the increasing dawn background.

The trail was photographed for triangulation purposes from two sites, 100 km east and 100 km north of the launch site, with K-24 cameras (each equipped with a 175 mm f/2.5 lens) on a RXP film using 5 seconds exposures (photography was performed by the Space Physics Laboratory of Georgia Institute of Technology). Spectra were obtained from the north site with a very fast slitless spectrograph with limited resolution, since accurate determination of band shape and intensity was not contemplated in this preliminary experiment. The spectrograph was of the slitless type designed and constructed by C. D. Cooper of the University of Georgia. It consisted of a 76 mm f/0.87 lens, and a 1800 line/mm reflection grating blazed for 5000A. A mirror mounted after the grating folded the zero order image into the 4400A region of the first order spectrum. Spectra were taken on RXP film using 30 second exposures. Since the trail image had a rather large width (subtending an angle of 1° from the observation site), the resolution was in the order of 100A, and the shape of the bands do not represent the rotational structure of the vibrational bands. Slit-type spectro-photometers with 10A

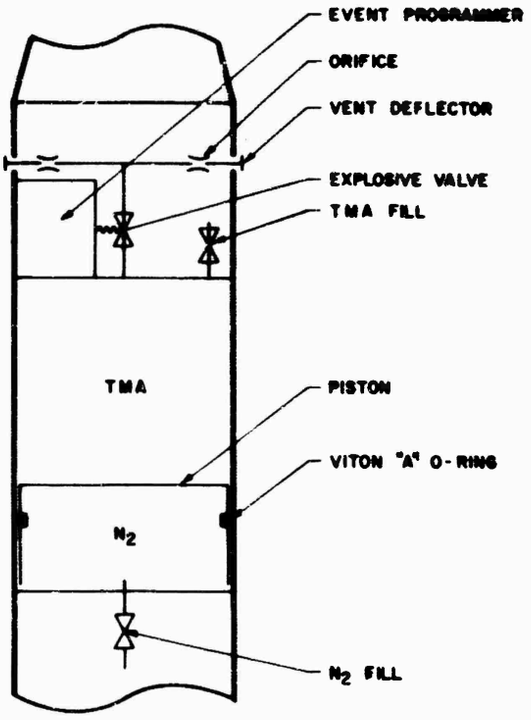

Figure 1. Schematic of the TMA Dispenser.

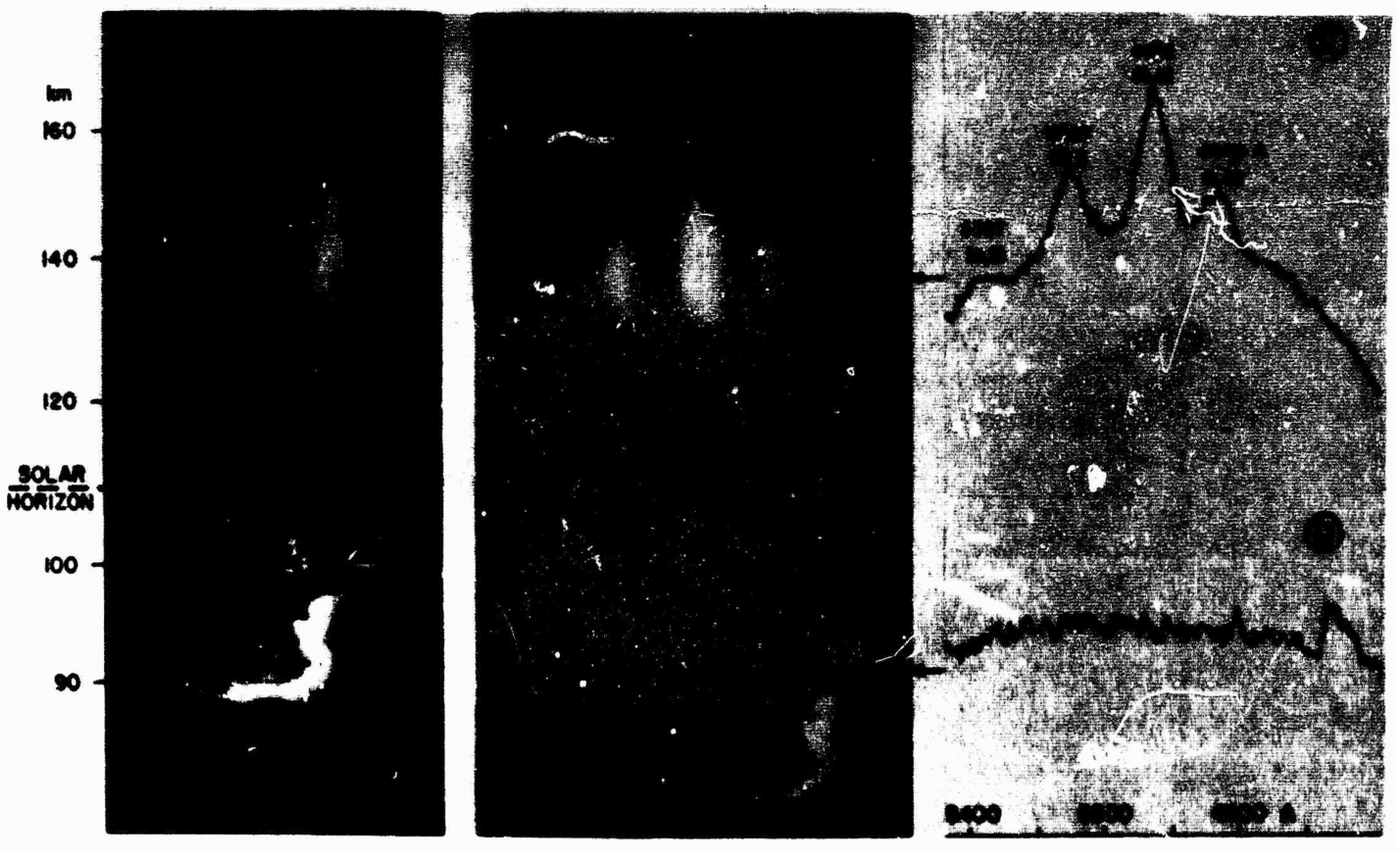

Figure 2. Photograph (A), Spectrum (B), and Densitometer Traces (C and D) of the Dark and Sunlit TMA Trail.

resolution will be required in future experiments for temperature measurements of the upper atmosphere.

3. OBSERVATIONS AND DISCUSSION

Photographic and spectrophotographic images are shown in Figure 2 which consists of four sections. Section A is the K-24 image of the trail taken 190 seconds after the release was started. Section B is the spectrographic image of the trail taken at the same time and enlarged to match the K-24 image. The folded zero order image of the trail appears in the 4400A region and displaced somewhat below the first order image. Section C is a densitometry tracing across the banded (sunlit) spectrum of the trail at 138 km altitude. Section D is a similar trace across the continuum (dark) spectrum of the trail at 92 km altitude.

The sunlit spectrum displays the blue-green AlO bands of the $A^2\Sigma^+ - X^2\Sigma^+$ transition. Similar spectra have been obtained in sunlit upper atmosphere explosions of aluminized grenades by Armstrong,[3] Authier et al.,[4] and Harang,[5] who have pointed out the utility of this radiation for temperature estimation of the ambient atmosphere. The advantage of the trail TMA release (compared with point explosions) for temperature measurement is that the altitude variation of temperature of the ambient atmosphere can be made with any desired degree of altitude resolution.

The banded spectrum does not appear below 130 km altitude, although the solar horizon at the time of the exposure was at the 110 km level. This may be due to attenuation and scattering of the exciting solar rays which had to pass through the dense lower layers of the earth's atmosphere, or to an unfavorable combination of reaction and excitation rates below 130 km. Further experiments are planned to determine the lowest altitude at which AlO bands can be observed.

The spectrum of the lower (chemiluminescent) trail is a continuum (Section D, Figure 2). It has been postulated previously[6] that AlO is an intermediary in the chemiluminescent reaction of aluminized compounds in the upper atmosphere. It was there suggested that light is emitted by the reaction sequence

$$AlO + O \rightarrow AlO_2^*$$

$$AlO_2^* \rightarrow AlO_2 + \text{pseudo-continuum.}$$

The appearance of the AlO spectrum in the sunlit trail tends to confirm this mechanism. It cannot be determined at this point whether AlO is formed in a reaction between TMA and ambient atomic or molecular oxygen.

References

1. N. W. ROSENBERG, D. GOLOMB and E. F. ALLEN, JR., Chemiluminescence of trimethyl aluminum released into the upper atmosphere, J. Geophys. Res. 68: 5895-5898, 1963.

2. N. W. ROSENBERG, Ionospheric Wind Patterns Through the Night, Fifth Conf. on Applied Meteorology, Atlantic City, 1964.

3. E. B. ARMSTRONG, Observations of luminous clouds produced in the upper atmosphere by exploding grenades, Planet. Space Sci. 11: 733-758, 1963.

4. B. AUTHIER, J. BLAMONT, G. CARPENTIER and M. HERSE, Mesure de la temperature de l'ionosphere a partir du spectre de vibration de la transition $X^2\Sigma^+ - A^2\Sigma^+$ de la molecule AlO, Compt. Rend. 256: 3870-3873, 1963.

5. O. HARANG, Excitation of AlO bands in the sunlit atmosphere and the temperature determination from the vibrational levels, Planet. Space Sci., in press 1964.

6. N. W. ROSENBERG, D. GOLOMB and E. F. ALLEN, JR., Chemiluminescent techniques for studying nighttime winds in the upper atmosphere, J. Geophys. Res. 68: 3328-3330, 1963.

XVIII. Ionospheric Wind Patterns Through the Night*

N. W. Rosenberg
Air Force Cambridge Research Laboratories
Bedford, Massachusetts

H. D. Edwards
Georgia Institute of Technology
Atlanta, Georgia

1. INTRODUCTION

Techniques for producing chemiluminous trails in the 90 to 150 km altitude region have been recently reported by this laboratory.[1, 2] The use of such trails to measure winds and shears in the ionosphere is similar to that extensively used for twilight sodium trails[3] and wind measurements throughout the night are therefore possible for the first time. Four measurements between 1720 and 2245 CST 3 December 1962 and four measurements between 1906 and 0406 CST 17 to 18 May 1963 from Eglin AFB, Florida are reported here, and correlations of wind motions with altitude time and season are examined. (No vertical motions are available from these trail studies, but previous point releases suggest vertical velocities below 5 m/sec at all altitudes of interest.)

---

* Paper delivered at the 5th conference on Applied Meteorology, Atlantic City, N. J. 1964.

2. DISCUSSION

Figures 1 and 2 present hodographs for the two nights. It will be seen that almost all wind vectors rotate clockwise (as viewed from above) with increasing altitude (that is, veer as opposed to back, which describes a counter clockwise rotation.)

In Figures 3 through 6 NS and EW components are presented for the two nights. In Figures 3 and 4 (December 3), it is seen that the altitude interval between wind nulls at a given time (that is, the half-wavelength) increases from about 5 km at 100 km, to about 20 km at 125 km. It is also seen that the maximum NS amplitudes increase from sunset to 2245, while the heights at which these maxima exist fall by about one-half wavelength over this five hour period. The EW amplitudes show similar wavelengths, and the only significant difference between the NS and EW components is that in the 100 km zone, the EW components decrease in amplitude with time, although two higher zones increase in amplitude with time.

In Figures 5 and 6 (May 17 to 18) excluding some complex patterns below 105 km, similar wavelengths and similar downward phase velocities to those of Figures 3 and 4 (December 3) are encountered, continuing through the night from sunset to sunrise. In this case, however, NS amplitudes decrease although EW amplitudes increase throughout the night.

In Figures 7 and 8 an alternate presentation of the time variation of wind patterns is made. The wind vectors at a given altitude are connected to show variation with time. Figure 7 shows a general trend of winds veering into night, at all altitudes except for the highest (130 km). Figure 8 (May 17 to 18) shows even more strikingly the wind veering with time at all altitudes from 100 to 130 km. Note that the 100 km pattern is offset from the zero axis by an (apparently) non-diurnal component. Note further that veer is greatest (1 1/2 turns sunset - sunrise) at the lowest altitude and least (1/2 turn sunset - sunrise) at the highest altitude.

The veering with height at a given time coupled with a downward phase velocity leads to the veering with time at a given height.

3. SUMMARY

The above discussion can be summarized as follows if the two nights are typical winter and summer nights and compared with the predictions of gravity waves as developed by Hines.[4]

(1) Horizontal ionospheric winds in the 90 to 150 km altitude region veer (that is, rotate clockwise viewed from above) with increasing altitude at all times of night both winter and summer.

(2) Individual (NS or EW) components of wind show a sinusoidal pattern at any given time of night. The wavelength of the pattern increases from about 10 km at 100 km, to 40 km at 125 km.

(3) A downward phase velocity is present throughout the night between 100 to 130 km with a downward velocity of about one wavelength per 12 hour night.

(4) In given zone (that is, region between two nulls), horizontal winds either increase throughout the night or decrease throughout the night. That is, in a given zone winds do not increase and then decrease in amplitude during the downward motion of the zone through the night.

(5) At any given altitude in the 100 to 130 km region, winds veer with time at a rate of about one cycle per 12 hour night, somewhat more at the lower altitudes, somewhat less at the higher altitudes.

(6) The only qualitative seasonal difference noted was that NS amplitudes increased during a winter night and decreased during a summer night. EW amplitudes increased during both nights, except in the lowest winter zone (100 km at sunset).

References

1. ROSENBERG, GOLOMB and ALLEN, J. Geophys. Res. 68: 3328, 1963
2. ROSENBERG, GOLOMB and ALLEN, J. Geophys. Res. 68: Oct 15 1963
3. MANRING, BEDINGER, KNAFLICH, J. Geophys. Res. 67: 3923, 1962
4. HINES Q. J. Roy Met Soc 89 No. 379, Jan 1963

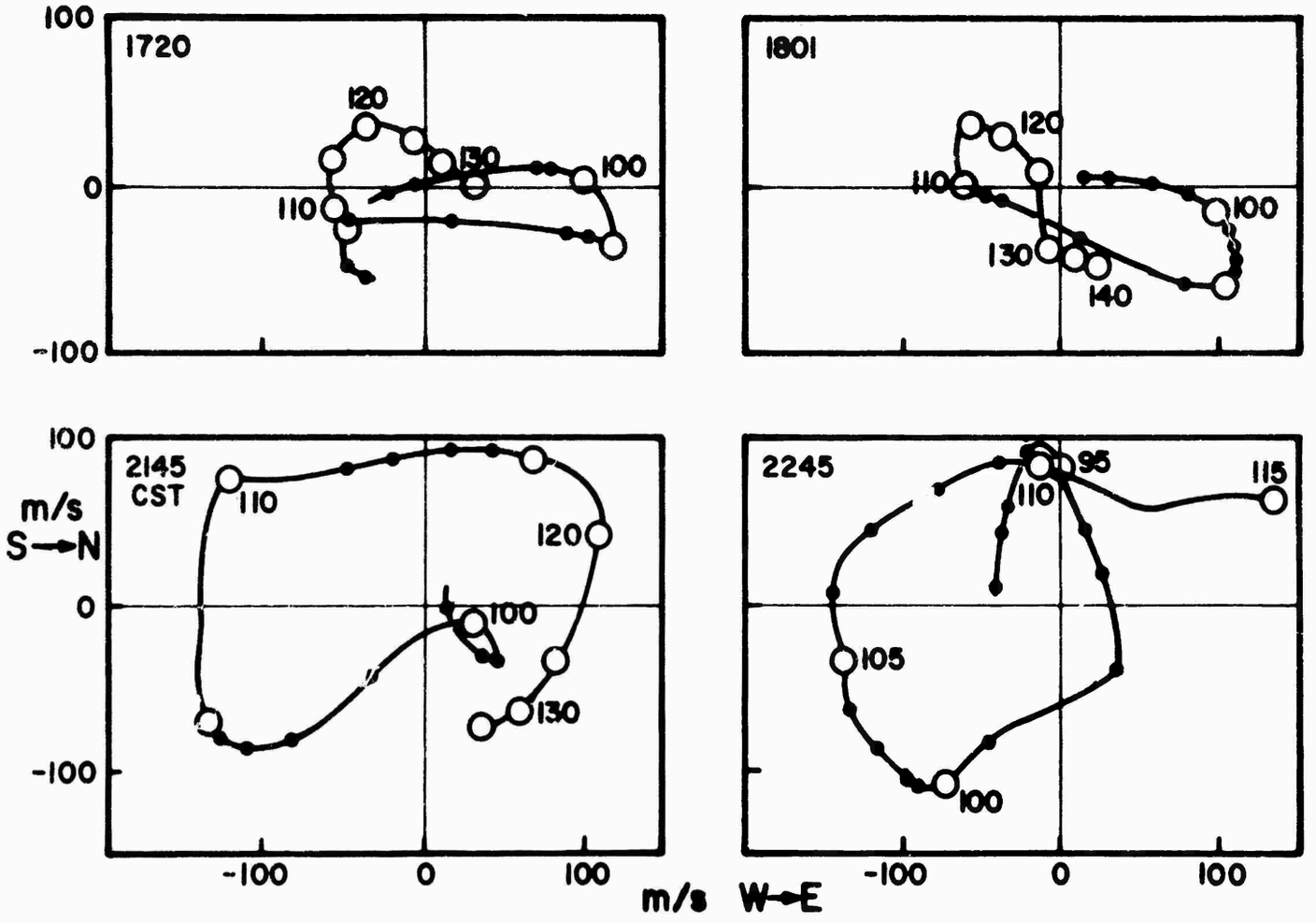

Figure 1. Wind Hodographs - Eglin AFB, Fla., 3 December 1962

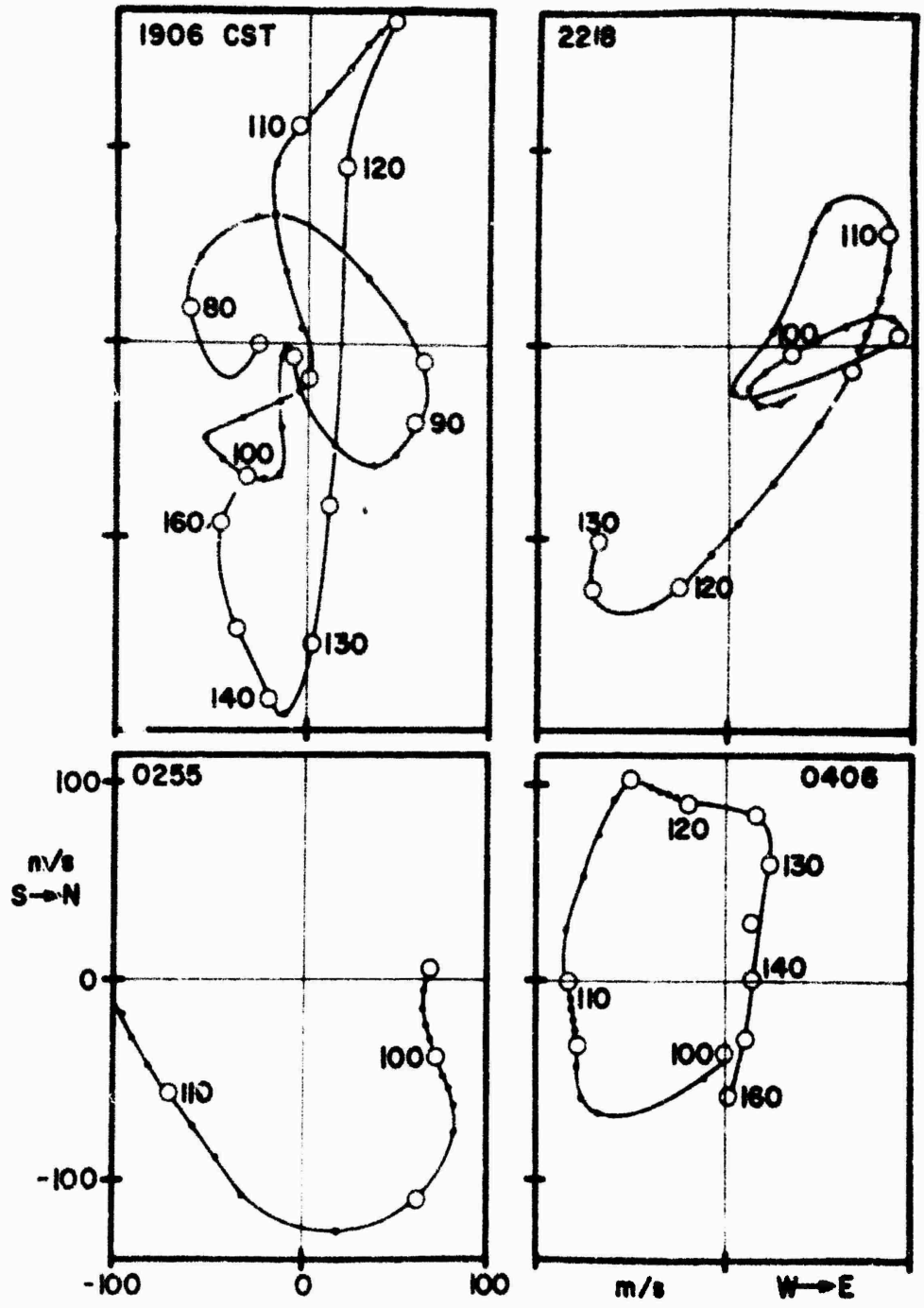

Figure 2. Wind Hodographs Eglin AFB, Fla., 17 to 18 May 1963

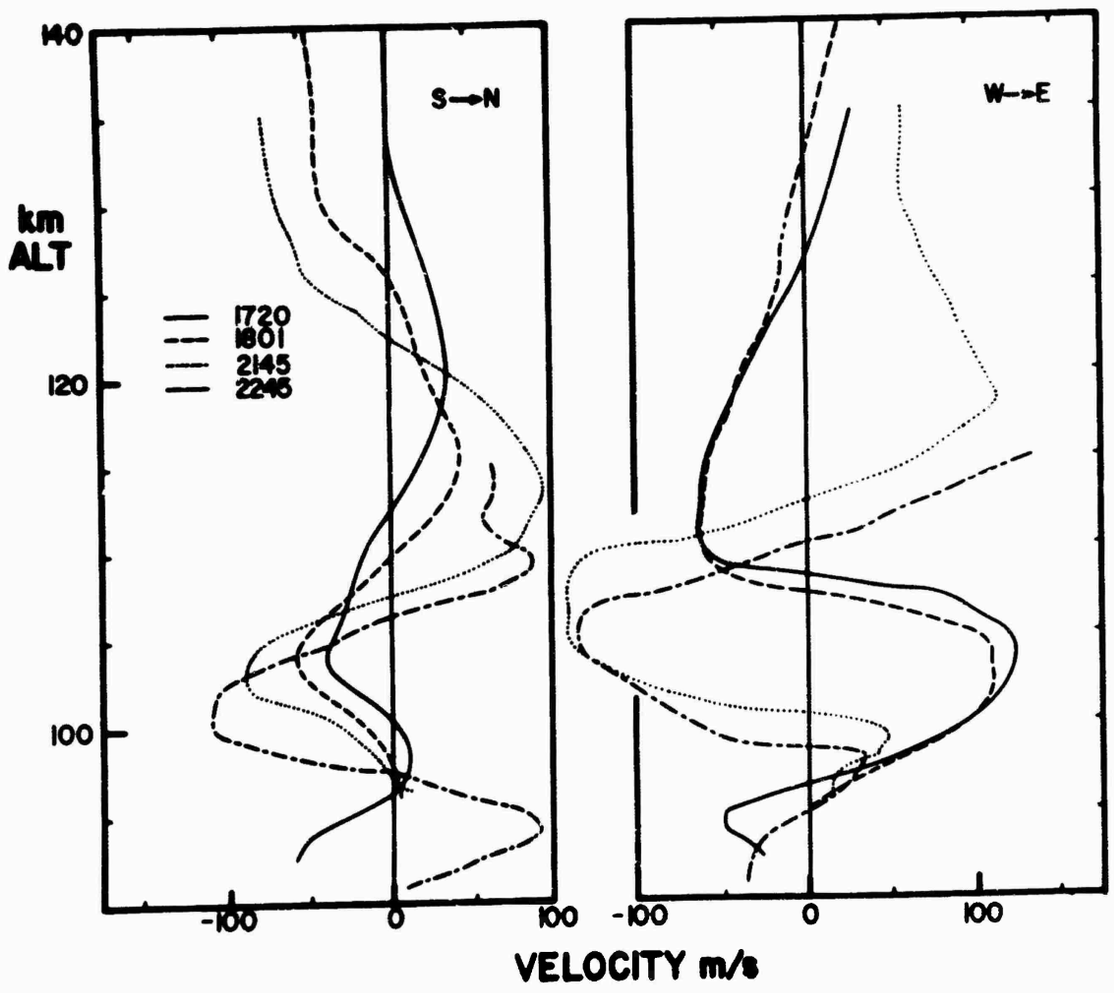

Figure 3. Wind Vectors Versus Altitude, 3 December 1962

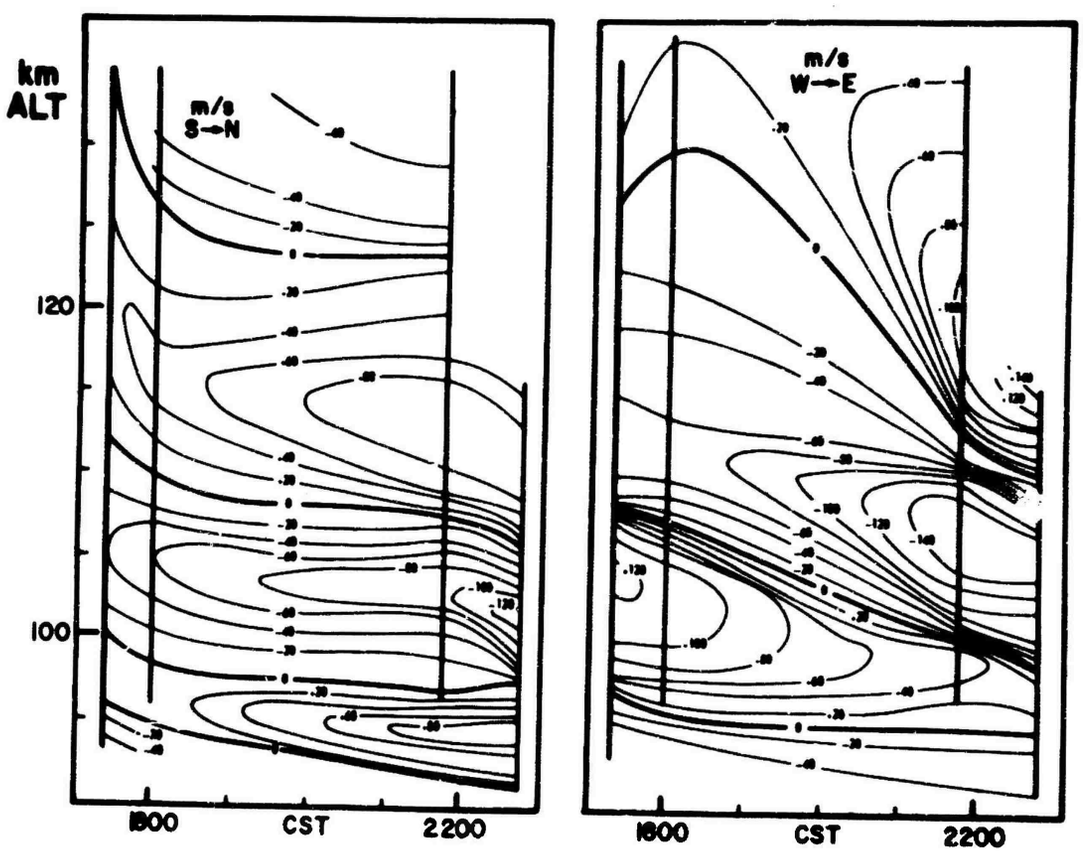

Figure 4. Wind Patterns - Eglin AFB, Fla., 3 December 1962

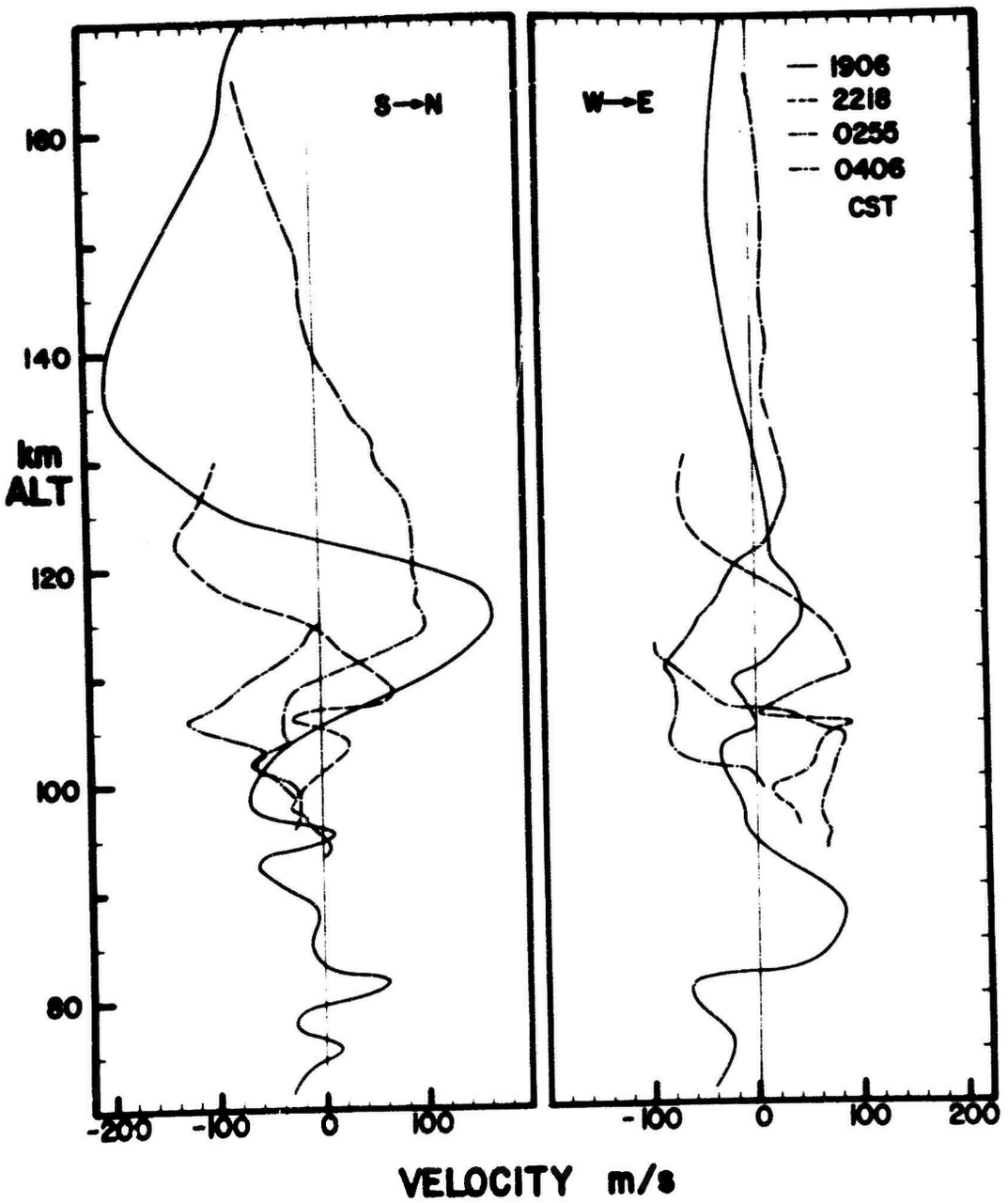

Figure 5. Wind Vectors Versus Altitude, 17 to 18 May 1963

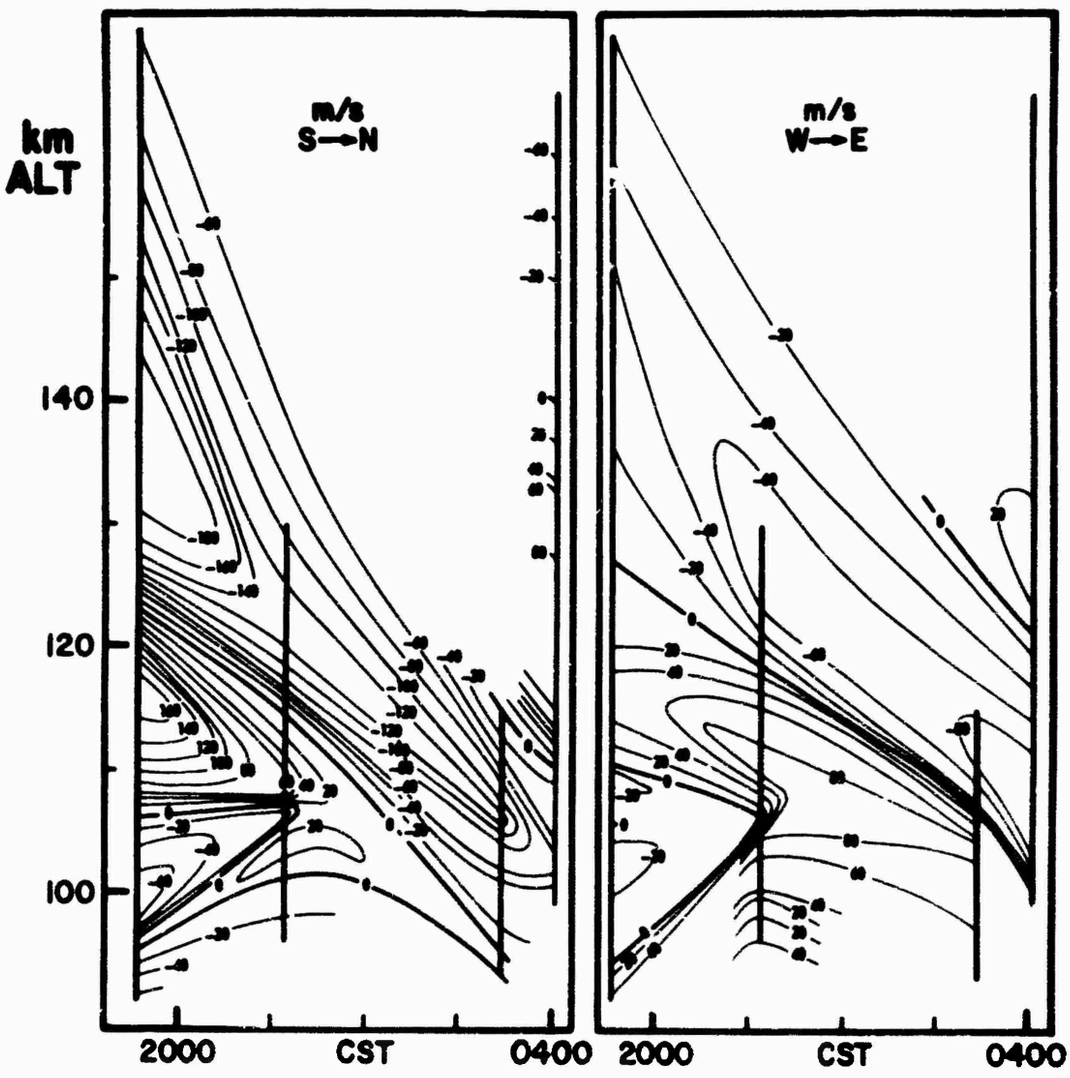

Figure 6. Wind Patterns - Eglin AFB, Fla., 17 to 18 May 1963

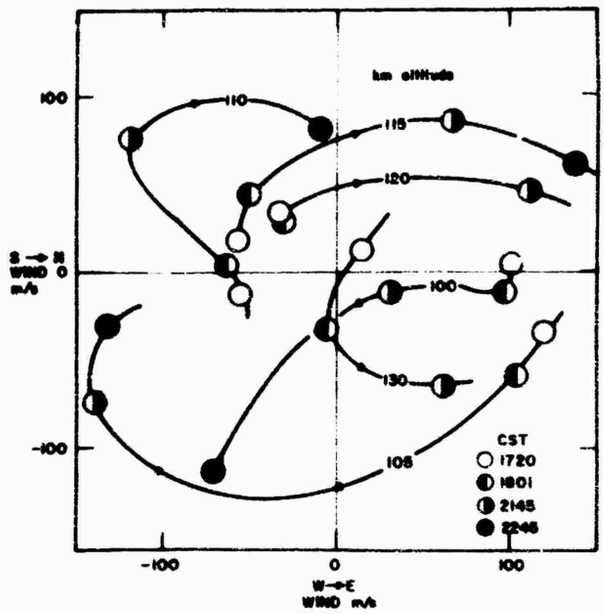

Figure 7. Wind Versus Time at Fixed Altitudes 100 to 130 km, Eglin AFB, Fla., (30°N 80°W), 3 December 1962

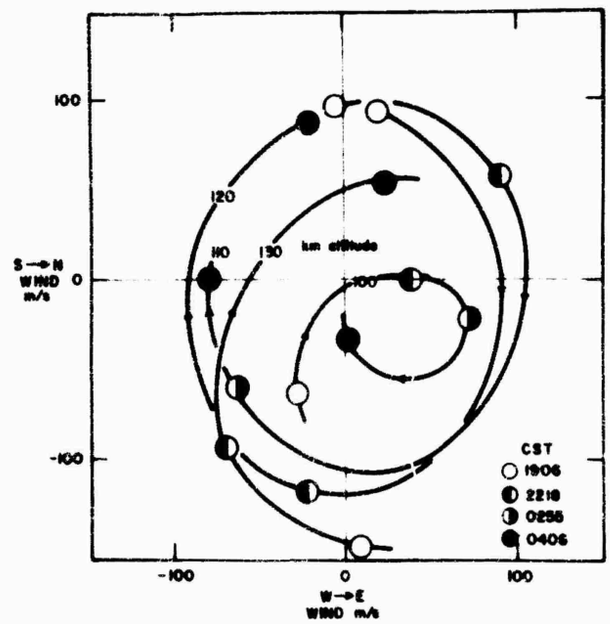

Figure 8. Wind Versus Time at Fixed Altitudes 100 to 130 km, Eglin AFB, Fla., (30°N 80°W), 17 to 18 May 1963

XIX. Acoustic Pulse Characteristics from Explosive Releases in the Upper Atmosphere

G. V. Groves
Department of Physics
University College London

Abstract

Calculations have been made of the main characteristics of a pressure pulse arriving at the ground from an explosive release in the upper atmosphere at heights between 20 and 180 km and for energies of 10^{14} to 10^{15} ergs. The quantities derived are the maximum pressure amplitude, the length of the positive pressure phase, the travel-time shortening due to the finite-amplitude of the wave, and the effect of neglecting this on temperature determination.

1. INTRODUCTION

The rocket-grenade technique for measuring upper atmosphere temperatures and wind speeds, involves the travel times of acoustical waves from grenades detonated at great heights to microphones on the ground. Temperatures are derived from the speed of sound, which is the quantity actually measured.

In the vicinity of an exploding charge the disturbance is a blast wave, which propagates eventually as a weak shock wave with a velocity approaching that of the speed of sound. The observed travel time is therefore shorter than that of a true

sound wave; that is, a wave of zero amplitude. Consideration has previously been given to the small time increment which needs to be added to the observed travel times in order to allow for this effect. [1, 2]

The problem of propagation is a complicated one, as the medium is one of varying density in which both blast-wave propagation from an explosive and the propagation of a weak pressure pulse to large distances occur. The procedure that has been followed is to divide the propagation into two regions:

(1) An initial phase where a strong shock wave is propagated in a uniform medium, and

(2) A subsequent phase where a weak shock wave propagates into a medium of increasing density.

In region (1), application is made of numerical calculations, and these then provide the initial conditions for region (2), which is treated theoretically. The transition between (1) and (2) is here taken at a point where the shock Mach number is 1.18, although this choice is arbitrary within limits. The contributions to the travel-time correction in the two regions are comparable. In region (1) the theory differs from that of Otterman in that the energy of the wave is not assumed constant, but account is taken of the non-linear hydrodynamic effects which become important over the large distance involved.

The purpose of the present paper is:

(1) To calculate the travel-time correction, and

(2) To determine the main characteristics of the pulse shape at ground level, as these are relevant to the problem of detection.

2. PROPAGATION OF A WEAK PULSE TO GREAT DISTANCES

The general features of a weak acoustical pulse which has originated from an explosion are:

(1) A pressure rise by means of a weak shock wave with over-pressure Δp_o,

(2) A positive over-pressure phase of length ℓ or duration ℓ/c_o, where c_o is the local speed of sound; and

(3) A recovery phase during which the pressure returns to its original value, with the possible presence of shock waves.

The main characteristics of the pulse will be represented in the following analysis by Δp_o, ℓ and a quantity σ which is defined in Eq. (11). The value σ depends on the pulse shape and, in turn, on the mechanism of its initial production, but is found to vary only slightly for different pulse profiles.

For a spherical sound wave originating from a source of radius r_o, Δp_o varies as r_o/r and the acoustical energy per unit surface area as $(r_o/r)^2$. Entropy changes are, however, present to order $(\Delta p_o/p_o)^3$, where p_o is ambient pressure, and over

large distances of propagation their effect becomes significant. If these are taken into account, Δp_o is found to decrease slightly more rapidly than r_o/r, in fact as $(r_o/r)(\ln r/r_o)^{-1/2}$ for a uniform medium.

When the propagation takes place in the atmosphere over vertical distances that are not small compared with one scale height, a non-spherical wavefront will arise because the upwards-moving portion must eventually accelerate to compensate for the decreasing atmospheric density. A further effect which will tend to make the wavefront non-spherical is the relative motion of the grenade with respect to the atmosphere, but as pointed out by Otterman, the asymmetry should be small as the kinetic energy of the grenade is only a small fraction of the energy of the explosion. When considering detection at the ground, only the downwards-moving portion is relevant and the amplitude of this decreases because of the increasing atmospheric density, as well as because of the geometrical effect. The wavefront Mach number M decreases to unity as

$$M = 1 + [(\gamma + 1)/4\gamma]\, \Delta p_o/p_o + 0(\Delta p_o/p_o)^2,$$

γ being the ratio of specific heats for air. For the downwards-moving part of the wavefront, a small wavefront element, therefore, propagates spherically at approximately the speed of sound if refraction by wind and temperature variations is neglected. One part of the pressure profile propagates at the speed of sound, and this is the point of zero pressure variation (N in Figure 1). The velocity of this point relative to the wavefront is $c_o(M - 1)$ and hence

$$d\ell/dt = c_o (M - 1). \tag{1}$$

But

$$dr/dt = c_o M$$

and therefore

$$d\ell/dr = 1 - 1/M = [(\gamma + 1)/4\gamma]\ \Delta p_o/p_o \tag{2}$$

If δE is the energy of a small area of the wavefront propagating at an angle θ to the downwards vertical within a solid angle $\delta\omega$ (Figure 2), then

$$\delta E = k\, \delta\omega\, r^2\, \ell\, \Delta p_o^2/p_o \tag{3}$$

where k depends on pulse shape and has been evaluated for the two cases[3] shown in Figure 1

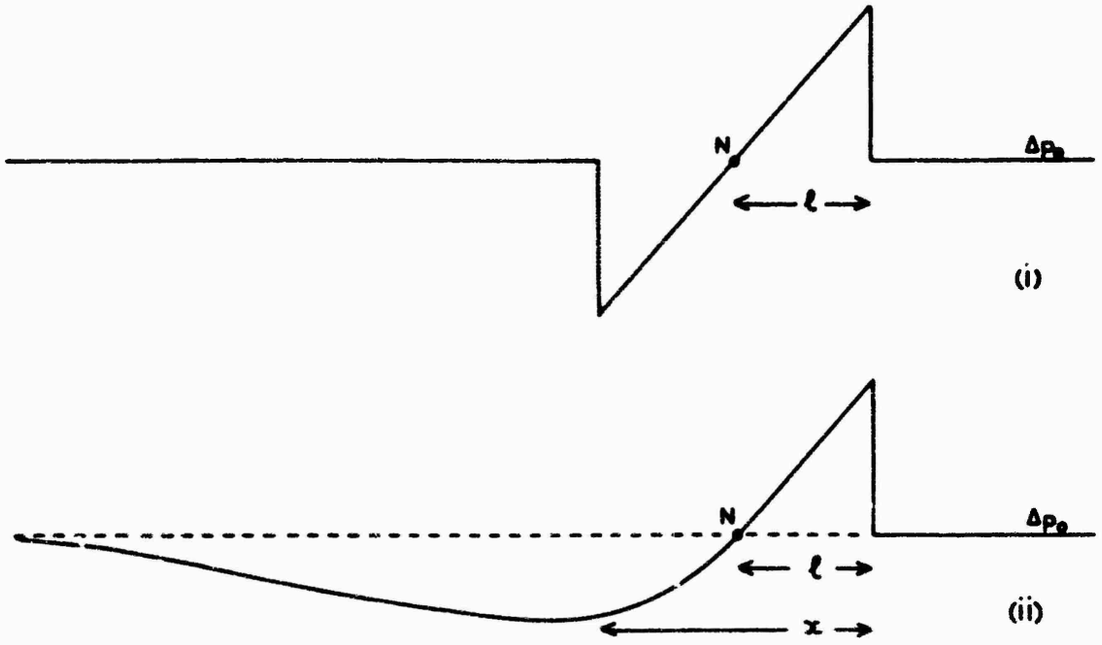

Figure 1. (i) Saw-Tooth Pulse

(ii) Linearly Decaying Pulse With Exponential Recovery

$\Delta p = (\Delta p_o)(1 - x/\ell)\, e^{-x/\ell}$

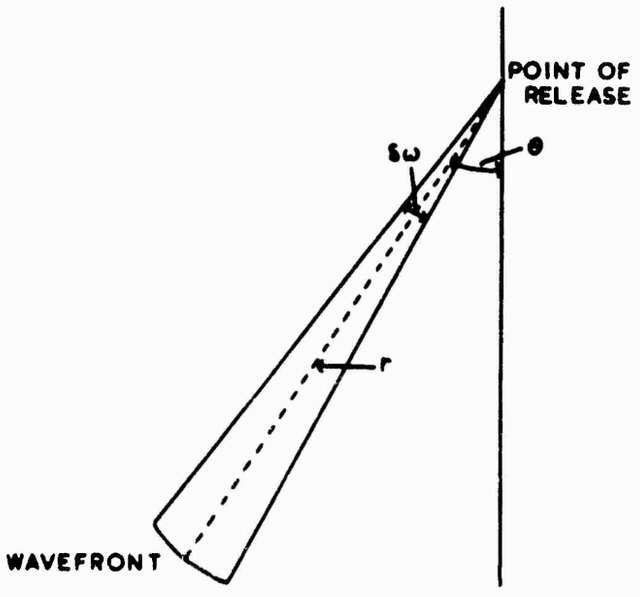

Figure 2. Propagation of Wavefront

$k = 2/3\gamma$ for Figure 1 (i)

$k = 1/4\gamma$ for Figure 1 (ii)

If distances are expressed as ratios of the length

$$\alpha = (E_{oo}/p_{oo})^{1/3} , \tag{4}$$

where E_{oo} is the explosive energy released and p_{oo} is the ambient pressure at the release height, then Eq. (3) becomes

$$y = k\lambda^2 \chi \Delta^2 (p_o/p_{oo}) \tag{5}$$

where

$$\lambda = r\alpha \qquad \chi = \ell/\alpha \qquad \Delta = \Delta p_o/p_o \qquad y = (\delta E/\delta\omega)/E_{oo} \tag{6}$$

Eq. (2) can then be written

$$d\chi/d\lambda = [(\gamma + 1)/4\gamma] \Delta \tag{7}$$

Dissipation of the acoustical energy of the pulse as heat in the atmosphere occurs in the wavefront shock and may also occur during the recovery phase, where shock waves may again be present. If ϵ is the ratio of the entropy increase in the back-shocks to that in the front shock, then it can be shown[3] that

$$dy/d\lambda = -(1 + \epsilon)\lambda^2 \Delta^3 (p_o/p_{oo})(\gamma + 1)/12\gamma^2 \tag{8}$$

Hence from Eqs. (5) and (8)

$$\frac{1}{y}\frac{dy}{d\lambda} = -\frac{(1 + \epsilon)\Delta(\gamma + 1)}{12k\gamma^2 \chi} = -(1 + \epsilon)(d\chi/d\lambda)/3k\gamma\chi \quad \text{by Eq. (7)}$$

Integration now gives

$$y\chi^{(1 + \epsilon)/3k\gamma} = \text{const.} \tag{9}$$

Eliminating y from Eqs. (5) and (9) gives

$$\lambda \chi^{\sigma} \Delta (p_o/p_{oo})^{1/2} = k \tag{10}$$

where k is a constant and

$$\sigma = \frac{1}{2}\left[1 + \frac{1+\epsilon}{3k\gamma}\right] \tag{11}$$

To obtain χ as a function of λ, we have from Eq. (7)

$$\lambda \chi^{\sigma} \frac{d\chi}{d\lambda}\left[\frac{p_o}{p_{oo}}\right]^{1/2} = k(\gamma+1)/4\gamma \tag{12}$$

This may be integrated by assuming an isothermal atmosphere of scale height H, so that

$$p_o/p_{oo} = e^{r\cos\theta/H} = e^{2k\lambda}, \tag{13}$$

where

$$k = \alpha \cos\theta/2H. \tag{14}$$

Eq. (12) then integrates to give

$$[(\chi/\chi_o)^{\sigma+1} - 1] = K[Ei(-k\lambda) - Ei(-k\lambda_o)], \tag{15}$$

where

$$Ei(-\theta) = -\int_{\theta}^{\infty} e^{-t} t^{-1}\, dt \tag{16}$$

$$K = k(\sigma+1)(\gamma+1)/4\gamma\chi_o^{\sigma+1} \tag{17}$$

The result mentioned above that Δp_o varies as $\lambda^{-1}(\ln\lambda)^{-1/2}$ for a medium of uniform density follows from Eqs. (10) and (12) with $p_o = p_{oo}$, if we put $\epsilon = 1$ and $k = 2/3\gamma$ in Eq. (11), corresponding to waveform Figure 1 (i) and thereby making $\sigma = 1$.

3. VALUES OF σ AND K

For a saw-tooth pressure pulse, $k = 2/3\gamma$, $\epsilon = 1$ and by Eq. (11) $\sigma = 1$. In the case of a linearly-decaying pulse, $k = 1/4\gamma$, $\epsilon = 0$ and $\sigma = 7/6$. If ϵ were taken as 1/2 instead of zero, then $\sigma = 3/2$. The values of σ considered in the following calculations range from 1 to 3/2, and dependence on σ has been found to be very slight.

K has been determined by fitting Eq. (15) to the numerical solution obtained by Brode[4] for the blast wave from a spherical charge of TNT. Only that part of the solution at later times is used, as Eq. (15) applies to weak shock propagation only

Since the numerical solution assumes a uniform medium, $H = \infty$, and Eq. (15) becomes

$$(\chi/\chi_o)^{\sigma+1} - 1 = K \log \lambda/\lambda_o \tag{18}$$

The region of Brode's solution to which this has been fitted is that where $\lambda \geq \lambda_o = 1$. In this region, the shock Mach number is less than 1.18. Initially $\chi = \chi_o = 0.185$ and $\tau_o = c_o t_o/\alpha = 0.541$, where t_o is the time after detonation. Values of $(\chi/\chi_o)^{\sigma+1} - 1$ have been plotted against $\log \lambda/\lambda_o$, as shown in Figure 3 for $\sigma = 1.25$, and a straight line fitted to obtain K. Taking other values of σ, it is found that

$$K \simeq 1.40 + (\sigma - 1.25) \tag{19}$$

for $1 \leq \sigma \leq 1.5$.

This application of Brode's solution is considered valid for a high-altitude release unless the release height exceeds the height h at which the initial blast wave begins to weaken and the amount of energy communicated to the atmosphere falls.[5] Values for h are given in Table 1.

TABLE 1. Heights at which the initial blast wave from an explosive of energy E_{oo} begins to weaken on account of decreasing ambient density (charge characteristics, $\gamma_o = 1.22$, $\bar{\gamma} = 1.28$)

E_{oo} (ergs)	10^{11}	10^{12}	10^{13}	10^{14}	10^{15}
h (km)	100	107	114	121	130

At heights greater than h, the method has nevertheless still been applied in order to obtain tentative results.

4. THE VALIDITY OF BRODE'S NUMERICAL SOLUTION FOR HIGH-ALTITUDE RELEASES

4.1 At Heights Below h

Since Brode's numerical solution was calculated for a certain density of TNT charge (1.5 gm/cc) and ambient sea-level conditions, consideration needs to be given to its application to high-altitude releases. The solution may be scaled to other ambient pressures and charge sizes, provided the explosive density is scaled appro-

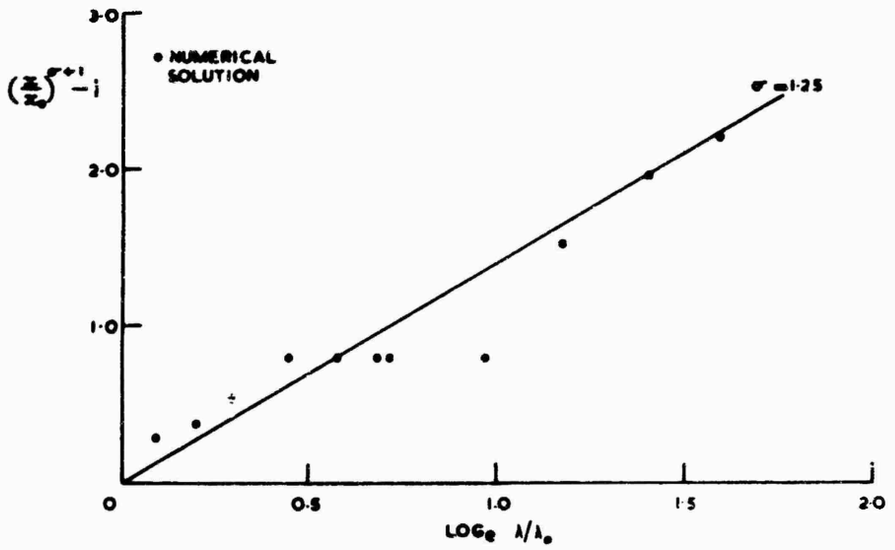

Figure 3. Comparison of Brode's Numerical Solution in Weak Shock Region With Equation (18)

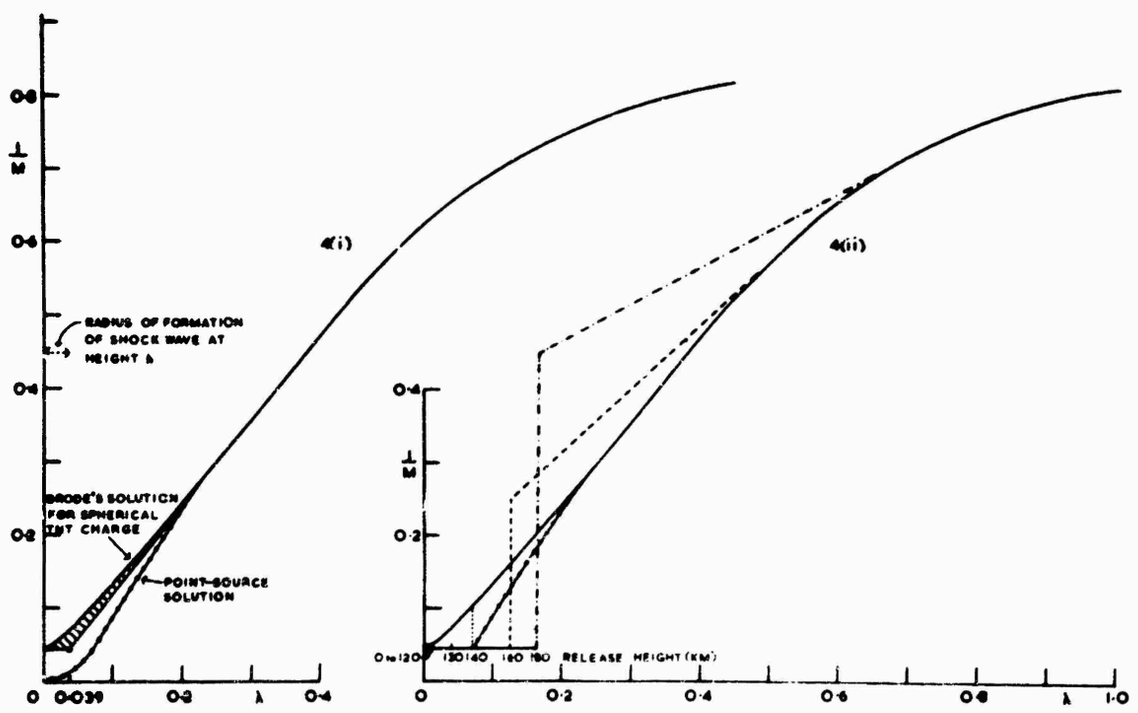

Figure 4. (i) I/M Against λ is The Same For All Release Heights Less Than h, Apart From The Shaded Area Which Represents an Almost Negligible Increase in The Vicinity of Height h

(ii) I/M Against λ Derived For $E_{oo} = 10^{15}$ Ergs at Release Heights Above h

priately; that is, as the ambient air density. As the range of values of possible charge densities is small, this would seem to leave little practical use for the solution at heights other than those very close to sea-level. However, comparison with the point-source solution, that is, that for infinite charge density, shows that the two solutions converge when the shock wave has propagated to a scaled radius of $\lambda_c = 0.25$ (see Figure 4).

Another way of expressing this condition is by the number of times N the mass of air engulfed by the shock wave at λ / λ_c is greater than the mass of the charge m_E. Then, if ρ_{oo} is ambient air density,

$$N = \frac{4\pi r_c^3 \rho_{oo}}{3m_E} = \frac{4\pi}{3} \frac{\lambda_c^3 \alpha}{g H}$$

where $\alpha = E_{oo}/m_E$ and $gH = p_{oo}/\rho_{oo}$. H is atmospheric scale height, and g is the acceleration due to gravity; and H, g and k can take only limited ranges of values. Hence N is roughly constant for all releases and release heights. Taking H = 8 km, g = 9.7 m/sec^2 and $\alpha = 4.8 \times 10^{10}$ ergs/gm, it is found that N = 4.

In the region in which Brode's solution is used to provide initial conditions for the weak shock region, that is $\lambda \geq 1$, $N \geq 256$, the solution is insensitive to charge density or release height.

In the region $\lambda < \lambda_c$, this is not the case, but as the speed of propagation is high, the uncertainty that can arise in the travel time correction is almost negligible. This is illustrated in Figure 4, where the travel time correction is proportional to the area about 1/M and below unity, and the shaded area is the almost negligible increase that can occur at height h.

4.2 At Heights Above h

In this region, the initial blast wave now weakens as the release height increases. Although no treatment of this case has been made, the initial radius and strength of the shock wave have been estimated[5] and on the basis of these values, curves for 1/M against λ have been devised as a means of providing tentative results above height h. Figure 4(ii) shows those used for $E_{oo} = 10^{15}$ ergs.

5. LENGTH OF POSITIVE PRESSURE PULSE, ℓ AT GROUND LEVEL

Eq. (15), with Eqs. (4) and (6), has been used to calculate R at ground level for vertical propagation with various release energies E_{oo} and various release heights. Figure 5 shows the results, and these lie within the thickness of the plotted lines for all values of σ between 1 and 1.5.

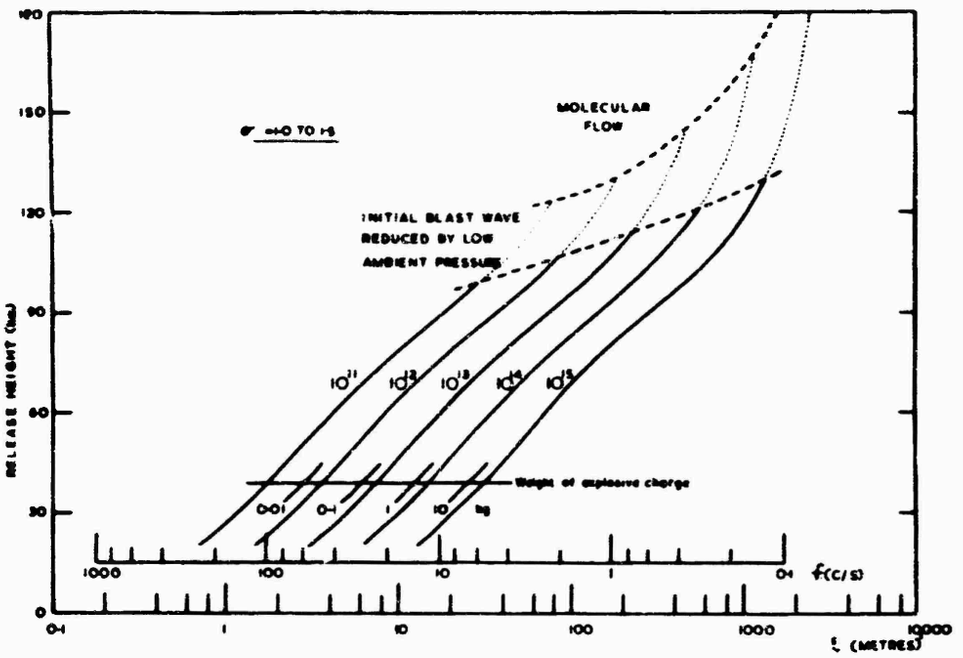

Figure 5. Length of Positive Pressure Pulse. Numbers on Curves Are E_{oo} in Ergs

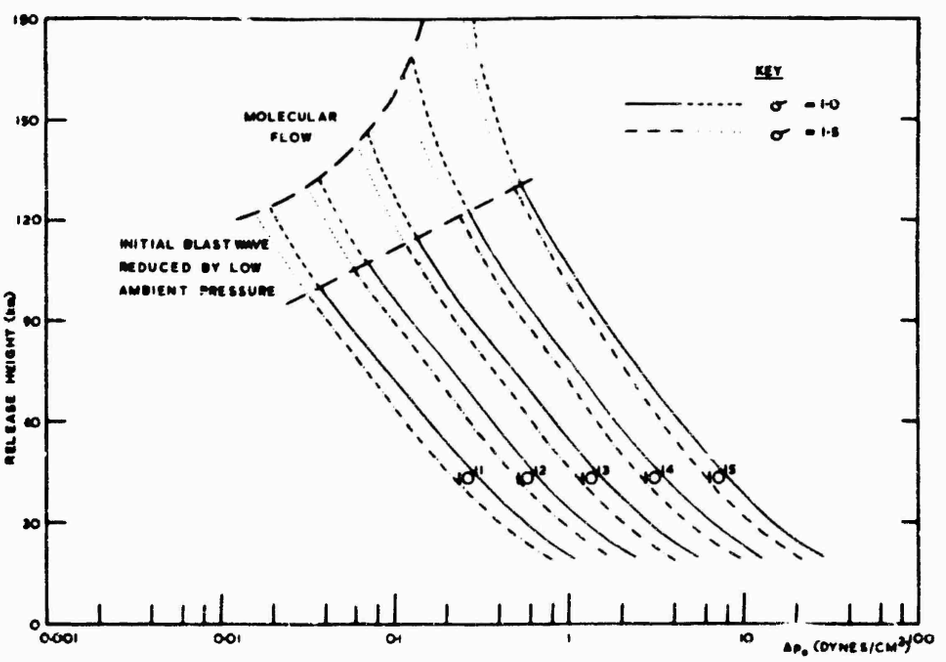

Figure 6. Pressure Amplitude at Ground Level of Vertically Transmitted Pulse. Numbers on Curves Are E_{oo} in Ergs

A scale is shown on Figure 5 of

$$f = c_o/2\ell \tag{20}$$

where c_o = 340 m/sec; that is, the frequency at which a half wavelength is ℓ. This would be expected to be the predominant frequency of the wave and should indicate the detector frequency required for maximum response.

6. PRESSURE AMPLITUDE Δp_o AT GROUND LEVEL

From Eqs. (10) and (17)

$$\Delta p_o/p_o = (p_{oo}/p_o)^{1/2}\, 4\gamma \chi_o^{\sigma+1}\, K/(\sigma+1)(\gamma+1)\chi^{\sigma}\lambda \tag{21}$$

Eq. (21) enables Δp_o to be calculated at ground level, and the results are shown in Figure 6 for vertical propagation. Values of p_{oo} have been taken from CIRA 1961, and γ has been taken to be 1.4. The dependence on σ is seen to be quite small.

7. TRAVEL TIME CORRECTION, Δt

Δt is the difference between the observed travel time and that which a sound wave would have in travelling between the explosion point and a microphone on the ground along the same path. Δt increases with height and explosive energy and depends slightly on the ray inclination. Write

$$\Delta\tau = c_o \Delta t/\alpha = \Delta\tau_1 + \Delta\tau_2 \tag{22}$$

where $\Delta\tau_1$ is the contribution from region (1) and $\Delta\tau_2$ from region (2). Now

$$\Delta\tau_1 = \lambda_o - \tau_o$$

since in non-dimensional terms, the shock wave travels a distance λ_o while a sound wave would travel a distance τ_o. Also

$$\Delta\tau_2 = \int_{\tau_o}^{\tau} (M-1)\, d\tau = \chi - \chi_o$$

by Eq. (1). From section 3, $\lambda_o = 1$, $\chi_o = 0.185$ and $\tau_o = 0.541$, and hence

$$\Delta\tau = \chi + 0.274 \tag{23}$$

By means of Eqs. (15) and (23), Δt may be calculated for various explosive energies and release heights, and the results are shown in Figure 7; with c_o being taken as 341 m/sec.

8. EFFECT OF TRAVEL-TIME CORRECTION ON TEMPERATURE DETERMINATION

The average speed of sound between two grenade bursts at heights z_1 and z_2 is

$$\bar{c} = \int_{z_1}^{z_2} c\, dz/(z_2 - z_1) = \left[\int_0^{z_2} c\, dz - \int_0^{z_1} c\, dz \right] / (z_2 - z_1) \qquad (24)$$

In general, the values of the two integrals in this expression are derived from observation of the travel times from two grenades to various microphones on the ground. In order to simplify the error analysis it will, however, be assumed that no winds are present, and that there is only one microphone situated vertically beneath both bursts to which the travel times are t_1 and t_2, respectively. Then, in the analysis of this experiment, we take

$$\int_0^{z_1} c\, dz = z_1^2 / (t_1 + \Delta t_1)$$

and similarly for the second burst, where Δt_1 and Δt_2 are the corrections for travel-time shortening. Writing

$$z_2 = z_1 + \delta z \qquad t_2 = t_1 + \quad t$$

we find that to the first order in small quantities δz, δt and $\Delta t_2 - \Delta t_1$, Eq. (24) gives

$$\bar{c} = \frac{2z_1}{(t_1 + \Delta t_1)} - \frac{z_1^2 (\delta t + \Delta t_2 - \Delta t_1)}{\delta z\, (t_1 + \Delta t_1)^2}$$

Taking $\Delta t_1 / t_1$ to be small, we have

$$\bar{c} = \frac{2z_1}{t_1} \left(1 - \frac{\Delta t_1}{t_1} \right) - \frac{z_1^2}{\delta z} \left[\frac{\delta t}{t_1^2} \left(1 - \frac{2\Delta t_1}{t_1} \right) + \frac{\Delta t_2 - \Delta t_1}{t_1^2} \right]$$

Let $\bar{c}_o$ be the result obtained without correcting for travel-time shortening. then

$$\bar{c} - \bar{c}_o = - \frac{2z_1 \Delta t_1}{t_1^2} + \frac{z_1^2}{\delta z} \left[\frac{2\, \delta t\, \Delta t_1}{t_1^3} - \frac{\Delta t_2 - \Delta t_1}{t_1^2} \right]$$

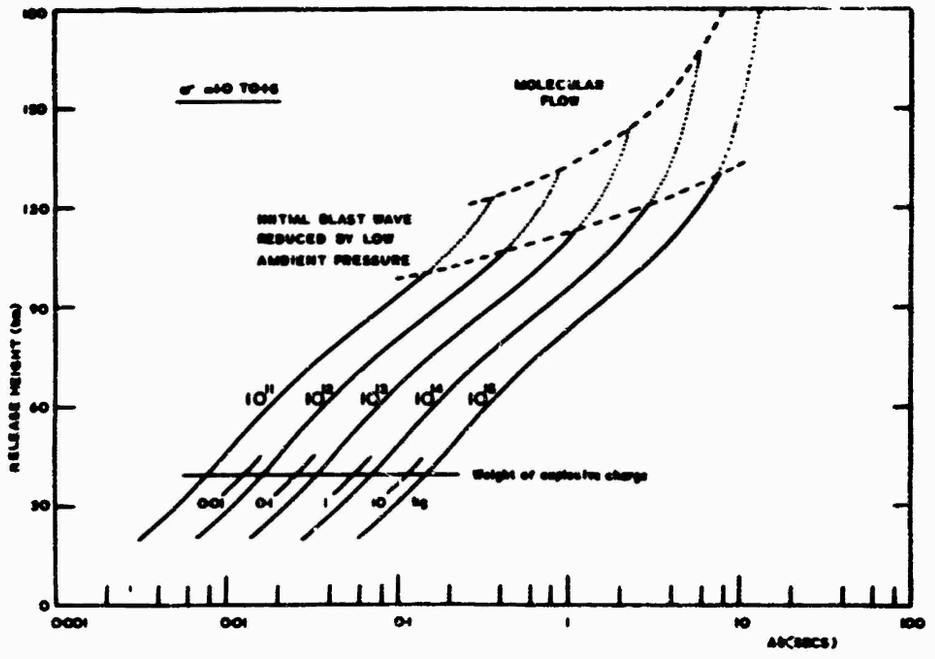

Figure 7. Travel Time Correction Against Release Height. Numbers on Curves Are E_{OO} in Ergs

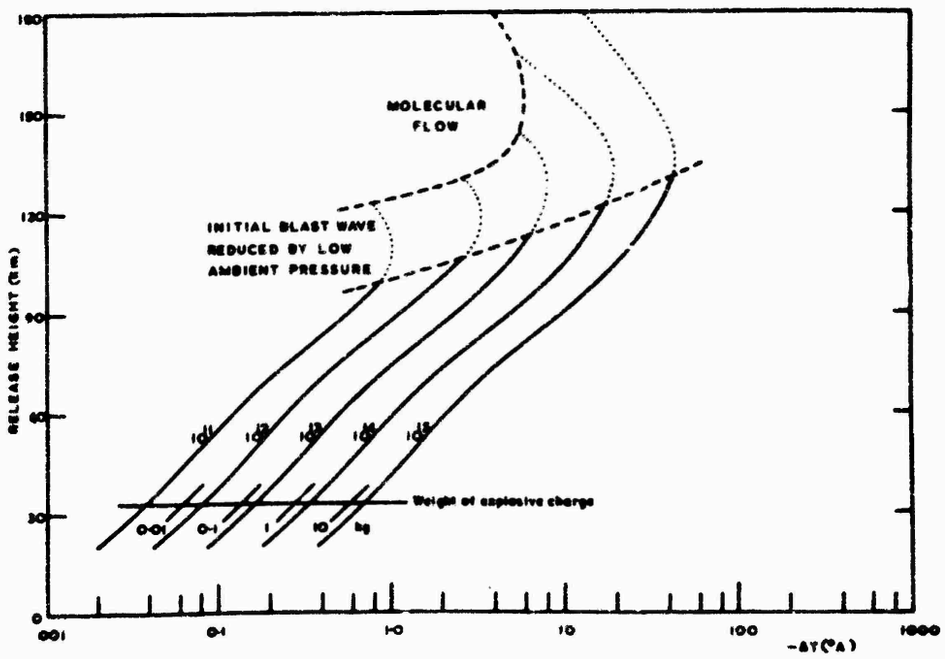

Figure 8. Correction to Grenade Experiment Temperatures For Finite-Amplitude Effect. Numbers on Curves Are E_{OO} in Ergs

Dropping the suffix 1 and writing $(\Delta t_2 - \Delta t_1)/\delta z = d(\Delta t)/dz$

$$\frac{\bar{c} - \bar{c}_o}{c_2} = - \frac{c_1}{c_2} \left[c_1 \frac{d(\Delta t)}{dz} + 2 \frac{c_2 - c_1}{c_2} \frac{\Delta t}{t} \right]$$

where

$$c_1 = z_1/t_1 = z_1 / \left[\int_0^{z_1} \frac{dz}{c(z)} \right] \tag{25}$$

$$c_2 = z/t \tag{26}$$

The error in temperature ΔT is then

$$\Delta T = - \frac{2c_1}{c_2} \left[c_1 \frac{d(\Delta t)}{dz} + 2 \frac{c_2 - c_1}{c_2} \frac{\Delta t}{t} \right] T \tag{27}$$

Figure 8 shows the error $-\Delta T$ calculated from Eq. (27), using the values of Δt given in Figure 7 and standard atmosphere values of c_1, c_2 and T. In all cases, neglect of the finite-amplitude correction Δt leads to an overestimation of temperature. For the maximum explosive charge considered, 10^{15} ergs, the error would be 10^{o} at 90 km, and 40^{o} at 120 km. Such errors would not invalidate the usefulness of the grenade technique above 90 km, and could be reduced by adding in a correction for the travel-time shortening.

References

1. G. V. GROVES, 1957.
2. J. OTTERMAN, Finite-amplitude propagation effect on shock-wave travel times from explosions at high altitudes. J. Acoust. Soc. Amer. 31: 470, 1959.
3. H. A. BETHE et. al, Shock hydrodynamics and blast waves. Los Alamos Report AECD, 2860, 1944.
4. H. L. BRODE, Blast wave from a spherical charge. Phys. of Fluids 2:217, 1959.
5. G. V. GROVES, Initial expansion to ambient pressure of chemical explosive releases in the upper atmosphere. J. Geophys. Res. 68:3033, 1963.

XX. Ionospheric Temperatures from Photography of Detonations*

N. W. Rosenberg
Air Force Cambridge Research Laboratories
Bedford, Massachusetts

Abstract

The overpressure in the shock wave accompanying the detonation of a high-explosive grenade at 108 km altitude was found to increase the brightness of a chemiluminous trail deposited just prior to the detonation. Motion of the bright overpressure region along the trail was photographed with a ground-based streak camera. The shock wave motion agreed with the calculations of Brode, and corresponded to an ambient sound speed of 350 m/sec. This speed is equivalent to a molecular scale temperature of 300°K ± 50°K, compared with the U. S. Standard Atmosphere value of 250°K. The technique should be useful for temperature measurements up to 140 km altitude.

1. INTRODUCTION

Measurements of acoustic velocities from detonations have provided the most reliable estimates of ambient temperatures at altitudes up to 85 km.[1] Ground-based acoustic detection of detonations at higher altitudes are difficult because of

* Submitted for publication to the J. of Geophys. Res.

the low frequency and low overpressure of the signal received from grenades of reasonable weight.[2] The maximum altitude of detonation for which ground-based acoustic detections have been reported are 85 km for 20g explosive,[3] 117 km for 4 kg,[4] and 160 km for 100 kg.[5]

This report discusses an experiment in which an alternate technique was utilized for recording acoustic pulses; that is, optical detection of the pulse in the vicinity of the detonation rather than ground-based acoustic detection. In this experiment a chemiluminous trail[6] was released from a rocket, followed by detonation of a grenade from the same rocket. The shock wave moved out as an approximately spherical shock intersecting the luminous trail. The overpressure of the shock created a brighter band of light moving a long the trail which was recorded by appropriate ground-based photography.

The experiment was carried out at 108 km altitude above Eglin AFB Florida (87^{o}W 30^{o}N) at 2230 CST 25 September 1963.

2. THEORETICAL CONSIDERATIONS

The blast wave from a spherical charge in the lower atmosphere has been theoretically analyzed by Brode.[7] The validity of the Brode solutions at high altitudes has been examined by Groves,[2] who has set forth appropriate corrections. The corrections are negligible if three conditions are fulfilled. The shock wave must have expanded to a radius large compared to the expanded fireball ($\sim$0.1 km). The radius must be small compared to an ambient scale height ($\sim$ 8 km). For shock formation at high altitudes, the expanded fireball must be large compared to the ambient mean free path, valid at altitudes below 120 to 150 km for charges of 0.1 to 10 kg of high explosive.

In the Brode treatment, a scaling length α is defined equal to $(E_o/P_a)^{1/3}$ where E_o is the explosive energy in ergs and p is the ambient pressure in dynes/cm^2. Radial distances and times are scaled in dimensionless units $\lambda \equiv r/\alpha$ and $\tau \equiv c_o t/\alpha$, respectively, where r is the radial distance from the explosion, t is the time after explosion, c_o is the speed of sound in the ambient atmosphere. Table 1 lists the distance in kilometers for $\lambda = 1$ and the time in seconds for $\tau = 1$, for explosive charges of 0.1 and 10 kg. It is for distances and times of this order that shock overpressures above 10% will be encountered. In the experiment actually executed and reported here (6kg high explosive at an altitude of 108 km), the scale radius was 1.4 km and the scale time was 4.0 seconds.

TABLE 1. Radii for $\lambda = 1$; times for $\tau = 1$

Altitude Km	Km radius		Seconds	
	0.1 kg HEx	10 kg HEx	0.1 kg HEx	10 kg HEx
100	0.26	1.2	0.9	4.0
120	0.60	2.8	1.6	7.2
140	0.88	4.0	1.4	6.4

Figure 1 adapted from Brode[7] represents the pressure profile at a series of times $\tau = 0.5$, 1.0, and 2.0. If a pressure sensor is moved into the shocked region towards the explosion (from right to left in Figure 1) at a given instant, for example $\tau = 1$, ambient pressure is observed until the shock surface is encountered at a radius $\lambda_s = 1.5$ where the pressure sharply rises to 23% above ambient. Further in, the pressure falls until at a 'null' radius $\lambda_n = 1.3$, ambient pressure is reached. Further in, a rarefaction is encountered until at a radius $\lambda_r = 1.1$, a minimum pressure 10% below ambient is reached. The pressure then rises slowly (with secondary maxima at second and third shocks) and the contact surface (CS) of the expanded fireball is reached at $\lambda = -0.23$ at near-ambient pressure with no significant discontinuity as this boundary is passed.

Figure 2 and Table 2, also adapted from Brode,[7] present the variation with time of selected parameters of the spherical overpressure shell which are important for photography. These parameters include the shock radius λ_s, the null radius λ_n, the thickness of the overpressure zone $\lambda_s - \lambda_n$, the maximum overpressure $(p_s/p_a)-1$ and the Mach number M_s of the shock surface. Between $\tau = 0.5$ and $\tau = 2$, they take on values which allow photographic records to be made; that is, overpressures of 50% to 10%; Mach numbers of 1.25 to 1.06; thicknesses of $\lambda = 0.18$ to 0.27, and radii of $\lambda = 1$ to 2.5.

TABLE 2. Shock wave history

τ	0.10	0.20	0.40	1.00	1.50	2.09	3.00	4.00
λ_s	0.34	0.54	0.82	1.55	2.11	2.65	3.70	4.73
M_s	2.40	1.53	1.29	1.17	1.09	1.07	1.05	1.03
$p_s/p_a - 1$	--	1.54	0.63	0.22	0.13	0.10	0.07	0.05
$\lambda_s - \lambda_n$	--	0.14	0.17	0.23	0.25	0.27	0.29	0.31

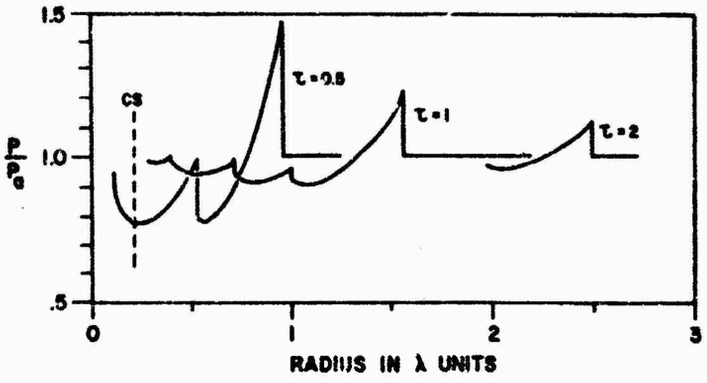

Figure 1. The Pressure Profile of a Spherical Shock Wave at Selected Times τ after Detonation, Adapted from Brode [1959]. p is the Pressure at a Radius λ, p_a is the Ambient Pressure. CS is the Final Position of the Contact Surface between the Detonation Product Gases and the Atmosphere, Reached at $\tau = 0.1$.

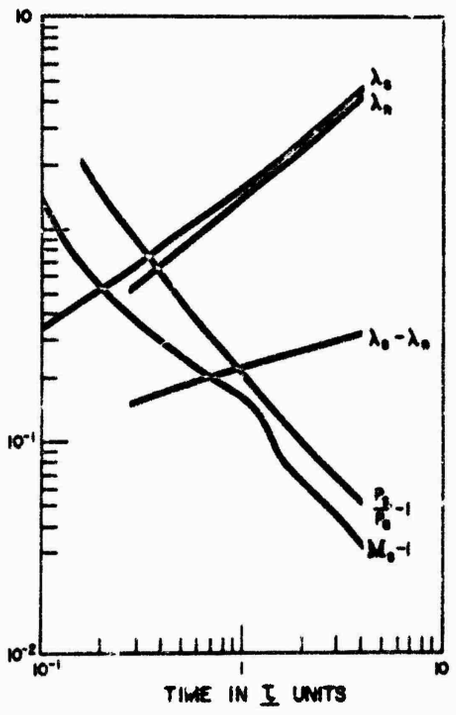

Figure 2. The History of Several Spherical Shock Parameters Following a Detonation, Adapted from Brode [1959]. $M_s - 1$, the Excess of the Shock Velocity over Acoustic Velocity, and $(p_s/p_a)-1$, the Excess of the Shock Pressure over Acoustic Pressure, are Almost Inversely Proportional to Time. The Shock Wave Thickness $\lambda_s-\lambda_n$ Increases Slightly with Time. The Shock Wave Position is Almost Directly Proportional to Time.

Let us next consider the realeased chemiluminous trail along which this pressure pulse will be imposed. A suitable gas (trimethyl aluminum) deposited at a rate of 50 g/km along a rocket trajectory, glows for tens of seconds following release with an intensity sufficient to permit photography with a fractional second exposure.[6] This gas expands within a fraction of a second after release to form a column of about 0.1 km dia, containing less than 1% released gas diluted by at least 99% ambient air. As the pressure is increased (that is, as the collisions per cm^3/sec are increased) the volumetric emission rate must rise, since the emission will be proportional to the collision frequency of some rate-limiting species. The detectability of a shock wave zone of increased pressure will depend on the relative brightness of that zone against the background glow of the rest of the trail at ambient pressure. In other words, the chemiluminous trail constitutes a marker for regions of differing pressure. The trail should be observed at a 90^{o} aspect angle to provide a maximum contrast between the region of overpressure and the undistrubed ambient, if the shock thickness is smaller than the trail diameter.

3. EXPERIMENTAL

The payload (26 kg gross weight) consisted of two cylindrical sections carried aboard a Nike Apache vehicle. The forward section carried a 2 kg payload of a liquid mixture (80 wt % trimethyl aluminum - 20 wt % triethyl aluminum). It contained a release programmer to dispense the liquid at 65 gm/sec beginning 70 seconds after launch (vehicle altitude 85 km). The vehicle velocity averaged 1.5 km/sec at this time, so that about 45 g/km was deposited. At 85 seconds after launch, a rear section containing 6 kg of high explosive (RDX) was detonated, releasing $3x10^{14}$ ergs at an altitude of 108.4 km. The liquid container was ruptured by the detonation, and the 1 kg of liquid not yet dispensed at the time of detonation was ejected and continued as vaporizing droplets along the ballistic trajectory at 1.5 km/sec for several kilometers.

The vehicle trajectory at this point was at an elevation angle of 84^{o}. With respect to the photographic recording site 134 km to the east of the launch site, the vehicle aspect was 130^{o}.

4. RESULTS AND DISCUSSION

Two types of photographic records were obtained: a framed movie sequence, and a streak photograph. The movie used a 76 mm f 0.87 lens at 2 frames/sec. Selected frames are shown in Figure 3A. The streak used a 50 mm f 1.5 lens and a film motion of 0.356 mm/sec perpendicular to the image of the trail. Royal X

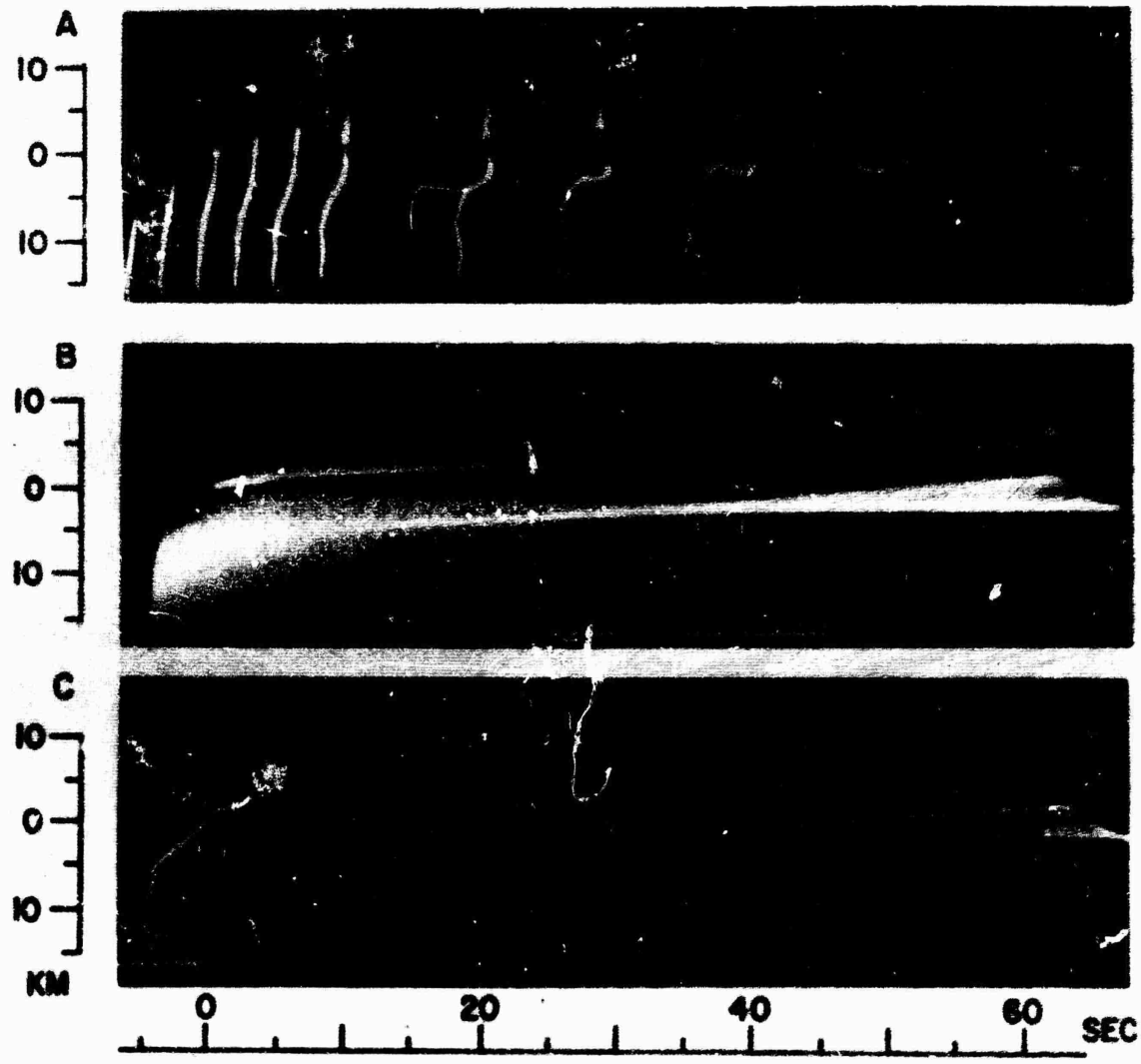

Figure 3. Shock Wave Photography. A is a Sequence of Frames Taken with 0.5 Second Exposures at Times Indicated Below the Picture. The First Two Frames were Taken Prior to the Detonation. The Scale to the Left is the Distance Along the Trail in Kilometers Upward or Downward from the Point of the Explosion at 108.4 km. No Shock Wave is Evident in the Framed Sequence. B is a Streak Photograph to the Same Scale as A. The Shutter was Opened Five Seconds Prior to Detonation, and Closed 60 Seconds Following Detonation, as the Film was Pulled from Right to Left. The Picture is Best Understood as a Smeared Version of Sequence A. The Shock Waves, Both Upward and Downward, are Obscure but Visible for Several Seconds as Lines at about a 20° Angle from the Detonation. C is a High Contrast Version of B (See Text), in Which the Shock Waves are Considerably More Visible.

Pan film was used in both cameras. The streak photograph is shown in Figure 3B at the same enlargement as the framed sequence. The scales to the left of the photographs are km distance along the trail from the point of detonation.

No visible shock wave was seen by field observers, and the framing sequence failed to show any moving band of light although it does show a remarkable development of eddy cells. The streak photograph, however, showed the expected effect although the high trail brightness overexposed the film. The streak photograph negative was used to make a contact positive transparency, which was registered slightly offset from the negative to give the high-key print shown as Figure 3C, and the enlargement shown as Figure 4. This technique enhanced contrast, and clearly showed the upward-moving shock to 10 sec and less clearly, the downward moving shock to 5 seconds.

A recently developed densitometry contour technique[8] was applied to the high-key offset. Contours of equal density are directly machine-formed by film scanning and presented in a map-like format as in Figure 5. Selected contours have been outlined to show the bands of high contrast caused by the shock wave moving up and down from the explosion. The pair of solid curved lines is the Brode solution for the case $E_o = 3 \times 10^{14}$ erg; $p_a = 0.11$ dynes/cm^2, $C_o = 350$ m/s. Agreement is excellent both in downward motion and in upward motion. For comparison, the dotted lines show Brode solutions for $C_o = 300$ and 400 m/s. It is evident that these velocities are clearly outside the experimental error, which is therefore set as $\pm$ 25 m/sec, an accuracy of $\pm$ 7%.

The ambient temperature T_M is related to the acoustic velocity by $T = M C_o^2 / \gamma R$ where T is the temperature, M the molecular weight, γ the ratio of specific heats, and R the gas constant. The uncertainties in γ and M are much less than the $\pm$7% uncertainty in C_o which becomes a 15% uncertainty in T. Using U. S. Standard Atmosphere 1962 values to estimate M as 28.64 and γ as 1.406, the observed acoustic velocity of 350 + 25 m/sec is equivlanet to a temperature of $300^o \pm 50^o$K. This may be compared to a temperature of 250^oK from the Standard Atmosphere tables for 108.4 km.

5. CAPABILITIES AND LIMITATIONS

Despite the unfortunate overexposure of the streak photograph which reduced its sensitivity, the high-key transparency showed clearly-marked shock waves to times of about 10 seconds (τ = 2.5) when peak overpressures of about 8% are expected. The analysis of Groves[2] suggests that shocks from 1 to 10 kg grenades will be severely attenuated above 140 km, setting an upper limit to the use of this technique. However, below that height, release of a series of six 1 kg explosive grenades along

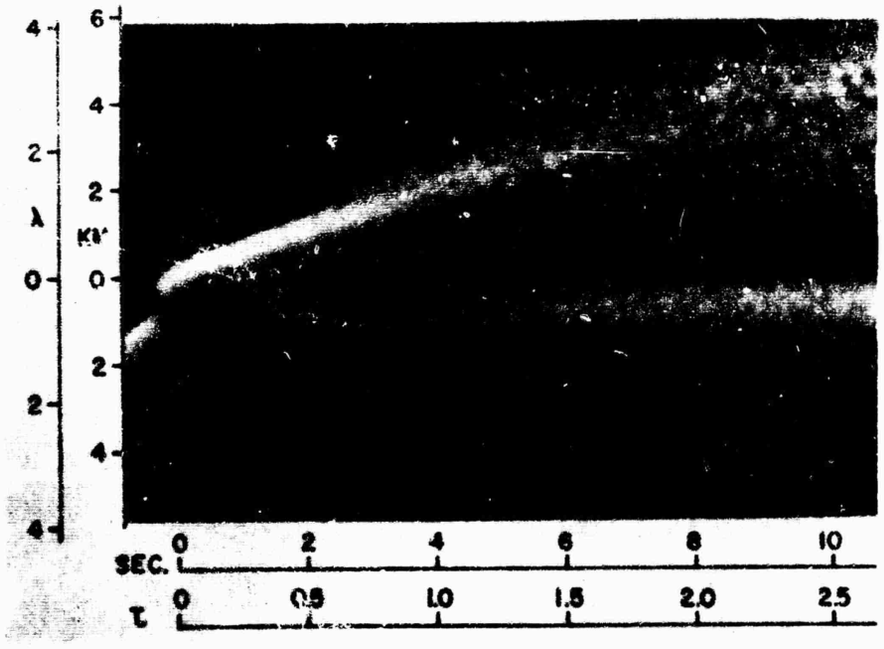

Figure 4. Enlargement of The Shock Wave Photograph of Figure 3C

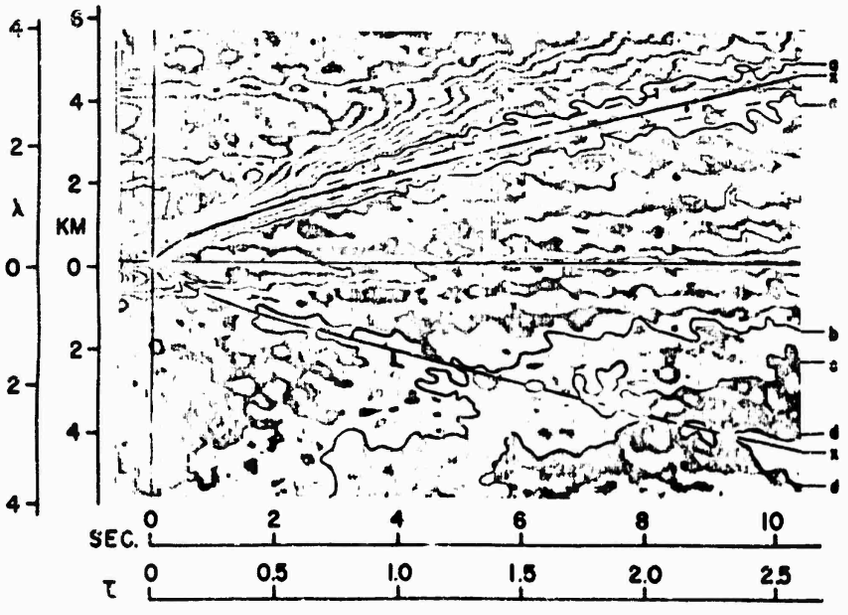

Figure 5. Density Contour Map of Figure 4. White, Gray, and Black Areas Represent Increasing Film Densities, a White Area next to a Black Area is a Higher Density than the Black and Starts a New White, Gray, Black Sequence. Density Increments are 0.025 Units. The Smooth Black Curve X-X is the Computed Shock Position at c_0 = 350 m/s. Selected Contours a-a, b, c, and d-d are Outlined, Their Distortion Showing the Location of the Shock Wave.

a simultaneously-deposited chemiluminous trail appears feasible in a 35 kg gross payload. This would permit temperature measurements at 10 km intervals from 90 to 140 km, together with simultaneous wind measurements from the trail distortion.

In view of the high trail intensity, evidenced by the overexposure of the streak photograph, a slow film of higher resolution and a slow lens of longer focal length could have been used. Both changes would result in a higher accuracy in locating the shock position, and in the temperature estimate derived from that measurement.

6. CONCLUSIONS

The measurement of acoustic velocity, and with minor uncertainty temperature, at 108.4 km altitude was accomplished by rendering a shock wave visible as it passed along a chemiluminous trail. An acoustic velocity of 0.35 km/sec, corresponding to a temperature of $300^{\circ}K \pm 50^{\circ}K$, was obtained, compared with a U. S. Standard Atmosphere[9] value of $250^{\circ}K$.

The agreement between the Brode[7] solutions for a sea-level spherical blast and the observed shock wave position was excellent, since the charge and the region under investigation met the Groves[2] criteria for applicability of the Brode solutions.

Extension of the technique to a multiple release determination of acoustic velocities between 90 and 140 km is contemplated as the next step in this program.

Acknowledgments

The author wishes to acknowledge the design work on the payload by Mr. Edward F. Allen, Jr., of Air Force Cambridge Research Laboratories, and the density contour map preparation by Mr. Fred Parsons and Dr. Irving Kofsky of Technical Operations, Inc.

References

1. W. NORDBERG and W. SMITH, Preliminary measurements of temperatures and winds above 50 km over Wallops Island, Technical Note D-1694, National Aeronautics and Space Administration, Washington, DC, 1963.

2. G. V. GROVES, Acoustic Pulse Characteristics from Explosive Releases in the Upper Atmosphere, in Project Firefly 1962-3, Air Force Cambridge Research Laboratories, L. G. Hanscom Field, Bedford, Massachusetts, 1964.

3. G. V. GROVES, Private communication, 1963.

4. H. F. ALLEN, Acoustic Detection at High Altitudes, Project Firefly 1962-3, Air Force Cambridge Research Laboratories, L. G. Hanscom Field, Bedford, Massachusetts, 1964.

5. J. E. BLAMONT, Private communication, 1962.

6. N. W. ROSENBERG, D. GOLOMB and E. F. ALLEN JR., Chemiluminescence of trimethyl aluminum released into the upper atmosphere, J. Geophys. 68: 5895-5898, 1963.

7. H. L. BRODE, Blast wave from a spherical charge, Phys. Fluids 2: 217-229, 1959.

8. I. KOFSKY, Private communication. The automatic equal-density contour-plotting machine used was recently developed by Technical Operations, Inc., Burlington, Massachusetts.

9. U. S. Standard Atmosphere 1962, Government Printing Office, Washington, DC, 1963.

XXI. Small-Scale Wind Structure Above 100 km*

Samuel P. Zimmerman
Air Force Cambridge Research Laboratories
Bedford, Massachusetts

Hines[1] has estimated the minimum scale size of atmospheric gravity waves by considering the variations from the mean of the wind velocity magnitude, that are observed in visible meteor trails at altitudes between 80 and 100 km. To get these estimates he superposes a constant shear upon the measured meteor-trail wind velocity, and then measures the altitude between the sequential points where the magnitude of this normalized wind velocity goes to zero. By this method he has subtracted out the effect of the mean wind shear upon the visible trail, which leaves atmospheric perturbations, such as gravity waves, to cause deformation of the trail.

This technique is valid only over the altitude range where the mean wind shear is constant. Any altitude variation of the mean wind velocity from a linear function will then introduce errors in the measurement of scale sizes. However, by measuring directly the altitude increment between inflection points of the magnitude of the wind velocity, as deduced from photographs of the trail deformation, the wavelengths or scale sizes of these small scale perturbations may be determined without the possible error introduced by the superposition of a correcting mean shear field. This technique is valid only for the condition where the wavelength of the mean wind velocity is large compared to the wavelength of the small scale velocity perturbations. Thus the effect of the altitude variation of the mean wind

*Reprinted from J. of Geophys. Res., 69, 784 (1964).

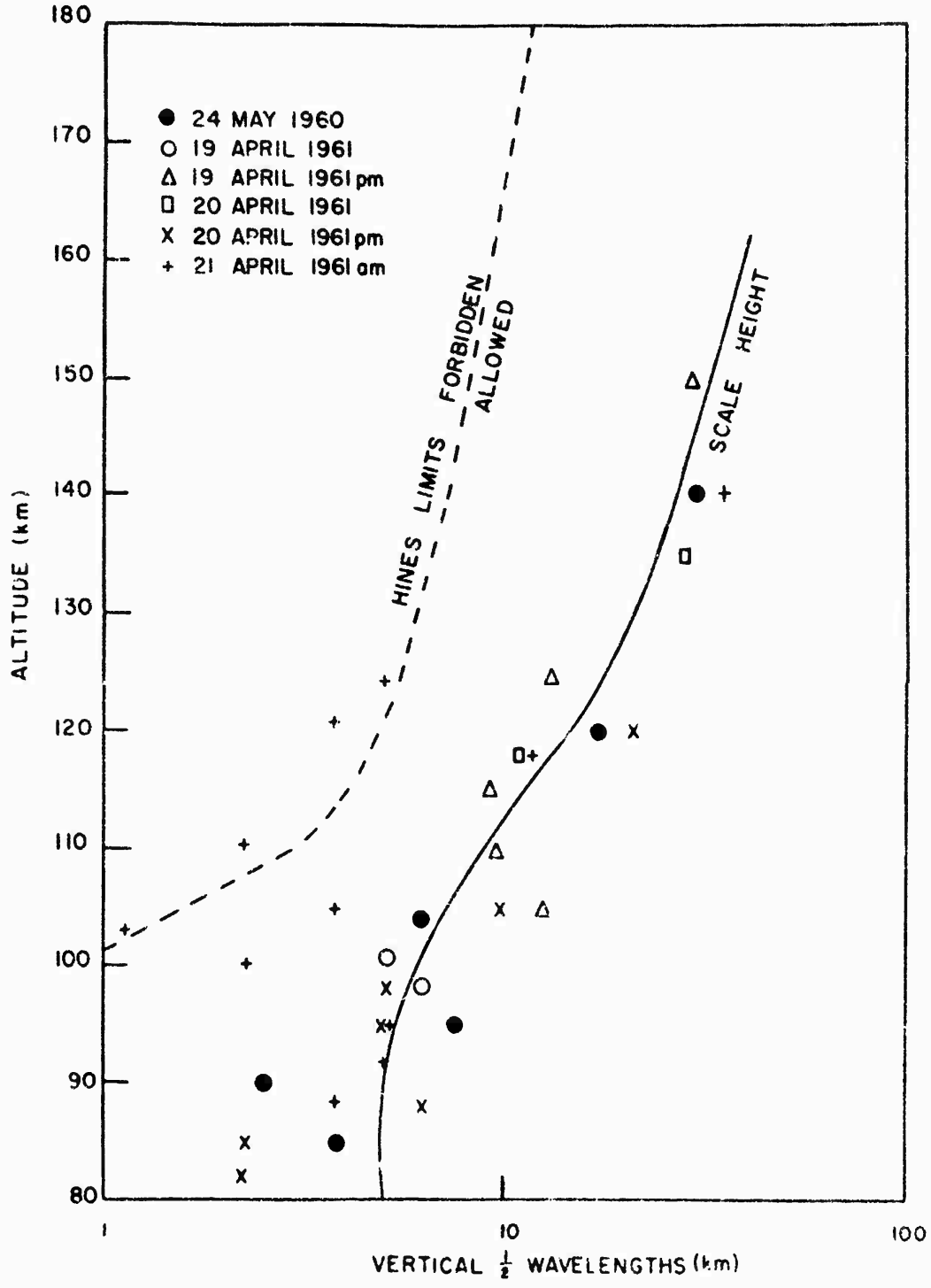

Figure 1. Summer Measurements of Vertical Half Wavelengths. The Data are from the NASA Report NAS5-215.

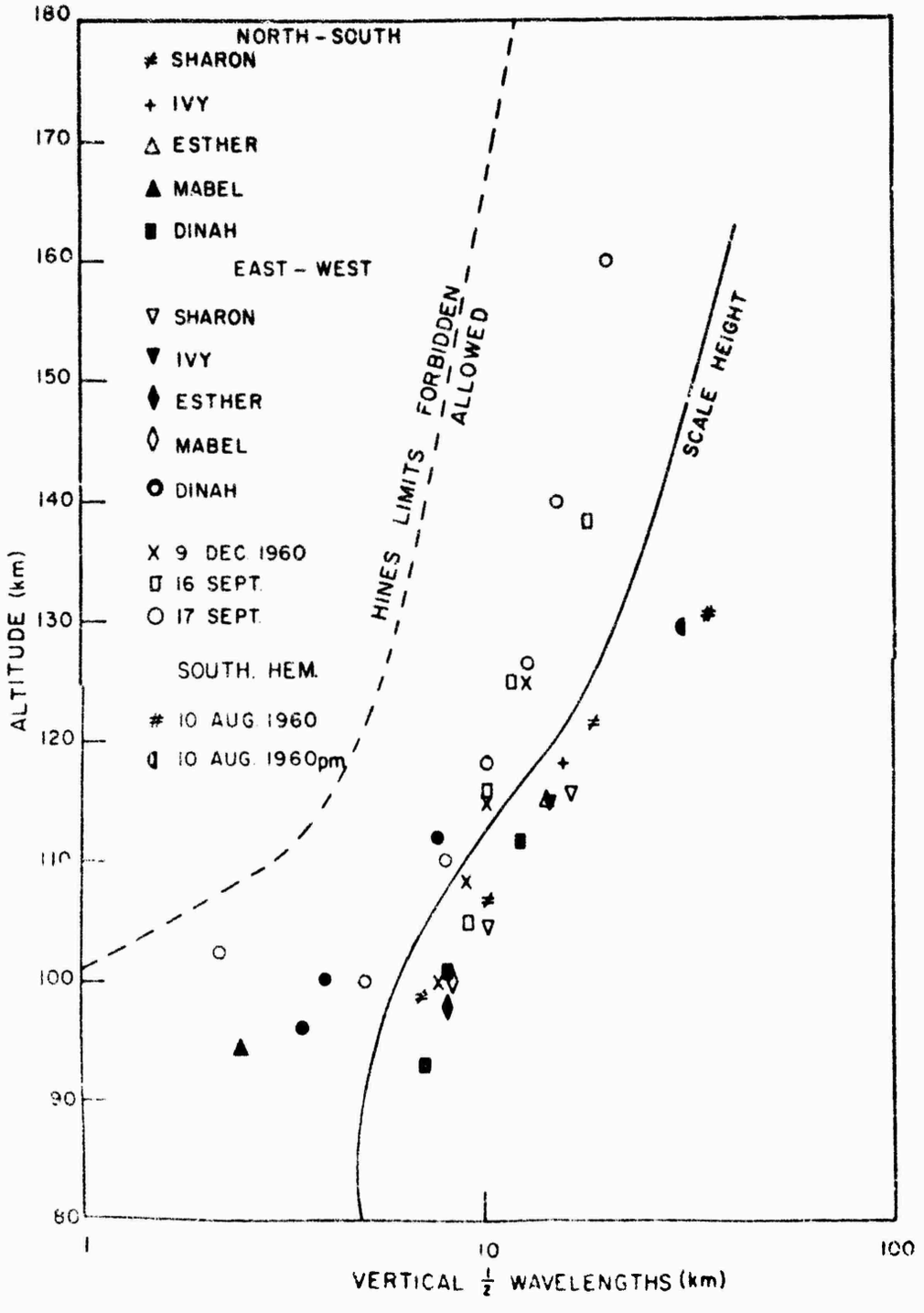

Figure 2. Winter Measurements of Vertical Half Wavelengths. The Data Labeled with Names are that of Rosenberg et al., December 1972, the Data Dated December and September are from the NASA Report NAS5-215, and the August 1960 Data Points are from Groves at Woomera, Australia. The Superposed Curves are the Same as in Figure 1.

upon the small scale inflection point to inflection point measurements will be that of a small perturbation. It is immediately recognizable that, for the case where the mean wind velocity has a linear altitude dependence, this technique will yield the same results as Hines.[1]

This type of analysis was applied to sodium trail releases that covered the altitude range of 80 to 160 km. The experiments were performed at Wallops Island, Va., by Manring,[2] at Eglin AFB, Fla., by Rosenberg et al.,[3] and at Woomera, Australia, by G. V. Groves.[4] The data were separated into winter and summer components as shown in Figures 1 and 2. Superposed on these is the viscous small-scale limitation hypothesized by Hines and the pressure scale height from the 1959 ARDC Model Atmosphere,[5] as another scale length of interest. From 100 to 125 km, the small-scale limit of Hines indeed shows a relationship to the measured value of these minor modes. However, at about 130 km, for the summer data, there appears to be an abrupt transition of the nodal sizes from Hines limit to a value proportional to the atmospheric pressure scale height. Since the 1959 ARDC Atmosphere was proposed for essentially a summer day, this suggests a possible connection between the parameters of scale height and the altitude variations of the wind velocity above 140 km.

These conclusions are obviously rough and highly debatable. However, the empirical fit to data gives some credence to them. It is also obvious that many more experiments of this nature must be performed, to gather more statistical evidence, before any definite conclusion can be reached.

References

1. C. O. HINES, Internal atmospheric gravity waves at ionospheric heights, Can. J. Phys. 38:1441-1481, 1960.
2. E. MANRING, Study of winds, diffusion and expansion of gases in the upper atmosphere, NASA Rept. NAS5-215, 1962.
3. N. W. ROSENBERG, H. D. EDWARDS, and J. W. WRIGHT, Ionospheric winds: Motions into night and sporadic E correlations, Proc. Intern. COSPAR Symp., 4th, Warsaw, North-Holland Publishing Company, Amsterdam, 1963.
4. G. V. GROVES, Private communication, 1960.
5. R. A. MINZNER, K. S. W. CHAMPION, and H. L. POND, The ARDC Model Atmosphere, 1959, Air Force Surveys in Geophysics No. 115, Air Force Cambridge Research Laboratories, Bedford, Mass., 1959.

XXII. Propagation by High Altitude Chemical Plasma Releases*

N. W. Rosenberg and D. Golomb
Air Force Cambridge Research Laboratories
Bedford, Massachusetts

Abstract

Physical or chemical techniques can be used to form localized regions of high electron density in the upper atmosphere. One method is described in detail wherein a mixture of cesium nitrate, aluminum powder and a high explosive is detonated in the 90 to 120 km altitude region of the upper atmosphere. The partially ionized reaction products expand to form a cloud from which radio waves can be reflected or scattered. In night releases, the free electrons are generated in the explosion by thermal ionization; in day releases additional photoionization of cesium occurs by absorption of solar UV. The reflected radio signal duration and intensity are dependent on altitude, time of day, and wind shears. In addition to thermal ionization and photoionization, major factors in determining the usefulness of chemical plasma clouds for radio wave propagation are their size, structure and orientation with respect to the transmission path.

1. INTRODUCTION

In this report a special application of 'ions in flames' is described; that is, the study of partially-ionized reaction products released into the upper atmosphere from

*Reprint from "Ions and Electrons in Combustion Systems", Amer. Inst. Aeronautics & Astronautics Series, Vol. XII (1963). Reprinted by permission.

vertical probe rockets. One objective of these experiments has been to create localized high electron densities (so-called electron clouds) for study of over-horizon propagation of radio frequency signals.

Over-horizon radio frequency propagation can be achieved in several ways:

(1) Reflection and scattering can occur from the natural E and F layers of the ionosphere, which are the normal modes of shortwave broadcasting. The transmitted electro-magnetic waves are 'bounced' back and forth between the ionized layers of the atmosphere and the ground until they reach the receiver. The reflection capability of these layers is dependent, among other things, on the electron density of the reflecting region which averages about 10^5 electrons/cm^3 at the 100 km altitude region called the E-layer, and 10^6 electrons/cm^3 at the 250 km altitude region called the F-layer.

The maximum radio frequency reflected at oblique incidence from a horizontal plasma sheet is given by

$$f = 0.009\, n^{1/2} \sec \phi \qquad (1)$$

where the frequency f is given in megacycles, n is the number of electrons per cm^3 in the plasma sheet, and ϕ is the angle of incidence measured from the vertical. The maximum attainable useful incidence angles from the vertical (in the F-layer) are about 70 to 75^o, permitting reflection of frequencies in the HF range; that is, 3 to 30 Mcps.

(2) Reflection of higher frequencies than those reflected by the normal E and F layers is possible from naturally-occurring passive reflectors of higher electron content than the ionosphere, such as meteor trails, formed by ionization of ambient air heated by meteor passage in the 90 to 110 km region. These trails attain a radar cross-section of 10^3 to 10^4 m^2 for frequencies between 30 and 100 Mcps. The major disadvantage of meteor trails as reflectors is, of course, their unpredictable occurrence. Reflection is obtained for a few seconds per trail, at a rate of one trail per minute, permitting over-the-horizon propagation for several minutes per hour.

(3) Reflection can be achieved by solid-surfaced passive reflectors, such as satellites, orbiting balloons and needles. Satellites and balloons are reflectors for wavelengths smaller than their radii and their small reflecting area requires powerful transmitters and receivers. Needles are even more selective in the transmittable frequencies. Active transponders such as the Telstar and Relay satellites receive at a pre-selected frequency which is amplified and re-transmitted.

(4) Artificial gaseous plasmas are most effectively generated in a relatively narrow altitude region extending between 90 and 120 km. Below this region the high collision frequencies increase the rate of electron loss mechanisms; above this altitude the increased diffusion rates cause a rapid dissipation of released gaseous material. Within the proper altitude region, however, the following methods

are presently being investigated for plasma generation: (a) striking of an electric arc from rocket-borne battery cells[1]; (b) cyclotron resonance heating of a region in the ionosphere by ground-based or rocket-borne high powered transmitters of the proper frequency[2]; (c) utilization of solar and chemical energy to photoionize and thermally ionize chemicals dispersed at the proper altitude. It is this last type of plasma generation which will be discussed in more detail with regard to ionization efficiency and propagation characteristics.

2. CHEMISTRY OF ELECTRON CLOUDS

The first successful electron cloud was formed in 1956 by release of 8 kg (275 moles) of nitric oxide at 95 km altitude in sunlight.[3] Nitric oxide, having an ionization potential of 9.25 eV, is readily photoionized by the solar Lymar - α, and a region of increased electron density was detected by radar echoes at the proper altitude for about 10 minutes following release. In subsequent experiments[4] nitric oxide was replaced by potassium and cesium, the ionization potentials of which are 4.32 and 3.86 eV, respectively. The nitrate salt of the desired alkali metal was mixed with aluminum powder in a ratio of 2.66 moles Al to 1 mole MNO_3, the total weight being about 25 kg. The mixture was packed into a canister equipped with a timer initiated igniter, set to ignite the mixture when the rocket attained an altitude of about 100 km. Upon ignition the mixture reacted, bursting the canister and expanding into a fireball composed mainly of alkali vapor, nitrogen and condensed Al_2O_3. At the high explosion temperature some of the alkali vapor was ionized, thus augmenting the solar photoionization with initial thermal ionization. In a series of day and night-time releases, distinct radar echoes were obtained both on back-scatter and on forward scatter circuits.[5] The nighttime effect was of shorter duration than the daytime effect, due to recombination and attachment processes, without photoionization. Ground tests indicated that the alkali nitrate-aluminum reaction is deflagrative; that is, on heating, the mixture reacts without detonation. In a closed vessel the reaction proceeds with pressure build-up until the vessel ruptures, scattering and extinguishing the unreacted portion of the mixture. Since the static burst pressure of the canister used was about 250 to 500 atm, the reaction proceeded until this pressure was attained. The void volume in the canister was such that only 3% of the above composition reacted before vessel rupture, which resulted in a low chemical yield. The estimated flame temperature of the reaction products at 500 atm is 4900°K, at which condition potassium is about 1% ionized.[6] However, substantial recombination, by as much as three orders of magnitude, can occur during the expansion process.

More recent experiments by Rosenberg and coworkers[7,8] improved the chemical yield to near 100% in detonation of 18 kg mixtures formed by adding a high ex-

plosive, such as RDX or TNT, to the cesium nitrate and aluminum. In such mixtures the equilibrium electron yield is relatively low due to the high pressure of the reaction zone and the presence of electron attaching species such as OH. Furthermore, it is generally agreed that aluminum does not fully react in the detonation zone; that is, considerable reaction occurs during expansion of the explosion products. Therefore, it is extremely difficult to estimate the number of electrons generated and decayed in the process of detonation and expansion of the above mixture. Radar returns obtained at a number of frequencies from high altitude releases immediately after the initial expansion is at present the best way to assess the thermal ionization yield of such reactions. Such assessments place the degree of ionization of the gaseous products after expansion in the order of 10^{-4}. Since cesium is 6% of the gaseous products, the degree of ionization of cesium is about 1.6×10^{-3}.

The major reaction products from the RDX-$CsNO_3$-Al explosion are CO, H_2, N_2, and Cs vapor, and condensed Al_2O_3. Altogether about 430 moles, or 2.5×10^{26} gaseous molecules, are liberated from the 18 kg payload. These gases expand to form a cloud of 100 to 1000 meters diameter, depending on altitude. Optical observations show that the clouds are initially spherical, and calculations may be based on cloud models where it is assumed that the clouds have a 'square-well' density distribution; or, alternately, a Gaussian density distribution, with the tails of the Gaussian being overlapped by the ambient which was pushed aside by the expanding gases (Figure 1). After completion of the (rapid) expansion, the total number density is assumed as a first approximation to be constant throughout the region and equal to the ambient number density. The radius of the spherical 'square-well' density cloud is given by

$$r \quad \left(\frac{3}{4\pi}\right)^{1/3} \left(\frac{N}{n_a}\right)^{1/3} \tag{2a}$$

where N is the total number of gaseous molecules released and n_a is the ambient number density at the release altitude. For a Gaussian cloud, the equivalent para-

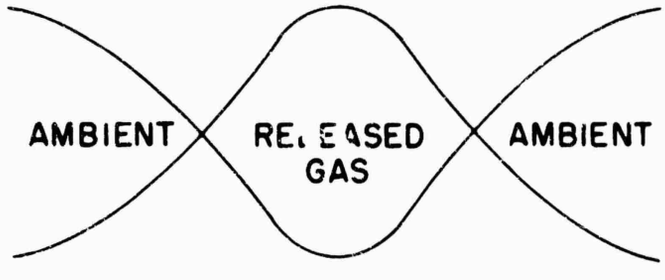

FIGURE 1. Model of Density Profile of Released Gases and Ambient

meter is the Gaussian half width; that is, the radial distance from the center where the density falls to 1/e of the center point density. The Gaussian half width, h, is given by

$$h = \frac{1}{\pi^{1/2}} \left(\frac{N}{n_a}\right)^{1/3} . \tag{2b}$$

Thus, r = 1.1h; that is, these parameters differ only by 10%, and for calculation of diffusion times it is quite immaterial which model one assigns to the density distribution. In Table 1 the Gaussian half-widths are calculated as a function of altitude based upon ambient density values of the CIRA standard atmosphere.[9]

TABLE 1. Gaussian half-width, h, for a cloud containing 2.5×10^{26} gaseous molecules as a function of altitude

Altitude (km)	n_a (particles/cm^3)	h (cm)
80	4.03×10^{14}	5.0×10^{3}
100	9.98×10^{12}	1.65×10^{4}
120	5.15×10^{11}	4.5×10^{4}
140	6.55×10^{10}	9.0×10^{4}

Based on these parameters, let us estimate the optimum altitude region for the deposition of reasonably long-lived RF reflecting electron densities. The upper altitude limit is determined by rapid diffusional loss. An electron cloud becomes 'invisible' to radio frequency waves of 10Mcps when the number of electrons per cm^3 drops below 10^6 at its center. The diffusion time of a spherical Gaussian cloud is given by[10]

$$t_u = \frac{h^2}{4D_a} (u^{2/3}-1) , \tag{3}$$

where t_u is the time in which the center point density reaches a value 1/u of its initial value and D_a is the ambipolar diffusion coefficient at a given altitude. We are interested in the time required to fall from a center point density of electrons

$$n_e(0) = 10^{-4} n_a \text{ to } n_e(t_u) = 10^6 \text{ cm}^{-3} ,$$

where 10^{-4} is the assumed degree of ionization. This time is set forth in Table 2

for various altitudes. From Table 2 it is seen that the life time of the cloud at 140 km altitude is 40 seconds and this height is probably the upper limit for reasonable life. In practice it was found that this altitude is closer to 120 km.

TABLE 2. Initial center point electron densities and the times necessary to reduce these to $10^6/cm^3$ by ambipolar diffusion

Altitude (km)	$n_e(0) = 10^{-4} n_a$ (electrons/cm^3)	D_a (cm^2/sec)	u	t_u (sec)
80	4×10^{10}	4.8×10^3	4×10^4	1.5×10^6
100	1×10^9	2.2×10^5	1×10^3	31000
120	5×10^7	6.9×10^6	50	920
140	6.5×10^6	1.3×10^8	6.5	40

Optical observations show that clouds deposited below 100 to 110 km usually grow by eddy diffusion (Figure 2) with turbulent diffusion rates higher by as much as two orders of magnitude than molecular diffusion rates. Therefore, the diffusion times for 80 and 100 km in Table 2 are perhaps overestimated by a factor of 10 to 100.

The lowest useful altitude is determined by losses due to recombination of electrons with positive ions and attachment of electrons to neutrals. Electron densities above $10^8 cm^{-3}$ cannot be maintained for considerable time periods, because a Bates, Kingston and McWhirter type collisional-radiative recombination[11] with an effective rate coefficient of $10^{-9} cm^3 sec^{-1}$ will take about 10 seconds to decrease the electron density from 10^{10} to $10^8 cm^{-3}$. When the electron density is in the order of $10^8 cm^{-3}$, the predominant loss mechanism at the lower altitudes is probably a three body attachment to the explosion products and to molecular oxygen diffusing into the cloud by molecular and turbulent diffusion. The rate coefficient for this process is about $5 \times 10^{-30} cm^{-6} sec^{-1}$ (Ref. 12). With a density of the attaching molecule and the third body of $\sim 4 \times 10^{14} cm^{-3}$ at 80 km, the time to decrease the electron density from 10^8 to $10^6 cm^{-3}$ is about 6 seconds; at 90 km ($n_a = 6 \times 10^{13} cm^{-3}$), the time is 250 seconds. This places the lower altitude limit at about 90 km, in agreement with experience. Thus, the 90 to 120 km altitude region is where long-lived electron clouds can be generated. In defining the optimum altitude region, we did not consider the effect of photoionization. However, photoionization can result in the prolongation of electron cloud life time within the optimum altitude region but will not extend this region, since the arguments about diffusion and recombination losses are not altered.

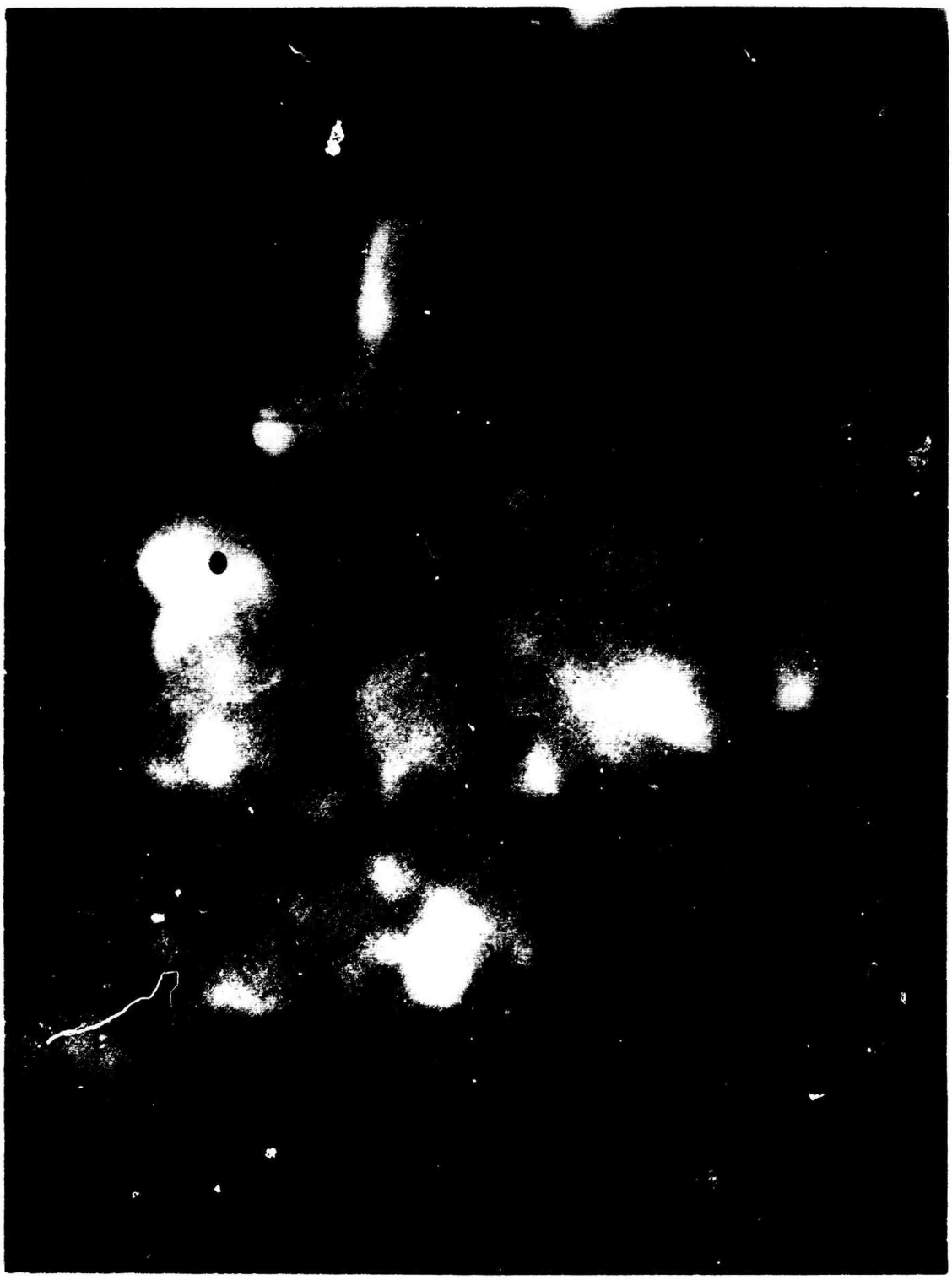

Figure 2. Typical Electron Cloud in The 100 km Altitude Region, 250 Seconds After Burst; Sunlit Against Dark Sky Background (Twilight Conditions). Note Turbulent Structure. Total Diameter 3 to 4 km.

It appears that improvement of the initial degree of ionization of the chemical reaction is not likely to increase the life time of electron clouds, because of rapid recombination losses during the early times when high electron densities are present. However, the size and structure of the cloud, which are dependent on the quantity of released material, the altitude of release, and atmospheric conditions (wind, turbulence, geomagnetic field, etc.) can affect the life time markedly, as discussed in the following section.

3. PROPAGATION CHARACTERISTICS OF ELECTRON CLOUDS

The mode of RF signal return from ionized regions is a complex phenomenon. The return at a given frequency can be evaluated empirically in terms of its intensity, polarization, phase delay, frequency spread and shift, and angular dependence. The scattering mechanism can only be inferred from such measurements and by construction of simplified theoretical models. For the point electron clouds three major modes of signal return seem to be operative.[13, 14]

(1) Perfect or partial reflection from a wholly overdense volume. In this case the received signal cross-section is proportional to the physical area of the reflector, the electron density is given by Eq. (1), and no short period fading of the signal is obtained.

(2) Reflective scattering from a large number of oversense irregularities. In this case the received signal cross-section is proportional to the number of irregularities and their scale, and considerable short period fading is observed due to interference.

(3) Booker-Gordon type scattering from underdense irregularities.[15] For this mode the scattered signal cross-section is proportional to $(\overline{\Delta n})^2$, the mean square departure of electron density from the mean, and the scale size of the (turbulent) irregularities. This mode will also result in signal fading.

Analysis of tens of electron cloud releases with regard to signal strength, duration, fading and angular dependence indicates that for electron clouds in the 100 km altitude region all three modes are operative simultaneously, with the contribution by each mode depending on the amount of turbulence, self-induced as well as atmospheric. After tens of minutes in sunlit releases and several minutes in night releases, the overdense reflectors decay and only the third mode remains significant.

3.1 Life Time of Electron Clouds

Figure 3 represents the life time of several electron clouds as a function of altitude and beam incidence angle for signals in the lower end of the VHF band.

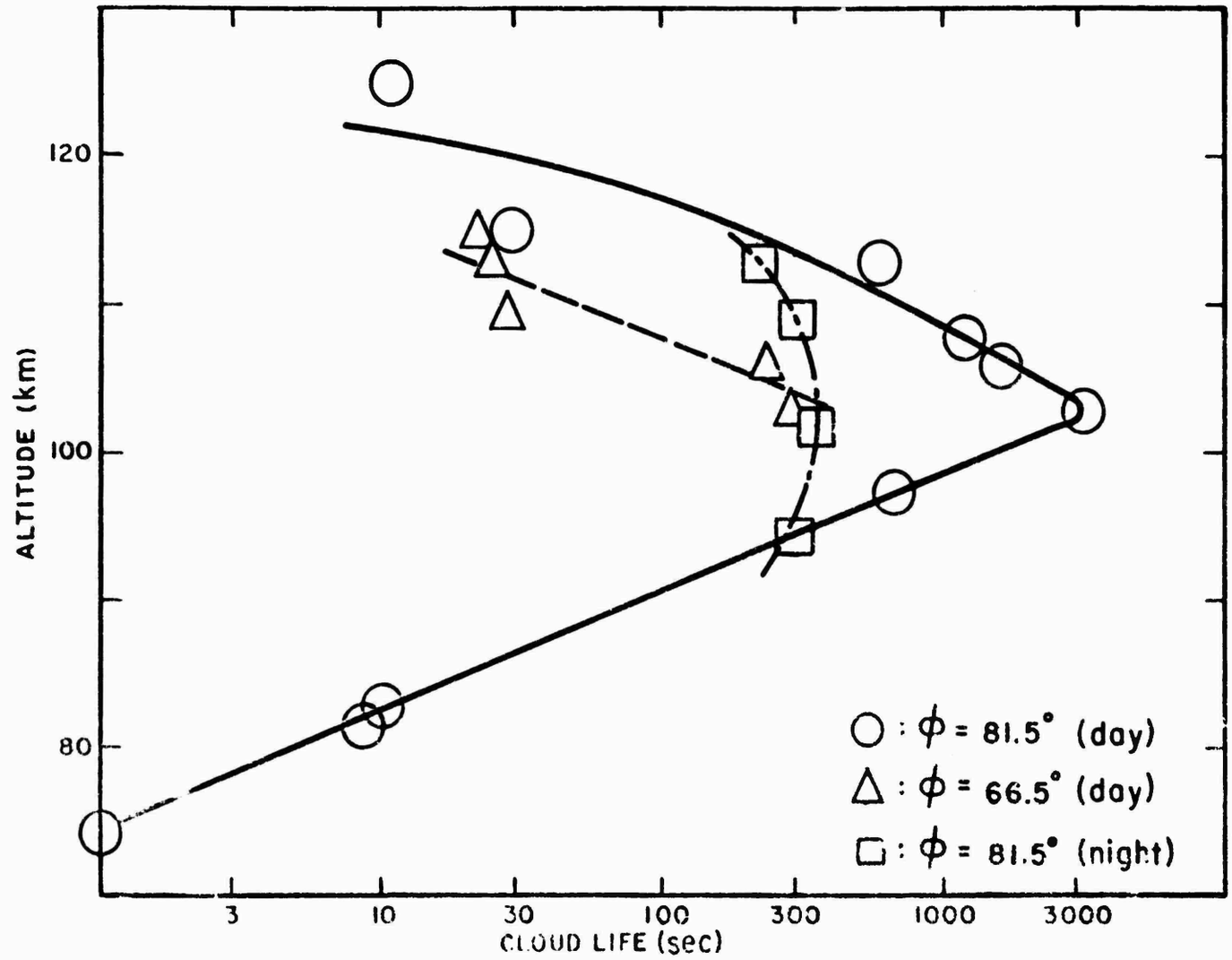

Figure 3. Cloud Life Time Versus Altitude

Sunlit clouds observed with an incidence angle $\phi = 81.5^{o}$, are denoted by circles. It is seen that clouds of considerable life times are obtained within the 90 to 120 km region, where signals are propagated for 100 to 3000 seconds. The optimum altitude appears to be in the 100 to 110 km region. The 103 km cloud may have been the best propagation cloud because it was deposited in the optimum altitude region, and also because it was dragged out by wind shears to large horizontal dimensions, as observed by optical tracking. Therefore, it seems that the size and orientation toward the transmission path are major factors in determining the life time of electron clouds as propagation links. Since wind velocities and directions may vary quite rapidly as a function of altitude, the optimum altitude for electron clouds can be expected to shift within the 100 to 110 km region, and it should not be inferred from Figure 3 that 103 km is always the best altitude. The size of the cloud is dependent also on the amount of released gases. From recent, not yet fully analyzed experiments, it was confirmed that 4 kg charges do result in shorter lived electron clouds with smaller radio cross-section than the 18 kg charges represented in Figure 3.

Night clouds (squares in Figure 3) last 3 to 10 times less for a given frequency and incidence angle than sunlit clouds, depending on altitude of release. Thus, useful propagation links of several minutes duration can be maintained with night releases, where photoionization does not play a role.

The life times denoted by triangles in Figure 3 were measured at a more obtuse incidence angle than those denoted by circles and are shorter by an order of magnitude. For the overdense reflection mode this is a consequence of Eq. (1), whereby a wave of a given frequency is reflected from lower electron densities at greater incidence angles to the normal. For instance, a 30 Mcps signal is reflected from a plasma sheet containing 2×10^{5} electrons per cm^{3} at $\phi = 81.5^{o}$, whereas 1.5×10^{6} electrons per cm^{3} are necessary for $\phi = 66.5^{o}$. By the same token, electron cloud life times for given incidence angle are inversely proportional to frequency.

3.2 Cloud Cross-sections

For the reflective cloud model, the radio cross-section at a given frequency is dependent on the effective reflection area of the overdense regions and on the scattering angle. For underdense scatter, the cross-section is dependent on the mean square departure of electron density from the mean and on the scale size of turbulent eddies in the cloud. All these variables are strongly time dependent, since the cloud is in a continuous dynamic condition (expansion, diffusion, turbulence) and the electron inventory is changing by dilution, recombination, attachment and photoionization. Figure 4 gives the time function of cross-sections at about 30 Mcps and $\phi = 81.5^{o}$ averaged over one minute intervals. The radar cross-sections display a similar altitude dependence as do overall signal durations, the

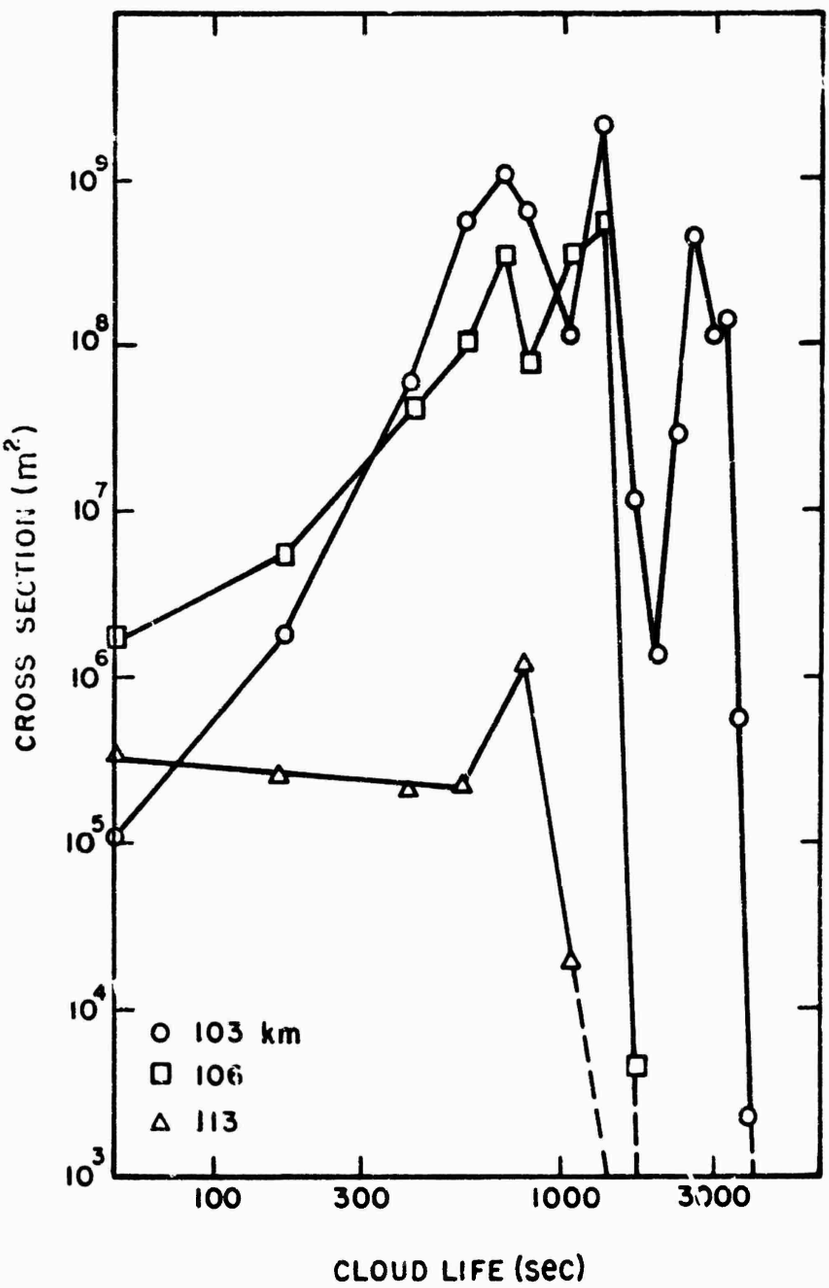

Figure 4. Cloud Radio Cross-Section Versus Time

103 km cloud attained in general the largest cross-sections, at lower and higher altitudes the averaged cross-sections decrease. It is seen that radar cross-sections in the order of 10^6 to $10^8 m^2$ are readily obtained for tens of minutes, but with significant fading and enhancement, due to interference and reinforcement of multipath signals.

Since the signals display a considerable short term fading, no clear-cut cross-section can be assigned to the clouds which would allow the assessment of their actual physical area (or volume) at a given time. Thus, it is difficult to use radar cross-sections from turbulent electron clouds to evaluate absolute electron densities as a function of time and space and to obtain the associated diffusion, recombination and attachment coefficients. This, of course, does not affect the possible use of artificial electron clouds as propagation links with properly designed systems. The tracking by radar of the gross movement of the clouds without knowing their intricate structure also gives important information on atmospheric winds and wind shears. Any acceptable cloud model which can be used to correlate the observed behavior of artificial electron clouds will also be of significant value in interpretation of radio frequency returns by natural events such as sporadic-E and meteor trails.

References

1. E. W. IRRE, Zimney Corp., Monrovia, Calif., formerly with ACF Electronics, Hyattsville, Maryland, private communication.
2. G. DESCHAMP, Univ. of Illinois, Urbana, Ill., Air Force Cambridge Research Laboratories, Bedford, Mass., Technical Rpt. 1071, 1962.
3. F. F. MARMO, J. PRESSMAN, L. M. ASCHENBRAND, A. S. JURSA and M. ZELIKOFF, J. Chem. Phys. 25:187, 1956.
4. F. F. MARMO, L. M. ASCHENBRAND and J. PRESSMAN, ARS Journal, 30: 523, 1960.
5. F. F. MARMO, L. M. ASCHENBRAND and J. PRESSMAN, Planet. Space Sci. 1:227, 1959, et seq.
6. A. W. BERGER, D. GOLOMB and J. O. SULLIVAN, J. Phys. Chem. 64:949, 1960.
7. N. W. ROSENBERG, Artificial Perturbation of the Ionosphere, in Space Research II, North-Holland Publ. Co., Amsterdam, 1961.
8. Project Firefly, Air Force Cambridge Research Laboratories, Bedford, Mass., Technical Report 256, 1961.
9. COSPAR International Reference Atmosphere, North-Holland Publishing Co., Amsterdam, 1961.
10. H. K. BROWN and J. PRESSMAN, Spherical Gaussian Diffusion in the Upper Atmosphere, Geophysics Corp. of America, Bedford, Mass. Technical Report 62-3-G, 1962.

11. D. R. BATES and A. DALGARNO in Atomic and Molecular Processes, D. R. Bates, ed., Academic Press, New York and London, pp. 253-257, 1962.

12. L. M. CHANIN, A. V. PHELPS and M. A. BIONDI, Phys. Rev. 128:219, 1962.

13. J. R. HERMAN and T. M. NOEL, AVCO Corp., Wilmington, Mass., in Project Firefly, Vol. IV, Air Force Cambridge Research Laboratories, Bedford, Mass., Technical Report 826, 1962.

14. H. G. CAMNITZ, Cornell Aeronautical Laboratory, Buffalo, N. Y., ibid.

15. H. G. BOOKER and W. E. GORDON, Proc. IRE, 38:401, 1950.

XXIII. A Systematic Study of Hydrocarbon Missile Exhaust Reactions with Atmospheric Constituents*

Neville Jonathan and G. Doherty
Geophysics Corporation of America
Bedford, Massachusetts

Abstract

Details are given of the performance of a laboratory apparatus designed for the simulation of the conditions which give rise to the light emission from missile trails during the boost and early post-boost phases.

Successful attempts to obtain measurements of the light emission from chemical reactions down to 8 microns Hg are described. Particular reference is made to the light emitting reactions of carbon monoxide and acetylene with atomic oxygen. A method is also given whereby atomic oxygen concentrations may be accurately measured at low pressures.

Future plans are outlined for further studies which should give additional information regarding missile trail chemiluminescence and possible ways of keeping its value to a minimum.

1. INTRODUCTION

One of the fundamental phenomena on the basis of which AICBM systems may be constructed is the emission of light from missile trails during the boost and early post-boost phases. Also, such emission from our own missiles may be used by

*This research was sponsored by ARPA under AF 19(628)-231 and monitored by GRD, AFCRL. Reprinted from AMIRAC Proceedings.

enemy detection systems as part of their warning network. Consequently, detailed studies of the nature of these light emissions, which include the mechanisms, the altitude dependence, the concentration dependence, and the over-all glow structure, are of importance in attempting to improve our AICBM capabilities and as a method also for decreasing the intensity of the light from our missile trails which would give away our launchings.

The detailed knowledge of the reactions involved in chemiluminescence should enable us to know more certainly what specific bands and lines offer the best possibility for detection. They also indicate what are the potentialities for altering the emission characteristics of the various types of missile chemical propulsion systems. This may be accomplished, for example, by chemical additives but such use of chemical additives must rest securely on a foundation of knowledge of the mechanisms involved in order to inhibit efficiently and diminish the most important lines or bands. Also, such fundamental studies will enable us to analyze more appropriately possible enemy attempts to reduce the boost and early post-boost luminescence.

In all probability, one of the main causes of the light emission which has been observed from the missile trails is a result of chemiluminescence. Chemiluminescence is a term which is applied to the emission of radiation from a system which is the direct result of a chemical reaction. Many examples of chemiluminescence have been reported in the open literature, involving either an atomic gas such as hydrogen, nitrogen, or oxygen, or ozone, with other gases, particularly unsaturated hydrocarbons. The degree of luminescence and its spectral position depends upon the gases which react. The spectral distribution is also dependent upon the type of excitation which is induced into the product species. The emissions arising from missile trails obviously come from species in excited electronic states. This can be shown since the critical potential, which is a measure of the energy difference between electronically excited states, is of the order of 5 E.V., that is, about 8×10^{-12} erg per molecule. Insertion of this value into the quantum theory equation $\epsilon = h\nu$, where h is Plank's constant, gives a value for the frequency of radiation accompanying an electronic transition of about 1.2×10^{15} vibrations per second. This is equivalent to a wavelength of 2500 A. In the same way it can be shown that pure vibrational level changes should give emission in the near infrared.

Any attempt to study the chemiluminescence arising from the reaction of unspent gases in missile trails with atmospheric constituents must take into account the conditions which exist in the region of suspected chemiluminescence. These conditions are predominantly (1) a very low pressure, (2) variable amounts of atomic species, (3) variable amounts of missile trail gases, and (4) variable amounts of other supposedly inactive constituents such as molecular oxygen.

In the 13th Annual AMRAC Meeting, some details were given of a proposed apparatus capable of carrying out the conditions of the preceding paragraph. Since

that time the apparatus has been put into full-scale operation and, after some minor modifications, has been found to function satisfactorily. As will be seen, it has proved to be an extremely valuable and versatile piece of equipment for the study of ultraviolet and visible chemiluminescence at low pressures.

2. EXPERIMENTAL

A block diagram of the complete apparatus is given in Figure 1. Molecular oxygen or a mixture of molecular oxygen and inert gas is passed, by a flowmeter and valve, through a microwave discharge unit. This partially dissociates the molecular oxygen which then enters the reaction vessel after first passing through a Wood's light trap and a device to control the number of oxygen atoms. The supposed missile trail gas enters the reaction vessel through a needle valve and a calibrated flowmeter. Gases used during the experiments are purified directly on the system. These included the nitric oxide and nitrogen dioxide which are used for titration of the oxygen and nitrogen atom concentrations. In this manner the danger of contamination of the gases by transfer from a purification apparatus to the experimental system is avoided.

In the 13th Annual AMRAC Meeting, a reaction cell was described which was anticipated to be of use for low pressure chemiluminescence studies. Extensive use of the cell has been made and successful attempts to detect chemiluminescence down to pressures of 8 microns of mercury have been effected. The cell consists of a 50 liter Pyrex flask which is evacuated by a N. R. C. 4-inch oil diffusion pump backed by a large Welsh mechanical pump (Figure 2). Using both pumps, a bulb pressure of 10 microns can be maintained when the input flow of gases is 70 standard ml per minute. The gas streams meet near the center of the cell and mix by diffusion. In effect the result is the same as a well stirred reactor. The light gathering power of the cell is increased by covering it with a layer of magnesium oxide which is an excellent diffuse reflector. The luminescence fills the cell and is, of course, difficult to focus through a conventional spectrometer since it in no way approximates to a point source. However, if the aperture through which the radiation leaves the cell is kept small, then the radiation will be mainly focused in a narrow beam. Provision is also made for heating the cell to a maximum of 700°K by means of the external heating jacket. The temperature of the cell is varied by changing the voltage in the heating circuit. The internal temperature was measured by means of a calibrated thermocouple wire inserted through one of the side arms.

The spectrum of the light emission was recorded between 2000 and 6000 A. using a conventional Perkin-Elmer monochromator equipped with a photomultiplier, as described previously. [1]

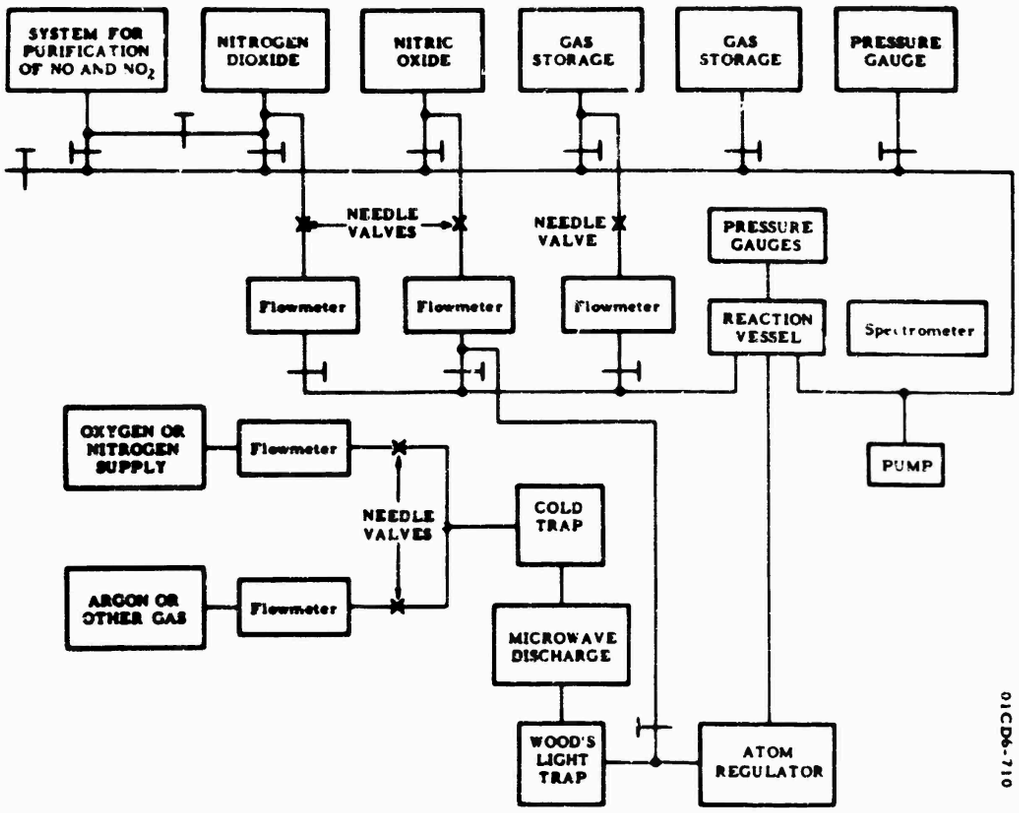

Figure 1. Block Diagram of Apparatus for Chemiluminescence Reaction Studies

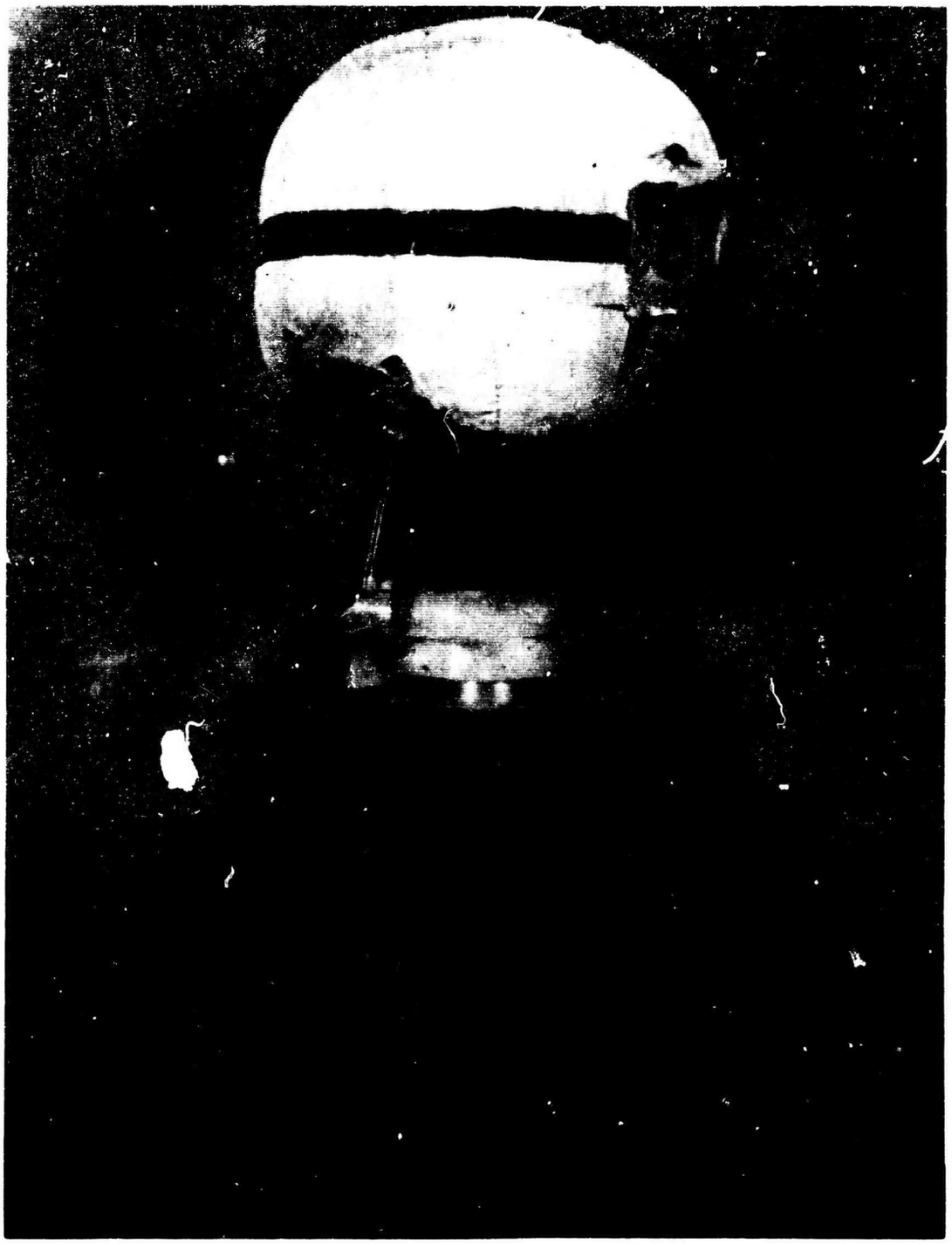

Figure 2. Reaction Cell

A modification of the usual technique for the titration of oxygen atom concentrations by nitrogen dioxide gas has been developed so that oxygen atoms can be measured accurately at pressures down to 10 microns of mercury. The method depends upon the two reactions

(1) $O + NO_2 \rightarrow NO + O_2$ (non light emitting)

(2) $O + NO \rightarrow NO_2^* \rightarrow NO_2 + h\nu$

Reaction (1) is very much faster than reaction (2) so that there is virtually no light emission when $[NO_2] = [O]$. When $[NO_2]$ is less than $[O]$ there will be light emission from the slower reaction. It can easily be seen that the maximum light emission will occur when $[NO_2] = 1/2\ [O]$. The usual method for titration of oxygen atoms has been to observe visually the position of non light emission as the amount of titrant NO_2 is varied. This procedure is unsuitable for work at low pressures and for work in a large volume. We have developed the technique whereby the light is observed with a standard photomultiplier and microammeter setup and the intensity is plotted as a function of nitrogen dioxide added. If one neglects all other considerations then one should obtain a symmetrical curve, as indicated by the broken line in Figure 3. Then the oxygen atom concentration can be calculated either from the NO_2 required to give maximum intensity or from that required to give minimum intensity. These two values should then agree. In practice, however, one finds that the curve has an asymmetry, as indicated by the solid line in Figure 3. This is due to the fact that at the end point A, the NO_2 is titrating the oxygen atoms which enter the cell. However, the point B will give a value of the steady state oxygen atom concentration in the cell since the NO + C reaction is much slower and some oxygen atoms which are measured at B will actually have recombined owing to wall collisions to give molecular oxygen. These values agree within 10% at 10 microns pressure since the residence time of the gases in the cell is small and so wall collisions are few. However, at pressures of 1 mm where under our conditions the residence time may be of the order of 60 seconds, the losses are large and the difference between the two values may be as much as 50%. It is, therefore, important to use the oxygen atom concentration which corresponds to the reaction speed. Hence, for the carbon monoxide-atomic oxygen reaction the peak intensity value was always used since the rate of this reaction is of the same order as that of O + NO. On the other hand, the atomic oxygen-acetylene reaction rapidly depletes the amount of atomic oxygen present and so the oxygen atom concentration corresponding to the end point nitrogen dioxide titration was always used.

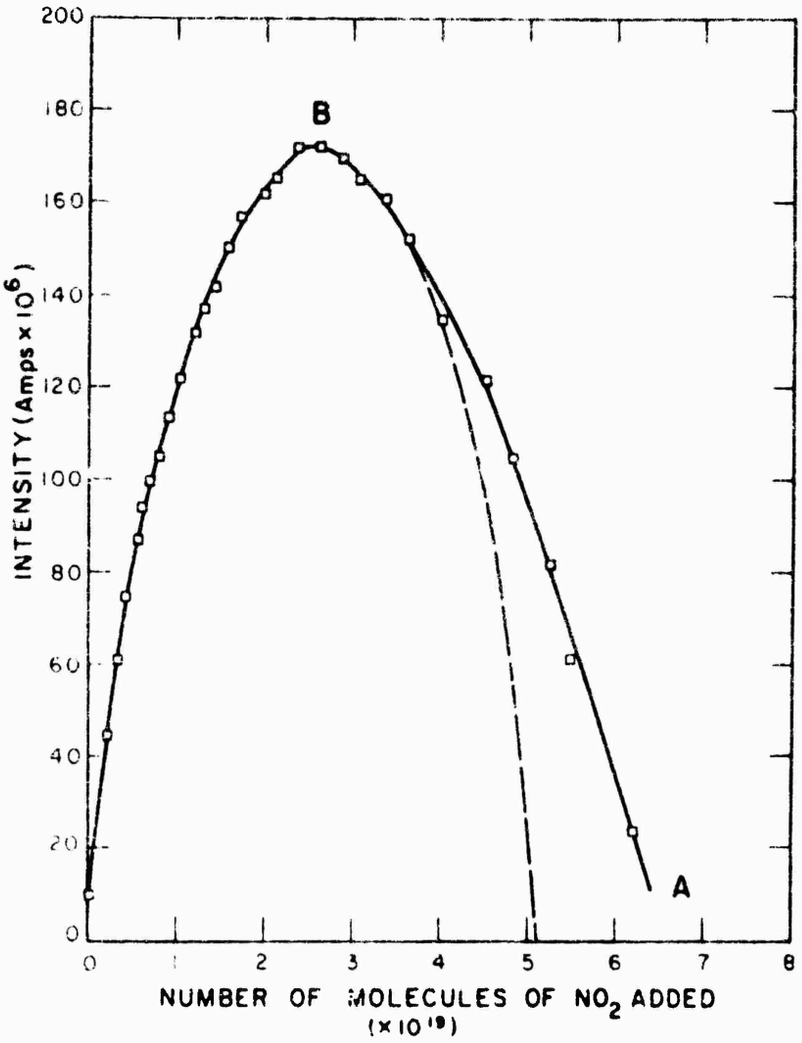

Figure 3. Plot of Light Intensity Versus Amount of NO_2 Added

3. RESULTS

It is proposed here to give an account of two of the reactions which we consider to be among the most likely to contribute to missile trail chemiluminescence. These reactions are those of atomic oxygen with acetylene and with carbon monoxide.

3.1 Reaction of Atomic Oxygen with Acetylene

Details have previously been given of the type of bands which have been observed. These are from OH, CH, and C_2 radicals and an apparent continuum which arises from an unestablished source. A typical spectrum is shown in Figure 4. Under higher resolution these bands can be readily identified as arising from those radicals mentioned above.

Figure 5 shows some results presented last year of a pressure variation study in the pressure region 230 to 1000 microns of mercury. The prediction was then made that the C_2 bands would decrease in importance according to the decrease in the pressure of the reaction. Our spectra which have since been obtained at 10 microns bear out this prediction. The intensity of the continuum has increased markedly in relation to the C_2 bands. This indicates that the continuum light emission arises from a two body reaction rather than a three body one. This would explain the lower intensities as higher pressures as being the result of quenching of the light emission by a third body.

Figure 6 shows the results of variation of the acetylene flow rate in the 10 micron pressure region. The over-all pressure remained essentially constant as did the molecular and atomic oxygen concentrations. These results have been duplicated a number of times and are given in Table 1.

TABLE 1. Acetylene flow rate (molecules/min) required to give maximum band intensities

Spectrum	O Atom Concentration (atoms/min)	O_2 Concentration (molecules/min)	Flow Rate for Max. Intensity			
			C_2	CH	OH	Continuum
1 A	6.5×10^{19}	5.0×10^{20}	6.0×10^{20}	2.3×10^{20}	2.9×10^{20}	5.0×10^{20}
2 A	9.5×10^{19}	7.5×10^{20}	7.0×10^{20}	2.3×10^{20}	2.3×10^{20}	Indefinite
3 A	6×10^{19}	10×10^{20}	10.0×10^{20}	2.2×10^{20}	3.0×10^{20}	4.0×10^{20}

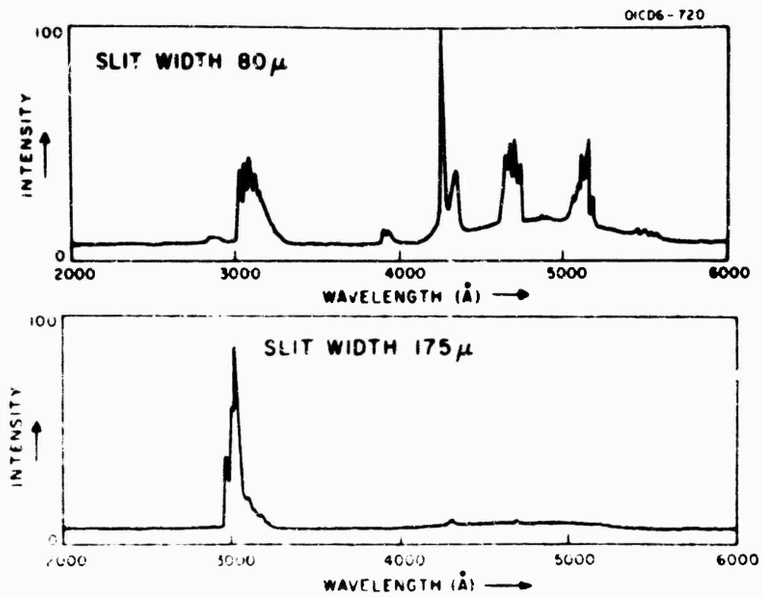

Figure 4. Spectrum of Light Emission from Atomic Oxygen Plus Acetylene (Upper) and Atomic Oxygen Plus Ethylene (Lower)

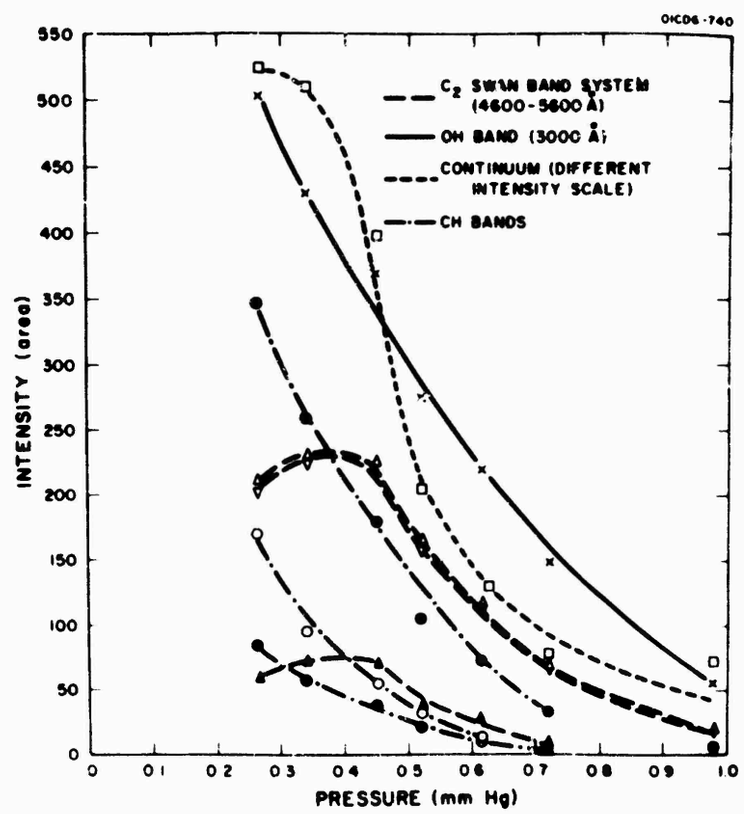

Figure 5. Typical Pressure Variation Study of Light Emission from O + Acetylene Reaction

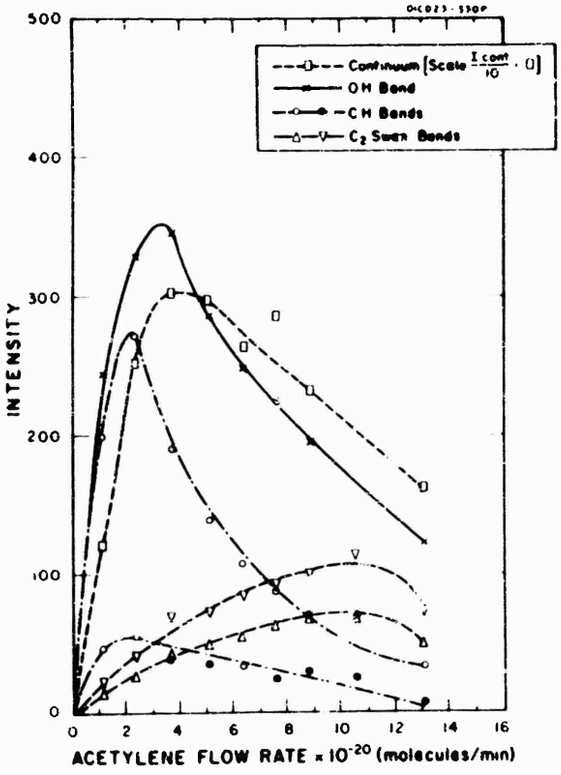

Figure 6. Variation of Band Intensities with Acetylene Flow Rate at Low Pressures

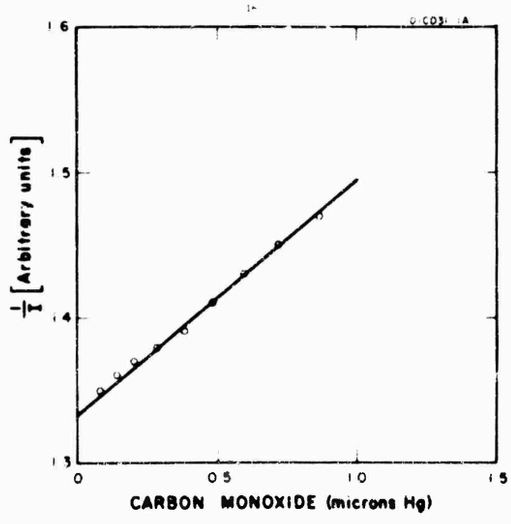

Figure 7. Atomic Oxygen 'Afterglow' Decrease in Accordance with Stern-Volmer Quenching Law

One can see from Table 1 and Figure 6 that the C_2 bands and continuum pass through their maximum intensities at much higher flow rates than the CH bands. The C_2 Swan bands seem to require an approximately equal number of oxygen and acetylene molecules to give maximum intensity. On the other hand, neither molecular nor atomic oxygen seems to affect greatly the maximum intensity position of the OH and CH bands. It would appear that these bands have a maximum intensity when the ratio of acetylene molecules to oxygen atoms is approximately three to one. This is an unlikely situation and it seems probable that both molecular and atomic oxygen are involved in the production of the radicals. A pressure variation study has not yet been completed but some preliminary observations from a study of the methyl acetylene-atomic oxygen light emission are probably relevant. It was noted that the over-all light emission at 100 microns was approximately equal to that at 10 microns although the concentration of each reactant has increased 10 times. This indicates that the light emissions are very sensitive to the over-all pressure, which would appear to show that quenching processes play a very large role in the reactions. The maximum intensities appearing at different acetylene flow rates would appear to be a clear indication that the radicals are formed at different stages of a multi-stage reaction.

A next step in the elucidation of the reaction mechanism must be a similar study in the absence of any molecular oxygen to that which has been made. Our apparatus is equipped to make these measurements and it is hoped to do so in the near future. These measurements should then give a good indication of the part which molecular oxygen plays in the over-all reaction mechanism.

3.2 Reaction of Atomic Oxygen with Carbon Monoxide

There have been several reports of the chemiluminescence arising from this reaction.[2,3,4] However, as far as we know, no attempt has been made to observe the luminescence below 500 microns of mercury. We have attempted to make some measurements at lower pressures in order to approximate more closely to the upper atmospheric conditions.

Using the apparatus already described, varying amounts of carbon monoxide were added to the fixed amounts of atomic and molecular oxygen in the reaction vessel. The over-all pressure was 8 microns of mercury and the atomic and molecular oxygen flow rates were 1.0×10^{20} and 15.5×10^{20} atoms/molecules per minute. The light emission was observed by a conventional standard photomultiplier setup. At all times there was a certain amount of emission from the so-called oxygen 'afterglow' arising from impurities in the tank oxygen used. This gives the O + NO light emission. Addition of carbon monoxide to this caused the 'afterglow' to diminish. As can be seen from Figure 7, the light emission actually decreases in accordance with the Stern-Volmer quenching law. Our conclusions from this ex-

periment are, therefore, that at 293°K and in the 10 micron pressure range, the carbon monoxide atomic oxygen luminescence does not occur to any significant extent and, in fact, carbon monoxide is quite an efficient quencher of luminescence, presumably acting in a third body process such as

$$O + NO \rightarrow NO_2^*$$

$$NO_2^* + CO \rightarrow NO_2 + CO$$

$$NO_2^* \rightarrow NO_2 + h\nu$$

The remainder of the experiments were carried out using the same apparatus at pressures between 250 microns and 1.5 mm of mercury. The luminescence arising from the reaction was very weak which meant that wide slits had to be employed on the monochromator. This consequently cut down on the degree of resolution available. However, under varying conditions of concentration and pressure, the emission always appeared as a continuum, varying only in intensity, between approximately 3000°A and 6200°A. In all probability this is the 'continuum' which has been reported as the carbon monoxide flame bands plus a large number of unidentified bands using photographic techniques.[4] Our results are not inconsistent with these since our degree of resolution with 2 mm slits would not be sufficient to resolve the bands suggested as being present.

The study of the light emission was continued using a standard photomultiplier setup. In all experiments it was found that there was a certain amount of 'afterglow' from the oxygen atoms owing to impurities, as described earlier. The light emission from the carbon monoxide reaction was obtained by subtraction of the microammeter readings obtained with and without carbon monoxide flowing.

The dependence of the glow on the concentration of carbon monoxide present was investigated in the following manner. Using a constant flow of molecular oxygen and maintaining a steady discharge, the flowrate of carbon monoxide was varied from 0 to 8 standard cc's per minute. The light emission was found to be linear with increasing carbon monoxide concentration.

The light emission variation as a function of atomic oxygen concentration was obtained in a similar way. The atomic oxygen concentration was varied while the carbon monoxide concentration was kept constant. The light emission was found to increase linearly with increase of atomic oxygen concentration.

The effect of changing the amount of third body present was next established. The molecular oxygen flowrate was varied from 63×10^{19} to 223×10^{19} molecules per minute, and varying amounts of carbon monoxide were added. The atomic oxygen concentration was measured in each case. The results are shown in Figure 8, which gives a clear indication of the lack of effect of varying amounts of the third body and of the first order dependence of the light emission on the atomic oxygen and carbon monoxide concentrations.

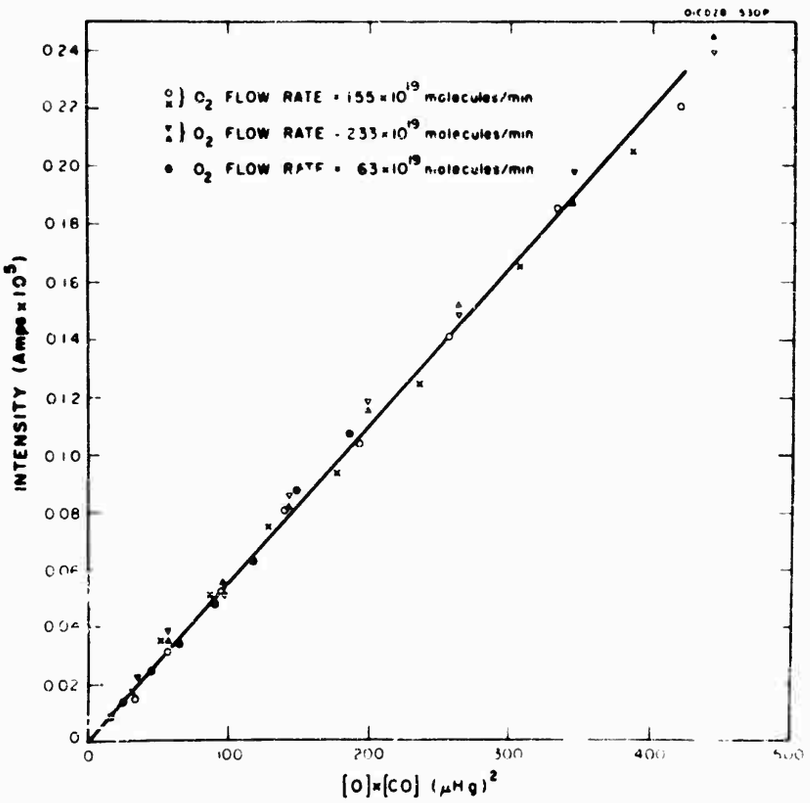

Figure 8. Variation of Intensity with Atomic Oxygen and Carbon Monoxide Concentration

The dependence of the light emission on the type of third body present was next investigated. The experiments were carried out by measuring the light emission using varying amounts of carbon monoxide with the molecular oxygen diluted with either helium or argon so that the predominant third was the inert gas. It was found that the light emission with argon or helium as the third body obeyed the same laws as when oxygen was the third body. However, the amount of light emitted per unit amount of [O] [CO] was different, showing that the light emission was dependent upon the nature of the third body present.

The light emission, as a function of pressure, was investigated over the pressure range 0.23 to 1.0 mm using molecular oxygen as a third body and from 0.5 to 1.0 mm using argon as the predominant third body. No significant change in the ratio of intensity to [O][CO] was observed over the pressure range studied. The ratio was, of course, dependent on the predominant third body, as explained above.

The results can be summarized by saying that the light emission was independent of both pressure and amount of third body present, but dependent upon the nature of the third body. In addition, the light yield showed a first order dependence on both atomic oxygen and carbon monoxide concentrations. These results are in agreement with the previous work of Clyne and Thrush but in apparent disagreement with that of Mahan and Solo who found that the light yield decreased with pressure. The latter workers also found that the amount of carbon dioxide formed is independent of the third body, which is not consistent with the reaction mechanism of Clyne and Thrush. A new mechanism which involves a three body process has been proposed in order to account for the data.[5] From the work we have done it is obvious that under room temperature conditions, the light emission would not be a source of importance in the upper atmosphere. However, it is to be noted that an increase in temperature of 90°K has caused an eight-fold increase in the light emission.[3] No work has yet been carried out on light emission above 284°K but if this figure is correct then one can anticipate a thirty-fold increase in the light emission at 650°K compared with 298°K. We hope to carry out the experimental study in the near future. The above figures mean that if the carbon monoxide from a missile trail was at a temperature of 2000°K when the reaction took place, then the light emission would be only of the order of a factor of ten less than the NO + O emission at 200°K, which are the conditions in the region of 100 km where it is known to give strong light emission. Therefore, at this stage, we cannot rule out the possibility of the carbon monoxide atomic oxygen reaction contributing appreciably to the light emission from missile trails.

4. CONCLUSIONS

This report has discussed a program for the systematic measurement of hydrocarbon chemiluminescent reactions with the upper atmosphere. These chemiluminescent reactions have been studied under variations of pressure and composition so as to understand the over-all variation of the rocket exhaust glow phenomena in the upper atmosphere. It is hoped that this type of systematic study will have consequences in the study of boost and early post-boost detection, programs for diminishing this type of emission from our missiles, and for an awareness as to possible enemy systems of detecting our missiles during these early phases.

Acknowledgments

We wish to thank Mr. D. Levine for valuable assistance in obtaining some of the data. Our thanks are also due to Dr. P. Warneck for many informative discussions.

References

1. N. JONATHAN, J. PRESSMAN and P. WARNECK, Experiments Simulating Chemiluminescent Reactions Between Missile Exhaust and Atmospheric Gases, 13th Annual Meeting of AMRAC, San Diego, 1962.
2. H. P. BROIDA and A. G. GAYDON, Trans. Far. Soc. 49:1190, 1953.
3. M. A. CLYNE and B. A. THRUSH, Proc. Roy. Soc. A269:404, 1962.
4. B. H. MAHAN and R. B. SOLO, J. Chem. Phys. 37:2669, 1962.
5. N. JONATHAN and G. DOHERTY, Unpublished data.

XXIV. Chemi-Ionization Processes in the Interaction of Missile Exhaust Products with Atmospheric Constituents

A. Fontijn
AeroChem Research Laboratories, Inc.
Princeton, New Jersey

Abstract

The upper atmospheric enhancement of rocket exhaust ionization is briefly discussed. A probable cause of this phenomenon is the occurrence of the reaction

$$CH + O \rightarrow CHO^+ + e^-$$

It is yet to be established whether the CH involved in this reaction is in its ground electronic state or in an excited state. Reasons are given to explain why this reaction may lead to a less diffuse ionization trail when it occurs in rocket exhaust gases than when it occurs due to upper atmospheric acetylene releases.

A laboratory research program, based on the reaction $O + C_2H_2$, is outlined, the goal of which is to fully elucidate the reaction mechanism and to quantitatively determine the efficiency of processes leading to upper atmospheric chemi-ionization.

The work is carried out in a Wood-Bonhoeffer type flow system and involves the measurement of ion concentration, light emission intensity and the concentration of reactants and reaction products. The apparatus built and the techniques used in each of these phases of the program are described. The few results obtained to date do not yet warrant any extensive discussion.

1. INTRODUCTION

The enhancement of rocket exhaust ionization in that region of the atmosphere where appreciable amounts of dissociated gases are present has been observed in

several instances.[1,2,3] For a review and discussion of this phenomenon reference is made to a recent AeroChem study.[4]

It is quite likely that these observations are due to a reaction of rocket exhaust gases with upper atmospheric oxygen atoms resulting in the formation of chemi-ions. An important step in this process is probably

(1) $CH + O \rightarrow CHO^+ + e^-$

It is still to be established whether the CH involved in reaction (1) is in its ground electronic state or in an excited state. Previous work at AeroChem has already shown that chemi-ionization occurs when O-atoms are reacted in a laboratory flow system with C_1 and C_2 hydrocarbons.[5,6] The highest ion concentrations were obtained in the reaction with acetylene, C_2H_2.

In order to test this explanation of upper atmospheric rocket exhaust ionization further, C_2H_2 was released in the upper atmosphere and attempts were made to observe the ion formation. These experiments were conducted in Project Firefly III, but unfortunately, no unambiguously interpretable results were obtained.[7,8] This may have been due to the narrowness of the acetylene trail, which at 100 km was initially only tens of meters in diameter, a size very difficult, if not impossible, to observe with the radar sounders used.[8] Another possible explanation of the apparent absence of appreciable upper atmospheric chemi-ion production from acetylene releases lies in the fact that several reaction steps are required to produce CH radicals, which are the necessary chemi-ion precursors of reaction (1). In an upper atmospheric acetylene release, considerable diffusion of the chemi-ion precursors may have occurred before the ions are actually produced. The resulting ion concentration would then be too low to be detected even though the same number of ions in a smaller region might easily have been detectable. In this respect, an acetylene release differs from a rocket exhaust, in which the gases may contain mole fractions of CH as high as 10^{-5} to 10^{-4}. Such high CH concentrations in solid propellant rocket exhaust gases were recently suggested by Calcote and Kurzius,[9] who based their calculations on the proposed rocket chamber equilibria

$$C_{solid} \rightleftharpoons C_{gas}$$

$$C_{gas} + H \rightleftharpoons CH$$

To further examine this problem it is necessary to conduct further upper atmospheric chemical releases with more suitable observation equipment, and to perform laboratory studies to clarify the reaction mechanism and obtain a quantitative evaluation of the efficiency of the chemi-ionization process. The present report is the first one on a laboratory study with these objectives.

2. DISCUSSION OF RESEARCH PROGRAM

After a study of the presently available knowledge, the following program for the study of the oxygen atom-acetylene reaction was outlined. A Wood-Bonhoeffer type discharge flow system is used in which O-atoms are produced free of O_2 (see Figure 1).[5,6] Pressures are in the range of 0.5 to 5.0 Torr and the temperature in the initial experiments is about 300°K but may be varied later. Measurements are made of initial concentrations, $[\ ]_o$, and concentrations after times t, $[\ ]_t$ corresponding to a distance ℓ, along the reaction tube. For each given flow system condition, $[O]_o$, $[C_2H_2]_o$, total ion concentration n_t^+, $[C_2H_2]_t$ and the light emission intensities of CH, CHO and C_2 at t are measured.* In a later stage, individual ion concentrations, for example, $[CHO^+]_t$, will be measured using a Bennett type rf mass spectrometer.

These measurements will yield the efficiency of the chemi-ionization reaction, that is, the number of ions produced per O and C_2H_2 reacted, the number of C_2H_2 molecules consumed per O-atom and the rate constant of $O + C_2H_2$. The most likely reaction responsible for chemi-ionization in this system is again[5,6]

(1) $CH + O \rightarrow CHO^+ + e^-$

The measurements will show whether the CH emission intensity is proportional to the rate of ion formation; this will help to clarify whether the reaction involves ground state or electronically excited CH. Ambipolar diffusion calculations show that it takes an ion, depending upon flow conditions, about 10^{-3} second (or about 1 cm length of the reaction tube) to diffuse to the wall where it is neutralized. Because of recombination, the ion mean lifetime in the flow system is actually less. The measured ion concentration n_t^+ will thus, in general, be representative of the locally formed ions. The lifetimes of CH $A^2\Delta$ and $B^2\Sigma$ are of the order of 10^{-6} second (Ref. 11), short enough to radiate in essentially the same volume element in which they are formed - which makes the CH emission intensities proportional to the local excited species concentrations - but long enough for some 10 percent of the excited CH molecules to collide with an O-atom under typical experimental conditions. It is thus, a priori, possible that reaction (1) involves excited CH molecules. It has been observed in hydrocarbon combustion flames that addition of CO_2 decreases the CH and C_2 emission but enhances the CHO emission.[12] Therefore, it is of considerable interest to use CO_2 as a major third body in some of our measurements

---

* The light emission measurements are made of the CH 4315 A System ($A^2\Delta - X^2\pi$), the CH 3900 A system ($B^2\Sigma^- - X^2\pi$), the Swan C_2 system ($A^3\pi_g - X^3\pi_u$) and Vaidya's hydrocarbon bands. Although these latter bands are very likely due to CHO this has not yet been established beyond doubt.[10]

to see whether it influences the chem -ionization rate. Because of the presence of CO_2 in rocket exhaust gases, an evaluation of the effect of CO_2, is not only important for the elucidation of the reaction mechanism but is also needed directly for a quantitative estimate of rocket exhaust ionization. Sugden[13] has suggested that the hydrocarbon flame bands may be due to

(2) $CH + O \xrightarrow{M} CHO^*$

hence there should be a close relation between the excitation of these bands and the production of chemi-ions. The described experiments should also serve to elucidate this point.

For full evaluation of upper atmospheric acetylene releases, it is necessary to understand the full mechanism of the $O + C_2H_2$ reaction. Kistiakowsky[14] has suggested that the oxidation of acetylene in shock tubes at 1200-3500°K occurs by

(3) $O + C_2H_2 \rightarrow C_2H + OH$

This scheme explains the C_4H_2 and H_2O formation but not the CO formation in his experiments. However, reaction (3) is probably endothermic by about 0.5 eV*, and certainly at the lower temperatures of our study addition of O-atoms to the triple bond seems, a priori, a more likely process. Such a mechanism rather than hydrogen abstraction has been shown to be predominant in O + olefin reactions.[16,17,18] For ethylene[16,17] the attack step is

(4) $O + C_2H_4 \rightarrow C_2H_4O^*$

in which $C_2H_4O^*$ denotes an energy-rich molecule which may decompose in a number of ways, the dominant reaction being

(5) $C_2H_4O^* \rightarrow CH_3 + CHO$

By analogy the reaction for acetylene would be

(6) $O + C_2H_2 \rightarrow C_2H_2O^* \rightarrow CH_2 + CO$

which is exothermic.* Fenimore and Jones[19] in their study of acetylene consumption in combustion flames and Haller and Pimentel[20] in their work on the $O + C_2H_2$ reaction in solid argon matrices both conclude that a direct O-atom attack on the carbon atom is the predominant mechanism. Any overall mechanism such as reaction (6) is, however, very speculative at the moment. We will make a study of the products formed in our system which hopefully will make it possible to decide which reaction scheme is most important. The influence of O_2 addition on the reaction products should also be studied.

---

*Based on a value of ΔH_f^o of 5.0 eV for C_2H, as calculated from the dissociation energy[15] of C_2H-H of 4.9 eV, and ΔH_f^o of the other components as given by the JANAF tables.

3. STATUS OF PROGRAM

In this section, the progress made to date on each phase of the program, as described in section 2, is discussed. Most effort has gone into building of apparatus and testing of techniques and equipment; mainly only preliminary results have been obtained so far. A correlation of the results of the various phases cannot as yet be made and the status of the work is consequently described separately for each phase.

3.1 Flow System

A previously used Pyrex-Vycor flow system[5, 6] was adapted to the present study. A schematic of the Pyrex reaction tube is shown in Figure 1. The reactant gases indicated in this figure are those for a particular experiment but the system can be quickly adapted to other experiments. For example, the indicated discharge through an O_2-He mixture followed, for the determination of $[O]_o$, by titration of the resulting O-atoms with NO_2 is replaced in some of the work by a discharge through N_2 followed by NO titration to the equivalence point of the resulting N-atoms. In the latter case, the initial O-atom flow is numerically equal to the pre-titration NO flow.[21] The actual O + C_2H_2 reaction zone begins at the position of the movable hydrocarbon inlet (hereafter to be referred to as the upstream movable nozzle). Shown inside the reaction tube is a double probe, the sensing wires of which are mounted on two axially movable teflon-covered tubes (see further section 3.2). The reaction tube is closed off at the bottom by a teflon-covered stainless steel base plate, which contains two Swagelok fittings to accommodate the probe tubes. Also fitted into the base plate is a stainless steel gas inlet tube to which is attached a length of teflon tubing-coiled around one of the probe tubes - the end of which serves as a second movable nozzle, the downstream movable nozzle. For other experiments the probes can be removed and replaced by a silver-plated screen upon which all the O-atoms recombine, thus terminating the reaction and allowing measurement of $[C_2H_2]_t$ by trapping downstream.

Upstream from the reaction tube are the flow meters which, for all gases but NO_2, are oil burettes or rotameters. A sonic orifice meter is used for NO_2. This device consists of a number of interchangeable orifices (3 and 5 mil diameter) placed inside nalgon tubing in a constant temperature water bath held at 308°K. The pressure upstream from the orifices is controlled by a Whitey 21-RF-4 fine control stainless steel needle valve and read on a di-n-butyl phthalate U-tube manometer. The flow of NO_2 as a function of pressure upstream from the orifices is calibrated inside the reaction tube against a known O-atom flow obtainable from the NO titration of N-atoms.

Reaction pressure is measured with a U-tube oil manometer equipped with a micrometer depth gauge; Dow-Corning 702 silicone oil is used. Downstream from

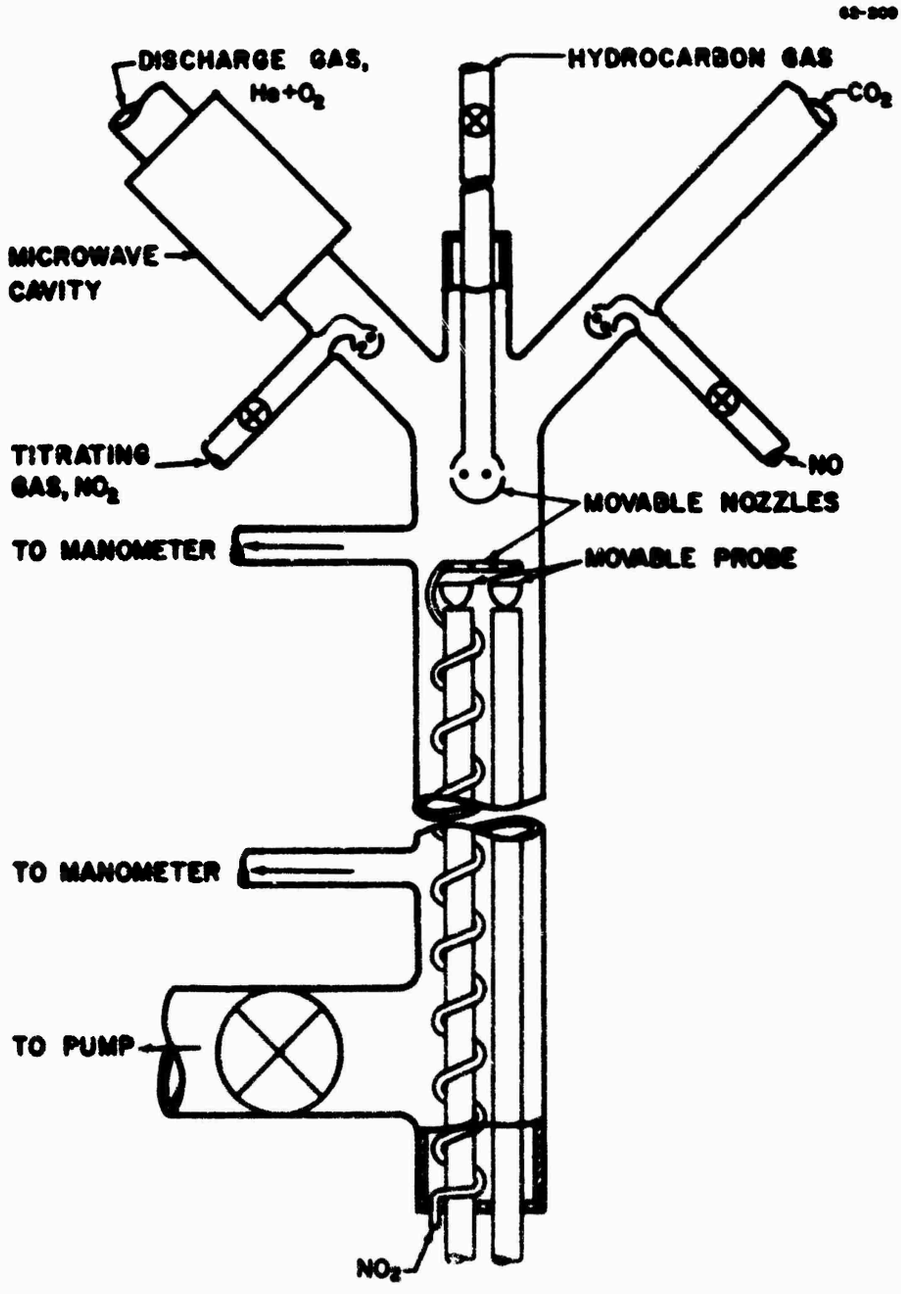

Figure 1. Schematic of Reaction Tube

the reaction tube there are, in parallel, three trapping systems and a bypass. Finally there is a ball valve which can be used to throttle the flow and a Kinney KD-30 vacuum pump.

3.2 Ion Concentration

3.2.1 PROBES AND ASSOCIATED ELECTRONICS

A schematic of the circuit diagram for the single (Langmuir) or double probe is shown in Figure 2. The circuit has three basic parts: the probes themselves, the power supply, and the current measurement and recording system. These will now be discussed.

The Langmuir probe consists of a sensing element of 90% Pt - 10% Rh wire, 1.3 cm long, 6×10^{-4} cm radius and a stainless steel screen.* The screen and sensing element are mounted on separate tubes which enable them to move independently over the full length of the reaction tube. This probe can be converted to a double probe by removing the stainless steel screen and replacing it with a second wire similar to the first. The stainless steel tubes on which the probes are mounted, completely surround the teflon-coated probe-input wires thus shielding them from noise pick-up. A teflon coating is used to insulate the steel tubes from the plasma. To insure the shielding, each steel tube is connected to ground by a soldered connection to a brass shield box in which the probe-input wires and the lead-in cables are joined. Similarly, the shields of both cables are connected to the respective shield boxes. Thus the whole probe system, except for the sensing element, is shielded from external noise sources through the grounded metal tubes, shield boxes, cable shields, and cabinets (Figure 2). Preliminary experiments had shown such shielding to be necessary because of the presence of noise sources in the laboratory. To complete the probe shielding, that is, to shield the probe wires themselves, the whole reaction tube (Figure 1) is surrounded by a grounded brass cylinder.** A slide-out window in this cylinder makes possible spectrophotometric measurements (section 3.3) and visual observation of the reaction when probe measurements are not being made.

Mounting each probe wire on an individual tube in the described fashion minimizes leakage current between them.*** It also enables one to change the distance

---

*This screen provides a reference potential for the Langmuir probe. In effect this probe arrangement can be considered as the limiting case of a double probe with unequal probe areas. In the conventional Langmuir probe, which was designed for use with electrical discharges having internal electrodes, the reference potential is provided by one of the electrodes.

**This cylinder also provides a dark background for spectrophotometric measurements.

***Careful checks performed by investigating various combinations of ground points showed that no alternate current paths through the plasma existed.

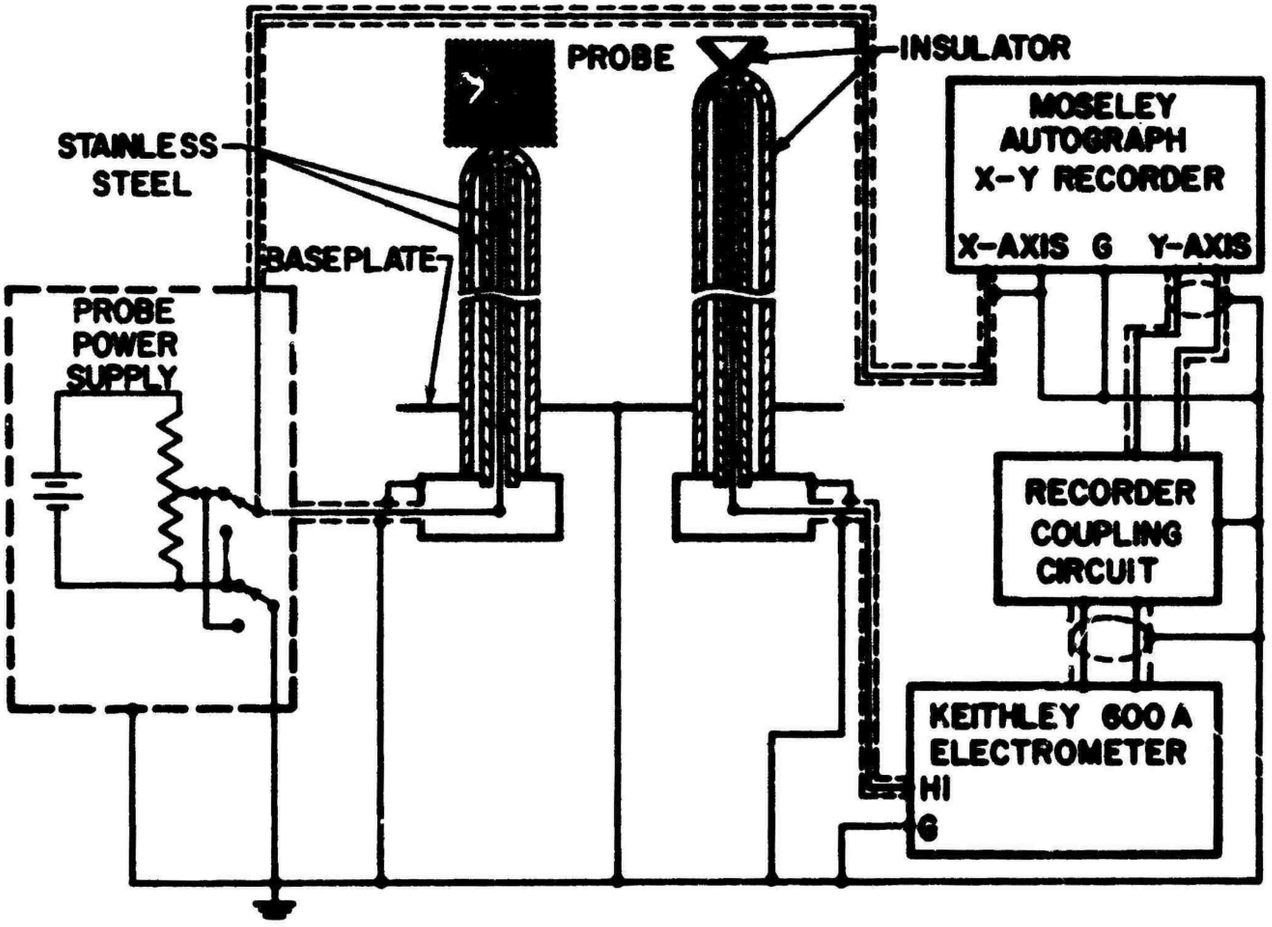

Figure 2. Schematic of Langmuir Probe Circuit

between the probe wires to ensure that the plasma distortion caused by one sensing element (or the screen) is not influencing the environment of the other sensing element. The grounded metal tubes surrounding each probe-input wire eliminate capacitive coupling to the other probe-input wire and the plasma. Such coupling would introduce significant errors at high sweep rates. In practice, these effects cannot be eliminated entirely since the metal tubes must not shield the probe sensing wires.

The probe power supply allows one to manually sweep the potential between the probe and the screen, or between the two probes, from -20 V to +20 V, or from -100 V to +100 V. Accuracy of the voltage output is better than 2% of value +0.02 V for the 20 V range; and 2% of value + 0.1 V for the 100 V range.

Currents are measured using a Keithley 600 A electrometer in its fast mode of operation. Current-potential curves are plotted using a Moseley Autograph X-Y recorder. Due to the design of the electrometer a recorder coupling circuit is needed to prevent the recorder from influencing the electrometer readings. The entire current measuring system was checked, in the absence of a plasma, for dynamic response and self-oscillations by using known input currents in the range of 10^{-7} to 10^{-12} amperes,[22] and found to be free of errors.

3.2.2 RESULTS

The probes as described above must still be considered as being in a state of development; they have not yet been tried out as double probes. When used as a Langmuir probe, the current-voltage characteristics obtained could not always be unambiguously interpreted. If curves that are unambiguous and well reproducible are obtained with the double probe, then no further probe development may be necessary. If such is not the case, then it is intended to do some experiments with probes that have been successfully used in combustion flame studies.[23] For this work we will generate our low temperature plasma in a combustion flame apparatus by introducing oxygen atoms into a hydrocarbon atmosphere in the same fashion as used previously (Ref. 5, section 2.2) for ion identification studies.

The development of a satisfactory means for measuring ion concentration is one of the most important problems to be worked on in the immediate future.

3.3 Light Intensity Measurements

Light intensity measurements are made using the Jarrell-Ash 82000 Ebert mounting monochromator equipped with a selected 1P28 photomultiplier tube. This instrument is fitted with a grating blazed for 7500 A and has a reciprocal linear dispersion of 32 A mm^{-1}. Spectrometer entrance and exit slit widths of 0.5 mm are used. A slit arrangement fastened to the spectrometer in front of the entrance slit limits observation to a 3 mm thick section of the Pyrex reaction tube perpendicular to the tube axis. The spectrometer is mounted on a platform that can be moved

vertically; that is, along the axis of the reaction tube. Measurements have been made thus far of the (O, O) bands of the CH 3900 A and 4315 A systems and the Swan C_2 system. The wavelength observed in all experiments is that of maximum intensity nearest to the band head. These wavelengths are respectively 3872, 4310 and 5159 A. The Swan C_2 system is observed in first order and both CH systems in second order. There is no interference of first order radiation with these latter measurements because of the insensitivity of the 1P28 tube to long wavelength (above approximately 6000-7000 A) radiation. This was further checked by placing a Corning CS 3-69 filter, which cuts off radiation of wavelengths shorter than approximately 5100 A, in the light path after second order measurements were made; at the wavelengths of interest no phototube currents higher than the noise level could be measured under these circumstances.

The change in intensity of each of the discussed band systems has been measured as a function of reaction time. The intensity of the (O, O) band of the 4315 A system decays more rapidly than the (O, O) band of the 3900 A system or the Swan C_2 system.* These observations were made with O-atoms from the N + NO reaction at pressures from 0.7 to 4.5 Torr, average gas velocities of 2 to 7.4 m sec^{-1} and $[C_2H_2]_o/[O]_o$ ratios varying from 0.33 to 5.5. The measurements extended over several orders of magnitude of light intensity. A typical plot of experimental results is shown in Figure 3.

It is interesting to note that this same behavior, that is, a more rapid decay of the 4315 system relative to the Swan system was observed in upper atmospheric acetylene releases (reference Figures 5 and 6 of Ref 24). The difference in behavior of the CH 4315 and 3900 A system may indicate that these systems have different excitation mechanisms.

Further intended work on this phase of the program includes measurement of Vaidya's hydrocarbon bands, the use of O-atoms from O_2-He mixtures, the effect of excitation quenching agents and correlation of the results with measurements on ion concentrations (section 2.2).

3.4 Concentration of Reactants and Reaction Products

3.4.1 OXYGEN ATOMS

A standard technique[25] for determining oxygen atom concentration in a reacting system is to determine the initial concentration $[O]_o$ with the NO_2 light titration technique and subsequently to add a small amount of NO upstream from the point of

*The lifetime of the C_2 ($A^3\pi_g$) molecules responsible for the Swan system emission in about 10^{-7} second (Ref. 26). Hence, like the discussed excited CH molecules, they radiate in essentially the volume element in which they were formed. No correction for the background continuum was made in these measurements. This will, however, be done in further experiments

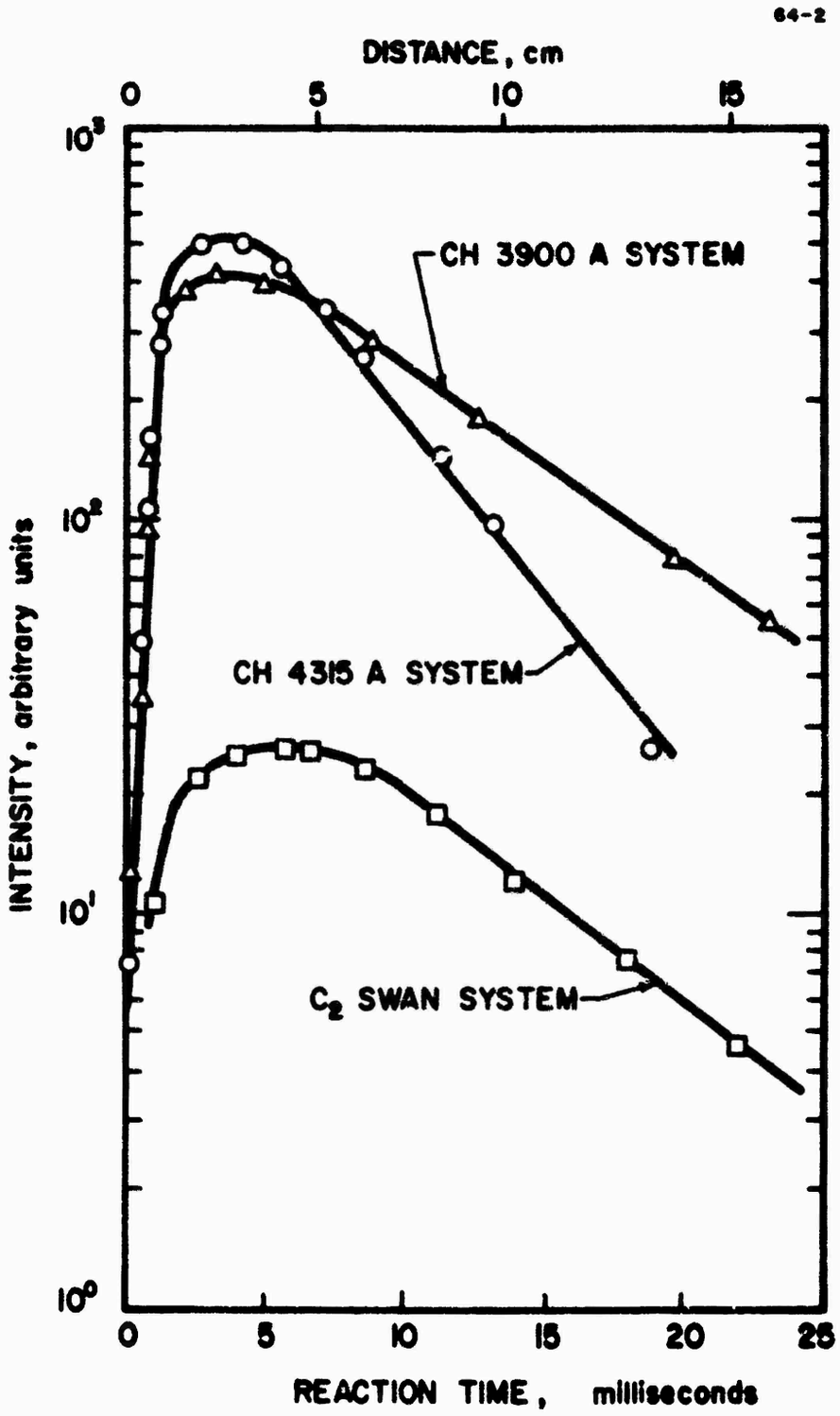

Figure 3. Chemiluminescent Intensity Variation with Reaction Time

Flow conditions: Linear flow rate 7.4 m sec^{-1};
$[N_2]$ = 6.85 x 10^{16} molecule cc^{-1};
$[O]_0$ = 2.19 x 10^{14} molecule cc^{-1};
$[C_2H_2]_o$ = 3.98 x 10^{14} molecule cc^{-1}

$[O]_o$ measurement to follow the O-atom decay by the air afterglow intensity, which is proportional to the product $[O]_t[NO]$. Small quantities of NO have to be used to keep the O-atom recombination due to the presence of NO negligible. This technique has been used successfully in studies of O-atom olefin reactions.[27,28]

Previous work in this laboratory[5,6] had shown that NO acts as a free radical scavenger in the $O + C_2H_2$ and C_2H_4 reactions, which also implies that NO is consumed by the free radicals produced in these reactions. To check the validity of the air afterglow technique in such systems, and to correct for any errors due to NO consumption, it was intended to introduce NO both upstream from the reaction zone and through the downstream movable nozzle. By comparing photometrically the intensity ratios of the air afterglow just upstream and just downstream of the movable nozzle, both in the absence and the presence of the hydrocarbon, it would then be possible to directly determine the amount of NO consumed by the reaction up to the position of the movable nozzle. Even though this amount may be negligible in the $O + C_2H_4$ reaction,[27,28] this may not be so in the $O + C_2H_2$ reaction where the much higher ion concentration[5] and light intensity (see below) indicate a much higher free radical concentration.

On trying out this technique, using the U. V. and visible sensitive 1P28 phototube, it was found that the light emission intensity of the $O + C_2H_2$ reaction, both of the banded spectrum and the background continuum, was so high - several orders of magnitude higher than that of $O + C_2H_4$ - that it was impossible to measure the air afterglow intensity even when concentrations of NO as large as $0.3\ [O]_o$ were added. At these concentrations, NO somewhat diminished the intensity of the CH and C_2 bands. At very high NO flow rates (10 to 100 times the initial O and C_2H_2 flow), no $O + C_2H_2$ emission was evident at all, it being entirely replaced by the air afterglow.* These observations demonstrate, not unexpectedly, that NO reacts with the free radical precursors of the light emitting species just as it does with the free radical precursors of the chemi-ions.[5,6]

It thus appears that the air afterglow technique cannot be used for O-atom measurement in the present system. It is, however, possible that in the 7000-12000 A region, where the air afterglow has considerable intensity,[29] the interference of $O + C_2H_2$ chemiluminescence is negligible (very little is known about its intensity in this region but observations on hydrocarbon combustion flames[26] indicate that it may be low for at least part of this region). If such is the case, then the technique can be employed using an infrared sensitive photomultiplier tube. Another method, direct NO_2 titration on the oxygen atoms inside the reaction zone, was shown to give a very sharp, easily determinable end point. This method may therefore be used in the present work, but it will, of course, be necessary to determine its quantitative

---

*Under these conditions the air afterglow intensity, at least at 5000 and about 5500 A, was not measurably influenced by the presence of C_2H_2.

validity. Previous work[30] had shown that the NO_2 titration can be in error, if used in reacting systems, due to the interference by excited molecules.

3.4.2 ACETYLENE AND REACTION PRODUCTS

The materials to be examined are distilled from the liquid nitrogen trap (section 2.1) to a sampling flask* having a side arm, closed off by a rubber septum, through which samples can be taken with a syringe for injection into a gas chromatograph. While the sampling flask is still attached to the system and partly submerged in a liquid nitrogen Dewar, it is filled with helium to about 270 Torr pressure. After warming up to room temperature the total pressure in the flasks is about 900 to 1000 Torr.** When all the necessary samples, usually three to four 1 cc samples, have been taken from the flask, its pressure is measured by puncturing the septum with a syringe needle which closes off one leg of a U-tube manometer, the other leg of which is open to the atmosphere; this measurement allows calculation of the fraction of the trapped products that was contained in the injected sample.*** From this quantity and the gas chromatogram peak areas, calibrated using known samples, the total amount of each material trapped is calculated.

This system has been checked so far only for unreacted acetylene and found to give well-reproducible (better than 5%) results. It was found necessary to use silicone vacuum grease in the sampling system; the use of Apiezon-N grease led to erroneous results due to absorption of acetylene. A 50-foot column of 25% diethyl malonate on non-acid-washed Chromosorb P (30-60 mesh) was used. Other columns that are intended to be used for analyses of condensable reaction products are β,β'-propionitrile on non-acid-washed Chromosorb P and Ethofat 60/25 on Columnpak T.[31]

Reaction products not condensable at liquid nitrogen temperature, for example, CO, can be sampled for gas chromatographic analysis using a Toepler pump which is located downstream from the liquid nitrogen traps (section 2.1). Molecular sieve columns will be used for these analyses.

4. CONCLUSIONS AND PLANS

In this report, a research program directed toward quantitative evaluation of upper atmospheric rocket exhaust ionization as a mechanism of production of free electron radar targets during the launch phase, and based on a study of the reaction

---

*The sampling flasks used have a volume of about 250 cc.

**In measurements of unconsumed acetylene, its partial pressure is about 10-50 Torr.

***The injected samples are always at atmospheric pressure even though the container from which they are taken is at a higher pressure.

$O + C_2H_2$ is outlined. This program consists of the measurement of ion concentration, light emission intensity, and concentration of reactants and reaction products as a function of initial reactant concentrations, pressure, reaction time, and the presence of several gases such as He, H_2, O_2, and CO_2. The techniques used are described and preliminary results discussed. Further work is continuing along the indicated lines.

Acknowledgments

The work was carried out with the assistance of J. M. Hogan, G. L. Baughman and T. Freda whose interest and enthusiasm is gratefully acknowledged. The work greatly benefited by the advice and assistance of W. Brenner and his electronics shop technicians.

References

1. H. A. POEHLER, Observation on Radio Interference by Exhausts of Operating Missiles (U), Space Technology Laboratories, Inc., Florida Division, GMPTM-5656, MT 62-82407, September 1962 (CONFIDENTIAL)
2. W. W. BALWANZ and P. T. STINE, The Plasmas of Missile Flight (U), U. S. Naval Research Laboratory, Washington, D. C., NRL-5636, July 1961. (CONFIDENTIAL)
3. M. R. BERG, et. al., Proceedings of the Study Group on Missile Launch Phase Phenomenology, SRI-1-266, Stanford Research Institute, pp. 25, 31, October 1961. (SECRET)
4. H. F. CALCOTE, A. FONTIJN and H. SILLA, Upper Atmospheric Effects (U), Section V-B of "Flame Plasma Effects Study (U)," RADC-TDR-63-, MRD-63-421-30, Rome Air Development Center, AFSC, Griffiss Air Force Base, N. Y., 1963. (SECRET)
5. A. FRONTIJN and G. L. BAUGHMAN, Influence of Oxygen Atoms in the Upper Atmosphere on the Production of Ions in Rocket Exhaust Afterburning, AeroChem TP-59, AD-297269, January 1963.
6. A. FRONTIJN and G. L. BAUGHMAN, J. Chem. Phys. 38:1784, 1963.
7. N. W. ROSENBERG and D. GOLOMB, Private communication.
8. N. W. ROSENBERG, Private communication.
9. H. F. CALCOTE and S. C. KURZIUS, Electron Production and Ion Mechanisms in Flame Plasmas (U), Section III of Flame Plasma Effects Study (U), RADC-TDR-63-, MRO-63-421-30, Rome Air Development Center, AFSC, Griffiss Air Force Base, N. Y., 1963. (SECRET)
10. W. M. VAIDYA, The Emitter of Hydrocarbon Flame Bands, Eighth Symposium (International) on Combustion, The Williams and Wilkins Co., Baltimore, Md. p. 252, 1962.

11. R. R. BENNETT and F. W. DALBY, J. Chem. Phys. 32:1716, 1960.

12. R. C. HERMAN, G. A. HORNBECK and K. J. LAIDLER, Science, 112:497, 1950.

13. T. M. SUGDEN, Ann. Rev. Phys. Chem. 13:369, 1962.

14. G. B. KISTIAKOWSKY, Proc. Chem. Soc., 289, 1962. See also:
J. N. BRADLEY and G. B. KISTIAKOWSKY, J. Chem. Phys. 35:264, 1961.
C. W. HAND and G. B. KISTIAKOWSKY, J. Chem. Phys. 37:1239, 1962.

15. B. E. KNOX and H. B. PALMER, Chem. Revs. 61:247, 1961.

16. R. J. CVETANOVIC, Can. J. Chem. 36:623, 1958.

17. R. J. CVETANOVIC, J. Chem. Phys. 23:1375, 1955.

18. R. J. CVETANOVIC, Can. J. Chem. 36:623, 1958. See also:
R. J. CVETANOVIC, J. Chem. Phys. 25:376, 1956.

19. C. P. FENIMORE and G. W. JONES, J. Chem. Phys. 39:1514, 1963.

20. I. HALLER and G. C. PIMENTEL, J. Am. Chem. Soc. 84:2855, 1962.

21. J. E. MORGAN, L. ELIAS and H. I. SCHIFF, J. Chem. Phys. 33:930, 1960.

22. J. PRAGLIN and W. A. NICHOLS, Proc. Inst. Radio Engrs. 48:771, 1960.

23. H. F. CALCOTE, Ion and Electron Profiles in Flames, Ninth Symposium (International) on Combustion, Academic Press, Inc., New York, p. 622, 1963.

24. C. D. COOPER, Data Reduction of Spectrometer and Spectrographic Data for Various Chemical Releases, University of Georgia, Physics Department, Athens, Georgia, Technical Report Contract AF 19(628)232, ARPA Order 42.

25 F. KAUFMAN, Reactions of Oxygen Atoms, Progress in Reaction Kinetics, Vol. 1, G. Porter, Ed., Pergamon Press, New York, p. 1, 1961.

26. W. S. BENEDICT and K. S. PLYLER, High-Resolution Spectra of Hydrocarbon Flames in the Infrared in Energy Transfer in Hot Gases, N. B. S. Circular 523, p. 57, March 10, 1954.

27. L. ELIAS, J. Chem. Phys. 38:989, 1963.

28. L. ELIAS and H. I. SCHIFF, Can. J. Chem. 38:1657, 1960.

29. A. FONTIJN, C. B. MEYER and H. I. SCHIFF, J. Chem. Phys. 40:64, 1964.

30. B. H. MAHAN and R. B. SOLO, J. Chem. Phys. 37:2669, 1962.

31. K. J. BOMBAUGH and W. C. BULL, Anal. Chem. 34:1237, 1962.

XXV. Gasdynamic Analysis of the Nitric Oxide Trail Experiment

Jacques A. F. Hill and Henry L. Alden
Mithras, Inc.
Cambridge, Massachusetts

Abstract

A gasdynamic analysis has been made of the flow generated by the release of NO from a supersonic vehicle in the upper atmosphere. The initial mixing between the NO and the ambient is found to occur in a layer forming approximately a paraboloid surrounding the vehicle. In this layer, the actual mixing zone is sandwiched between two shockwaves. For one actual experiment, a calculation has been made of the size and shape of the mixing layer and of the amount of ambient entrained. With increasing altitude it is found that the mixture changes from being at first rich to finally lean in NO.

1. INTRODUCTION

As part of the Firefly program of chemical releases in the upper atmosphere, some experiments have been run in which a quantity of Nitric Oxide was released from a vehicle over a period of about 70 seconds while it rose from 95 km to 150 km. This release produced a bright visible trail generated by a chemiluminescent reaction between the NO and atomic O in the atmosphere.

Since the number of photons emitted per unit volume can be computed from the photographic observations of the trail, it is very interesting to consider the possibility of using the data to calculate the concentration of O in the atmosphere. For this purpose one of the things we need to know is the size of the atmospheric sample which can react with NO. The purpose of this report is to provide this knowledge for the actual conditions of a particular NO release.

The problem we consider, then, is the mixing between the NO flowing from a tank in the vehicle and the airstream flowing past the vehicle. We consider that this mixing occurs in two distinct regions. In the first region the mixing is associated with the expansion of the NO to ambient pressure. The second region extends far downstream and comprises the wake of the initial expansion. Only the first region, which corresponds to the observed 'head glow', is considered in this report.

2. THE FLOW PATTERN

A sketch of the overall flow pattern past a vehicle releasing a gas into the atmosphere is shown in Figure 1. The frame of reference for this picture is fixed in the vehicle and the vehicle motion is replaced by a moving airstream. Over most of the trajectory of the release to be analyzed, this flow is supersonic (see Appendix A). The upper sketch is an idealized picture which neglects the effects of viscosity, diffusion, etc., and considers both the NO and air to be ideal gases. The lower sketch indicates where the ideal picture has to be modified when these effects are considered. It thus shows where the observed reaction takes place in the flow.

2.1 The Inviscid Flow Model

In the theoretical model of the flow surrounding the NO release, the gas container and its plumbing are replaced by a point source of known strength. The NO expands from this source as if into a vacuum until it encounters the inner shock sketched in Figure 1a. This shock is required to decelerate the highly supersonic expanding flow to a subsonic speed. It locates itself in the flow such that the pressure of the NO after passing through it balances at each point the pressure generated by the moving airstream.

Outside of the source shock is a 'film layer' containing the ejected NO (note that in this preliminary inviscid model there is no mixing with the ambient). The thickness of this layer can be calculated in terms of the normalized injection momentum

$$\frac{\rho_2 V_2^2}{\rho_\infty V_\infty^2} \qquad (1)$$

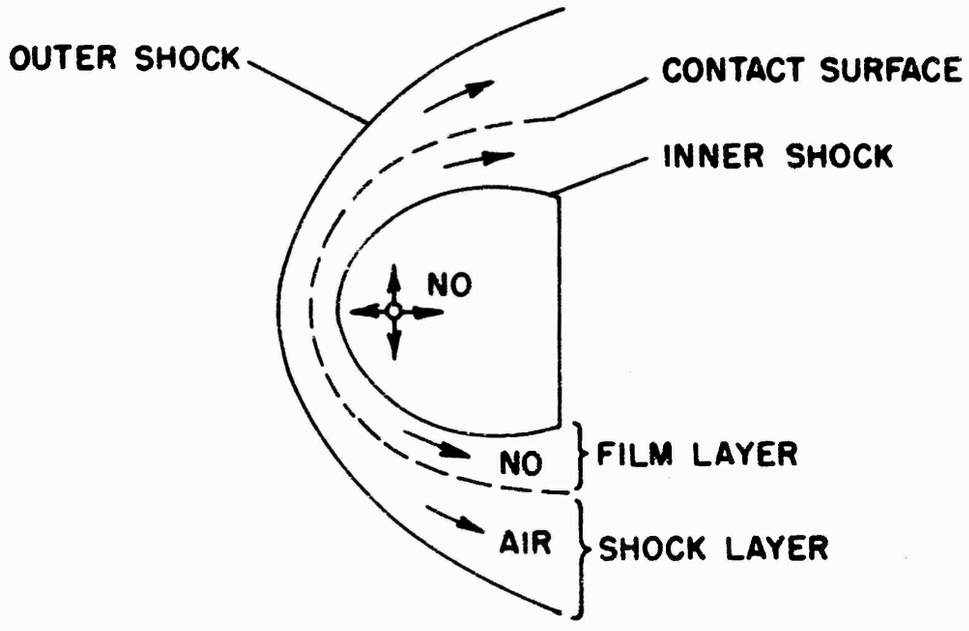

(a.) Inviscid Flow Pattern

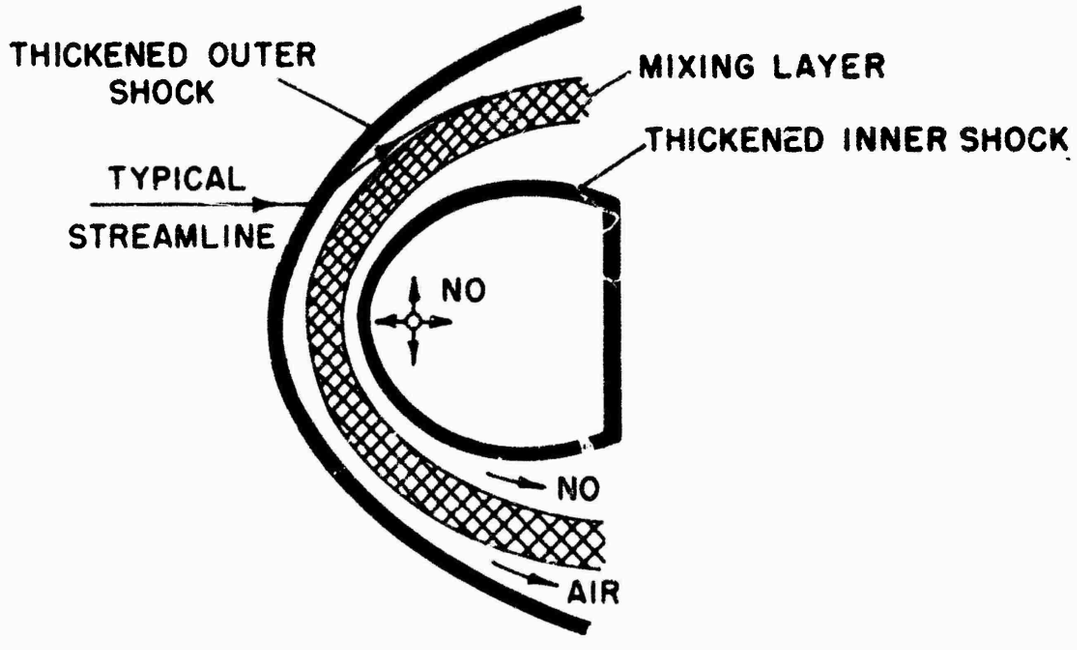

(b.) Viscous Flow Pattern

Figure 1. Flow Pattern Schematic

as shown in section 4. The outer edge of the film layer is the contact surface between the NO and the ambient. As far as the external flow is concerned, this is the effective body surface.

The external flow is the usual blunt-body flow with detached shock wave in the ambient, since the vehicle speed is supersonic.

2.2 Viscous Flow Model

The more realistic flow pattern including the effects of viscosity, conductivity, and diffusion differs from the inviscid model chiefly in that mixing spreads out in both directions from the contact surface, as sketched in Figure 1b. Near the nose of any blunt body the mixing layer thickness is approximately constant if the injection velocity is constant.

At the high altitudes of interest here, viscosity also plays a role in broadening the shock wave so that it can no longer be treated as a mathematical discontinuity. This shock thickness grows less rapidly than the mixing layer thickness as the density is reduced.

As both the shock and mixing layer become thicker with increasing altitude, they eventually will merge into a combined shock and mixing layer. The mixing layer will also spread inwards towards the source shock and eventually absorb the entire inviscid layer. Criteria for judging when these effects take place are discussed in section 5, where the viscous flow field is described in more detail.

To summarize this qualitative discussion of the flow pattern, we note that a merged layer is formed between the expanding NO and the ambient airstream. Both edges of this layer are shockwaves, and mixing between the NO and the ambient is confined to the region between these shockwaves. Our problem is first to calculate the shape and size of the layer and then the degree of mixing within it. Mixing is molecular diffusion.

At the high altitudes at which the experiment is conducted, turbulent flow cannot develop and this mixing takes place by molecular diffusion in a laminar flow.

3. MERGED LAYER SHAPE

The merged layer between the NO and the ambient is thin throughout the release except towards the end where the vehicle speed becomes close to sonic. We shall initially regard it as a contact surface and calculate its shape by applying a force balance across it as sketched in Figure 2.

Neglecting the centrifugal force on the flow along the merged layer, we equate at each point the normal pressures due to the external and internal flows. For the sake of simplicity we compute these normal pressures by the Newtonian formula

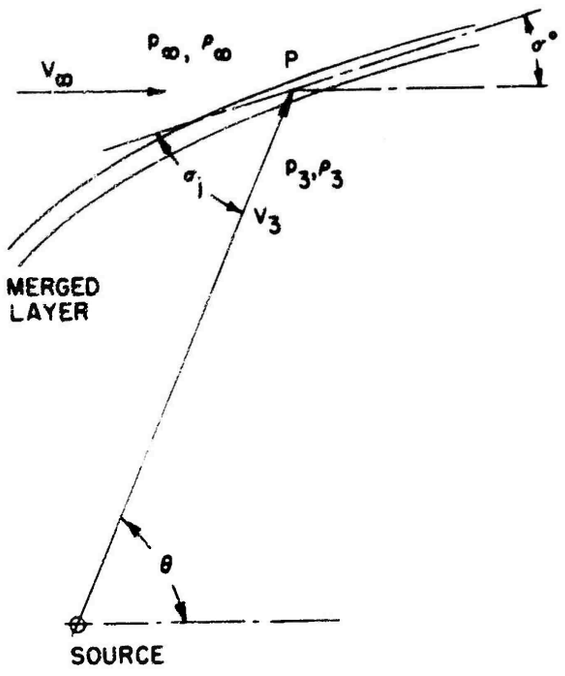

Figure 2. Normal Force Balance at the Merged Layer

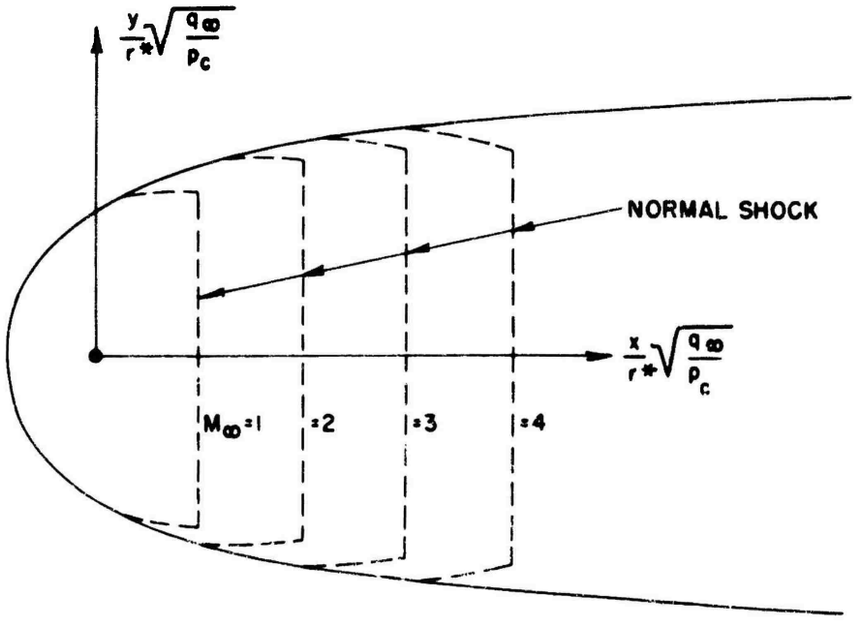

Figure 3. Merged Layer Shape

$$p_1 = p_\infty \gamma M_\infty^2 \sin^2 \delta = p_{s1} \sin^2 \delta \tag{2}$$

where δ is the angle through which the flow is turned and p_∞ is the static pressure of the impinging flow.

The flow inside the merged layer is a spherical source flow which has expanded through a very large pressure ratio. The velocity is everywhere along the radius vector, and its magnitude is nearly constant at the limiting value

$$V_1 = \sqrt{2 \, cp \, T_o} \tag{3}$$

where T_o is the temperature of the NO in the tank. Since the mass flow across all spheres centered on the source is constant, the density must fall off with distance according to the law

$$\rho V_1 r^2 = \text{constant} \tag{4}$$

The ram pressure in the Newtonian force formula is

$$p_{s3} = p_2 \gamma M_3^2 \approx \rho_3 V_e^2 \tag{5}$$

and thus falls off as $1/r^2$ along each radius vector. We can normalize this pressure with respect to the storage pressure in the tank and the radius with respect to the radius r* of the sphere surrounding the source across which the flow is sonic. For $\gamma = 1.4$, then

$$\frac{p_{s3}}{p_c} \approx 1.81 \left(\frac{r^*}{r}\right)^2 \approx \frac{1.81}{\bar{r}^2} \tag{6}$$

The force balance at the point P in Figure 2 is then

$$2 q_\infty \sin^2 \sigma^o = 1.81 \, pc \left(\frac{1}{\bar{r}^2}\right) \sin^2 \sigma j \tag{7}$$

so that

$$\sin \sigma j = 1.05 \sqrt{q_\infty / p_c} \; \bar{r}^2 \sin \sigma^o \tag{3}$$

Using the relations

$$\sin \sigma^o = \sin (\theta - \sigma j) \tag{9}$$

and

$$\cot \sigma_j = - \frac{1}{r} \frac{dr}{d\theta} \tag{10}$$

we can obtain the linear first order differential equation

$$\frac{d\bar{r}}{d\theta} + \bar{r} \cot \theta + \frac{0.95}{\sin \theta} \sqrt{\frac{p_c}{q_\infty}} = 0 \tag{11}$$

or

$$\frac{d}{d\theta} (\bar{r} \sin \theta) + 0.95 \sqrt{\frac{p_c}{q_\infty}} = 0 \tag{12}$$

which has the general solution

$$\bar{r} = \frac{0.95}{\sin \theta} \sqrt{\frac{p_c}{q_\infty} (\theta_o - \theta)} \tag{13}$$

where θ_o is the arbitrary constant of integration. In order to have a finite value of $\bar{r}$ at the nose, $\theta = \pi$, we must have $\theta_o = \pi$. This shape is illustrated in Figure 3. Some quantities which can be readily derived from this equation are:

(1) The upstream displacement of the vertex of the merged layer from the source

$$\bar{r}_{\text{nose}} = 0.95 \sqrt{\frac{p_c}{q_\infty}} \tag{14}$$

(2) The radius of curvature at the vertex

$$R_N = 1.4 \sqrt{\frac{p_c}{q_\infty}} \tag{15}$$

(3) The asymptotic width as $\theta \to 0$

$$\bar{r} \sin \theta \cong 3 \sqrt{\frac{p_c}{q_\infty}} \tag{16}$$

The latter quantity and the downstream shape of the profile generally are not very reliable because the flow turning angles at the merged layer become too small for the Newtonian pressure formula to be a good approximation. Furthermore, we expect a closed curve for the shock layer profile with a normal shock across the base of the profile, located so as to compress the expanding NO to approximately ambient pressure. This normal shock location depends on the flight Mach number as illustrated on the universal plot of Figure 3. The actual shape of the downstream portion of the shock layer has not been calculated and is only sketched here.

4. INVISCID FILM AND SHOCK LAYER THICKNESS

Corresponding to the inviscid model of the flow, there exist several quite accurate methods for computing the properties of the film layer on a sphere.[1,2] For our purposes a simple approximate method is satisfactory and we shall develop one based on the 'oversimplified' model of Reshotko,[3] which applies directly to the shock layer.

4.1 Film Layer

Using Newtonian theory for the pressure distribution on the contact surface we have, as before,

$$p(\theta) = p_{s1} \cos^2 \theta = p_{s1} (1 - \theta^2 + - - -) \tag{17}$$

near the stagnation point. Now regarding the contact surface as a streamline of the film flow, we have for the pressure along it

$$p(\theta) = p_s - \frac{1}{2} \rho_2 u_2^2 \tag{18}$$

assuming a constant density ρ_2. With $p_s \approx 0.9 \rho_\infty V_\infty^2$ (modified Newtonian value), we may write

$$p(\theta) \approx p_s \left(1 - .55 \frac{\rho_2 u_2^2}{\rho_\infty V_\infty^2} \right) \tag{19}$$

Equating Eqs. (17) and (19), we obtain

$$\frac{u_2}{V_\infty} \approx 1.35 \sqrt{\frac{\rho_\infty}{\rho_2}} \theta \tag{20}$$

along the inner side of the contact surface.

Now consider a mass balance for the flow in the film layer up to the angle θ. If the thickness of the layer is Δ_F, the flow along it is

$$\pi \Delta_F \rho_2 u_2 R_N \theta \tag{21}$$

assuming a linear velocity profile (see Figure 4). This must equal the mass flow flux injected up to this angle which is approximately

$$\pi R_N^2 \theta^2 \rho_2 V_2 \tag{22}$$

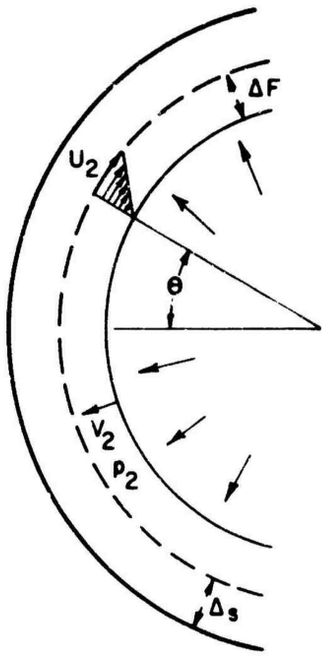

Figure 4. Film Layer Schematic

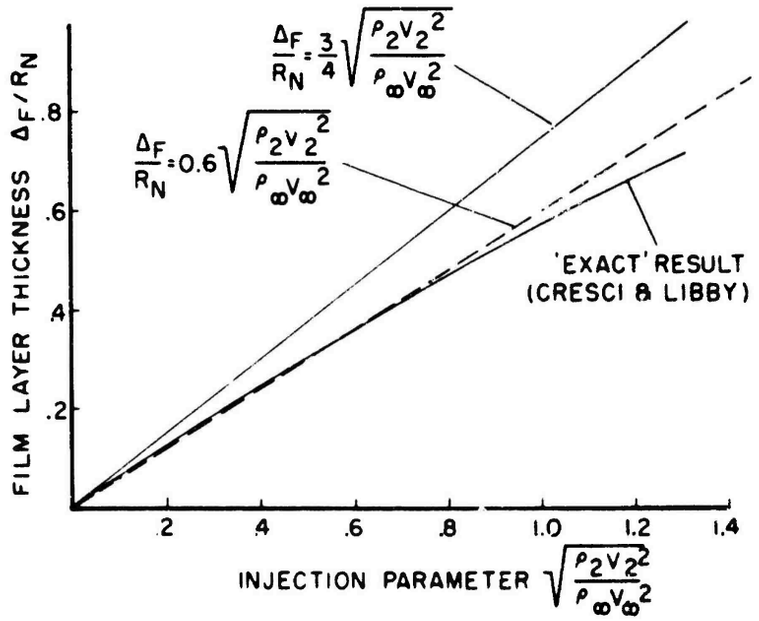

Figure 5. Comparison of Film-Layer Thickness Formula with 'Exact' Result

where V_2 is the injection velocity downstream of the source shock. Equating these two expressions we get

$$\frac{\Delta_F}{R_N} \approx \frac{V_R \theta}{u_2} \approx \frac{3}{4} \sqrt{\frac{\rho_2 V_2^2}{\rho_\infty V_\infty^2}} \tag{23}$$

near the stagnation point.

In Figure 5, this result is compared with the prediction of Cresci and Libby.[2] On the basis of this comparison, we shall adjust our numerical constant and write

$$\frac{\Delta_F}{R_N} = 0.6 \sqrt{\frac{\rho_2 V_2^2}{\rho_\infty V_\infty^2}} \tag{24}$$

4.2 Shock Layer

The oversimplified theory of Reshotko[3] calculates the thickness of the shock layer in a manner similar to that just used for the film layer. When it is refined slightly it can be written

$$\frac{\Delta_s}{R_s} = \frac{k}{1 + \sqrt{2k}} \tag{25}$$

where k is the density ratio $\frac{\rho_\infty}{\rho_1}$ across the shock, and R_s is the radius of curvature of the shock. Although this analysis applies strictly only in hypersonic flow, its results check exact theories for Mach numbers as low as M = 2 in air.

In Figure 6 we have plotted the thickness of the film and shock layers versus altitude for the trajectory described in Appendix A.

4.3 Velocity Ratio Across the Contact Surface

Across the contact surface the pressures are everywhere locally balanced. As the flow accelerates away from the stagnation point, it expands through equal pressure ratios on either side. Since $r \cong 1.4$ for both air and NO, this means that the Mach numbers are locally equal in the two gases. The velocity ratio is therefore equal to the ratio of sound velocities or to the square root of the temperature ratio.

The supply temperature of the nitric oxide is assumed initially to be 290°K. This drops in the tank as the pressure drops, but there is some reheating in the valves and plumbing. We shall assume that the temperature is approximately constant.

The air temperature at the start of the flow around the contact surface is the stagnation temperature corresponding to the ambient temperature and flight Mach

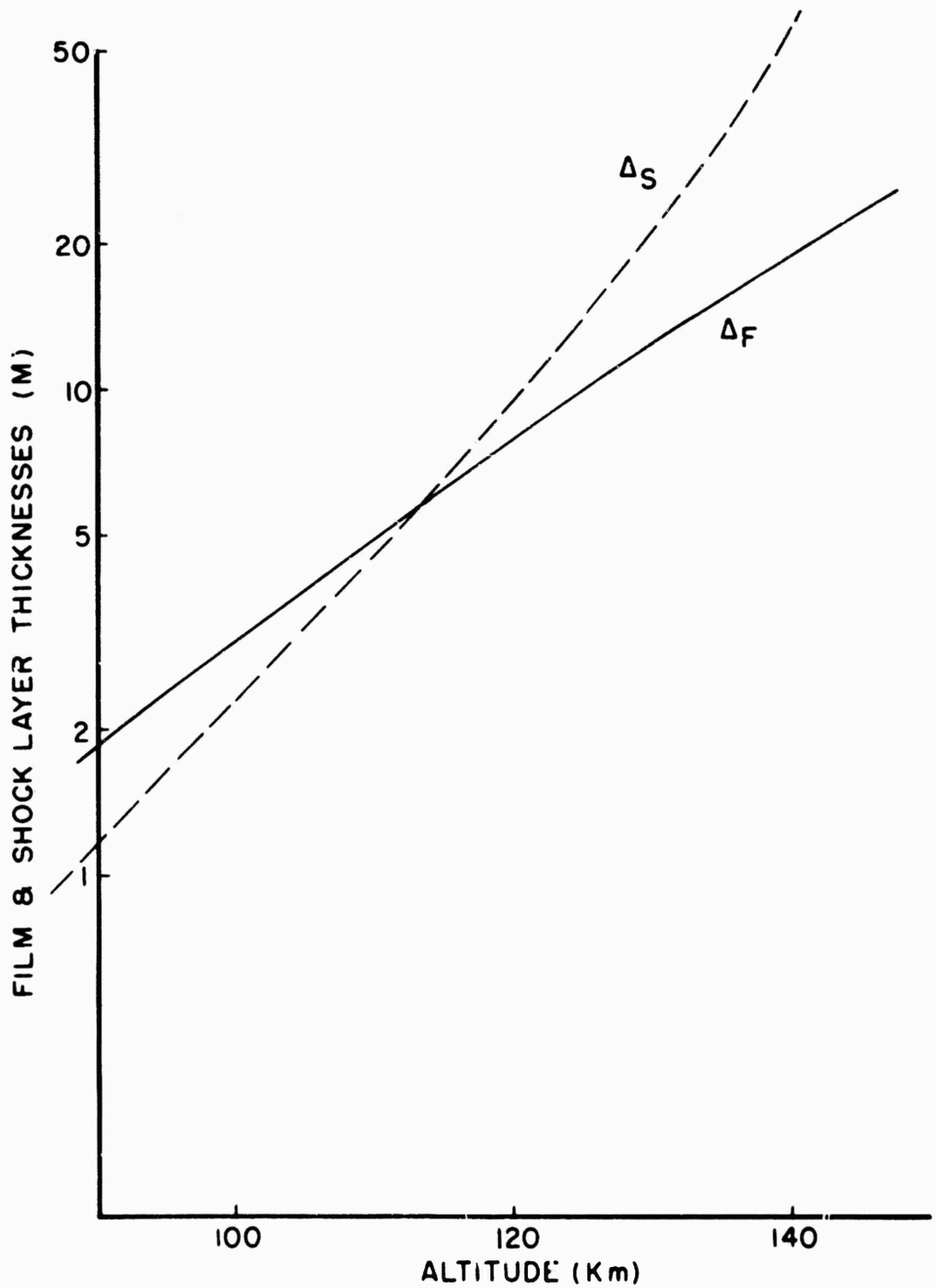

Figure 6. Thickness of Film and Shock Layers

number. The former rises as the latter drops in such a way that the stagnation temperature variation is quite small. For the given trajectory we have approximately

$$800^{\circ}K < T_{s1} < 950^{\circ}K \tag{26}$$

which implies a range of velocity ratios across the contact surface;

$$1.6 < \frac{u_1}{u_2} < 1.8 \tag{27}$$

The air velocity in the shock layer is always higher than the velocity of the NO in the shock layer.

5. VISCOUS FLOWS

5.1 Flow Regime

At the altitude at which the experiment is conducted, the mean free path varies from a few centimeters to tens of meters. Compared with the size of the flow pattern, it begins as a small fraction and finally becomes approximately equal to it. We expect, therefore, that viscous effects will penetrate very far into the inviscid flow between the free-stream and source shocks, and that the inviscid region may disappear completely at the upper altitudes.

One criterion which may be used to study the merging of the external shock and mixing layer is the shock Reynolds number

$$R_e = \frac{\rho_\infty V_\infty R_c}{\mu_s} \tag{28}$$

where in this case R_c is the radius of the contact surface and μ_s is the viscosity behind the normal shock. According to a very recent calculation for a boundary layer on a sphere,[4] the inviscid region disappears at $R_e \approx 100$.

Figure 7 illustrates the variation of R_e with altitude for the given trajectory. Obviously most of the experiment falls into merged-layer regime and there is no inviscid shock layer.

As the density drops with increasing altitude, the inviscid film layer may also disappear. A criterion for this occurrence may be expressed in terms of the injection parameter f_w of Libby[5] where

$$-f_w \approx 0.[illegible] \frac{\rho_2 V_2}{\rho_\infty V_\infty} \sqrt{R_e (\;)^{1/4}} \tag{29}$$

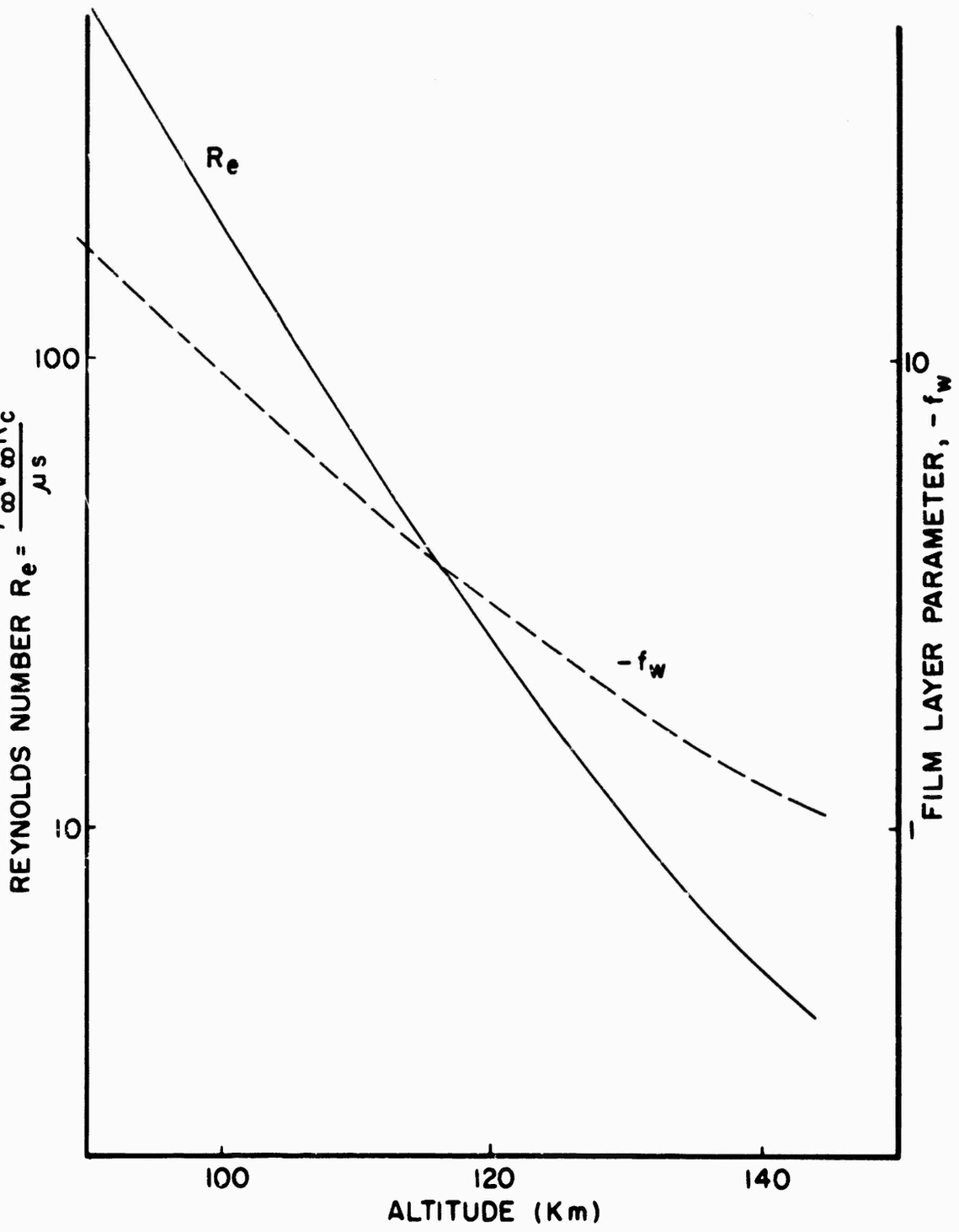

Figure 7. Reynolds Number and Film Layer Parameter

and the inviscid layer disappears for $|f_w| < 2$. The variation of fw with altitude is illustrated in Figure 7. It is interesting to note that the inviscid region in the film disappears at a somewhat higher altitude than in the shock layer.

5.2 Viscous Flow Patterns

The different flow regimes through which the NO Release passes correspond to somewhat different flow patterns. We shall here describe two patterns: one corresponding to the viscous layer flow at the lower altitude, and one corresponding to the merged layer flow at the upper altitude.

5.2.1 VISCOUS LAYER FLOW

For Re > 100 (or altitude below 106 km), the mixing layer is a distinct region in the flow pattern with inviscid flow between it and either shock wave. This flow pattern is sketched in Figure 1b. The thickness of the mixing layer may be estimated approximately from the solutions published by Libby[5] for homogenous boundary layers with large rates of injection. Figure 1b is drawn approximately to scale for an altitude 100 km. The outer edge has been arbitrarily defined where the velocity is 99 percent of the external velocity, and the inner edge where the temperature has changed 1 percent from the value at the inner shock.

Using the same solutions, we have sketched the streamline pattern between the shock and the mixing layer, connecting corresponding points on the shock and on the outer edge of the mixing layer. The streamlines give us some idea of how big a tube of ambient is swallowed into the mixing layer.

5.3.1 MERGED LAYER FLOW

At higher altitudes, the mixing region of the NO and the ambient occupy the entire layer between the two shockwaves, at least in the stagnation region. Air mixes with NO immediately after passing through the bow shock.

As far as the head glow is concerned, the stream tube of interest is that intercepted by the bow shock up to the point corresponding to the maximum diameter of the inner shock, as sketched in Figure 8. This flow pattern can only be estimated since there are no published solutions of the equations of motion like those for the viscous layer.

6. NUMERICAL ESTIMATES OF THE AIR ENTRAINED

The general results derived above have been used to calculate the amount of air entrained by the NO release described in Appendix A. The following schemes have been used in the two regimes of the merged and viscous layers.

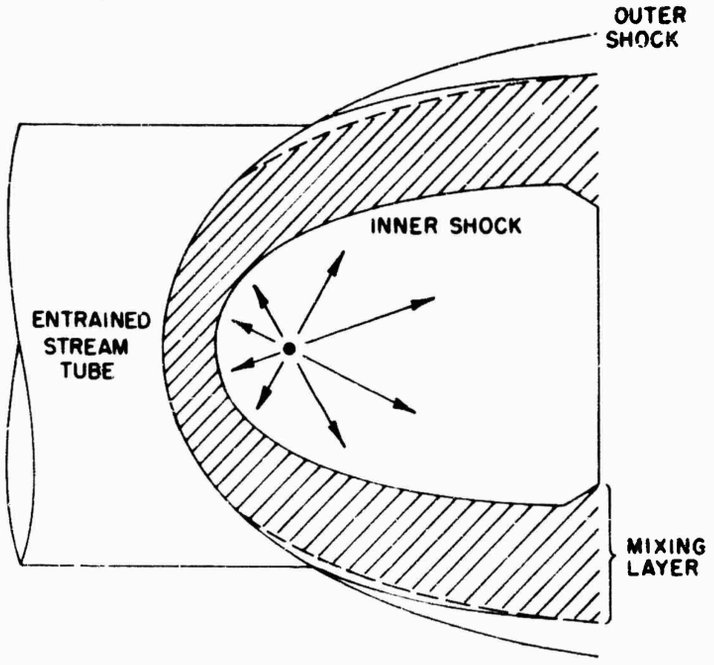

Figure 8. Merged Layer Entrainment

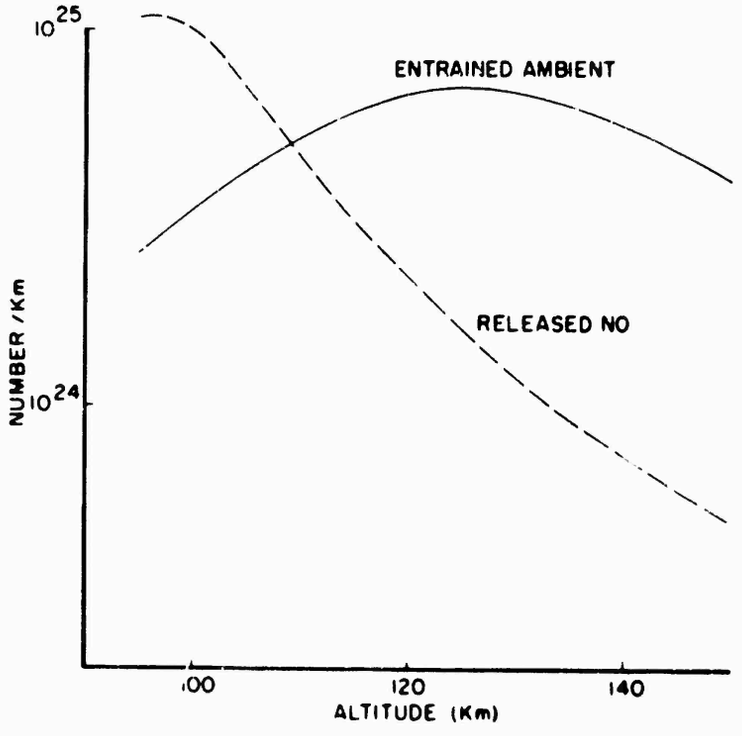

Figure 9. Air Entrainment Along the Track of tne Nitric Oxide Release

6.1 Merged Layer (Above 106 Km)

(1) The maximum radius of the internal shock (NO shock) has been read from Figure 3, using the appropriate normal shock location as a function of flight speed.

(2) The combined film and shock layer thicknesses have been added to this radius to give the total radius of the entrained stream tube.

6.2 Viscous Layer (Below 106 Km)

(1) The maximum radius of the internal shock has been calculated as above.

(2) The flow conditions in the inviscid shock layer have been computed by the formulas of section 4.

(3) For these flow conditions, the mass flow in the viscous layer has been obtained from the calculations of Libby.[4]

6.3 Final Results

The final result of these calculations is illustrated in Figure 9. The calculated radii of the entrained stream tubes have been combined with atmospheric data to yield the number of particles entrained per kilometer along the vehicle track. Also shown is the rate of deposit of NO particles along the track. Note that the air entrainment represents only that which may be associated with the head glow. The further mixing of air and NO which may occur in the downstream 'wake' of the flow is neglected here.

7. CONCLUSIONS

The flow pattern associated with the release of NO from a moving vehicle at high altitudes has been found to be quite complex. The scale of this flow pattern increases with altitude (as the pressure drops) to a diameter of the order of 200 meters, and this is large enough compared with the ambient mean free path so that the equations of continuum flow can be applied.

Although it is very difficult to obtain solutions of the equations of motion for all regions of the flow field, it is possible to obtain good estimates of the mixing between the released NO and the ambient. This mixing takes place in a layer which surrounds the vehicle and lies between two shock waves. One shockwave is in the ambient and corresponds to the usual detached shock ahead of a blunt body in supersonic flow. The other is in the expanding flow of NO from the vehicle and exists to decelerate this flow from a very highly supersonic speed to a subsonic one. At all but the lowest altitudes of interest, the mixing occurs over the entire thickness of this layer between the two shockwaves. Below about 106 km, however, pure air flows along the outer part of the layer and pure NO along the inner part.

The total amount of air swallowed into the mixing pattern at the head of the trail has been calculated as a function of altitude and compared with the rate of release of the NO. It is found that the mixture is initially rich in NO but becomes lean over the second half of the trajectory.

References

1. M. VINOKUR and R. W. SANDERS, Inviscid Hypersonic Flow Around Spheres with Mass Injection, Lockheed Missiles and Space Division Report. LMSD-288209, January 1960.
2. R. J. CRESCI and P. A. LIBBY, The Downstream Influence of Mass Transfer at the Nose of a Slender Cone, Polytechnic Institute of Brooklyn PIBAL Report No. 634, May 1961. Also, of the Aerospace Sciences, July 1962.
3. RESHOTKO, Estimate o Shock Standoff Distance Ahead of a General Stagnation Point, NASN TN D-10[illegible], August 1961.
4. M. C. KAO, A Study of Viscous Hypersonic Flow Near the Stagnation Point of a Sphere, Presented at AIAA Conference on Physics of Entry into Planetary Atmospheres, M. I. T., August 1963. AIAA Preprint 63-437.
5. P. A. LIBBY, The Homogeneous Boundary Layer at an Axisymmetric Stagnation Point with Large Rates of Injection, Polytechnic Institute of Brooklyn PIBAL Report No. 605, August 1960. Also, J. of the Aerospace Sciences, January 1962.

Appendix A

Detailed trajectory information on a particular NO release has been obtained from D. Golomb. Figure A1 shows the variation of vehicle speed and ambient sound speed with altitude.

The rate of release of NO along the flight path may be computed from the tank pressure variation with altitude shown in Figure A2.

For convenience in estimating the rate of the chemical reaction between O and NO, the histories of the pressure and temperature at the vertex of the mixing layer are also shown in Figure A2. At this location both pressure and temperature have their peak values. Average values over the whole mixing layer are of the order of half the peak values.

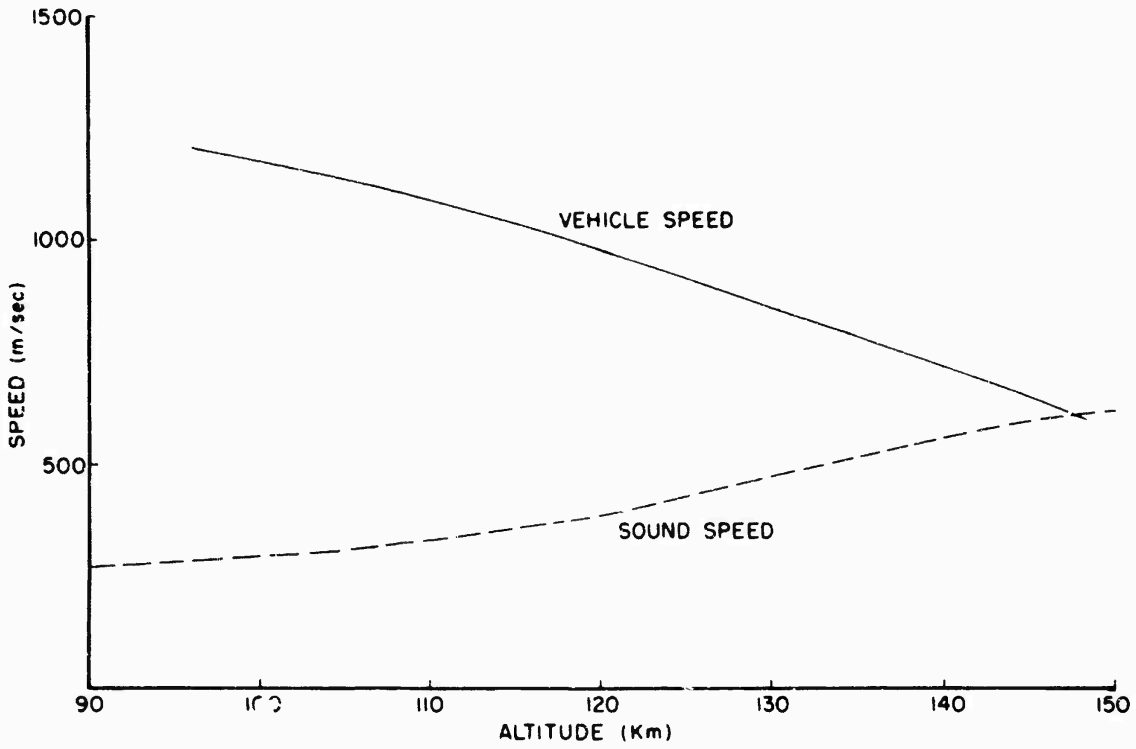

Figure A1. Trajectory Data for the NO Release

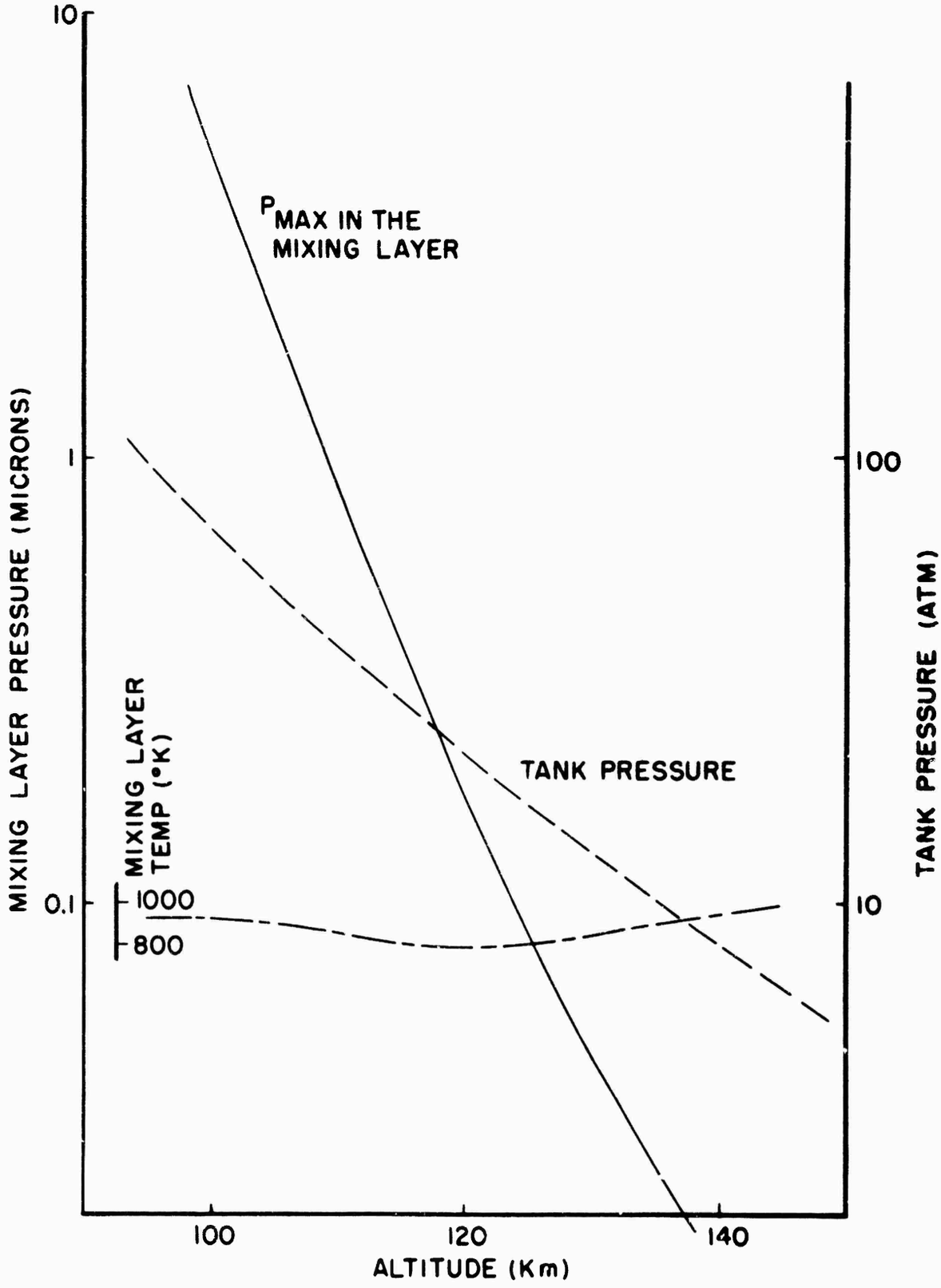

Figure A2. Pressure and Temperature Histories for the NO Release